Springer Proceedings in Physics 221

Olena Fesenko
Leonid Yatsenko *Editors*

Nanocomposites, Nanostructures, and Their Applications

Selected Proceedings of the 6th International Conference Nanotechnology and Nanomaterials (NANO2018), August 27-30, 2018, Kyiv, Ukraine

Springer

Springer Proceedings in Physics

Volume 221

The series Springer Proceedings in Physics, founded in 1984, is devoted to timely reports of state-of-the-art developments in physics and related sciences. Typically based on material presented at conferences, workshops and similar scientific meetings, volumes published in this series will constitute a comprehensive up-to-date source of reference on a field or subfield of relevance in contemporary physics. Proposals must include the following:

- name, place and date of the scientific meeting
- a link to the committees (local organization, international advisors etc.)
- scientific description of the meeting
- list of invited/plenary speakers
- an estimate of the planned proceedings book parameters (number of pages/ articles, requested number of bulk copies, submission deadline).

More information about this series at http://www.springer.com/series/361

Olena Fesenko • Leonid Yatsenko
Editors

Nanocomposites, Nanostructures, and Their Applications

Selected Proceedings of the 6th International Conference Nanotechnology and Nanomaterials (NANO2018), August 27-30, 2018, Kyiv, Ukraine

Springer

Editors
Olena Fesenko
National Academy of Sciences of Ukraine
Institute of Physics
Kyiv, Ukraine

Leonid Yatsenko
National Academy of Sciences of Ukraine
Institute of Physics
Kyiv, Ukraine

ISSN 0930-8989 ISSN 1867-4941 (electronic)
Springer Proceedings in Physics
ISBN 978-3-030-17758-4 ISBN 978-3-030-17759-1 (eBook)
https://doi.org/10.1007/978-3-030-17759-1

Preface

This book highlights the most recent advances in nanoscience from leading researchers in Ukraine, Europe, and beyond. It features contributions from the participants of the sixth International Research and Practice Conference "Nanotechnology and Nanomaterials" (NANO-2018), held in Kyiv, Ukraine, on August 27–30, 2018. This event was organized jointly by the Institute of Physics of the National Academy of Sciences of Ukraine, Taras Shevchenko National University of Kyiv (Ukraine), University of Tartu (Estonia), University of Turin (Italy), and Pierre and Marie Curie University (France). Internationally recognized experts from a wide range of universities and research institutes shared their knowledge and key results in the areas of nanocomposites and nanomaterials, nanostructured surfaces, microscopy of nano-objects, nanooptics and nanophotonics, nanoplasmonics, nanochemistry, nanobiotechnology, and surface-enhanced spectroscopy.

Today, nanotechnology is becoming one of the most actively developing and promising fields of science. Numerous nanotechnology investigations are already producing practical results that can be applied in various areas of human life from science and technology to medicine and pharmacology. The aim of these books is to highlight the latest investigations from different areas of nanoscience and to stimulate new interest in this field. Volume I of this two-volume work covers such important topics as nanostructured interfaces and surfaces, and nanoplasmonics.

This book is divided into two sections: Part I, *Nanocomposites and Nanostructures*, and Part II, *Applications.* Sections covering Nanophotonics and Nanooptics, Nanobiotechnology, and Applications can be found in Volume II: *Nanophotonics, Nanooptics, Nanobiotechnology, and Their Applications*.

The papers published in these five sections fall under the broad categories of nanomaterial preparation and characterization, nanobiotechnology, nanodevices and

quantum structures, and spectroscopy and nanooptics. We hope that both volumes will be equally useful and interesting for young scientists or PhD students and mature scientists alike.

Kyiv, Ukraine — Olena Fesenko
Kyiv, Ukraine — Leonid Yatsenko

Contents

Contributors

A. N. Alekseev Taras Shevchenko National University of Kyiv, Physical Faculty, Kyiv, Ukraine

S. A. Alekseev Taras Shevchenko National University of Kyiv, Physical Faculty, Kyiv, Ukraine

M. A. Alieksandrov Taras Shevchenko National University of Kyiv, Kyiv, Ukraine

M. Androulidaki Institute of Electronic Structure & Laser (IESL) of Foundation for Research & Technology Hellas (FORTH), Heraklion, Greece

A. E. Artyukhov Processes and Equipment of Chemical and Petroleum-Refineries Department, Sumy State University, Sumy, Ukraine

A. Y. Artyukhov Processes and Equipment of Chemical and Petroleum-Refineries Department, Sumy State University, Sumy, Ukraine

N. O. Artyukhova Processes and Equipment of Chemical and Petroleum-Refineries Department, Sumy State University, Sumy, Ukraine

Ihor Astrelin Department of Inorganic Substances Technology, Water Treatment and General Chemical Engineering of National Technical University of Ukraine "Igor Sikorsky Kyiv Polytechnic Institute", Kyiv, Ukraine

T. G. Avramenko Taras Shevchenko National University of Kyiv, Kyiv, Ukraine

I. V. Bacherikova Institute for Sorption and Problems of Endoecology, National Academy of Sciences of Ukraine, Kyiv, Ukraine

Z. Ya. Blikharskyy Institute of Building and Environmental Engineering, Lviv Polytechnic National University, Lviv, Ukraine

Daryn Borgekov Astana branch of the Institute of Nuclear Physics, Nur-Sultan, Kazakhstan

L. N. Gumilyov Eurasian National University, Astana, Kazakhstan

I. V. Brazhnyk Gimasi SA Ukraine R&D Centre, Via Luigi Lavizzari, Mendrisio, Switzerland

L. A. Bulavin Taras Shevchenko National University of Kyiv, Physical Faculty, Kyiv, Ukraine

T. Butyrina Ukrainian State University of Chemical Technology, Dnipro, Ukraine

D. Chalyy Lviv State University of Life Safety, Lviv, Ukraine

Nikolay Chernyak National Science Center "Kharkiv Institute of Physics and Technology", Kharkiv, Ukraine

O. V. Chukova Taras Shevchenko National University of Kyiv, Kyiv, Ukraine

L. Didukh Ternopil Ivan Puluj National Technical University, Ternopil, Ukraine

R. V. Dinzhos Mykolaiv V.O. Sukhomlynskyi National University, Mykolayiv, Ukraine

N. V. Diyuk Taras Shevchenko National University of Kyiv, Kyiv, Ukraine

O. A. Diyuk Institute for Sorption and Problems of Endoecology, National Academy of Sciences of Ukraine, Kyiv, Ukraine

O. P. Dmytrenko Taras Shevchenko National University of Kyiv, Kyiv, Ukraine

Yu. Dovhopyaty Ternopil Ivan Puluj National Technical University, Ternopil, Ukraine

Alina V. Dvornichenko Sumy State University, Sumy, Ukraine

Yurii Fedenko Department of Inorganic Substances Technology, Water Treatment and General Chemical Engineering of National Technical University of Ukraine "Igor Sikorsky Kyiv Polytechnic Institute", Kyiv, Ukraine

O. M. Fesenko Institute of Physics of National Academy Sciences of Ukraine, Kyiv, Ukraine

L. Frolova Ukrainian State University of Chemical Technology, Dnipro, Ukraine

Angelina Gab Institute for Engineering & Technology, University "Ukraine", Kyiv, Ukraine

I. I. Gab Frantsevich Institute for Problems of Materials Science of National Academy Sciences of Ukraine, Kyiv, Ukraine

Zygmunt Gburski Institute of Physics, University of Silesia, Katowice, Poland

Silesian Centre of Education & Interdisciplinary Research, Chorzów, Poland

Oleksandr Goretskiy Institute for Engineering & Technology, University "Ukraine", Kyiv, Ukraine

Krzysztof Górny Institute of Physics, University of Silesia, Katowice, Poland

Silesian Centre of Education & Interdisciplinary Research, Chorzów, Poland

Y. E. Grabovskii Taras Shevchenko National University of Kyiv, Physical Department, Kyiv, Ukraine

I. Hadzaman Drohobych State Pedagogical University, Drohobych, Ukraine

S. Hamamda Laboratory of Thermodynamics and Surface Treatment of Materials, University of Frères Mentouri Constantine 1, Constantine, Algeria

Iuliia Harahuts Faculty of Chemistry, Taras Shevchenko National University of Kyiv, Kyiv, Ukraine

K. I. Hnatiuk Taras Shevchenko National University of Kyiv, Physical Faculty, Kyiv, Ukraine

A. Ingram Opole University of Technology, Opole, Poland

Iryna Ivanenko Department of Inorganic Substances Technology, Water Treatment and General Chemical Engineering of National Technical University of Ukraine "Igor Sikorsky Kyiv Polytechnic Institute", Kyiv, Ukraine

K. O. Ivanenko Taras Shevchenko National University of Kyiv, Kyiv, Ukraine

A. V. Ivaniia Processes and Equipment of Chemical and Petroleum-Refineries Department, Sumy State University, Sumy, Ukraine

Egor Kaniukov Institute of Chemistry of New Materials of the NAS of Belarus, Minsk, Belarus

Ann. V. Karakurkchi National Technical University "Kharkiv Polytechnic Institute", Kharkiv, Ukraine

I. Karbovnyk Ivan Franko National University of Lviv, Lviv, Ukraine

Inesh Kenzhina Astana branch of the Institute of Nuclear Physics, Nur-Sultan, Kazakhstan

L. N. Gumilyov Eurasian National University, Astana, Kazakhstan

Dmitrii O. Kharchenko Institute of Applied Physics, National Academy of Sciences of Ukraine, Sumy, Ukraine

Vasyl O. Kharchenko Institute of Applied Physics, National Academy of Sciences of Ukraine, Sumy, Ukraine

Ye. V. Kharchenko Institute of Building and Environmental Engineering, Lviv Polytechnic National University, Lviv, Ukraine

N. V. Khutoryanskaya Taras Shevchenko National University of Kyiv, Kyiv, Ukraine

H. Klym Lviv Polytechnic National University, Lviv, Ukraine

N. S. Kopachevska Institute for Sorption and Problems of Endoecology, National Academy of Sciences of Ukraine, Kyiv, Ukraine

M. Koptiev Solid State Physics and Optoelectronics Department, Oles Honchar Dnipro National University, Dnipro, Ukraine

A. M. Korol Laboratory on Quantum Theory in Linkoping, ISIR, Linkoping, Sweden

Ilya Korolkov Astana branch of the Institute of Nuclear Physics, Nur-Sultan, Kazakhstan

A. M. Korostil Institute of Magnetism of NAS of Ukraine and MES of Ukraine, Kyiv, Ukraine

Yu Kostiv Lviv Polytechnic National University, Lviv, Ukraine

B. D. Kostyuk Frantsevich Institute for Problems of Materials Science of National Academy Sciences of Ukraine, Kyiv, Ukraine

I. G. Kovzun F.D.Ovcharenko Institute of Biocolloid Chemistry of NAS of Ukraine, Kyiv, Ukraine

Artem Kozlovskiy Astana branch of the Institute of Nuclear Physics, Nur-Sultan, Kazakhstan

L. N. Gumilyov Eurasian National University, Astana, Kazakhstan

O. Kramar Ternopil Ivan Puluj National Technical University, Ternopil, Ukraine

M. M. Krupa Institute of Magnetism of NAS of Ukraine and MES of Ukraine, Kyiv, Ukraine

M. P. Kulish Taras Shevchenko National University of Kyiv, Kyiv, Ukraine

M. M. Kurmach L. V. Pisarzhevskii Institute of Physical Chemistry, National Academy of Sciences of Ukraine, Kyiv, Ukraine

Nataliya Kutsevol Faculty of Chemistry, Taras Shevchenko National University of Kyiv, Kyiv, Ukraine

Maksim Kutuzau Scientific-Practical Materials Research Centre, NAS of Belarus, Minsk, Belarus

V. Kyryliv Karpenko Physico-Mechanical Institute of the NAS of Ukraine, Lviv, Ukraine

Yaroslav Kyryliv Lviv State University of Life Safety, Lviv, Ukraine

O. M. Lavrynenko State Institution “Institute of Environmental Geochemistry of NAS of Ukraine”, Kyiv, Ukraine

I.M. Frantsevych Institute of Material Science Problems of NAS of Ukraine, Kyiv, Ukraine

M. M. Lazarenko Taras Shevchenko National University of Kyiv, Physical Faculty, Kyiv, Ukraine

T. Lebyedyeva V.M. Glushkov Institute of Cybernetics, National Academy of Sciences of Ukraine, Kyiv, Ukraine

V. M. Ledovskykh National Aviation University, Kyiv, Ukraine

Serhii Lesik Department of Inorganic Substances Technology, Water Treatment and General Chemical Engineering of National Technical University of Ukraine "Igor Sikorsky Kyiv Polytechnic Institute", Kyiv, Ukraine

S. V. Levchenko National Aviation University, Kyiv, Ukraine

Oleg V. Lozitsky Department of Physics, Taras Shevchenko National University of Kyiv, Kyiv, Ukraine

Tetiana Lukashenko Institute for Engineering & Technology, University "Ukraine", Kyiv, Ukraine

D. Lukashevych Lviv Polytechnic National University, Lviv, Ukraine

Antonina A. Maizelis National Technical University "Kharkiv Polytechnic Institute", Kharkiv, Ukraine

O. Maksymiv Karpenko Physico-Mechanical Institute of NAS of Ukraine, Lviv, Ukraine

Viktor Malyshev Institute for Engineering & Technology, University "Ukraine", Kyiv, Ukraine

Oleksandr Mats National Science Center "Kharkiv Institute of Physics and Technology", Kharkiv, Ukraine

Luidmila Yu. Matsui Departments of Physics, Taras Shevchenko National University of Kyiv, Kyiv, Ukraine

Maryna V. Mayba National Technical University "Kharkiv Polytechnic Institute", Kharkiv, Ukraine

N. V. Medvid' National University for Food Technologies, Kyiv, Ukraine

Oleksandr Morozov National Science Center "Kharkiv Institute of Physics and Technology", Kharkiv, Ukraine

H. Yu. Mykhailova G. V. Kurdyumov Institute for Metal Physics of the NAS of Ukraine, Kiev, Ukraine

Oksana Nadtoka Faculty of Chemistry, Taras Shevchenko National University of Kyiv, Kyiv, Ukraine

Antonina Naumenko Faculty of Physics, Taras Shevchenko National University of Kyiv, Kyiv, Ukraine

S. M. Naumenko Taras Shevchenko National University of Kyiv, Kyiv, Ukraine

S. Nedilko Physics Faculty, Taras Shevchenko National University of Kyiv, Kyiv, Ukraine

S. G. Nedilko Taras Shevchenko National University of Kyiv, Kyiv, Ukraine

O. Nesterov Solid State Physics and Optoelectronics Department, Oles Honchar Dnipro National University, Dnipro, Ukraine

O. M. Nikipelova SA "Ukrainian Research Institute of Medical Rehabilitation and Balneology, Ministry of Health of Ukraine", Odessa, Ukraine

M. M. Nischenko G. V. Kurdyumov Institute for Metal Physics of the NAS of Ukraine, Kiev, Ukraine

H. Nykyforchyn Karpenko Physico-Mechanical Institute of NAS of Ukraine, Lviv, Ukraine

Yu. Olenych Ivan Franko National University of Lviv, Lviv, Ukraine

V. O. Oliinyk F.D. Ovcharenko Institute of Biocolloid Chemistry of NAS of Ukraine, Kyiv, Ukraine

Viktor V. Oliynyk Department of Radiophysics, Electronics, and Computer Systems, Taras Shevchenko National University of Kyiv, Kyiv, Ukraine

A. I. Olkhovyk Processes and Equipment of Chemical and Petroleum-Refineries Department, Sumy State University, Sumy, Ukraine

Iryna V. Ovsiienko Departments of Physics, Taras Shevchenko National University of Kyiv, Kyiv, Ukraine

Mateusz Pabiszczak Institute of Physics, University of Silesia, Katowice, Poland

Silesian Centre of Education & Interdisciplinary Research, Chorzów, Poland

A. V. Panko F.D. Ovcharenko Institute of Biocolloid Chemistry of NAS of Ukraine, Kyiv, Ukraine

A. Papadopoulos Institute of Electronic Structure & Laser (IESL) of Foundation for Research & Technology Hellas (FORTH), Heraklion, Greece

O. Yu. Pavlenko I.M. Frantsevych Institute of Material Science Problems of NAS of Ukraine, Kyiv, Ukraine

O. Petrov Institute of Solid State Physics, Darmstadt Technical University, Darmstadt, Germany

T. M. Pinchuk-Rugal Taras Shevchenko National University of Kyiv, Kyiv, Ukraine

V. A. Prokopenko F.D. Ovcharenko Institute of Biocolloid Chemistry of NAS of Ukraine, Kyiv, Ukraine

National Technical University of Ukraine “KPI”, Kyiv, Ukraine

Przemysław Raczyński Institute of Physics, University of Silesia, Katowice, Poland

Silesian Centre of Education & Interdisciplinary Research, Chorzów, Poland

S. L. Revo Taras Shevchenko National University of Kyiv, Kyiv, Ukraine

Konstantin Rozhalovets Institute for Engineering & Technology, University “Ukraine”, Kyiv, Ukraine

Ya. Rybak Physics Faculty, Taras Shevchenko National University of Kyiv, Kyiv, Ukraine

O. V. Sachuk Institute for Sorption and Problems of Endoecology, National Academy of Sciences of Ukraine, Kyiv, Ukraine

Galina V. Saenko Departments of Physics, Taras Shevchenko National University of Kyiv, Kyiv, Ukraine

Nikolay D. Sakhnenko National Technical University “Kharkiv Polytechnic Institute”, Kharkiv, Ukraine

Nataliya Sas Stepan Gzhytskyi National University of Veterinary Medicine and Biotechnologies, Lviv, Ukraine

Z. Sawlowicz Institute of Geology, Jagiellonian University, Krakow, Poland

Julius Schuster Faculty of Chemistry, University of Vienna, Vienna, Austria

B. H. Shabalin State Institution “Institute of Environmental Geochemistry of NAS of Ukraine”, Kyiv, Ukraine

D. B. Shakhnin University “Ukraine”, Kyiv, Ukraine

Dmytro Shakhnin Institute for Engineering & Technology, University “Ukraine”, Kyiv, Ukraine

S. M. Shcherbakov M.G. Kholodny Institute of Botany of the National Academy of Science of Ukraine, Kyiv, Ukraine

V. V. Shlapatska L.V. Pisarghevskiy Institute of Physical Chemistry NAS of Ukraine, Kyiv, Ukraine

L. V. Shmeleva Taras Shevchenko National University of Kyiv, Kyiv, Ukraine

P. Shpylovyy V.M. Glushkov Institute of Cybernetics, National Academy of Sciences of Ukraine, Kyiv, Ukraine

Alena Shumskaya Scientific-Practical Materials Research Centre, NAS of Belarus, Minsk, Belarus

Yu. Skorenkyy Ternopil Ivan Puluj National Technical University, Ternopil, Ukraine

M. Skoryk NanoMedTech LLC, Kyiv, Ukraine

A. A. Slepets Taras Shevchenko National University of Kyiv, Kyiv, Ukraine

A. I. Sokolenko National University for Food Technologies, Kyiv, Ukraine

I. V. Sokolenko National University for Food Technologies, Kyiv, Ukraine

V. L. Starchevskyy National University «Lviv Polytechnic», Lviv, Ukraine

A. Stelmashchuk Ivan Franko National University of Lviv, Lviv, Ukraine

Yaroslav B. Stetsiv Ukrainian Academy of Printing, Lviv, Ukraine

Andrew E. Stetsko Ukrainian Academy of Printing, Lviv, Ukraine

Yaryna T. Stetsko Ivan Franko National University of Lviv, Lviv, Ukraine

T. V. Stetsyuk Frantsevich Institute for Problems of Materials Science of National Academy Sciences of Ukraine, Kyiv, Ukraine

E. I. Stratakis Institute of Electronic Structure & Laser (IESL) of Foundation for Research & Technology Hellas (FORTH), Heraklion, Greece

A. D. Suprun Taras Shevchenko National University of Kyiv, Kyiv, Ukraine

R. Szatanik Opole University of Technology, Opole, Poland

V. M. Tkach V. Bakul Institute for Superhard Materials NAS of Ukraine, Kyiv, Ukraine

M. Trubitsyn Solid State Physics and Optoelectronics Department, Oles Honchar Dnipro National University, Dnipro, Ukraine

Tatiana L. Tsaregradskaya Departments of Physics, Taras Shevchenko National University of Kyiv, Kyiv, Ukraine

O. A. Tsyganovich F.D. Ovcharenko Institute of Biocolloid Chemistry of NAS of Ukraine, Kyiv, Ukraine

National technical University of Ukraine “KPI”, Kyiv, Ukraine

B. D. Vasyliv Karpenko Physico-Mechanical Institute of the NAS of Ukraine, Lviv, Ukraine

Maryna V. Ved’ National Technical University “Kharkiv Polytechnic Institute”, Kharkiv, Ukraine

V. V. Vira Institute of Building and Environmental Engineering, Lviv Polytechnic National University, Lviv, Ukraine

M. Vogel Institute of Solid State Physics, Darmstadt Technical University, Darmstadt, Germany

T. A. Voitenko Taras Shevchenko National University of Kyiv, Kyiv, Ukraine

M. Volnianskii Solid State Physics and Optoelectronics Department, Oles Honchar Dnipro National University, Dnipro, Ukraine

Luidmila L. Vovchenko Departments of Physics, Taras Shevchenko National University of Kyiv, Kyiv, Ukraine

Yu. P. Vyshnevska National Technical University of Ukraine "Igor Sikorsky Kyiv Polytechnic Institute", Kyiv, Ukraine

Institute for Renewable Energy NAS of Ukraine, Kyiv, Ukraine

Olena S. Yakovenko Department of Physics, Taras Shevchenko National University of Kyiv, Kyiv, Ukraine

Oleksandr Yasko Institute for Engineering & Technology, University "Ukraine", Kyiv, Ukraine

Iryna Yu. Yermolenko National Technical University "Kharkiv Polytechnic Institute", Kharkiv, Ukraine

Oleg Yeshchenko Faculty of Physics, Taras Shevchenko National University of Kyiv, Kyiv, Ukraine

S. M. Yezhov Taras Shevchenko National University of Kyiv, Kyiv, Ukraine

Y. F. Zabashta Taras Shevchenko National University of Kyiv, Physical Faculty, Kyiv, Ukraine

Volodymyr V. Zagorodnii Department of Radiophysics, Electronics, and Computer Systems, Taras Shevchenko National University of Kyiv, Kyiv, Ukraine

V. A. Zazhigalov Institute for Sorption and Problems of Endoecology, National Academy of Sciences of Ukraine, Kyiv, Ukraine

V. O. Zazhigalov Institute for Sorption and Problems of Endoecology, National Academy of Sciences of Ukraine, Kyiv, Ukraine

Maxim Zdorovets Astana branch of the Institute of Nuclear Physics, Astana, Kazakhstan

L. N. Gumilyov Eurasian National University, Astana, Kazakhstan

Ural Federal University named after the first President of Russia Boris Yeltsin, Ekaterinburg, The Russian Federation

Volodymyr Zhurba National Science Center "Kharkiv Institute of Physics and Technology", Kharkiv, Ukraine

O. Zvirko Karpenko Physico-Mechanical Institute of NAS of Ukraine, Lviv, Ukraine

Part I
Nanocomposites and Nanostructures

Chapter 1
A Microscopic Description of Spin Dynamics in Magnetic Multilayer Nanostructures

A. M. Korostil and M. M. Krupa

1.1 Introduction

Stacks of alternating ferromagnetic and nonmagnetic metal layers exhibit giant magnetoresistance (GMR), because their electrical resistance depends strongly on whether the moments of adjacent magnetic layers are parallel or antiparallel. This effect has allowed the development of new kinds of field-sensing and magnetic memory devices [1]. The cause of the GMR effect is that conduction electrons are scattered more strongly by a magnetic layer when their spins lie antiparallel to the layer's magnetic moment than when their spins are parallel to the moment. Devices with moments in adjacent magnetic layers aligned antiparallel thus have a larger overall resistance than when the moments are aligned parallel, giving rise to GMR. At the same time, there is the converse effect: just as the orientations of magnetic moments can affect the flow of electrons, a polarized electron current scattering from a magnetic layer can have a reciprocal effect on the moment of the layer. As shown in [2, 3], an electric current passing perpendicularly through a magnetic multilayer may exert a torque on the moments of the magnetic layers. This effect which is known as "spin transfer" may, at sufficiently high current densities, alter the magnetization state. It is a separate mechanism from the effects of current-induced magnetic fields. Experimentally, spin-current-induced magnetic excitations such as spin waves [4–9] and stable magnetic reversal [6, 7] have been observed in multilayers, for current densities greater than 10^7 A/cm^2.

The spin-transfer effect offers the promise of new kinds of magnetic devices and serves as a new means to excite and to probe the dynamics of magnetic moments at the nanometer scale. To controllably utilize these effects, however,

A. M. Korostil (✉) · M. M. Krupa
Institute of Magnetism of NAS of Ukraine and MES of Ukraine, Kyiv, Ukraine

O. Fesenko, L. Yatsenko (eds.), *Nanocomposites, Nanostructures, and Their Applications*, Springer Proceedings in Physics 221,
https://doi.org/10.1007/978-3-030-17759-1_1

it is necessary to achieve a better quantitative understanding of current-induced torques. A derivation of spin-transfer torques using a one-dimensional (1D) WKB approximation with spin-dependent potentials presented in [3] only take into account electrons which are either completely transmitted or completely reflected by the magnetic layers. For real materials the degree to which an electron is transmitted through a magnetic/nonmagnetic interface depends sensitively on the matching of the band structures across the interface [10, 11]. It is important to incorporate such band structure information together with the effect of multiple reflections between the ferromagnetic layers, into a more quantitative theory of the torques generated by spin transfer. This could be done using the formalism [12] based on kinetic equations for spin currents. Instead, it can be made by employing a modified Landauer-Büttiker formalism, in which the ferromagnetic layers are modeled as generalized spin-dependent scatterers [13]. In this case, the calculations are carried out for a quasi-one-dimensional geometry, for which formulas for the torque generated on the magnetic layers are derived when a current is applied to the system, for either ballistic or diffusive nonmagnetic layers.

Controlling spin flow in the mentioned magnetic nanostructures at ultrafast time scales using femtosecond laser pulses opens intriguing possibilities for spintronics [14]. These laser-induced perturbations [15, 16] stir up the extreme regime of spin dynamics, which is governed by the highest energy scale associated with magnetic order: the microscopic spin exchange that controls the ordering temperature T_C. In contrast, at microwave frequencies the ferromagnetic dynamics in the bulk are well described by the Landau-Lifshitz-Gilbert (LLG) phenomenology [17], which has been successfully applied to the problem of the ferromagnetic resonance (FMR). At finite temperatures below T_C, the spin Seebeck and Peltier effects [18, 19] describe the coupled spin and heat currents across interfaces in magnetic heterostructures.

Despite their different appearances, the microwave, thermal and ultrafast spin dynamics are all rooted in the exchange interactions between electrons. It is thus natural to try to advance a microscopic describing of the ultrafast dynamics based on the established phenomena at lower energies. Although some attempts have been made [20, 21] to extend the LLG phenomenology to describe ultrafast demagnetization in bulk ferromagnets, no firm connection exists between the ultrafast spin generation at interfaces and the microwave spin-transfer and spin-pumping effects [22] or the thermal spin Seebeck and Peltier effects.

Solving the above-mentioned problem involves unification of the energy regimes of microwave, thermal, and ultrafast spin dynamics in magnetic heterostructures from a common microscopic point of view, so that the parameters that control the high and low energy limits of spin relaxation originate from the same electron-magnon interactions [23]. In addition to the unified framework, these unique contributions are the history-dependent, nonthermalized magnon distribution function and the crucial role of the out-of-equilibrium spin accumulation among itinerant electrons as the bottleneck that limits the dissipation of spin angular momentum from the combined electronic system.

The paper is organized as follows. In Sect. 1.2, the interconnection between the spin current and spin dynamics via the spin-dependent scattering and an accom-

panying spin torque effect in ferromagnetic (F)/normal metal (N)-based magnetic multilayer nanostructure is studied. Section 1.3 is devoted to the description of the impact of electron-magnon spin-flop scattering on out-of-equilibrium spin dynamics in F/N-based magnetic nanostructures.

1.2 Spin-Dependent Interface Scattering-Induced Torques in Magnetic Multilayer Nanostructures

1.2.1 Features of Spin-Features of Spin Transfer Effect

In this section, a simple intuitive picture of the physics behind the spin-transfer effect is considered. The connection between current-induced spin-transfer torques and the spin-dependent scattering that occurs when electrons pass through a magnetic-nonmagnetic interface can be illustrated most simply by considering the case of a spin-polarized current incident perpendicularly on a single thin ferromagnetic layer F, as shown in Fig. 1.1.

The layer lies in the y-z plane, with its magnetic moment uniformly pointed in the z direction, and it is assumed that the current is spin-polarized in the $z-x$ plane at an angle θ to the layer moments. The incoming electrons can therefore be considered as a coherent linear superposition of basis states with spin in the $+z$ direction (amplitude $\cos\theta/2$) and $-z$direction (amplitude $\sin\theta/2$). At first, it is assumed that the layer is a perfect spin filter, so that spins aligned with the layer moments are completely transmitted through the layer, while spins aligned antiparallel to the layer moment are completely reflected. For incident spins polarized at an angle θ, the average outgoing current will have the relative weights $\cos^2\theta/2$ polarized in the $+z$ direction and transmitted to the right and $\sin^2\theta/2$ polarized in the $-z$ direction and reflected to the left. Consequently, both of the outgoing electron spin fluxes (transmitted and reflected) lie along the z axis, while the incoming (incident)

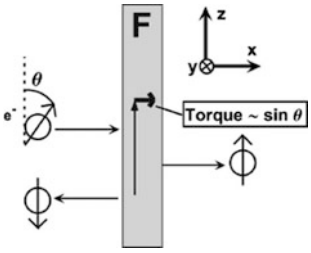

Fig. 1.1 Schematic of exchange torque generated by spin filter. Spin-polarized electrons are incident perpendicularly on a thin ideal ferromagnetic layer. Spin filtering removes the component of spin angular momentum perpendicular to the layer moments from the current; this is absorbed by the moments themselves, generating an effective torque on the layer moments

electron flux has a component perpendicular to the magnetization, along the x axis, with magnitude proportional to $\sin\theta$. This x component of angular momentum must be absorbed by the layer in the process of filtering the spins.

Because the spin-filtering is ultimately governed by the *s-d* exchange interaction between the conduction electrons and the magnetic moments of the layer, the angular momentum is imparted to the layer moments and produces a torque on them. This exchange torque [24], which is proportional to the electron current through the layer and to $\sin\theta$, is in the direction to align the moments with the polarization of the incident spin current. The symmetry of this model precludes any generation of torque from the spin filtering of a current of unpolarized electrons. To generate the effect, then, a second ferromagnetic layer is needed to first spin polarize the current (Fig. 1.1). In that case, spin angular momentum is transferred from one layer to the flowing electrons and then from the electrons to the second layer.

The presence of this second layer has the additional effect of allowing for multiple scattering of the electrons between the two layers, which gives rise to an explicit asymmetry of the torque with respect to current direction. This asymmetry is an important signature which can be used to distinguish spin-transfer-induced torques from the torques produced by current-generated magnetic fields. To see how the asymmetry arises, consider the ferromagnet/normal-metal/ferromagnet (F/N/F) junction shown in Fig. 1.2.

It consists of two ferromagnetic layers F_a and F_b, with moments pointing in directions m_a and m_b, separated by a normal metal spacer N. Normal metal leads on either side of the trilayer inject an initially unpolarized current into the system. When the current enters the sample from the left (Fig. 1.2a), electrons transmitted through F_a will be polarized along m_a. As long as the normal metal spacer is smaller than the spin-diffusion length (100 nm for Cu), this current will remain

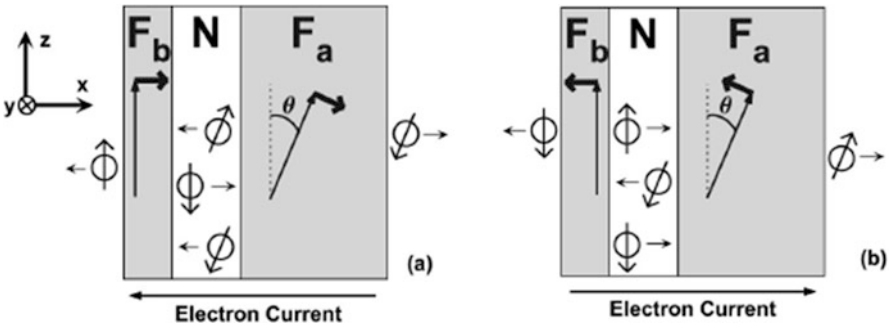

Fig. 1.2 Qualitative picture of asymmetry of spin-transfer torque with respect to current bias in a F/NF junction. For left-going electrons (**a**), initially polarized by a magnetic layer F_a, the moments of layer F_b experience a torque so as to align them with layer F_a. The electron current reflected from layer F_b, in turn, exerts a torque on layer F_a so as to antialign it with the moment of layer F_b. Subsequent reflections between the layers reduce but do not eliminate this torque. If the current is reversed (**b**) the overall sign of the torque is reversed, encouraging the moment of layer F_b to align antiparallel with layer F_a

spin-polarized when it impinges on F_b and will exert a torque on the moment of F_b in a direction so as to align m_b with m_a.

Repeating the argument for F_b, we find that the spin of the electrons reflected from layer F_b is aligned antiparallel to m_b, and, hence in turn, exerts a torque on the moment of F_a trying to align m_a antiparallel with m_b. Subsequent multiple reflections of electrons between F_a and F_b can serve to reduce the magnitudes of the initial torques, but they do not eliminate or reverse them, as the electron flux is reduced upon each reflection. If there were no anisotropy forces in the sample, the net result would be a motion with both moments rotating in the same direction (clockwise in Fig. 1.2a), as described previously in [3]. When the current is injected from the right, the directions of the torques are reversed. The flow of electrons exerts a torque on F_a trying to align its moment parallel with m_b, while it exerts a torque on F_b so as to force the moment in layer F_b antiparallel with m_a.

In [3, 6], the layer F_a was taken to be much thicker than F_b, so that intralayer exchange and anisotropy forces will hold the orientation of m_a fixed. In that case, one is only interested in the torque on F_b, which serves to align m_b either parallel or antiparallel with the fixed moment m_a depending on the current direction. This asymmetric current response has been employed in both a point-contact geometry [7] and in a thin-film pillar geometry [8] to switch the moments in F/N/F trilayers from a parallel to an antiparallel configuration by a current pulse in one direction, and then from antiparallel to parallel by a reversed current. For weakly interacting layers, either orientation can be stable in the absence of an applied current, so that the resistance versus current characteristic is hysteretic, and the devices can function as simple current-controlled memory elements.

Often, the transport properties of magnetic multilayers are described using "two-current" models [8], in which one assumes that the effects of spin-polarized currents can be described completely in terms of incoherent currents of spin-up and spin-down electrons. Normally, only the cases of purely parallel or purely antiparallel magnetic layers are considered, and the spin currents are conserved upon passing through each normal-metal–ferromagnet interface.

In the mentioned case, there can be no current-induced torque on either magnetic layer. It is important to recognize that such two-current models are not appropriate to calculate current-induced torques for the more general case of arbitrary tilt angle between the moments in a magnetic multilayer, as the simple example discussed in this section demonstrates. Tilting of the spin axis is an essential point of the physics [9], and this must be described in terms of a coherent sum of spin-up and spin-down basis states. In the general case, the spin flux is not conserved upon passing through a magnetic layer, so that a torque is applied to each magnetic layer. As it is turned out, this is a simple consequence of different transmission amplitudes for the spin-up and spin-down components of the electron flux.

1.2.2 Passing the Electric Current Through the F/N Contact

Treating the ferromagnetic layers as perfect spin filters provides important qualitative insights into spin transfer, but for a complete qualitative and quantitative picture, a more general approach is required. This can be realized by introduction a scattering matrix description of the F/N/F junction which allows to deal with nonideal (magnetic and nonmagnetic) layers. It is important to relate the torque τ_b exerted on layer F_b by an unpolarized incident electron beam to the scattering properties of the layers. Although restriction by formulas to the F/N/F junction (see Fig. 1.3), the mentioned method is applicable for an arbitrary array of magnetic-nonmagnetic layers.

The spin flux $\boldsymbol{J}$ in the x direction (the direction of current flow) can be written in the form [13]

$$\boldsymbol{J}(x) = \frac{\hbar^2}{2m} \operatorname{Im} \int dydz \left(\phi^{\dagger}(x) \boldsymbol{\sigma} \phi(x) \right), \tag{1.1}$$

where $\phi(x)$ is a spinor wave function and $\boldsymbol{\sigma}$ is the vector of Pauli matrices

$$\phi(x) = \begin{pmatrix} \phi_{\uparrow}(x) \\ \phi_{\downarrow}(x) \end{pmatrix}, \qquad \boldsymbol{\sigma} = \begin{pmatrix} \sigma_x \\ \sigma_y \\ \sigma_z \end{pmatrix}.$$

Note that no local equation of conservation can be written for the spin flux, since in general, the Hamiltonian (of the itinerant electrons) does not conserve spin. Specifically, the magnetic layers can act as sources and sinks of spin flux, so that the spin flux on different sides of a F layer can be different. When the angle θ is 0 or π (typical situation for GMR), the commutativity between the Hamiltonian and the (electron) spins is restored (in the absence of spin-flip scattering). It should be stressed that the Hamiltonian of the full system (electrons plus local moments of the

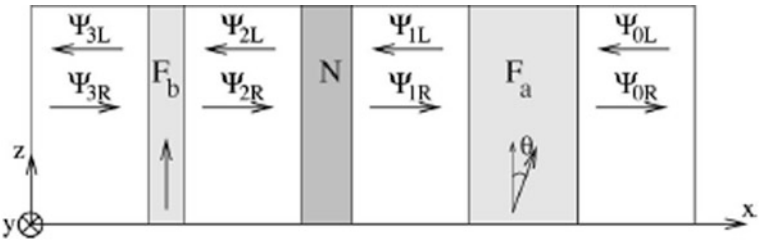

Fig. 1.3 Schematic of the setup used for the definition of the scattering matrices of the F and N layers. The two layers F_b and F_a are ferromagnetic layers whose magnetic moment is oriented as shown in the bottom of the figure. The layer N is a nonmagnetic metal spacer. Amplitude of left and right moving propagating waves are defined in fictitious ideal leads 0, 1, 2, and 3 between the layers and between the layers and the reservoirs

ferromagnets plus the environment) does commute with the total spin. Therefore, the spin lost by the itinerant electrons has to be gained by the other parts of the system.

Figure 1.3 shows the F/N/F junction where (fictitious) perfect leads (labeled 0, 1, 2, and 3) have been added in between the layers F and N and between the F layers and the electron reservoirs on either side of the sample. The introduction of these leads allows for a description of the system using scattering matrices. In the perfect leads, the transverse degree of freedom is quantized, giving N_{ch} propagating modes at the Fermi level, where $N_{\mathrm{ch}} \sim A/\lambda_F^2$, A is the cross section area of the junction and λ_F is the Fermi wave length. Expanding the electronic wave function in these modes, we can describe the system in terms of the projection $\Psi_{i,\mathrm{j}}$ of the wave function onto the left ($j = 1$) or right ($j = 2$) going modes in the region $i = (0, 1, 2, 3)$. The Ψ_{ij} is $2N_{\mathrm{ch}}$-component vector, counting the N_{ch} transverse modes and spin. The amplitudes of the wave function in two neighboring ideal leads are connected through the scattering matrices $S_1 = S_a$, $S_2 = S_N$ and $S_3 = S_b$ that relate amplitudes of outgoing modes and incoming modes at the layer (see [25]) by the relation

$$\begin{pmatrix} \Psi_{i,1} \\ \Psi_{i-1,2} \end{pmatrix} = S_i \begin{pmatrix} \Psi_{i,2} \\ \Psi_{i-1,1} \end{pmatrix}, \quad i = (1, 2, 3) \tag{1.2}$$

The scattering matrix S_i is $4N_{\mathrm{ch}} \times 4N_{\mathrm{ch}}$ unitary matrices. The generalized matrix S_i is decomposed into $2N_{\mathrm{ch}} \times 2N_{\mathrm{ch}}$ reflection and transmission matrices

$$S_i = \begin{pmatrix} r_i & t_i' \\ t_i & r_i' \end{pmatrix}. \tag{1.3}$$

Normalization is done in such a way that each mode carries unit current. Due to the spin degree of freedom, $r_i = \left\| r_{i,\sigma\sigma'} \right\|$ and $\sigma, \sigma' = (\uparrow, \downarrow)$, where the reflection and transmission matrices can be written in terms of four $N_{\mathrm{ch}} \times N_{\mathrm{ch}}$ blocks: where the subscripts $\uparrow$, $\downarrow$ refer to spin up and down in the z-axis basis. The scattering matrix of the magnetic layers depends on the angle θ the moments may make with the z axis. The matrix $S_i(\theta)$ is related to $S_i(0)$ through a rotation in spin space:

$$\begin{aligned} r_i(\theta) &= R_\theta r_i(0) R_{-\theta}, \quad r_i'(\theta) = R_\theta r_i'(0) R_{-\theta}, \\ t_i(\theta) &= R_\theta t_i(0) R_{-\theta}, \quad t_i'(\theta) = R_\theta t_i'(0) R_{-\theta}, \end{aligned} \tag{1.4}$$

where

$$R_\theta = \begin{pmatrix} \cos\frac{\theta}{2} & -\sin\frac{\theta}{2} \\ \sin\frac{\theta}{2} & \cos\frac{\theta}{2} \end{pmatrix} \otimes 1_N. \tag{1.5}$$

The nonmagnetic metallic layer will not affect the spin states, i.e., $r_{N\uparrow\downarrow} = r_{N\downarrow\uparrow} = 0$ and $r_{N\uparrow\uparrow} = r_{N\downarrow\downarrow}$. We need to keep track of the amplitudes

within the system in order to calculate the net spin flux deposited into each magnetic layer. Therefore, we define $2N_{\text{ch}} \times 2N_{\text{ch}}$ matrices Γ_{ij} and Λ_{ij} $(i = (0, 1, 2, 3))$ so that all the $\Psi_{i,\,\text{j}}$ can be expressed as a function of the amplitudes incident from the two electrodes (regions 0 and 3):

$$\begin{pmatrix} \Psi_{i,1} \\ \Psi_{i,2} \end{pmatrix} = \begin{pmatrix} \Gamma_{i1} & \Lambda_{i1} \\ \Gamma_{i2} & \Lambda_{i2} \end{pmatrix} \begin{pmatrix} \Psi_{0,1} \\ \Psi_{3,1} \end{pmatrix} \tag{1.6}$$

with the convention that $\Gamma_{01} = \Lambda_{32} = 1$ and $\Gamma_{32} = \Lambda_{01} = 0$. In order to calculate the torque exercised on layer F_b for a current entering from the left, we need the matrix Γ_{21}, which for simplification is denoted as $\Omega(\Omega = \Gamma_{21})$. The matrix Ω relates the amplitudes Ψ_{21} to the incoming amplitudesΨ_{01}. Putting that $\Psi_{32} = 0$ and using (1.2), the matrix of the Eq. (1.6) can be explicitly expressed via elements of the scattering matrices S_i. Consequently, the following expression can be obtained for the matrix Ω:

$$\Omega = \frac{1}{1 - r_n r_b'} t_n' \frac{1}{1 - r_a t_n r_b' \left(1 - t_n r_b'\right) t_n' - t_a r_n'} t_a', \tag{1.7}$$

which will enter in determination of the torque on the moment of the ferromagnetic layer F_b.

If the system is connected to two unpolarized electron reservoirs on its two sides, then in equilibrium, the modes in the reservoirs are filled up to the Fermi level ε_F. The spin current through the system is generated when the chemical potential in the left (right) reservoir is slightly increased by $\delta\mu_3(\delta\mu_0)$. The spin current J_i in each region $i = 0, 1, 2, 3$ is the difference of the left going and right going contributions. In according to (1.1) and (1.6)

$$\frac{\partial J_i}{\partial \mu_0} = \frac{1}{4\pi} \text{Re}\left[\text{Tr}\sigma\ \Gamma_{iR}\Gamma_{iR}^{\dagger} - \text{Tr}\sigma\ \Gamma_{iR}\Gamma_{iR}^{\dagger}\right], \tag{1.8}$$

$$\frac{\partial J_i}{\partial \mu_3} = \frac{1}{4\pi} \text{Re}\left[\text{Tr}\sigma\ \Lambda_{iL}\Lambda_{iL}^{\dagger} - \text{Tr}\sigma\ \Lambda_{iL}\Lambda_{iL}^{\dagger}\right]. \tag{1.9}$$

Since the spin flux on both sides of F_b is different, angular momentum has been deposited in the F_b. This creates a torque $\tau_b = J_3 - J_2$ on the moment of the ferromagnet. Setting $\delta\mu_0 = eV_0$ gives

$$\frac{\partial r_b}{\partial V_0} = -\frac{e}{4\pi} \text{Re}\,\text{Tr}_{2N_{ch}}\left[\Sigma\ \Omega\ \Omega^{\dagger}\right], \quad \Sigma = \sigma - t''^{\dagger}{}_b \sigma t_b' - r'^{\dagger}{}_b \sigma r_b' \tag{1.10}$$

This equation can be simplified further if the spin-transfer effect is due entirely to spin filtering (as argued in 1.3) as opposed to spin-flip scattering of electrons from the magnetic layers. That is at $\tau_{b\uparrow\downarrow} = \tau_{b\downarrow\uparrow} = \tau_{a\uparrow\downarrow}(\theta = 0) = \tau_{a\downarrow\uparrow}(\theta = 0) = 0$, then

$$\frac{\partial r_b}{\partial V_0} = -\frac{e}{4\pi}\,\mathrm{Re}\,\mathrm{Tr}_{N_{\mathrm{ch}}}\left[\left(\Omega_{\uparrow\uparrow}\Omega^{\dagger}_{\downarrow\uparrow} + \Omega_{\uparrow\downarrow}\Omega^{\dagger}_{\downarrow\downarrow}\right)\ \left(1 - r'_{b\uparrow\uparrow}r'^{\dagger}_{b\downarrow\downarrow} - r'_{b\uparrow\uparrow}r'^{\dagger}_{b\downarrow\downarrow}\right)\right], \tag{1.11}$$

where off-diagonal spin-flip terms are related to spin-flip scattering both in normal and magnetic layers. There is no spin flux conservation in this system, $\partial J_i/\partial\mu_3$ can be different from $\partial J_i/\partial\mu_0$ and, hence, there can be a nonzero spin flux even when the chemical potentials are identical in the two reservoirs.

The existence of a zero-bias spin flux and the resulting torques reflect the well-known itinerant-electron-mediated exchange interaction (also known as the RKKY interaction) between two ferromagnetic films separated by a normal-metal spacer. This interaction can in fact be described within a scattering framework [26–29]. The zero-bias torque has to be added to the finite-bias contribution (given by 1.11). Since the former is typically a factor N_{ch}^{-1} smaller and vanishes upon ensemble averaging [25], the zero-bias contribution to the torque can be neglected. Then the bias-induced torque satisfies the equation $\partial r_b/\partial V_0 = \partial r_b/\partial V_3$.

1.2.3 Averaging Over the Normal Metal Layer

The torque on the moments of the ferromagnetic layers F_a and F_b not only depends on the scattering matrices S_a and S_b of these layers, but also of the scattering matrix S_N of the normal metal layer in between. If the normal layer is disordered, τ_a and τ_b depend on the location of the impurities; if N is ballistic, the torque depends sensitively on the electronic phase shift accumulated in N. In general, sample to sample fluctuations of the torque will be a factor N_{ch}^{-1} smaller than the average [25]. Hence, if N_{ch} is large, the torque is well characterized by its average. After averaging, the zero-bias spin-transfer current, corresponding to the RKKY interaction described above, vanishes, and only the torque caused by the electron current remains. Because all effects of quantum interference in the N layer will disappear in the process of averaging, the derived results are unchanged if the reflection and transmission matrices include processes in which the energy of the electron changes during scattering [30].

1.2.3.1 The Torque for Disordered Normal Metal Layers

The scattering matrix of the normal layer can be written using the standard polar decomposition [25]

$$S_a = \begin{pmatrix} U & 0 \\ 0 & V' \end{pmatrix}\begin{pmatrix} \sqrt{1-T} & i\sqrt{T} \\ i\sqrt{T} & \sqrt{1-T} \end{pmatrix}\begin{pmatrix} U' & 0 \\ 0 & V \end{pmatrix}, \tag{1.12}$$

where U, V, $U^{'}$ and $V^{'}$ are $2N_{\mathrm{ch}} \times 2N_{\mathrm{ch}}$ unitary matrices and T is a diagonal matrix containing the eigenvalues of $t_n t_n^{\dagger}$. Since S_n is diagonal in spin space, matrices U, $U^{'}$, V and $V^{'}$ are block diagonal: $U(U^{'}) = \begin{pmatrix} u\,(u') & 0 \\ 0 & u\,(u') \end{pmatrix}$ and similar definitions for v and $v^{'}$. The outer matrices in (1.12) thus mix the modes in an ergodic way while the central matrix contains the transmission properties of the layer, which determine the average conductance of N.

It is necessary to average (1.11) over both the unitary matrices and T. A diagrammatic technique for such averages has already been developed in [31] and can be used to calculate $\partial \rho_b / \partial V_0$ in leading order in $1/N_{\mathrm{ch}}$. It is a general property of such averages that the fluctuations are a factor of order N_{ch} smaller than the average. This justifies the statement above, that the ensemble-averaged torque is sufficient to characterize the torque exerted on a single sample.

The resulting expression for $\partial \rho_b / \partial V_0$ can be written in a form very similar to the one for (1.11) if one uses a notation that involves 4×4 matrices. Then, the average over the transmission eigenvalues T can be obtained taking into account that the average of a function is the function of the average, to leading order in $1/N_{\mathrm{ch}}$. Thus the average over T amounts to the replacement

$$\hat{t}_n = \frac{g_N}{N_{\mathrm{ch}}} \mathrm{l}_4, \quad \hat{r}_n = \left(1 - \frac{g_N}{N_{\mathrm{ch}}}\right) \mathrm{l}_4 \tag{1.13}$$

where g_N is the conductance of the normal layer and l_4 is the 4×4 unit matrix. Entering the 4×4 block matrix $\hat{\Sigma}$ with the first and fourth rows equal to $(\Sigma_{\uparrow\uparrow}\ \Sigma_{\uparrow\downarrow}\ \Sigma_{\downarrow\uparrow}\ \Sigma_{\downarrow\downarrow})$ and the zero second and third rows, it can be obtained that

$$\left\langle \frac{\partial r_b}{\partial V_0} \right\rangle = -\frac{e}{4\pi} \mathrm{Re}\, \mathrm{Tr}_4 \left[\hat{\Sigma}\ \Omega^{\dagger} \right] \tag{1.14}$$

where $\hat{\Sigma}$ coincide with Ω after the formal replacements $r_n \to \hat{r}_{nn}$ and $t_n \to \hat{t}_n$. In the absence of spin-flip scattering (1.14) reduces to

$$\left\langle \frac{\partial r_b}{\partial V_0} \right\rangle = -\frac{e}{2\pi} \mathrm{Re} \left[\left(\hat{\Omega}_{3,1} + \hat{\Omega}_{3,4} \right) \times \mathrm{Tr}_{N_{\mathrm{ch}}} \left(1 - r'_{b\uparrow\uparrow} r'^{\dagger}_{b\downarrow\downarrow} - t'_{b\uparrow\uparrow} t'^{\dagger}_{b\downarrow\downarrow} \right) \right]. \tag{1.15}$$

The same formalism can be used to calculate the conductance g of the system using the Landauer formula. One gets $\langle g \rangle = (N_{\mathrm{ch}}/h) \left[\hat{t}'_{1,1} + \hat{t}'_{1,4} + \hat{t}'_{4,1} + \hat{t}'_{4,4} \right]$, where $t^{'}$ being the total matrix$t' = t'_b \Omega$.

Note that, while our theory started from a full phase coherent description of the F/N/F trilayer, including the full $4N_{\mathrm{ch}} \times 4N_{\mathrm{ch}}$ scattering matrices of the F/N interfaces, the final result can be formulated in terms of 2×4 parameters, represented by the matrices $\hat{r}_a$ and $\hat{r}'_b$(2×16 parameters in the case of spin-flip

scattering). This confirms the statement that for a diffusive normal-metal spacer all effects of quantum interferences are absent [25].

The torque is characterized by symmetry properties. Due to the conservation of current, the total torque deposited on the full system is antisymmetric with respect to current direction and the equation

$$\partial\tau_b/\partial V_0 + \partial\tau_a/\partial V_0 = -\left[\partial\tau_b/\partial V_3 + +\partial\tau_a/\partial V_3\right]$$

must be held before averaging. The averaging results in $\langle\partial\tau_b/\partial V_0\rangle = \langle\partial\tau_b/\partial V_3\rangle$. Thus, for $N_{\mathrm{ch}} \gg 1$, the linear response of the torque to a small bias voltage is described by the expression

$$\tau_\beta = \left\langle \frac{\partial\tau_b}{\partial V_0} \right\rangle (V_0 - V_3) \tag{1.16}$$

In the given geometry, where F_a and F_b are in the x-z plane, the only nonzero component of the torque is τ_b^x. The torque vanishes when the moments are completely aligned or antialigned (all the matrices are diagonal in spin space and therefore no x component of the spin can be found). Around these two limits, the torque is symmetric in respect to the angle $\theta \rightarrow -\theta$ and $\pi - \theta \rightarrow \pi + \theta$. There is no symmetry between θ and $\pi - \theta$. In addition, the two layers are not equivalent, and exchanging the scattering matrices of F_a and F_b also changes the torque.

The Eq. (1.14) can be simplified in some particular cases. In the case of ideal spin filter, so that majority (minority) spins are totally transmitted (reflected) by either layer, it reduces to

$$\left\langle \frac{\partial r_b^x}{\partial V_0} \right\rangle = -\frac{e}{2\pi}\frac{g_N \sin\theta}{3+\cos\theta} = -\frac{h}{4\pi e}\langle g\rangle \frac{\tan\theta/2}{2}, \tag{1.17}$$

where $\langle g\rangle = 4(e^2/h)g_N\cos^2\theta/(3 + \cos\theta)$ is the average magnetoconductance. As expected, for left-going electrons ($V_0 < 0$) the torque is positive, so it acts to align the moment of the magnetic layer F_b toward the one of F_a.

In the considered case of weak *s-d* exchange coupling, i.e., when the scattering coefficients depend only weakly on spin, with no spin-flip scattering in the ferromagnetic layers, g_a and g_b can be defined as the average conductance per spin of the two layers (in unit of e^2/h). Then, the conductance of F_a alone is $g_a + \delta g_a$ and $g_a - \delta g_a$ for, respectively, the majority and minority spins, which defines the spin scattering asymmetryδg_a. In that case, in lowest nontrivial order in δg_a and δg_b

$$\left\langle \frac{\partial\tau_b^x}{\partial V_0} \right\rangle = \frac{e}{2\pi}\frac{\sin\theta}{2\,(1-g_b/N_{\mathrm{ch}})}\frac{g_N^2\delta g_a\delta g_b^2}{\left(g_a g_b + g_N\left(g_a+g_b-2g_a g_b/N_{\mathrm{ch}}\right)\right)^2}, \tag{1.18}$$

This formula shows that the torque is always nonzero for arbitrary small spin scattering asymmetry. This proves the statement that multiple reflections between the F layers, fully taken into account here, cannot completely eliminate the torque. The torque is not symmetric with respect to interchanging the layer F_a andF_b, in contrast to the conductance. If one changes δg_a to $-\delta g_a$, the sign of the torque is reversed. However, $\partial \tau_b^x / \partial V_0 \propto \delta g_b^2$, so if one changes δg_b to $-\delta g_b$, the sign of the torque is unchanged. The sign of the torque on a ferromagnetic layer therefore depends on whether the other layer is a positive or negative polarizer, but not on the sign of filtering for the layer experiencing the torque.

This is true also in the general case. The quantity g_N^2 appears through its square. Indeed, in order for some spin to be deposited in the layer F_b, some left going electrons have to be reflected by F_b and exit the system from the right-hand side. Therefore, these electrons cross the normal layer at least twice and this leads to the factorg_N^2. On the other hand, the conductance is linear in g_N. Therefore, in order to maximize the torque deposited per current, one has to use the cleanest possible normal metal spacer. This statement is true in this limit of weak filtering, but not in general. Note that in the previous case (perfect spin filtering) the torque is proportional to g_N instead of the expected g_N^2. Indeed, in that case, once the electron has been reflected by the layer F_b, it cannot go through F_a which works as a perfect wall for it. Therefore, current conservation implies that it goes out of the system through the right. For $g_N \ll N_{\mathrm{ch}}$, the torque is actually proportional to g_N^2 for arbitrary spin asymmetry (except perfect filtering), and one gets

$$\left\langle \frac{\partial \tau_b^x}{\partial V_0} \right\rangle \propto g_N^2 \sin\theta, \quad g_N \ll N_{\mathrm{ch}}, \tag{1.19}$$

where the factor of proportionality being a complicated function of the transmission robabilities of the layers.

1.2.3.2 The Torque for Ballistic Normal Metal Layers

If the normal metal layers N is very clean, and the interfaces are very flat, it is reasonable to assume that the electrons propagate ballistically inside the normal layer. The different modes will not be mixed in that case, and the electron wave function only picks up a phase factor $\exp(ik_iL)$ where L is the width of N and k_i is the momentum of channel i. For a sufficiently thick normal layer (i.e., $L \gg \lambda_F$), small fluctuations of k_i lead to an arbitrary change in the phase factor, and it is justified to consider $\exp(ik_iL)$ as a random phase and to average over it. This is different from the case of a disordered metal spacer, where the average involves unitary matrices$u$, u', ... that mix the channels (see 1.25). In the case where $r_{a\downarrow}$, $r_{a\uparrow}$, ... are proportional to the identity matrix (i.e., the reflection amplitudes do not depend on the channel), the ballistic model reduces to the disordered model of (1.32) for $g_N = N_{\mathrm{ch}}$.

The reflection matrices of N being zero, the matrix Ω reads

$$\Omega = \exp\ (ik_i L)\ \frac{1}{1 - \exp\,(2ik_i L)\, r_a r'_b} \tag{1.20}$$

Neglecting spin-flip scattering, denoting $z = \exp\ (2ik_i L)$, and choosing $r_{a11} = r_{a\uparrow}$,$r_{a22} = r_{a\downarrow}$, ... where $r_{a\uparrow}$, $r_{a\downarrow}$, ... are diagonal matrices, one gets after some algebra

$$\frac{\partial r_b^x}{\partial V_0}(z) = -\frac{ev}{4\pi}\mathrm{Tr}\,\mathrm{Re}\,\frac{A(z)}{z|D(z)|^2}\sin\theta, \tag{1.21}$$

where $A(z)$ and $D(z)$ stand for

$$A(z) = \left(1 - t'_{b1}t'^*_{b2} - r'_{b1}r'^*_{b2}\right)\sum_{i=1,2}\left|t'_{ai}\right|^2\left(1 - zr_{ai'}r'_{bi'}\right)\left(z - r^*_{ai'}r'^*_{bi}\right), \tag{1.22}$$

where $i = (1,2) = (\uparrow,\downarrow)$, $i' = 1$ at $i = 2$ and $i' = 2$ at $i = 1$,

$$D(z) = 1 - z\left[\cos^2\tfrac{\theta}{2}\left(r_{a\uparrow}r'_{b\uparrow} + r_{a\downarrow}r'_{b\downarrow}\right) + \sin^2\tfrac{\theta}{2}\left(r_{a\downarrow}r'_{b\uparrow} + r_{a\uparrow}r'_{b\downarrow}\right)\right] + z^2 r_{a\downarrow}r_{a\uparrow}r'_{b\downarrow}r'_{b\uparrow}. \tag{1.23}$$

A similar formula can be written for the conductance $g(z)$:

$$g(z) = \frac{e^2}{h}\mathrm{Tr}\frac{B(z)}{z|D\,(z)|^2}, \tag{1.24}$$

$$B(z) = \sum_{i,j=(1,2)}\left|t'_{ai}\right|^2\left|t'_{aj}\right|^2 R_{ij}\,(\theta)\left(1 - zr_{ai'}r'_{bj'}\right)\left(z - r^*_{ai'}r'^*_{bj'}\right) \tag{1.25}$$

where $i', j' = (1,2)(1 = \uparrow, 2 = \downarrow)$ are determined by the relations $i' \neq i$, $j' \neq j$, $R_{ij}(z) = (\delta_{i,\,\mathrm{j}}\cos^2\theta/2 + (1 - \delta_{i,\,\mathrm{j}})\sin^2\theta/2)$. Taking the average over the phases now amounts to contour integration for $z{:}\langle f\rangle = (1/2\pi)\oint dzf(z)/z$, where the integration is done along the unit circle. The result is then given by the sum of the poles that are inside the unit circle. The two poles of $D(z)$ are outside the unit circle, while the two poles z_1 and z_2 of $z^2D(1/z)$ are inside the circle. They have the form

$$\begin{aligned} z_i = {} & \tfrac{1}{2}\Delta^+_{11,22}\cos^2\tfrac{\theta}{2} + \Delta^+_{21,12}\sin^2\tfrac{\theta}{2} \\ & + \tfrac{1}{2}(-1)^i\left[\left(\Delta^-_{11,22}\right)^2\cos^4\tfrac{\theta}{2} + 2\Xi\cos^2\tfrac{\theta}{2}\sin^2\tfrac{\theta}{2} + \left(\Delta^-_{11,22}\right)^2\sin^4\tfrac{\theta}{2}\right]^{1/2}, \end{aligned} \tag{1.26}$$

where

$$\Delta^{+(-)}_{ii',jj'} = \left(r_{ai}r'_{bi'} \pm r_{aj}r'_{bj'}\right), \quad \Sigma = r'_{b\downarrow}r'_{b\uparrow}\left(r_{a\uparrow} - r_{a\downarrow}\right)^2 + r_{a\downarrow}r_{a\uparrow}\left(r'^2_{b\uparrow} + r'^2_{b\downarrow}\right).$$

The averaged torque and conductance are then simply given by

$$\left\langle \frac{\partial \tau_b^x}{\partial V_0} \right\rangle = \frac{ev}{4\pi} \frac{\sin\theta}{z_1 - z_2} \mathrm{Tr}\left(\frac{A(z_1)}{D(z_1)} - \frac{A(z_2)}{D(z_2)}\right) \tag{1.27}$$

and

$$g = \frac{e^2}{h} \frac{1}{z_1 - z_2} \mathrm{Tr}\left(\frac{B(z_1)}{D(z_1)} - \frac{B(z_2)}{D(z_2)}\right) \tag{1.28}$$

In the case where all the channels are not identical, these results can be generalized by introducing a k dependence of the different transmission-reflection amplitudes.

1.2.4 Current-Driven Magnetic Switching

Application to current-driven magnetic switching involves calculation of torques for scattering parameters which are more appropriate for the transition metal trilayers. In this case, the torque per unit current I, $\tau_b^x/I = \langle (1/g) \times \partial\tau_b^x/\partial V \rangle$. The main features of the mentioned system are that the θ dependence of the torque is not of a simple $\sin\theta$ form, and that the torque per unit current diverges at $\theta = 0$.

The main feature of this system is that the θ dependence of the torque is not of a simple $\sin\theta$ form, and that the torque per unit current diverges at $\theta = 0$. In the imperfect case, when one of the layer (F_b) is a nearly perfect polarizer while the other one is not, the character behavior of the torque is represented in Fig. 1.4.

As can be seen in Fig. 1.4 on the left, although the divergence at $\theta = \pi$ is regularized, τ_b^x/I remains sharply peaked near $\theta = \pi$. This is relevant for the critical current needed to switch the magnetization of F_b from $\theta = \pi$ to $\theta = 0$. The switching of the domains follows from a competition between the spin-transfer torques on the one hand and restoring forces from local fields, anisotropy, exchange coupling, etc. The competition between these forces has been considered phenomenologically [7, 32] using a Landau-Lifschitz-Gilbert equation. The torques for θ close to 0 and π determine the critical currents to overturn a metastable parallel (antiparallel) alignment of the moment in F_a and F_b. Hence the critical current should be different at $\theta = 0$ and $\theta = \pi$. Features of the dependence of the derivative of the torque (with respect to θ closely to 0) on the conductance of the normal layer g_N in the same system with one perfectly polarizing F layer and one partially polarizing layer are represented in Fig. 1.4 on the right.

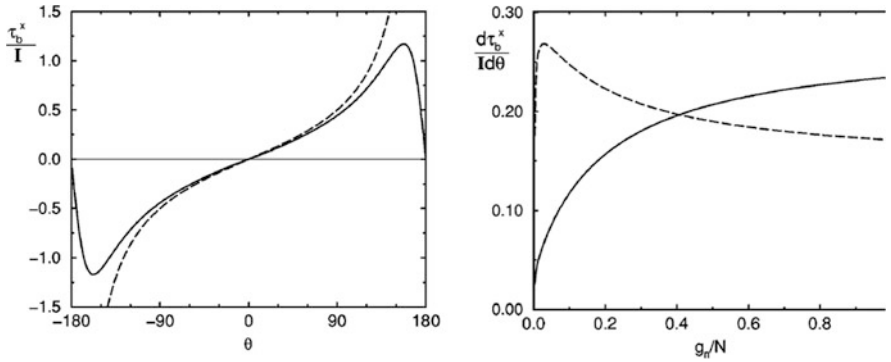

Fig. 1.4 The normalized torque as a function of θ (on the left) and its derivative as a function of the normalized conductance g_N at $\theta = 0$ (on the right) per unit current for the case, where F_b is a nearly perfect polarizer ($|t_{b\uparrow}|^2 = 0.999$, $|t_{b\downarrow}|^2 = 0.001$ and F_a is not ($|t_{a\uparrow}|^2 = 0.3$, $|t_{a\uparrow}|^2 = 0.01$) (solid line). On the left, the case of perfect polarizers is described by the Eq. (1.17) (dashed line). On the right, the dashed line corresponds to the case, when F_a is a nearly perfect polarizer and F_b is not

Switching the two layers has a drastic effect on the torque, even at a qualitative level. In the case where F_a is the nearly perfect layer (dashed line), a maximum of the torque is found for$g_N/N_{\text{ch}} \ll 1$, i.e., in that case, a dirty metal spacer would give a higher torque (per unit of current) than a clean one.

In the abovementioned description, the scattering matrices of the ferromagnetic layers appear as free input parameters. However, it can be calculated from first principle calculations for specific materials. Such an approach has been taken in [10, 11] and the results can be used to give some estimates of torques that can be expected in realistic systems.

1.3 Out-of-Equilibrium Spin Dynamics in *F/N*-Based Structures

1.3.1 Features of Spin Dynamics

The first reports on ultrafast demagnetization in Ni [33] challenged the conventional view of low-frequency magnetization dynamics at temperatures well below T_C. A multitude of mechanisms and scenarios have been suggested to explain the observed quenching of the magnetic moment. Some advocate direct coherent spin transfer induced by the irradiating laser light as the source of demagnetization [34]. Alternative theories argue that ultrafast spin dynamics arise indirectly through incoherent heat transfer to the electron system [35]. Recent experiments have demonstrated that nonlocal laser irradiation also induces ultrafast demagnetization,

and atomistic modeling supports the view that heating of magnetic materials is sufficient to induce ultrafast spin dynamics [16, 36].

Terahertz (THz) magnon excitations in metallic ferromagnets have recently been proposed as an important element of ultrafast demagnetization [37, 38]. The elementary interaction that describes these excitations is the electron-magnon scattering. The proposed approach is based on kinetic equations, which were used for the low-frequency spin and charge transport associated with the microwave magnetization dynamics in heterostructures [39] and with the linear spin-caloritronic response [19, 40]. One treats far-from-equilibrium spin dynamics, in which transport is dominated by magnons and hot electrons. Electron-magnon scattering plays a critical role in this regime. Description of this interaction is related to the transverse spin diffusion in the bulk and the spin-mixing physics, e.g., spin transfer and spin pumping [40], at the interfaces.

1.3.2 The Model of the Out-of-Equilibrium Spin Dynamics

Characteristic properties of the out-of-equilibrium ultra-fast spin dynamics are described by the quantum-mechanical model bilayer system comprising ferromagnetic (F) and normal metal layers, in which the localized spins are distinct from the itinerant electrons at the energy scales of interest. According to the accepted description of relaxation in ferromagnetic metals, the loss of energy and angular momentum from localized d electrons is mediated by the exchange interaction to the itinerant s electrons. The spin transfer from d to s states is accompanied by the relaxation of the s electron spins to the lattice through an incoherent spin-flip process caused by the spin-orbit coupling.

Ultra-fast spin dynamics in bulk ferromagnetic metal is described by the quantum kinetic equations. The F/N interfacial spin transport due to electron-magnon interactions follows a similar essential structure, unifying the bulk and interfacial spin dynamics in magnetic heterostructures. The Hamiltonian that describes F is $H = H_0 + H_{sd}$, where H_0 consists of decoupled s- and d- electron energies, including the kinetic energy of the itinerant electron bath, the d-d exchange energy, dipolar interactions, and the crystalline and Zeeman fields. The s-d interaction is

$$H_{sd} = J_{sd} \sum_j \boldsymbol{S}_j^d \boldsymbol{s}\left(\boldsymbol{r}_j\right), \tag{1.29}$$

where J_{sd} is the exchange energy and $\boldsymbol{S}_j^d$ $\left(\boldsymbol{s}\left(\boldsymbol{r}_j\right)\right)$ is the d-electron (s-electron) spin vector (spin density) at lattice point j. The s-d interaction can be expressed in terms of bosonic and fermionic creation and annihilation operators:

$$H_{sd} = \sum_{qkk'} V_{qkk'} a_q c^{\dagger}_{k\uparrow} c_{k'\downarrow} + \text{H.c.} \tag{1.30}$$

where $a_q^{\dagger}$ $\left(a_q\right)$ is the Holstein-Primakoff creation (annihilation) operator for magnons with wave number q and $c^{\dagger}_{k\sigma}$ $(c_{k\sigma})$ is the creation (annihilation) operator for s electrons with momentum k and spin σ. H_{sd} describes how an electron flips its spin while creating or annihilating a magnon with momentum q and spin σ. The scattering strength is determined by the matrix element $V_{qkk'}$.

In (1.30), terms of the form$a^{\dagger}_q a_{q'} c^{\dagger}_{k\sigma} c_{k'\sigma}$, which describe multiple-magnon scattering and do not contribute to a net change in magnetization along the spin-quantization axis, have been disregarded. Higher-order terms associated with the Holstein-Primakoff expansion are also disregarded. Fully addressing magnonic correlation effects in the ultrafast regime would require a rigorous approach, e.g., using nonequilibrium Keldysh formalism [41]. However, when the s-d coupling (1.29) is not the dominant contribution to H, a mean-field approach and Fermi's golden rule were used to compute the spin transfer between the s and d subsystems. Additionally, it is assumed that all relevant energy scales are much smaller than the Fermi energy $\varepsilon = k_B T_F$ of the itinerant s electrons. In this limit, the electronic continuum remains largely degenerate, with electron-hole pairs present predominantly in the vicinity of the Fermi level.

In the given bilayer system, localized spin density points in the negative z direction at equilibrium, with saturation value S (in units of $\hbar$). In the presence of a magnon density n_d, the longitudinal spin density becomes $S_z = n_d - S$. The magnons are assumed to follow a quadratic dispersion relation $\varepsilon_q = \hbar\omega = \varepsilon_0 + Aq^2$, where ε_0 is the magnon gap and A parameterizes the stiffness of the ferromagnet. $\left\langle a^{\dagger}_q a_{q'} \right\rangle = n\left(\varepsilon_q\right)\delta_{qq'}$defines the magnon distribution function $n(\varepsilon_q)$, which is related to the total magnon density through $n_d = \int_{\varepsilon_0}^{\varepsilon_b} d\varepsilon_q D\left(\varepsilon_q\right) n\left(\varepsilon_q\right)$, where $D(\varepsilon_q) = (\varepsilon_q - \varepsilon_0)^{1/2}/(4\pi^2 A^{3/2})$ is the magnon density of states. The integral over $D(\varepsilon_q)$ is cut off at an energy corresponding to the bandwidth, $\varepsilon_b = k_B T_C$.

Because of the s-d interaction (1.29), the itinerant s electrons have a finite spin density at equilibrium, as it is represented in Fig. 1.5.

One of the key driving forces of the out-of-equilibrium spin dynamics is the spin accumulation $\mu_s = \delta\mu_{\uparrow} - \delta\mu_{\downarrow}$. The bands for spin-up and spin-down electrons are split by$\Delta_{xc} \sim J_{sd} S a^3$, where a is the lattice constant of F. By introducing a dynamic exchange splitting, we can write $\mu_s = \delta n_s/D - \Delta_{xc}$ [42], where δn_s is the out-of-equilibrium spin density of the s electrons, $D = 2D_{\uparrow}D_{\downarrow}/(D_{\uparrow} + D_{\downarrow})$, and $D_{\uparrow(\downarrow)}$ is the density of states for spin-up (spin-down) electrons at the Fermi level. Because the mean-field band splitting due to the s-d exchange vanishes when the d orbitals are fully depolarized, $\delta\Delta_{xc}/\Delta_{xc} = \pm\, n_d/S$, where the sign determines whether the s and d orbitals couple ferromagnetically $(-)$ or antiferromagnetically $(+)$.

The rate of spin transfer (per unit volume) between the s and d subsystems due to electron-magnon spin-flop processes is determined from (1.30) by Fermi's golden rule [40]:

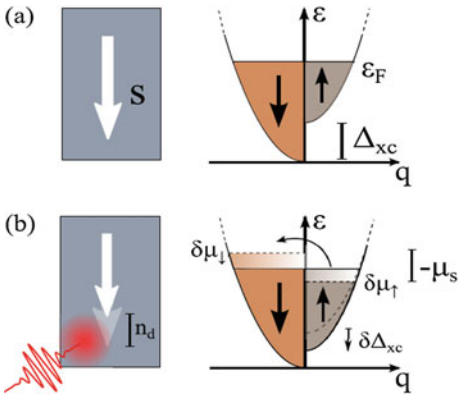

Fig. 1.5 (**a**) Sketch of the density of s electron states in a ferromagnetic metal with saturation spin density S. At equilibrium, the exchange splitting Δ_{xc} shifts the bands for spin-up and spin-down electrons. (**b**) A laser pulse heats the s electron bath. The out-of-equilibrium spin accumulation $\mu_s = \delta\mu_\uparrow - \delta\mu_\downarrow$ results from two different mechanisms: electron-magnon scattering induces a spin density among the s electrons, and the meanfield exchange splitting is shifted by $\delta\Delta_{xc}$ by the induced magnon density n_d

$$I_{sd} = \int_{\varepsilon_a}^{\varepsilon_b} d\varepsilon_q \Gamma\left(\varepsilon_q\right)\left(\varepsilon_q - \mu_s\right) D\left(\varepsilon_q\right)\left[n_{BE}\left(\varepsilon_q - \mu_s\right) - n\left(\varepsilon_q\right)\right], \tag{1.31}$$

where $\Gamma(\varepsilon_q)$ parameterizes the scattering rate at energy ε_q. In the derivation of (1.31), it has been assumed that the kinetic energy of the itinerant electrons and the empty states (holes) thermalize rapidly due to Coulombic scattering and that they are distributed according to Fermi-Dirac statistics. Correspondingly, it can be shown that the electron-hole pairs follow the Bose-Einstein (BE) distribution function, $n_{BE}(\varepsilon_q - \mu_s) = \{\exp[\beta_s(\varepsilon_q - \mu_s)] - 1\}^{-1}$at the electron temperature $T_s = 1/(k_B\beta_s)$. The number of available scattering states is influenced by the spin accumulation μ_s.

In contrast to the low-energy treatment in [40], the derivation of (1.31) does not constrict the form of the magnonic distribution $n(\varepsilon_q)$ to the thermalized BE distribution function. When the time scale of the *s-d* scattering is faster than the typical rates associated with magnon-magnon interactions, magnons are not internally equilibrated shortly after rapid heating of the electron bath, as also predicted by atomistic modeling [43]. Consequently, the occupation of the magnon states can deviate significantly from the BE distribution on the time scale of the demagnetization process. Such treatment differs from that, in which the excited magnons are assumed to be instantly thermalized with an effective spin temperature and zero chemical potential and the thermally activated electron bath is assumed to be unpolarized.

1.3.3 Heat Pulse-Induced Spin Dynamics

The *s-d* scattering rate can be phenomenologically expanded as $\Gamma(\varepsilon_q) = \Gamma_0 + \chi(\varepsilon_q - \varepsilon_0)$, where Γ_0 (which vanishes in the simplest Stoner limit) parameterizes the scattering rate of the long-wavelength magnons and $\chi(\varepsilon_q - \varepsilon_0) \propto q^2$ describes the enhanced scattering of higher-energy magnons due to transverse spin diffusion [44]. In general, one might expect other terms of higher order in q to be present in this expansion as well. The quantity $\Gamma(\varepsilon_q)$is extrapolated up to the bandwidth ε_b that should be sufficient for qualitative purposes. Neglecting any direct relaxation of magnons to the static lattice or its vibrations (i.e., phonons), $\partial_t n_d = I_{sd}/\hbar$. The equations of motion for the *s*-electron spin accumulation and the *d*-electron magnon distribution function are

$$\partial_t \mu_s = -\frac{\mu_s}{\tau_s} + \frac{\rho}{\hbar} I_{sd}, \tag{1.32}$$

$$\partial_t n\left(\varepsilon_q\right) = \frac{\Gamma\left(\varepsilon_q\right)}{\hbar}\left(\varepsilon_q - \mu_s\right)\left[n_{BE}\left(\varepsilon_q - \mu_s\right) - n\left(\varepsilon_q\right)\right], \tag{1.33}$$

where ρ determines the feedback of the demagnetization on μ_s and τ_s is the spin-orbit relaxation time for the *s* electron spin density relaxing to the lattice. Here, τ_s is typically on the order of picoseconds [45] and represents the main channel for the dissipation of angular momentum out of the combined electronic system. In general, τ_s also depends on the kinetic energy of the hot electrons after laser-pulse excitation. However, it is assumed that τ_s is independent of energy. $\rho = \rho_D + \rho_\Delta = -1/D + \Delta_{xc}/S$ includes effects arising from both the out-of-equilibrium spin density and the dynamic exchange splitting. For ferromagnetic (−) *s-d* coupling, these effects add up, whereas for antiferromagnetic (+) coupling, they compete.

At low temperatures, low-frequency excitations result in purely transverse spin dynamics. In the classical picture of rigid magnetic precession, the transverse relaxation time τ_2 is determined by the longitudinal relaxation time τ_1 via the relation, $1/\tau_2 = 1/(2\tau_1) = \alpha\omega$, where α is the Gilbert damping parameter and ω is the precession frequency. Indeed, in the limit $(q, T_s) \to 0$, $\partial_t n_d \to (\Gamma/\hbar)\varepsilon_0 n_d$, which is identical to the LLG phenomenology, indicating that $\varepsilon_0 = \hbar\omega$ and thus $\Gamma_0 = 2\alpha$. This result establishes the important link between the scattering rate Γ_0 in this treatment and the Gilbert damping parameter that is accessible through FMR experiments.

In the opposite high-frequency limit, pertinent to ultrafast demagnetization experiments, the layer *F* to be in a low temperature equilibrium state before being excited by a THz laser pulse at $t = 0$, upon which the effective temperature of the itinerant electron bath instantly increases such that $T_s \geq T_C$. This regime is clearly beyond the validity of the LLG phenomenology, which is designed to address the low energy extremum of magnetization dynamics. Dissipation in the LLG equation,

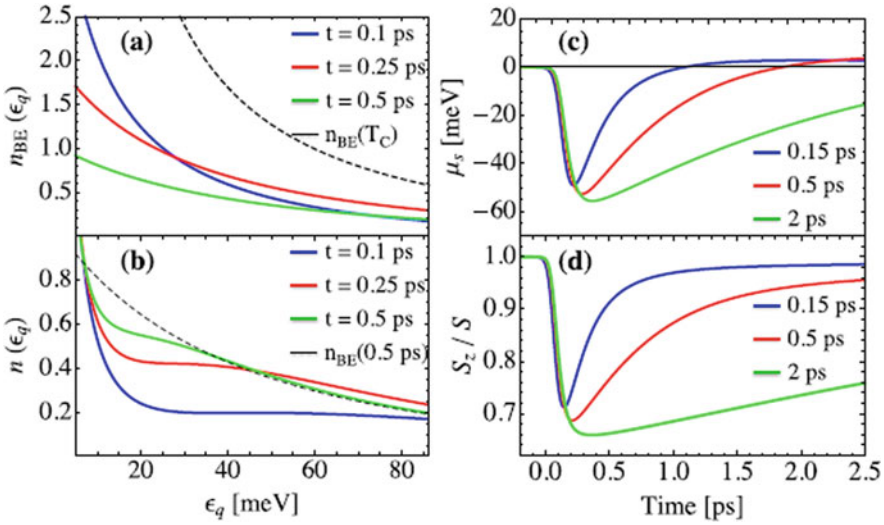

Fig. 1.6 Numerical solutions of Eqs. (1.32) and (1.33) after T_s is increased from 10^2 to 10^3 K (T_C) within 50 fs with a decay time of 2 ps. ε_0=5 meV, A = 0.6 meV/nm^2, $\rho = 6$ meV/nm^3, $\tau_s = 2$ ps, and $\alpha^* = 10\alpha = 0.1$. (**a**) The itinerant electron-hole pair distribution $n_{\mathrm{BE}}(\varepsilon - \mu_s)$ is rapidly depleted by the spin accumulation μ_s that is built up via electron-magnon scattering. (**b**) In the magnon distribution $n(\varepsilon_q)$ the high-energy magnon states are rapidly populated, whereas the low-energy states remain unaffected on short time scales. (**c**) Time evolution of the spin accumulation $\mu_s(t)$ and (**d**) the longitudinal spin density $-S_z(t)$ with different decay times of T_s: 0.15, 0.5, and 2 ps

including relaxation terms based on the stochastic Landau-Lifshitz-Bloch treatment [46], is subject to a simple Markovian environment without any feedback or internal dynamics. This perspective must be refined for high frequencies when no subsystem can be viewed as a featureless reservoir for energy and angular momentum.

The nonthermalized nature of the excited magnons can be appreciated in the limit in which μ_s is small compared with ε_0 and no magnons are excited ($n(\varepsilon_0 = 0)$) for $t < 0$. After rapid heating of the itinerant electrons at $t = 0$, the time evolution of the magnonic distribution follows

$$n\left(\varepsilon_q, t\right) \approx n_{BE}\left(\varepsilon_q, t\right)\left[1 - \exp\left(\Gamma\left(\varepsilon_q, t/\hbar\right)\right)\right]. \tag{1.34}$$

This result implies that, initially, the high-energy states are populated much faster than low-energy states. When μ_s becomes sizable, the coupled Eqs. (1.32) and (1.33) must be solved subject to a suitable $T_s(t)$. Fig. 1.6 (a, b) presents numerical solutions of (1.32) and

Equation (1.33) when T_s is increased from 10^2 to 10^3 K within 50 fs with a decay time of 2 ps. By comparison, internal magnon-magnon interactions equilibrate the distribution function on the time scale $\tau_{eq}^{-1} \sim \hbar^{-1}\varepsilon_m(\varepsilon_m/(k_B T_C))^3$ [40], where ε_m is a characteristic energy of the thermal magnon cloud. For short times, I_{sd} (see

1.31) dominates the magnon dynamics, and the magnon population is significantly different from the thermalized BE distribution.

When $T_s > T_C$, the thermally excited electron-hole pairs are populated in accordance with the classical Rayleigh-Jeans distribution, $n_{BE}(\varepsilon_q - \mu_s) \rightarrow k_B T_s/(\varepsilon_q - \mu_s)$. Assuming, for simplicity, that the expansion for $\Gamma(\varepsilon_q)$ is valid throughout the Brillouin zone, (1.31) yields

$$\partial_t n_d|_{t\rightarrow 0} = I_s(0)/\hbar = (\Gamma_0 + 3\chi\,(\varepsilon_b - \varepsilon_0)\,/5)\,k_B T_s/\hbar.$$

Thus, the demagnetization rate is initially proportional to the temperature of the electron bath but is reduced by the lack of available scattering states for high energy magnons within the time scale of the demagnetization process. Fig. 1.6(c, d) illustrates the time evolution of the out-of-equilibrium spin accumulation $\mu_s(t)$ and the longitudinal spin density $-S_z(t)$ for different decay times of T_s.

In the ultrafast regime, the electron-magnon spin-flop scattering is governed by the effective Gilbert damping parameter $\alpha^* = \chi(\varepsilon_b - \varepsilon_0)$. Experimental investigations of the magnon relaxation rates on Co and Fe surfaces confirm that high-q magnons have significantly shorter lifetimes than low-q magnons [38]. It is reasonable to assume that the same effects are also present in the bulk. The initial relaxation time scale in the ultrafast regime is $\tau_i \sim (\alpha^* \hbar^{-1} k_B T_s)^{-1}$. This generalizes the result of [20] for the ultrafast relaxation of the longitudinal magnetization to arbitrary α^* based on the transverse spin diffusion [44].

The notion of magnons becomes questionable when the intrinsic linewidth approaches the magnon energy, which corresponds to $\alpha^* \sim 1$. Staying well below this limit and consistent with [40], it is assumed that $\alpha^* = 0.1$. For $T_C = 10^3$ K the initial relaxation time scale $\tau_i \sim 10^2 (T_C/T_s)$ fs, which is generally consistent with the demagnetization rates observed for ultrafast demagnetization in Fe [47].

It can be shown that the interfacial scattering follows a structure similar to that of the bulk scattering in a unified description based on the electron-magnon interaction. Figure 1.7 presents a schematic illustration of an F/N interface. In magnetic heterostructures and for stand-alone ferromagnets on a conducting substrate, the demagnetization dynamics of F are also affected by the spin accumulation in N $\mu_N(x)$, which can impact how nonlocal laser irradiation (e.g., the heating of N alone) induces ultrafast demagnetization of F [15]. By adding terms of the form $\sim \sum_{qkk'} U_{qkk'} a_q c^\dagger_{k\uparrow} c_{k'\downarrow}$ to H_{sd}, where $c^\dagger_{k\uparrow}(c_{k'\downarrow})$ describes the creation (annihilation) of an electron with spin up (down) at the F/N interface, the interfacial spin transfer (per unit area) due to electron-magnon spin-flop scattering is [40]

$$I_i = \int_{\varepsilon_0}^{\varepsilon_b} d\varepsilon_q \Gamma^i\left(\varepsilon_q\right)\left(\varepsilon_q - \mu_N^0\right) D\left(\varepsilon_q\right)\left[n_{BE}\left(\varepsilon_q - \mu_N^0\right) - n\left(\varepsilon_q\right)\right], \qquad (1.35)$$

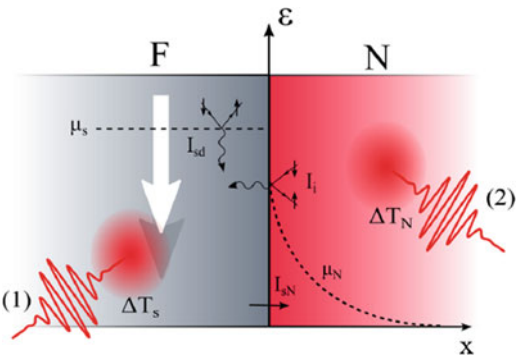

Fig. 1.7 Sketch of a metallic ferromagnet (F) coupled to a normal metal (N). In the ultrafast regime, both the rapid heating of s electrons in F by ΔT_s (labeled (1)) and the heating of N by ΔT_N (labeled (2)) can demagnetize F. I_{sd} induces the spin accumulation μ_s in F, whereas I_i induces the spin accumulation μ_N^0 at the F/N interface. Subsequently, $\mu_N(x)$diffuses into N until it vanishes due to spin-flip dissipation to the lattice. The additional interfacial spin current I_{sN}, due to the thermodynamic biases $\delta\mu = \mu_s - \mu_N^0$ and $\delta T = T_s - T_N$, can be described by conventional thermoelectric parameters for longitudinal spin-dependent transport

where $\mu_N^0 = \mu_N(0)$ is the spin accumulation at the interface and $\Gamma^i(\varepsilon_q)$ parameterizes the interfacial scattering rate.

The scattering of coherent long-wavelength magnons at the F/N interface can be described in the language of spin pumping/spin Seebeck effects [40], parameterized by the spin mixing conductance $g_{\uparrow\downarrow}$ (per unit area) [39]. Motivated by $\Gamma(\varepsilon_q)$ in the bulk, the interfacial scattering rate can be written as $\Gamma^i\left(\varepsilon_q\right) = g^*_{\uparrow\downarrow}\left(\varepsilon_q\right)/(\pi S)$, where $g^*_{\uparrow\downarrow}$ reduces to $g_{\uparrow\downarrow}$ for low energy scattering, $\varepsilon_q \to \varepsilon_0$. The interface scattering (see 1.35) dominates the microwave spin relaxation in thin ferromagnetic layers of thickness $d_F \leq 10$nm [39, 48]. This trend should continue for higher frequencies and is relevant for ultrafast spin dynamics in thin magnetic layers in heterostructures.

The energy dependence of the effective spin-mixing conductance is relatively weak compared to that of the bulk scattering $\Gamma(\varepsilon_q)$, which can be severely constrained at low energies due to momentum conservation. For a finite temperature bias δT across the interface and for magnons thermalized at the temperature $T < T_C$, the connection to the thermal spin Seebeck and Peltier effects is made by identifying $S = \partial_t I_i$ and $\Pi = TS$ [49] as the Seebeck and Peltier coefficients, respectively. Contact, as well as the spin pumping, is governed by a mixing conductance.

1.4 Conclusions

The spin-transfer-induced torques on the magnetic moments of F/N/F systems caused by a flowing current have been described in the framework of the scattering

matrix formalism. This description deals with the effects of multiple scattering between the layers using the scattering matrices of the *F*/*N* interfaces as input parameters. Both the cases of a diffusive and ballistic normal metal spacer are considered. In the diffusive case, the high-dimensional scattering matrices of the *F*/*N* interfaces only appear through the averaging over the normal metal layers. This allows to make qualitative predictions about the role of the interface transparency, normal metal resistance, etc., without detailed knowledge of the microscopic details of the system.

The description has focused on the effects of "spin filtering" as the mechanism for current-induced torque, i.e., the difference in the transmission and reflection probabilities for electrons with spins parallel and antiparallel to the moments of the ferromagnetic layers (the diagonal terms in the matrices for the reflection and transmission amplitudes). A different source of spin-dependent scattering related to spin-flip scattering is described by the off diagonal terms in the scattering matrices. Its effect can be twofold. In the normal spacer, it would decrease the effective polarization, and therefore the torque. However, in the ferromagnet, the rate of spin-flip scattering is symmetric with respect to minority and majority spins, and therefore spin-flip scattering may also be an additional source of torque.

The concepts of transverse spin diffusion in bulk ferromagnets and the interfacial spin-mixing physics have extended to address the ultrafast spin dynamics observed in rapidly heated magnetic heterostructures. In the ultrafast regime, the relative importance of the bulk scattering and the interfacial scattering can be extracted from measurements of demagnetization strength and spin currents in magnetic heterostructures. For metallic ferromagnets in the bulk, treating the magnonic subsystems as quasiequilibrated and parameterized by an effective temperature is insufficient to describe the far-from-equilibrium spin dynamics induced by pulsed laser heating. The magnon distribution function remains nonthermalized on the relevant time scale of the demagnetization process, in which the relaxation of the out-of-equilibrium spin accumulation limits the dissipation of spin angular momentum from the combined electronic system considered.

References

1. Akerman J (2005) Toward a universal memory. Sciences 308:508
2. Berge L (1996) Emission of spin waves by magnetic multilayer transverse by current. Phys Rev B 54:9353
3. Slonczewski JC (1996) Current-driven excitation of magnetic multilayers. J Magn Magn Mater 159:L7
4. Tsoi M, Jznsen AGM, Bass J, Chiang WC, Seck MV, Wider P (1998) Excitation of magnetic multilayer by an electric current. Phys Rev Lett 80:4281
5. Sun Z (1999) Current-driven magnetic switching in manganite trilayer junctions. J Magn Magn Mater 202:157
6. Myer EB, Ralph DC, Katine JA, Louie RN, Buhrman RA (1999) Current-induced switching of domains in magnetic multilayer devices. Science 285:867

7. Katine JA, Albert FJ, Buhrman RA, Muers EB, Ralph DC (2000) Current-driven magnetization reversal and spin-wave excitations in Co/Cu pillars. Phys Rev Lett 84:3148
8. Valet T, Fert A (1993) Theory of perpendicular magnetoresistance in magnetic multilayers. Phys Rev B 48:7099
9. Camblong HE, Levy PM, Zhang S (1995) Electron transport in magnetic in homogeneous media. Phys Rev B 48:7099
10. Stiles MD (1996) Oscillatory exchange coupling in Fe/Cr multilayers. Phys Rev B 54:14679
11. Schep KM, van Hoof HBAN, Kelly PJ, Bauer GEW, Inglesfield JE (1997) Interface resistances of magnetic multilayers. Phys Rev B 56:10805
12. Brataas A, Nazarov YV, Bauer GEW (2000) Finite-element theory of transport in ferromagnet-normal metal systems. Phys Rev Lett 84:2481
13. Waintal X, Myers EB, Brouwer PW, Ralph DC (2000) Role of spin-dependent interface scattering in generating current-induced torque in magnetic multilayers. Phys Rev B 62:12317
14. Choi GM, Min BC, Lee KL, Cahill DG (2014) Spin current generated by thermally driven ultrafast demagnetization. Nat Commun 5:4334
15. Kirilyuk A, Kimel AV, Rasing T (2010) Laser-induced magnetisation dynamics and reversal in ferrimagnetic alloys. Rev Mod Phys 82:2731
16. Kirilyuk A, Kimel AV, Rasing T (2010) Laser-induced magnetisation dynamics and reversal in ferrimagnetic alloys. Rep Prog Phys 76:026501
17. Lifshitz EM, Pitaevskii LP (1980) Cours of theoretical physics. Part 2, vol 9, 3rd edn. Pergamon, Oxford
18. Xiao J, Bauer GEW, Uchida KC, Maekawa S (2010) Theory of magnon-driven spin Seebeck effect. Phys Rev B 81:214418
19. Bauer GEW, Saitoh E, van Wees BJ (2012) Spincaloritronics. Nat Mater 11:391
20. Koopmans B, Ruigrok JJM, Dalla F, Jonge WJM (2005) Ultrafying ultrafast magnetization dynamics. Phys Rev Lett 95:267207
21. Walowski J, Műller G, Djordjevic M, Műnzerberg M, Klaui M, Vaz CAF, Bland JAC (2008) Energy equilibrium processes of electrons, magnons, and phonons at the femtosecond time scale. Phys Rev Lett 101:237401
22. Brataas A, Kent AD, Ohno H (2012) Current-induced torque in magnetic materials. Nat Mater 11:372
23. Tveten EG, Brataas A (2015) Electron-magnon scattering in magnetic heterostructures far out of equilibrium. Phys Rev B 92:180412
24. Berger L (1984) Exchange interaction between ferromagnetic domain wall and electric current in very thin metallic films. J Appl Phys 55:1954
25. Beenakker CWJ (1997) Random-matrix theory of quantum transport. Rev Mod Phys 69:731
26. Hathaway KB, Cullen JR (1992) A free electron model for the exchange coupling of ferromagnets through paramagnetic metals. J Magn Magn Mater 104:1840
27. Slonzhewski JC (1993) Mechanism of interlayer exchange in magnetic multilayers. J Magn Magn Mater 126:374
28. Bruno P (1995) Theory of interlayer magnetic coupling. Phys Rev B 52:411
29. Edwards DM, Frederici F, Mathon J, Umerski A (2005) self-consistent theory of current-induced switching of magnetization. Phys Rev B 71:05440
30. Brataas A, Nazarov YV, Gerrit EW (2001) Spin-transport in multi-terminal normal metal-ferromagnet systems with non-collinear magnetization. Eur Phys J B 22:99
31. Brouer PW, Beenakker CWJ (1996) Diagram method of integration over the unitary group with application to quantum transport in mesoscopic systems. J Math Phys 37:4904
32. Slonzhewski JC (1993) Excitation of spin wave by electric current. J Magn Magn Mater 195:L261
33. Beaurepaire JC, Merle JC, Daunois A, Bigot JY (1996) Ultrafast spin dynamics in ferromagnetic nickel. Phys Rev Lett 76:4250
34. Bsgot JY, Vomir M, Beaurepaire JC (2009) Coherent ultrafast magnetism induced by femtosecond laser pulses. Nat Phys 5:515

35. Schellekens AJ, Koopmans B (2013) Microscopic model for ultrafast magnetization dynamics of multisublattice magnets. Phys Rev B 87:020407
36. Eshenlohr A, Battitato M, Maldonado P, Pontius N, Kachel T, HolldackK MR, Fönlisch A, Oppeneer PM, Stamm C (2013) Ultrafast spin transport as key to femtosecond demagnetization. Nat Mater 12:332
37. Illg C, Haag M, Fähnle M (2013) Ultrafast demagnetization after laser irradiation in transition metals: *Ab initio* calculation of the spin-flip electron-phonon scattering with reduced exchange splitting. Phys Rev B 88:214404
38. Zhang Y, Chuang TH, Zakeri K, Kirschner J (2012) Relaxation time of terahertz magnons excitated at ferromagnetic surfaces. Phys Rev Lett 109:087203
39. Tserkovnyak Y, Brataas vA, Bauer GEW, Halperin BI (2005) Nonlocal magnetization dynamics in ferromagnetic heterostructures. Rev Mod Phys 77:1375
40. Bender SA, Tserkovnyak Y (2015) Interfacial spin and heat transfer between metals and magnetic insulator, vol 91, p 140402
41. Jauho AP, Wingreen NS, Meir Y (1994) Time-dependent transport in interacting and noninteracting resonant-tunneling systems. Phys Rev B 50:55285544
42. Mueller BY, Baral A, Vollar S, Cinchetti M, Aeschlimann M, Schneider HS, Rethfeld B (2013) Feedback effect during ultrafast demagnetization dynamics in ferromagnets. Phys Rev Lett 111:167204
43. Barker J, Atxitia U, Ostler TA, Hovorka O, Chubykalo-Fesenko O, Chantrell W (2013) Two-magnon bond state causes ultrafast thermally induced magnetization switching. Sci Rep 3:3262
44. Tserkovnyak Y, Hankiewicz EM, Vignale G (2009) Transverse spin diffusion in ferromagnets. Phys Rev B 79:094415
45. Messervey R, Tedrow PM (1994) Spin-polarized electron tunneling. Phys Rep 238:473
46. Atxitia U, Chubykalo-Fesenko O, Walowski J, Mann A, Műnzerberg M (2010) Evidence for thermal mechanism in laser-induced femtosecond spin dynamics. Phys Rev B 81:147401
47. Weber A, Pressacco F, Gűnter S, Mancini E, Oppeneer PM, Back CH (2011) Ultrafast demagnetization dynamics of thin Fe/W(110) films: comparison of time- and spin-resolved photoemission with time-resolved magneto-optic experiments. Phys Rev 84:132412
48. Liu Y, Wesselink RJH, Starikov AA, Kelly PJ (2014) Interface enhancement of Gilbert damping from first principles. Phys Rev Lett 113:207202
49. Hoffman S, Sato K, Tserkovnyak Y (2013) Landau-Lifshitz theory of the longitudinal spin Seebeck effect. Phys Rev B 88:064408

Chapter 2
Development of the Nano-mineral Phases at the Steel-Bentonite Interface in Time of the Evolution of Geological Repository for Radioactive Waste

B. H. Shabalin, O. M. Lavrynenko, and O. Yu. Pavlenko

2.1 Introduction

Today, the optimal prototypes for geological storage (GS) facilities (GS) that are planned to be located in crystalline rocks of Chernobyl Exclusion Zone or adjacent regions of Ukraine are geological repositories (GR) of high-level waste (HLW) and spent nuclear fuel (SNF) that are situated in Precambrian crystalline rocks (granites) of Sweden and Finland [34]. The GR safety concept is based on the usage of multiple barriers in the disposal systems that perform protective functions over different time periods. Standard design of the storage facilities foresees the following barriers: matrix with HLW, metal canister for the matrix, clay buffer between the canister and the containing rock, and filler for main tunnels and other underground workings (the backfill) – engineered barrier system (EBS) – including the host rock in contact with or near the EBS and the environment as a whole that separates EBS from the geosphere and biosphere. The canisters relate to the most important elements of EBS, which are usually made of iron alloys (carbon steel, cast iron, stainless steel, etc.) [37]. A main function of the clay buffer is to isolate the waste container from the environment due to its high ability to retain radionuclides in the engineered barrier system (EBS) and to prevent entry of groundwaters [9].

B. H. Shabalin
State Institution "Institute of Environmental Geochemistry of NAS of Ukraine", Kyiv, Ukraine

O. M. Lavrynenko (✉)
State Institution "Institute of Environmental Geochemistry of NAS of Ukraine", Kyiv, Ukraine

I.M. Frantsevych Institute of Material Science Problems of NAS of Ukraine, Kyiv, Ukraine

O. Yu. Pavlenko
I.M. Frantsevych Institute of Material Science Problems of NAS of Ukraine, Kyiv, Ukraine

O. Fesenko, L. Yatsenko (eds.), *Nanocomposites, Nanostructures, and Their Applications*, Springer Proceedings in Physics 221,
https://doi.org/10.1007/978-3-030-17759-1_2

In the conceptual decisions of a number of GR, clay buffer material is considered to be natural bentonite (montmorillonite clay) of the MX-80 grade produced in states of Wyoming and North Dakota (USA), as well as pure sodium or calcium forms of montmorillonite. Its composition contains up to of 75% Na-montmorillonite, 15% quartz, 5–8% feldspar, 1% carbonate, 0.3% pyrite, and 0.4% C org. Numerous bentonite clay deposits are situated in Ukraine, namely, in Cherkaska, Vinnytska, Zakarpatska, and Chernivetska Oblasts and other parts of the country. Chemical and mineral composition, crystallochemical features, and ion-exchange properties have been studied for samples of some repositories [8].

Steel packaging provides radionuclide isolation from groundwater flow for one thousand years, but bentonite buffer may increase this period, at least by one order of magnitude [20, 41]. At the same time, the isolating properties of the bentonite buffer in a multibarrier disposal system can change over time and negatively affect the safety of the GR [49]. Three stages in GR evolution are distinguished:

1. Early aerobic (with the presence of oxygen) phase (100–200 years; the stage where waste is disposed of into storage facilities and some period after its closure)
2. Transition from aerobic to anaerobic phase (up to 1000 years)
3. Long-term anaerobic phase (more than 10,000 years) [26]

   Saturation of the water repository may occur in both phases (transitional and long-term anaerobic), and it depends on the rate of groundwater filtration.

The aim of the review is to analyze the phase transformation of bentonite clay at the steel-bentonite interface in the radioactive waste geological repository system and to evaluate the impact of newly formed mineral phases of corrosive and geochemical origin on the isolating properties of bentonite buffer and the long-term safety of the GR as well.

2.2 Characterization of Primary Nanoscale Structures of Corrosive Origin

The primary mineral phases formed on the steel surface during the corrosion process are Fe(II)-Fe(III) layered double hydroxides (Fe(II)-Fe(III) LDH of Green Rust) and ferrihydrite (Fh). The main factors that determine the chemical composition and structure of such primary particles are the anionic composition of dispersion medium, the presence of ferric or ferrous aqua hydroxyl forms, and the reductive-oxidative conditions in the system.

2.2.1 *Fe(II)-Fe(III) Layered Double Hydroxide (LDH) Structures, the Mechanism of Their Formation and Their Phase Transformations*

Fe(II)-Fe(III) LDH structure consists of hydroxide layers formed by $Fe^{II\text{-}III}(OH)_6$ octahedrons. Water molecules and anions that are coordinated by the hydroxide layers, which provide the compensation of ferric charge in the crystal lattice and give electroneutrality to the entire structure of the mineral, are located in the interlayer space of Green Rust. Depending on the kind of coordinated anions in the interlayer space, Fe(II)-Fe (III) LDH are referred to the first or second types, which determine their crystallochemical properties: the ability to gradually change Fe^{2+}/Fe^{3+} cation ratio in the Green Rust I lattice and constancy of this ratio in the Green Rust II structure [44]. Thus, the typical Fe(II)-Fe (III) LDH which can be formed when the steel surface is in contact with groundwater is the hydroxycarbonate Green Rust-(CO_3^{2-}). Its crystallochemical formula can be written as $Fe^{II}_4Fe^{III}_2(OH)_{12}CO_3 \bullet nH_2O$, where $n = 2$ or 3. The sample of Fe(II)-Fe(III) LDH which corresponded to the second type is hydroxysulfate Green Rust-(SO_4^{2-}). Its crystallochemical formula is written as $Fe^{II}_4Fe^{III}_2(OH)_{12}SO_4 \sim 8H_2O$ [46].

The Green Rust-(CO_3^{2-}) formation occurs through several mechanisms: (1) chemical interaction of ferrous aqua hydroxyl forms and oxygen-containing carbonate species under oxidative conditions [47], (2) their interaction with pre-deposited ferric hydroxide, and (3) solid-state interaction of ferrous and ferric hydroxides in the presence of oxygen-containing carbonates species. At the same time, the formation of Fe(II)-Fe(III) LDH structures can occur via coagulation of so-called green complexes and is associated with hydrolysis and polymerization of ferric and ferrous aqua hydroxyl forms in the reaction area near the steel surface [1]. Green Rust phase formation occurs via topotactic transformation without oxidative destruction of a natural amakinite $Fe(OH)_2$ in the presence of ferrous cations and SO_4^{2-} or CO_3^{2-} anions [2].

Kinetic regularities of Fe(II)-Fe(III) LDH formation on the steel surface was reported in the work of [30]. According to obtained data, the relative quantity of Green Rust phase did not stand constant. It depended on chemical composition of the dispersion medium and reductive-oxidative conditions at the interface between the steel surface and dispersion medium. Hence, it may increase or decrease due to the phase transformation of Green Rust into other ferric oxygen-containing mineral phases: ferrihydrite, ferric oxyhydroxides, or magnetite. The main criteria which determined the process of Green Rust transformations are the redox potential (ROP) of the system, the chemical composition of the dispersion medium, the pH value, temperature, and, probably, the presence of various microorganisms.

2.2.1.1 "Green Rust-Ferrihydrite" System (Green Rust-Fh)

The study of the process of ferrihydrite formation via oxidation of ferrous hydroxide water suspension in the presence of HCO_3^- anions (in the range of the pH value from 7.5 to 9) shows that Fh is a transitional product between Green Rust-(CO_3^{2-}) and goethite α-FeOOH [15]. Phase transformation of Green Rust-(Cl^-) into ferrihydrite may be estimated as a result of ferrous hydrated cations and Green Rust itself fast oxidation [18].

At the same time, the transformation of ferrihydrite as well as mixed oxidized forms of Fe(III)-Green Rust into ferrous cations is possible in natural systems [16].

2.2.1.2 "Green Rust-Goethite" System

Formation of α-FeOOH goethite during oxidation of Fe(II)-Fe(III) LDH by dissolved oxygen was shown for the mineral phases of Green Rust-(SO_4^{2-}), Green Rust-(Cl^-) [18], and Green Rust-(CO_3^{2-}) [55]. The mechanism of such transformation went through the stages of Green Rust dissolution and re-precipitation accompanied by subsequent deposition of well-ordered ferric oxyhydroxide structures [7]. At the same time, Green Rust-(CO_3^{2-}) of corrosive origin turns into α-FeOOH goethite in 0.1 M solution of $NaHCO_3$ without intermediate formation of the ferric hydroxide [11].

Growth of redox potential from (−0.45) to (−0.3) V [55] is observed in the solution when Fe(II)-Fe(III) LDH phase was transformed into goethite α-FeOOH (pH value ~9.5). Usually, the formations of goethite particles lead to decrease in the pH value of the dispersion medium.

2.2.1.3 "Green Rust-Akaganeite" System

According to published data, the determinative condition for the transformation of Green Rust into akaganeite β-FeOOH is the relatively high concentration of dissolved ferrous and chloride species [36].

2.2.1.4 "Green Rust-Lepidocrocite" System

The formation of lepidocrocite γ-FeOOH under the slow oxidation of Green Rust (pH ~ 7.0) occurs in two stages [40]. The first stage gives place to partial oxidation of ferrous cations in the Fe(II)-Fe(III) LDH structure, hydrolysis, and re-precipitation of ferric cations into poorly crystalline hydrated ferrihydrite phase. Here, Fh can quickly react with ferrous cations and turn into Green Rust again. The reaction order of the secondary formation of Green Rust is limited by the deposition of Fh and concentration of ferrous cations. Re-precipitation of lepidocrocite particles occurs at the second stage.

During oxidation of Green Rust, magnetite as an intermediate phase may be included into Green Rust crystal lattice. Further oxidation of the system involves the destruction of both mineral phases and the following precipitation of needlelike γ-FeOOH particles. Transformation of natural fougerite into lepidocrocite when the last was contacting with dispersion medium in the presence of high quantities of carbonates, aluminum aquaforms, and silicate species was shown in [52].

2.2.1.5 "Green Rust-Feroxyhyte" System

A mixture of weakly crystallized ferrihydrite and feroxyhyte (ferric Green Rust) structures was obtained during phase transformation of Green Rust-(CO_3^{2-}) of corrosive origin under oxidation conditions of the system [11].

2.2.1.6 "Green Rust-Magnetite" System

Formation of Fe_3O_4 magnetite in aqueous suspension of Green Rust is also associated with dissolution and re-precipitation of the unstable structures Fe(II)-Fe(III) LDH [21]. At the pH value 9 and the ferrous/ferric ratio 0.5 and 1, the formation of hexagonal particles of GR(SO_4^{2-}) lasts ~ 6 min, and then they quickly transform into magnetite. At the same time, Green Rust-(SO_4^{2-}) phase remains stable when the pH value decreases to 7. Moreover, when the ferrous/ferric ratio equals 0.5, the magnetite phase is not formed. Decrease of pH < 7 leads to dissolution of Green Rust structure and saturation of the dispersion medium with ferrous cations. In time ferrous species are gradually oxidized and precipitated as the ferric oxyhydroxide phases [31].

The main results of modern studies related to Green Rust synthesis under laboratory conditions, its structure, properties, as well as its formation in the natural environment and interaction with various chemical species are summarized in the review papers [5, 6]. So, the formation of Green Rust structures on the steel and iron surfaces, due to its strong reductive properties, sorption, and chemical activity in respect to high toxically chemical elements and compounds, together with the ability to phase transformation accompanied by involvement of different cations, may be an important additional contribution to fixation of radionuclides in case of the steel vessel usage in geological repository of radioactive waste.

2.2.2 Phase Transformation of Ferrihydrite

Ferrihydrite (Fh) is another primary mineral phase that can be formed on the steel surface via the corrosion process. It belongs to the Fe(III) (oxy)hydroxysalt group and is closely connected to the iron oxides by supergene phase formation processes [39]. Synonyms of ferrihydrite are "hydrated oxide of ferric iron" (HFeO),

"amorphous hydroxide of ferric iron," "colloidal hydroxide of ferric iron," and "$Fe(OH)_3$."

So, ferrihydrite as a metastable ferrous-hydroxide phase is easily transformed into more stable disperse minerals, such as goethite and hematite [12]. The main factors influencing the chemical mechanisms of the ferrihydrite formation and the composition of the transformation products are chemical composition and pH value of the dispersion medium, temperature, reductive-oxidative conditions, etc. [10]. Because the phase transformation of ferrihydrite into goethite belongs to the typical processes in natural systems, it is extensively covered in the literature sources.

The main mechanism for such a transformation is dissolution/re-precipitation that is catalyzed by ferrous cations of aqueous medium [50]. Dissolution of ferrihydrite and its precipitation into α-FeOOH in the presence of ferrous cations completes under standard conditions within 24 h, while ferrihydrite remains stable for a long time when the solution is free of ferrous cations. Taking into account that solubility of Fh (10^{-39}) is higher than solubility of its transformation products – α-FeOOH (10^{-41}) and α-Fe_2O_3 (10^{-43}) – their formation via dissolution-re-precipitation mechanism is quite expectable.

In general, two- and six-line ferrihydrites are formed by hydrolysis of ferric cations and polymerization of their dimeric species $Fe_2(OH)_4{}^{4+}$ at pH < 4.1, whereas the most favorable conditions for Fh transformation are pH values 4 and 12, when corresponding complexes $Fe(OH)_2{}^{+}$ and $Fe(OH)_4{}^{-}$ are formed in the water medium. According to other data, the optimal conditions for ferrihydrite transformation into goethite correspond to pH = 9 and T ~ 40 °C, where the polymerization of ferric hydroxocomplexes may occur [17].

2.3 The Study of Corrosion Processes on the Surface of Steel Containers

Much of the world canisters for vitrified HLW are made of steel containing <0.3 wt.% carbon, where Mn, Si, Cu, Cr, Ni, Mo, W, V, and Zr may also be present among additional chemical components. The guaranteed lifetime of such kind of canisters is determined within 1000 years, and the main destructive process for them may be corrosion [27]. The main reasons for the corrosion of steel are its chemical composition; the physical-chemical conditions in the geological repositories, such as temperature; oxidation potential; alkalinity and mineralization of groundwater; and the presence of bentonite buffer and other structural materials in the repository system, in particular, cement [9].

Oxidizing conditions in the RW repository will be kept several hundred years at the stage of waste deposition and some period after repository closure. After that, the repository will be characterized by anaerobic reduction regime, set as a result of reactions in EBS. Generally speaking, aerobic corrosion has very limited significance for analyzing multilayer container behavior, because it takes place

during the relatively short operational stage of the repository and some period after its closure. During this time, only the outer packaging can be damaged. After all oxygen has been used in the ESB reduction-oxidation reactions, anaerobic corrosion of the container in a water-saturated environment starts to play the main role. These conditions are corresponded by two types of steel container corrosion that change its properties, which can cause deterioration of metal functions and the whole barrier system. Also, corrosion can be divided into general and local and crevice corrosion. General corrosion occurs throughout the surface and at a constant speed. In aqueous media, this is an electrochemical process having at least one oxidation reaction: $(M^{X+}, xe^-) \rightarrow (M^{X+}) + x(e^-)$ and cathode reduction: $Ox^{q+} + x(e^-) \rightarrow Red^{(q-x)+}$, where Ox and Red are oxidized and reduced forms of elements. Under aerobic conditions, cathode reaction runs according to the scheme:

$$O_2 + 2H_2O + 4e^- \rightarrow 4O,$$

while as in anaerobic conditions, it occurs with hydrogen formation:

$$H_2O + e^- \rightarrow 0.5H_2 + OH^-.$$

Thickness of metal would decrease in time, if corrosion products are soluble in water, or the surface iron oxide layer is formed. In other cases, the overall thickness does not change. In the first case, active corrosion process is accompanied by transfer of charges and matter, and in the second one, passive corrosion process leads to the appearance of dense protective film of newly formed mineral phases. So, at the near-neutral pH values, the formation of protective layer is an important aspect of steel corrosion in water solutions.

Generally, the protective layer on the steel surface can affect SNF container corrosion process in a different way:

- To limit transfer of outer matter and reagents to corroding surface and, correspondingly, corrosion products from corroding surface
- To protect the steel surface against the following dissolution (if the film has no conductive properties)
- To change anode and cathode areas and their ratio (if the film is conductive enough to maintain electrochemical reactions)

Among effects listed above, surface protection and limitation of matter transport to the surface and from it may be called. In both cases, we achieve decrease of corrosion process, as it was proved by experimental work, including obtained in underground research laboratories.

Numerous works were devoted to the study of carbon steel behavior under conditions of GR. Long-term experiments (6000 h) under conditions simulating HLW disposal facility of clays showed that the rate of steel destruction in water at $T = 90\ ^\circ C$ is less than 10^{-3} cm per year [13], whereas by the contact of seawater (at $T = 80\ ^\circ C$) with steel under aggressive conditions, it is slightly higher – $2 \cdot 10^{-3}$ cm per year [48].

In the first decades after the repository closure and its filling with water under aerobic stage, the process of local container corrosion with microfracture formation under the influence of current will dominate. In the ongoing anaerobic stage, the main degradation reasons will be general container corrosion and its destruction due to the appearance and action of hydrogen [37]. Usually, carbon steel has high corrosion rate (0.06 mm/year) within the aerobic stage when it is contacting with water having 2.5 g per liter mineralization that is achieved in the presence of Na^+, Ca^{2+}, Cl^-, $SO_4{}^{2-}$, and sulfuric and carbonic acids. Herein, the corrosion rate is increased by 30–50 percent when the temperature increases from 30 to 50 °C [59].

The rate of corrosion of low carbon steel in 1 M NaCl solution in the pH range from 8.4 to 11 is independent of alkalinity. It decreases from 30 μm/h, at the beginning of the experiment, to 1–3 μm/h after 4600 h of the contact of steel with the solution. Under anaerobic conditions, the rate of corrosion becomes less than 5 μm/h after 300–600 h of contact of the steel surface with water that equilibrated with bentonite [43].

According to other data [37], at moderate temperatures in anaerobic conditions, corrosion of carbon steel occurs at a rate of the first microns per year. Thereat, radiation does not significantly influence the rate of corrosion, and it can lead to slight increase or even decrease the corrosion process, but under large radiation loads a negative accelerating effect on the destruction of steel becomes more evident.

Stainless steel is more stable in comparison to carbon steel. Its average corrosion rate under hypothetical RW repository conditions is estimated at 0.01 μm/h, expected corrosion is 31.8 mm per 1000 years. So, the real values of the corrosion rate are 2–20 mm in 10,000 years [60].

For Belgian HLV repository situated in Boom clay formation, the corrosion rates of stainless steel lies in the range from 0.003 to 0.15 μm/h [35]. Its total corrosion in water equilibrated with cement is 0.03–0.5 μm/year in aerobic medium and 0.001–0.01 μm/year under anaerobic conditions. Corrosion of steel slows down during the time when the pH of water medium grows, but it increases when temperature, oxidation potential, and water mineralization rise.

As it was shown in the works [25, 54], the rate of anaerobic corrosion of steel during first tens of hours reached 70 μm/h, and next it decreased up to the first microns per year due to the formation of a protective layer consisting of corrosion products – iron oxides (magnetite, maghemite) and carbonates (siderite $FeCO_3$). Whereas the increase in pH value of water led to reduction of the rate of corrosion of steel and hydrogen generation by two orders of magnitude – from several dozens to one tens of liters per square meter per year – irradiation caused its increase [45]. Temperature accelerated the formation of protective layer on the steel surface in contact with 0.1 M ($HCO_3{}^- + CO_3{}^{2-}$) solution [19].

A corrosion layer formed by the similar structures was obtained in an 8-month experiment by the contact of steel and argillites at 90 °C under anaerobic conditions [13]. External dense layer of iron carbonate ($FeCO_3$) corrosion products and an internal interchange layer of iron oxides and silicates can be highlighted.

The corrosion rate of steel in contact with water medium in the presence of bentonite was decreased over time, reaching stationary state of 1–3 microns per year. Such result was achieved under experimental conditions after hundreds of hours when the steel surface was placed into bentonite suspension or water equilibrated with bentonite, as well as after one thousand hours in contact of the steel with compacted bentonite. The increase in the pH value suppressed the steel corrosion because the poorly soluble ferric hydroxide phases were formed on the surface of the steel container.

Thus, the corrosion rate is strongly dependent on the physical-chemical properties of the metal and the determinative environmental factors (Eh-pH value, temperature, the chemical composition and total mineralization of groundwater, etc.), together with processes taking place in the EBS, for instance, the formation of iron oxide and hydroxide particles in the corrosion layer.

At the aerobic stage (in the presence of oxygen) following waste disposal into storage facilities, corrosion of steel slows down in time due to increase in the pH value, but if the temperature, oxidation potential, and water mineralization grow, the corrosion rate would increase. So, the main criteria in reducing corrosion rate at this stage are the formation of protective iron oxide layer on the steel surface, high pH values in contact with bentonite, and when the temperature is growing.

At the beginning of the anaerobic period, a previously formed film consisting of a porous layer of ferric-ferrous corrosion products (magnetite or other spinel ferrite phases) may be present on the steel surface. Such structures will have the same effect on the corrosion process as a porous film formed in anaerobic corrosion. Also, if the main protective function of spinel ferrite film is to block the surface only, the appearance of primary porous film under anaerobic conditions would not be important. However, if the corrosion layer limits the matter transfer in the direction to and from the steel surface, the thickness of the previously formed ferric oxyhydroxide film would be important for the following overall thickness of the film, and, thus, it determines the rate of corrosion.

2.4 The Phase Transformation of Bentonite Clays at the Steel-Bentonite Interface Under Conditions of Geological Repository

Bentonite belongs to montmorillonite clays that are characterized by high sorption capacity, plastic property, and swelling when they are saturated by water. The specificity of montmorillonite structure lies in the presence of a three-layer package including tetrahedron-octahedron-tetrahedron. The bonding between all the packages is weak, and water can penetrate into this interlayer space causing strong swelling of the mineral. Its capacity of cation exchange reaches 80–120 mg-eq per 100 g. Montmorillonite content in bentonite reaches 55–95%, and hydromica, chlorite, kaolinite, and quartz are present in their composition as additional minerals.

Genetically the largest deposits of bentonite are formed via decomposition of volcanic ash and tuffs under subaqueous conditions [4, 23].

The transformation of bentonite buffer at the initial stage of GR evolution depends on the degree of its saturation by water: first, dehydration due to bentonite heating in the presence of radioactive waste and, second, rehydration due to the penetration of groundwater into the GR. When bentonite is saturated with groundwater, it swells and fills empty spaces between the buffer, canister of waste, and rock cracks near to the buffer.

Mineral composition of bentonite clays and their isolating properties can change due to the influence of high temperature, chemical composition of groundwater, products of dissolution of the radioactive waste, related microbiological processes, and chemical composition of corroded canisters, which are made of steel or other materials. Complex influence of these factors and the possible synergistic effect cannot be predicted. Chemical and physical-chemical evolution of the buffer is regulated by thermodynamic conditions in GR system that contributes to form and transform new nanosized minerals and is closely related to the quantitative ratios of the dispersed phase and the dispersion medium (solution) [29]. Duration of thermal, hydrodynamic, and mechanical processes can be determined from several hundred to 1000 years, but mineralogical-geochemical reactions caused by corrosion of canisters or products of destruction of structural and associated materials will occur during the entire time of GR evolution.

Temperature is one of the key factors that affect the rate and degree of transformation of smectite (montmorillonite) mineral phase. At the same time, it is well known that at the beginning of evolution, the temperature in GR will be relatively low (<150 °C), moreover it is predicted the trend to its steady decrease. According to the prognosis [33], the maximum expected temperature in GR will be 45.5 °C within 1000 years, and after 10,000 years 20.5 °C. Consequently, it is likely that chemical composition of the water environment will control bentonite buffer evolution with respect to transformations of the mineral phases [51].

It can be assumed that the chemical composition of porous water in bentonite buffer should be influenced by diffusion of ferric/ferrous aqua hydroxyl forms, obtained during canister corrosion, and other compounds that went from containing rock. At the same time, bentonite is characterized by high acid-alkaline buffer capacity that is provided by protonation-deprotonation of surface hydroxyl groups. As a result, the chemical composition of bentonite porous water will remain stable for very long time [14], and it is almost similar to the composition of groundwater in contact with it [38]. Moreover, if bentonite contacts with groundwater from granites located in GR, the buffer sorption capacity and clay's ability to cation exchange practically would not decrease. So, it should promote sorption retardation of individual forms of radionuclides.

Probably, Na-form of montmorillonite will be changed to its calcium form during evolution of the geological repository, but to date, there has been no experimental evaluation of the actual speed and extent of these changes. It is expected that the transformation of bentonite into its Ca-dominating composition will contribute to long-term stability of the buffer, since calcium-containing smectite is characterized

by high water-holding (isolating) properties, high sorption capacity, and resistance to dissolution when it is in contact with strongly alkaline groundwaters. Natural bentonites (MX-80, Cherkaskii) contain not only Ca^{2+} and Na^{+} cations but also cations Mg^{2+} and K^{+}, which have low effect on the cation exchange process; therefore, it is almost impossible to achieve mono-cation composition of bentonite buffer under the GR conditions.

One of the important questions concerning the phase transformation of bentonite and, consequently, changes in its physical and chemical properties, are processes of interaction buffer with corrosion products of steel container. When bentonite buffer is saturated with groundwater and contacted with steel surface, mineralogical changes of bentonite can occur by two ways of saponitization and/or beidellitization according to the following scheme, low-charged montmorillonite → high-charged beidellite + saponite + quartz [32, 56], and or illitization [53].

Saponitization does not critically influence the isolating properties of the buffer, because newly formed saponite, likes bentonite, is capable of swelling, and, so, it can be used as a buffer material too; however, the formation of beidellite may critically affect the isolating properties of the buffer.

Thermodynamic calculations suggest processes of montmorillonite dissolution and precipitation of ferric-/ferrous-enriched minerals under conditions of the GR. The most probable products of montmorillonite transformation are ferrum smectites (e.g., Fe-saponite), berthierine, or chlorite, which was confirmed experimentally [58]. At the same time, the transformation of montmorillonite in contact with the steel surface at $T > 50$ °C remains controversial, and the obtained results are contradictory. Most of them were reported according to the French Radioactive Waste Management Program [32]. Thus, as it was shown in some experiments, the newly formed iron-oxide phases were not detected at $T = 80$ °C; in others, only corrosion products, magnetite, hematite, and goethite, were found; in the third, berthierine, nontronite, and saponite were found. Formation of chlorite and saponite, which corresponds to smectite characterized by high ferrum content, was reported at temperatures 250–300 °C. But the general conclusion regarding the processes of bentonite transformation in GR conditions in contact with the steel surface is that under the isothermal conditions the ratio of dispersed phase/dispersion medium is in the inverse correlation, depending on the change of mineralogical composition of the bentonite buffer. In particular, according to [24], the reductive ability of bentonite to swell due to its interaction with the container metal (iron) remains limited in space to several centimeters over a long period of time. The main source of the ferrum is newly formed siderite particles and ferrous cations from porous water of unchanged buffer.

According to the results of the long-lasting (8.2–10 years) experimental modeling of the phase transformation of MX-80 bentonite in contact with iron (cast iron) placed in a copper container, diffusion front of ferric/ferrous species into bentonite does not exceed 7–8 mm from iron surface [28]. Saturation of the initial solution (0.5 M NaCl) with Mg^{2+}, Ca^{2+}, and SO_4^{2-} ions resulted in increase of solution alkalinity up to 8 and formation of the following mineral phases on the bentonite surface: gypsum, quartz, aragonite, and hematite. At the same time, bentonite in

contact with cast iron was cemented to a certain extent due to increase of the content of illite fraction.

Converted montmorillonite was characterized by decrease in the ability to swell and swelling pressure, but its hydraulic conductivity practically was not changed. In general, ferrum was incorporated into the montmorillonite structure, whereas the silicon oxide is released from it. The amount of exchanged iron in the bentonite structure was increasing in direction to the cast iron. The redox conditions in external solution and porous water were strongly reducing within 8.6 years. The gas phases contained H_2, which probably evolved as a result of the corrosion of cast iron cylinders, and CO_2, which source had been the calcite dissolution.

At the same time, as it has been shown in serial IAEA tests, the transformation of bentonite occurred more intensively when the iron to clay ratio and pH value of dispersion medium were simultaneously increasing. Montmorillonite in contact with steel lost its swelling ability and turned into another clay containing phases of serpentine and berthierine when it was kept in 0.3–0.6 M NaCl solutions and, partly, in 0.1 M $NaHCO_3$ solution. Silicon oxide was released as a result of montmorillonite transformation.

In samples that were kept in distilled water and in 0.05 M solution of sulfate in distilled water solution, a montmorillonite fraction was isolated that contained magnetite and pyrite admixtures. In general, the montmorillonite component of bentonite MX-80 after 8–10 years of contact with iron practically did not change. There was also no evidence of complete montmorillonite transformation into non-swelling mineral. But if the pH value and content of ionized iron at the iron-bentonite interface are increased, such transformation would be accelerated.

Taking into account the presence of K^+ cations in the granite groundwater (mainly because of feldspars presence in granites), which have the largest energy of absorption by montmorillonite in comparison to other cations [3], the illitization of bentonite buffer can become a real threat to the safety of the storage facility. The gradual transformation of montmorillonite into illite takes place by replacing interlayer Na^+ or Ca^{2+} cations with K^+. At that, the mixed layers of illite/montmorillonite are formed as a result of illitization process. In this case, pure illite does not have the ability to swell, and for the mixed illite-montmorillonite layer, such ability is significantly limited. In addition, gradual changes in the mineralogical characteristics and physical-chemical properties of the buffer, such as the specific surface area, cation exchange properties, hydraulic conductivity, etc., have been observed.

At the same time, kinetics of the transformation of montmorillonite into illite, performed for KBS-3-type repository conditions [42], has proved practical impossibility illitization process because of low temperature in the repository. At temperatures below 100 °C, the rate of bentonite transformation will be small and will not lead to loss of buffer's isolating properties during the period when the buffer should perform safety functions. However, taking into account that the process of montmorillonite into illite transformation is also influenced by many other factors, such as the degree of bentonite saturation with water or ratio of dispersed phase to dispersion medium, pH value, and concentration of alkaline cations (in particular,

K^+), evaluation of illitization process probability should be carried out separately for each GR site.

Detailed investigations of the thermal transformation of bentonite into illite were performed for various samples in a wide range of physical and chemical conditions. So, the results of the study of illitization in the natural systems have proved [22] that montmorillonite can be existed in stable state for more than one million years at temperatures below $T = 100$ °C. The authors of the work [22] have concluded that noticeable illitization at temperatures of 100–130 °C will not occur even for 10 years. The review paper [57] that is devoted to the study of bentonite stability at $T < 100$ °C, assumed that the transformation of smectite into illite depends on temperature, time, and concentration of K^+ in porous water. At the same time, it was reported that in wet conditions at $T = 120$ °C, no significant changes in hydraulic and mechanical properties were detected for bentonite, whereas noticeable effects of cementation and possible illitization were observed only at $T > 150$ °C. In dry conditions, montmorillonite (bentonite) remains stable up to $T = 300$ °C.

According to prognostic estimates made for the state of Olkiluoto geological repository (Finland) [29], the processes of illitization and cementation of bentonite buffer by silicon dioxide or iron oxides are unlikely due to the current and expected natural conditions (composition and localization of groundwater and possible temperature changes). However, the usage of external materials in the construction of repository, similar to cement-based fillings, can lead to the release of K^+ and SiO^{2-} and increase pH > 13, which also can accelerate cementation/illitization processes and may start other phase transformations such as saponitization and/or beidellitization. In particular, it is believed that the formation of zeolites occurs even at a pH < 11. It is expected that initial leaching products in the repository will have the pH value ~ 10.5–11.5, but further redistribution of the substance under such conditions is not determined.

Thus, in spite of the prognostic estimation that does not show the destructive influence of the container shell on the physical and chemical properties of the buffer within 105 years, the phase transformation processes at the steel-bentonite interface should be taken into account when calculating the isolating characteristics of the buffer material. In particular the potential impact of ferrous aquaforms on the sorption centers of bentonite should also be considered during GR creation. But preliminary experimental results indicate that front of the ferrum transfer from the container surface will not penetrate deeply into the buffer for a long time. On the contrary, the corrosion process zone and formation of highly dispersed and sorption-active particles of ferric/ferrous hydroxides and oxides can play the role of effective sorbents and reducing agents (in the case of formation of Fe(II)-Fe(III) LDH and magnetite). This role helps to receive redox conditions aqua(hydroxo) forms of uranium (VI), plutonium, technetium, and selenium.

2.5 Conclusion

1. Bentonite clay that is usually used as a buffer material in the design of geological repository of radioactive waste can change its mineralogical-geochemical, geomechanical, and hydraulic properties under conditions of the repository evolution because of the influence of a number of factors that can significantly decrease the insulating properties of the buffer. Special attention is needed in the analysis of processes that take place at the interface between bentonite buffer and the surface of steel container. According to thermodynamic calculations, the most probable products of the mineralogical transformations in the disposal facility will be ferrum smectite (Fe-saponite), berthierine, or chlorite.
2. Due to the contact of bentonite buffer saturated by groundwater and the steel surface, mineralogical changes of bentonite can be directed to saponitization, beidellitization, or illitization. Whereas saponitization is not critical for buffer's isolating properties because of the saponite's ability to swell, the formation of beidellite may lead to critical decrease in insulating properties of the buffer.
3. One of the main processes that can become critical for bentonite's isolating properties is the illitization of montmorillonite. Its rate depends on temperature, chemical composition of the aqueous medium (pH value and concentration of alkaline cation, especially K^+), degree of bentonite saturation with water, and the ratio between dispersed phase and dispersion medium. While a preliminary estimate shows impossibility of buffer illitization due to low temperature, the usage of external building materials, in particular, cements, may shift the balance and causes transformation of bentonite into illite.
4. Preliminary studies have shown that diffusion of the ferrum-containing components into bentonite is limited to a few centimeters for a long time. Moreover, the formation of the primary ferrum-bearing structures such as Green Rust and ferrihydrite on the steel surface and their transformations into the sorption-active oxyhydroxides and oxides can become an additional mechanism for the fixation of radionuclide's mobile forms and their reduction into less mobile and toxic state.
5. In order to predict the long-term stability of the bentonite buffer and assess the safety of the storage facility, taking into account mineralogical-geochemical processes caused by corrosion of the container, and the possible transformation of bentonite buffer under conditions of the geological repository, the integral experimental research should be introduced into the future concept and program of creation of a geological repository in Ukraine. One of the important aspects of such study should be to analyze the phase formation processes at the steel-bentonite interface and to determine the effect of newly formed nanosized structures on the process of radionuclide migration and isolating properties of buffer material as well.

References

1. Lavrynenko OM, Prokopenko VA, Lebovka NI, Mamunia SV (2008) Colliid Journ 70(3), RU, 1–8
2. Chuhrov FV, Ermilova LP, Gorshkov AI et al (1975) Gipergennyie okislyi zheleza v geologicheskih protsessah, Nauka, Moskov, RU, 207 p
3. Holdberg VM, Skvortsov NP (1986) Pronitsaemost i filtratsiya v glinah, Nedra, Moskov, RU, 160 p
4. Drits VA, Kossovskaya AG (1990) Glinistyie mineralyi: smektityi, smeshanosloynyie obrazovaniya: Monografiya, Nauka, Moskov, RU, 214 p
5. Lavrynenko OM (2009) Nanostrukturnoe materialovedenie, № 3, RU, pp 15–40
6. Lavrynenko OM (2009) Nanostrukturnoe materialovedenie, № 4, RU, pp 16–53
7. Nanomineralogiya. Ultra- i mikrodispersnoe sostoyanie mineralnogo veschestva (2005) Nauka, St.Petersburg, RU, 581 p
8. Shabalin BH, Lavrynenko OM, Kosorukov PO, Buhera SP (2018) Mineral Journ, T. – №.4, Kyiv, UA, pp (in Print)
9. Bennett DG, Gens R (2008) J Nucl Mater 379:1–8
10. Burleson DJ, Penn RL (2006) Langmuir V(22):402–409
11. Abdelmoula M, Refait P, Drissi SH et al (1996) Corros Sci 38(4):623–633
12. Cornell RM, Schwertmann U (2003) The iron oxides: structure, properties, reactions, occurrence and uses/R. M. Cornell, U. Schwertmann 2nd ed. Wiley, Weinheim, 703 p
13. Corrosion and alteration of nuclear materials (2010) Paris: CEA. 160 p
14. Curti E, Wersin P (2009) Assessment of porewater chemistry in the bentonite backfill for the Swiss SF //HLW repository. Nagra. Technical report 02–09. 78 p
15. Benali O, Abdelmoula M, Refait P, Genin J-MR (2001) Geochim Cosmochim Acta 65(11):1715–1726
16. Lair V, Antony H, Legrand L, Chausse A (2006) Corros Sci. V 48:2050–2063
17. Flynn CM (1984) Chem Rev 84:31–41
18. Refait P, Benali O, Abdelmoula M, Genin J-MR (2003) Corr Sci 45:2435–2449
19. Fukaya Y, Akashi M (1999) Mat Res Symp Proc 556:871–878
20. disposal G (2014) A review of the development of bentonite barriers in the KBS-3V disposal concept. In: NDA technical note no. 21665941, p 84
21. Sumoondur A, Shaw S, Ahmed I, Benning LG (2008) Mineral Magazine 72(1):201–204
22. Ishikawa H, Shibata M, Fujita T (1994) Journal of the Clay Science Society of Japan., V 34:149–156
23. Kamei G, Yusa Y, Sasaki N (1992) Mater Res Soc Symp Proc., V 257:505–512
24. Karnland O, Olsson S, Nilsson U (2006) Mineralogy and sealing properties of various bentonites and smectite–rich clay minerals // SKB technical report TR-06-30
25. King F (2008) Corrosion of carbon steel under anaerobic conditions in a repository for SF and HLW in Opalinus Clay. Technical Report 08–12. Wettingen: Nagra, 44 p
26. King F, Kolar M (2009) Theory manual for the steel corrosion model version 1.0 Report No.: NWMO TR-2009-07
27. King F, Shoesmith DW (2010) In: Ahn J, Apted MJ (eds) Geological repository systems for safe disposal of spent nuclear fuels and radioactive waste. Woodhead Publishing Ltd, Cornwall, pp 379–420
28. Kumpulainen S, Kiviranta L, Carlsson T, Muurinen A, Svensson D, Sasamoto H, Yui M, Wersin P, Rosch D (2010) Long-term alteration of bentonite in the presence of metallic iron. // POSIVA.Working Report 2010-71. 98 p
29. Laine H, Karttunen P (2010) Long-term stability of bentonite: a literature review (working report 2010–53), Olkiluoto, Posiva OY, Finland, 132 p
30. Lavrynenko OM, Korol YaD, Netreba SV. Prokopenko VA (2010) Khimiia, fizyka ta tekhnolohiia poverkhni, T. 1, № 3, pp 338–342
31. Lewis DG (1997) Adv Geoecol 30:345–372

32. Meunier A, Velde B, Griffault L (1998) Clay Miner 33:187–196
33. NUMO. Proceedings of the International Workshop on Bentonite-Cement Interaction in Repository Environments 14-16 April 2004, Tokyo, Japan. NUMO Technical Report No. NUMO-TR-04-05
34. Pettersson S, Lönnerberg B (2008) International conference underground disposal unit design & emplacement processes for a deep geological repository. 6-18 June 2008, Prague, pp (20)1–12
35. Project Opalinus Clay Safety Report. Demonstration of disposal feasibility for spent fuel, vitrified high-level waste and long-lived intermediate-level waste. Technical report 02–05. Wettingen: NAGRA, 2002. 472 p
36. Ph R, Genin J-MR (1997) Corros Sci 39:539–553
37. Rodriguez MA (2014) JOM 66(3):503–525
38. Samper J, Lu C, Montenegro L (2008) PhysChemEarth 33:306–316
39. Schwertmann U, Cornell RM (2000) Compl. Rev. and Ext. Ed. Wiley-VCH, Weinheim, p 185
40. Schwertmann U, Fechter H (1994) Clay Miner,. V 29:87–92
41. Shestopalov VM, Shybetskyi IuA, Proskura MI, Zinkevich LI, Temny RG (2016) International approaches for nuclear waste disposal in geological formations: geological challenges in radioactive waste isolation—fifth worldwide review. Faybishenko B, Birkholzer J, Sassani D, Swift P, editors, LBNL-1006984, doi:https://doi.org/10.2172/1353043
42. SKB. Long-Term Safety for KBS-3 Repositories at Forsmark and Laxemar – a First Evaluation (Main Report of the SR-Can Project). SKB Technical Report TR-06-09. Svensk Kärnbränslehantering AB, Stockholm, Sweden. 2006
43. Smart NR, Blackwood DJ, Werme LO (2001) The anaerobic corrosion of carbon steel and cast iron in artificial groundwaters. SKB Technical Report TR-01-22; Smart RN, Rance AP, Werme LO (2004) MRS Symp Proc 807: 441–446
44. Genin J-MR, Abdelmoula M, Ch R, Ch U (2006) CRGeosci 338:402–419
45. Stammoze D, Vokal A (2012) Preliminary interpretation of experimental results on gas generation. FORGE Report D2.3-R, 34 p
46. Simon L, François M, Refait P, Renaudin G et al (2003) Sol St Sci 5(2):327–334
47. Tamura H (2008) Corros Sci,. V 50:1872–1883
48. Taniguchi N, Honda A, Ishikawa H (1998) MRS Symp Proc 506:495–501
49. The management system for the disposal of radioactive waste, 2008, IAEA safety standards series N°. GS-G-3.4, Vienna
50. Tronc E, Belleville P, Jolivet JP, Livage J (1992) Langmuir 8:313–319
51. Tripathy S, Thomas HR, Stratos P (2017) Geosciences 7(3):53–57
52. Trolard F (2006) Compt Rendus Geosci 338:1158–1166
53. Tsutomu S, Takashi M, Hiroshi I, Toshihiko O (1995) Mater Res Soc Symp roc 353:239–246
54. Turnbull A (2009) A review of the possible effects of hydrogen on lifetime of carbon steel nuclear waste canisters. Technical Report 09–04, Nagra, Wettingen, 51 p
55. Pozas R, Ocana M, Morales MP, Serna CJ (2002) J Coll Interf Sci 54:87–94
56. Wersin P, Birgersson M, Olsson S, Karnland O, Snellman M (2007) Impact of corrosion-derived iron on the bentonite buffer within the KBS-3H disposal concept – the Olkiluoto Site as Case Study, POSIVA. Working Report 2007-11, 78 p
57. Wersin P, Johnson LH, McKinley IG (2006) Phys Chem Earth Parts A/B/C 32(8–14):780–788
58. Wilson J, Cressey G, Cressey B, Cuadros J, Vala Ragnarsdottir K, Savage D, Shibata M (2006) Geochim Cosmochim Acta 70:323–336
59. Xu QF, Wang W, Pang XL et al (2014) Corrosion Eng Sci Technol. 49(6):480–484
60. Yoshikawa H, Gunji E, Tokuda M (2008) J Nucl Mater 379:112–117

Chapter 3
Development of a Controlled in Situ Process for the Formation of Porous Anodic Alumina and Al Nanomesh From Thin Aluminum Films

T. Lebyedyeva, M. Skoryk, and P. Shpylovyy

3.1 Introduction

The researches on the formation of porous anodic alumina (PAA) films for use of their nanoscale properties can be divided into two main areas: growing oxide on a bulk aluminum and foils and on films deposited onto the substrate. The development of technological processes of PAA creation on bulk aluminum usually presumes the improvement of methods of ordered structures creation with implementation of a two-stage process of anodizing. This is where significant success has already been achieved [1]. However, the method of growing of ordered PAA on deposited thin aluminum films is yet to be discovered. Only the processes of nanopore ordering for PAA on thin Al films by pre-texturing by special stamps can be considered as those that secured proved results [2]. The structural difference in PAA films, grown on the bulk aluminum (plates or folds) and on the deposited films of aluminum, is usually attributed to the fact that on contrary to the annealed and subjected to the electrochemical polishing surface of bulk aluminum, the surface of the deposited film has high surface roughness, and films themselves may be disordered small-grain structure with a considerable difference in grain sizes and a large number of randomly distributed inter-grain boundaries. Aluminum films produced under various conditions also differ from each other—according to structural parameters, density of grains packing, and average values of surface roughness [3–5].

Nevertheless there are a lot of publications devoted to the nanostructures on substrates of various materials, including semiconductors, metals, dielectrics, and

T. Lebyedyeva (✉) · P. Shpylovyy
V.M. Glushkov Institute of Cybernetics, National Academy of Sciences of Ukraine, Kyiv, Ukraine

M. Skoryk
NanoMedTech LLC, Kyiv, Ukraine
e-mail: skoryk@nanomedtech.com.ua

O. Fesenko, L. Yatsenko (eds.), *Nanocomposites, Nanostructures, and Their Applications*, Springer Proceedings in Physics 221,
https://doi.org/10.1007/978-3-030-17759-1_3

polymers that can be produced by anodic alumina nanopatterns. Among them aluminum nanomesh thin films (nano-sized networks non-anodized Al on a substrate) made by electrochemical anodizing and wet etching of porous anodic alumina have special importance as one of the promising candidates for transparent conductive layers (TCLs) which possess both high conductivity and high optical transparency [6–10].

Transparent conductive layers (TCLs) which possess both high conductivity and high optical transparency have many actual and potential applications. Areas of application are optoelectronics, plasmonics, biosensorics, and sources of "green energy." Transparent conducting electrodes are used in light-emitting and solar cells, different kinds of displays, touch screens, etc. [11–15]. Traditionally, films of conductive oxides are used. These are mainly indium tin oxide (ITO) as well as zinc and tin oxides, including doped ones [12, 13]. TCLs on conducting polymers have been also developed [15]. Alternative materials with new operational properties, structure, and morphology are also being searched [14–21]. Nanostructured metal-based thin films as metallic nanowires, metallic and hybrid nanogratings, and metal nanotrough networks are among these materials [19–22].

Aluminum nanomesh thin films made by electrochemical anodizing and wet etching of porous anodic alumina (PAA) are promising candidates for manufacturing of TCL [6–10]. Such Al nanomeshes are electrically conductive, optically transparent, and flexible. The size of the PAA cells and, accordingly, the cells of Al nanomesh can be varied in the range of 10 nm to 1000 nm by varying the electrolyte composition and the anodization regime. The uniform pores arrangement allows improvement of the optical and electrical performance up to ITO layers. The study has shown that the transparency of Al nanomesh on glass can be 10–90% and the conductivity 10–1000 Ω sq^{-1} for 400–800 nm wavelength [6, 10]. Such Al nanomesh can be used in next-generation optoelectronic devices—such as thin-film solar cells, touch screens, and flexible displays [6, 7]. In liquid crystal displays, a nanoset aluminum film can simultaneously be used as a TCL and an orienting surface for nematic crystals [8, 9].

To be widely applicable, the production of nanostructures should be inexpensive and compatible with industrial thin-film technology for manufacturing of optoelectronic devices. These requirements are met by a simple and cheap technology for the production of Al nanomesh from aluminum films deposited on glass, Si, and other substrates.

The possibility of forming Al nanomesh by anodic oxidation is closely related to the structural features of PAA. The nanostructured PAA (Fig. 3.1a) is ideally described as a honeycomb structure that consists of hexagonal cells of a D diameter. The relationship between cell size and anodization voltage can be expressed as a linear dependence $D = \lambda_D \bullet U$, where the coefficient λ_D is approximately 2.5 nm•V^{-1}. In the center of each cell is a pore of $d_p = \lambda_d \bullet U$, λ_d diameter, which equals approximately to 1.3 nm•V^{-1} [23, 24]. The bottom of the pore is separated from the aluminum base by a hemispherical layer of barrier oxide with a thickness h_b. The barrier layer thickness was found to be proportional to the anodizing voltage with a ratio of ~1.2 nm •V^{-1} [23, 24]. In practice, the geometric parameters of

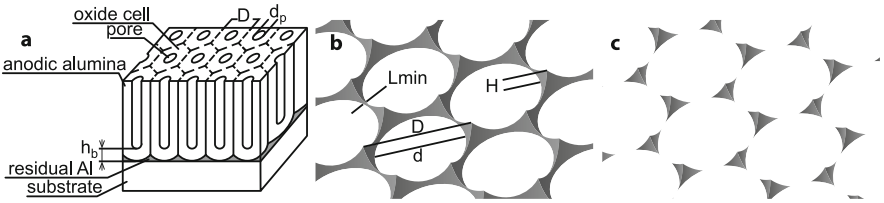

Fig. 3.1 Schematic representation of porous anodic alumina and nanostructures from residual aluminum on a substrate. (**a**) porous anodic alumina; (**b**) Al nanomesh; (**c**) Al nanoprism system

the PAA depend on the anodizing regime (the composition and temperature of the electrolyte, the current or voltage of the anodizing, the duration of anodizing) and aluminum purity [24–26].

The thickness of the walls and the bottom of the pores of the PAA can be reduced by chemical etching, forming the desired pore configuration, for example, for the further production of nanostructures by deposition into pores [27, 28]. It is possible to remove PAA completely and to form a nanostructured surface of aluminum with the purpose of, for example, carrying out the second stage of anodic oxidation [29]. The nanostructured aluminum surface at the oxide/metal interface is a set of concave hemispheres, i.e., has a relief surface with protuberances in the places where the PAA cells meet (Fig. 3.1a). If the formation of PAA is carried out from an aluminum film, then as the bottom surface of the PAA hemispheres reaches the substrate, a continuous aluminum film under the oxide is transformed into a porous aluminum mesh film [6–10]. Al nanomesh on the substrate can be formed by selective etching of the porous oxide (Fig. 3.1b) [6–10].

The size of the cells of Al nanomesh D is equal to the size of the PAA cells. The maximum height H of the aluminum is half the diameter of the PAA pore. The pore diameter d in Al mesh depends both on the anodization voltage and on its duration. The height and thickness of the aluminum mesh decrease as the diameter of the contact surface between the bottom of the PAA pore and the substrate increases during anodic oxidation [16]. By increasing the oxidation time, it is possible to form a nanostructure from individual aluminum nanopyramids (Fig. 3.1c), realized as aluminum hexagonal dot array [30]. Using the dependence of the geometrical parameters on the characteristics of the anodizing process, it is possible to control the morphology of the Al nanostructure and its electrical and optical characteristics [6–10].

The formation of conductive transparent Al nanomesh thin films on substrates includes the following processes (Fig. 3.2):

(a) Vacuum deposition of an aluminum film onto a substrate
(b) Anodic oxidation of the aluminum film to form a PAA (single-stage or two-stage) with stopping when the protruding parts of the anodization front reach the substrate
(c) Elimination of PAA by selective chemical etching

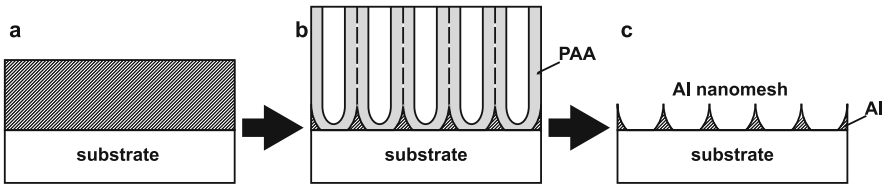

Fig. 3.2 Schematic depictions show the stages of preparing Al nanomesh thin films on the substrate. (**a**) deposited Al films on substrate; (**b**) PAA and Al nanomesh after anodic oxidation; (**c**) Al nanomesh after elimination of PAA by wet etching

The formation of an ordered Al nanomesh is a way of improving optic-electronic properties by minimizing the number of breakages in aluminum lines and the number of disconnected islands [10]. The homogeneity and ordering of Al nanomesh are determined primarily by the structure of the PAA.

The formation of PAA from deposited Al films differs from the formation of PAA on a massive metal (plate or foil). The structural difference between PAA films grown on massive aluminum and on deposited Al films is connected with differences in the structure of the anodized materials.

To form homogeneous ordered PAA on massive aluminum, annealed and electrochemically polished samples of high-purity aluminum, which have a structure of densely packed large grains and a smooth surface, are usually used. To obtain PAA with homogeneous ordered pores from a bulk aluminum, processes such as annealing of the initial material, electrochemical surface polishing, long anodizing time, and a two-stage anodic oxidation [24–30] are used. As a result of the application of these techniques on massive aluminum, PAA with pores of the same size and having an almost perfect hexagonal ordered structure were obtained.

The use of methods for ordering PAA on massive aluminum is often impossible to apply for deposited aluminum films because of their small thickness and structural features. Vacuum-deposited aluminum films have a granular structure with a considerable difference in sizes of grains and a large number of chaotically located grain boundaries. Their surface may have a high roughness. The density of the aluminum film, the grain size, the degree of randomness of the grain boundaries, and the surface roughness depend on the method and mode of deposition [4, 31–33].

Because of promising perspectives for ordered PAA on substrates to be used for the formation of various nanostructures, a lot of studies has been devoted to this issue [34–38]. The influence of the aluminum film structure on the growth of PAA is being studied. In order to increase the ordering of PAA on aluminum films, two-stage anodizing is sometimes being tried [35, 36, 42], but stable success has not been obtained in this direction so far. Preliminary texturing of the surface by ion beam etching through an electron beam lithography fabricated mask [40] or by transferring patterns from the hard master stamp onto the surface [2, 41] is being successfully applied.

An important point in the formation of PAA and especially Al nanomesh from deposited aluminum films is good adhesion to the substrate. It is necessary to prevent

Al peeling from the substrate during anodizing and etching. The transition metals, active to oxygen, usually Cr, Ta, or Ti [43], are used as an adhesive layer. The Nb layer can also serve as an excellent adhesive layer for thin aluminum films [5]. A careful study of thin Al/Nb films deposited by a magnetron showed that a continuous layer of aluminum is formed even at a 3 nm thickness due to the high affinity of aluminum to niobium [44].

Important issues in the production of Al nanomesh thin films are the control of the stopping time of the anodizing during the formation of Al nanomesh on a substrate and the control of the complete etching of the PAA. Therefore, it is desirable to find an in situ control method, at least for testing the technology. When Al nanomesh formed from Al film, the thickness of the PAA before etching is, as a rule, several hundred nanometers. The effective thickness of the remaining aluminum film lies in the nanometer range. Such thin-film structures of PAA-Al exhibit plasmon and/or waveguide properties. Similar structures served as the basis for the development of optical sensors on metal-clad waveguide (MCWG) with a porous sensor layer [45–48]. The method of optical control directly in the process of formation of the structures of PAA-Al, which comprises monitoring of the angular dependence of reflection on monochromatic light, was used by us earlier for MCWG PAA-Al production. It was used both for the formation of the PAA-Al structures by anodic oxidation and for the widening of pores by wet etching [47]. Since the angular dependencies of the reflection curves of the PAA-Al structures vary both with a change in the dielectric layer and with the slightest change in the thickness of Al, the method can be applied to control the etching of the PAA, as well as to control the remaining Al nanomesh.

This work is devoted to the development and investigation of in situ controlled process for the formation of Al nanomesh from thin aluminum films deposited by a direct current magnetron on glass substrates with an adhesive layer of Nb. In order to control in situ anodic oxidation processes during the formation of the PAA-Al nanomesh structure and the removal of PAA by etching, the method of monitoring of an angular reflection curves was applied. The obtained Al nanomesh was studied by the SEM method. Particular attention is paid to the connection between the features of the initial thin-film structures and the formed Al nanomesh.

3.2 Experiment

The plates of optical polished glass with $n_D = 1.609$, 20×25 mm in size, and 1 mm thick were used as substrates. The substrates were previously cleaned in chromic acid solution for 6 hours. After washing in deionized water, they were treated in the high-frequency oxygen plasma. Immediately prior to the deposition, the final cleaning of the substrate was carried out in the vacuum chamber by bombarding their surface with argon ions with an energy of 400 eV for 10 minutes. Adhesive layer of niobium with a thickness of 2–5 nm and aluminum films with a thickness of 340 nm were deposited in a vacuum chamber equipped with a turbomolecular

pump by magnetron sputtering at a constant current. Optimization of the deposition regime of aluminum films was carried out by us earlier [5]. The parameters related to the deposition of aluminum films are:

Target	Aluminum (99.999% purity)
Gas	Argon (99.95% purity)
Base pressure	$1 \cdot 10 - 6$ Torr
Argon pressure	$1.8 \cdot 10 - 3$ Torr
Substrate-to-target distance	45 mm
Deposition rate	1.1 nm/s

Anodic oxidation of aluminum films was carried out in a two-electrode cell. Anodization modes and control of chronometric dependencies were provided by means of a self-made computerized device. A vacuum-deposited gold film on a glass substrate served as the cathode. The formation of PAA was carried out in the potentiostatic regime, but in the beginning the oxide was grown in a constant current regime. The area for the formation of PAA (100 mm^2) was limited by a mask of photoresist. To avoid etching the aluminum surface in a photoresist developer, the mask was stamped. A 0.3 M solution of oxalic acid was used as the electrolyte. The electrolyte was stirred with a magnetic stirrer, and its temperature was 17 °C. The anodic oxidation was stopped when a sharp jump down appeared on the $I(t)$ curve. Angular reflection curves at a wavelength of 670 nm were monitored using the "Plazmontest" sensor device developed by us [47].

Then selective etching of PAA in an etchant composition of 10% H_3PO_4 + 2% CrO_3 at a temperature of 18 °C was carried out. The change in the reflection curves during etching of PAA was monitored with a self-made instrument providing a large range of light angles incidence.

Samples of aluminum films, PAA, and Al nanomesh have been studied by SEM Tescan Mira 3 LMU. Before the SEM investigations, the Au layer thickness of 8–10 nm was thermally evaporated in vacuum on the surface of the specimens to form a conducting film to avoid the charging problem.

3.3 Results and Discussion

The chronometric dependencies obtained during single-stage anodic oxidation of aluminum films with a thickness of 340 nm at a voltage of 40 V are shown in Fig. 3.3a, b. It is seen from Fig. 3.3b that the stationarity of PAA growth on an aluminum film of 340 nm thickness in this anodization regime is not achieved. We should note that on the curve $I(t)$ (Fig. 3.3b), when the anodization front approaches the substrate, there is always a smooth current drop (Sect. 3.1 on the insert), then a sharp current jump down (Sect. 3.2), and a further gradual decrease (Sect. 3.3). We believe that this jump is due to the fact that the anodization front has reached an

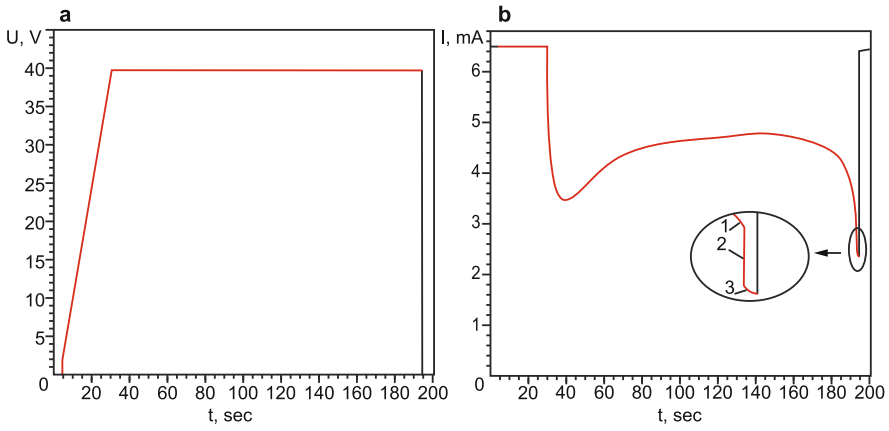

Fig. 3.3 Chronometric dependencies obtained during anodic oxidation of the Al (340 nm)/Nb (adhesive layer) thin-film structure on glass substrate. (**a**) voltage-time characteristic; (**b**) current-time characteristic

adhesive layer. This adhesive layer is probably a mixture of niobium and aluminum atoms due to metal interdiffusion, and it also may be partially oxidized prior to the deposition of aluminum because of the getter properties of niobium. The jump on the curve $I(t)$ we consider as a signal that continuous aluminum has been converted to nanoscale. Further, in the centers of the Al nanomesh cells, nanotips from a mixture of niobium and aluminum oxides are formed, and thinning of the Al lines continues. We stopped the anodizing, as soon as Sect. 3.2 appeared on curve $I(t)$. The decrease in current as the anodization front approaches the substrate occurs very rapidly, and it is difficult to control the time of anodization stoppage reproducibly. To ensure the steady-state growth of the PAA and to ensure the reproducibility of the stopping time, it seems that the anodizing temperature must be lowered.

The minimum angle on the reflection curve of the produced waveguide thin-film structures of PAA/Al was about 64 degrees (in water).

After thorough washing and drying of the samples, we carried out controlled etching of PAA. The control of PAA etching was made by a self-made computerized device with a light source of 670 nm wavelength, *p*-polarizer, and a photodiode. The range of light incidence angles of 40–68 degrees was provided by a stepping motor.

Figure 3.4a shows the scheme for measuring the reflection curves obtained by etching of PAA/Al nanomesh structures. The time interval between the reflection curves was 20 minutes (Fig. 3.4b). The initial curve 1 in Fig. 3.4b is a first-order waveguide mode of a thin-film structure of PAA/Al. In the etching process, the porous oxide layer is gradually etched and converted to a combination of a thin alumina barrier layer and/or PAA residues lying on the surface of the Al nanomesh. The waveguide minimum shifts to the left (curves 2, 3, 4) and gradually disappears, and in the viewing angle region, the left part of the SPR minimum appears (curve 5). When etching proceeds, curve 6 is formed from curve 5. Curve 6 corresponds to

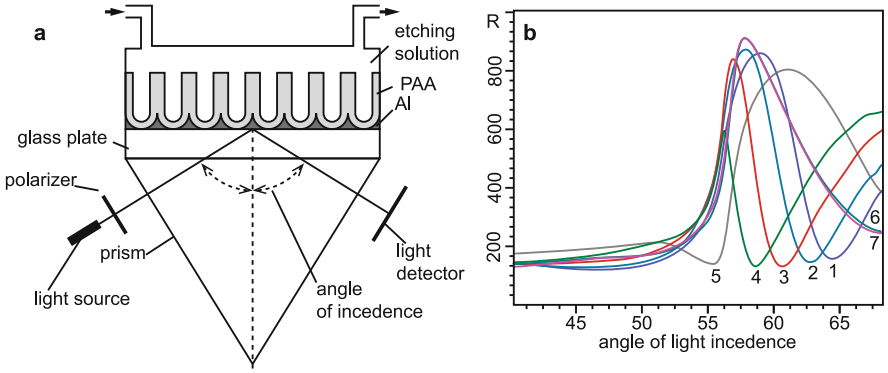

Fig. 3.4 Measurement of the reflection curves during the process of the etching of PAA-Al structure. (**a**) scheme of measurement; (**b**) the reflection curves obtained during the etching of PAA-Al structure

surface plasmon resonance on a nanoscale aluminum film. Due to the limited range of the device angles, we see only the left side of the SPR curve. The invariance of the SPR curve with further etching (curve 7 coincides with curve 6) indicates that PAA is completely etched away. There remained only Al nanomesh, which remained unchanged under this etching regime.

The measured sheet resistance values of such Al nanomesh samples were from 30 Ω/sq. to 45 Ω/sq.

The SEM images shown in Fig. 3.5a, b correspond to the reflection curves 1 and 8 in Fig. 3.4b, respectively. Figure 3.5a is the SEM of the PAA surface after the anodic oxidation. The inset in Fig. 3.5a shows the SEM surface of the original aluminum, which, according to [5], consists of a base aluminum film with protruding crystallites. On the surface of the PAA (Fig. 3.5a), small disordered pores partially covered with gold are seen both on the base surface and on the protruding crystallites. An image of the surface of the sample from which the PAA is etched away shows a surface of Al nanomesh (Fig. 3.5b). Most of the cells have a hexagonal shape, but there are also cells with 5 and 4 vertices. Size of the cells ranges from 90 nm to 120 nm. The nanostructure is heterogeneous, and the discontinuities of Al lines are visible in some places. The width of the aluminum lines is generally about 20 nm. A bright spot measuring 20–25 nm is at the center of almost every cell, apparently a gold-coated bump from an anodic niobium oxide (or a mixture of niobium and aluminum oxides).

SEM of various sections of Al nanomeshes produced from Al films on an adhesive sublayer of Nb are also shown in Fig. 3.6. Figure 3.6a, b correspond to homogeneous and inhomogeneous regions of the nanoscale of aluminum obtained from a film with a thickness of 340 nm. Figure 3.6c is an area of the nanoscale of aluminum obtained from an Al film with a thickness of 1000 nm with protruding crystallites.

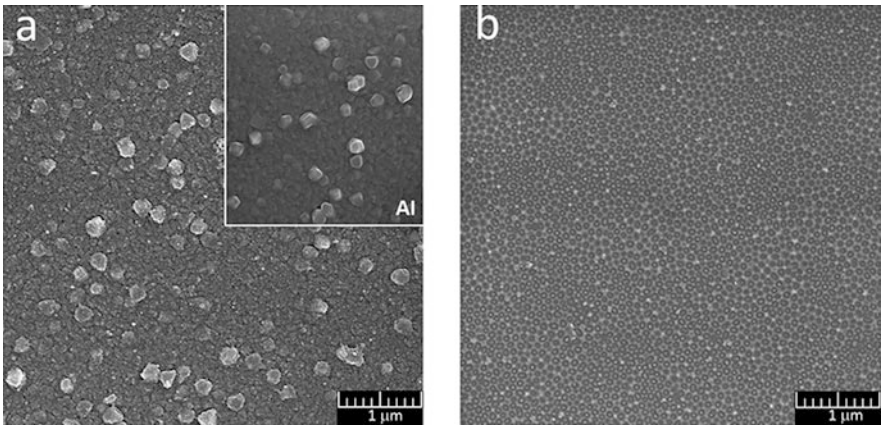

Fig. 3.5 SEM of the PAA and Al nanomesh surface. (**a**) PAA surface after anodic oxidation; (**b**) surface of Al nanomesh after etching of the PAA. The inset in (**a**) shows the surface of the initial aluminum film

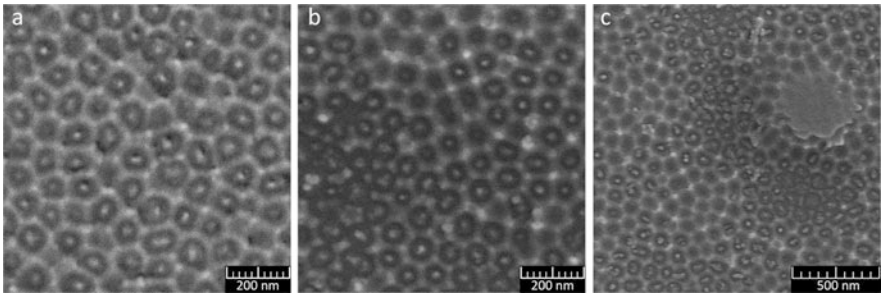

Fig. 3.6 Different sections of Al nanomesh produced from Al films on an adhesive sublayer of Nb. (**a**, **b**) Al nanoscale obtained from Al film with a thickness of 340 nm; (**c**) an area of Al nanoscale obtained from Al film with a thickness of 1000 nm

From the SEM data, we can see that the Al nanomesh reflects to a certain extent the structure of the aluminum film from which it was formed. Places with wider Al lines correspond to places of aluminum film of greater thickness. They are surrounded by the parts of the nanoscale with narrower lines, up to the line ruptures. It seems to us that there are so many reasons that can cause heterogeneity of the Al nanomesh.

First, an Al nanomesh with a nanometer thickness and a width of lines "reacts" to heterogeneity of the thickness of initial Al film. As it was shown earlier [5], the aluminum film (insert in Fig. 3.5a) contains above the "base" the aluminum film, protruding crystallites, and grooves at the grain boundaries. AFM analysis of the relief showed that the roughness of surface (RMS) is 3 nm, difference of the film thickness on areas between protruding crystallites is 10–15 nm, and height of big crystallites is 50–150 nm. The difference in the thickness of the Al film

leads to the fact that different sections of the anodization front reach the substrate not simultaneously. In places where the thickness of aluminum is less, the lower boundary of the barrier layer of PAA reaches the substrate earlier than in places with a greater thickness of aluminum. At these thinner places, formation of nanoscale from aluminum begins earlier. The height and thickness of the Al mesh decrease with the increase in the diameter of the bottom of the pore of the PAA and the substrate, i.e., they decrease with increasing the time of mesh formation [9]. The longer formation time of the nanoscale after touching the bottom of the pore of the cover leads to a thinning of the aluminum lines in places with a lower thickness of the aluminum film. In these places the breaks in the aluminum lines may appear until the anodization stops. As our studies have shown, an increase in the thickness of the initial aluminum film leads to an increase in the inhomogeneity of its thickness [5] and to an increase in the inhomogeneity of the Al nanostructure remaining after the formation of PAA. SEM of the area of Al nanomesh obtained from a film with a thickness of 1000 nm (Fig. 3.6c) clearly shows that the nanoscale formation on the big grain has not yet occurred, whereas around the Al grain, nanomesh already has breaks.

Second, it is likely that the local increase in temperature caused by the current flow in places where the Al nanoset is thinner can further accelerate the oxidation.

Third, the question of the relationship between the purity of aluminum into grains and on grain boundaries remains open, and the purity affects the formation of PAA and, consequently, Al nanoset.

Figure 3.7 shows a schematic representation of the cross section of the samples at different stages of production of Al nanomesh from an Al film on a thin Nb layer corresponding to the SEM images in Figs. 3.5 and 3.6. When drawing up the scheme, we relied on the results of studies on the formation of arrays of nanotips on thin-film Al-Nb structures [49–51]. They show that under the bottom of the pore of the PAA, oxidation of the underlying niobium without its contact with the electrolyte occurs due to the transfer of niobium ions and oxygen by an electric field through a layer of barrier alumina. The migration of O^{2-} and Nb^{5+} ions occurs in each pore along the narrow channel perpendicular to the surface of the substrate. Under the barrier alumina, niobium oxide (or a mixture of niobium and aluminum oxides) is formed, and the aluminum oxide is gradually dissolved. Since niobium oxide has less ion current resistance than alumina, the oxidation of niobium occurs faster than of the neighboring aluminum [49]. Thus, even a very thin adhesive sublayer

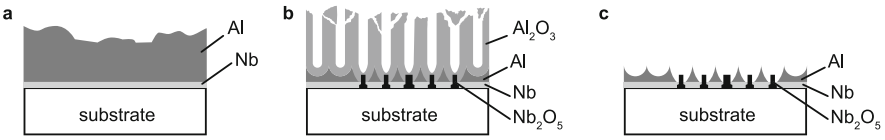

Fig. 3.7 Schematic representation of the cross section of the samples at different stages of fabrication of Al nanomesh from the Al film on the Nb sublayer. (**a**) Al film on Nb adhesive layer; (**b**) appearing of Nb oxide nanotips at the end of anodic oxidation; (**c**) Al nanomesh with Nb oxide nanotips after etching of PAA

of niobium can help preserve the nanoscale from aluminum until the oxidation of niobium under the bottom of the pore is complete.

3.4 Conclusions

An in situ controlled process for the formation of porous anodic alumina and Al nanomesh from thin aluminum films deposited by a direct current magnetron on glass substrates with an adhesive layer of niobium was developed. It was shown that the method of monitoring of the angular reflection curves can be successfully applied in situ not only for monitoring of the anodic oxidation and pore-widening processes in the formation of the structure of PAA-Al [47] but also for monitoring the etching of PAA in Al nanomesh formation.

SEM images of the obtained Al nano-networks show that most cells have a hexagonal shape. A bump from an anodic niobium oxide (or mixtures of niobium and aluminum oxides) is located in the center of almost every cell. We believe that, since the anodic oxidation of Nb occurs faster than that of the neighboring Al, the thin Nb sublayer not only increases the adhesion of aluminum to the substrate but can contribute to the preservation of Al nanomesh when it is formed by anodic oxidation of the aluminum film on the substrate.

Studies by SEM showed that the heterogeneity of the formed Al nanomesh is connected with the structural features of thin aluminum films containing protruding crystallites and cavities at the grain boundaries that disrupt the uniformity of the anodization front during the formation of PAA and Al nanomesh.

The homogeneity of anodic porous alumina and Al nanomesh, in our opinion, can be improved by increasing the uniformity of the thickness of Al films, possibly by precision electrochemical polishing and by using nanopatterning of the aluminum surface prior to anodizing. For the reproducibility of the moment when the formation of the Al nanomesh stops, work should be carried out to optimize the composition of the electrolyte and to decrease the anodic oxidation temperature.

References

1. Losic D, Santos A (2015) Nanoporous alumina: fabrication, structure, properties and applications, Springer Series in Materials Science, vol 219. Springer, Cham
2. Choi J, Nielsch K, Reiche M, Wehrspohn RB, Gosele U (2003) Fabrication of monodomain alumina pore arrays with an interpore distance smaller than the lattice constant of the imprint stamp. J Vac Sci Technol B 21:763–766
3. Ottone C, Laurenti M, Bejtka K, Cauda V (2014) Effects of the film thickness and roughness in the anodization process of very thin aluminum films. J Mater Sci Nanotech 1(1):1–9
4. Lita A, Sanchez JE (1999) Characterization of surface structure in sputtered Al films: correlation to microstructure evolution. J Appl Phys 85(2):876–882

5. Lebyedyeva T, Kryvy S, Lytvyn P, Skoryk M, Shpylovyy P (2016) Formation of nanoporous anodic alumina by anodization of aluminum films on glass substrates. Nanoscale Res Lett 11:203
6. Li Y, Chen Qiu M, Yu H, Zhang X, Sun XW, Chen R (2016) Preparation of aluminum nanomesh thin films from an anodic aluminum oxide template as transparent conductive electrodes. Sci Rep. https://doi.org/10.1038/srep20114
7. Kazarkin B, Mohammed AS, Stsiapanau A, Zhuk S, Satskevich Y, Smirnov A (2014) Transparent conductor based on aluminum nanomesh. J Phys Conf Series. https://doi.org/10.1088/1742-6596/541/1/012027
8. Smirnov A, Stsiapanau A, Mohammed A, Mukha E, Kwok HS, Murauski A (2011) Combined nanostructured layers for display applications. Proceedings SID symposium display week-2011 Los-Angeles, USA, pp 1385–1387
9. Dadivanyan AK, Belyaev VV, Chausov DN, Stepanov AA, Smirnov AG, Tsybin AG, Osipov MA (2015) Nanomesh aluminum films for LC alignment. Theoretical and experimental modeling. Mol Cryst Liq Cryst 611(1):117–122
10. Hubarevich A, Marus M, Stsiapanau A, Smirnov A, Zhao J, Fan W, Wang H, Sun X (2015) Transparent conductive nanoporous aluminium mesh prepared by electrochemical anodizing. Phys Status Solidi A Appl Mater Sci 212(10):2174–2178
11. Gao J, Kempa K, Giersig M, Akinoglu EM, Han B, Li R (2016) Physics of transparent conductors. Adv Phys 65(6):553–617
12. Stadler A (2012) Transparent conducting oxides – an up-to-date overview. Materials 5:661–683
13. Kumar A, Zhou C (2010) The race to replace tin-doped indium oxide: which material will win? ACS Nano 4:11–14
14. Ellmer K (2012) Past achievements and future challenges in the development of optically transparent electrodes. Nat Photon 6:809–817
15. Song TB, Li N (2014) Emerging transparent conducting electrodes for organic light emitting diodes. Electronics 3(1):190–204
16. Zhou Y, Azumi R (2016) Carbon nanotube based transparent conductive films: progress, challenges, and perspectives. Sci Technol Adv Mater 17(1):493–516
17. Park S, Vosguerichian M, Bao Z (2013) A review of fabrication and applications of carbon nanotube film-based flexible electronics. Nanoscale 5(5):1727–1752
18. Rana K, Singh J, Ahn JH (2014) A graphene-based transparent electrode for use in flexible optoelectronic devices. J Mater Chem C 4(2):2646–2656
19. Sannicolo T, Lagrange M, Cabos A, Celle C, Simonato JP, Bellet D (2016) Metallic nanowire-based transparent electrodes for next generation flexible devices: a review. Small 12(44):6052–6075
20. Guo C, Ren Z (2015) Flexible transparent conductors based on metal nanowire networks. Mater Today 18(3):143–154
21. Luo M, Liu Y, Huang W, Qiao W, Zhou Y, Ye Y, Chen LS (2017) Towards flexible transparent electrodes based on carbon and metallic materials. Micromachines 8(12):1–16
22. Wu H, Kong D, Ruan Z, Hsu PC, Wang S, Yu Z, Carney TJ, Hu L, Fan S, Cui Y (2013) A transparent electrode based on a metal nanotrough network. Nat Nanotechnol 8(6):421–425
23. Nielsch K, Choi J, Schwirn K, Wehrspohn RB, Gosele U (2002) Self-ordering regimes of porous alumina: the 10% porosity rule. Nano Lett 2:677–680
24. Sulka G (2008) Highly ordered anodic porous alumina formed by self-organized anodizing, Chapter 1. In: Eftekhari A (ed) Nanostructured materials in electrochemistry. Wiley-VCH, Weinheim
25. Zhang J, Kielbasa JE, Carroll DL (2010) Controllable fabrication of porous alumina templates for nanostructures synthesis. Mater Chem Phys 122:295–300
26. Abd-Elnaiem AM, Gaber A (2013) Parametric study on the anodization of pure aluminum thin film used in fabricating nano-pores template. Int J Electrochem Sci 8:9741–9751

27. Rahman M, Garcia-Caurel E, Santos A, Marsal LF, Pallarès J, Ferré-Borrull J (2012) Effect of the anodization voltage on the pore-widening rate of nanoporous anodic alumina. Nanoscale Res Lett 7(1):474
28. Sulka G, Zaraska L, Stępniowski W (2011) Anodic porous alumina as a template for nanofabrication. In: Nalwa HS (ed) Encyclopedia of nanoscience and nanotechnology, vol 11, 2nd edn. American Scientific Publishers, Stevenson Ranch, pp 261–349
29. Masuda H, Fukuda K (1995) Ordered metal nanohole arrays made by a two-step replication of honeycomb structures of anodic alumina. Sci 268(5216):1466–1468
30. Shingubara S, Murakami Y, Sakaue H, Takahagi T (2001) Formation of Al dot hexagonal array on Si using anodic oxidation and selective etching. Jpn J Appl Phys 41:L340–L343
31. Petrov I, Barna PB, Hultman L, Green JE (2003) Microstructural evolution during film growth. J Vac Sci Technol A 21(5):S117–S128
32. Bordo K, Rubanh HG (2012) Effect of deposition rate on structure and surface morphology of thin evaporated Al films on dielectrics and semiconductors. Mater Sci/Medziagotyra 18(4):313S
33. Her SC, Wang YH (2015) Temperature effect on microstructure and mechanical properties of aluminum film deposited on glass substrates. Indian J Eng Mat Sci 22:268–272
34. Lei Y, Cai W, Wilde G (2007) Highly ordered nanostructures with tunable size, shape and properties: a new way to surface nano-patterning using ultra-thin alumina masks. Prog Mater Sci 52:465–539
35. Chin IK, Yam FK, Chai Y, Hassan Z (2015) Comparative study of porous anodic alumina: effects of aluminium deposition methods. Mater Sci Technol 31(6):709–714
36. Upreti S, Mukherjee K, Palit M, Bag A, Mallik S, Chattopadhyay S, Maiti SK (2014) Porous anodic alumina template formation: deposition technique dependence. In: Physics of semiconductor devices. Springer, Cham, pp 725–728
37. Es-Souni M, Habouti S (2014) Ordered nanomaterial thin films via supported anodized alumina templates. Front Mater 1:1–9
38. Chu SZ, Wada K, Inoue S, Segawa HJ (2011) Direct growth of highly ordered crystalline zirconia nanowire arrays with high aspect ratios on glass by a tailored anodization. Electrochem Soc 158:148
39. Arslan HC, Yusufoglu I, Aslana MM (2014) Structural and optical characterizations of porous anodic alumina–aluminum nanocomposite films on borofloat substrates. Opt Eng 53(7):071822
40. Wang CE, Tanaka S, Saito K, Shimizu T, Shingubara S (2014) Fabrication of ordered arrays of anodic aluminum oxide pores with interpore distance smaller than the pitch of nano-pits formed by ion beam etching. J Mater Sci & Nanotech 1(1):1–6
41. Yasui K, Nishio K, Nunokawa H, Masuda H (2005) Ideally ordered anodic porous alumina with sub-50 nm hole intervals based on imprinting using metal molds. J Vac Sci Technol B 23:L9
42. Chahrour KM, Ahmed NM, Hashim MR, Elfadill NG, Maryam W, Ahmad MA, Bououdina M (2015) Effects of the voltage and time of anodization on modulation of the pore dimensions of AAO films for nanomaterials synthesis. Superlattice Microst 88:489–500
43. Foong TRB, Sellinger A, Hu X (2008) Origin of the bottlenecks in preparing anodized aluminium oxide (AAO) templates on ITO glass. ACS Nano 2(11):2250–2256
44. Imamura T, Hasuo S (1992) Fabrication of high quality Nb/AlOx/-Al/Nb Josephon junctions. II. Deposition of thin Al layers on Nb films. IEEE Trans Appl Supercond 2:84–94
45. Yamaguchi A, Hotta K, Teramae N (2009) Optical waveguide sensor based on a porous anodic alumina/aluminum multilayer film. Anal Chem 81(1):105–111
46. Hotta K, Yamaguchi A, Teramae N (2010) Properties of a metal clad waveguide sensor based on a nanoporous metaloxide/metal multilayer film. Anal Chem 82(14):6066–6073
47. Voitovich ID, Lebyedyeva TS, Rachkov OE, Gorbatiuk OB, Shpylovyy PB (2015) Anodic alumina-based nanoporous coatings for sensory applications. In: Fesenko O, Yatsenko L (eds) Nanoplasmonics, nano-optics, nanocomposites, and surface studies. Springer, Cham, pp 423–431

48. Biednov M, Lebyedyeva T, Shpylovyy P (2015) Gold and aluminum based surface plasmon resonance biosensors: sensitivity enhancement. Proceedings 9506, optical sensors 95061P. https://doi.org/10.1117/12.2177992
49. Surganov V, Gorokh G (2000) Array of niobium nanotips formed in porous anodic alumina matrix. Proc SPIE. https://doi.org/10.1117/12.382321
50. Mozalev A, Sakairi M, Saeki I, Takahashi H (2003) Nucleation and growth of the nanostructured anodic oxides on tantalum and niobium under the porous alumina film. Electrochim Acta 48(20):3155–3170
51. Mozalev A, Vázquez RM, Bittencourt C, Cossement D, Gispert-Guirado F, Llobet E, Habazaki H (2014) Formation–structure–properties of niobium-oxide nanocolumn arrays *via* self-organized anodization of sputter-deposited aluminum-on-niobium layers. J Mater Chem C 2:4847–4860

Chapter 4
Electrooxidation of Ethanol on Nickel-Copper Multilayer Metal Hydroxide Electrode

Antonina A. Maizelis

4.1 Introduction

The electrocatalytic oxidation of some alcohols is of great interest due to a wide range of application. The reaction is used not only in electrosynthesis of organic compounds but in direct alcohol fuel cells (DAFCs) too. Fuel cells require highly reactive fuels with high-energy density and low toxicity [1–4]. One of the key points to develop a cost-effective electrolysis is to decrease the cost of electrocatalysts for the oxidation. The commercial use of highly effective catalysts containing Pt and Pd is limited due to having high cost and global scarcity [5]. Alkaline electrolytes allow the use of inexpensive transitional metals and metal oxides. Such electrolytes have higher efficiency of both anodic and cathodic processes. There is almost no sensitivity to the surface structure and negligible poisoning effects in alkaline solutions [4].

Among the most promising alternative catalytic materials are cheap Ni-based catalysts having excellent electrochemical activity, stability, and high catalytic abilities toward the alcohol oxidation reaction [6–12]. The electrochemical behavior of electrode made of pure copper and other different copper-based composite electrodes has been studied toward alcohol oxidation in alkaline medium [2, 13, 14]. The copper-nickel alloy is proposed as potential substrate for production of anode component of fuel cells [15]. The methanol electrooxidation at the Ni-Cu alloy (40% Cu)-modified electrode was significantly larger than that at pure Ni [16–18].

To increase the surface area of electrode, the highly porous metallic nickel matrices as Raney electrodes, carbon-supporting materials such as graphene, carbon nanofibers (CNFs), mesoporous carbon, carbon nanotubes (CNTs), and

A. A. Maizelis (✉)
National Technical University "Kharkiv Polytechnic Institute", Kharkiv, Ukraine

O. Fesenko, L. Yatsenko (eds.), *Nanocomposites, Nanostructures, and Their Applications*, Springer Proceedings in Physics 221,
https://doi.org/10.1007/978-3-030-17759-1_4

noncarbonaceous-based materials such as hybrid supports materials and conducting polymers are proposed [5, 19, 20].

In this chapter the results of the study of catalytic activity of the multilayer nickel-copper metal hydroxide electrode with an electrochemically accessible developed surface is presented. Electrode coating was electrodeposited in polyligand pyrophosphate-ammonia electrolyte that allows to obtain multilayer nickel-copper coating with high adhesion to various substrates [21, 22], good mechanical properties [23, 24], and catalytic activity in the oxidation of methanol [25].

4.2 Experimental

Multilayer coatings were deposited in pyrophosphate-ammonia polyligand electrolyte containing 0.1 mol L^{-1} $CuSO_4 \cdot 5H_2O$, 0.5 mol L^{-1} $NiSO_4 \cdot 7H_2O$, 1.0 mol L^{-1} $K_4P_2O_7$, 4.0 mol L^{-1} ammonia as a mixture of 0.4 mol L^{-1} NH_4Cl, and 3.6 mol L^{-1} NH_4OH, pH 8.5. The counter electrode was combined of copper and nickel. The obtained multilayer coatings were tested in electrolyte containing 1 mol L^{-1} KOH and electrolyte additionally containing 0.5 mol L^{-1} ethanol. Electrochemical studies were carried out using potentiostat P-45X. The working electrodes were made of copper wire with an open surface area of 0.152 cm^2. The real surface area of the electrodes with and without coating in the stabilized oxidized state was determined by electrochemical double layer capacitance measurements using cyclic voltammetry (CVA) in 0.5 KOH by the method used in [26] taking in account for comparison the capacity of the oxidized metal surface as 60 mkF cm^{-2}. The counter electrode was made of platinum. A saturated silver/silver chloride electrode was used as the reference electrode.

4.3 Experimenal Results and Discussion

On the CVA curve (Fig. 4.1) on a platinum electrode (staring potentials scan in the cathode direction), there is a wave of limiting current of copper deposition (in the potential range of $-0.45 \ldots -0.85$ V). Then (in the potential range of $-1.19 \ldots -1.25$ V) a wave of limiting current of a nickel-copper alloy deposition appears. After it (under conditions of intensive hydrogen evolution), the copper and nickel hydroxy compounds as well as hydrides deposit with alloy. When scanning potentials in the anodic direction, the alloy deposition is facilitated due to both surface development and its enrichment with nickel. At the first peak of the anode branch of the CVA, the copper-rich phase dissolves from the deposit. Then nickel-rich phase dissolves in the second peak. The copper content in the coating (33%) was determined similarly to [27, 28] by the method of anodic voltammetry in an ammonia-glycinate electrolyte, which allows selective dissolution of copper and nickel.

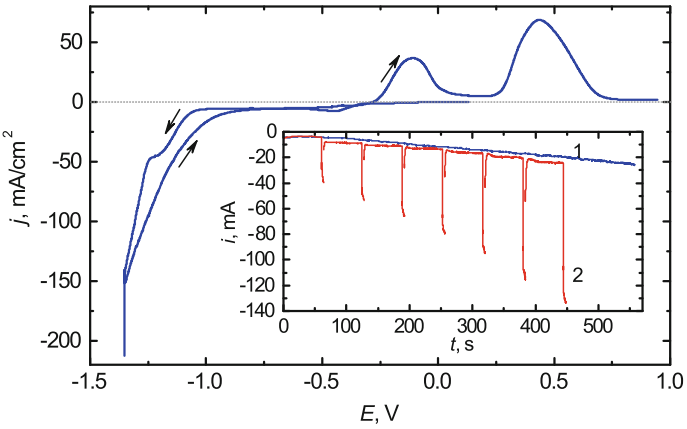

Fig. 4.1 CVA on Pt in pyrophosphate-ammonia electrolyte. Potential scan rate is $10\,\mathrm{mV\,s^{-1}}$. Insert: $E-t$ curves of Ni-Cu alloy coating deposition (1) at a potential of -1.175 V and NiCu(ML) coating deposition (2)

The multilayer nickel-copper metal hydroxide coating NiCu(ML) was formed by a two-pulse potentiostatic method with periodic potential change from -1.175 V (between two limiting currents on CVA Fig. 4.1) to -1.35 V (above the second wave). In this case the nickel-copper alloy layer is deposited at potential of -1.175 V, and the layer containing mixture of metals and its hydroxides is deposited at potential of -1.35 VV. Insert at Fig. 4.1 shows the chronoamperograms of multilayer coating deposition (curve 1) and nickel-copper alloy coating deposition at potential of -1.175 V (curve 1). The deposition current increases in both cases, indicating the increase in surface area of the samples during the deposition process both at potential of -1.35 V and at a potential of -1.175 V. Both coatings were deposited until the deposition current at potential of -1.175 V reached 24 mA. Therefore the samples with coating had approximately the same surface area available for deposition. The approximate calculated thickness of alloy layers varies from 430 to 110 nm. The thickness of metal hydroxide layers decreases from 260 to 40 nm during electrodeposition. For comparison, a sample with porous nickel coating electrodeposited in Watts bath was obtained.

After coating deposition all the samples were cycled in 1 M KOH solution (Fig. 4.2) in the range potentials corresponding to the reaction [6]:

$$Ni(OH)_2 \rightarrow NiOOH + H^+ + e^-. \tag{4.1}$$

The oxidation current in the first cycle at the initial section of anodic branch of CVA is much higher on the samples with alloy coating (curve 2) and multilayer coating (curve 1) than on nickel surface (curve 3) due to more active oxidation of copper in this region of potentials. The anodic peak of the first cycle is located at more positive potentials than the peaks of subsequent cycles on all samples. The

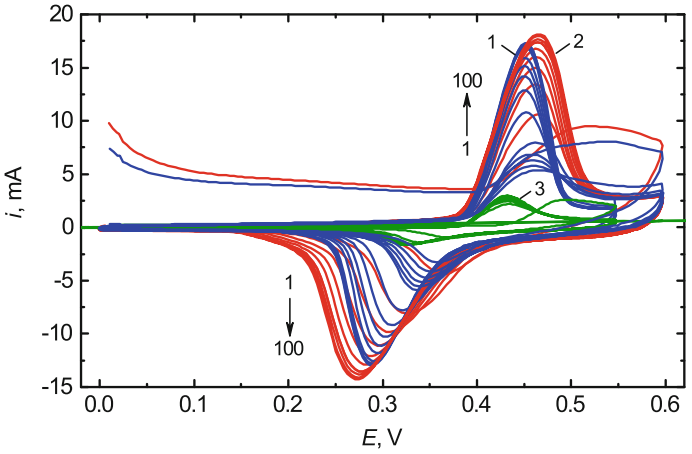

Fig. 4.2 CVA in 1 mol L^{-1} KOH on electrodes with NiCu(ML) (1), Ni-Cu alloy (2), and Ni (3) coatings. Potential scanning rate of 50 mV s^{-1}. Every 10th cycle is shown

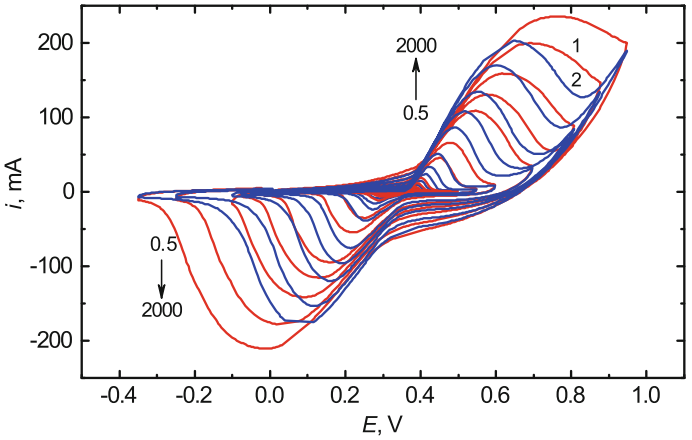

Fig. 4.3 CVA in 1 mol L^{-1} KOH on electrodes with NiCu(ML) (1) and Ni-Cu alloy (2) coatings

height of the anodic and cathodic peaks corresponding to the flow of reaction (1) in the cathodic and anodic directions increases. As the surface of the samples is saturated with active sites, the height of these peaks stabilizes. Further studies were performed on the stabilized surface of the electrodes. The real area of the stabilized surface of the electrodes, determined out of capacity value, was 5.0 and 5.26 cm^2 for samples with Ni-Cu alloy and NiCu (ML) coatings, respectively.

As the potential scan rate increases from 0.5 to 2000 mV s^{-1} (Figs. 4.3 and 4.4), the height of both the cathode and anode peaks increases. The potential difference between them also increases, indicating increase in the degree of irreversibility of redox processes on all investigated electrodes. The height of the peaks linearly

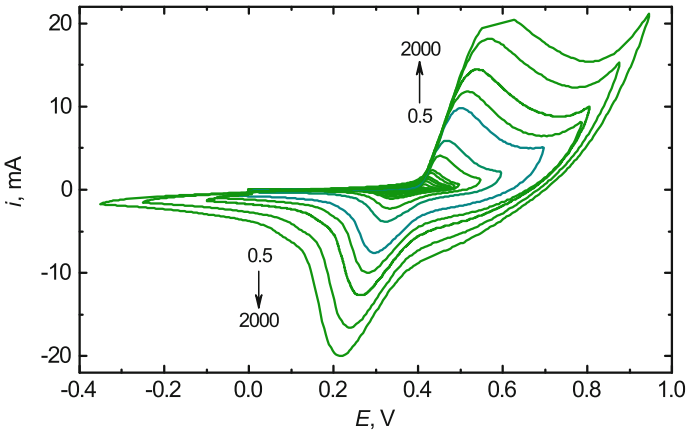

Fig. 4.4 CVA in $1\,\text{mol}\,\text{L}^{-1}$ KOH on electrode with Ni coating at potential scan rate of $0.5\ldots2000\,\text{mV}\,\text{s}^{-1}$

depends on the square root of the potential sweep rate, reflecting the contribution of proton diffusion (reaction Eq. (4.1)) to electrode reactions of nickel hydroxide oxidation and nickel oxyhydroxide reduction. Figure 4.5 shows CVA in the range of small values of potential scan rates (0.5–$40\,\text{mV}\,\text{s}^{-1}$). The surface of nickel is oxidized less actively than the surface of the alloy and multilayer coatings as the oxidation of surface starts at more positive potentials and the slope of the rising ascending branch is smaller. The peak currents i_p at low potential scan rates are proportional to the potential scan rate v. The surface coverage Γ^* of $Ni(OH)_2$/NiOOH redox species of electrode surface can be calculated using the slope of the $i_p - v$ dependencies by Eq. [29]:

$$i_p = (n^2F^2/4RT)vS\Gamma^*, \tag{4.2}$$

where n is number of transferred electron, F is Faraday constant, and S is apparent area of the electrode.

The surface coverage Γ^* of $Ni(OH)_2$/NiOOH redox species of the alloy and multilayer electrodes are 3.66×10^{-6} and $4.8 \times 10^{-6}\,\text{mol}\,\text{cm}^{-2}$ deriving from the average of the anodic and the cathodic results. The Γ^* of electrode with multilayer surface is 1.31 times higher than Γ^* of electrode with coating of alloy, though the real surface area is exceeded by only 1.05 times. The Γ^* value of the NiCu(ML) coating surface is about one order of magnitude higher as compared to the oxidized surface of porous nickel. It is higher as compared to other nickel-containing surfaces [4, 8], and it is at the level of the Γ^* value of the surface of Ni-B coating modified nanoporous Cu ($3.44\times10^{-6}\,\text{mol}\,\text{cm}^{-2}$, [6]).

When ethanol is added to the alkaline electrolyte a wave of ethanol oxidation (Fig. 4.6, curve 1') is observed in the region of nickel hydroxide oxidation potentials (curve 1). In the same potential region, the surface of the copper electrode (curve

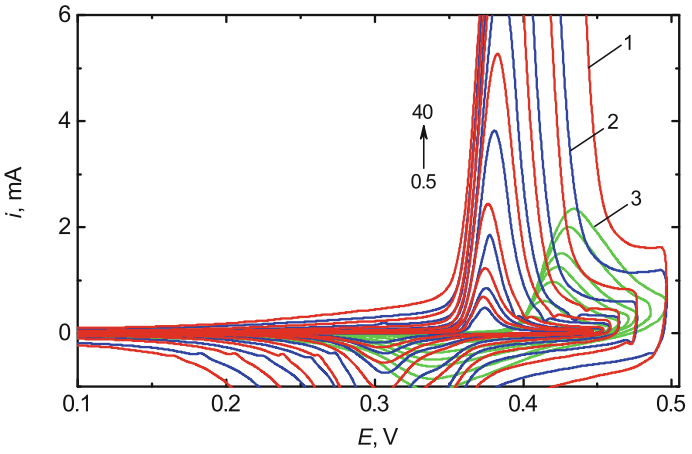

Fig. 4.5 CVA in 1 mol L^{-1} KOH on electrode with NiCu(ML) (1), alloy (2), and Ni (3) coatings, at potential scan rate of 0.0. . . 40 mV s^{-1}

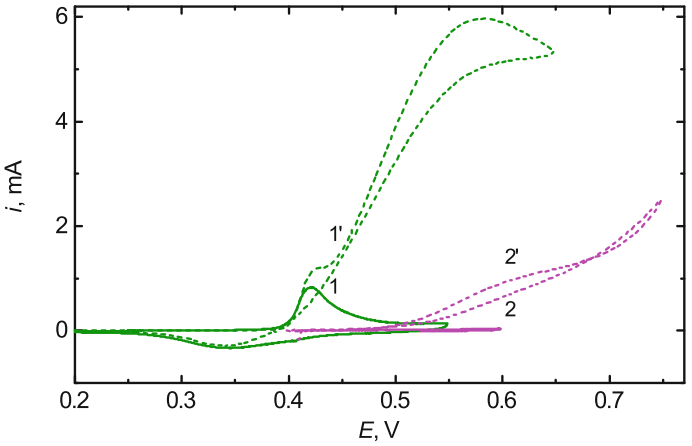

Fig. 4.6 CVA in 1 mol L^{-1} KOH (1, 2) and with the addition of 0.5 mol L^{-1} ethanol (1', 2') on copper (2, 2') and nickel-coated (1, 1') electrodes. Potential scan rate is 10 mV s^{-1}

2) practically does not show catalytic activity (curve 2'), though its geometric area (3.1 cm^2) exceeding the surface area of the studied electrodes by an order of magnitude, and the real surface area (4.8 cm^2) approximately equals the real surface area of the electrodes with Ni-Cu and NiCu(ML) coatings.

A NiCu(ML) coating shows higher catalytic activity as compared to the porous nickel coating (Fig. 4.7). As the potential scan rate increases, ethanol oxidation peak height decreases (Fig. 4.7a–e). Figure 4.7f shows the change in the coefficient k reflecting the relative increase in the ethanol oxidation peak height as compared to the anodic peak height of nickel hydroxide oxidation. A decrease in value of k

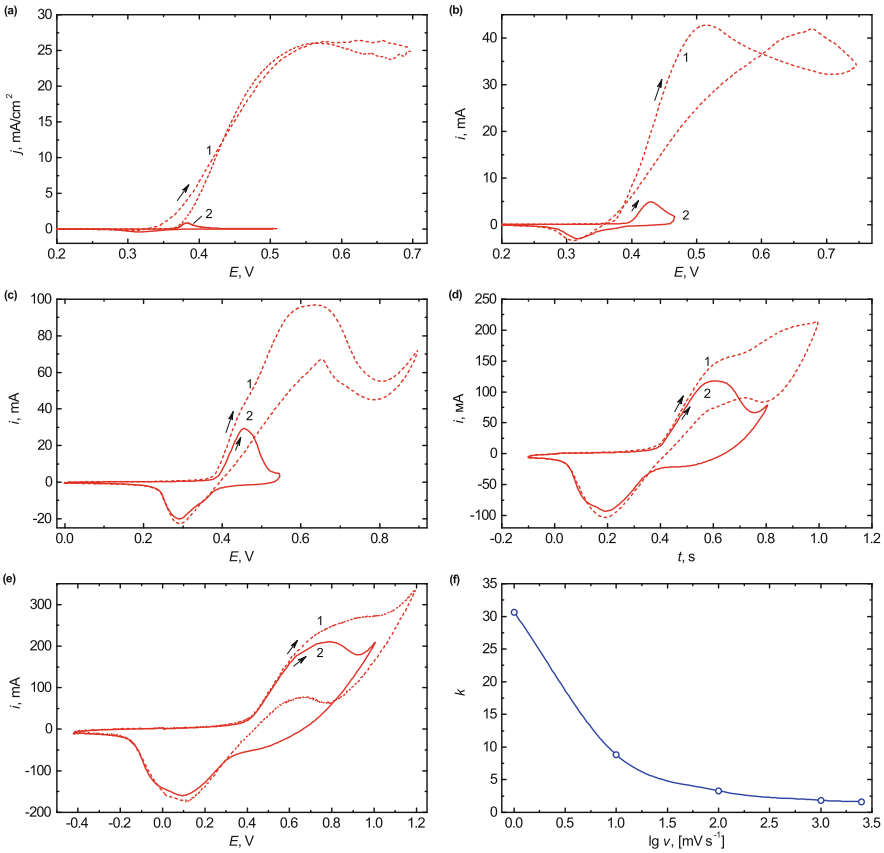

Fig. 4.7 CVA in 1 mol L^{-1} KOH (2) and with the addition of 0.5 mol L^{-1} ethanol (1) on electrode with NiCu(ML) coating at a potential scan rate of 1 mV s^{-1} (**a**), 10 mV s^{-1} (**b**), 100 mV s^{-1} (**c**), 1000 mV s^{-1} (**d**), 2500 mV s^{-1} (**e**); semi-logarithmic dependence (**f**) of the coefficient k (the ratio of the peak current of methanol oxidation to the peak current of nickel hydroxide oxidation) on the potential scan rate

with the increase in potential scan rate indicates slower ethanol oxidation reaction as compared to oxidation reaction of catalytically active surface.

The long-term studies of electrodes in alkali solution (Fig. 4.8, curves 1' and 2') show that the peak height of nickel hydroxide oxidation increases in the first cycles, but in alkaline solution containing alcohol (curves 1 and 2), the peak height of ethanol oxidation in the first cycles decreases. Further cycling in all cases leads to slight increase in peak height. Degradation of the electrodes was not observed. The coefficient k of the relative increase in ethanol oxidation peak height as compared to the peak height of nickel hydroxide oxidation of NiCu(ML) coating ($k = 3.3$) is higher than the value of k for a nickel-copper alloy coating ($k = 2.7$). This indicates

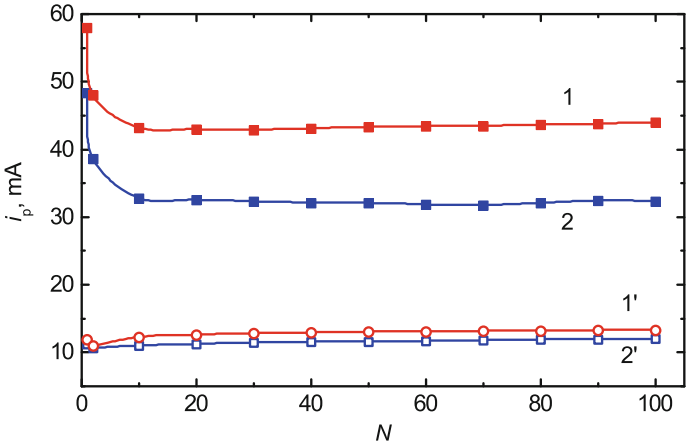

Fig. 4.8 Change in the anode peak current in 1 mol L^{-1} KOH (1', 2') and in 1 mol L^{-1} KOH with the addition of 0.5 mol L^{-1} ethanol (1, 2) when cycling in the potential range of 0.0…+0.7 V at the potential scan rate of 50 mV s^{-1}

a higher catalytic activity of the electrode with a multilayer coating as compared to the electrode with alloy layer.

4.4 Conclusions

A multilayer nickel-copper metal hydroxide electrode coating obtained from a polyligand pyrophosphate-ammonia electrolyte and consisted of alternating layers of nickel-copper alloy and a mixture of metals with hydroxides has higher developed surface, higher surface coverage of redox species, and higher catalytic activity as compared to alloy coating deposited from the same electrolyte.

References

1. Ong BC, Kamarudin SK, Basri S (2017) Direct liquid fuel cells: a review. Int J Hydrog Energy 42:10142–10157. https://doi.org/10.1016/j.ijhydene.2017.01.117
2. Bezghiche-Imloul T, Hammache-Makhloufi H, Aitahmed N (2016) Electrocatalytic oxidation of alcohols on Cu2O/Cu thin film electrodeposited on titanium substrate. Surf Rev Lett 23(5):1650041. https://doi.org/10.1142/S0218625X16500414
3. Barbosa AFB, Oliveira VL, van Drunen J, Tremiliosi-Filho G (2015) Ethanol electro-oxidation reaction using a polycrystalline nickel electrode in alkaline media: temperature influence and reaction mechanism. J Electroanal Chem 746:31–38. https://doi.org/10.1016/j.jelechem.2015.03.024

4. Ehsani A, Mahjani MG, Jafarian M, Naeemy A (2012) Electrosynthesis of polypyrrole composite film and electrocatalytic oxidation of ethanol. Electrochim Acta 71:128–133. https://doi.org/10.1016/j.electacta.2012.03.107
5. Zhang J, Li Q, Zhang J, Fan Y (2016) Advanced anode catalysts for direct alcohol fuel cells. In: Wang Y (ed) Nanomaterials for direct alcohol fuel cell. Pan Stanford Publishing, Singapore, pp 15–76
6. Zhang SJ, Zheng YX, Yuan LS, Zhao LH (2013) Ni-B amorphous alloy nanoparticles modified nanoporous Cu toward ethanol oxidation in alkaline medium. J Power Sources 247:28–436. https://doi.org/10.1016/j.jpowsour.2013.08.129
7. Nikiforova TG, Stepanova AA, Datskevich OA, Maleev VV (2013) Porous nickel deposits formed in the oxidation of alcohols in an alkaline medium. Rus J Appl Chem 86(11):1713–1718. https://doi.org/10.1134/S107042721311013X
8. Hassan HB, Hamid ZA (2011) Electrodeposited Ni-Cr2O3 nanocomposite anodes for ethanol electrooxidation. Int J Hydrog Energy 36(8):5117–5127. https://doi.org/10.1016/j.ijhydene.2011.01.024
9. Li YS, Zhao TS, Liang ZX (2009) Performance of alkaline electrolyte-membrane-based direct ethanol fuel cells. J Power Sources 187(2):387–392. https://doi.org/10.1016/j.jpowsour.2008.10.132
10. Kim JW, Park SM (2005) Electrochemical oxidation of ethanol at nickel hydroxide electrodes in alkaline media studied by electrochemical impedance spectroscopy. J Korean Electrochem Soc 8(3):117–124. https://doi.org/10.5229/JKES.2005.8.3.117
11. Kim JW, Park SM (2003) In situ XANES studies of electrodeposited nickel oxide films with metal additives for the electro-oxidation of ethanol. J Electrochem Soc 150(11):E560–E566. https://doi.org/10.1149/1.1613671
12. Sincheskul A, Pancheva H, Loboichenko V, Avina S, Khrystych O, Pilipenko A (2017) Design of the modified oxide-nickel electrode with improved electrical characteristics. East Eur J Enterp Technol 5(6):23–28
13. Heli H, Jafarian M, Mahjani MG, Goba F (2004) Electro-oxidation of methanol on copper in alkaline solution. Electrochim Acta 49:4999–5006. https://doi.org/10.1016/j.electacta.2004.06.015
14. Yuan LS, Zheng YX, Jia ML, Zhang SJ, Wang XL, Peng C (2015) Nanoporous nickel-copper-phosphorus amorphous alloy film for methanol electro-oxidation in alkaline medium. Electrochim Acta 154:54–62. https://doi.org/10.1016/j.electacta.2014.12.055
15. Sen Gupta S, Mahapatra SS, Datta J (2004) A potential anode material for the direct alcohol fuel cell. J Power Sources 131:169–174. https://doi.org/10.1016/j.jpowsour.2004.01.009
16. Antolinia E, Gonzalez ER (2010) Alkaline direct alcohol fuel cells. J Power Sources 195:3431–3450. https://doi.org/10.1016/j.jpowsour.2009.11.145
17. Danaee I, Jafarian M, Forouzandeh F, Gobal F, Mahjani MG (2008) Electrocatalytic oxidation of methanol on Ni and NiCu alloy modified glassy carbon electrode. Int J Hydrog Energy 33:4367–4376. https://doi.org/10.1016/j.ijhydene.2008.05.075
18. Jafarian M, Moghaddam RB, Mahjani MG, Gobal F (2006) Electro-catalytic oxidation of methanol on a Ni-Cu alloy in alkaline medium. J Appl Electrochem 36(8):913–918. https://doi.org/10.1007/s10800-006-9155-6
19. Jin GP, Ding YF, Zheng PP (2007) Electrodeposition of nickel nanoparticles on functional MWCNT surfaces for ethanol oxidation. J Power Sources 166(1):80–86. https://doi.org/10.1016/j.jpowsour.2006.12.087
20. Zhang S, Zheng Y, Yuan L, Wang X, Zhao L (2014) In situ synthesis of nickel-boron amorphous alloy nanoparticles electrode on nanoporous copper film/brass plate for ethanol electro-oxidation. Int J Hydrog Energy 39(7):3100–3108. https://doi.org/10.1016/j.ijhydene.2013.12.116
21. Maizelis AA, Tul'skii GG, Bairachnyi VB, Trubnikova LV (2017) The effect of ligands on contact exchange in the NdFeB-Cu^{2+}-$P_2O_7^{4-}$-NH_4^+ system. Russ J Electrochem 53(4):417–423. https://doi.org/10.1134/S1023193517040085

22. Fletcher S, Halliday CS, Gates D, Westcott M, Lwin T, Nelson G (1983) The response of some nucleation/growth processes to triangular scans of potential. J Electroanal Chem Interfacial Electrochem 159(2):267–285. https://doi.org/10.1016/S0022--0728(83)80627-5
23. Maizelis AA, Bairachniy BI, Trubnikova LV, Savitsky BA (2012) The effect of architecture of the Cu/(Ni-Cu) multilayer coatings on their microhardness. Funct Mater 19(2):238–244
24. Maizelis AA, Bairachniy BA (2017) Copper nucleation on nickel from pyrophosphate-based polyligand electrolyte. In: International conference on nanotechnology and nanomaterials. Springer, Cham, pp 443–457. https://doi.org/10.1007/978-3-319-92567-7_28
25. Maizelis A, Bairachniy B (2016) Electrochemical formation of multilayer metal and metal oxide coatings in complex electrolytes. In: International conference on nanotechnology and nanomaterials. Springer, Cham, pp 557–572. https://doi.org/10.1007/978-3-319-56422-741
26. Gira MJ, Tkacz KP, Hampton JR (2016) Physical and electrochemical area determination of electrodeposited Ni, Co, and NiCo thin films. Nano Convergence 3(1):6. https://doi.org/10.1186/s40580-016-0063-0
27. Maizelis A, Bairachny B (2017) Voltammetric analysis of phase composition of Zn-Ni alloy thin films electrodeposited from weak alkaline polyligand electrolyte. J Nano-Electron Phys 9(5):1–7. https://doi.org/10.21272/jnep.9(5).05010
28. Maizelis A (2017) Voltammetric analysis of phase composition of Zn-Ni alloy thin films electrodeposited under different electrolyze modes. In: IEEE 7th international conference on nanomaterials: applications and properties 02NTF13. IEEE. https://doi.org/10.1109/NAP.2017.8190373
29. Bard AJ, Faulkner LR (2005) Electrochemical methods, fundamentals and applications. Chemical Industry Press, Beijing, p 409

Chapter 5
Metal Surface Engineering Based on Formation of Nanoscaled Phase Protective Layers

V. M. Ledovskykh, Yu. P. Vyshnevska, I. V. Brazhnyk, and S. V. Levchenko

5.1 Introduction

Surface engineering for obtaining nanoscale protective and functional coatings with enhanced properties constitutes a multidiscipline challenge and requires combination of fundamental knowledge from different areas, including electrochemistry, physics of condensed matter, and chemistry of nanoscaled systems. One of the approaches for implementing such surface modification is the purposeful engineering of the specific conditions and utilization of spontaneous processes including the process of metal ionization in a controlled manner to achieve the formation of coatings with desired structure, thickness, morphology, and alignment.

Over a past decade, the theoretical models that represent the mechanism of action of the inhibitive additives on the dissolution and degradation processes of the metal surface in different media have been significantly improved. For the additives that are capable of forming slightly soluble compounds with the metal ions, the modern models predict the formation of thin phase layers on the metal surface. Such layers may serve as protective, functional, or multifunctional coatings, while their composition, structure, and morphology may be adjusted in a wide range by tuning the additive concentrations and engineering favorable conditions and deposition

V. M. Ledovskykh · S. V. Levchenko
National Aviation University, Kyiv, Ukraine

Yu. P. Vyshnevska (✉)
National Technical University of Ukraine “Igor Sikorsky Kyiv Polytechnic Institute”, Kyiv, Ukraine

Institute for Renewable Energy NAS of Ukraine, Kyiv, Ukraine

I. V. Brazhnyk
Gimasi SA Ukraine R&D Centre, Via Luigi Lavizzari, Mendrisio, Switzerland

O. Fesenko, L. Yatsenko (eds.), *Nanocomposites, Nanostructures, and Their Applications*, Springer Proceedings in Physics 221,
https://doi.org/10.1007/978-3-030-17759-1_5

regime. Of particular interest are the binary inhibitive mixtures that include additives of different nature and mechanism of action that demonstrate extremely protective efficiency. At the same time, the complete theoretical representation for combined action of the individual inhibitive and modification mixture components on the formation of phase protective layers in such multicomponent systems to date has not been proposed.

In this work, the influence of concurrent and complement effects within inhibitive mixtures on the thickness, structural parameters, and barrier properties of the obtained coatings has been investigated.

5.2 Materials and Experimental Methods

Individual inhibitors and their binary compositions based on XO_n^- anions, and based on anions, that may form the slightly soluble salts with Fe^{2+} cations (SiO_3^{2-} and polyhexametylene guanidine (PHMG)), for inhibiting the carbon steel corrosion in neutral media, are investigated. Aqueous saline solutions have the following composition: 0.3 g/l NaCl, 0.3 g/l Na_2SO_4, and 0.3 g/l $NaHCO_3$.

Determination of the inhibitor efficiency was performed gravimetrically according to the standard procedure. Exposure time at 25 °C temperature of carbon steel 08kp in neutral solutions was 168 h. The ratio of the solution volume (ml) to the area of metal sample (cm^2) was 10:1. The inhibition efficiency was determined by the equation $Z = \left[\left(K_m - K_m^{'}\right)/K_m\right] \cdot 100\%$ and the inhibition coefficient by the equation $\gamma = K_m/K_m^{'}$, where K_m, $K_m^{'}-$ is the corrosion rate of metal in solutions without and with inhibitor ($K_m = \Delta m/(S \cdot \tau)$, where Δm is the loss of the sample weight, g; S is the sample area, m^2; and τ is the exposure time, h).

Polarization measurements were carried out in the potentiostatic regime in a three-electrode cell with separated cathodic and anodic compartments. Carbon steel 08kp was used as the working electrode, platinum as the counter-electrode, and an Ag|AgCl|KCl (sat.) electrode as the reference one. In this paper, the potential values are given with respect to the normal hydrogen electrode potential.

Investigation of the morphological characteristics and elemental composition of the surface protective films of the inhibitive compositions and distribution of elements into the phase film were carried out with the scanning electron microscope (EVO-50, Zeiss, Germany) equipped with the energy-dispersive detector (INCA PENTA FET × 3, Oxford Instruments, Co., UK) and using Auger microprobe JAMP-9500F in the scanning electron microscopy mode. The energy of the electron beam was 3 keV and the current was 0.5 μA. During the profiling, the surface of the samples was bombarded with argon ions (ion etching) with an energy of 4 keV. The pickling rate is 40 Å/min.

5.3 Results and Discussion

Formation of phase layers on a metal surface is extensively used for metal protection. In particular, such mechanism is utilized by the passivation-type inhibitors for protection of steel in aqueous saline solutions where the dissolved molecular oxygen is found to be the main corrosive agent. Due to a possibility of direct and lateral depolarizer transport toward the metal surface, the inhibition of the cathodic reduction reaction may be complicated to be achieved in practice. For this reason, passivators mainly target the anodic reaction of metal ionization via formation of phase protective films on the metal surface.

In most cases, the mechanism implies the formation of the protective oxide layers (oxide passivation) or deposition of slightly soluble salts in a form of a dense film that blocks the metal surface (salt passivation). The first group includes oxyanions XO_n^- (nitrites, clorates, chromates, and others), while the second group may be illustrated with silicates, phosphates, as well as guanidine derivatives that may form slightly soluble complex salts with iron cations [1–6].

Protective efficiency may be further improved via development of inhibitive mixtures that utilize synergistic effects within its individual components wherein the optimal concentration ratio virtually complete protection can be achieved [7–10]. Extremely high protective efficiency combined with the ability to control the composition of the formed phase layers by optimizing the mixture components and concentration ratio predetermines the expediency of in-depth research for building theoretical representation of the processes and regularities of synergistic phenomena in such multicomponent systems.

The thermodynamic approach for analysis of redox transformations of the reagents and products is the key for understanding the reaction mechanism in studied multicomponent systems. The Pourbaix diagram [11] for the Fe-H_20 system (Fig. 5.1) provides an ability to determine the conditions for the formation of oxide films on the metal surface depending on the electrode potential of possible equilibria and pH value of the medium.

The pH value of the blank solution greatly affects the state of the system and in particular the metal surface. In the case of a shift above pH 9 and crossing the *line 7* of the diagram, the system is being transferred from the hydrated Fe (II) ions toward the hydrated iron (II) hydroxide according to the following reaction:

$$Fe^{2+} + 2H_2O = Fe(OH)_2 + 2H^+$$

SEM images confirm the significant morphology changes caused by the oxide films formed under different pH conditions in blank solution (Figs. 5.2 and 5.3). Thus, pH 9 constitutes the hydrogen value of hydrate formation for iron (II) that is a thermodynamically stable form under these conditions. This is found to be in a good agreement with elemental composition of the surface layer that contains a significant amount of oxygen and delivers very slight reduction in the corrosion rate owing to deceleration of the anodic reaction of metal ionization. This is also in line

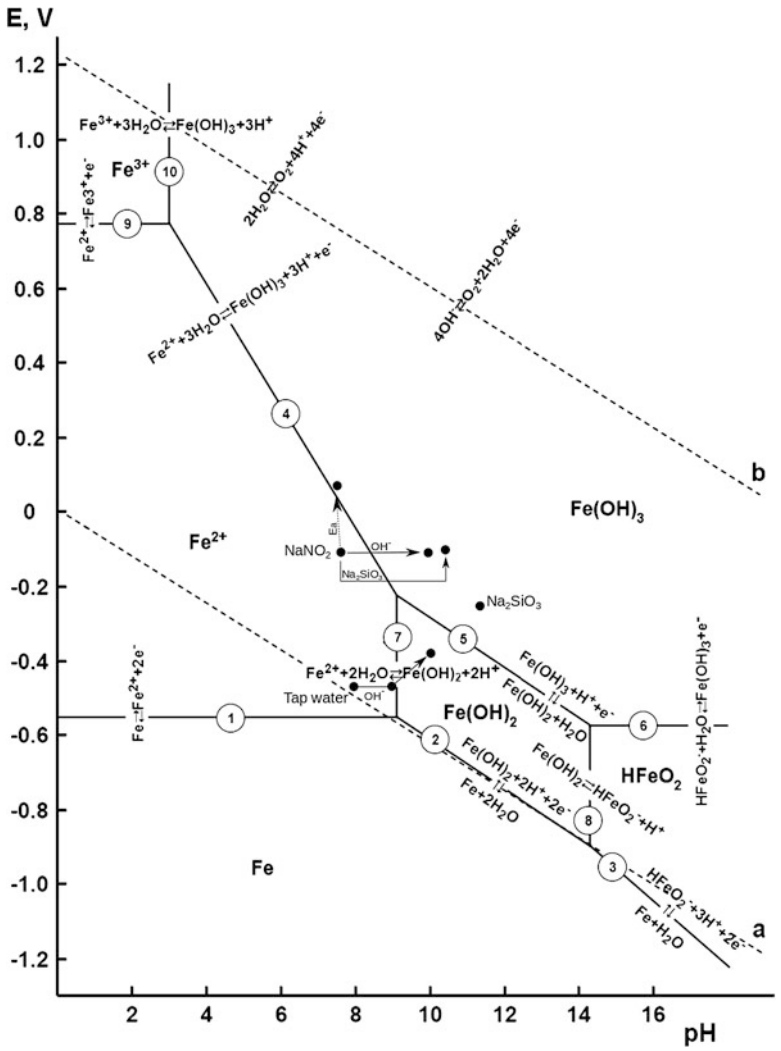

Fig. 5.1 Pourbaix diagram of the Fe-H_2O system

with Evans and Rozenfeld representation that casted a doubt on the possibility of achieving the efficient passivation of steel using deposited iron (II) hydroxides [1].

Oxyanions with oxidative action like NO_2^- have the active electron pair on the sp^2−hybridized orbital on the central nitrogen atom that results in its adsorption properties on the metal surface.

This representation is supported by the fact that the nitrate ion, despite being coordinated analogue virtually, does not affect the corrosion process due to lack of such electron pairs [6].

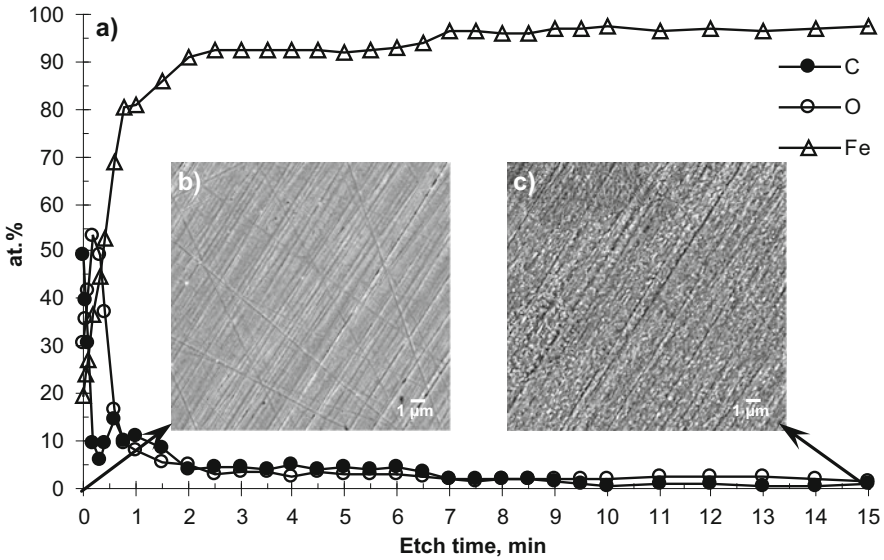

Fig. 5.2 Elemental composition of the surface of an unexposed sample obtained using Auger spectroscopy with ion etching against etching time (**a**) and surface morphology before (**b**) and after etching (**c**)

Infusion of NO_2^- to neutral aqueous saline solution leads to a shift of the steel corrosion potential toward a positive direction from $E_{corr} \cong -0.42$ V to -0.1 V and decrease in the corrosion rate due to inhibition of anodic reaction (Fig. 5.4). At the same time, the additive virtually does not affect the kinetics of the cathodic reaction while the anodic process of metal ionization remains in active area (Figs. 5.1 and 5.4).

Under these conditions, the morphology studies show generally a uniform film structure with marked signs of local corrosion damage (Fig. 5.5), while the ion etching of the surface show the presence of a nanoscale protective layer with typical thickness of 15–20 nm (Fig. 5.6).

The presence of nitrite ions has been confirmed using Auger spectroscopy that showed presence of 4% of nitrogen within a surface layer of the sample (Fig. 5.6). The surface profiling using ion etching showed sharp decrease in nitrogen concentration falling to zero levels after 1 min of etching that is also in line with theoretical expectations (Fig. 5.6).

It should also be noted that the morphology of the support plate under a protective layer is greatly affected by the film formation process during exposition (Fig. 5.6b). Figure 5.3c shows a typical phase domain structure after removing the surface layer using ion etching. In contrast, the morphology of the support plate after etching of the film formed in the presence of $NaNO_2$ shows a marked relief structure with a partially nonlinear pattern that does not match typical signs of mechanical treatment. Such results also could not be explained by the assumption that the

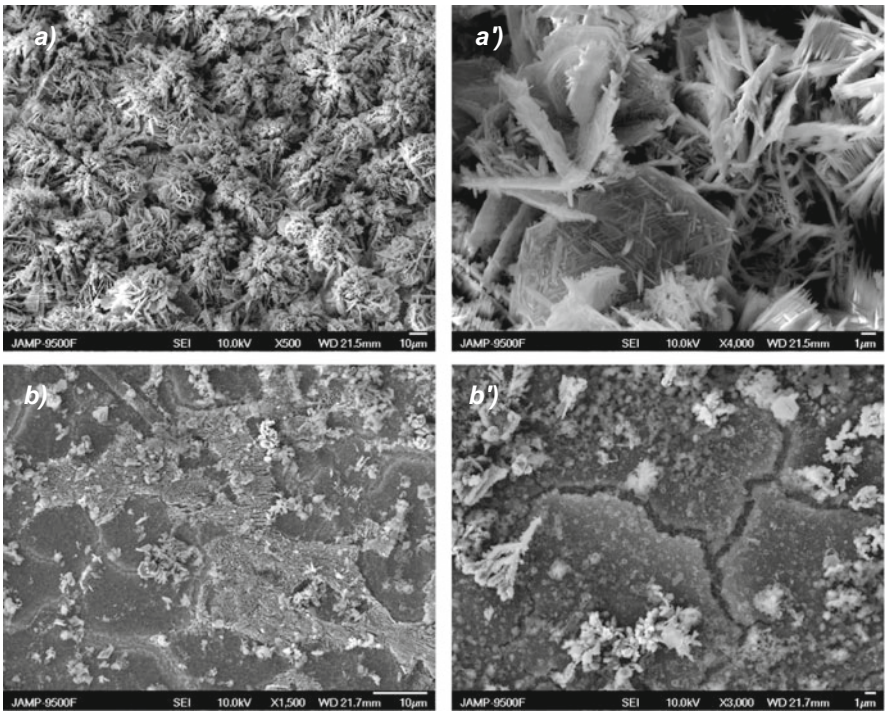

Fig. 5.3 Sample morphology: (***a, a′***) after 168 h exposition in blank solution at pH 7.3, (***b, b′***) after 168 h exposition in blank solution at pH 10

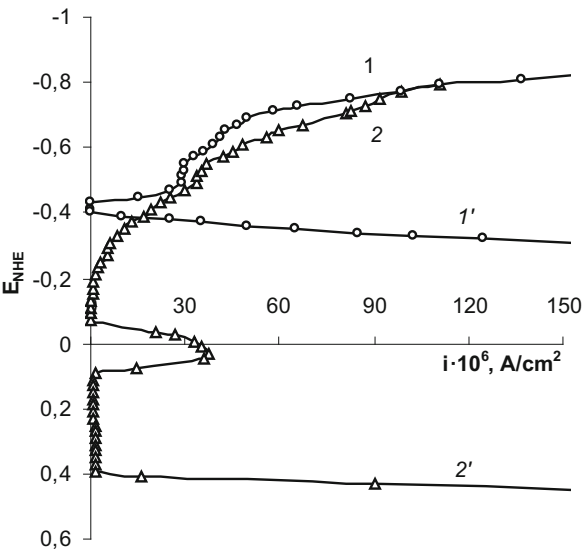

Fig. 5.4 Cathodic (1, 2) and anodic (*1′*, *2′*) polarization curves for carbon steel in *1, 1′*, background aqueous saline solution; *2*, *2′*, in the presence of $NaNO_2$ (30 mmol/l) at pH 7.38

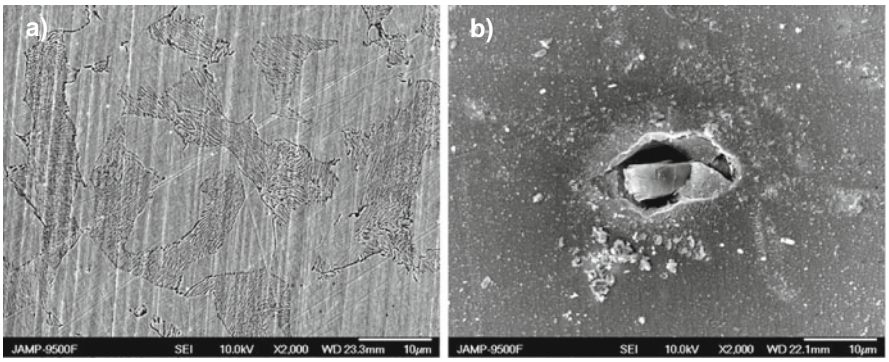

Fig. 5.5 Morphology of the protective film after 18 h (**a**) and 168 h (**b**) of exposition in the presence of $NaNO_2$ (30 mmol/l) at pH 7.38

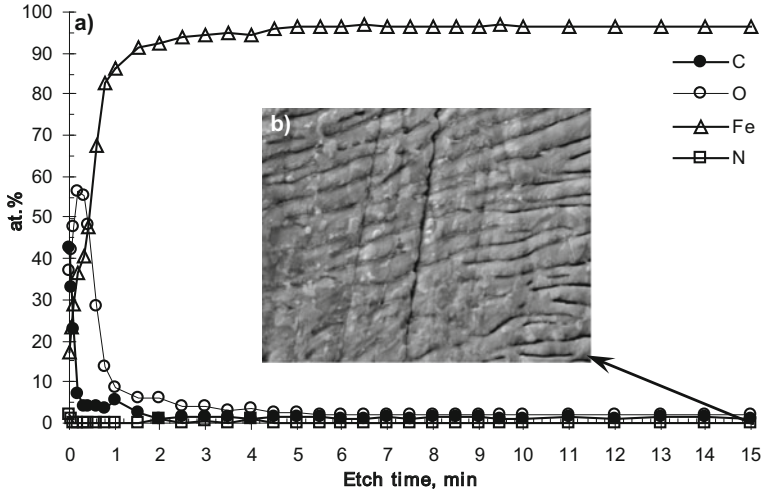

Fig. 5.6 Elemental composition of the protective film formed in the presence of $NaNO_2$ (30 mmol/l) obtained using Auger spectroscopy with ion etching against etching time (**a**) and surface morphology after etching (**b**)

protective film has been etched only partially as the elemental composition stabilizes as expected for plain steel values after 5 min of ion etching. Based on the obtained results, we may conclude that the presence of NO_2^- ions may affect the metal ionization process on such an extent that it could lead to a macroscopic change in the morphology of the metal surface.

Analysis of the polarization measurements shows the electrode potential must be shifted to 1.0 V for transferring the metal surface to a passive state. According to the Pourbaix diagram, such shift corresponds to a transition toward a state of thermodynamically stable hydrated ions of iron (III) (Fig. 5.1) that are capable of forming protective phase layers on the metal surface.

The pH value of the medium also affects the protective efficiency and mechanism of action of the NO_2^- ion. Near the *line 4* of the Pourbaix diagram, inhibitive efficiency of the nitrite ion rises significantly that may be attributed to a phenomenon when under this condition the reduction of the inhibitor with assimilation of the electron that is released during oxidizing of iron (II) to iron (III) ions. Shifting the Fe-H_2O system toward a state with thermodynamically stable hydrated iron (III) oxides leads to a formation of dense phase layers on the metal surface according to the reaction:

$$Fe^{2+} + 3H_2O = Fe(OH)_3 + 3H^+ + \overline{e}$$

Higher inhibitive efficiency at a higher pH value is also in line with the SEM images that reveal a much smoother morphology of the protective film, while the analysis of its elemental composition shows significant decrease in the nitrogen content that is on one order of magnitude lower than at pH 7.38 (Fig. 5.7).

Investigation of the kinetics of the electrode processes in the presence of $NaNO_2$ under pH 10 using the polarization measurements shows notable increase in the cathodic reaction rate, while the anodic one is significantly decelerated owing to a passivation of the metal surface with protective oxide film (Fig. 5.8).

In contrast to oxyanions, the inhibitive properties of silicates, phosphates, and carbonates of alkaline metals are due to their ability to form slightly soluble salts with iron cations with subsequent formation of dense phase protective layers on the metal surface. At the same time, analysis of the protective mechanism of such compounds should take into account their ability to undergo hydrolysis in aqueous solutions by the anion of weak acid that will lead to a significant alkalization of the medium. For this reason, the protective performance of such additives should be assessed in conjunction with the sole alkalinization effect without inhibitor that will ensure comparable conditions and reliability of the results.

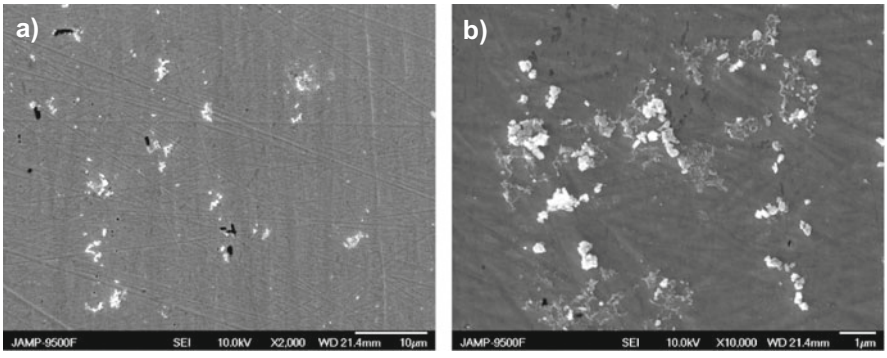

Fig. 5.7 SEM images of the sample after immersion into solution with $NaNO_2$ (30 mmol/l) at pH 10

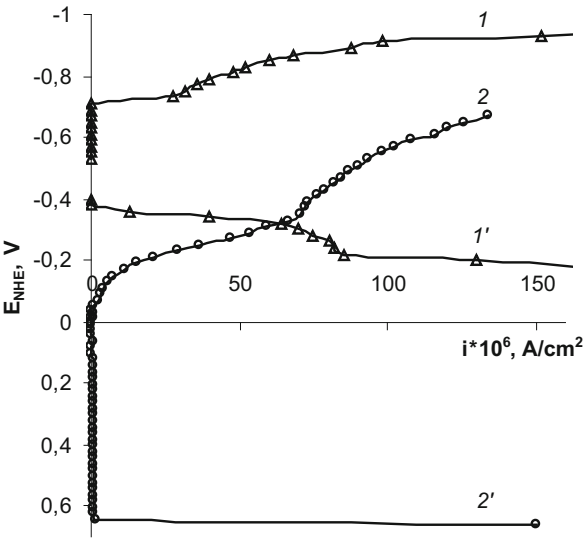

Fig. 5.8 Cathodic (*1, 2*) and anodic (*1′, 2′*) polarization curves for carbon steel in *1, 1′*, background aqueous saline solution; *2, 2′*, in the presence of $NaNO_2$ (30 mmol/l) at pH 10

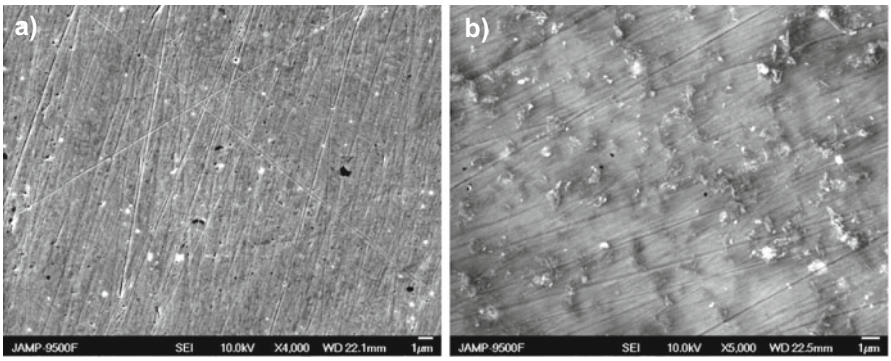

Fig. 5.9 Morphology of the protective film after 18 h (**a**) and 168 h (**b**) exposition in solution with Na_2SiO_3 (30 mmol/l) at pH 11.2

Increase in pH value and shift of the corrosion potential of steel result in the formation of nanoscaled uniform protective layers on the metal surface (Figs. 5.9 and 5.10). It should be noted that after 168 h of exposition (Fig. 5.9b), marks of mechanical treatment may still be observed.

Thus, in contrast to nitrite, Na_2SiO_3 does not tend to provoke metal ionization and is capable of better preserving the original structure of the metal surface under the protective film that is in line with theoretical expectation based on the difference in the mechanism of action.

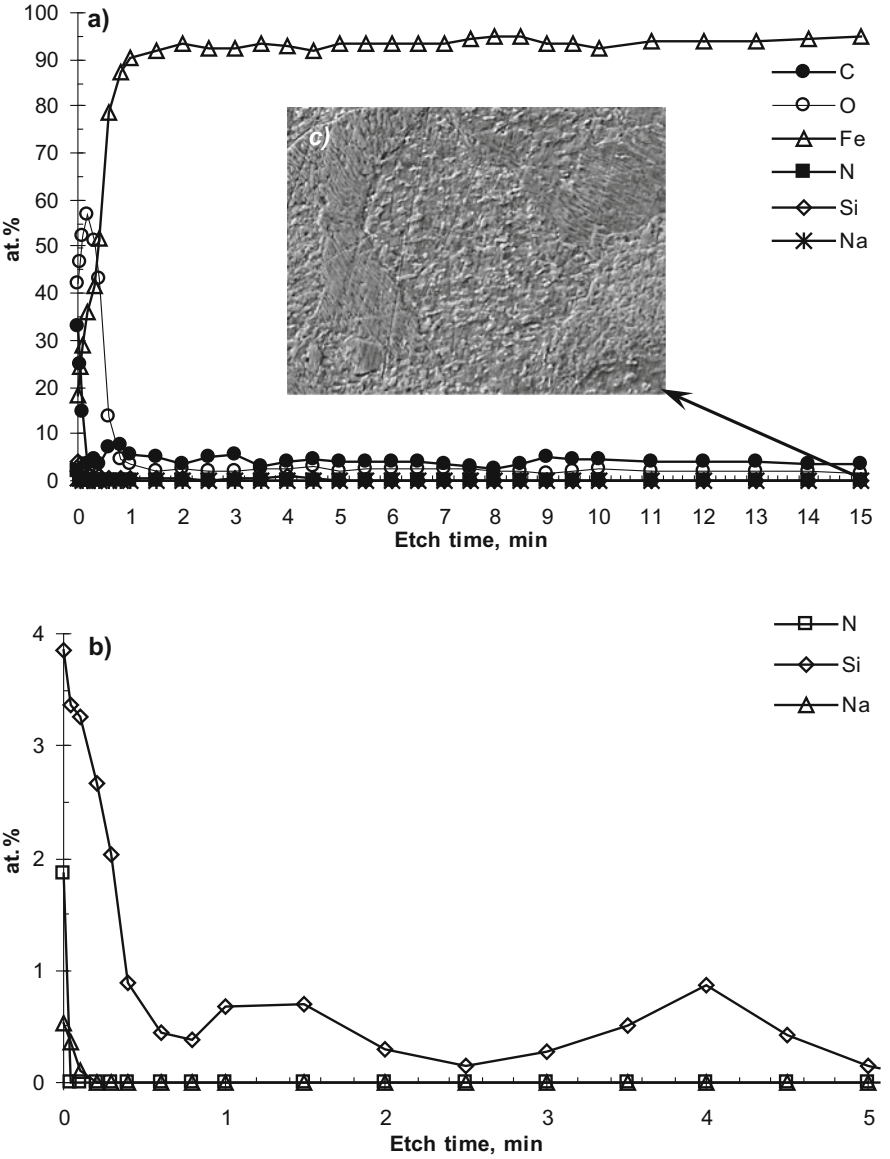

Fig. 5.10 Elemental composition of the protective film formed in the presence of Na_2SiO_3 (30 mmol/l) at pH 11.2 obtained using Auger spectroscopy with ion etching against etching time (**a**), nitrogen, silicon, and sodium atom distribution within the surface layer (**b**), and sample morphology after ion etching (**c**)

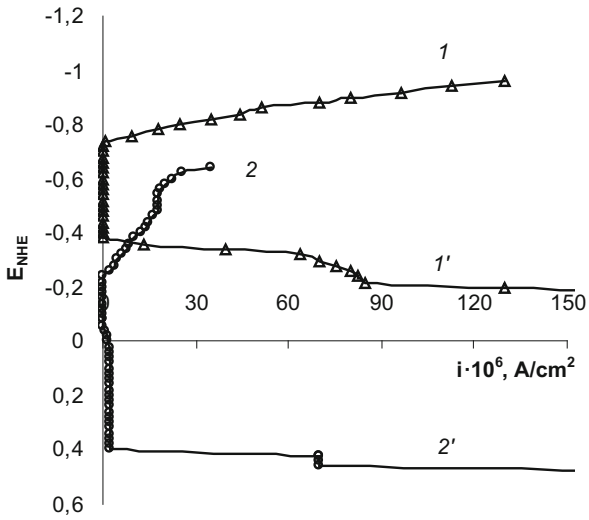

Fig. 5.11 Cathodic (*1*, *2*) and anodic (*1′*, *2′*) polarization curves for carbon steel: *1*, *1′*, background aqueous saline solution at pH 10; *2*, *2′*, in the presence of Na_2SiO_3 (30 mmol/l)

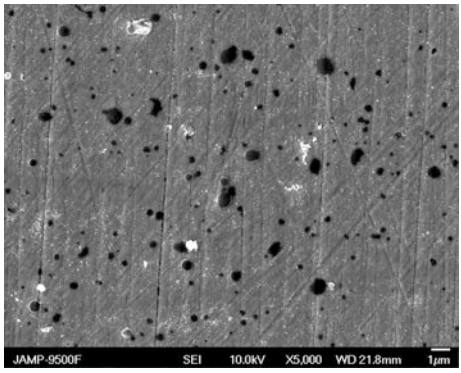

Fig. 5.12 Morphology of the protective film formed in the presence of PHMG (30 mmol/l)

Auger spectra analysis with ion etching revealed the elemental composition and its distribution within the protective layer. The film thickness is found to be ~40 nm with significantly increased content of silicon and oxygen (Fig. 5.10).

According to the polarization measurements, the presence of silicate additive leads to passivation of the metal surface and emergence of the complete passivation zone in the anodic portion of polarization curve (Fig. 5.11).

Similar results may be obtained with organic ligands that are capable of forming slightly soluble complex salts with the metal cations, in particular with polyhexamethylene guanidine (PHMG). Formation of the phase layer of Fe-PHMG complexes (Fig. 5.12) delivers slight metal protection, while its efficiency is significantly lower than in acidic medium [7].

Auger analysis confirms the formation of a phase layer with significant content of carbon and nitrogen of 49.3 and 20.6 at.%, respectively, while the iron content is 12.2 at.% that is found to be in good agreement with theoretical expectations.

It should be noted that despite uniform morphology without signs of local corrosion damage, the protective efficiency of sole PHMG under these conditions falls below other studied inorganic additives reaching typical values of 40%. Such efficiency may be attributed to the fact that PHMG as a complexing type inhibitor requires sufficient amount of iron cations in order to form a dense phase layer. Thus, we may predict that in the case of successful engineering of favorable conditions for complexation process, the PHMG protective efficiency may be significantly improved.

One of the approaches for achieving higher efficiency as well as better control over the protective layer composition, microstructure, and morphology is the development of theoretical representation of the combined action of the additives in multicomponent systems.

It was found, that binary mixtures that combine inhibitive additives with different mechanisms of action may exhibit synergistic effects and deliver improved protective performance. The dependence of protective efficiency against concentration ratio of their components in such cases is found to be extreme where in maxima the most significant protective effect may be achieved [12].

The mechanism of action of synergistic inhibitive compositions is largely determined by their individual characteristics: the additives of oxidative oxoanions contribute to the formation of nanoscaled oxide films on the metal surface, while the inhibitors of salt passivation may alkalize the medium and modify the films with the slightly soluble salts with the iron cations, which eliminates the negative factor of pitting formation as a result of the local damage of the passive layers.

In particular, the synergistic mixtures of $NaNO_2 + Na_2SiO_3$ ensure the formation of a uniform protective layer without signs of local damage that is typical for sole $NaNO_2$ (Fig. 5.13).

The elemental composition of the surface phase layers formed in the presence of synergistic mixtures of $NaNO_2 + Na_2SiO_3$ at pH 10.2 showed a decrease in

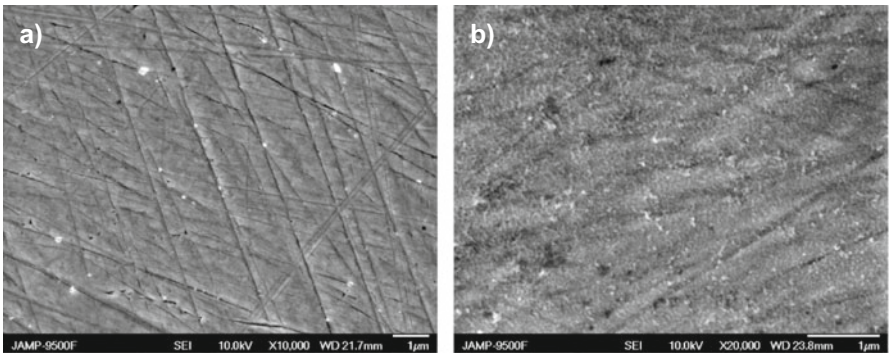

Fig. 5.13 Morphology of the surface layers formed in the presence of synergistic inhibitive mixture of $NaNO_2$ (10 mmol/l) + Na_2SiO_3 (20 mmol/l) at pH 10. Exposure time: (**a**) of 18 h and (**b**) 168 h

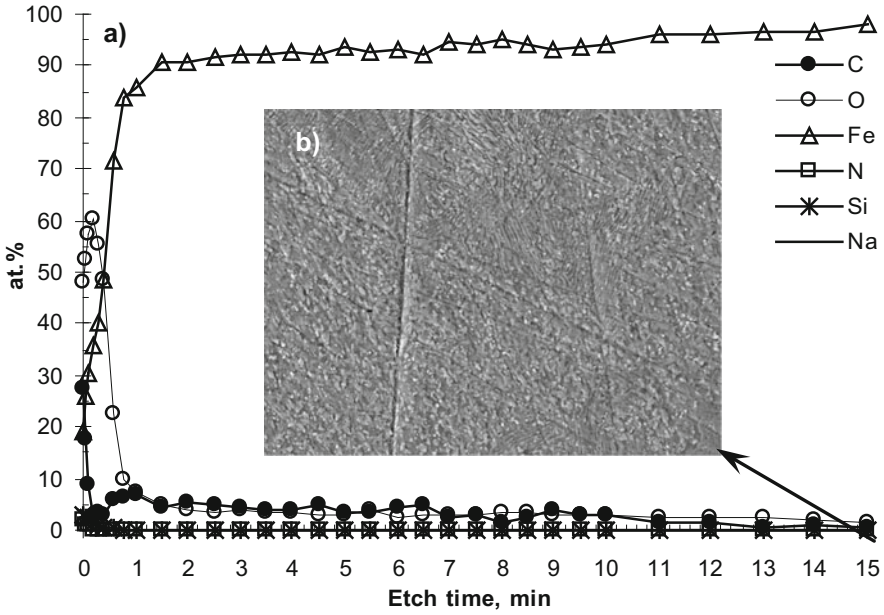

Fig. 5.14 Elemental composition of the protective film formed in the presence of synergistic mixture of $NaNO_2$ (10 mmol/l) + Na_2SiO_3 (20 mmol/l) at pH 10.2 obtained using Auger spectroscopy with ion etching against etching time (**a**) and sample morphology after ion etching (**b**)

nitrogen content and increased silicon content, similar to what is observed in the case of individual inhibitors (Fig. 5.14).

It should be noted that the surface morphology after ion etching shows characteristic signs of both additives. Mechanical treatment marks largely preserved as in the case of silicate, while some signs of metal dissolution process may also be observed as with sole nitrite. Taking into account the ability of $NaNO_2$ for a notable extent to promote the metal ionization process either individually or within a binary mixture, it is possible to use it for engineering optimal phase layer deposition conditions for complexing type inhibitors.

The isomolar series method has been employed for determining the optimal concentration ratio of the $NaNO_2$-PHMG binary mixture. It was found that the protective efficiency of the mixture against the concentration ratio has extreme character reaching a peak value of 99.8% at the $NaNO_2$/PHMG ratio as 2:1.

The SEM image of the surface layer after 168 h exposition revealed slight morphology changes compared to initial condition with marked smoothing of the mechanical treatment traces (Fig. 5.15).

The elemental composition of the protective film formed in the presence of synergistic mixtures of $NaNO_2$ + PHMG at optimal concentration ratio shows that the nitrogen content increased slightly from 20.6 to 25.5 at.% compared to sole PHMG that adequately corresponds to the presence of NO_2^- ions (Table 5.1).

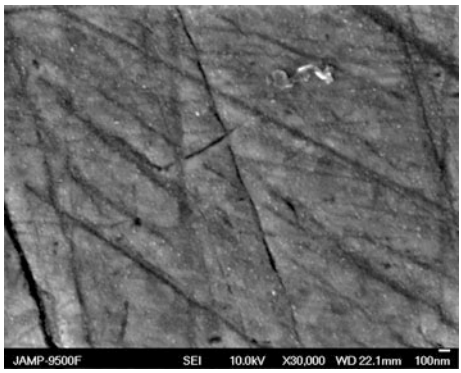

Fig. 5.15 Morphology of the surface after 168 h exposition in the presence of the $NaNO_2$ (20 mmol/l) + PHMG (10 mmol/l)

Table 5.1 Elemental composition of the carbon steel surface (by the results of Auger spectroscopy) after treatment in 1–30 mmol/l PHMG, 2–10 mmol/l PHMG, and 20 mmol/l $NaNO_2$

Spectrum	C	N	O	Na	Si	S	Cl	Fe	Total
1	49.3	20.6	17.7	–	–	0.1	–	12.2	100.00
2	48.1	25.5	22.3	0.5	1.8	0.1	0.1	10.9	100.00

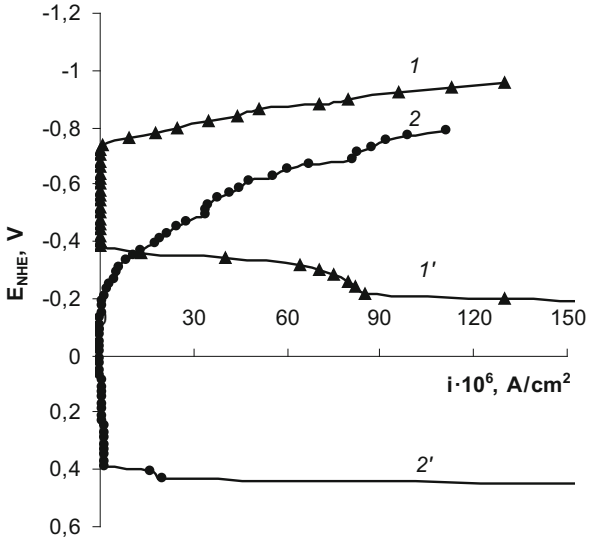

Fig. 5.16 Cathodic (*1, 2*) and anodic (*1′*, *2′*) polarization curves for carbon steel: *1, 1′*, background aqueous saline solution; *2*, *2′*, in the presence of $NaNO_2$ (10 mmol/l) + Na_2SiO_3 (20 mmol/l) at pH 10.2

Due to the formation of dense composite passive layers on the metal surface, the synergistic compositions of the inhibitors cause significant shift of the corrosion potential to the positive direction and form a long passivation zone in a wide range of potentials (1 V), and the potential of pitting formation is considerably distant from the corrosion that allowed to achieve full reliable protection of metals (Fig. 5.16).

In contrast, the efficiency of PHMG + Na_2SiO_3 mixture is unstable in the case of slight shift from the optimal concentration ratio of 1:1. This effect may be attributed

to mechanism concurrency as both mixture components require the metal cations to be able to form a phase layer.

Thus, the analysis of possible concurrent and complement effects between individual mechanisms and specific action of the mixture components is a crucial requirement for developing the efficient metal surface modification methods based on the formation of phase protective layers in multicomponent systems.

5.4 Conclusions

The processes of formation of phase protective layers in the presence of numerous individual inhibitors and their mixtures have been investigated. Thermodynamic approach for the analysis of possible interactions and equlibria based on the Pourbaix diagram has been demonstrated. It was shown that the pH value of the medium may significantly affect the protective efficiency and mechanism of action of the additives, as well as morphology of the formed phase layers.

Auger spectroscopy with ion etching enabled to confirm the mechanism of action of the additives and determine the thickness of phase layers and the composition distribution within protective films. Depending on the additives used for the formation process, the phase layer thickness varies in range from 15 to 50 nm.

Based on the obtained results, the generalized design recommendations may be proposed. The most efficient inhibitive mixtures may be composed using additives with different mechanisms of action that exhibit synergistic effects. In contrast, it was shown that additives with similar protective mechanism may demonstrate unreliable results due to mechanism concurrency.

Thus, the challenge of elaboration of modern surface engineering methods may be addressed by improving veracity of the theoretical models that represent the interaction in target systems in conjunction with recent advancements in the field of nanoscale systems.

References

1. Rozenfeld IL (1977) Corrosion Inhibitors. Khimiya, Moscow
2. Antropov LI, Makushin EM, Panasenko VF (1981) Inhibitors of the corrosion of metals. Tekhnika, Kiev
3. Tzaneva B (2013) Effect of pH on the corrosion behaviour of high nitrogen stainless steel in chloride medium. J Chem Technol Metall 48(4):383–390
4. Cui J, Yuan W, Yuan D, Pei Y (2017) Effect of pH on the passivation of carbon steel by sodium borosilicate controlled-release inhibitor in simulated recirculating cooling water. Ind Eng Chem Res 56(25):7239–7252. https://doi.org/10.1021/acs.iecr.7b01433
5. Hussain RR (2014) Passive layer development and corrosion of steel in concrete at the nano-scale. J Civil Environ Eng 4:e116. https://doi.org/10.4172/2165-784X.1000e116
6. Ledovskykh VM, Vyshnevska YP, Brazhnyk IV, Levchenko SV (2017) Metal surface modification for obtaining nano- and sub-nanostructured protective layers. Nanoscale Res Lett 12:186–191. https://doi.org/10.1186/s11671-017-1964-5

7. Ledovs'kykh VM, Vyshnevs'ka YP, Brazhnyk IV, Levchenko SV (2017) Development and optimization of synergistic compositions for the corrosion protection of steel in neutral and acid media. Mater Sci 52(5):634–642. https://doi.org/10.1007/s11003-017-0002-1
8. Ledovskikh VM (1983) Synergetic inhibition of steel corrosion in neutral media by nitrogenous organic alkalis with sodium nitrite. Prot Met 19(1):84–91
9. Min J, Park JH, Sohn H-K, Park JM (2012) Synergistic effect of potassium metal siliconate on silicate conversion coating for corrosion protection of galvanized steel. J Ind Eng Chem 18(2):655–660. https://doi.org/10.1016/j.jiec.2011.11.057
10. Truc AT, Pébère N, Xuan Hang T, Hervaud Y, Boutevin B (2002) Study of the synergistic effect observed for the corrosion protection of a carbon steel by an association of phosphates. Corros Sci 44:2055–2071. https://doi.org/10.1016/S0010-938X(02)00013-6
11. Pourbaix M (1974) Atlas of electrochemical equilibria in aqueous solutions. National Association of Corrosion Engineers, Houston, p 551
12. Ledovs'kykh VM, Levchenko SV, Tulainov SM (2013) Synergistic extrema of the mixtures of corrosion inhibitors for metals in aqueous salt solutions. Mater Sci 49(6):827–832. https://doi.org/10.1007/s11003-014-9680-0

Chapter 6
Electrical Conductivity and ^{7}Li NMR Spin-Lattice Relaxation in Amorphous, Nano- and Microcrystalline Li_2O-7GeO_2

O. Nesterov, M. Trubitsyn, O. Petrov, M. Vogel, M. Volnianskii, M. Koptiev, S. Nedilko, and Ya. Rybak

6.1 Introduction

Applications in modern electronics and power engineering stimulate active studies of ionic conduction in dielectric solids [1, 2]. As a rule, the structures of ionic conductors contain a large number of vacant positions which can be occupied by mobile ions. Besides vacant positions should be separated by not too high potential barriers and connected by channels that enable ionic migration through the lattice framework. Such structural features provide for fast ionic conduction at moderate temperatures. The crystals of the lithium germanate family are considered as perspective matrixes to create new materials with high ionic conductivity. By now, about ten representatives of the Li_2O-GeO_2 family have been synthesized [3], and special attention is devoted to the ferroelectric crystals of lithium tetragermanate ($Li_2Ge_4O_9$) and lithium heptagermanate ($Li_2Ge_7O_{15}$) which are typical dielectrics with an energy gap of about 5 eV width [4]. The structures of these crystals have framework type and are formed by germanium-oxygen octahedra [GeO_6] and tetrahedra [GeO_4], which are connected by polyhedral edges or by bridging oxygen atoms [5–7]. The Li^+ ions are located within the cavities, formed by the germanium-oxygen structural skeleton. Electrical conductivity in pure and 3d-ion-

O. Nesterov · M. Trubitsyn (✉) · M. Volnianskii · M. Koptiev
Solid State Physics and Optoelectronics Department, Oles Honchar Dnipro National University, Dnipro, Ukraine

O. Petrov · M. Vogel
Institute of Solid State Physics, Darmstadt Technical University, Darmstadt, Germany
e-mail: michael.vogel@physik.tu-darmstadt.de

S. Nedilko · Ya. Rybak
Physics Faculty, Taras Shevchenko National University of Kyiv, Kyiv, Ukraine
e-mail: snedilko@univ.kiev.ua

O. Fesenko, L. Yatsenko (eds.), *Nanocomposites, Nanostructures, and Their Applications*, Springer Proceedings in Physics 221,
https://doi.org/10.1007/978-3-030-17759-1_6

doped $Li_2Ge_7O_{15}$ crystals was studied in previous works [8–12]. It was shown that charge transfer was determined by Li^+ interstitial ions hopping through the channels of the $Li_2Ge_7O_{15}$ structure [10–12].

Today nanostructuring is actively used to create dielectrics with a high ionic component of the electrical conductivity. Reducing the size of structural inhomogeneities down to the nanometer range makes it possible to increase ionic conductance and even to induce a transition to a superionic phase [1, 2]. Spatially heterogeneous solid electrolytes, which consist of more than one phase, are of particular interest. The relative volume of the phases and size of the homogeneous regions as well as their spatial distribution become the essential factors for such materials. One of the effective ways to obtain nanostructured materials is heat treatment and partial crystallization of initial amorphous phases. It is known that the maximal increase of the number of crystal nuclei and the maximal growth of the size of the nuclei occur at different temperatures. Thus, selecting the regimes of glass heat treatment allows one to control the mean size of nanoregions, enabling a preparation of highly dispersed states which have the same chemical composition as the homogeneous medium, but significantly different properties. Varying stoichiometry and temperature regimes of glass devitrification, one can control chemical composition, structure and morphology of ordered and interfacial regions.

Recently the preparation of Li_2O-$x$$GeO_2$ glasses and their crystallization on heating were studied in [13–17]. It was shown that amorphous phases crystallized in stages depending on the proportion x of the starting reagents. In this paper, we study electrical properties (conductivity σ and complex impedance ρ*) of the states obtained from crystallization of Li_2O-$7GeO_2$ glass. In order to determine the mechanisms of charge transfer, the ^{7}Li NMR spin-lattice relaxation (SLR) rate was measured in Li_2O-$7GeO_2$ glass, intermediate nanocrystalline state and polycrystal. The NMR SLR data are compared with the results of conductivity and complex impedance studies.

6.2 Experimental Details

Lithium heptagermanate Li_2O-$7GeO_2$ glass was prepared by fast quenching of the melt. In general, Li_2O-$x$$GeO_2$ glasses can be crystallized by heating or by isothermal heat treatment [17, 18]. Here we devitrified Li_2O-$7GeO_2$ glass only on heating. The temperatures characterizing glass devitrification were determined by differential scanning calorimetry (DSC) (Mettler STARe SW derivatograph). The structure and morphology of the heterogeneous states, obtained at glass crystallization, were studied by X-ray phase analysis (DRON-3) and atomic force microscopy (AFM) (Integra Prima Basic NT-MDT microscope) [19, 20]. Electrical properties were measured in an AC field by using a bridge method (AC bridges E7-10, Tesla BM-507). ^{7}Li NMR spin-lattice relaxation measurements were performed at a Larmor frequency of 139.9 MHz using a saturation-recovery sequence in combination with

solid-echo detection. Further details of the ^{7}Li NMR experimental setup can be found in previous work [21].

6.3 Results and Discussion

6.3.1 *Structure and Morphology of the States Resulting from Glass Devitrification*

Crystallization of the Li_2O-$7GeO_2$ glass was studied by DSC. The data obtained were consistent with previous results for the Li_2O-$xGeO_2$ family [13–17]. The DSC thermogram (Fig. 6.1) showed a weak anomaly at the glass transition temperature T_g and two exothermic peaks, indicating stepwise crystallization of the amorphous phase. The DSC anomalies were detected only during the first heating run of the original glass, while they were absent during subsequent temperature cycling as a result of the preceding complete glass crystallization.

Phase compositions of the states appearing at glass crystallization were investigated by X-ray phase analysis (Fig. 6.2) [19]. The samples in the intermediate state were prepared by heating the glass to temperatures between the first and the second DSC peaks ($T_1 < T < T_2$) and subsequent cooling to room temperature. The polycrystalline samples were obtained by heating the glass to temperatures above the second DSC peak ($T > T_2$) and subsequent cooling to room temperature.

It was concluded that the first DSC peak is associated with an appearance of nuclei of lithium tetragermanate $Li_2Ge_4O_9$ and lithium heptagermanate $Li_2Ge_7O_{15}$ phases. Heating above T_2 led to complete crystallization of the thermodynamically stable $Li_2Ge_7O_{15}$ phase. The lithium tetragermanate phase disappeared and transformed to the lithium heptagermanate one in accord with $Li_2Ge_4O_9 + 3GeO_2 \rightarrow Li_2Ge_7O_{15}$. As it was discussed in [7], transformation of $Li_2Ge_4O_9$ nuclei into $Li_2Ge_7O_{15}$ ones was possible, because lithium tetragermanate

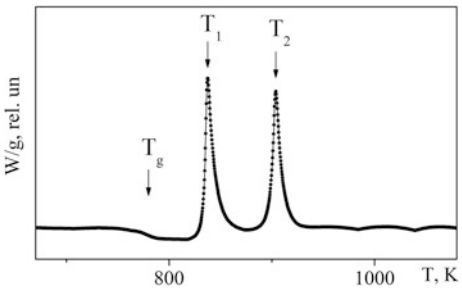

Fig. 6.1 DSC thermogram measured on heating the original Li_2O-$7GeO_2$ glass. Three anomalies were detected: inflection at the glass transition point $T_g = 775$ K and two exothermic peaks at $T_1 = 838$ K and $T_2 = 904$ K. Temperature was increased with a rate of 10 K/min

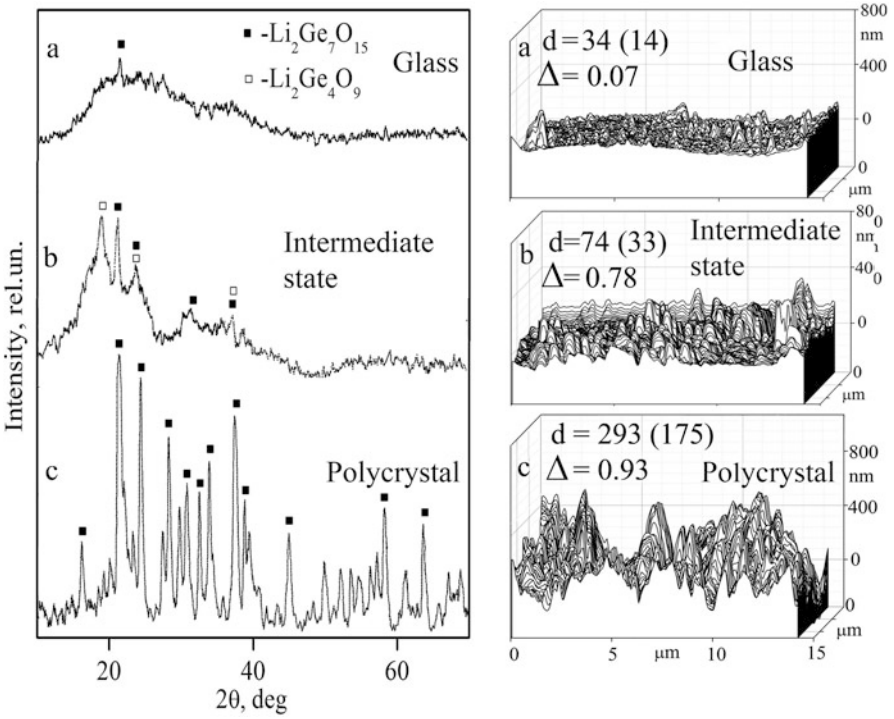

Fig. 6.2 X-Ray diffraction patterns (on the left) and profiles of AFM images (on the right) for the states formed during Li_2O-$7GeO_2$ glass crystallization: glass (**a**), intermediate state (**b**) and polycrystal (**c**) [19, 20]. Average linear size d of the ordered regions (in nm) and ordered phase fraction Δ are indicated on the AFM images

and lithium heptagermanate have similar crystal structures formed by octahedral and tetrahedral germanium-oxygen polyhedra.

The morphology of the states obtained at glass devitrification was studied by AFM [20]. Figure 6.2 shows the profiles of AFM images. Moreover, the mean linear size d of the ordered nuclei and the relative fraction Δ of the ordered regions are indicated. One can see that in the intermediate state, the ordered phases with nanometer-sized nuclei ($d = 74$ nm) occupy about three quarters of the sample volume, whereas amorphous surroundings occupy the rest one quarter. In the polycrystalline samples, the crystallites with micrometer-ranged average size ($d \approx 0.3$ μm) occupy nearly the whole sample volume.

6.3.2 Electrical Conductivity

Preliminary data of the conductivity σ of Li_2O-7GeO_2 as-quenched glass were presented in the previous work [20]. The results were obtained during the first heating run up to temperatures in the interval between T_1 and T_2 of DSC anomalies (Fig. 6.1). It was shown that σ sufficiently increased in the intermediate nanocrystalline state. Nevertheless, for the nonstoichiometric composition Li_2O-11.5GeO_2 [18], it was demonstrated that the glass could be completely crystallized not only by heating over T_2 but also by isothermal heat treatment at a temperature in the interval between T_g and T_1. This means that the intermediate nanocrystalline state is in fact metastable. It is of interest to clarify the conditions which allow one to stabilize such nanostructured state with increased conductivity. Therefore, in this study, we used the following temperature cycles. At first, the as-quenched glass was heated up to a temperature of T_g – 100 K and then cooled to room temperature. The upper limit in this cycle was chosen to avoid changes of the amorphous state of the sample during the measurements. Next the sample was heated up to T_1 + 9 K, transformed to the intermediate nanocrystalline state and immediately after that cooled to room temperature. Finally the sample was heated over the second DSC peak up to T_2 + 27 K, underwent complete crystallization and subsequently cooled to room temperature. The heating and cooling rates were 3.3 K/min. The conductivity σ was measured in an AC field (f = 1 kHz) during the above-described temperature runs.

Figure 6.3 shows the results in an Arrhenius plot. One can see that a nearly linear behavior of $\sigma(1/T)$ observed for the glass is changed to a steeper increase when heating through T_g as a result of glass softening. In the range between T_1 and T_2, the conductivity of the sample significantly increases until it eventually drops sharply on crossing T_2.

According to [9–12], charge transfer in single crystalline $Li_2Ge_7O_{15}$ is determined by Li^+ interstitials hopping along the structural channels. Thus, the increase of σ with temperature is governed by thermal activation of the charge carrier's mobility. Based on this data, one can assume that the conductivities of Li_2O-7GeO_2 glass, intermediate nanocrystalline state and polycrystal are determined by Li^+ ions which are mobile enough owing to weak bonds with germanium-oxygen structural framework [6].

A thermally activated increase of the conductivity is usually described by the expression

$$\sigma(T) = \frac{A}{T}\exp\left(-E_\sigma \Big/ k_B T\right), \tag{6.1}$$

where E_σ is the activation energy of conductivity; k_B the Boltzmann constant, $A = nq^2\delta^2\nu/(zk_B)$; n, q and δ the carrier's concentration, charge and hopping length, respectively; ν the frequency of lattice vibrations; and z the number of nearest available positions. The values of the parameters in Eq. 6.1 obtained for the studied states are presented in Table 6.1. One can see that at 500 K conductivity of the

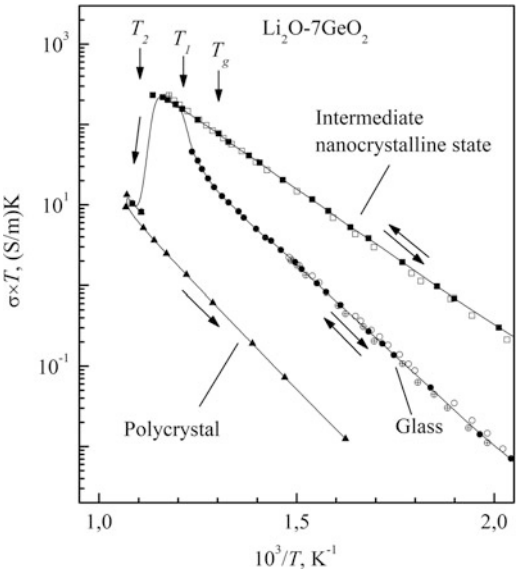

Fig. 6.3 Conductivity of Li_2O-7GeO_2 states vs. $1/T$. Measurements were carried out in an AC field ($f = 1$ kHz) by using the temperature regimes described in the text. The temperatures of DSC anomalies (Fig. 6.1) are shown by arrows

Table 6.1 Conductivity and values of the parameters in Eq. 6.1 determined from the linear regions in the Arrhenius plot shown in Fig. 6.3

Li_2O-7GeO_2 states	Conductivity σ, S/m, ($T = 500$ K)	Factor A, $\times 10^5$, (S/m)·K	Activation energy, eV	
			E_σ	E_{SLR}
Glass	2.4×10^{-5}	100 (30)	0.89 (2)	0.45(1)
Intermediate nanocrystalline state	4.8×10^{-4}	25(5)	0.69(1)	0.26(1)
Polycrystal	~1.6×10^{-6}	24(5)	1.01(1)	0.58(3)

The right column shows the values of the activation energy determined from NMR SLR data (Sec. 6.3.4)

nanocrystalline state is one order higher than for the glass and two orders higher than for the polycrystal grained in the micrometer range. Consistently the E_σ has the lowest value for the intermediate nanocrystalline state. The charge transport in the glass is characterized by an intermediate value of E_σ, while the highest activation energy is observed for the polycrystal. One can assume that noticeable differences in E_σ values reflect distinct potential energy reliefs and diverse heights of the potential barriers in which thermally activated charge carriers overcome in the glass, nanocrystalline state and polycrystal. One may note that, in comparison with the data in [20], the E_σ values for the nanocrystalline state and polycrystal (Table 6.1) were determined from much broader temperature intervals in this work and, hence, can be assumed to be more accurate.

In accord with [18, 20], the increase of the conductivity between T_1 and T_2 (Fig. 6.3) can be attributed to a presence of nanometer-sized crystal nuclei in the intermediate state. Complete crystallization occurs through a formation of micrometer-sized crystallites (Fig. 6.2), resulting in a sharp and irreversible decrease of σ in the polycrystal. The above-described temperature cycling shows that the glass and the intermediate state were quite stable, and electrical properties did not change at temperatures below the glass transition point T_g. Hence, thermal treatment allows one to prepare highly dispersed intermediate states with increased conductivity, and such states can be stabilized by sufficiently fast cooling to temperatures well below T_g. It should be noted that nonstoichiometric Li_2O-$11.5GeO_2$ glass could be devitrified in a similar manner [18].

6.3.3 Complex Impedance Spectra

For the glass, intermediate nano- and polycrystalline states of Li_2O-$7GeO_2$ we studied spectra of the complex impedance $\rho^*(\omega)$. The samples were prepared by heating to certain temperatures in accord with the regimes described in Sec. 6.3.1. The measurements were carried out in the frequency range of 10^1–2×10^5 Hz and in the temperature interval up to 700 K, i.e. well below T_g, in order to keep the state of samples unchanged during the measurements.

Figure 6.4 shows the experimental data. One can see that for glass and polycrystal, the hodographs (Fig. 6.4a, c) consist of single arcs. Within the equivalent circuit approach [22], such hodographs can be described by the impedance of a parallel *RC* circuit. The centers of the arcs shift slightly downward on the abscissa ρ' axis, which is typical for real systems owing to a distribution of relaxation times $\tau = RC$. Usually such deviation is described by replacing the ordinary capacitance by a generalized frequency-dependent one, $C_n^* = B \cdot (i\omega)^{n-1}$ (ω – cyclic frequency, $0 \leq n \leq 1$) in the expression for the impedance of the parallel *RC* circuit:

$$\rho^*(\omega) = (S/l) \cdot \left(R^{-1} + B(i\omega)^n\right)^{-1}, \tag{6.2}$$

where S is the area of the electrodes and l the thickness of the sample.

Hodographs for the nanocrystalline state (Fig. 6.4b) differ from the diagrams for glass and polycrystal (Fig. 6.4a–c) and consist of two arcs. Such spectra can be simulated by the impedance of two serially connected parallel RC^* circuits:

$$\rho^*(\omega) = (S/l) \cdot \left(\frac{1}{R_1^{-1} + B_1 (i\omega)^{n_1}} + \frac{1}{R_2^{-1} + B_2 (i\omega)^{n_2}} \right). \tag{6.3}$$

Two arcs in the hodographs in Fig. 6.4b can be attributed to the coexistence of the nanometer-sized nuclei and the amorphous internuclei medium in the intermediate state. In previous works [18, 20], it was argued that the increased conductivity

of the nanocrystalline state results from its high dispersity. Accordingly, the high-frequency arc in the hodographs of Fig. 6.4b can be attributed to Li^+ ion motion within the crystalline nuclei, while the low-frequency arc corresponds to charge transport within the amorphous internuclei regions. One may note that the hodographs for the nanocrystalline state of nonstoichiometric Li_2O-11.5GeO_2 composition consist of only a single arc [23]. We assume that such discrepancy reflects different distributions of Li ions in the nanocrystalline states of stoichiometric (Li_2O-7GeO_2) and nonstoichiometric (Li_2O-11.5GeO_2) compositions, the latter of which contains an excess of GeO_2. The comparative analysis of the hodographs for Li_2O-7GeO_2 and Li_2O-11.5GeO_2 will be presented elsewhere soon.

Figure 6.5 shows an Arrhenius plot of the impedance relaxation rates $\tau^{-1}(1/T)$ for the glass and nanocrystalline state of Li_2O-7GeO_2. For the latter sample, we plot the relaxation rates τ^{-1} of both the high-frequency arc, which is assumed to reflect the charge transfer within ordered nuclei, and the low-frequency arc attributed to charge carrier motion within the embedding amorphous medium. The data for the polycrystal are omitted because of a low accuracy of τ^{-1} determination (see Fig.6.4c). Assuming that τ^{-1} can be related to the hopping rate of the charge carriers, one can conclude that the conductivity of the nanocrystalline state increases due to high Li^+ ion mobility within the nanometer-sized nuclei.

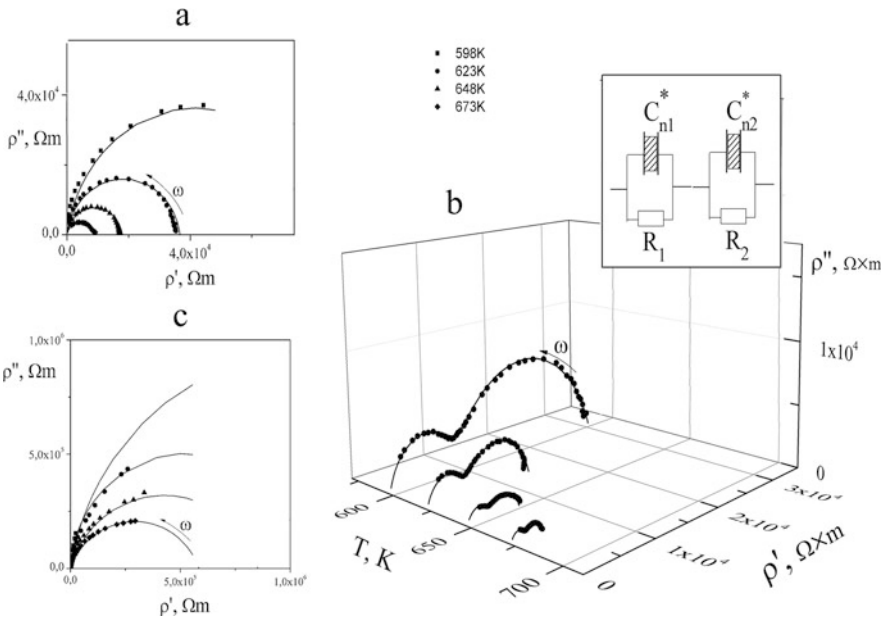

Fig. 6.4 Impedance spectra $\rho^*(\omega,T)$ for Li_2O-7GeO_2: (**a**) glass, (**b**) nanocrystalline state, and (**c**) polycrystal. Symbols represent the experimental data; solid lines are calculated by using Eqs. 6.2 and 6.3. The insert of panel (**b**) shows the equivalent circuit used to simulate the impedance of the nanocrystalline state

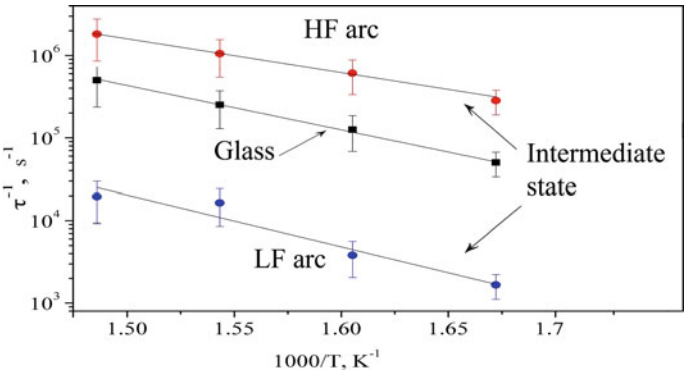

Fig. 6.5 Impedance relaxation rate τ^{-1} vs. $1/T$ for Li_2O-7GeO_2 states. For the nanocrystalline intermediate state, τ^{-1} is plotted for the high-frequency (HF) arc and the low-frequency (LF) arc

6.3.4 NMR Spin-Lattice Relaxation of ^{7}Li Isotope Nuclei

Measurements of ^{7}Li NMR SLR rates $T_1{}^{-1}$ provide information about local dynamics of Li^+ ions [24, 25]. Within the continuous diffusion model [24–30], the SLR rate $T_1{}^{-1}$ can be related to the correlation time τ_C describing the mean lifetime of the ions in some fixed positions. In the simplest case, which requires, e.g. the existence of an exponential correlation function of ion dynamics, the SLR rate $T_1{}^{-1}$ is given by

$$T_1{}^{-1}(\omega_L, T) \sim \begin{cases} \tau_C(T), & \text{if } (\omega_L \tau_C << 1), \\ \frac{1}{(\omega_L)^2}(\tau_C(T))^{-1}, & \text{if } (\omega_L \tau_C >> 1), \end{cases} \tag{6.4}$$

where $\omega_L \tau_C >> 1$ is fulfilled in the low-temperature interval (slow motion limit) and $\omega_L \tau_C << 1$ is valid in the high-temperature regime (fast motion limit). Motivated by the findings of the above conductivity and impedance studies, we assume in the following analysis that the correlation time obeys an Arrhenius law, $\tau_C(T) = \tau_0 \exp(E_{SLR}/k_B T)$.

The temperature-dependent ^{7}Li SLR rates $T_1{}^{-1}$ of the Li_2O-7GeO_2 glass, nanocrystalline state and polycrystal are plotted in Fig. 6.6. One can see that $T_1{}^{-1}$ increases when the temperature is increased for all Li_2O-7GeO_2 states. According to Eq. 6.4, this means that the slow motion limit applies and $T_1{}^{-1}$ is inversely proportional to the correlation time τ_C.

Comparing the data in Fig. 6.6, we observe that the intermediate nanocrystalline state has the highest SLR rate $T_1{}^{-1}$ and, hence, the fastest ion dynamics, followed by the glass and, finally, the polycrystal with the lowest SLR rate and slowest Li^+ motion. These findings are in qualitative agreement with the results of our impedance studies (Figs. 6.4 and 6.5). The SLR and impedance relaxations are fastest for the nanocrystalline state and slowest for polycrystalline state. These

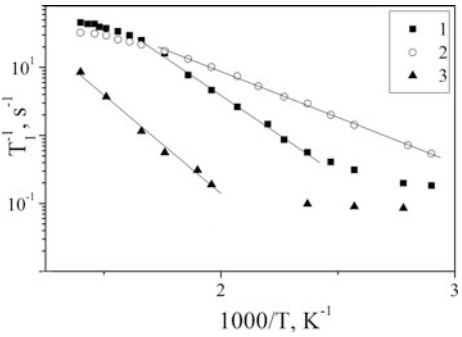

Fig. 6.6 ^{7}Li SLR rate $T_1{}^{-1}$ vs. $1/T$ for Li_2O-$7GeO_2$: (1) glass, (2) intermediate nanocrystalline state, and (3) polycrystal

observations indicate that the increased conductivity of the nanocrystalline state is due to a high mobility of Li^+ ions.

Activation energies E_{SLR}, determined from the SLR data, are added to Table 6.1 for comparison. One can see that for all states studied, the E_{SLR} values are appreciably smaller than the E_σ values. A similar discrepancy is observed for many other compounds [24, 25]. Such difference is actually expected when the correlation function of ion dynamics is not exponential, a situation met also for the present samples, as implied by the results of the above impedance studies. Then, the temperature dependence of $T_1{}^{-1}$ in the slow motion limit reflects not only the slowdown of the ion dynamics but also the stretching of the correlation loss, leading to a weaker increase upon cooling [24, 25]. As a consequence, E_{SLR} is smaller than E_σ under such circumstances. Despite these effects, both methods yield the same order of activation energies for the studied Li_2O-$7GeO_2$ states. The highest activation energy is found for the polycrystalline state, followed by the values for the glass, and the lowest activation energy is obtained for the nanocrystalline state.

Like impedance measurements, SLR analysis provides evidence for a hopping motion of Li^+ ions and allows us to link the enhanced conductivity of the nanocrystalline state with a high mobility of these charge carriers. This in turn can be attributed to a high dispersion of the intermediate state with nanometer-sized crystal nuclei, as indicated by our AFM studies. The transformation of the nanometer nuclei to micrometer crystallites upon formation of the polycrystalline state is accompanied by a sharp decrease of conductivity.

6.4 Conclusions

The electrical conductivity was measured during Li_2O-$7GeO_2$ glass crystallization upon heating. It was shown that heat treatment of Li_2O-$7GeO_2$ glass enabled to obtain a nanocrystalline state with increased electrical conductivity. Such nanocrystalline state could be stabilized by sufficiently fast cooling to temperatures below the glass transition point T_g. Complete glass crystallization happened through

transformation of nanometer-sized nuclei into micrometer-sized crystallites. It was accompanied by a sharp decrease of conductivity. Charge transport in the studied Li_2O-7GeO_2 states can be attributed to Li^+ ions that are mobile due to weak bonds to the germanium-oxygen structural framework.

Impedance spectra were recorded for glass, nanocrystalline and polycrystalline samples. Charge transport within the crystalline nuclei and their amorphous surroundings were distinguished for the nanocrystalline state. It was observed that the corresponding relaxation rates differ by about two orders of magnitude.

Measurements of ^{7}Li NMR SLR rates confirmed that the charge transport in the studied Li_2O-7GeO_2 compounds results from Li^+ ion motion. It was shown that the SLR rate and the impedance relaxation rate are highest and, hence, the ionic jumps are fastest in the nanocrystalline state. We conclude that the increase of the conductivity in the nanocrystalline state is caused by a high mobility of the Li^+ ions within nanometer-sized nuclei.

References

1. Maier J (2004) Ionic transport in nano-sized systems. J Solid State Ionics 175:7–12. https://doi.org/10.1016/j.ssi.2004.09.051
2. Maier J (2005) Nanoionics: ion transport and electrochemical storage in confined systems. J Nat Mater 4(11):805–815. https://doi.org/10.1038/nmat1513
3. Murthy MK (1964) Studies in germanium oxide systems: I, phase equilibria in the system Li_2O–GeO_2. J Am Ceram Soc 47(7):328–331. https://doi.org/10.1111/j.1151-2916.1964.tb14433.x
4. Haussuhl S, Wallrafen F, Recker K, Eckstein J (1980) Growth, elastic properties and phase transition of orthorhombic $Li_2Ge_7O_{15}$. Z Kristallogr 153:329–337
5. Vollenke H, Wittman A, Nowotny H (1970) Die kristall-structure des lithiumhepttagermanats $Li_2Ge_7O_{15}$. Monatch Chem 101:46–45
6. Iwata Y, Shibuya I, Wada M, Sawada A, Ishibashi Y (1987) Neutron diffraction study of structural phase transition in ferroelectric $Li_2Ge_7O_{15}$. J Phys Soc Jpn 56(7):2420–2427. https://doi.org/10.1143/JPSJ.56.2420
7. Ilyushin GD, Dem'yanets LN (2000) Crystal chemistry of germanates: characteristic structural features of Li, Ge-germanates. Crystallography Rep 45(4):626–632. https://doi.org/10.1134/1.1306574
8. Liebert BE, Huggins RA (1976) Ionic conductivity of Li_4GeO_4, Li_2GeO_3 and $Li_2Ge_7O_{15}$. Mat Res Bull 11(5):533–538. https://doi.org/10.1016/0025-5408(76)90235-X
9. Volnyanskii MD, Trubitsyn MP, Obaidat YAH (2008) Anisotropy of the electrical conductivity of lithium heptagermanate crystals. Phys Solid State 50(3):422–424. https://doi.org/10.1134/S1063783408030049
10. Trubitsyn MP, Volnyanskii MD, Obaidat YAH (2008) Ionic conduction in $Li_2Ge_7O_{15}$ crystals doped with Cr and Mn ions. Phys Solid State 50(7):1234–1237. https://doi.org/10.1134/S106378340807007X
11. Volnyanskii MD, Plyaka SN, Trubitsyn MP, Obaidat YAH (2012) Ion conduction and space-charge polarization processes in $Li_2Ge_7O_{15}$ crystals. Phys Solid State 54(3):499–503. https://doi.org/10.1134/S1063783412030353
12. Volnianskii M, Plyaka S, Trubitsyn M, Obaidat Y (2014) Frequency dispersion of conductivity and complex impedance in $Li_2Ge_7O_{15}$ single crystal. Ferroelectrics 462(1):74–79. https://doi.org/10.1080/00150193.2014.890880

13. Pernice P, Aronne A, Marotta M (1992) The non-isothermal devitrification of lithium tetragermanate glass. Mater Chem Phys 30(3):195–198. https://doi.org/10.1016/0254-0584(92)90223-u
14. Pernice P, Aronne A, Marotta M (1992) Crystallizing phases and kinetics of crystal growth in Li_2O-$_{19}GeO_2$ glass. J Mater Sci Lett 11:427–429
15. Marotta A, Pernice P, Aronne A, Catauro M (1993) The non-isothermal devitrification of lithium germanate glasses. J Ther Anal 40(1):181–188. https://doi.org/10.1007/BF02546568
16. Aronne A, Catauro M, Pernice P, Marotta A (1993) Gel synthesis and crystallization of Li_2O - $7GeO_2$ glass powders. Thermochim Acta 216:169–176
17. Volnyanskii MD, Nesterov AA, Trubitsyn MP (2012) Thermal and electrical properties of glass-ceramics based on lithium heptagermanate. Phys Solid State 54(5):945–946. https://doi.org/10.1134/S1063783412050459
18. Nesterov OO, Trubitsyn MP, Volnyanskii DM (2015) Metastable state of the Li_2O–$11.5GeO_2$ glass ceramics with a high electrical conductivity. Phys Solid State 57(4):683–688. https://doi.org/10.1134/S1063783415040204
19. Volnianskii MD, Nesterov OO, Trubitsyn MP (2014) Devitrification of the Li_2O – $x(GeO_2)$ glass. Ferroelectrics 466(1):126–130. https://doi.org/10.1080/00150193.2014.895173
20. Nesterov OO, Trubitsyn MP, Nedilko SG, Volnianskii MD, Plyaka SM, Rybak YO (2018) Ionic conductivity in multiphase Li_2O-$7GeO_2$ compounds. Acta Phys Polonica 133(4):892–896. https://doi.org/10.12693/APhysPolA.133.892
21. Gabriel J, Petrov OV, Kim Y, Martin SW, Vogel M (2015) Lithium ion dynamics in Li_2S+GeS_2+GeO_2 glasses studied using ^{7}Li NMR field-cycling relaxometry and line-shape analysis. Solid State Nucl Magn Reson 70:53–62. https://doi.org/10.1016/j.ssnmr.2015.06.004
22. Barsoukov E, Macdonald JR (2005) Impedance spectroscopy. Theory, experiment and applications, 2nd edn. Wiley, New York, p 616. ISBN: 978-0-471-64749-2
23. Nesterov OO, Trubitsyn MP, Plyaka SM, Volnyanskii DM (2015) Complex impedance spectra of glass and glass ceramic Li_2O–$11.5GeO_2$. Phys Solid State 57(9):1759–1763. https://doi.org/10.1134/S1063783415090255
24. Böhmer R, Jeffrey KR, Vogel M (2007) Solid-state Li NMR with applications to the translational dynamics in ion conductors. Prog Nucl Magn Reson Spectrosc 50(2–3):87–174. https://doi.org/10.1016/j.pnmrs.2006.12.001
25. Böhmer R, Storek M, Vogel M (2018) NMR studies of ionic dynamics. In: Hodgkinson P (ed) Modern methods in solid-state NMR: a practitioners guide, vol 7. Royal Society of Chemistry, pp 193–230. https://doi.org/10.1039/9781788010467-00193
26. Torrey HC (1953) Nuclear spin relaxation by translational diffusion. Phys Rev 92(4):962–969. https://doi.org/10.1103/physrev.92.962
27. Kimmich R, Voigt G (1978) Zeitschrift fur Naturforschung. Astrophysik. Physik und Physikalische Chemie 3BA:1294–1306
28. Deutch JM (1972) J Chem Phys 56:6076–6081
29. Avogadro A, Villa M (1977) Nuclear magnetic resonance in a two dimensional system. J Chem Phys 66(6):2359–2367. https://doi.org/10.1063/1.434272
30. Bjorkstam JL, Villa M (1980) Second-order quadrupolar and low-dimensionality effects upon NMR resonance spectra. Phys Rev B 22(11):5025–5032. https://doi.org/10.1103/physrevb.22.5025

Chapter 7
Influence of Surface Ultrafine Grain Structure on Cavitation Erosion Damage Resistance

Yaroslav Kyryliv, V. Kyryliv, and Nataliya Sas

7.1 Introduction

Many operational properties of metallic materials, such as fatigue strength, frettage, resistance to wear, corrosion and electrochemical characteristics, and cavitation and erosion damage resistance, depend on the physical and mechanical properties of the surface layer. Destruction of the material begins from the surface. Therefore, the optimization of the surface layer's properties is very important for improving the service life of machine parts and new technologies of metal surfaces processing based on the creation of nanocrystalline (NCS), and ultrafine-grained structures (UFGS) in surface layers are of great interest. In particular, one of the ways to create NCS and UFGS is the grinding of grains in the superficial layer of material to nanometer size. Previous studies have shown that NCS and UFGS can be formed, in particular, by severe plastic deformation (SPD) of the surface. One of these methods is vibration-centrifugal hardening (VCH) [1, 2]. The results of these studies have shown that the VCH forms a high microhardness structure and a significant (up to 7 mm) depth due to the large mass of the strengthening tool. Such structure has better electrochemical characteristics and resistance to wear.

The developed VCH method allows to adjust the mass of the strengthening tool in a wide scope (from 3.5 to 7.5 kg) without increasing the diameter of the balls. Such conditions increase the depth and microhardness of the surface layer by increasing

Y. Kyryliv (✉)
Lviv State University of Life Safety, Lviv, Ukraine

V. Kyryliv
Karpenko Physico-Mechanical Institute of the NAS of Ukraine, Lviv, Ukraine

N. Sas
Stepan Gzhytskyi National University of Veterinary Medicine and Biotechnologies, Lviv, Ukraine

O. Fesenko, L. Yatsenko (eds.), *Nanocomposites, Nanostructures, and Their Applications*, Springer Proceedings in Physics 221,
https://doi.org/10.1007/978-3-030-17759-1_7

the contact loads in the processing zone [1, 2]. This provides fragmentation and increases the imperfection of the surface layer's structure and allows improving its properties. The main parameters that influence the physical and mechanical properties of the surface layer during the vibration processing are the amplitude and frequency of oscillations, the mass of the tool, the diameter of the balls, and the processing time [1, 2]. In some cases machine parts work under conditions of cavitation erosion damage (CED). The behavior of machine parts after VCH during operation in the CED conditions has not been studied.

The purpose of the work is to study the influence of VCH on cavitation erosion damage resistance and to find optimal VCH modes for increasing cavitation erosion damage resistance of the 40Kh steel.

7.2 Materials and Methods

Rings made from 40Kh steel were used as the samples for research. External and internal diameters of the samples were 75 and 60 mm, respectively, and the width of the samples was 20 mm. Garnished rings of the same steel for the comparative studies of resistance to wear reached the hardness of HRC 52–54. To study the CED, rectangular samples (140 × 12 × 6 mm; see Fig. 7.1) were made from the rings. Surface *A* of each rectangular sample was strengthened by the VCH. Strengthening was carried out on a special vibration-centrifugal hardening unit [2] with a special massive tool. Balls that were 13 mm in diameter were fixed in the tool. The unit provided vibrations of a certain amplitude and rotation of the tool, as well as its movement along the cylindrical surface. Samples were fixed on a mandrel. The treatment was performed with the following parameters: amplitude of oscillation $A = 5$ mm; frequency of oscillations $f = 24$ Hz; working tool mass $m = 3.5$–7.5 kg; treatment time $\tau = 12$–36 min; and eccentricity $\varepsilon = 10$ mm.

During the VCH treatment, shock dynamic loads act on the surface of a cylindrical sample that carries out vibration oscillations of a certain amplitude and frequency. The loads are made by a special tool of increased mass in the form of a ring with balls fixed in it, which rolls along the outer cylindrical surface of the sample. The material is strengthened as a result of the SPD. The construction of the tool and its mass makes it possible to obtain high contact loads at constant dimensions of the balls. The balls are fixed in the ferrule in the radial direction to the sample. Providing movement of the balls in necessary direction allows increasing the depth of hardening [2].

Microhardness and depth of hardening were measured on the PMT-3 unit according to the standard method (loading on the pyramid was 100 g). The microstructure was investigated on EVO 40XVP scanning electron microscope.

Erosion losses were measured gravimetrically. Before and after tests on cavitation erosion, the samples were washed with acetone and then with ethanol and then dried, and only after that they were weighed on an analytical grade VLA-200 M with an accuracy of ±0.00005 g.

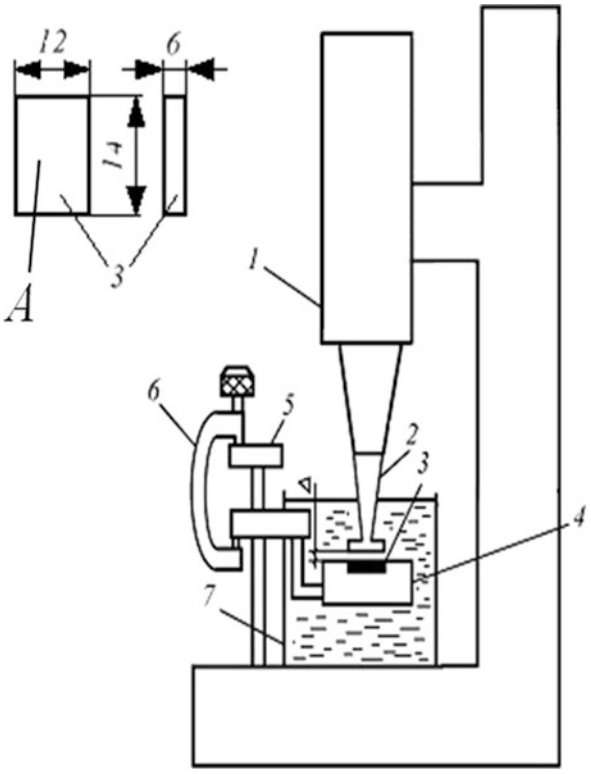

Fig. 7.1 Schematic illustration of magnetostrictive unit of CED resistance investigation with an undermounted sample

Products of corrosion were usually removed from the surface mechanically, and in some cases samples were steeped into an inhibited pickling solution (5% HCl + 0.15% acid corrosion inhibitor HOSP-10) [3]. After tests, the samples were washed with acetone and ethanol and dried.

The rate of cavitation erosion damage W (g/min•mm^2) was determined by the following formula [4]:

$$W = (m–m_0) / (S \times t)\,, \tag{7.1}$$

where m and m_0 are the masses of the sample before and after the experiment, g; S is the working area of the sample, mm^2; and τ is the exposure time, min.

The CED resistance was investigated by using the vibration method (using magnetostrictive vibration generator) [4]. According to obtained measurements of cavitation erosion losses, two types of dependencies were constructed. These dependencies characterized the CED of the material and made it possible to evaluate CED resistance of the material. First, for all the studied hydrodynamic modes with oscillation amplitude A (in the case of a magnetostrictive method), the CED kinetic diagrams were constructed in coordinates lg W–lgτ (W, the rate of CED, g/min•mm^2; τ, exposure time, min). They are known to have four main areas [4–6]:

(1) the incubation time τ (involves the time before the registration of mass losses), (2) increasing of W to the maximum value, (3) decreasing of W, and (4) the period of steady destruction, which is characterized by a relatively constant rate of CED (W_{st}). The incubation period of CED in a liquid environment was considered to finish at a time when the CED rate of the material exceeded the rate of corrosion. During the incubation period (as well as under test conditions, when the damage of the cavity surface of the sample was determined by its general corrosion) for calculating W, the working surface of the sample was taken into account. After visual determination of CED, only the part of the surface, on which the traces of damage were detected by the metallographic analysis, was considered for calculating W. According to the kinetic diagrams of the CED, the dependences $\lg W_{st}$–A and $\lg\tau$–A were constructed.

Serial unit UZDN-2 T containing a magnetostrictive generator with a working vibration frequency of 22 kHz was used. The sample, immersed in the liquid, is attached to the tip (Figs. 7.1 and 7.2). The cavitation zone in the unit is created by longitudinal oscillations of the emitter – a nickel rod. These oscillations are excited at the resonant frequency by a magnetostrictive generator. A low pressure area is created under the lower part of the sample which leads to formation of bubbles. During lowering motion, the pressure increases and the bubbles are closed. The amplitude of the oscillations at the UZDN-2 T can be changed within 10–50 μm.

Magnetostrictive tests were carried out with an amplitude of 30 μm in container 7 [4–10] according to the scheme with undermounted sample 3 (Figs. 7.1 and 7.2). Rectangular samples were mounted directly on magnetostrictor emitter 1. Due to the scheme, oscillation concentrator 2 was attached to emitter 1, and sample 3 in the form of a parallelepiped with dimensions of 14 × 12 × 6 mm was fixed in mandrel

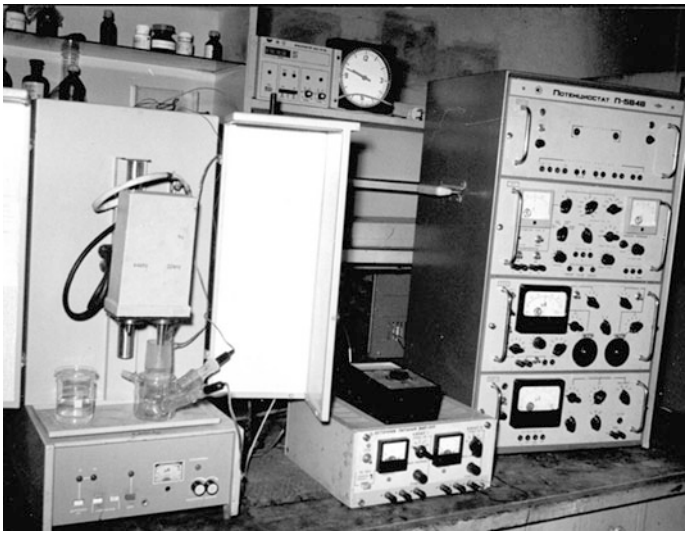

Fig. 7.2 Magnetostrictive unit of CED resistance investigation

4. The mandrel slided on a tripod 5. A micrometer 6 was used to obtain the required physical gap Δ. The value of Δ can significantly affect the CED rate according to such scheme of the tests [4]. During the tests, the gap was fixed at a constant value of $\Delta = 0.5$ mm. According to [4], such value of Δ could lead to obtaining the maximum CED rate. The general view of the test unit is shown in Fig. 7.2.

The tests for cavitation erosion damage (CED) were performed in water with medium hardness (pH 6.3–6.8, hardness 3.8–4.1 mg equivalents/liter). The magnetostrictive tests for undermounted samples were performed according to [11]. Stabilized CED rate W_{st} and incubation period of CED τ_i were chosen as damage parameters.

During the tests, special attention was paid to providing a constant amplitude of oscillations, as there is a direct connection between the amplitude of oscillations and mass loss of the sample.

7.3 Results and Discussion

Preliminary studies, conducted in [1, 2] showed that the optimal parameters for obtaining high microhardness, depth of hardening, favorable corrosion, and electrochemical characteristics are as follows: oscillation amplitude $A = 5$ mm; oscillation frequency $f = 24$ Hz; working tool mass $m = 3.5$, 4.5, and 7.5 kg; and eccentricity $\varepsilon = 10$ mm. Under these treatment conditions, $t = 28$ min, $\delta = 6$ mm, the microhardness reaches 8.9 GPa (Fig. 7.3), and single-phase structure of the

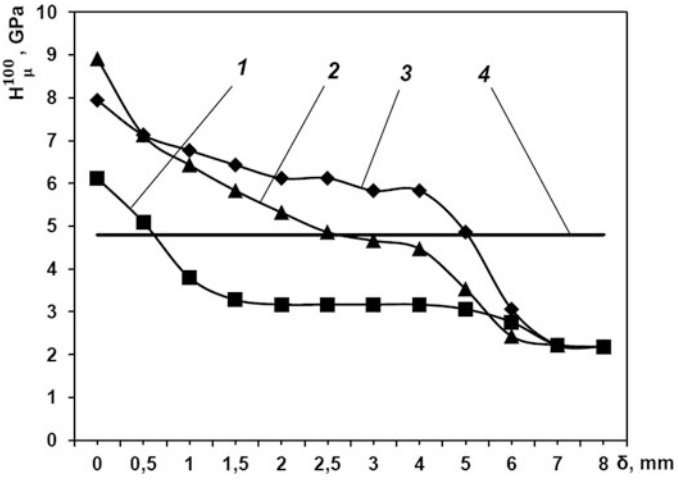

Fig. 7.3 Microhardness of the hardened 40Kh steel layer under various processing methods: (1) VCH ($m_i = 3.5$ kg, $\tau = 20$ min), (2) VCH ($m_i = 4.5$ kg, $\tau = 28$ min), (3) VCH ($m_i = 7.5$ kg, $\tau = 28$ min), and (4) hardening with low tempering (200 °C)

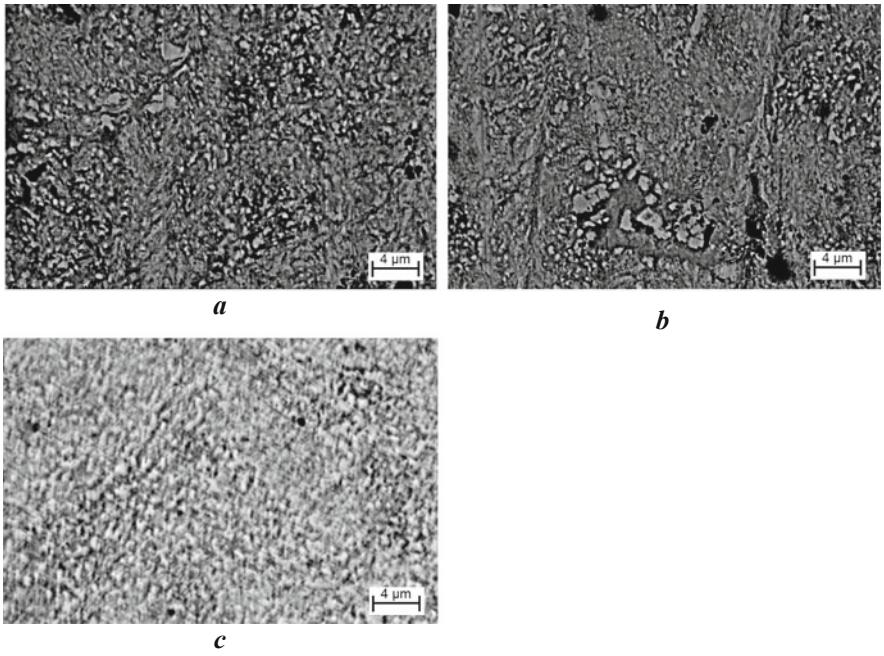

Fig. 7.4 The microstructure of 40Kh steel after VCH at depths: (**a**) 100 μm, (**b**) 1000 μm, and (**c**) matrix structure of 6 mm (×3000) under the following processing modes: $A = 5$ mm; $m = 4.5$ kg; $\tau = 28$ min; and $\varepsilon = 10$ mm

ferritic class (Fig. 7.4) with a grain size on the surface up to 190 nm and a high dislocation density up to 0.84×10^{12} cm^{-2} can be obtained [1, 2, 12].

After the VCH, the microstructure is highly fragmented near the surface at a depth of 100 μm (Fig. 7.4a). The grains are fragmented unevenly by separate blocks. At a depth of 1000 μm (Fig. 7.4b), the picture is similar, and the distribution of grain size decreases, apparently due to a more even distribution of deformation during the impact of the balls' surfaces and smoothly passes to the initial matrix structure (Fig. 7.4c). The steel structure is formed at the optimal processing time $t = 28$ min and the mass of the working tool $m = 4.5$ kg (Fig. 7.4).

One α-phase can be seen in the initial ferritic-pearlitic structure. There are no cementite lines on X-ray patterns, which agrees well with [2] on the decomposition of cementite as a result of cold plastic deformation. In conditions typical for a VCH, such decomposition is possible also at temperatures below the austenite phase existence. The ferrite structure was detected by X-ray studies at all depths within the range of 1 mm. The nature of the lines (110) and (220) [2] indicates large stress in the lattice of the deformed metal. The density of dislocations in the 1 mm section decreases gradually the depth of the metal [2], and this provides a gradient character of the grain size increase. The main increase in microhardness was obtained due to the large voltages in the lattice and the high density of dislocations.

The UFGS has an increased lattice parameter, which decreases in depth. Carbon may segregate at grain boundaries and on dislocation cores or in the form of small graphite precipitates. Dissolution of cementite during the cold deformation leads to redistribution of carbon, which, being placed on the grain boundaries, plays the role of "useful impurities" and blocks the returning processes. High stress in the lattice is the driving force of such redistribution [2].

In order to provide maximum microhardness, the depth of the hardened layer and favorable electrochemical characteristics (Table 7.1) VCH of the samples was performed under the following modes: $m_i = 3.5$ kg, $\tau = 20$ min; $m_i = 4.5$ kg, $\tau = 28$ min; and $m_i = 7.5$ kg, $\tau = 28$ min. By comparison, cavitation erosion tests of steel 40Kh were also performed after samples' processing by traditional technological methods (normalization and machining).

Technological processing methods, including VCH, provide different levels of surface deformation [13]. This has a different influence on the corrosion and electrochemical behavior of 40Kh steel (Table 7.1, Fig. 7.5) as well as cavitation erosion damage resistance. The optimal values of H_μ and the depth of the hardened layer were achieved during VCH under optimal conditions (Fig. 7.3, curves 1–3). VCH provides a significant depth (up to 7 mm) of the hardened layer with a microhardness exceeding the maximum possible value of H_μ (4.8 GPa), which can be achieved by hardening with low tempering (200 °C). The microhardness of 40Kh steel after VCH is higher in comparison with the initial microhardness, and its $H_\mu{}^{max}$ (4.8 GPa) is lower than the microhardness obtained after VCH. Since the CED resistance of materials is determined by the microhardness of the surface, and by corrosion resistance, the above described changes affect the CED resistance of 40Kh steel.

CED resistance of 40Kh steel samples after various technological processing methods differ significantly (Fig. 7.6). The sample after VCH ($m = 7.5$ kg, $\tau = 28$ min) is the most stable in terms of the incubation time τ_i (Fig. 7.6, curve 5). Since the incubation time largely depends on the corrosion resistance of the material, the effectiveness of the technological processing methods' influence on this parameter can be evaluated by the corrosion and electrochemical characteristics of 40Kh steel after processing (Table 7.1, Fig. 7.5).

The positive effect of VCH ($m = 7.5$ kg, $\tau = 28$ min), which is associated with higher corrosion and electrochemical parameters of 40Kh steel after this processing (Table 7.1, Fig. 7.5, curve 5), as well as high level of microhardness and depth of hardened layer, provides surface stability at the stage of damage accumulation. Normalization (Fig. 7.6b, curve 1) also provides some increase of τ_i, but it is lower in comparison to hardening with low tempering because relaxation and redistribution of considerable residual tensile stresses affect the corrosion properties. These residual tensile stresses are usually formed during machining of the samples. VCH under the modes $m = 3.5$ kg, $\tau = 20$ min, and m = 4.5 kg, $\tau = 28$ min, not only does not increase the incubation time but also reduces it in comparison with 40Kh steel in the initial state. After the VCH under these modes, a hardened layer with low level of electrochemical characteristics (Table 7.1 and Fig. 7.5, curves 3 and 4) close to the state of the surface overhardening is

Table 7.1 Mechanical and electrochemical characteristics of 40Kh steel after VCH

Number	Sample state		Surface microhardness $H_{\mu}{}^{100}$, GPa	Strengthening depth δ, mm	-E_{cor}, V	R_p, MΩ/m^2	$I_a{}^{max}$, A/cm^2
	Treatment	Treatment time τ, min					
1.	Normalization	–	2.25	–	0.43	64.23	0.0020
2.	Normalization and machining	–	2.8	0.12	0.57	47.13	0.0055
3.	VCH ($m_i = 3.5$ kg)	6	5.08	4.9	0.45	30.92	0.0020
4.		12	5.83	5.8	0.525	23.14	0.0017
5.		20	6.12	5.8	0.48	26.85	0.0019
6.		28	7.13	5.8	0.46	32.24	0.0025
7.		36[a]	4.12[a]	6.0	0.44	35.87	0.0032
8.	VCH ($m_i = 4.5$ kg)	6	5.83	5.4	0.47	25.66	0.00057
9.		12	6.43	5.4	0.39	68.06	0.00024
10.		20	7.94	6.7	0.44	72.79	0.00027
11.		28	8.91	6.4	0.49	31.69	0.0030
12.		36[a]	7.94[a]	6.7	0.57	16.83	0.0064
13.	VCH ($m_i = 7.5$ kg)	6	7.13	6.4	0.53	32.67	0.0028
14.		12	7.13	6.4	0.52	42.74	0.0026
15.		20	7.13	6.4	0.50	45.89	0.0045
16.		28	7.94	6.9	0.39	95.78	0.00036
17.		36	7.94	7.1	0.40	104.28	0.00014

[a]Overhardening

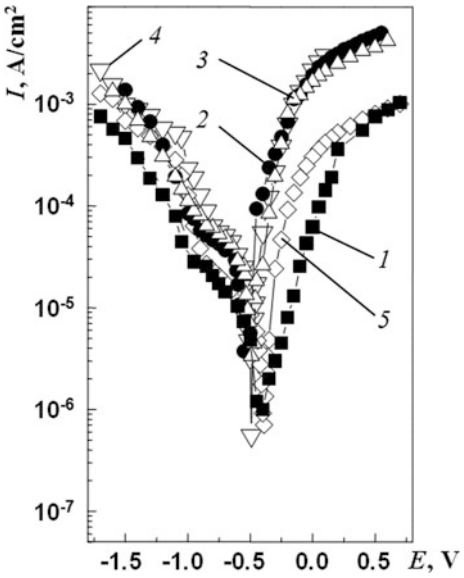

Fig. 7.5 Polarization curves of 40Kh steel after various processing methods: (1) normalization, (2) turning, (3) VCH ($m_i = 3.5$ kg, $\tau = 20$ min), (4) VCH ($m_i = 4.5$ kg, $\tau = 28$ min), and (5) VCH ($m_i = 7.5$ kg, $\tau = 28$ min)

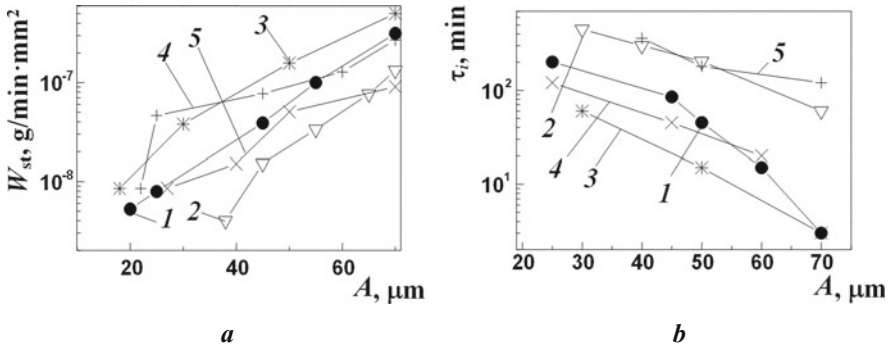

Fig. 7.6 Dependence of the stabilized CED rate (**a**) and the incubation time (**b**) on the amplitude of testing 40Kh steel samples after technological processing methods: (1, 1) normalization, (2, 2) hardening with low tempering (200 °C), (3, 3) VCH ($m = 3.5$ kg, $\tau = 20$ min), (4, 4) VCH ($m = 4.5$ kg, $\tau = 28$ min), and (5, 5) VCH ($m = 7.5$ kg, $\tau = 28$ min)

formed. According to [14], the corrosion and electrochemical behavior of steels is associated with the degree of their surface deformation, and in particular, in case of overhardening, dislocations reach the metal surface and become dissolution centers [14].

According to the criterion of the stabilized CED rate W_{st} (Fig. 7.6a), the most effective VCH mode is as follows: $m = 7.5$ kg, $\tau = 28$ min. VCH under the modes

$m = 3.5$ kg, $\tau = 20$ min, and $m = 4.5$ kg, $\tau = 28$ min, is not effective according to the criterion τ_i (Fig. 7.6b, curves 3 and 4). These modes provide maximum microhardness due to the achievement of a high defectiveness of the surface layer, close to the overhardening. Since it is believed that the CED occurs according to microfatigue mechanism [15, 16], the presence of a heterogeneous corrosive-active surface with significant defects greatly facilitates the damage of the material. This is due to the relatively insignificant depth and microhardness of the hardened layer in comparison with the depth of CED process (Fig. 7.6, curves 1 and 3).

So, the VCH technology improves the wearing quality of machine parts operating under CED conditions. However, the modes, which bring the material closer to the overhardening according to the degree of the structure imperfection ($m = 3.5$ kg, $\tau = 20$ min, and $m = 4.5$ kg, $\tau = 28$ min), are unsuitable. Modes characterized by lower microhardness, but higher corrosion resistance, are more effective. Such vibration-centrifugal hardening modes, as can be seen from Fig. 7.6, increase the cavitation erosion damage resistance by two times after stabilizing the destruction rate and by ten times at the incubation time.

7.4 Conclusions

Vibration-centrifugal hardening forms on the 40Kh steel surface, an ultrafine-grained ferritic structure with a grain size of 190 nm, dislocation density of 0.84×10^{12} cm^{-2}, and microhardness of 8.9 GPa.

Under certain processing modes, VCH increases the cavitation erosion damage resistance of the surface layer of the strengthened material, mainly due to the increase of the microhardness of the material and the improvement of its corrosion and electrochemical properties. Since the cavitation erosion damage resistance of the material is directly related to the degree of its surface deformation, overhardening of the material leads to decreasing of its CED resistance. For machine parts made of 40Kh steel, working under friction conditions, the best CED resistance is obtained under the following modes of processing: $m = 4.5$–7.5 kg; $\tau = 20$–28 min.

It is shown that vibration-centrifugal hardening increases the cavitation erosion damage resistance by two times after stabilizing the destruction rate and by ten times at the incubation time.

References

1. Aftanaziv IS, Bassarab AI, Kyryliv YB (2002) Mechanical and corrosion characteristics of 40Kh steel after vibration-centrifugal hardening treatment. Mater Sci 38(3):436–441
2. Kyryliv V, Kyryliv Y, Sas N (2018) Formation of surface ultrafine grain structure and their physical and mechanical characteristics using vibration-centrifugal hardening. Adv Mater Sci Eng 2018:3152170

3. Bassarab AI, Zhovnirchuk VM, Tsyrul'nyk OT (2001) Effect of the acid-inhibitor treatment on the resistance of 30Kh GSNA steel to the cavitation-erosion fracture in water. Mater Sci 37(5):820–822
4. Srinivasan Y., Vedula K. (1989) Mechanisms of combined erosion-corrosion of steels at elevated temperatures. A. Levy Ed. Minerals, Metals and Materials Society, Warrendale
5. Pirsol I (1972) Cavitation. Mills And Boon Ltd, London
6. Plesset FJ, Devine RE (1966) Effect of exposure time on cavitation damage. J Basic Eng 68(4):691–705
7. Singh R, Tiwari SK, Mishra SK (2012) Cavitation erosion in hydraulic turbine components and mitigation by coatings: current status and future needs. J Mater Eng Perform 21:1539–1551
8. Knapp R.T., Daily J.W., Hammitt F.G. (1970) Cavitation. McGraw-Hill New York
9. Yabuki A, Noishiki K, Komori K, Matsumura M (2001) The surface behavior of metallic materials during the incubation period of cavitation erosion. ASTMSTP 1339:357–369
10. Karasyuk YA, Kocherov VI, Benino VV, Galaktionova NL (1977) Relationship between corrosion and erosion factors in the cavitation failure of metals. Mater Sci 12(5):537–540
11. Hurei IV, Kyryliv VI, Bassarab AI (2004) Erosion resistance of 40kh steel after mechanical-pulse treatment. Mater Sci 40(2):296–301
12. Nykyforchyn H, Kyryliv V, Maksymiv O (2017) Wear resistance of steels with surface nanocrystalline structure generated by mechanical-pulse treatment. Nanoscale Res Lett 12:150
13. Kyryliv V, Chaikovs'kyi B, Maksymiv O et al (2016) Contact fatigue of 20KHN3A steel with surface nanostructure. Mater Sci 51:833–838
14. Gutman E. M. (1998) Mechanochemistry of materials. Cambridge International Science
15. Ricman RH, McNaughton WP (1990) Correlation of cavitation erosion behavior with mechanical properties of metals. Wear 140:63–82
16. Nykyforchyn HM, Kyryliv VI, Bassarab AI, Voloshyn VA (2002) Wear resistance of mechanical-pulse treated 40kh steel during abrasive friction and cavitation. Mater Sci 38(6):873–879

Chapter 8
The Effect of Mechanochemical and Ultrasonic Treatments on the Properties of Composition CeO_2–MoO_3 = 1:1

V. A. Zazhigalov, O. A. Diyuk, O. V. Sachuk, N. V. Diyuk, V. L. Starchevsky, Z. Sawlowicz, I. V. Bacherikova, and S. M. Shcherbakov

8.1 Introduction

Two-component compositions, which contain the molybdenum and cerium oxides, are promising materials used in modern electronics, adsorption, catalysis, and photocatalytic processes [1–10]. There are publications that show that the formation of nanodispersed materials in these compositions greatly improves their functional characteristics. Well-known traditional methods such as coprecipitation, thermal solid-phase, template, and sol-gel synthesis, which have a significant number of disadvantages when used for the synthesis of nanosized composites. These disadvantages are primarily related to use in the synthesis of metal salts, which determines the need for the further removal of anions, the use of fairly significant temperatures in calcination or synthesis, and the formation of harmful waste. Thus, the development of new alternative methods of synthesis that permit improvement of the conditions of nanodimensional composite preparation is a current objective.

V. A. Zazhigalov · O. A. Diyuk · O. V. Sachuk (✉) · I. V. Bacherikova
Institute for Sorption and Problems of Endoecology, National Academy of Sciences of Ukraine, Kyiv, Ukraine
e-mail: zazhigal@ispe.kiev.ua

N. V. Diyuk
Taras Shevchenko National University of Kyiv, Kyiv, Ukraine

V. L. Starchevsky
National University «Lviv Polytechnic», Lviv, Ukraine

Z. Sawlowicz
Institute of Geology, Jagiellonian University, Krakow, Poland

S. M. Shcherbakov
M.G. Kholodny Institute of Botany of the National Academy of Science of Ukraine, Kyiv, Ukraine

O. Fesenko, L. Yatsenko (eds.), *Nanocomposites, Nanostructures, and Their Applications*, Springer Proceedings in Physics 221,
https://doi.org/10.1007/978-3-030-17759-1_8

Among such methods, mechanochemical (MChT) and ultrasonic treatment (UST) have attracted attention. The application of these methods permits the use of metal oxides as raw materials, characterized by a small amount of harmful waste, which designates them as "environmentally friendly" technologies [11–13], the acquisition of nanoparticles, the modification of the properties of initial materials, etc. [14–17]. Data on the influence of these perspective methods on the properties of the oxide Ce/Mo system are practically absent in the scientific literature. Therefore, in this publication, the results of the mechano- and sonochemical treatment of the CeO_2–MoO_3 = 1:1 mixture and the comparison of the properties of the compositions obtained are presented.

8.2 Experimental

The powders of CeO_2 and MoO_3 (molar ratio 1:1) were used as the raw materials of the initial mixture. This mixture was treated in a planetary ball mill *Pulverisette–6* (Fritsch) in an air atmosphere for 2 h with balls measuring 5 mm in diameter and a balls to powder mass ratio (BPR) of 10:1 at a rotation frequency of 550 rpm. The technique of UST is described in our previous publication [18]. The samples obtained were studied by physical–chemical methods, which are presented below.

Powder X-ray diffraction (XRD) of the samples was conducted using PW 1830 Philips apparatus with Cu Kα radiation. Nitrogen sorption was used to determine the specific surface areas of the powders at the temperature of liquid nitrogen (−196 °C) in a Quantachrome instrument (NOVA-2200 Gas Sorption Analyzer). The scanning electron microscopy (SEM) investigations of the samples were realized on a Jeol JSM-6490 instrument in conjunction with an energy-dispersive spectrometer after deposition of a nanolayer of gold on the samples. Transmission electron microscopy (TEM) of the samples was carried out on a Jeol JEM 1230 device after their preliminary UST dispersion in a water–alcohol emulsion. H_2-TPR analysis was carried out (the instrument is presented in the Fig. 8.1) in a H_2-Ar atmosphere (H_2:Ar = 1:1) within the temperature range 30–800 °C at a heating rate of 5 °C/min, a feed rate of the mixture of 80 ml/min, a sample weight of 50 mg, a scale sensitivity of $3.4 \cdot 10^{-5}$ g, and a rate of registration of data of 10 point/min.

Electron paramagnetic resonance (EPR) spectra of the samples were obtained on a Bruker Elexsys E580 FT/C at room temperature at a frequency of 9.2–9.9 GHz.

The catalytic activity of the samples in the ethanol oxidation was tested in a flow fixed-bed stainless steel microreactor at atmospheric pressure within the temperature range of 25–310 °C. The catalyst (V = 0.5 cm^3 with fraction 0.25–0.50 mm) was loaded into a reactor. Gas mixture containing 1 vol % C_2H_5OH in air was passed through the reactor at a total flow rate of 20 cm^3/min. Initial components and reaction products have been analyzed on-line with the use of two gas chromatographs. On the device Chrom 5, with the use of a flame ionization detector (FID), the ethanol and acetic aldehyde were analyzed, and a Selmi-Chrom-1 with thermal conductivity detectors (TCD) was used to determine the amounts of

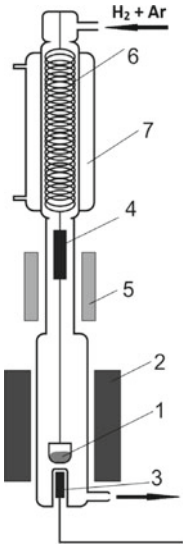

1 – sample;
2 – thermo-programmed furnace;
3 – thermocouple;
4 – ferrite core;
5 – solenoid;
6 – tungsten spring;
7 – thermostated case.

Fig. 8.1 Schematic diagram equipment of H_2-TPR tests

CO_x, CO, and C_2H_4. The reaction of ethanol partial oxidation to acetaldehyde (Ac) is shown in Eq. (8.1):

$$CH_3CH_2OH + 1/2O_2 \rightarrow CH_3CHO + H_2O \tag{8.1}$$

The parameters of the catalytic activity of modified samples were calculated according to the following formulas:

$$X_{EtOH} = C_{EtOH}\,(in) - C_{EtOH}\,(out)\,/\,C_{EtOH}\,(in) \times 100\% \tag{8.2}$$

$$S = C/C_{EtOH}\,(in) - C_{EtOH}\,(out) \times 100\% \tag{8.3}$$

$$Y = X_{EtOH} \times S/100\% \tag{8.4}$$

$$N = k\frac{Y_{Ac}}{m_{cat}} \tag{8.5}$$

where X_{EtOH} is ethanol conversion %, S is the selectivity of the product %, Y is the product yield %, C_{EtOH} (in) is the initial ethanol molar concentration, C_{EtOH} (out) is the ethanol molar concentration after the reactor, C is the product molar concentration after the reactor, N is catalyst productivity for acetic aldehyde, mol/kg_{cat}·h, and k (coefficient taking into account the amount of product produced in 1 h) is $5{\cdot}10^{-3}$ mol/h.

8.3 Results and Discussion

The XRD patterns of the initial CeO_2–MoO_3 = 1:1 mixture and the samples after MChT and UST are presented in Fig. 8.2. The initial oxide mixture (Fig. 8.2a) shows the presence of all characteristic reflexes of initial oxides with the dominant reflection of the α-MoO_3 orthorhombic modification from the plane (020). The decrease in the reflex intensity of the mixture components with their simultaneous broadening was observed after MChT of the sample over a period of 2 h (Fig. 8.2b), which can be connected to a decrease in particle size (the results of particle size calculations are presented in Table 8.1). It should be noted that the reflexes of phase α-MoO_3 from the planes (020) and (150) fully disappear and that the ratio of reflex intensity of the planes (040) and (060) is changed. $I_{(040)/(060)}$is equal to 1:1 for the sample after treatment whereas in an initial sample $I_{(040)/(060)}$ = 1:2. It may be due to the anisotropic destruction of α-MoO_3 crystal as a result of MChT activation, which leads to partial amorphization of this phase also. At the same time, from Fig.8.2b it can be seen that the reflex from the plane (111) of the CeO_2 phase of the cubic structure becomes dominant in the MChT sample without changes in the ratio of intensity of the reflexes $I_{(111)/(200)}$ = 3.2. However, according to the results presented in Table 8.1, a decrease in crystallite size of CeO_2 calculated to the plane (111) occurred after treatment. It is possible to propose that the chaotic destruction of this oxide without its amorphization takes place at MChT of the mixture.

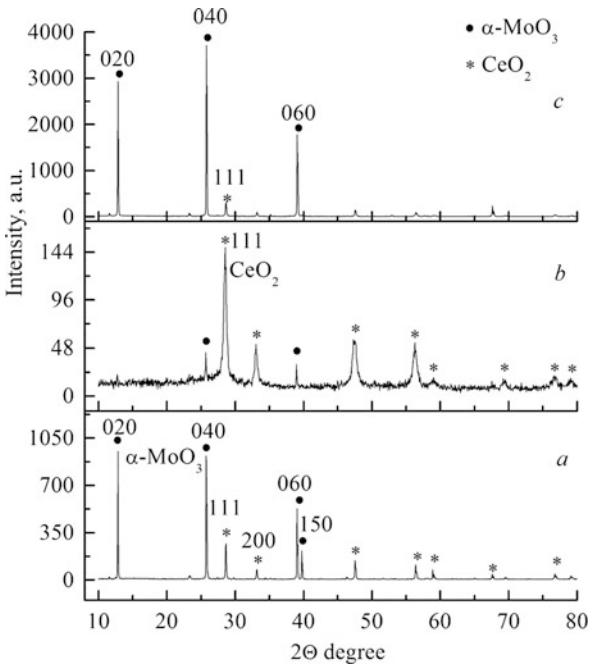

Fig. 8.2 X-ray diffraction (XRD) patterns of composition of Ce/Mo = 1:1: (**a**) initial sample, (**b**) after mechanochemical treatment (MChT), (**c**) and ultrasonic treatment (UST)

Table 8.1 X-ray diffraction (*XRD*) data of patterns of the CeO_2–MoO_3 system

Treatment type	Duration of treatment, h	L, nm[a]		S_{BET}, m^2/g
		MoO_3 (020)	CeO_2 (111)	
Initial	0	93	53	2
MChT	2	52	21	5
UST	1	70	30	6

MChT mechanochemical treatment, *UST* ultrasonic treatment
[a]Average crystallite size

Table 8.2 Energy-dispersive spectroscopy (EDS) analysis of the CeO_2–MoO_3 system

Element	Initial			After 2 h MChT						UST		
	A	B	FS	A	B	C	D	E	FS[a]	A	B	FS[a]
Mo	96.5	0	50.2	51.3	51.8	52.2	50.1	46.5	50.5	100	4.0	51.1
Ce	3.5	100	49.8	48.7	48.2	47.8	49.9	53.5	49.5	0	96.0	48.9

FS full surface

But some other changes in the sample were observed after the sonochemical process. From Fig. 8.1c the change in intensity of the main reflexes of MoO_3 from the planes (020) and (040) without a change in the reflex intensity ratio from the planes (040) and (060). Therefore, the anisotropic destruction of molybdenum oxide at UST proceeds in different direction is carried out, than that in the case of MChT. At the same time, no changes in the relative intensity of the reflexes of cerium oxide were observed after treatment. It worth noting that after sonochemical treatment, the MoO_3 reflexes remain dominant on a diffractogram, but a broadening of the reflexes of both oxides was observed. As result, a decrease in the particle size of both oxides was established (Table 8.1), but its value was less than that with MChT.

The results obtained allow the conclusion that after MChT and UST of oxide cerium-molybdenum mixture, the chaotic destruction of ceria and the anisotropic deformation of MoO_3 occurs. The direction of the last deformation depends on the method of treatment used.

Simultaneously, it was found that MChT and UST led to some changes in the porous structure, namely the formation of mesopores and an increase in the specific surface area of the systems (Table 8.1).

The decrease in oxide particle size in MChT and UST was confirmed by SEM data. It is necessary to pay attention to the results of the surface analysis, which are obtained by energy-dispersive spectroscopy (EDS; Table 8.2). Comparison of SEM and EDS analysis (Fig. 8.3a, Table 8.2) shows that in the initial mixture, the big crystals measuring 200–300 nm belong to MoO_3, whereas small particles with sizes 50–70 nm are characteristic of cerium oxide.

It was found that after MChT in the sample there are also larger particle sizes, but their morphology differs from that of the initial MoO_3. Simultaneously, the results of analysis of the composition of these particles (Table 8.2) show the equivalent content of molybdenum and cerium as in other places on the surface, where the presence of fine particles is observed.

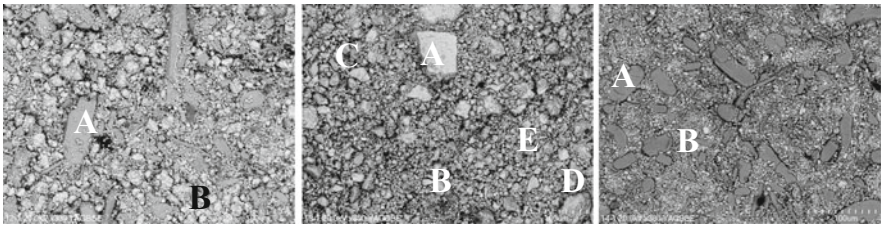

Fig. 8.3 Scanning electron microscopy (SEM) images of (**a**) the initial composition of Ce/Mo = 1:1 –and after its (**b**) MChT –and (**c**) UST

Thus, the results of the EDS analysis show an equable distribution of oxides on the whole sample surface independently from the particle dimensions, and, on the other hand, slightly lower cerium content in most places can indicate that the surface of cerium oxide is to a small degree covered by molybdenum oxide.

Other changes were observed after UST of the sample. From Fig. 8.3c it can be seen that large particles decrease in size and become more rounded (A), but that their analysis demonstrates the presence of MoO_3 only (Table 8.2). The small particles (B) reduce in size, but contain practically only cerium oxide. Analysis of the full surface of the sample after activation shows that the ratio of Ce/Mo in the composition is equal to 1.

Thus, the XRD and SEM data show the difference between MChT and UST of the CeO_2–MoO_3 mixture. In the first case, the destruction of both oxides with partial amorphization of molybdenum oxide and good mix of the small oxide particles (the presence of large forms can be connected to the agglomeration of small particles) was observed. In the second case, the partial destruction of the oxides without their mixing may be proposed.

Additional information about the processes that occur at MChT and UST of CeO_2–MoO_3 = 1:1 composition was obtained from TEM data (Fig. 8.4). The initial sample is characterized by the presence of large particles (dark places) with dimensions close to 100–200 nm (MoO_3) and elongated crystals with a smaller size, 50–100 nm (CeO_2). These results correspond to SEM data and show that large particles observed by SEM are conglomerates of smaller particles. MChT of the sample (Fig. 8.4b) leads to the formation of complex particles with an average size of about 100 nm. These particles contain the core, with the dimensions of 10–50 nm and a shell of thin, needle-like particles (thickness 2–3 nm, length 50–70 nm). Part of these complexes can be agglomerated with the formation of more large particles, which can be observed in the top right corner of the photo. Data obtained by XRD, SEM, and EDS permit us to suppose that dark crystals can be attributed to CeO_2, whereas the needle-like transparent particles present the partly amorphous molybdenum oxide. It is possible to suppose that the needle-like crystals belong to hydrated molybdenum oxide ($MoO_3 \cdot 0.5H_2O$), the formation of which was observed after the treatment of MoO_3. Simultaneously, it is necessary to note that the

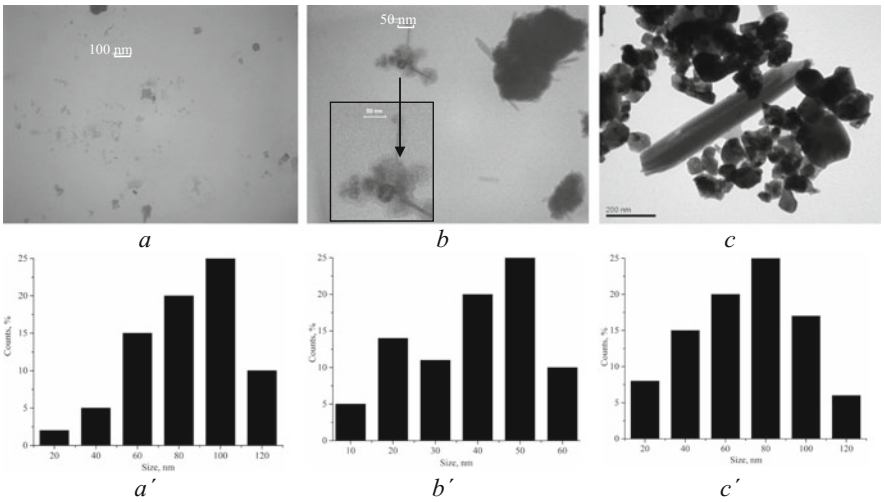

Fig. 8.4 Transmission electron microscopy (TEM) images and particle size distribution (´) of CeO_2–MoO_3 composition: (**a**) initial ***(a´)***, (**b**) after MChT ***(b´)***, and (**c**) UST ***(c´)*** of these samples respectively

Table 8.3 Catalytic properties of the composition CeO_2–MoO_3 after MChT and UST

Sample	$T_{reaction}$, °C		Product yield at $X_{ethanol} = 100\%$			N_{Ac}, mol/kg_{cat}·h
	$X_{50\%}$	$X_{100\%}$	CH_3CHO	C_2H_4	CO_x	
Initial	234	310	78	17	5	0.6
MChT	186	230	95	5	–	0.9
UST	158	200	87	–	13	0.7

N_{Ac} catalyst productivity for acetaldehyde

formation of the core–shell heterostructure, where the ceria is the core (25–35 nm) and amorphous MoO_3 is a transparent shell, was clearly observed in Zazhigalov et al. [19] after a longer period of MChT. The formation of the core–shell structure as early as 2 h of treatment is in good agreement with EDS data, which show the uniform distribution of Mo and Ce at different points of the surface (Table 8.3).

The data obtained for the sonochemically treated composition Ce/Mo = 1:1 (Fig. 8.4c (c´)) show the grinding of the particles MoO_3 up to 50–100 nm and the change in their crystal form from oblong to round. Simultaneously, the decrease in the crystal size of ceria from 50–150 nm to 25–35 nm was observed. No formation of complex crystallite was observed, which agrees with the results of XRD, SEM, and EDS.

In the first instance, for an understanding of the mixture samples transformation, the H_2-TPR analysis of initial oxides MoO_3 and CeO_2 was carried out.

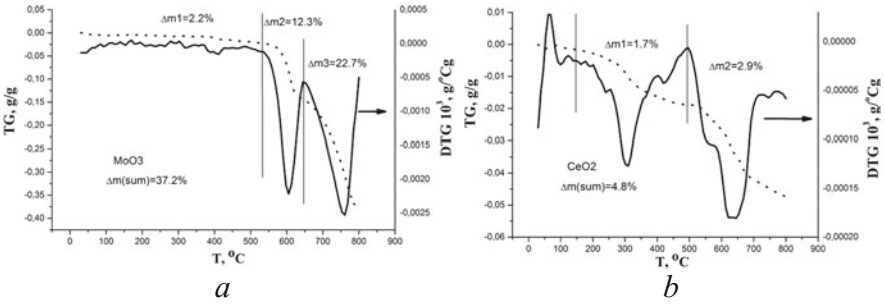

Fig. 8.5 Thermogravimetric profile and relative derivative curve: (**a**) MoO_3 initial, (**b**) CeO_2 initial

It is known that H_2-TPR of CeO_2 proceeds according to the general Scheme (8.6) [20]:

$$CeO_2 + xH_2 + CeO_{2-x} + xH_2O \tag{8.6}$$

From Fig. 8.5b a weight loss of 1.7% within the temperature range 150–500 °C can be seen, which corresponds to the formation of $CeO_{1.82}$. In the temperature range 500–800 °C, the sample is characterized by a weight loss of 2.9%, which corresponds to a further reduction in $CeO_{1.82}$ to Ce_2O_3 [21, 22].

As presented in Goswami et al. [23], the reduction of MoO_3 occurs consistently according to Scheme (8.7):

$$MoO_3 \rightarrow Mo_9O_{26} \rightarrow Mo_8O_{23} \rightarrow Mo_4O_{11} \rightarrow MoO_2 \rightarrow Mo. \tag{8.7}$$

The process of reduction to each of the next oxides is accompanied by a fixed weight loss. In Fig.8.5a, the H_2-TPR of MoO_3 is shown. There are several effects on the derivative thermogravimetric (DTG) curve, which can be explained by the stepwise reduction of MoO_3 to Mo. The complete weight loss at reduction of MoO_3 to Mo is 37.2%, whereas the theoretical value of weight loss is 33%. It can be connected to the sublimation of MoO_3. The H_2-TPR diagram of MoO_3 can be conditionally split into three parts:

(i) At T = 30–530°C, with weight loss $\Delta m_1 = 2.2\%$ corresponds to the removal of chemisorbed water and an initial reduction of MoO_3, and can be written as the following theoretical Schemes (8.8, 8.9, and 8.10) with appropriate weight loss:

$$9MoO_3 + H_2 = Mo_9O_{26} + H_2O \ (\Delta m = 1.2\%) \tag{8.8}$$

$$8MoO_3 + H_2 = Mo_8O_{23} + H_2O \ (\Delta m = 1.4\%) \tag{8.9}$$

$$5MoO_3 + H_2 = Mo_5O_{14} + H_2O \ (\Delta m = 2.2\%) \tag{8.10}$$

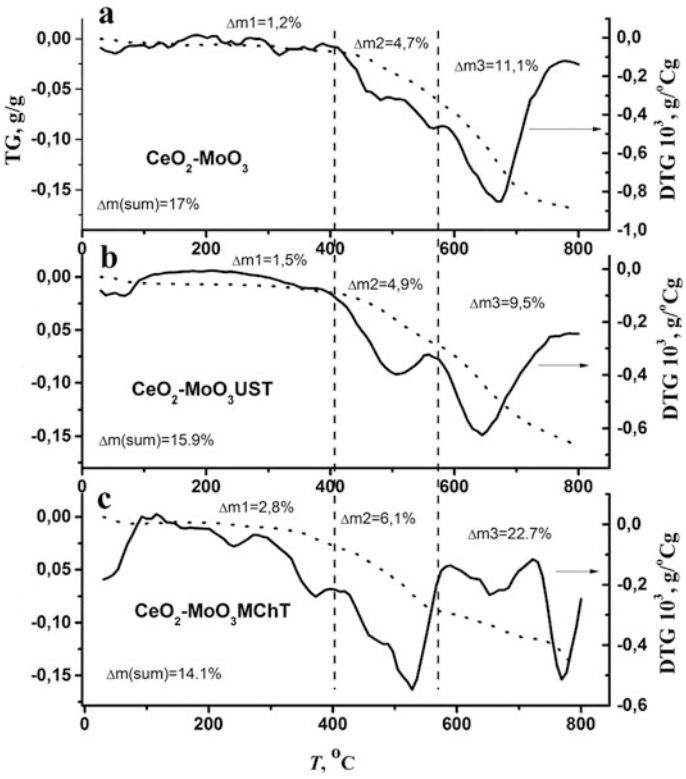

Fig. 8.6 Thermogravimetric profile and relative derivative curve: (**a**) initial CeO_2–MoO_3, (**b**) CeO_2–MoO_3 UST, –(**c**) CeO_2–MoO_3 MChT–

(ii) At T = 530–650°C with a mass loss of $\Delta m_2 = 12.3\%$, corresponding to a reduction of MoO_3:

$$MoO_3 + H_2 = MoO_2 + H_2O \ (\Delta m = 11.1\%) \tag{8.11}$$

(iii) This part is characterized by the complete reduction of oxide to molybdenum at T = 650–800°C, $\Delta m_3 = 22.7\%$:

$$MoO_2 + 2H_2 = Mo + 2H_2O \ (\Delta m = 22.2\%) \tag{8.12}$$

The thermogravimetric (TG) and DTG dependence of the hydrogen reduction of the CeO_2–MoO_3 compositions before and after treatments is presented in Fig. 8.6.

It was shown that the reduction of the initial CeO_2–MoO_3 sample begins at 400 °C, that is, 100 °C less than the reduction of MoO_3. The theoretical calculation of the total weight loss for nontreatment CeO_2–MoO_3 composition is 21%; however, the experimental weight loss of this sample is only 17%. This made it possible

to conclude that a mutual influence of oxides leads to changes in the reduction properties of the composition – the reducing beginning earlier, but system's initial CeO_2–MoO_3 is more stable for high-temperature reduction.

The UST and MChT of the sample (Fig. 8.6b, c) lead to the significant activation of the surface layer and an appearance of the defect in its structure, which is accompanied by an increase in oxygen mobility and a change in the character of the TG and DTG curves at controlled reduction. TG and DTG curves can be conditionally split into three parts: (i) at T = 30–410°C; (ii) 400–570°C; and (iii) 570–800°C. In the first part at T = 30–410°C, for the initial CeO_2–MoO_3 sample, the weight loss was $\Delta m_1 = 1.2\%$, but for CeO_2–MoO_3 after UST $\Delta m_1 = 1.5\%$, and the largest weight loss $\Delta m_1 = 2.8\%$ was observed for the CeO_2–MoO_3 sample after MChT. The second part at T = 410–570°C: for the initial CeO_2–MoO_3 system, the weight loss was $\Delta m_2 = 4.7\%$; for CeO_2–MoO_3 after UST there was a similar mass loss of $\Delta m_2 = 4.9\%$; and for the MChT sample a corresponding maximal weight loss of $\Delta m_2 = 6.1\%$ was observed. The third part at T = 570–800°C has another tendency: the largest weight loss $\Delta m_3 = 11.1\%$ was observed for the initial CeO_2–MoO_3 sample; in the case of CeO_2–MoO_3 after UST composition, the weight loss was $\Delta m_3 = 9.5\%$; and for MChT the CeO_2–MoO_3 weight loss had the smaller value of $\Delta m_3 = 5.2\%$, because for this pattern the main reduction occurred at lower temperatures. The comparison of the H_2-TPR results show that the sample is better able to undergo reduction after MChT than after UST. Obviously, the reduction of molybdenum oxide is the main contributor to weight loss in H_2-TPR. In our opinion, the greatest weight loss was observed in the MChT CeO_2–MoO_3 pattern within the temperature range 30–570°C, which can be explained by a decrease in the crystallite size of MoO_3, its partial amorphization, which was determined from XRD, and a deposition of nanoparticles of MoO_3 on CeO_2 with formation of core-shell structures (see Fig. 8.4b). All these facts make the CeO_2–MoO_3 MChT sample more susceptible to low-temperature reduction.

The EPR spectrum of the initial sample (Fig. 8.7a) demonstrates the presence of signal with g-factors $g_x = 1.926$, $g_y = 1.947$, and $g_z = 1.977$. According to the literature data [24, 25] this signal belongs to tetra- or hexacoordinated ions Mo^{5+} in axially distorted [MoO_6] octahedron respectively. The signal $g = 1.971$, whose presence can be connected to structural defects of industrial MoO_3, belongs to the Mo^{5+} ion with rhombic distortion, which also corresponds to the signals $g = 1.977$ and 1.979. The latter signal was observed in the spectrum of the sample after UST. It worth noting that the spectrum of the sonomodified sample is similar to the spectrum of initial composition. In the sample after MChT, it was found that the appearance of signal with parameters $g_{||} = 1.941$ and $g = 1.956$ (Fig. 8.7b), whose formation is due to the presence of a hexacoordinated Mo^{5+} ion in the MoO_3 crystal and the transition of the Mo^{5+} ion from the tetra- to the pentagonal coordination respectively, was observed to indicate the weakening of the Mo–O bond in the octahedron.

The signal $g = 2.02$, which is observed in the spectrum of the modified Ce/Mo = 50:50 sample, is the isotropic signal of ion-radical O_2^-, which is located

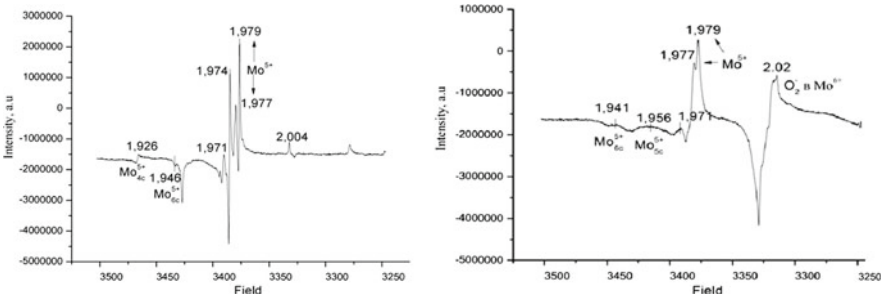

Fig. 8.7 The EPR spectra of (**a**) the initial Ce/Mo = 1:1 sample and (**b**) the sample after MChT

on Mo^{6+} ions [26]. These data are in agreement with XRD results of the anisotropic destruction of MoO_3 crystal.

The growth production of bio-ethanol (Et) from raw nonfood, primarily cellulose, creates opportunities for the production of valuable chemicals on this basis, for example, acetic aldehyde (Ac) (according to Scheme 8.13).

$$\mathbf{CH_3CH_2OH} \overset{k_1}{\rightleftharpoons} \mathbf{"CH_3CH_2O"} \overset{k_2}{\rightleftharpoons} \mathbf{CH_3CHO} \overset{k_3}{\rightarrow} \mathbf{CH_3COOH} \qquad (8.13)$$
$$k_4 \downarrow$$
$$\mathbf{CO_x}$$

This Scheme clearly indicates that the reaction proceeded via Ac before forming acetic acid [27]. Experimental data show that acetic acid is not a source of CO_X. The formation of CO_x can be presumed to originate from the full oxidation of an adsorbed intermediate reaction. Ac is selectively produced when k2≫k3>k4, whereas acetic acid is selectively produced when k3≫k2> k4 [27]. Recently, systems with high catalytic characteristics in the reaction of the selective oxidation of ethanol to Ac have been synthesized [18, 27–33]. Thus, vanadium-containing catalysts show 50% conversion of ethanol and Ac selectivity is about 100% at T = 160°C. However, an increase in temperature and in ethanol conversion leads to the appearance and a sharp increase in CO_x without the formation of acetic acid [28].

The study of Ce/Mo = 1:1 in an ethanol oxidation reaction shows that the main reaction method is ethanol dehydrogenation to acetic aldehyde according to Eq. (8.1). It was found that in an initial sample, the maximal conversion is achieved at 310 °C with an Ac yield of 78% (Fig. 8.8a). MChT for 2 h leads to significant decrease in the temperature reaction and the maximal yield of Ac is equal to 95% at 100% ethanol conversion, which is achieved at 230 °C (Fig. 8.8b).

From Fig. 8.8c it can be seen that UST allows the maximal values of selectivity and yield of Ac (87%) to be obtained at 200 °C, whereas in the initial sample at the same temperature, the yield of the main product is only 4%.

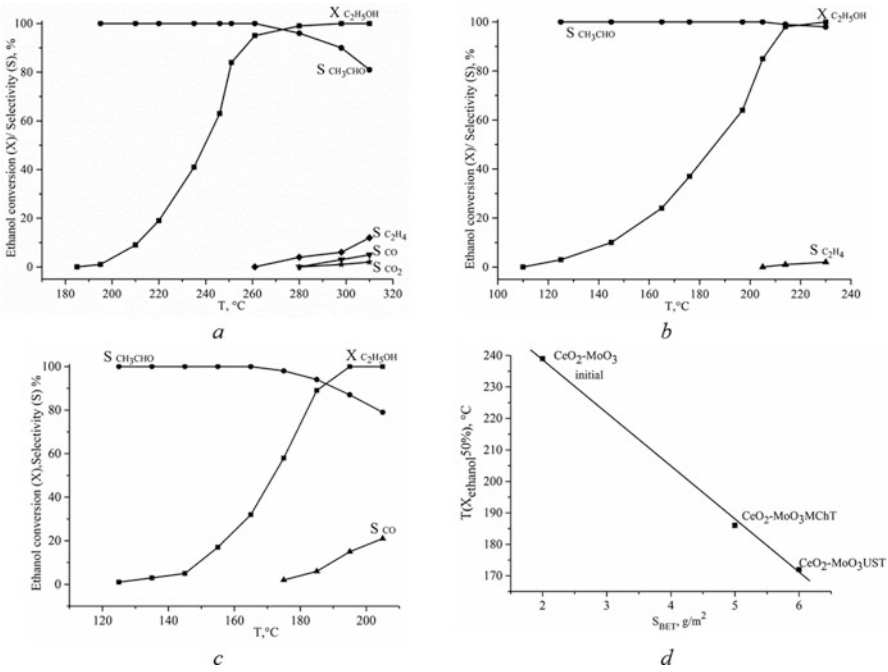

Fig. 8.8 Temperature dependence of ethanol conversion and selectivity of reaction product formation on (**a**) the initial sample, (**b**) after MChT, (**c**) UST, (**d**) correlation between the specific surface area and catalyst activity (temperature of the achievement of 50% ethanol conversion)

An interesting fact is that the catalytic testing of the initial oxide mixture leads to the formation of both C_2H_4 and CO_x as by-products. The increase in the temperature leads to an increase in the selective formation of ethylene and does not affect CO_x formation. MChT leads to the formation of only C_2H_4 as a by-product, whereas UST is accompanied by a formation of CO as a single by-product in the reaction of the selective oxidation of ethanol. This fact may indicate the different nature of the "active catalytic sites" formed as a result of MChT and UST.

The correlation between a specific surface area and catalyst activity (temperature of the achievement of 50% ethanol conversion) is presented in Fig. 8.8d. In our opinion, the increase in the catalytic activity of treated compositions can be explained by a decrease in particle size (Table 8.1) as a result of treatment and a corresponding increase in their specific surface area, i.e., the number of catalytically active centers. In addition, the increase in catalyst activity after MChT can be caused by the presence of tetrahedral coordinated Mo^{5+} ions in amorphous molybdenum oxide (Fig. 8.5b), which can easily coordinate oxygen with the formation of Mo^{6+}–O_2^- pairs, and oxygen ions can activate the process. It can be assumed that the shell of molybdenum oxide is a selective component of these catalysts.

8.4 Conclusion

The influence of the MChT and UST of the CeO_2–MoO_3 = 50:50 composition on its structural, catalytic, and reducing properties was investigated. It was shown that in both processes, a decrease in crystallite size of the initial oxides with the formation of nanodispersed particles occurs. These changes are accompanied by a decrease in the temperature reaction in ethanol oxidation and make it possible to obtain Ac with a maximal yield of 95% at 230 °C. The results obtained confirm that a high activity of the sample in the formation of Ac process in ethanol oxidation is determined by the presence of dispersed MoO_3. In the study of reduced properties, it was found that after MChT, the sample of CeO_2–MoO_3 is more actively reducing at a temperature of 200—600°C than initial and sonotreated samples.

Acknowledgments This work was financially supported by the NASU Programs: Fundamental Research "New Functional Substances and Materials for Chemical Engineering" (project 7–17/18) and the Program for Young Scientists (project 41: "Synthesis of new nanodispersed photocatalysts of environmental protection processes").

References

1. Jin Y, Li N, Liu H, Hua X, Zhang Q, Chen M, Teng F (2014) Highly efficient degradation of dye pollutants by Ce-doped MoO_3 catalyst at room temperature. Dalton Trans 43(34):12860–12870
2. Zhao S, Li J, Wang L, Wang X (2010) Degradation of rhodamine B and safranin-T by MoO_3:CeO_2 nanofibers and air using a continuous mode. Clean (Weinh) 38(3):268–274
3. Sobhani-Nasab A, Maddahfar M, Hosseinpour-Mashkan SM (2016) $Ce(MoO_4)_2$ nanostructures: synthesis, characterization, and its photocatalyst application through the ultrasonic method. J Mol Liq 216:1–5
4. Mohamed MM, Katib SMA (2005) Structural and catalytic characteristics of MoO_3/CeO_2 catalysts: CO oxidation activity. Appl Catal A Gen 287(2):236–243
5. Chang H, Jong MT, Wang C, Qu R, Du Y, Li J, Hao J (2013) Design strategies for P-containing fuels adaptable CeO_2-MoO_3 catalysts for $DeNO_x$: significance of phosphorus resistance and N_2 selectivity. Environ Sci Technol 47(20):11692–11699
6. Zhu J, Gao F, Dong L, Yu W, Qi L, Wang Z, Dong L, Chen Y (2010) Studies on surface structure of $M_xO_y/MoO_3/CeO_2$ system (M = Ni, Cu, Fe) and its influence on SCR of NO by NH_3. Appl Catal B Environ 95(1–2):144–152
7. Peng Y, Qu R, Zhang X, Li J (2013) The relationship between structure and activity of MoO_3–CeO_2 catalysts for NO removal: influences of acidity and reducibility. Chem Commun 49:6215–6217
8. Nasser H, Rédey Á, Yuzhakova T, Kovács J (2009) Thermal stability and surface structure of Mo/CeO_2 and Ce-doped Mo/Al_2O_3 catalysts. J Therm Anal Calorim 95(1):69–74
9. Matsuoka Y, Niwa M, Murakami Y (1990) Morphology of molybdena supported on various oxides and its activity for methanol oxidation. J Phys Chem 94:1477–1482
10. Rao BG, Sudarsanam P, Rangaswamy A, Reddy BM (2015) Highly efficient CeO_2–MoO_3/SiO_2 catalyst for solvent-free oxidative coupling of benzylamines into N-benzylbenzaldimines with O_2 as the oxidant. Catal Lett 145(7):1436–1445

11. Chatel. G (2018) How sonochemistry contributes to green chemistry? Ultrasonics Chem Part B 40:117–122
12. Quaresma S, André V, Fernandes A, Duarte MT (2017) Mechanochemistry – a green synthetic methodology leading to metallodrugs, metallopharmaceuticals and bio-inspired metal-organic frameworks. Inorganica Chimia Acta, Part 2 455:309–318
13. Buyanov RA, Molchanov VV (1996) Application of the method of mechanochemical activation in low-waste energy-saving technologies for the production of catalysts and carriers. J. Chemical Industry 3:152–157
14. Bang BJH, Suslick KS (2010) Applications of ultrasound to the synthesis of nanostructured materials. Adv Mater 22:1039–1059
15. Mason TJ, Lorimer J (2003) Applied sonochemistry: uses of power ultrasound in chemistry and processing. Wiley, Weinheim, p 303
16. Balaz P (2008) Mechanochemistry in nanoscience and minerals engineering. Springer, Berlin, p 412
17. Boldyrev VV et al (2009) Fundamental principles of mechanical activation of mechanosynthesis and mechanochemical technologies. Publish.Hous SORAN, Novosibirsk, p 343
18. Zazhigalov VA, Sachuk OV, Diyuk OA, Starchevskyy VL, Kolotilov SV, Sawlowicz Z, Shcherbakov SM, Zakutevskyy OI (2018) The ultrasonic treatment as a promising method of nanosized oxide CeO_2-MoO_3 composites preparation. In: Fesenko O, Yatsenko L (eds) Nanochemistry, biotechnology, nanomaterials, and their applications, and their applications, Springer Proceedings in Physics 214. Springer International Publishing AG, part of Springer Nature, Cham, pp 297–308
19. Zazhigalov VA, Wieczorek-Ciurowa K, Sachuk OV, Diyuk EA, Bacherikova IV (2018) Mechanochemical synthesis of nanodispersed molybdenum oxide catalysts. Theor Exp Chem 54(4):225–234
20. Fierro J, Sanz JSJ, Rojo J (1987) Induced changes in Ceria by thermal treatments under vacuum or hydrogen. J Solid State Chem 66:154–162
21. Laachir A, Perrichon V, Badri A, Lamotte J, Catherine E, Lavalley JC, El Fallah J, Hilaire L, Le Normand F, Quéméré E, Sauvion GN, Touret O (1991) Reduction of CeO_2 by hydrogen. Magnetic susceptibility and Fourier-transform infrared, ultraviolet and X-ray photoelectron spectroscopy measurements. J Chem Soc Faraday Trans 87(10):1601–1609
22. Marrero-Jerez J, Chinarro E, Peña-Martínez J, Núñez P (2015) CGO20–CuO composites synthesized by the combustion method and characterized by H_2-TPR. Ceram Int 41(9):10904–10909
23. Goswami R, Herman H, Sampath S, Jiang X (2001) Plasma sprayed Mo-Mo oxide nanocomposites: synthesis and characterization. Surf Coat Technol 141(2):220–226
24. Boudlich D, Haddad M, Nadiri A, Berger R, Kliava J (1998) Mo^{5+} ions as EPR structural probes in molybdenum phosphate glasses. J Non-Cryst Solids 224:135–142
25. Dyrek K, Łabanowska M (1991) Electron paramagnetic resonance investigation of the paramagnetic centres in polycrystalline MoO_3. J Chem Soc Faraday Trans 87(7):1003–1009
26. Il'ichev AN, Kuli-zade AM, Korchak VN (2005) ESR study of the formation of radical anions on oxidized CeO_2 and CeO_2/ZrO_2 adsorbing a $CO + O_2$ mixture O-2. Kinet Catal 46(3):396–402
27. Jørgensen B, Christiansen SE, Thomsen MLD, Christensen CH (2007) Aerobic oxidation of aqueous ethanol using heterogeneous gold catalysts: efficient routes to acetic acid and ethyl acetate. J Catal 251:332–337
28. Takei T, Iguchi N, Haruta M (2011) Synthesis of acetoaldehyde, acetic acid, and others by the dehydrogenation and oxidation of ethanol. Catal Surv Jpn 15(2):80–88
29. Yoshitake H, Aoki Y, Hemmi S (2006) Mesoporous titania supported-molybdenum catalyst: the formation of a new mesophase and use in ethanol-oxygen catalytic reactions. Microporous Mesoporous Mater 93(1–3):294–303

30. Beck B, Harth M, Hamilton NG, Carrero C, Uhlrich JJ, Trunschke A, Shaikhutdinov S, Schubert H, Freund H-J, Schlögl R, Sauer J, Schomäcker R (2012) Partial oxidation of ethanol on vanadia catalysts on supporting oxides with different redox properties compared to propane. J Catal 296:120–131
31. Kim D-W, Kim H, Jung Y-S, Song IK, Baeck S-H (2008) Synthesis of tungsten–vanadium mixed oxides for ethanol partial oxidation. J Phys Chem Solids 69:1513–1517
32. Tesser R, Maradei V, Di Serio M, Santacesaria E (2004) Kinetics of the oxidative dehydrogenation of ethanol to acetaldehyde on V_2O_5/TiO_2-SiO_2 catalysts prepared by grafting. Eng Chem Res 43:1623–1633
33. Quaranta NE, Soria J, Corberan VC, Fierro JLG (1997) Selective oxidation of ethanol to acetaldehyde on $V_2O_5/TiO_2/SiO_2$ catalysts effect of TiO_2-coating of the silica. Support J Catal 171:1–13

Chapter 9
Behavior of Tempered Surface Nanocrystalline Structures Obtained by Mechanical-Pulse Treatment

O. Maksymiv, V. Kyryliv, O. Zvirko, and H. Nykyforchyn

9.1 Introduction

Nanocrystalline structures (NCS) and technologies of their production have been a source of great interest to scientists and engineers in recent years because of their unique properties [1]. Obtaining of NCS with high mechanical properties (strength, plasticity, wear resistance, etc.) is particularly important. The technology of mechanical-pulse treatment (MPT) [2, 3] has been recently developed and successfully used for steels to produce surface NCS by severe plastic deformation (SPD) [4], which is generated by energy of high-speed friction. MPT is based on the principle of grinding and can be realized on slightly modified lathes and grinding machines. The physics of MPT consists in a heating of surface layers of treated metal during high-speed friction with the rotational cylindrical tool above the phase transformation temperature (above 850 °C). The peculiarity of the MPT technology is using special fluids, so-called technological media (TM), which are supplied to the friction contact zone and play two roles: (a) enabling structural-phase transformations to occur in the material due to its rapid cooling and (b) saturation of the metal surface layer by chemical elements (carbon, nitrogen, etc.) as a result of thermal and mechanical destruction of TM components within the friction contact zone and intensive mass transfer. Therefore, during MPT two very important processes are realized: (a) metal surface nanostucturization by SPD and (b) metal surface alloying by chemical elements from TM combined with thermal treatment similar to quenching.

Subsequent tempering of NCS is one of the ways to improve its mechanical properties [5]. An important detail for MPT technology is the fact that alloying elements,

O. Maksymiv · V. Kyryliv (✉) · O. Zvirko · H. Nykyforchyn
Karpenko Physico-Mechanical Institute of NAS of Ukraine, Lviv, Ukraine
e-mail: kyryliv@ipm.lviv.ua

O. Fesenko, L. Yatsenko (eds.), *Nanocomposites, Nanostructures, and Their Applications*, Springer Proceedings in Physics 221,
https://doi.org/10.1007/978-3-030-17759-1_9

saturating the metal surface layer, are mainly concentrated at the grain boundaries. Therefore, they suppress the process of recrystallization with temperature increase and facilitate stabilization of NCS [6, 7]. Under the influence of thermal field, force field, and irradiation and during long-term service even at ambient temperatures as well, NCS undergo processes of recrystallization, segregation, homogenization, and relaxation, phase transformation, amorphization, and agglomeration of the nanopores (nanocapillaries) [8]. Differentiation of their impact on mechanical properties of NCS is rather complicated, but almost all of the abovementioned factors significantly influence on properties and service characteristics of NCS. The additional thermal treatment could have the opposite effect on NCS: stabilization of NCS properties [9] on the one hand and their degradation due to partial loss of the initial nanoscale of NCS on the other hand.

The aim of this research was to study the influence of tempering temperature on the structure and mechanical properties of NCS surface layer produced by MPT on 40Kh (0.4C-1Cr) steel.

9.2 Materials and Experimental Methods

MPT was applied to 40Kh steel specimens of two geometries: flat and cylindrical. Flat specimens for X-ray analysis and microhardness measurements were machined from the round bar 25 mm in diameter. The bar was forged to the strip size of 4×32 mm and annealed at the temperature of 860 °C, and after that the specimens with size of $2 \times 20 \times 30$ mm were machined. MPT was applied to both sides of specimens using flat surface grinding machine SPC-20 at the following treatment regimes: tool rotation speed 50 m/s, linear velocity of stage movement 0.0017 m/s, cross-sectional tool advance 0.5 mm on a double-stage movement, and depth of run 0.3 mm (the value characterizes a pressing force of the tool to the treated specimen). Strengthening tool was made of 40Kh steel. Special TM (I-12A industrial oil, GOST 20799-75, with addition of low-molecular-weight polyethylene) was used during MPT for carburizing of the metal surface layer [10].

Cylindrical specimens (rings) 40 mm in diameter and 10 mm thick for wear resistance studies were machined from the round bar and treated by MPT using a slightly modified grinding machine 1 K62 [11] applying the same TM for carburizing at the following regimes: tool rotation speed 50 m/s, rotational speed of treated specimen 0.04 m/s, and depth of run 0.3 mm. Inserts were produced from VCh-60 cast iron (3.3C-2.6Si-0.6Mn-0.3Ni-0.1Cr) in the as-received state. All specimens made of 40Kh steel after MPT were tempered at 200, 300, 400, and 500 °C during 1 h. Wear resistance studies were carried out on friction machine MI-1 M according to ring (specimen)-insert (counter body) scheme [12] in oil medium (I-20A industrial oil, GOST 20799-75) at the load of 2 MPa and sliding velocity of 0.9 m/s. The weight loss ΔG of tested specimens after a certain duration of time (6 h) was considered as the wear parameter. The specimen's weight loss was determined using an analytical balance with a precision of ±4 mg.

Microhardness H_μ was measured using PMT-3 equipment at the load of 100 g. Phase composition, average grain size, and value of relative stresses in the lattice of the specimen surface layer after strengthening treatment were determined by X-ray analysis using the diffractometer DRON-3 with a CuK_α X-ray source (voltage of 30 kV and intensity of 20 mA), applying a step of 0.05° and exposition of 4 s. The diffractograms were post-processed using the software CSD [13]. The X-ray diffraction patterns were analyzed using the JCPDS-ASTM index [14].

9.3 Results and Discussion

The metallographic studies of the cross section of the flat specimen in depth from the surface revealed the strengthened surface layer as the unetched area (so-called white layer) (Fig. 9.1a). The microhardness of the surface layer of the treated specimen was measured on its cross section (Fig. 9.1b.). It can be visually observed that the size of microhardness indentation imprints in the strengthened layer was smaller than in the matrix material which points to its higher microhardness. The quantitative assessments of H_μ in a depth δ from the surface and from the side of the section (Fig. 9.1a) showed that microhardness varied from maximal value ~ 8.5 GPa on the surface to 2.8 GPa in the matrix material, which was three times less. The thickness of the strengthened layer was ~ 130 μm, and it corresponded with the thickness of the unetched area revealed at the metallographic analysis. Such correspondence points to the responsibility of the unique structure of the strengthened layer for its mechanical property H_μ.

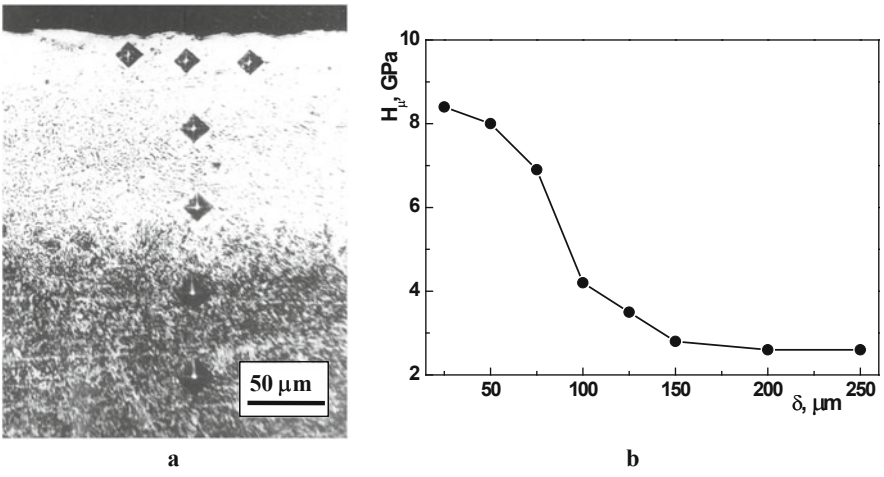

Fig. 9.1 Microstructure (**a**) and microhardness H_μ in depth from surface δ (**b**) of 40Kh steel after MPT

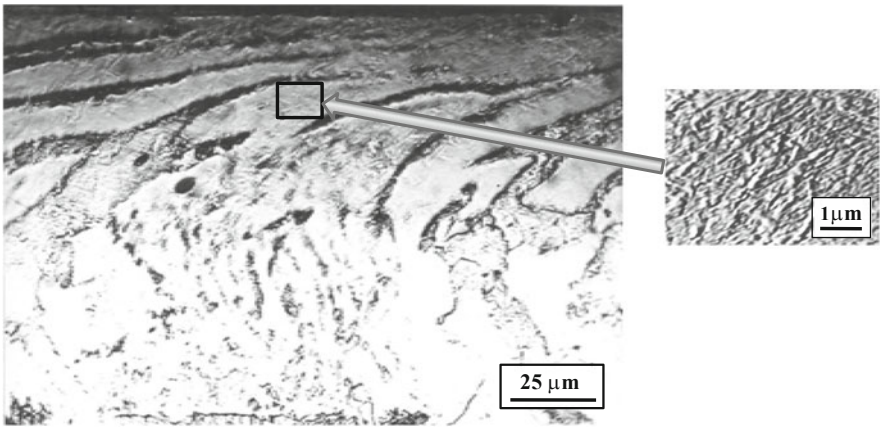

Fig. 9.2 Texture of deformation and fragment of the surface layer of 40Kh steel after MPT

At higher magnifications, the texture of deformation [7] was observed nearly on the surface (Fig. 9.2), which confirmed intense shear deformation necessary for surface nanostructurization during MPT. Dark areas on the surface represent only other crystallographic orientations of theirs compared with light ones, but don't represent an occurrence of another phase. The fragmentation of the structure in the form of unequiaxed stretched areas was observed at even higher magnifications. It allows us to assume that NCS consists of unequiaxed grains as well.

According to X-ray analysis, the steel after MPT had a microstructure, which consisted of pure ferrite α-Fe (Fig. 9.3) with grain size ~ 60 nm. It should be noted that MPT causes heating of surface layers to temperatures above the temperature of phase transformations. Therefore, the appearance of phases, which usually consisted in steel after cooling of austenite, was expected: creation of martensite due to rapid cooling or, at least, formation of cementite, if the cooling rate of the metal was insufficient for martensite transformation. However, martensite and cementite weren't detected on the steel surface after MPT. It could be also assumed that in condition of high-speed heating, there wasn't enough time for formation of an austenite structure, and, accordingly, the initial pearlite structure consisted basically of ferrite and cementite was cooled. Moreover, those phases should be detected by X-ray analysis. In this case, the absence of cementite in the structure of the surface layer was fundamental and could be described in two ways: (a) carbon from cementite dissolved in austenite during heating and martensite didn't form during cooling and (b) cementite decomposed during MPT.

The solubility of carbon in iron lattice at ambient temperatures under equilibrium conditions is negligibly small compared with its content in the steel. So, it can be assumed that all carbon was located at the grain boundaries in atomic state when martensite was absent in the microstructure. Such unconventional state of carbon for ferrite-pearlite steel could be explained by the fact that the total area of grain boundaries in NCS is several orders higher than in the microcrystalline

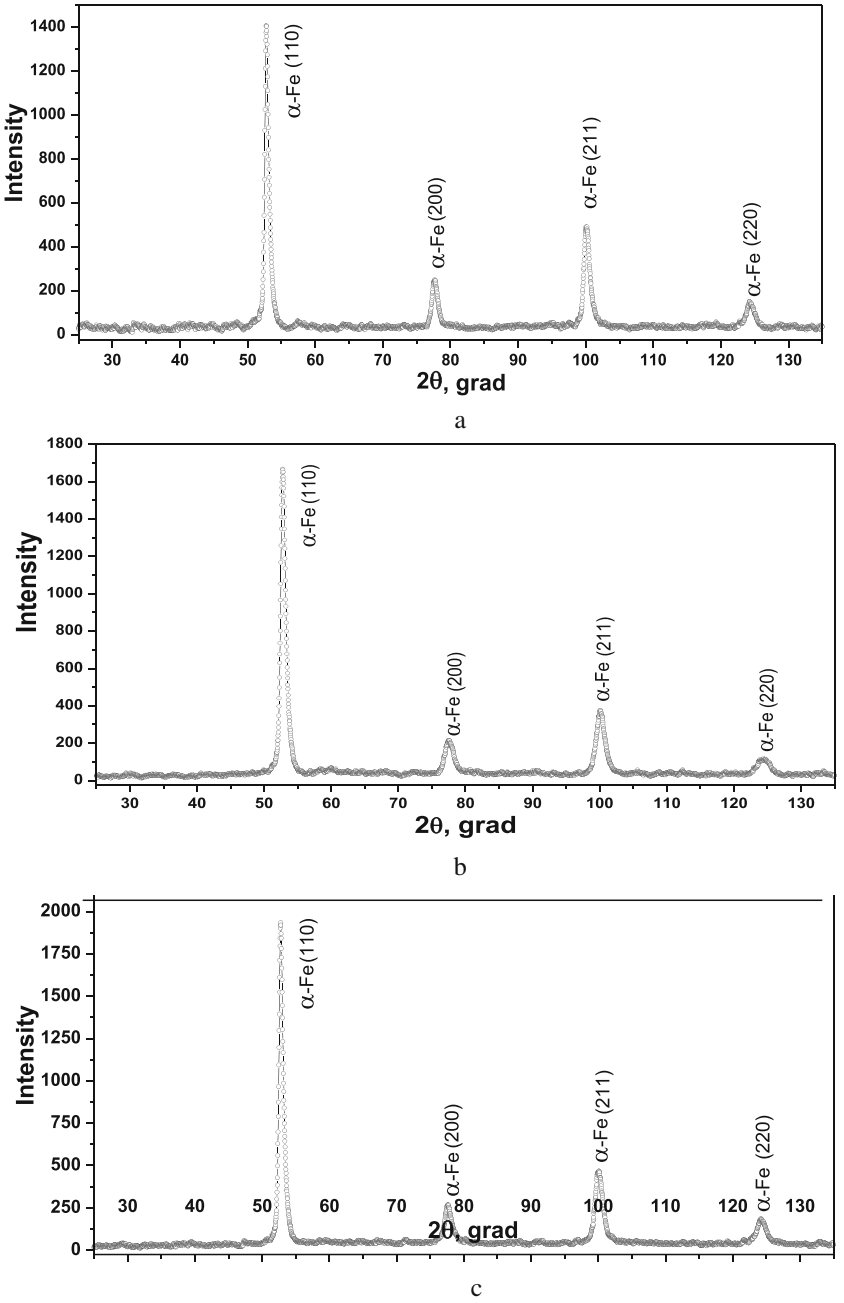

Fig. 9.3 The fragments of diffractograms of surface layers on 40Kh steel after MPT at different tempering temperatures: (**a**) MPT, (**b**) MPT + tempering at 200 °C, (**c**) MPT + tempering at 300 °C, (**d**) MPT + tempering at 400 °C, and (**e**) MPT + tempering at 500 °C

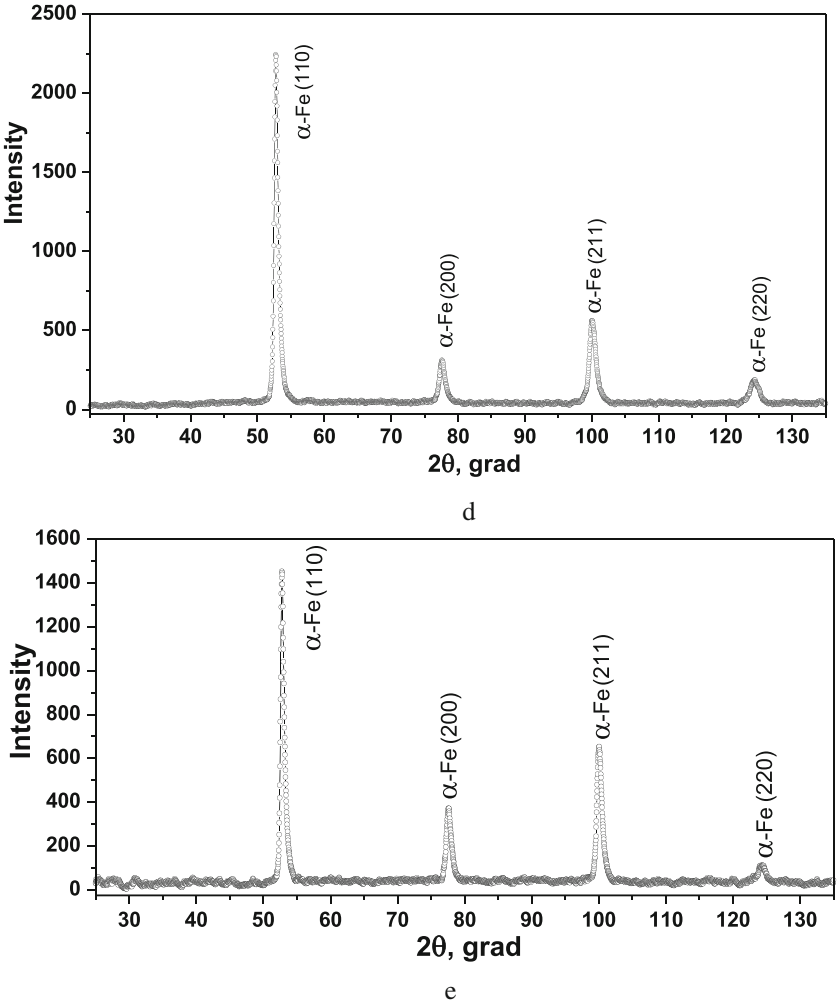

Fig. 9.3 (continued)

one. Therefore, the influence of carbon contained in cementite on mechanical properties of microcrystalline steels differs from its influence on the same properties of NCS structures when it is in atomic state at grain boundaries. So, not only extra small grain size but also anomalous carbon state in the steel should be considered at analyzing NCS. It could be expected to detect higher carbon content on the surface NCS layer because of the usage of special TM for carburizing during MPT. Nevertheless, according to carried out analysis, carbon was in atomic state at grain boundaries.

The structural-phase state of steel's NCS layer hadn't been changed after tempering: another component, besides ferrite, wasn't detected (Fig. 9.3b–e). One

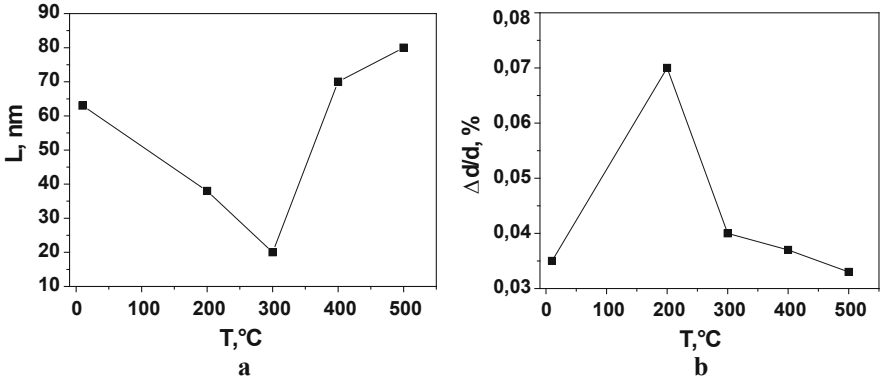

Fig. 9.4 The dependence of the nanocrystalline's grain size L (**a**) and relative stresses of the lattice $\Delta d/d$ (**b**) of surface NCS on different tempering temperatures

Table 9.1 Effect of MPT and subsequent tempering on surface microhardness Hμ of 40Kh steel, GPa

		Tempering at the temperature after MPT			
As-received state	MPT without tempering	200 °C	300 °C	400 °C	500 °C
2.5	8.5	8.4	5.8	5.5	4.4

of the features of MPT treatment is retardation of cementite formation in the studied steel at tempering in such range of tempering temperatures.

Tempering significantly influenced the grain size (Fig. 9.4a), relative stresses in the lattice (Fig. 9.4b), and microhardness of the surface NCS (Table 9.1). Thus, with increase of tempering temperature, the microhardness of the surface layer decreased. However, the microhardness of the surface layer was more than two times higher even after tempering at 500 °C compared with the as-received state. It could be the result of not only retaining of NCS but also enriching of the surface layer by carbon.

The grain size decreased up to about 20 nm with increase in tempering temperature up to 300 °C and then increased. The decreasing of the grain size was unexpected. However, it should be noted that unidirectional shear thermoplastic deformation leads to formation of unequiaxed stretched grains in the surface layer. Then, the fragmentation of unequiaxed grains to more equiaxed grains at the tempering temperature in the range of 200–300 °C was possible, and it resulted in the decrease of grain size L [7]. On the other hand, grain fragmentation needs some level of stresses, which occurred due to tempering. In the studied case, it was shown that the value of relative stresses $\Delta d/d$ in the lattice increased at the tempering temperature of 300 °C compared with the untempered state. This process evidently caused grain fragmentation.

At tempering temperatures above 300 °C, increase of the grain size was accompanied with decreasing stresses in the lattice which indicated the correlation between L and $\Delta d/d$ in all tempering temperature ranges. It should be noted

that the growth of nanograins of the investigated steel occurred at a temperature considerably lower than the temperature of recrystallization. High defectiveness of NCS obtained by SPD creates the field of elastic stresses [15–17]. Complicated structural changes, associated with processes of return, recrystallization, and grain growth, take place during their heating [8]. It should be also noted that heating of NCS to a temperature of 200 °C leads to a sharp reduction of vacancy concentration, and dislocation density is strongly reduced in the temperature range of 200–500 °C [17].

Wear resistance of 40Kh steel with surface NCS depends on the tempering temperature. The highest wear resistance was inherent to the specimens without tempering or after tempering at 200 and 300 °C. In that case, the grains of NCS were the smallest and the microhardness was the highest. At higher tempering temperatures, microhardness and wear resistance of the surface significantly decreased. In general, there was the correlation between H_μ and ΔG. At the same time, it should be emphasized that wear resistance of the surface layer obtained by applying the treatment MPT + tempering at 300 °C (curve 3) was almost the same as at the treatment MPT without tempering (curve 1) or MPT + tempering at 200 °C (curve 2) as it can be seen in Fig. 9.5, but the microhardness H_μ was significantly lower (Table 9.1). On the other hand, MPT + tempering at 300 °C owned the smallest grains of surface NCS (Fig. 9.4a). Hence, it was assumed that the grain refining of NCS was responsible for maintaining of a rather high wear resistance of the surface layer. NCS was characterized by extra low friction coefficient [12, 18, 19], and the positive effect of MPT on wear resistance of the surface layer with reduced microhardness after tempering at 300 °C could be associated with it. Consequently, stable high wear resistance of the surface layer resulted in two confronting factors: decreasing of microhardness and subsequent grain fragmentation. Such unique combinations of properties of NCS, namely, high wear resistance, low friction

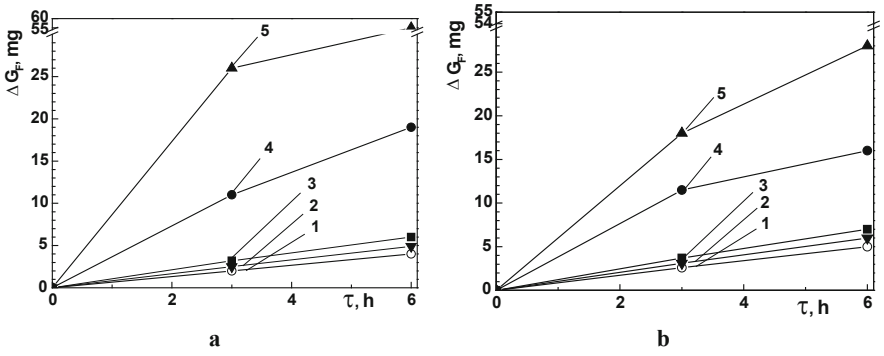

Fig. 9.5 Wear kinetics of rings (**a**) and inserts (**b**) of a pair of 40Kh steel – VCh60 iron tested at a loading of 2 MPa in an oil environment: (1) MPT, (2) MPT + tempering at 200 °C, (3) MPT + tempering at 300 °C, (4) MPT + tempering at 400 °C, and (5) MPT + tempering at 500 °C

coefficient, and low relative stresses, are very important for components working under high-cycle fatigue, corrosion fatigue, and contact loads [20, 21].

9.4 Conclusions

1. Strengthened surface layer obtained by MPT on 40Kh steel formed NCS with defined texture of deformation with unequiaxed grains. It is indirectly confirmed by further refinement of NCS during tempering up to 300 °C.
2. X-ray analysis revealed that the NCS surface layer strengthened by MPT consisted in grains of ferrite only; cementite and martensite were absent. Therefore, all carbon in the NCS surface layer was in atomic state at grain boundaries.
3. Surface NCS without tempering and tempered at temperatures up to 300 °C were characterized by the highest wear resistance. There were two confronting factors that influenced wear resistance: decreasing of microhardness and subsequent grain fragmentation.

References

1. Kurzydlowski KJ (2004) Microstructural refinement and properties of metals processed by severe plastic deformation. Bul Polish Acad Sci Tech Sci 52:301–311
2. Nykyforchyn H, Kyryliv V, Maksymiv O et al (2016) Formation of surface corrosion-resistant nanocrystalline structures on steel. Nanoscale Res Lett 11:51
3. Nykyforchyn H, Lunarska E, Kyryliv V, Maksymiv O (2015) Chapter 32: influence of hydrogen on the mechanical properties of steels with the surface nanostructure. In: Fesenko O, Yatsenko L (eds) Nanoplasmonics, nano-optics, nanocomposites, and surface studies. Springer, Heidelberg/Cham, pp 457–465
4. Umemoto M (2003) Nanocrystallization of steels by severe plastic deformation. Mater Trans 44(10):1900–1911
5. Nykyforchyn H, Kyryliv V, Maksymiv O (2015) Effect of nanostructurisation for structural steels on their wear hydrogen embrittlement resistance. Solid State Phenom 225:65–70
6. Firstov S, Rogul T, Shut O (2018) Hardening in the transition to nanocrystalline state in pure metals and solid solutions (ultimate hardening). Powder Metal Metal Ceram 57:161–174
7. Yurkova A, Belots'ky A, Byakova A (2006) Mechanical behavior of nanostructured layer formed by severe plastic deformation under diffusion flow of nitrogen. Mater Sci Forum 503-504:645–650
8. Andrievski RA (2003) Review Stability of nanostructured materials. J Mater Sci 38:1367–1375
9. Vasiliev MO, Prokopenko GI, Filatova VS (2004) Nanocrystallization of metallic surfaces with using the methods of intense plastic deformation (review). PHYS-USP 5:345–399
10. Kyryliv VI (1999) Surface saturation of steel with carbon during mechanical-pulse treatment. Mater Sci 35:853–858
11. Kalichak TN, Kyryliv VI, Fenchin SV (1989) Mechanopulsed hardening of long components of the hydraulic cylinder rod type. Sov Mater Sci 25:96–99
12. Nykyforchyn H, Kyryliv V, Maksymiv O (2017) Wear resistance of steels with surface nanocrystalline structure generated by mechanical-pulse treatment. Nanoscale Res Lett 12:150

13. Akselrud LG, Gryn' YM, Zavaliy PY et al (1993) Use of the CSD program package for structure determination from data. In: Abstract of the European powder diffraction Conference, Enshede, Netherlands, 1992. Materials Science Forum, vol 41, pp 335–342
14. Powder Diffraction File 1973 (1974) Search manual alphabetical listing and search section of frequency encountered phases. Inorganic, Philadelphia
15. Valiev R, Aleksandrov I (1999) Bulk nanostructured materials from severe plastic deformation. Nanostruct Mater Sci 45:103–189
16. Segal VM (2005) Deformation mode and plastic flow in ultra fine grained material. Mater Sci Eng A 406:205–216
17. Gleiter H (2000) Nanostructured materials: basic concepts and microstructure. Acta Mater 48:1–29
18. Buckleu DH (1981) Surface effects in adhesion, friction, wear, and lubrication. Elsevier, Amsterdam
19. Nykyforchyn H, Kyryliv V, Maksymiv O et al (2018) Wear resistance of the surface nanocrystalline structure under an action of diethylene glycol medium. Applied Nanoscience, Heidelberg, pp 1–6
20. Kyryliv V, Chaikovs'kyi B, Maksymiv O et al (2018) Fatigue and corrosion fatigue of the roll steels with surface nanostructure. J Nano Res 51:92–97
21. Kyryliv V, Chaikovs'kyi B, Maksymiv O et al (2016) Contact fatigue of 20KhN3A steel with surface nanostructure. Mater Sci 51:833–838

Chapter 10
Nano-sized Adsorbate Island Formation in Adsorptive Anisotropic Multilayer Systems

Vasyl O. Kharchenko, Alina V. Dvornichenko, and Dmitrii O. Kharchenko

10.1 Introduction

Nano-sized patterning in thin films attains an increasing interest from theoretical and practical viewpoints due to usage of nano-sized objects in new electronic devices and, generally, in optoelectronics. A manipulation with atomic sizes allows one to manufacture new materials with exceptional functionality such as giant magnetoresistance [1], tunable optical emission [2], high-efficiency photovoltaic conversion [3], and ultralow thermal conductivity [4]. These advantages of new materials are used in magnetoresistive sensors, memory devices, quantum dot lasers, and detectors which can be exploited at quantum communications. During the last few decades, it was shown experimentally, and by theoretical modeling, that nano-sized objects can be produced at vapor or ion-beam deposition [5–8], ion-beam sputtering [9–13], pulsed laser irradiation [14–16], and molecular beam epitaxy [17–23].

As far as industrial applications of nano-sized patterns have become more and more complex, it is of great scientific and technological interest to understand a role of main mechanisms governing and controlling nanostructured thin films. A modeling texture formation and their evolution are of primary importance in the study of thin film growth. By exploiting different technics for deposition, one can use effectively mechanisms for nano-sized island growth (adsorption/desorption, diffusion, interaction of adatoms) leading to formation of different types of patterns:

V. O. Kharchenko · D. O. Kharchenko (✉)
Institute of Applied Physics, National Academy of Sciences of Ukraine, Sumy, Ukraine
e-mail: vasiliy@ipfcentr.sumy.ua; dikh@ipfcentr.sumy.ua

A. V. Dvornichenko
Sumy State University, Sumy, Ukraine
e-mail: alina.dvorni4enko@ukr.net

O. Fesenko, L. Yatsenko (eds.), *Nanocomposites, Nanostructures, and Their Applications*, Springer Proceedings in Physics 221,
https://doi.org/10.1007/978-3-030-17759-1_10

periodic array of vacancy islands [24], elongated islands of adsorbed semiconductors [25, 26], and metals [27, 28]. It was shown that elongated adsorbate clusters are governed by formation of dimers and their reconstructions [29] representing nonequilibrium chemical reactions.

The continuous approach related to reaction-diffusion models is able to study the system dynamics on wide range of time scales and considers dynamics of pattern formation on length scales from nano- to micrometers. This approach was successfully applied to study nano-sized surface patterns in reaction-diffusion systems (see, e.g., Refs. [30–40]). A progress in studying primary and secondary mechanisms leading to formation of nano-sized patterns and morphology change of adsorbate islands was reported in Refs. [41–43].

Most of theoretical studies relevant for nano-sized pattern formation at condensation from a gaseous phase deal with one-layer problem. The two-layer system and its possible generalization to multilayer system with transference interaction between layers was studied in Ref. [37]. In this work authors considered one-dimensional problem. It was shown that in multilayer system, cascades of first-order phase transitions can be realized, where transition profiles manifest staircase structure. Multilayer growth during thin film deposition was studied in Refs. [39, 40]. Here dynamics of nano-sized pattern formation was analyzed under assumption that adatoms can move between layers in a diffusion-like manner. This assumption admits an equiprobable motion of adatoms between layers. From the physical viewpoint, such equiprobable motion can be broken by introduction of additional external fields (e.g., electric field). It can result in anisotropy of transference reactions when adatom can move between neighbor layers with different probabilities. At the same time, questions related to an influence of transference interactions between layers onto formation of adsorbate nano-islands remain open. The main aim of this work is to study an influence of transference reactions onto dynamics of nanostructured thin films growth in adsorptive multilayer systems. In the present paper, we solve the following problems: (i) to describe a cascade of first-order phase transitions at patterning; (ii) to find critical supersaturation and critical radius of adsorbate islands governing formation of islands on a new layer of the thin film; and (iii) to study a morphology change of nano-patterns.

In our study, we generalize multilayer models proposed in Refs. [37, 39, 40] allowing us to consider an adsorptive system with equilibrium, nonequilibrium, and transference reactions. We restrict ourselves by taking into account substratum mediated interactions only. One-, two-, and three-layer systems are studied analytically in stationary regime in order to show a cascade of phase transitions of first order. Here spatial instability and type of patterns emergent in different layers for these models are discussed. Multilayer systems with isotropic and anisotropic transference of adatoms between neighbor layers are studied numerically. Here emergence of anomalous dynamics of island formation is shown. A crossover of dynamical regimes for linear size of islands will be illustrated.

The work is organized as follows. In Sect. 10.2, we introduce a generalized model for multilayer adsorptive system. Section 10.3 is devoted to stability analysis of homogeneous and inhomogeneous systems with one, two, and three layers.

Numerical study of pattern formation in isotropic and anisotropic systems is presented in Sect. 10.4. We conclude in Sect. 10.5.

10.2 Model

In our consideration, we adopt continuous description for a growing surface. We will monitor the local coverage $c_i(\mathbf{r}, t)$ in the i-th layer (monoatomic level), where t is the time variable and $\mathbf{r} = \{x, y\}$ is the space coordinate. Studying the multilayer system, we introduce a vector $\mathbf{c}(\mathbf{r}, t)$ having the components $\{c_i(\mathbf{r}, t)\}_{i=1}^{n}$, where n is the total number of layers. Dynamics of this vector is governed by both equilibrium and nonequilibrium quasi-chemical reactions. Equilibrium reactions correspond to adsorption and desorption processes, whereas nonequilibrium ones relate to interactions of adatoms with formation of dimers, associates, resulting to a decrease in separated adatoms concentration. In problems of multilayer growth, one has to take into account additional contribution to this dynamics corresponding to adatom transference between two neighboring layers. The total set of reactions in each i-th layer can be described by the reaction term $f_i(\mathbf{c}(\mathbf{r}, t))$. These terms can be combined into one vector, $\mathbf{f}(\mathbf{c}(\mathbf{r}, t)) = \{f_i(\mathbf{c}(\mathbf{r}, t))\}_{i=1}^{n}$. As far as all adatoms are mobile species, one needs to take into account a corresponding diffusion flux $\mathbf{J}_i(\mathbf{c}(\mathbf{r}, t), \nabla)$, where $\nabla \equiv \partial/\partial\mathbf{r}$. For n-layer system the set of fluxes can be combined into one vector, $\mathbf{J}(\mathbf{c}(\mathbf{r}, t), \nabla) = \{\mathbf{J}_i(\mathbf{c}(\mathbf{r}, t), \nabla)\}_{i=1}^{n}$. Therefore, the generalized model for the adsorptive multilayer system can be written as follows:

$$\partial_t \mathbf{c}(\mathbf{r}, t) = \mathbf{f}(\mathbf{c}(\mathbf{r}, t)) - \nabla \cdot \mathbf{J}(\mathbf{c}(\mathbf{r}, t), \nabla). \tag{10.1}$$

Let us consider, initially, components of $\mathbf{f}$ in details. Adsorption processes on i-th layer are characterized by constant k_{ai} and a partial pressure p of the gaseous phase. Moreover, adsorption is only possible to the free sites on the current layer and admits free sites on upper layers with nonzero adatoms concentration on $(i-1)$-th layer. It means that on the i-th level, the adsorption rate is $k_{ai}\, p c_{i-1} \prod_{j=i}^{n}(1 - c_j)$, where $c_0 = 1$ corresponds to initial substrate. Adsorption rate can be defined through the adsorption energy E_{ai}, temperature T measured in energetic units, and frequency factor ν as $k_{ai} = \nu e^{-E_{ai}/T}$. Desorption processes occur with a rate $k_{di} = k_d^0 \exp(U_i(\mathbf{r})/T)$, where k_d^0 is the desorption rate for noninteracting particles, $U_i(\mathbf{r})$ gives contribution due to strong local bond (substratum-mediated interactions). Desorption rate $k_{di}^0 = \nu e^{-E_{di}/T}$ relates to the life time scale of adatoms $\tau_{di} = [k_{di}^0]^{-1}$, where E_{di} is the desorption energy. Therefore, the desorption processes are defined by a contribution $-k_{di} c_i (1 - c_{i+1})$, where we take into account that desorption is possible if the corresponding site on upper layer is free. Introducing this term, we admit that only substratum-mediated interactions are possible. In such a case, this term describes desorption of adatom into gaseous phase or it motion to upper layer if the corresponding site is empty. Nonequilibrium chemical reactions responsible to a formation of dimers in each i-th layer can

be described by a rate $-k_{ri}c_i^2\prod_{j=i+1}^{n}(1-c_j)$, where k_{ri} is the constant. We assume that dimers can be formed on the growing layer only. A motion of adatoms between two neighboring layers occurs at different rates and possible only on free sites on the corresponding layer. This transfer can be described by a contribution $k_{i+1\to i}c_{i+1}(1-c_i)+k_{i-1\to i}c_{i-1}(1-c_i)-k_{i\to i+1}c_i(1-c_{i+1})-k_{i\to i-1}c_i(1-c_{i-1})$, where $\{k_{i\to j}\}$ are rate constants for transitions from i-th to j-th level.

For the components $\mathbf{J}_i$, one should take into account free diffusion of adsorbed particles described by the term $-D_i\nabla c_i$, where $D_i = D_0e^{-E_{Di}/T}$ is the diffusion coefficient in i-th layer (D_0 is the prefactor, $E_{Di} \simeq E_{ai}/3$ is the activation energy for diffusion) and a component caused by action of the force $F_i = -\nabla U_i$. This force affects the adsorbed particles attaining a velocity $v_i = (D_i/T)F_i$. The associated particle flux is proportional to v_ic_i and possible only at the $(1-c_i)$ free sites. Therefore, the total flux in i-th layer can be written as follows:

$$\mathbf{J}_i = -D_i\nabla c_i - (D_i/T)c_i(1-c_i)\nabla U_i. \tag{10.2}$$

In our study, we take into account that there are substratum-mediated attractive interactions among particles separated by a distance r. For the potential U_i, we assume a self-consistent approximation. In such a case for the lower layer, we can write $U_1 = -\int u_1(r-r')c_1(r')\mathrm{d}r'$, where the integration is provided over the whole surface. Here $u_1(r)$ is the attraction potential having symmetrical form, i.e., $\int r^{2n+1}u_1(r)\mathrm{d}r = 0$. Following Ref. [34] we choose the Gaussian profile for the interaction potential $u_1(r)$ in the standard form:

$$u_1(r) = \frac{2\epsilon_1}{\sqrt{4\pi r_{01}^2}}\exp\left(-\frac{r^2}{4r_{01}^2}\right), \tag{10.3}$$

where ϵ_1 is the interaction strength and r_{01} is the interaction radius. Assuming that the diffusion length $L_{Di} = \sqrt{D_i/k_{di}^0}$ is large comparing to the interaction radius r_{0i}, and the coverage behaves slowly comparing to $u_1(r)$, we can use an expansion: $\int u_1(\mathbf{r}-\mathbf{r}')c_1(\mathbf{r}')\mathrm{d}\mathbf{r}' \simeq \int u_1(\mathbf{r}-\mathbf{r}')\sum_n \frac{(\mathbf{r}-\mathbf{r}')^n}{n!}\nabla^n c_1(\mathbf{r})\mathrm{d}\mathbf{r}'$. By retaining only three nonvanishing terms and using expression (10.3), we get: $\int u_1(r)\mathrm{d}r = 2\epsilon_1$, $\int u_1(r)c_1(r)\mathrm{d}r = 2\epsilon_1c_1$, $\frac{1}{2}\int u_1(r)r^2\nabla^2c_1(r)\mathrm{d}r = 2\epsilon_1r_{01}^2\nabla^2c_1$, $\frac{1}{4!}\int u_1(r)r^4\nabla^4c_1(r)\mathrm{d}r = \epsilon_1r_{01}^4\nabla^4c_1$. Finally, for the interaction potential, u_1 one has:

$$\int u_1(\mathbf{r}-\mathbf{r}')c_1(\mathbf{r}')\mathrm{d}\mathbf{r}' \simeq \epsilon_1c_1(\mathbf{r}) + \epsilon_1(1+r_{01}^2\nabla^2)^2c_1(\mathbf{r}). \tag{10.4}$$

Next, following Ref. [37] let us use the simplification assuming that the potential $u(r)$ among particles in each layer is the same, i.e., $u(r) \equiv u_i(r)$ and $\epsilon \equiv \epsilon_i$. This implies that $r_0 \equiv r_{0i}$. Therefore, for the substratum-mediated interactions for the 2-nd layer, one has the definition $U_2(r) = c_1(r)\left\{-\int u(r-r')c_2(r')\mathrm{d}r'\right\}$. Hence, in the general case, one can use the expression

$$U_i(\mathbf{r}) \simeq -\epsilon c_{i-1}(\mathbf{r}) \left\{ c_i(\mathbf{r}) + (1 + r_0^2 \nabla^2)^2 c_i(\mathbf{r}) \right\} \tag{10.5}$$

with $\nabla U_i = -\epsilon c_{i-1}(\mathbf{r}) \nabla \left\{ c_i(\mathbf{r}) + (1 + r_0^2 \nabla^2)^2 c_i(\mathbf{r}) \right\}$. Above self-consistent approximation for the interaction potential is used well in studying nano-sized island formation not only in problems of condensation from gaseous phase (see Refs. [35–43]). It was exploited to study pattern formation in chemical systems [44] and pyramidal island growth at molecular beam epitaxy [20, 21].

In order to simplify the notations, we take $L_D = L_{Di}$ (implying $k_d^0 = k_{di}^0$) and use scaling parameters: $r' = r/L_D$, $\varepsilon \equiv \epsilon/T$, $t' \equiv t k_d^0$ (next we drop primes for convenience). To reduce the number of parameters, we consider the simplest case when adsorption in each layer occurs at the same constant rate, i.e., $k_a = k_{ai}$, and we put $k_r = k_{ri}$. This allows one to introduce dimensionless rates: $\alpha \equiv k_a p/k_d^0$, $\beta \equiv k_r/k_d^0$. Considering exchanging rates $k_{i+1\to i}$ and $k_{i\to i+1}$, we take in mind that a probability to move from upper level toward lower one can be different. In our study we consider a general case $k_{i+1\to i} \geq k_{i\to i+1}$. Next we introduce dimensionless exchange rates $w \equiv k_{i+1\to i}/k_d^0$, $u \equiv k_{i\to i+1}/k_d^0$, $w/u \geq 1$. The case $w/u = 1$ corresponds to isotropic vertical diffusion of adatoms, whereas the anisotropic case $w/u > 1$ can be realized in the presence of an external field or at pressure-induced motion of adatoms from upper to lower layers. The last model is of our main interest.

By using above definitions and introducing a dimensionless interaction radius $\rho_0 = r_0/L_D$, we arrive at dimensionless evolution equations for adsorptive multilayer system in the form:

$$\begin{aligned}
\partial_t c_i = {} & \alpha c_{i-1} \prod_{j=i}^{n} (1 - c_j) - c_i (1 - c_{i+1}) e^{-2\varepsilon c_i c_{i-1}} - \beta c_i^2 \prod_{j=i+1}^{n} (1 - c_j) \\
& + w \left[c_{i+1}(1 - c_i) - c_i (1 - c_{i-1}) \right] + u \left[c_{i-1}(1 - c_i) - c_i (1 - c_{i+1}) \right] \\
& + \nabla \cdot \left[\nabla c_i - \varepsilon c_i (1 - c_i) c_{i-1} \times \nabla \left\{ c_i + (1 + \rho_0^2 \nabla^2)^2 c_i \right\} \right] + \xi_i(\mathbf{r}, t).
\end{aligned} \tag{10.6}$$

Here, we introduce fluctuating terms ξ_i responsible for statistical description of the system dynamics. These stochastic sources are taken in the form of Gaussian statistically independent noises with properties: $\langle \xi_i \rangle = 0$, $\langle \xi_i(\mathbf{r}, t) \xi_j(\mathbf{r}', t') \rangle = \delta_{i,j} \delta(t - t') \delta(\mathbf{r} - \mathbf{r}')$.

In further consideration, we pay the most of attention to study multilayer growth when particles can move between layers with different relations between u and w. We will analyze statistical properties of stationary adsorbate island formation and investigate the related growth dynamics for multilayer system controlled by transfer rates w and u.

10.3 Stability Analysis

Let us study stability of the homogeneous system. To this end, we neglect all spatial dependencies and consider stationary regime by taking $\partial_t c_i = 0$, for all i. In such a case, we arrive at a system of a set of coupled algebraic equations which can be solved numerically only.

Phase diagrams illustrate formation of bistable states (see Fig. 10.1a, b). In Fig. 10.1a, we plot phase diagram for one- and two-layer systems in the plane (α,ε) at different values of the exchange rate w. Here dot line corresponds to one-layer system, whereas dash and solid lines relate to the two-component system. Domains I and II correspond to unimodal and bimodal states, respectively. At small value of exchange rate ($w = 0.01$), there are two separated domains of system parameters, where bistable regime emerges (see dash lines in Fig. 10.1a). At large w single cusp at elevated α, related to large adatoms concentration on each level, is realized. Hence, it follows that in two-layer system, an increase in the vertical diffusivity caused by exchange rate w leads to degeneracy of the bistable state at small values of adsorption coefficient. Phase diagram that illustrate this effect for two-layer model is shown in Fig. 10.1b in plane (α,w) at different values of adsorbate interaction energy ε. It is seen that at small ε, there is one domain of bistable states realized at small α and small w (see dot line in Fig. 10.1b). An increase in ε leads to emergence of the second domain of bistability at elevated α. Here at small w, two-layer system is characterized by two domains with bistable states, whereas at large w, only one domain is possible at elevated α. It is seen that the critical maximal value of exchange rate grows with increase in ε. Therefore, the bimodality in systems admitting two-layer growth is possible at low temperatures small vertical diffusivity and elevated pressure of the gaseous phase. It follows that in multilayer adsorptive systems, we get an emergence of a cascade of first-order phase transitions

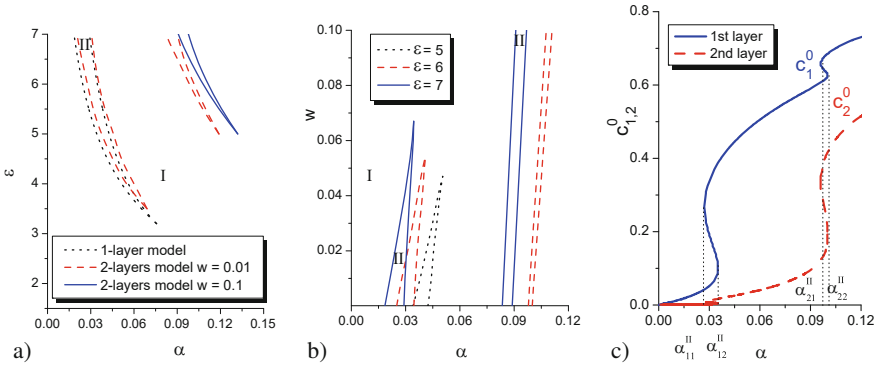

Fig. 10.1 (**a**) Phase diagram for the homogeneous system in the parameter plane (ε,α) at $\beta = 0.1$ and different $w = u$. (**b**) Phase diagram for the homogeneous two-layer system at different ε and $\beta = 0.1$. In the domains I, the system is monostable; in domains II the system is bistable. (**c**) Bifurcation diagram for the two-layer model at $\beta = 0.1$, $\varepsilon = 6.0$, $w = 0.1$, $u = 0.01$

in successive layers. For the multilayer system at $w/u > 1$ in vertical direction of the thin film, one has no standard diffusion. Here an adatom on i-th level has larger probability to move down on $(i-1)$-th level comparing to probability to move on $(i+1)$-th level. Corresponding isotherms $c_i^0(\alpha)$ for two-layer systems are shown in Fig. 10.1c. It follows that in two-layer system, two hysteresis loops can be observed. The first one relates to adsorbate interactions inside the layer. The second hysteresis is caused by two layers coupling and is realized at elevated values of α. A width of the hysteresis loops at fixed other system parameters are denoted by values (α_1^I, α_2^I) for one-layer system and $\{(\alpha_{11}^{II}, \alpha_{12}^{II}); (\alpha_{21}^{II}, \alpha_{22}^{II})\}$ for two-layer system. Therefore, it follows that in n-layer system, one can get n hysteresis loops, where the system manifests bimodality.

Next, let us consider stability of the inhomogeneous system. In the framework of the linear stability analysis, we study dynamics of deviations from the corresponding stationary values c_i^0: $\delta c_i \equiv c_i - c_i^0 \propto e^{\lambda_i(\kappa)t} e^{\mathrm{i}\kappa r}$, where the dimensionless wave number $\kappa = kL_D$ is introduced. The corresponding increments are of the form

$$\lambda_i(\kappa) = \lambda_i(0) - \kappa^2[1 - \varepsilon\mu_{i,i-1}(1 + (1 - \rho_0^2\kappa^2)^2)], \tag{10.7}$$

where $\lambda_i(0) \equiv \partial_{c_i}\phi_i|_{c_i^0}$ are defined through

$$\phi_i \equiv \alpha c_{i-1}\prod_{j=i}^{n}(1-c_j) - \beta c_i^2\prod_{j=i+1}^{n}(1-c_j) - c_i(1-c_{i+1})e^{-2\varepsilon c_i c_{i-1}}$$
$$+ w\,[c_{i+1}(1-c_i) - c_i(1-c_{i-1})] + u\,[c_{i-1}(1-c_i) - c_i(1-c_{i+1})]\,;$$

here we use the notation $\mu_{i,i-1} \equiv c_{i-1}^0 c_i^0(1-c_i^0)$ with $c_0^0 = 1$.

Analysis of the increments (10.7) for one- and two-layer systems allows us to obtain corresponding stability diagrams shown in Fig. 10.2a. For the one-layer model (see insertion in Fig. 10.2a), we have two domains A and B only. In the domain A at small α, no spatial modulations characterized by adsorbate islands are realized. At elevated α in the domain B, adsorbate islands can emerge. For the two-layer system, we have three domains A, B, and C. The domain A denotes system parameters where no adsorbate islands can emerge. In the domain B, adsorbate islands on the first layer can be realized without spatial modulation on the second layer. The domain C realized at large α is characterized by formation of adsorbate islands on both first and second layers (islands on the second layer are possible only on islands formed on the first layer). At large values of the exchange rate, w domains of adsorbate island emergence on both levels are shifted toward large α and large ε. For the three-layer system, we get additional domains in the stability diagram (see Fig. 10.2b). Here in the domain C', the first layer is characterized by vacancy clusters inside adsorbate matrix; adsorbate islands emerge on the second layer. In the domain D, we get adsorbate islands on the third layer formed on islands on the second layer, which are arranged on adsorbate islands on the first layer. In the domain D', the first layer is filled by adatoms, and only vacancy islands

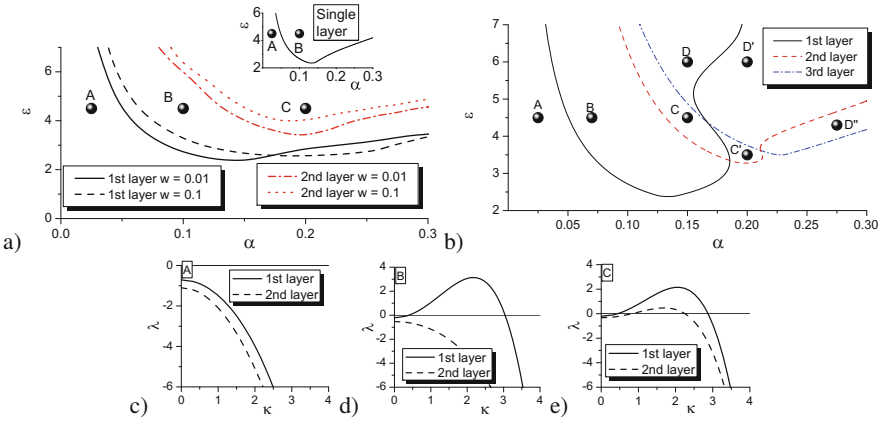

Fig. 10.2 Stability diagrams of the uniform state to inhomogeneous perturbations at $\beta = 0.1$ (**a**) for one- and two-layer models with $u = w$ and (**b**) for three-layer model at $w = 0.1$, $u = 0.01$. (**c**)–(**e**) Stability exponents for the two-layer model taken in points A, B, and C, respectively

can emerge. In the domain D'', we get pattern with vacancy islands on both first and second layers with adsorbate island emergence on the third layer. Therefore, it follows that in n-layer system, pyramidal patterns with different morphologies can be organized. Figure 10.2c–e shows dependencies of the stability exponents $\lambda_{1,2}$ from the two-layer model at system parameters, taken at points A, B, and C in the stability diagram Fig. 10.2a.

10.4 Numerical Simulations

To describe system behavior quantitatively, we use numerical simulations considering four-layer model. All simulations were done on the lattice with triangular symmetry of the linear size $L = 512\ell$ with periodical boundary conditions and a mesh size $\ell = 0.5$; $\Delta t = 0.00025$ is the time step. In the case of the triangular/hexagonal symmetry, there are three wave vectors separated by $2\pi/3$ angles. The total size of the system is $L = 25.6L_D$. As initial conditions we take: $\langle c_i(\mathbf{r}, 0)\rangle = 0$ for $i = 1 \ldots n$, $\langle(\delta c_1(\mathbf{r}, 0))^2\rangle = 0.1$, $\langle(\delta c_{i\neq 1}(\mathbf{r}, 0))^2\rangle = 0.0$.

10.4.1 Isotropic Transference Between Layers

The main task of this section is to investigate the morphology of the structures of the adsorbate in a multilayer system by varying the adsorption rate. To that end, we fix $\beta = 0.1$, $\varepsilon = 4.0$ and $w = u = 0.1$. The typical evolution of the system at different

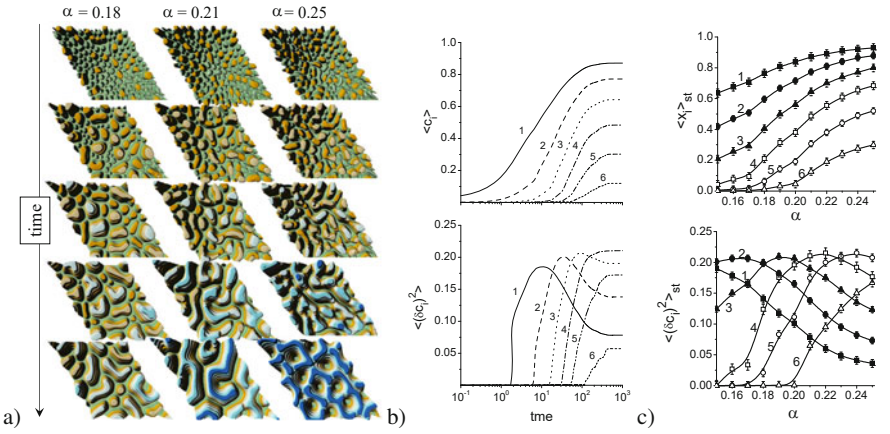

Fig. 10.3 (**a**) Typical evolution of the six-layer system at different values of the adsorption coefficient. (**b**) Evolution of the mean adsorbate concentration $\langle x_i \rangle$ (top panel) and dispersion of the coverage field (order parameter) $\langle (\delta x_i)^2 \rangle$ (bottom panel) on i-th layer at $\alpha = 0.21$. (**c**) Dependencies of the stationary values $\langle x_i \rangle_{st}$ (top panel) and $\langle (\delta x_i)^2 \rangle_{st}$ (bottom panel) on the adsorption coefficient α on each layer

values of the adsorption coefficient α is shown in Fig. 10.3a. It is seen that in the initial stages of the system evolution, adsorbate structures on the first (lower) layer are formed. At this stage, the adsorption coefficient does not have a significant effect on the system. In the course of evolution, the structure of the adsorbate structures begin to appear on next layers. In the case of small values of the adsorption coefficient (left column), one gets separated adsorbate structures on the substrate. At elevated values of α, we have a situation where the adsorbate structures, due to interaction, begin to merge into larger clusters and extended structures (see middle and right columns). At late stages of the system evolution, the upper layers are also characterized by the presence of adsorbate structures. In the quasi-stationary boundary (lower row), the type of surface structures essentially depends on the value of the adsorption coefficient. Thus, at small values of the adsorption coefficient, separated adsorbate structures (nano-dots) are formed. At large values of the adsorption coefficient, we have the opposite picture, when the adsorbate covers the layers in such a way that vacancy structures (nano-holes) are formed. At moderate values, a labyrinth structure is realized that can be characterized as a transition between nano-holes and nano-dots with an increase in the adsorption coefficient.

In Fig. 10.3b we present the dependencies of the main statistical moments $\langle x_i \rangle$ (on the top) and $\langle (\delta x_i)^2 \rangle$ (on the bottom) at $\alpha = 0.21$. The quantity $\langle (\delta x_i)^2 \rangle$ is a criterion for structuring and can be considered as an order parameter for patterning. It is seen that the average concentration of adsorbate on each layer of the six-layer system monotonically increases with time and reaches a stationary value $\langle x_i \rangle_{st}$. The order parameter at early stages takes zero value, which indicates a homogeneous

distribution of adsorbate on the first layer (see curve 1 on the bottom panel in Fig. 10.3b). When the adsorbate concentration on the first layer reaches a critical value, the order parameter starts to grow with time, indicating the beginning of the ordering processes (formation of adsorbate structures). At late stages of the system evolution, $\langle(\delta x_i)^2\rangle$ attains a stationary value $\langle(\delta x_i)^2\rangle_{st}$, indicating that the first layer is formed. A similar situation is realized on other layers.

Dependencies of $\langle x_i\rangle_{st}$ and $\langle(\delta x_i)^2\rangle_{st}$ on the adsorption coefficient α are shown in Fig. 10.3c. It is seen that the stationary average concentration of adsorbate on each layer of a multilayer system monotonically increases with the adsorption coefficient (see top panel). The order parameter at small α increases, reaches the maximum value, and then decreases. In the limit case $\alpha \to 0$, due to the small amount of adsorbate on the substrate, the order parameter on each layer will goes to zero. In the case $\alpha \to \infty$ due to dense coverage of all layers by adsorbate, one gets $\langle(\delta x_i)^2\rangle_{st} \to 0$. Thus, by varying the adsorption coefficient (gas phase pressure), one can control the structuring processes of the growing surface.

Processes of adsorbate island growth can be studied by monitoring dynamics of the average island size $\langle R_{ai}\rangle$ on i-th layer. To calculate the radius of islands, we proceed in the following manner: (i) we neglect percolating and large elongated clusters; (ii) assuming that all other islands have spherical form, we calculate corresponding areas and obtain the radius $\langle R_{ai}\rangle$. The corresponding typical dependencies are shown in Fig. 10.4a. It is seen that the mean linear size of adsorbate islands on each level $\langle R_{ai}\rangle$ grows in time and takes quasi-stationary value $\langle R_{ai}\rangle \sim 10L_D$ at large exposing time. It means that at elevated values of α, percolating clusters of adsorbate are formed; they transform into adsorbate matrix with vacancy cluster on each layer (right column in Fig. 10.3a). The distributions of island sizes on different layers in stationary regime are shown in Fig. 10.4b at $\alpha = 0.25$. It follows that the most probable size of nano-holes decreases with the layer number growth and varies in the interval $0.45 \div 1.1L_D$ from the lower to upper layer.

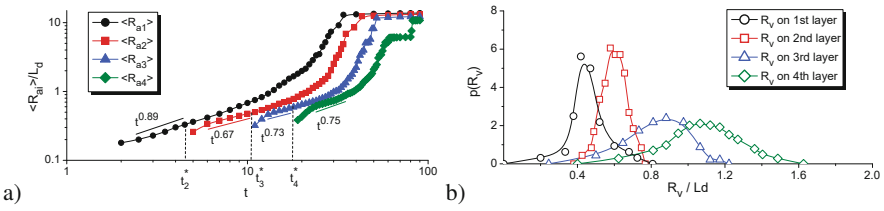

Fig. 10.4 (**a**) Dynamics of the averaged linear size of islands on each layer. Here t_i^* denotes time instant when i-th layer starts to grow; (**b**) distribution functions over nano-hole size in stationary regime for each layer at $\alpha = 0.25$

10.4.2 Pressure-Induced Anisotropic Transference

Next, let us discuss dynamics of pattern formation in actual case of adsorptive multilayer model at $\alpha = 0.25$, $\beta = 0.1$, $\varepsilon = 4.0$, and $w/u > 1$ in details. Quasi-stationary structure is shown in Fig. 10.5a at. It is seen that in the stationary case, vacancy islands are organized on low layers. The upper layer is characterized by adsorbate island emergence.

One can elucidate that islands on $(i + 1)$-th layer can be arranged only if an averaged coverage $\langle c_i \rangle$ over the i-th layer attains some critical value $\langle c_i \rangle^{cr}$ governed by adsorption/desorption rates, adsorbate interaction energy, rate for nonequilibrium reactions, and rates for adatoms motion between layers. At the same time, a size of island on the $(i - 1)$-th layer should be enough to provide diffusion and interaction of adatoms in i-th layer. It means that there is a critical value for adsorbate island size $\langle R_{ac} \rangle$ when new layer can be arranged. Both $\langle c_i \rangle^{cr}$ and $\langle R_{ac} \rangle$ are calculated at the time t^* when $\langle (\delta c_{i+1}))^2(t) \rangle$ starts to increase in the corresponding protocol. In such a case at $t > t^*$, islands of adsorbate can be arranged on the $(i + 1)$-th layer. This procedure is repeated for next layers. Critical values $\langle c_i \rangle^{cr}$ limiting growth of the $(i + 1)$-th layer are shown in Fig. 10.5b on the top panel at different w/u. It is seen that these quantities take elevated values when the rate for adatoms motion toward lower layer grows. The corresponding dependencies can be approximated by exponential decaying functions $\langle c_i \rangle^{cr} = \langle c_1^* \rangle^{cr} - i \cdot \Delta - Ae^{-w/w_c}$, where $\langle c_1^* \rangle^{cr} \simeq 0.74$, $\Delta \simeq 0.17$, $A \simeq 0.22$, $w_c = 2.11$ ($u = 0.01$). It is important that all fitting constants are independent on w. It follows that any next layer can grow at lower coverage of the current layer. Hence, one can elucidate that the second layer can grow at elevated coverage for the first layer, whereas the upper layer starts to grow at very low values of the coverage on the third layer. As was denoted above, an additional condition for the island growth on a new layer is the sufficient area covered by adsorbate in the current layer. In the bottom panel in Fig. 10.5b, we

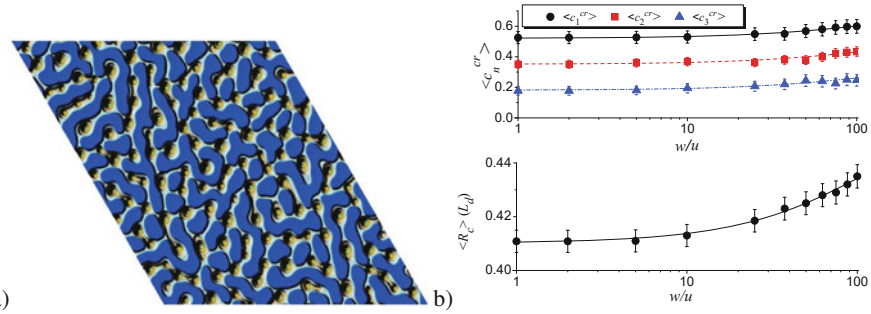

Fig. 10.5 (**a**) Typical quasi-stationary structure formed in systems with four layers at $u = 0.01$ and $w = 0.1$. (**b**) Critical values of the averaged coverage on i-th layer (top panel) and corresponding critical radius of island (bottom panel) limiting growth of $(i + 1)$-th layer *versus* w/u calculated at $w \in [0.1, 1.0]$, $u \in [0.01, 0.1]$

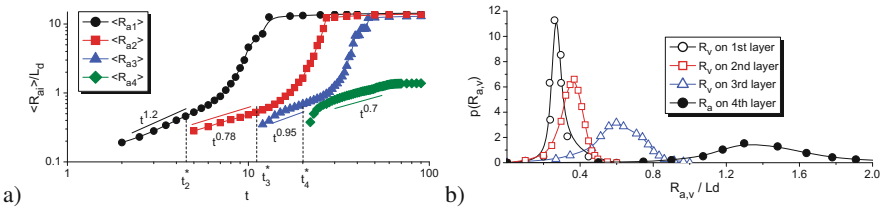

Fig. 10.6 Dynamics of the averaged linear size of islands on each layer (**a**) and distribution functions over island size in stationary regime for each layer (**b**) (curves with empty markers correspond to vacancy islands, curve with filled markers relates to adsorbate island distribution function) at $w = 0.1$, $u = 0.01$

plot values of critical linear size $\langle R_{ac} \rangle$ of the adsorbate islands limiting formation of adsorbate islands in new layer. It is seen that $\langle R_{ac} \rangle$ slightly grows with w/u. It should be noted that $\langle R_{ac} \rangle$ remains constant and does not vary with i.

In Fig. 10.6a we show dynamics of the average island size $\langle R_{ai} \rangle$ on i-th layer. The time dependence $\langle R_{ai}(t) \rangle$ is very complicated that relates to competition between several main mechanisms governing adsorbate island growth. Mechanisms playing most essential role are as follows. The first one is the usual diffusion leading to coarsening of islands. The second one is caused by adsorption of atoms from the gaseous phase. The last mechanism corresponds to a decrease in the island size due to motion of adatoms toward lower layer. A combination of above mechanisms into one scenario promotes complex time dependence of $\langle R_{ai}(t) \rangle$ shown in Fig. 10.6a. This competition results in three characteristic stages of island growth on any layer, namely, (i) island formation, (ii) island growth, and (iii) coalescence of adsorbate islands. In the domain $t < t_2^*$, islands of adsorbate emerge on the lower layer only. The time t_2^* bounds time interval for next layer growth. In the time domain $t_2^* < t < t_3^*$, adsorbate islands grow on the second layer. In this time domain, there is a crossover in time dependence $\langle R_{a1}(t) \rangle$. The same picture is observed when islands on the third layer are formed in the time domain $t_3^* < t < t_4^*$. In this domain one can observe crossover of the time dependence $\langle R_{a2}(t) \rangle$. At $t > t_4^*$ one has adsorbate islands on the last fourth layer. Therefore, any above crossover in time dependencies $\langle R_{ai}(t) \rangle$ relates to formation of new layer with adsorbate islands. It follows that each time instant t_i^* decreases with an increase in adsorption coefficient α and does not change with wary in relation w/u. In Fig. 10.6b we plot distribution functions of adsorbate (filled symbols) and vacancy (empty symbols) islands over their sizes in quasi-stationary regime (see Fig. 10.5a). Vacancy islands organized on the first layer are characterized by the most probable island size $\simeq 0.3L_D$. On the second layer, one has vacancy islands with the most probable linear size $\simeq 0.4L_D$. Most of vacancy islands on the third layer have linear size $\simeq 0.6L_D$. On the upper layer, one gets adsorbate islands with most probable size $\simeq 1.38L_D$. It is important that all above most probable values of island sizes coincide with the corresponding average values. It means that in weak approximation obtained, numerical data can be fitted by ordinary Gaussians.

10.4.3 Anisotropic Plasma-Condensate Systems

By considering plasma-condensate system, one should take into account that the vertical diffusion of adatoms becomes anisotropic due to the applied electric field with the strength $\mathbf{E} = -\nabla\phi$, where ϕ is the electric potential difference. In such system the substance is sputtered in the magnetron sputterer and accumulated near the substrate, which is located in a hollow cathode. Under the plasma influence, the main part of deposited atoms are re-evapourated to be later ionized again and returned onto an energetically favorable position on upper adsorbate layer under the influence of electric field [45]. Therefore, such ionized atoms condense on upper layers of growing surface. The corresponding additional vertical flux of adsorbate induced by electric field takes the form: $\mathbf{J}^E_{i||} = \left(\mathbf{E}ZeD_{||}/T\right)c_i$, where Z is the valence of ion and e is the electron charge. By taking into account that this flux is possible only on free sites on neighbor layers, one can put $u/w > 1$ in the multilayer adsorptive model (10.6) with $u = u + u_E$, where $u_E = |\mathbf{E}|Ze/T$ denotes the anisotropy strength of vertical diffusion of adsorbate induced by the electrical field near substrate.

In this study we are aimed to analyze an influence of anisotropy strength u_E onto statistical properties of adsorbate nano-islands. Hence, in all simulations we fix $\alpha = 0.2$ and $\varepsilon = 4$ and put $\beta = 0$. To study an influence of the anisotropy strength u_E onto structural transformations between the configuration of vacancy islands (holes) and the configuration of adsorbate islands in detail, next we provide statistical analysis considering stationary two-point correlation function $C(r) = \langle c(r)c(0)\rangle$, which can be represented in a form: $C(r) = Ae^{-r/R_c}\cos(2\pi r/R_0 + \phi)$, where R_c and R_0 are the correlation radius and the mean distance between structures, respectively. The quantity R_0 is useful to characterize the morphological transformation in a system. A dependence of the R_0 in units of diffusion length L_D *versus* anisotropy ratio $u/w > 1$ is shown in Fig. 10.7a with typical stationary snapshots for different u/w. It follows that R_0 grows with an increase in the anisotropy strength. In the vicinity of u/w_c, the mean distance between structures takes maximal value and decreases with further growth in u/w. Hence, at $u/w = u/w_c$ one gets the picture like in phase separation with $\langle c\rangle = 1/2$: at $1 \le u/w < u/w_c$ during exposing, one gets holes in adsorbate matrix; at $u/w > u/w_c$ separated adsorbate islands will grow on a substrate. Typical stationary snapshots illustrating this morphological transformation are shown in the top in Fig. 10.7a at different values of u/w. Correlation functions $C(r)$, manifesting oscillatory behavior with different periods, are shown in insertion in Fig. 10.7a.

Next we will discuss a change in the mean linear size of adsorbate islands $\langle R\rangle$ on a half-height of the growing surface with an increase in the ratio u/w. Temporal dependencies $\langle R(t)\rangle$ in units of diffusion length L_D at different values of u/w are shown in Fig. 10.7b. It is seen that at small values of anisotropy strength (see curve with black squares at $u/w = 3$), the mean linear size $\langle R\rangle$ of adsorbate islands on a half-height of a growing surface grows in time even at large time scales. With an increase in the anisotropy strength u/w (see curve with blue triangles at $u/w = 4$ in

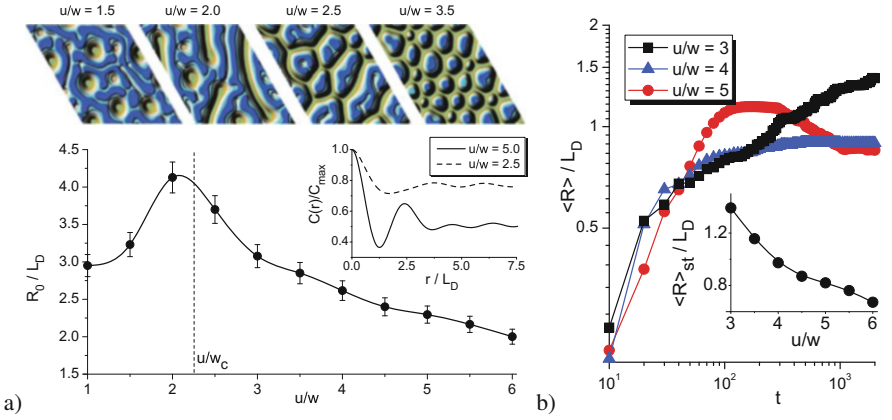

Fig. 10.7 (**a**) Dependence of the mean distance between structures R_0 *versus* anisotropy strength u/w with snapshots in the stationary limit; the corresponding stationary two-point correlation functions at different values of the anisotropy strength u/w are shown in inset. (**b**) Evolution of the mean linear size of adsorbate islands at different values of anisotropy strength; dependence of the stationary values of the adsorbate structures on anisotropy strength u/w is shown in inset

Fig. 10.7b) after the stage of adsorbate island growth (increasing dynamics of $\langle R \rangle$), the mean linear size of adsorbate islands takes stationary value at large time scales. At large values of u/w, the dependence $\langle R(t) \rangle$ changes crucially (see curve with red circles at $u/w = 5$ in Fig. 10.7b): the mean linear size of adsorbate islands increases attaining its maximal value and then decreases to the stationary value. A decrease in $\langle R(t) \rangle$ means that motion of adatoms to upper layers at large u/w provides more compact structure of adsorbate islands [46]. It follows that the stationary value of the mean linear size of adsorbate islands decreases with the anisotropy strength growth. The corresponding dependence $\langle R_{st}(u/w) \rangle$ is shown in the insertion in Fig. 10.7b.

Finally, we will discuss an influence of the anisotropy strength u/w onto stationary distribution $\varphi(R)$ of adsorbate islands over sizes, measured in units of diffusion length L_D. In Fig. 10.8 (left panel) we present calculated distributions $\varphi(R)$ for different values of anisotropy strength u/w. It is seen that at small u/w, the distribution $\varphi(R)$ has nonsymmetrical form with respect to the most probable size R_{mp} and has the form of Lifshitz-Slyozov-Wagner distribution. With an increase in u/w from three to four, one has modality change of the distribution of adsorbate islands over sizes in stationary limit: distribution $\varphi(R)$ is bimodal and is characterized by one peak located at small R and another one at large R. It means that in the stationary regime, one can observe on a substrate large amount of large adsorbate clusters and small number of small clusters. The most probable value of the linear size of adsorbate structures R_{mp}, which correspond to the largest peak of $\varphi(R)$, decreases, comparing to the case of $u/w = 3$. With an increase in the anisotropy strength, the stationary distribution $\varphi(R)$ transforms back to unimodal Lifshitz-Slyozov-Wagner distribution, and the most probable size R_{mp} decreases (see plot at $u/w = 5$). At large u/w both the most probable value R_{mp} and

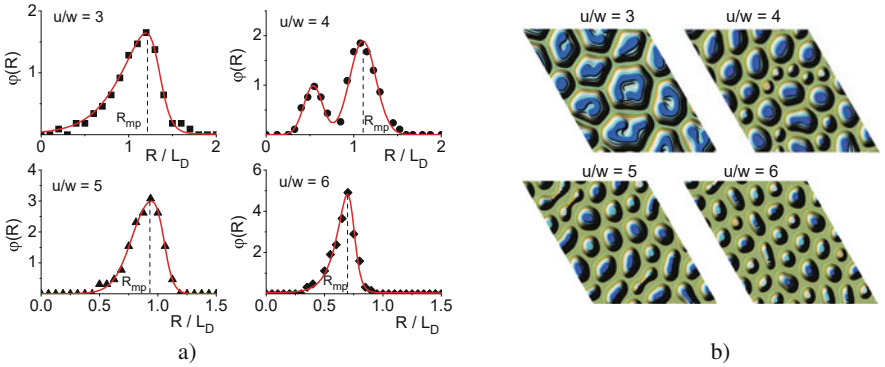

Fig. 10.8 Distribution functions of adsorbate islands over sizes in stationary limit on a half-height of a growing surface (**a**) and typical snapshots of surface patterns (**b**) at different values of anisotropy strength u/w

the dispersion of this unimodal distribution decrease. The last means that most of adsorbate structures are characterized by the same linear size.

In Fig. 10.8 on the right-hand side, we present typical snapshots of surface patterns at different values for anisotropy strength u/w. It follows that at small anisotropy $u/w = 3$, the surface is characterized by large adsorbate clusters. In the case of $u/w = 4$, both large and small adsorbate clusters are realized. With a further increase in u/w, adsorbate clusters become smaller with preferentially spherical lateral shape; they tend to have equivalent sizes.

10.4.4 Estimations

To estimate linear size of obtained structures, we consider a prototype system $Ge/Si(100)$, where the activation energy of adatom formation is $E_a = 0.6\,\text{eV}$, $E_d = 1.3\,\text{eV}$ is the activation energy for desorption, $E_D = 0.65\,\text{eV}$ is the activation energy for diffusion, and $\nu = 10^{12}\,\text{s}^{-1}$ is the lattice oscillation frequency. Using lattice constant $a = 5.6 \times 10^{-10}\,\text{m}$ for Ge and taking adatom interaction energy $\epsilon \approx 0.27\,\text{eV}$ at temperature $T = 773\,\text{K}$, one gets: $k_d = 1/\tau_d$ with $\tau_d = \nu^{-1} e^{E_d/T} \approx 3 \times 10^{-4}\,\text{s}$, $D = a^2 \nu e^{-E_D/T} \approx 1.8 \times 10^{-9}\,\text{m}^2/\text{s}$, $L_D = 7.4 \times 10^{-8}\,\text{m}$. According to definition of the critical adsorbate islands, we obtain $\langle R_c \rangle \simeq 0.42 L_d \simeq 30\,\text{nm}$. Estimation for the size of stationary adsorbate islands gives $\langle R_a \rangle \simeq 0.75 L_D \div 1.25 L_D \simeq 60 \div 100\,\text{nm}$, whereas vacancy islands have linear sizes $\langle R_v \rangle \simeq (0.3 \div 0.6) L_d \simeq (20 \div 40)\,\text{nm}$.

10.5 Conclusions

We have studied processes of adsorbate clusters formation in model of multilayer adsorptive system with isotropic and anisotropic motion of adatoms between neighbor layers. By using stability analysis, it is shown that for n-layer system, one gets n first-order transitions governing patterns formation on all layers. Phase diagrams manifesting emergence of spatial instabilities on each layer were obtained.

In the case of isotropic multilayer system with equiprobable motion of adatoms between neighbor layers, it is shown that an increase in the adsorption coefficient reduced to the gaseous phase pressure promotes structural transformation in the growing surface from separated multilayer pyramidal-like adsorbate islands on the substrate toward separated vacancy clusters inside adsorbate matrix.

In the case of pressure-induced anisotropic motion of adatoms between neighbor layers with preferential motion from upper toward lower layers, it is found that sufficient conditions for formation of adsorbate islands on the current layer are both the critical coverage and the critical size of the adsorbate island on the precursor layer serving as substrate for the current layer. It was found that evolution of the mean adsorbate island size is governed by major mechanisms related to standard diffusion, adsorption from the gaseous phase, and transference interaction. Their competition leads to complicated dynamics and crossover of dynamical regimes of adsorbate island growth processes on each layer. Coarsening regime on each layer is characterized by its own exponent. Distribution functions of adsorbate/vacancy islands over their sizes are studied in details.

It is shown that in plasma-condensate systems with preferential motion of adatoms from lower to upper layers, induced by the electrical field near substrate, an increase in the anisotropic strength leads to the structural transformation of the growing surface morphology: from patterns characterized by holes inside adsorbate matrix toward separated adsorbate structures on a substrate. It is shown that the anisotropy strength controls the dynamics of adsorbate island growth and distribution of adsorbate islands over sizes. At small values of the anisotropic strength, the mean linear size of adsorbate islands grows in time even at large time scales. The distribution has the form of Lifshitz-Slyozov-Wagner distribution. At intermediate values of the anisotropic strength, the mean size of adsorbate islands attains stationary value at large times, and the corresponding distribution transforms into bimodal one. In such a case in the stationary limit, stable adsorbate islands are characterized by small and large sizes comparing to the mean size. At large values of the anisotropic strength, the distribution of adsorbate islands over sizes has the form of the Lifshitz-Slyozov-Wagner distribution.

Obtained within this work, results can be useful to predict self-organization of adatoms into 3-D clusters in gas-/plasma-condensate systems for different materials (metals, semiconductors, etc.). We expect that our nontrivial findings will stimulate further theoretical and experimental studies of nano-size adsorbate island formation in anisotropic multilayer systems.

Acknowledgements Support of this research by the Ministry of Education and Science of Ukraine, project No. 0117U003927, is gratefully acknowledged.

References

1. Hirota E, Sakakima H, Inomata K (2002) Giant magneto-resistance devices. Springer, Berlin, Heidelberg, New York, Barcelona, Hong Kong, London, Milan, Paris, Tokyo
2. Warburton RJ, Schäflein C, Haft D et al (2000) Optical emission from a charge-tunable quantum ring. Nature 405:926
3. Shah A, Torres P, Tscharner R et al (1999) Photovoltaic technology: the case for thin-film solar cells. Science 285:692
4. Zhao L-D, Lo S-H, Zhang Y et al (2014) Ultralow thermal conductivity and high thermoelectric figure of merit in SnSe crystals. Nature 508:373
5. Wadley HNG, Zhou X, Johnson RA et al (2001) Mechanisms, models and methods of vapor deposition. Prog Mater Sci 46:329
6. Sree Harsha KS (2006) Principles of physical vapor deposition of thin films. Elesevier, Amsterdam/Boston/London
7. Perotto G, Bello V, Cesca T et al (2010) Nanopatterning of silica with mask-assisted ion implantation. Nucl Instrum Methods Phys Res B 268:3211
8. Bernas H (2010) Can ion beams control nanostructures in insulators? Nucl Instrum Methods Phys Res B 268:3171
9. Bradley RM, Harper JME (1988) Theory of ripple topography induced by ion bombardment. J Vac Sci Technol A 6(4):2390
10. Karmakar P (2013) Nanostructures in thin films by keV ion beams. In: Som T, Kanjilal D (eds) Nanofabrication by ion-beam sputtering. Taylor & Francis Group, LLC, Singapore
11. Lian J, Zhou W, Wei QM et al (2006) Simultaneous formation of surface ripples and metallic nanodots induced by phase decomposition and focused ion beam patterning. Appl Phys Lett 88:093112
12. Kharchenko DO, Kharchenko VO, Lysenko IO, Kokhan SV (2010) Stochastic effects at ripple formation processes in anisotropic systems with multiplicative noise. Phys Rev E 82:061108(13)
13. Kharchenko VO, Kharchenko DO (2011) Morphology change of the silicon surface induced by Ar^+ ion beam sputtering. Condens Matter Phys 14(N2):23602
14. Yutakam Y, Norihito S, Seiichi W et al (2011) Self-organized two-dimensional vidro-nanodot array on laser-irradiated Si surface. Appl Phys Express 4(5):055202
15. Huang SM, Hong MH, Lu YF et al (2002) Pulsed-laser assisted nanopatterning of metallic layers combined with atomic force microscopy. J Appl Phys 91(5):3268
16. Lu Y, Chen SC (2003) Nanopatterning of a silicon surface by near-field enhanced laser irradiation. Nanotechnology 14:505
17. Venables JA, Spiller GDT, Hanbücken M (1984) Nucleation and growth of thin films. Rep Prog Phys 47:399
18. Pimpinelli A, Villian J (1998) Physics of crystal growth. Cambridge University Press, Cambridge
19. Caflisch RE (2006) Proceedings of the international congress of mathematicians, Madrid, Spain, p 1419
20. Kharchenko DO, Kharchenko VO, Lysenko IO (2011) Phase-field modeling of epitaxial growth in stochastic systems with interacting adsorbate. Phys Scr 83:045802
21. Kharchenko DO, Kharchenko VO, Zhylenko TI et al (2013) A study of pyramidal islands formation in epitaxy within the generalized phase-field model. Eur Phys J B 86(4):175
22. Kharchenko DO, Kharchenko VO, Kokhan SV (2014) Universality and self-similar behaviour of non-equilibrium systems with non-Fickian diffusion. Condens Matter Phys 17:33004

23. Kharchenko VO, Kharchenko DO, Dvornichenko AV (2015) Scaling properties of pyramidal Islands formation process at epitaxial growth. Eur Phys J B 88:3
24. Pohl K, Bartelt MC, de la Figuera J et al (1999) Identifying the forces responsible for self-organization of nanostructures at crystal surfaces. Nature 397:238
25. Mo YW, Swartzentruber BS, Kariotis R et al (1989) Growth and equilibrium structures in the epitaxy of Si on Si(001). Phys Rev Lett 63:2393
26. Cirlin GE, Egorov VA, Sokolov LV, Werner P (2002) Ordering of nanostructures in a $Si/Ge_{0.3}Si_{0.7}/Ge$ system during molecular beam epitaxy. Semiconductors 36(N11):1294–1298
27. Bucher JP, Hahn E, Fernandez P et al (1994) Transition from one-to two-dimensional growth of Cu on Pd (110) promoted by cross-exchange migration. Europhys Lett 27:473
28. Besenbacher F, Pleth Nielsen L, Sprunger PT (1997) Surface alloying in heteroepitaxial metal-on- metal growth (Chapter 6). In: King DA, Woodruff DP (eds) The chemical physics of solid surfaces, vol 8. Elsevier, Amsterdam, p 207
29. Brune H (1998) Microscopic view of epitaxial metal growth: nucleation and aggregation. Surf Sci Rep 31:121–229
30. Mikhailov A, Ertl G (1995) Pattern formation by adsorbates with attractive lateral interactions. Chem Phys Lett 238:104
31. Hildebrand M, Mikhailov AS (1996) Mesoscopic modeling in the kinetic theory of adsorbates. J Phys Chem 100:19089
32. Batogkh D, Hildebrant M, Krischer F, Mikhailov A (1997) Nucleation kinetics and global coupling in reaction-diffusion systems. Phys Rep 288:435
33. Hildebrand M, Mikhailov AS, Ertl G (1998) Traveling nanoscale structures in reactive adsorbates with attractive lateral interactions. Phys Rev Lett 81:2602(4)
34. Hildebrand M, Mikhailov AS, Ertl G (1998) Nonequilibrium stationary microstructures in surface chemical reactions. Phys Rev E 58:5483(11)
35. Mangioni SE, Wio HS (2005) Interplay between noise and boundary conditions in pattern formation in adsorbed substances. Phys Rev E 71:056203
36. Mangioni SE (2010) Nano-pattern stabilization by multiplicative noise. Physica A 389:1799
37. Casal SB, Wio HS, Mangioni S (2002) Phase transitions and adsorption isotherm in multilayer adsorbates with lateral interactions. Physica A 311:443
38. Walgraef D (2002) Nanostructure initiation during the early stages of thin film growth. Physica E 15:33
39. Walgraef D (2003) Nanostructure evolution during thin film deposition. Physica E 18:393
40. Walgraef D (2004) Reaction-diffusion approach to nanostructure formation and texture evolution in adsorbed monoatomic layers. Int J Quantum Chem 98:248
41. Kharchenko VO, Kharchenko DO (2012) Nanosize pattern formation in overdamped stochastic reaction-diffusion systems with interacting adsorbate. Phys Rev E 86:041143
42. Kharchenko VO, Kharchenko DO, Dvornichenko AV (2014) Statistical properties of nanosized clusters on a surface in overdamped stochastic reaction-Cattaneo systems. Surf Sci 630:158
43. Kharchenko VO, Kharchenko DO, Kokhan SV et al (2012) Properties of nano-Islands formation in nonequilibrium reaction-diffusion systems with memory effects. Phys Scr 86:055401
44. Kharchenko DO, Kokhan SV, Dvornichenko AV (2009) Noise induced patterning in reaction-diffusion systems with non-Fickian diffusion. Physica D 238:2251
45. Perekrestov VI, Olemskoi AI, Kosminska YuO, Mokrenko AA (2009) Self-organization of quasi-equilibrium steady-state condensation in accumulative ion-plasma devices. Phys Let A 373:3386
46. Kharchenko VO, Kharchenko DO, Yanovsky VV (2017) Nano-sized adsorbate structure formation in anisotropic multilayer system. Nanoscale Res Lett 12:337

Chapter 11
The Effect of Ultrasonic Treatment on the Physical–Chemical Properties of the ZnO/MoO_3 System

V. O. Zazhigalov, O. V. Sachuk, O. A. Diyuk, N. S. Kopachevska, V. L. Starchevskyy, and M. M. Kurmach

11.1 Introduction

A number of publications [1–8] are devoted to the use of ultrasonic treatment (UST) in various areas, including the preparation of nanodispersed materials. Analysis of the results presented in these publications shows that ultrasonic vibrations lead not only to ultrafine grinding, which, as a rule, can be realized by other methods, but also permit a specific surface area, rate, and percentage of chemical reaction effectuated during the processing to be increased. Herewith, the cavitation is a working effect. This phenomenon is characterized by the formation in the droplet of fluid cavities filled with gas, steam or a mixture (so-called cavitation bubbles or cavities). Currently, the process of cavitation in solutions has not been fully studied, and the mechanism of its influence on oxide materials, including binary oxide systems, in particular Zn and Mo, is not sufficiently established. The zinc and molybdenum oxides, and composites based on them are most promising in view of their practical utilization. This is because of their wide use as luminescence materials in the field of energy-saving and geological research to find highly efficient energy sources [9–11], photocatalysts in the decomposition of organic dyes [12, 13], and catalysts in a number of hydrocarbon processes – hydrofining, hydrocracking,

V. O. Zazhigalov (✉) · O. V. Sachuk · O. A. Diyuk · N. S. Kopachevska
Institute for Sorption and Problems of Endoecology, National Academy of Sciences of Ukraine, Kyiv, Ukraine
e-mail: zazhigal@ispe.kiev.ua

V. L. Starchevskyy
National University «Lviv Polytechnic», Lviv, Ukraine

M. M. Kurmach
L. V. Pisarzhevskii Institute of Physical Chemistry, National Academy of Sciences of Ukraine, Kyiv, Ukraine

O. Fesenko, L. Yatsenko (eds.), *Nanocomposites, Nanostructures, and Their Applications*, Springer Proceedings in Physics 221,
https://doi.org/10.1007/978-3-030-17759-1_11

reforming, isomerization, polymerization, metathesis, etc. [14–16]. Also, Zn/Mo oxide composites are used in the creation of electrode batteries as one of the most economical convective water heaters, in the production of gas sensors, and bolometers for measuring the energy of high-frequency radiation [15, 16]. However, investigations of nanostructured molybdates are highly limited because of the complex synthesis methods used for the preparation of different molybdates. Thus, the development of the simple methods of the synthesis of molybdate nanostructures is a promising pathway for the widespread use of further molybdates. It is necessary to note that in the papers by Sachuk et al. and Zazhigalov et al. [17–20]the results of the mechanochemical treatment (MChT) approach were reported as an alternative sampling method to the synthesis of molybdates in the ZnO/MoO_3 system and the physicochemical properties of the prepared products were studied.

In this present study, the effect of UST on a series of compositions of ZnO/MoO_3 with molar oxide ratios equal to 15:85, 25:75, 50:50, and 75:25 has been investigated. We report a facile sonochemical approach (as a type of MChT in a solution) to the synthesis of the nanodimensional needle-like structure of zinc molybdate ($ZnMoO_4$).

11.2 Experimental

11.2.1 Materials

The complex binary ZnO/MoO_3 system with molar ratios of ZnO/MoO_3 = 15:85, 25:75, 50:50, and 75:25 was prepared by mixing zinc and molybdenum oxides. The aqueous solutions of the samples were sonicated for 1 h using a UZDN instrument, which operates in acoustic cavitation mode at a frequency of 40 kHz. During the reaction, the temperature of the solution was maintained at 80 °C by circulating cold water around the reactor. After treatment, the emulsions obtained were separated on a centrifuge and powders were dried in the air at 110 °C.

11.2.2 Techniques

X-ray powder diffractograms of initial and sonoactivated samples were determined by using a diffractometer (Philips PW 1830). The patterns were run with Cu Kα radiation with an Ni filter and working in continuous mode with a step size of 0.05° 2Θ in combination with the Inorganic Crystal Structure Database (ICSD). *Particle size* (L) for the most intense reflexes was calculated *using* the *Scherrer formula* (11.1):

$$L = \frac{K\lambda}{\beta \cos \Theta} \tag{11.1}$$

where L is the crystallite size, K is the Scherrer constant (0.89), λ the X-ray wavelength, β the full-width at half-maximum of the main diffraction peaks of crystalline phases present, and Θ is the diffraction angle.

The specific surface area (S_{BET}) was determined from nitrogen adsorption isotherms measured at 77 K using a Quantachrome NOVA-2200e instrument. Before conducting measurements, each sample was degassed under vacuum 10^{-5} Torr at 180°C for 20 h.

Fourier transform infrared spectra were recorded at room temperature in the air on a "Spectrum One" spectrometer with KBr as a diluting agent and operated within the range of 4000–400 cm^{-1}.

Transmission electron microscopy (TEM) images were obtained on a JEM-2010 apparatus (JEOL) at an accelerating voltage of 80 kV after preliminary ultrasonic dispersion of the samples in a water–alcohol solution.

The surface morphology of the samples was studied using scanning electron microscopy (SEM) on a JSM-6490 device (JEOL, Japan) in combination with an energy dispersive spectrometer (Haruta).

The catalytic properties of the samples in the ethanol oxidation reaction were determined in a flow-type installation using the stainless steel microreactor within a temperature range of 25–300°C. The sample load was 0.5 ml (fraction 0.25–0.5 mm). The reaction mixture contained 1% ethanol in air. The starting materials and reaction products were analyzed on-line on gas chromatographs with flame-ionization (FID) and thermal conductivity detectors (TCD). The formulas of the calculation of ethanol conversion, acetaldehyde selectivity, and its yield are presented in Zazhigalov et al. [21]. The productivity of the catalyst was calculated according to Eq. 11.2:

$$N = k\frac{Y_{Ac}}{m_{cat}} \tag{11.2}$$

where N is the catalyst productivity of acetic aldehyde, mol/kg_{cat} · h, k (coefficient taking into account the amount of product produced in 1 h) is $5{\cdot}10^{-6}$, Y_{Ac} is the percentage acetaldehyde yield, and m_{cat} is the mass of catalyst in milligrams.

11.3 Results and Discussion

X-ray diffraction patterns of zinc–molybdenum oxide mixtures are shown in Fig. 11.1. The diffractogram of the initial samples (Fig. 11.1a; independent of the molar ratio ZnO/MoO3) shows a presence of peaks of α-MoO3 orthorhombic modification (ICSD – 005-008) as a dominant reflex with maximum intensity from the plane (040) and diffraction peaks of ZnO (ICSD – 01-080-0075). After UST, a broadening of the characteristic peaks and a decrease in their intensity were observed (Fig. 11.1), which indicates the formation of structural defects and can also be connected to a decrease in crystallite size (Table 11.1). The formation

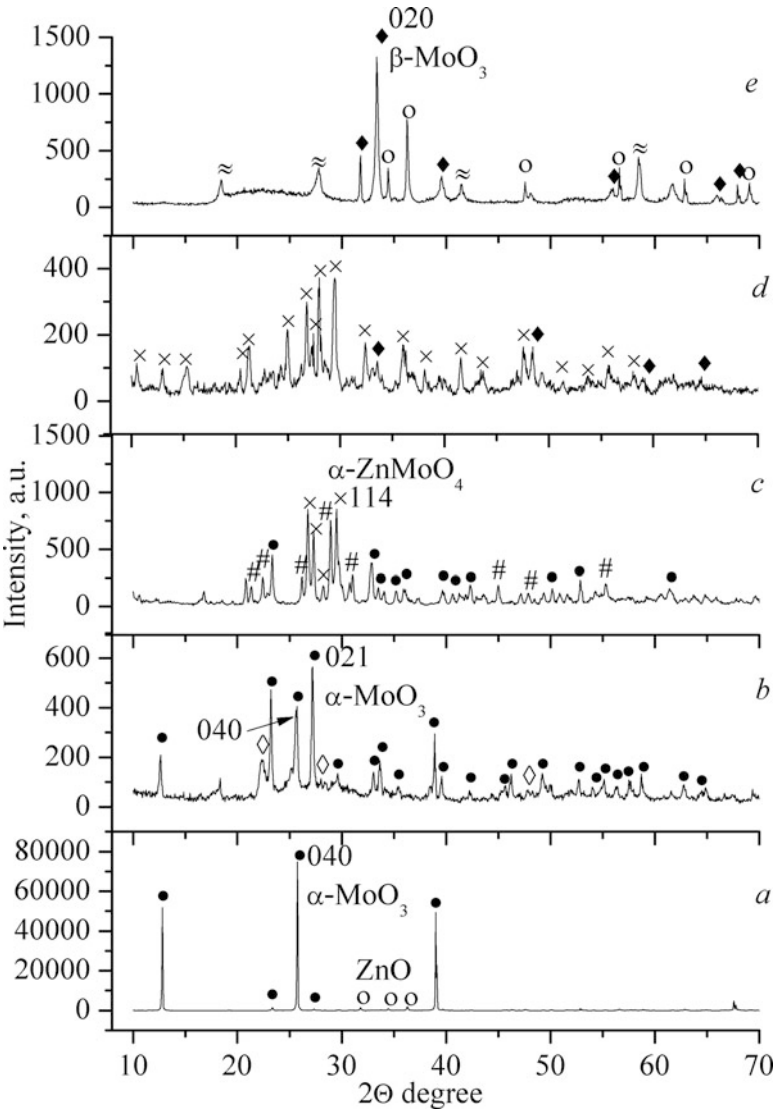

Fig. 11.1 X-ray diffractograms of (**a**) the initial sample Zn/Mo = 50:50, and after ultrasonic treatment (UST) of compositions (**b**) Zn/Mo = 15:85, (**c**) 25:75, (**d**) 50:50, (**e**) 75:25

of new reflexes characteristic of the zinc molybdate α-$ZnMoO_4$ and molybdenum suboxides (Mo_4O_{11} and Mo_8O_{23}, Magneli phases) was established. Some features of the changes of phase composition for each of the mixtures studied are presented below.

It was established that UST of the composition ZnO/MoO_3 = 15:85 (Fig. 11.1b) is accompanied by a change in the maximum intensity reflex α-MoO3 from the

Table 11.1 Some characteristics of the ZnO/MoO_3 compositions

Parameter	Molar ratio ZnO/MoO_3				
	Sample state	15:85	25:75	50:50	75:25
L, nm[a]	Initial	116	95	81	72
	UST 1 h	38	23	33	28
S_{BET}, m^2/g	Initial	1	1	2	3
	UST 1 h	3	6	3	14

S_{BET} Brunauer–Emmett–Teller specific surface area, *UST* ultrasonic treatment

[a]*L* is a size of crystallites, calculated to the most intense reflexes to use Scherrer's equation

planes (040) to (021) caused by the anisotropic deformation of MoO_3. Also, the formation of minor amounts (15.4%) of γ-Mo_4O_{11} orthorhombic modification was observed, which can be connected to a reduction process of MoO_3 by hydrogen, which could be formed as a result of water sonolysis. This result is in agreement with a suggestion by Burch [22], who proposed that Mo_4O_{11} is an intermediate product of the reduction reaction of MoO_3 to MoO_2 (Scheme 11.1):

$$MoO_3 \xrightarrow{H_2} Mo_4O_{11} \xrightarrow{H_2} MoO_2 \tag{11.3}$$

It is necessary to note that the reduction of MoO_3 by hydrogen was studied by Ressler et al. and Lalik [23, 24] and the influence of the temperature process on Mo_4O_{11} formation from MoO_3 was postulated, which was experimentally confirmed by other investigators [25–29]. On the other hand, the sonolysis process of the water molecules splitting leads to the formation of free radicals (Reaction 11.4):

$$H_2O \rightarrow H^{\cdot} + OH^{\cdot} \tag{11.4}$$

In Margulis et al. and Bang and Suslick [30, 31], it was shown that these radicals can recombine with the formation of molecular products (H_2 and H_2O_2), according to Scheme 11.3, but their high reactivity to the reduction of the solids must be greater than that of molecular hydrogen and the reduction of the oxides in this case can proceed at a low temperature. It is necessary to note that the reduction of vanadium and molybdenum oxides after their MChT in water was established in Zazhigalov et al. and Bogutskaya et al. [32, 33].

$$H_2O \text{—}))) \; H^{\cdot}, OH^{\cdot}, H_2, H_2O_2 \tag{11.5}$$

After sonochemical activation of the $ZnO/MoO_3 = 25{:}75$ sample (Fig. 11.1c), the diffractogram contains the reflexes of the initial compound α-MoO_3 and a new phase – β-Mo_8O_{23} – of monoclinic modification. The formation of a metastable phase of suboxide Mo_8O_{23} can be explained analogically by the hydrogen reduction

of molybdenum oxide and a crystallographic shift in MoO_3. Such a shift occurs on intense ultrasound action accompanied by the diffusion of oxygen atoms from the surface as a result of the formation of oxygen vacancies. It is necessary to note that the formation of the suboxide Mo_8O_{23} was also observed in the MChT process of Zn/Mo = 50:50 mixture in water medium [18]. Any diffraction peaks of ZnO were observed for this mixture after treatment, which can be connected to the existence of this phase in an X-ray amorphous state or amorphous zinc molybdate phase formation.

$\bullet\alpha\text{-}MoO_3, \lozenge\, \gamma - Mo_4O_{11}, \times\alpha\text{-}ZnMoO_4, \blacklozenge\, \beta\text{-}MoO_3, \#\beta\text{-}Mo_8O_{23}, \approx \eta\text{-}Mo_4O_{11}, \bigcirc\, ZnO.$

The investigations of the $ZnO/MoO_3 = 50{:}50$ composition show that UST leads to a solid phase reaction between initial components ZnO and MoO_3 with formation of a zinc molybdate phase. The peaks detected in the sample diffractogram (Fig. 11.1d) were specified as zinc molybdate $\alpha\text{-}ZnMoO_4$ triclinic modification (JCPD card 01-072-1486) with a dominant reflex from the plane (114). It is possible to suppose that a mechanism of α-zinc molybdate formation connected to the interaction between hydrated oxides of zinc and molybdenum analogous to those proposed in Zhang et al., Keereeta et al., and Karekar et al. [11, 34, 35]. It is necessary to note that the formation of reflexes of this phase in small amounts was observed in the sonochemical process of the sample $ZnO/MoO_3 = 25{:}75$. Simultaneously, the weak peaks of the $\beta\text{-}MoO_3$ monoclinic modification are presented in a diffractogram, the formation of which can be connected to the anisotropic destruction of $\alpha\text{-}MoO_3$ crystal. Thus, it is possible to suppose that the formation of this modification can accelerate the process of zinc molybdate formation or that this phase can be an initial compound in the process of zinc molybdate formation. As a result, the ultrasonic method of obtaining this phase was protected by us in a Ukrainian patent [36].

The diffractogram of the sample Zn/Mo = 75:25 (Fig. 11.1e) exhibits the reflexes of initial zinc oxide and $\beta\text{-}MoO_3$ with a dominant reflex from the plane (020). Simultaneously, new and low-intensity peaks were identified at 2Θ values of 18.5° (012), 27.8° (202), 41.5° (−126), and 58.4° (411), which correspond to the monoclinic modification $\eta\text{-}Mo_4O_{11}$ (JCSD 01-086-1269).

Thus, the observed changes in the XRD X-ray diffraction profiles of the oxide mixtures and the formation of new reflections as a result of UST can be explained by the formation of shear defects in MoO_3 due to ultrasound irradiation.

The data presented in Table 11.1 show that the sonochemical modification of the powders leads to a decrease in the average crystallite size (by 2–4 times) and an increase in their Brunauer–Emmett–Teller (BET) specific surface areas in comparison with initial oxide mixtures. The latter can be due to the following three phenomena: (i) dispersion of the samples, which was established using XRD; (ii) phase transformation of MoO_3; and (iii) the formation of a secondary porous structure.

The data obtained by SEM demonstrate the change of the oxides mixtures morphology as result of treatment (Fig.11.2). The initial compositions show (Fig. 11.2a)

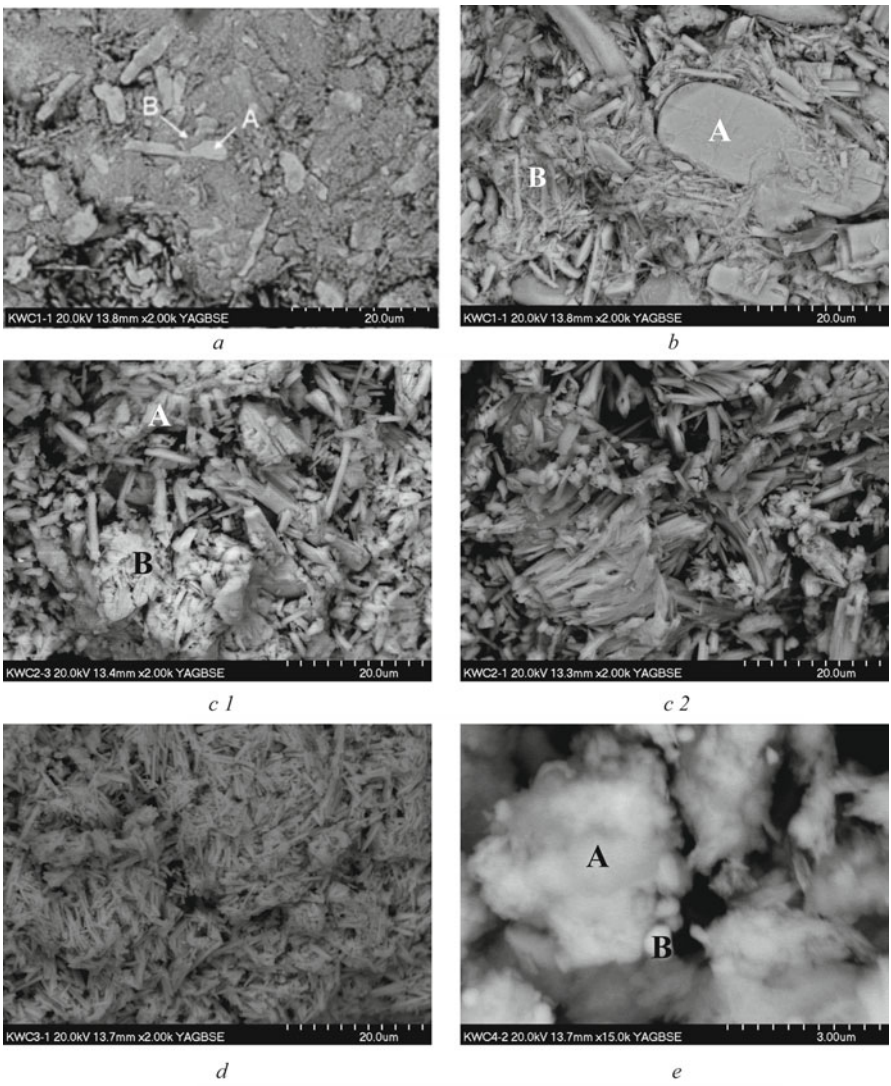

Fig. 11.2 Scanning electron microphotographs of (**a**) the initial sample Zn/Mo = 50:50 and after UST of compositions (**b**) Zn/Mo = 15:85, (**c**) 25:75 (*1* and *2*), (**d**) 50:50, and (**e**) 75:25

an irregularity in shape that is due to presence of two types of the particles: big irregular form crystals (A), which according to energy dispersive spectroscopy (EDS) analysis (Table 11.2) belong to MoO_3 and finely dispersed crystals (B) which are correspond to ZnO. The ration between these particles depends from initial mixture composition. It was established that UST of the sample Zn/Mo = 15:85 (Fig. 11.2b) leads to a destruction of MoO_3 big crystals with formation of rounded

Table 11.2 Results of the samples by energy dispersive spectroscopy analysis

Sample	Analysis size	Element content, % at.	
	(Fig. 11.2)	Zn	Mo
Initial Zn/Mo = 50:50	A	4.4	95.6
	B	97.0	3.0
	After UST		
Zn/Mo = 15:85	A	–	100
	B	2.5	97.5
	FS	5.2	94.8
Zn/Mo = 25:75	A (*c1*)	47.6	52.4
	B (*c1*)	15.3	84.7
	FS (*c2*)	49.3	50.7
Zn/Mo = 50:50	FS	48.9	51.1
Zn/Mo = 75:25	A	–	100
	B	88.5	11.5
	FS	70.8	29.2

FS full surface

oblong plates and small particles. The data of EDS analysis (Table 11.2) show that both large (A) and small (B) particles belong to oxide(s) molybdenum. So, the excess of molybdenum oxide on sample surface which covers zinc oxide is observed.

After treatment of the samples Zn/Mo = 25:75 and 50:50, a significant number of elongated crystals, which can characterize the zinc molybdate, are observed on the Fig. 11.2, c1 and c2, d, Fig. 11.3b and c. In the sample Zn/Mo = 25:75, except for oblong crystals (Fig. 11.2c1 (A), c2), particles of undefined shape (Fig. 11.2c1 (B)) are presented on SEM microphotographs, when the surface of the second composition is more homogeneous (Fig. 11.2d).

The data presented in Table 11.2 show that the ratio of Zn/Mo in elongated (needle-like) crystals is about 1:1, which is in agreement with XRD data and permits them to be attributed to α-$ZnMoO_4$. A significant excess of molybdenum is characteristic of particles of type B (Table 11.2); thus, they can belong to molybdenum suboxides. A completely different morphology was observed in the sample Zn/Mo = 75:25 (Fig. 11.2e), where large agglomerations (A), which, according to analysis (Table 11.2) are molybdenum oxide(s), and nanosized particles (B), which correspond to zinc oxide, were found.

The data of TEM analysis of the samples after UST presented in Fig. 11.3 confirm the presence in the sample Zn/Mo = 15:85 (Fig. 11.3a1, a2) of two types of crystals, which correspond to initial compounds – zinc and molybdenum oxides, but with smaller dimensions in comparison with the initial mixture. It was found that for the compositions Zn/Mo = 25:75 and 50:50, the presence of nanosized needle-like crystals is characteristic after treatment (Fig. 11.3b, c1, c2). It worth noting that for the second composition their sizes are much smaller (in cross-section, 70–130 nm). After UST of the composition with ZnO excess (Zn/Mo = 75:25), few crystal types

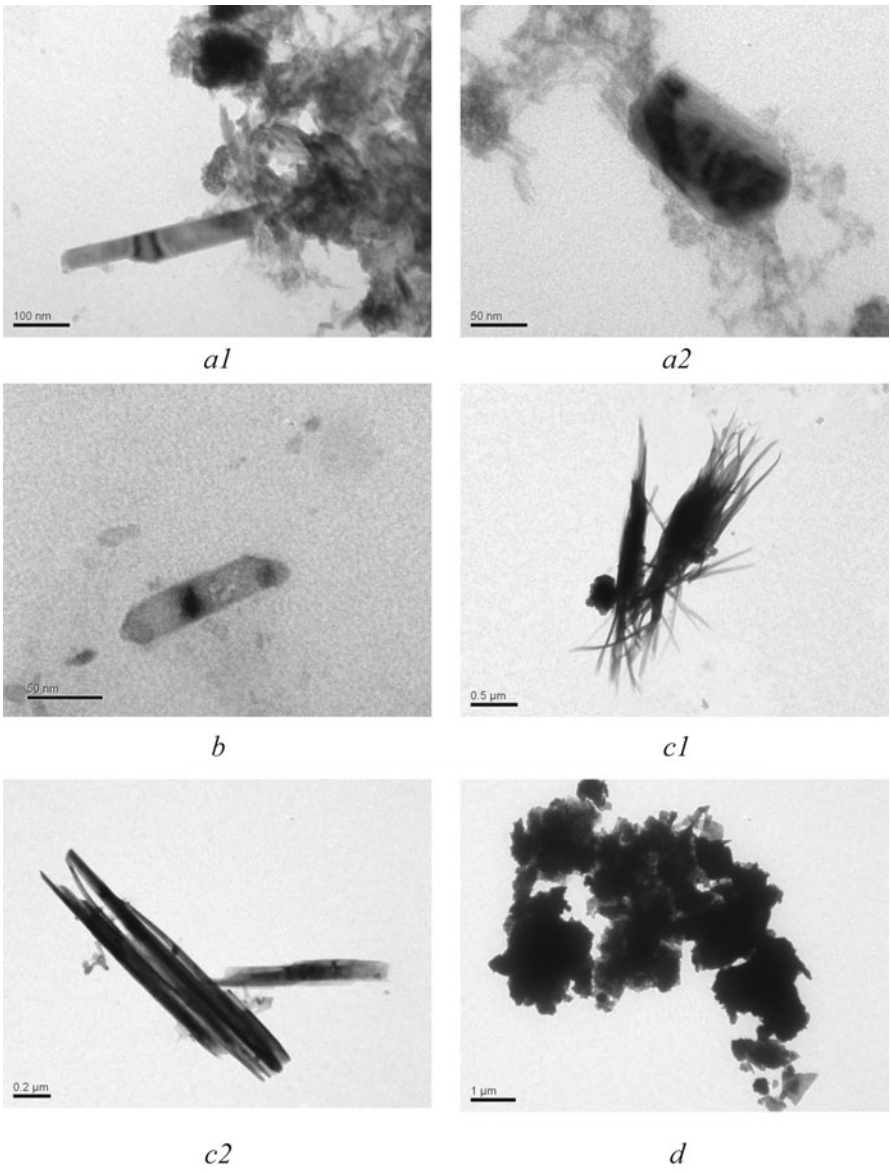

Fig. 11.3 Transmission electron microscopy images after UST of the samples (**a1**,**a2**) Zn/Mo = 15:85, (**b**) 25:75, (**c**) 50:50 (*1* and *2*), (**d**) 75:25

with a smaller size than in the initial sample were observed (Fig. 11.3d). Herewith, some of them have a defined form that differs from the initial oxides. It can be explained by the formation of a reduced molybdena phase and a small amount of zinc molybdate.

Table 11.3 Fourier transform infrared data of modified samples of the ZnO/MoO_3 system

Absorption band	Wave number, cm^{-1}					
Sample	Mo = O	Linear Mo-O-Mo	Zn-O	Angular Mo-O-Mo	Mo-O	Mo-O-Zn
Initial	988	860	500	–	–	
15:85	950	897	497	–	577	
25:75	962, 924	832, 882	495	746	655	
50:50	924	897	500	–	655	531
75:25	922	864	445	691, 792	–	–

The morphological change in the samples and the decrease in crystallite sizes as a result of intense sonochemical treatment accompanied by a change in the infrared (IR) spectra of the samples. The IR spectra of initial mixtures (Table 11.3) independently on the molar ratio ZnO/MoO_3 show the presence of absorption bands at 988, 860, and 500 cm^{-1}, which correspond to the stretching modes of the Mo = O terminal bond, the Mo_2O (Mo-O-Mo) entity [37, 38], and the stretching vibrations of the Zn-O bond [39, 40] respectively.

As a result of sonochemical treatment, some shift of the absorption bands and vibrations, and the appearance of new bonds were observed. In the spectrum of the Zn/Mo = 15:85 sample (Table 11.3) the drastic decrease in intensity for the band of the asymmetric stretching modes of the Mo = O bond and its shift up to 950 cm^{-1} was established. The shift of the band of stretching modes of the Mo-O-Mo bond in a high-frequency region (897 cm^{-1}), which can be caused by an increase in the bridging bond length, was also observed. The appearance of the band at 577 cm^{-1}, assigned to stretching vibrations of Mo_2O_2 (Mo-O) units, which can be formed by an edge shared with MoO_6 octahedra, was registered. These changes correspond well with the destruction of the large initial crystals of MoO_3 observed by XRD, SEM, and TEM. The spectrum of the composition ZnO/MoO_3 = 25:75 demonstrates the presence of absorption bands centered at 832 and 746 cm^{-1}, which are characteristic of the linear Mo-O-Mo and angular Mo-O-Mo bonds of Mo_8O_{23} [41] respectively (Table 11.3). Besides the spectrum of this sample also contains the bands of linear Mo-O-Mo bond at 882 cm^{-1} and the terminal Mo = O bond at 962 cm^{-1}, which is in agreement with XRD data on α-MoO_3 phase existence. Two absorption bands at 924 and 655 cm^{-1} belong to terminal Mo = O (its further shift can be noted) and linear bridging O-Mo-O bonds respectively can testify the formation of the zinc molybdate phase [42]. The higher intensity of these absorption bands is well observed for the sample Zn/Mo = 50:50, where an appearance of the characteristic for the zinc molybdate phase band at 531 cm^{-1} was also fixed. The spectrum of the sample Zn/Mo = 75:25 demonstrates the presence of a weak absorption band at 445 cm^{-1} that is assigned to the vibrations of ZnO_4 units in zinc oxide and its shift can be connected with oxide destruction established by SEM and TEM. Two bands at 691 and 792 cm^{-1} are attributed to the angular bridging Mo-O-Mo bond of η-Mo_4O_{11}, as the band, which is characteristic of the Mo-O-Mo linear bridging bond, with strong intensity at 864 cm^{-1}. The stretching vibrations of the

terminal Mo = O bond visible at 922 cm^{-1} can characterize the low quantity of zinc molybdate formation. Thus, the data on IR spectroscopy correspond well to the results of these study samples by means of XRD, SEM, and TEM.

The study of the catalytic properties of the ZnO/MoO_3 system (samples with Zn/Mo = 50:50 were examined) in bioethanol oxidation shows that only acetic aldehyde and ethylene are the products of this reaction (Fig. 11.4 and Table 11.4).

Comparison of the initial sample and after UST shows that the UST essentially increases the catalytic activity (Table 11.4).

The conversion of ethanol equal to 100% in the case of the treated sample can be achieved at 62 °C lower (at 255 °C) in comparison with the initial sample. On the other hand, a decrease in acetaldehyde formation selectivity with an increase in ethanol conversion is observed for an initial sample, but in the case of treated samples, the small change in this product selectivity up to ethanol conversion equal to 100% was established (Fig. 11.4). An increase in catalytic activity of the sample after treatment can be explained by a decrease in catalyst particle size and a corresponding increase in the specific surface area, which leads, respectively, to an increase in the number of catalytic active centers available for reagents. Conversely, the stability of acetaldehyde formation selectivity at the suppression of the parallel reaction of ethylene formation can be due to the formation of α-$ZnMoO_4$ as a result of treatment. It is necessary to note that the sample prepared using a simple method (UST) from oxide mixture demonstrates a high acetaldehyde yield equal to 94% at a low reaction temperature (255 °C) and its productivity equal to 1.08 mol/kg·h. These

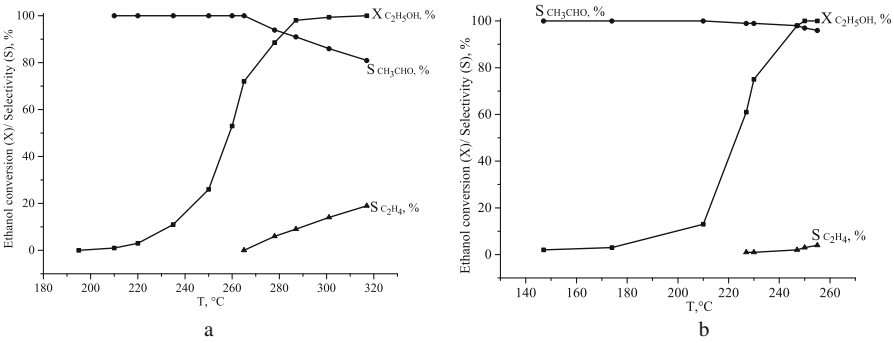

Fig. 11.4 Temperature dependence of ethanol conversion (*X*) and the selectivity of product reaction formation (*S*) on (**a**) initial Zn/Mo = 50:50 catalyst and (**b**) after UST

Table 11.4 Catalytic properties of a Zn/Mo = 50:50 sample in an ethanol oxidation reaction

	$T_{reaction}$, °C		Yield at X = 100%		
Sample	$X_{50\%}$	$X_{100\%}$	CH_3CHO	C_2H_4	N, mol/kg·h at X = 100%
Initial	260	317	81	19	0.44
UST	223	255	94	6	1.08

X ethanol conversion, *N* productivity of the catalyst for acetic aldehyde at 100% ethanol conversion

results permit us to consider this reaction on prepared catalyst as an alternative to the known Wacker process of acetaldehyde manufacture.

11.4 Conclusion

The presented research shows that UST of the microcrystal mixtures of zinc and molybdenum oxides leads to a decrease in the size of initial components up to nanodimensions, a change in their porous structure, and an increase in the specific surface area. The formation of the new nanodispersed suboxides M_4O_{11} and Mo_8O_{23} and also the solid phase reaction between zinc and molybdenum oxides with the formation of needle-like nanoparticles of triclinic modification α-$ZnMoO_4$ occur. It was shown that prepared nanostructured ZnO/MoO_3 compositions possess high catalytic activity in ethanol oxidation reaction with a high acetaldehyde yield (94%) at a low reaction temperature (255 °C).

Acknowledgments This work was financially supported by NASU Programs: Fundamental Research "New Functional Substances and Materials for Chemical Engineering" (project 7-17/18) and Program for Young Scientists (project 41: "Synthesis of new nanodispersed photocatalysts of environmental protection processes").

References

1. Bang JH, Suslick KS (2010) Application of ultrasound to the synthesis of nanostructural materials. Adv Mater 22:1039–1059
2. Chatel G (2018) How sonochemistry contributes to green chemistry? Ultrasonics Chem 40:117–122
3. Mason TJ, Lorimer JP (2002) Applied sonochemistry: uses of power ultrasound in chemistry and processing. Copyright, Weinheim, p 293
4. Yusof NSM, Babgi B, Alghamdi Y, Aksu M, Madhavan J, Ashokkumar M (2016) Physical and chemical effects of acoustic cavitation in selected ultrasonic cleaning applications. Ultrason Sonochem 29:568–576
5. Leong T, Ashokkumar M, Kentish S (2011) The fundamentals of power ultrasound – a review. Acoustics Australia 39(2):54–63
6. Suslick KS, Price GJ (1999) Applications of ultrasound to materials chemistry. Annu Rev Mater Sci 29(1):295–326
7. Mason TJ (1997) Ultrasound in synthetic organic chemistry. Chem Soc Rev 26:443–451
8. Thompson LH, Doraiswamy LK (1999) Sonochemistry: science and engineering. Ind Eng Chem Res 38(4):1215–1249
9. Choi GK, Kim JR, Yoon SH, Hong KS (2007) Microwave dielectric properties of scheelite (A = Ca, Sr, Ba) and wolframite (A = Mg, Zn, Mn) $AMoO_4$ compounds. J Eur Ceram Soc 27:3063–3067
10. Ryu JH, Koo SM, Yoon JW, Lim CS, Shim KB (2006) Synthesis of nanocrystalline $MMoO_4$ (M = Ni, Zn) phosphors via a citrate complex route assisted by microwave irradiation and their photoluminescence. Mater Lett 60:1702–1705

11. Zhang G, Yu S, Yang Y, Jiang W, Zhang S, Huang B (2010) Synthesis, morphology and phase transition of the zinc molybdates $ZnMoO_4 \times 0.8H_2O$/α-$ZnMoO_4$/$ZnMoO_4$ by hydrothermal method. J Cryst Growth 312:1866–1874
12. Li Y, Weisheng G, Bo B, Kaijie G (2009) Yeast-directed hydrothermal synthesis of $ZnMoO_4$ hollow microspheres and its photocatalytic degradation of auramine O. International conference on energy and environment technology IEEE. https://doi.org/10.1109/ICEET.2009.631
13. Ramezani M, Hosseinpour-Mashkani SM, Sobhani-Nasab A, Estarki HG (2015) Synthesis, characterization, and morphological control of $ZnMoO_4$ nanostructures through precipitation method and its photocatalyst application. J Mater Sci Mater Electron 26(10):7588–7594
14. Sotani N, Suzuki T, Nakamura K, Eda K, Hasegawa S (2001) Change in bulk and surface structure of mixed MoO_3-ZnO oxide by heat treatment in air and in hydrogen. J Mater Sci 36:703–713
15. Nakamura K, Eda K, Hasegawa S, Sotani N (1999) Reactivity for isomerization of 1-butene on the mixed MoO_3–ZnO oxide catalyst. Appl Catal A Gen 178(2):167–176
16. Maezawa A, Okamoto Y, Imanaka T (1987) Physicochemical characterization of ZnO/Al_2O_3 and ZnO–MoO_3/Al_2O_3 catalysts. J Chem Soc Faraday Trans 1 Phys Chem Condensed Phases 83(3):665–674
17. Sachuk OV, Zazhigalov VO, Kuznetsova LS, Tsiba MM (2016) Properties of Zn-Mo oxide systems, synthesized by mechano-chemical processes. Chem Phys Surface Technol 7(3):309–321
18. Zazhigalov VA, Sachuk EV, Kopachevskaya NS, Bacherikova IV, Wieczorek-Ciurowa K, Shcherbakov SN (2016) Mechanochemical synthesis of nanodispersed compounds in the ZnO–MoO_3 system. Teor Exp Chem 52(2):97–103
19. Sachuk O, Zazhigalov V, Kobuley O (2016) Mechanochemical activation and photocatalytic activity of oxide zinc-molybdenum composition. NaUKMA 183:26–30
20. Pat.116067 Ukraine, MPK C01G 39/02, C01G 9/02. Patent for utility model Mechanochemical method of obtaining nanosized B-ZnO4 rods // Sachuk O.V., Zazhigalov, V.O.; The owner is the Institute of Sorption and Endoecology Problems of the National Academy of Sciences of Ukraine - № u 2016 10715; stated 25.10.2016; posted 10.05.2017. Bul №
21. Zazhigalov VA, Sachuk OV, Diyuk OA, Starchevskyy VL, Kolotilov SV, Sawlowicz Z, Shcherbakov SM, Zakutevskyy OI (2018) The ultrasonic treatment as a promising method of nanosized oxide CeO_2-MoO_3 composites preparation, vol 214. Springer, Cham, pp 294–309
22. Burch R (1978) Preparation of high surface area reduced molybdenum oxide catalysts. J Chem Soc Faraday Trans 1(74):2982–2990
23. Ressler T, Jentoft RE, Wienold J, Gunter MM, Timpe O (2000) In situ XAS and XRD studies on the formation of Mo suboxides during reduction of MoO_3. J Phys Chem B 104(6):360–370
24. Lalik E (2011) Kinetic analysis of reduction of MoO_3 to MoO_2. Catal Today 169:85–92
25. Słoczynski J, Bobinski W (1991) Autocatalytic effect in the processes of metal oxide reduction. II. Kinetics of molybdenum oxide reduction. J Solid State Chem 92:436–348
26. Słoczyński J (1995) Kinetics and mechanism of molybdenum (VI) oxide reduction. J Solid State Chem 118:84–92
27. Schulmeyer WV, Ortner HM (2002) Mechanisms of the hydrogen reduction of molybdenum oxides. Int J Refract Met Hard Mater 20:261–269
28. Enneti RK, Wolfe TA (2012) Agglomeration during reduction of MoO_3. Int J Refract Met Hard Mater 31:47–50
29. Dang J, Zhang G-H, Chou K-C (2014) Phase transitions and morphology evolutions during hydrogen reduction of MoO_3 to MoO_2. High Temp. Mater. Proc. 33(4):305–312
30. Margulis MA (1984) Basics of AcoustoChemistry (chemical reactions in sound fields) // M .: Higher. sch.
31. Bang JH, Suslick KS (2010) Applications of ultrasound to the synthesis of nanostructured materials. Adv Mat 22:1039–1059
32. Zazhigalov VA, Haber J, Stoch J, Kharlamov AI, Bogutskaya LV, Bacherikova IV, Kowal A (1997) Influence of the mechanochemical treatment on the reactivity of V-containing oxide systems. Solid State Ionics 101–103:1257–1263

33. Bogutskaya LV, Khalameida SV, Zazhigalov VA, Kharlamov AI, Lyashenko LV, Byl' OG (1999) Effect of mechanochemical treatment on the structure and physicochemical properties of MoO3. Theor Experim Chem 35(4):242–246
34. Keereeta Y, Thongtem T, Thongtem S (2014) Effect of medium solvent ratios on morphologies and optical properties of α-$ZnMoO_4$, β-$ZnMoO_4$ and $ZnMoO_4{\cdot}0.8H_2O$ crystals synthesized by microwave-hydrothermal/solvothermal method. Superlattice Microst 69:253–264
35. Karekar SE, Bhanvase BA, Sonawane SH, Deosarkar MP, Pinjari DV, Pandit AB (2015) Synthesis of zinc molybdate and zinc phosphomolybdate nanopigments by an ultrasound assisted route: advantage over conventional method. Chem Eng Process 87:51–59
36. Pat.117264 Ukraine, MPK C01G 39/02, C01G 9/02. Patent for utility model Sonochemical method for obtaining a nanosized phase of alpha-ZnMoO4 // Sachuk OV, Zazhigalov VO, Starchevskii VL; The owner is the Institute of Sorption and Endoecology Problems of the National Academy of Sciences of Ukraine - № u 2016 12989; stated 20.12.2016; posted 26.06.2017. Bul №12
37. Chiang TH, Yeh HC (2013) The synthesis of α-MoO_3 by ethylene glycol. Materials 6:4609–4625
38. Irmawati R, Shafizah M (2009) The production of high purity hexagonal MoO_3 through the acid washing of as-prepared solids. Int J Basic Appl Sci 9(9):241–244
39. Cavalcante LS, Moraes E, Almeida MAP, Dalmaschio CJ, Batista NC, Varela JA, Longo E, Siu Li M, Andrés J, Beltrán A (2013) A combined theoretical and experimental study of electronic structure and optical properties of β-$ZnMoO_4$ microcrystals. Polyhedron 54:13–25
40. Talam S, Karumuri SR, Gunnam N (2012) Synthesis, characterization and spectroscopic properties of ZnO nanoparticles. ISRN Nanotechnol 2012:1–6
41. Gruber H, Krautz E, Fritzer HP, Gatterer K, Popitsch A (1986) Changes of electrical conductivity, magnetic susceptibility, and IR spectra in the ternary system $Mo_{n\text{-}x}W_xO_{3n\text{-}1}$. Phys Status Solidi 98:297–304
42. Mancheva M, Iordanova R, Kamenova AA, Stoyanova A, Dimitriev Y, Kunev B (2007) Influence of mechanical treatment on morphology of the MoO_3 nanocrystals. Nanosci Nanotechnol 7:74–76

Chapter 12
Hybrid Nanocomposites Synthesized into Stimuli Responsible Polymer Matrices: Synthesis and Application Prospects

Nataliya Kutsevol, Iuliia Harahuts, Oksana Nadtoka, Antonina Naumenko, and Oleg Yeshchenko

12.1 Introduction

Stimuli-responsive polymers can undergo a tuneable phase transition in response to external stimuli [1]. Among them, poly(N-isopropylacrylamide) (PNIPAAm) [2–4] is the most studied polymer. Several reviews related to the employment of PNIPAAm in the field of biomedicine have been published in the last few years. Among biomedical applications, the most explored areas are drug delivery, tissue engineering, biosensors, and bioimaging. PNIPAAm is extensively investigated due to its solubility in water and its Lower critical solution temperature (LCST) close to human body temperature [5]. The reversibility of the hydrophilic/hydrophobic state occurs by varying the temperature below or above a critical value. Below LCST the polymers are soluble [6]. When the temperature is raised above the LCST, these polymers first undergo a phase transition; they then collapse and form aggregates. Linear PNIPAM has an LCST value of approximately 32 °C. PNIPAAm is soluble at room temperature, but its phase separates at physiological temperature (37 °C) and therefore can be used as a linear polymer, a hydrogel, or a copolymer for biomedical application [7, 8], for example, for drug targeting in solid tumors with local hyperthermia and in thermosensitive coatings or micelles for controlled release of the drug. In addition, PNIPAM polymers are used in eye drop preparations and as a new embolic material in neurosurgery and cancer therapy [6, 8]. Any successful applications of such intelligent polymers-nanocarriers are dependent on their physical properties and the possibility to control the hydrophobic-hydrophobic balance of the macromolecule at physiological body temperature.

N. Kutsevol (✉) · I. Harahuts · O. Nadtoka
Faculty of Chemistry, Taras Shevchenko National University of Kyiv, Kyiv, Ukraine

A. Naumenko · O. Yeshchenko
Faculty of Physics, Taras Shevchenko National University of Kyiv, Kyiv, Ukraine

O. Fesenko, L. Yatsenko (eds.), *Nanocomposites, Nanostructures, and Their Applications*, Springer Proceedings in Physics 221,
https://doi.org/10.1007/978-3-030-17759-1_12

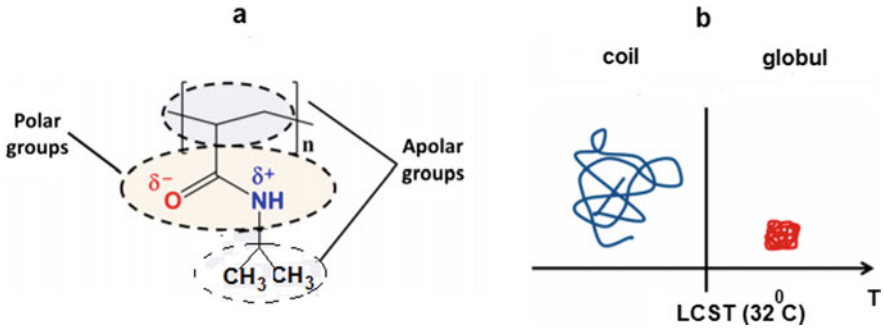

Fig. 12.1 Chemical formula of PNIPAAm (**a**) and representation of phase transition in PNIPAAm solution in the region of LCST (**b**)

The solubility of PNIPAAm in H_2O at temperatures below 32 °C is related to the ability of the macromolecule to form H bonds with H_2O molecules via the amide functional groups. On the other hand, the apolar N-isopropylamide groups induce a considerable ordering of an aqueous solvent. When an aqueous solution of linear PNIPAAm is heated to 32 °C (the cloud point or LCST), phase transition is observed (Fig. 12.1) [9].

Polymer side chains-H_2O interactions have been confirmed by experimental results [9]. This ordering of H_2O causes large negative contributions to both the enthalpy of mixing and the entropy of mixing. At LCST, the entropy contribution to the free energy of mixing will overcome the negative enthalpy of solution, and the phase separation of the polymer solution takes place [9]. Thus, PNIPAAm is a stimulus-responsive polymer that can change the conformation in water from an expanded state (coil) below the LCST (32 °C) to a globular state above the LCST.

A possible tuning of the hydrophobicity of these polymers and the regulation of the region of phase transition and size of hydrophobic domains would be a real achievement in pharmaceutical materials science and could extend their application. It was shown that LCST depends on polymer molecular structure [10]. The temperature-induced phase transition of poly(N-isopropylacrylamide) provides the ideal tool to study the influence of internal molecular structure of branched polymers, namely, their grafting density on the reversible temperature-induced phase separation [10].

We have focused our efforts on the synthesis of starlike dextran-graft-poly(N-isopropylacrylamide) copolymers and nanosystems prepared into these branched polymers. The aim of this research was to study the possibility to vary the macromolecular structure of copolymer by changing the amount of PNIPAAm grafts, to shift the region of the phrase transition by the internal polymer structures of branched PNIPAM, and to synthesize and study the hybrid nanosystems in the region of conformational transition of the polymer matrix for possible anticancer application.

12.2 Materials and Methods

12.2.1 Synthesis of Dextran-Graft-Poly(N-Isopropylacrylamide) Copolymers

Dextrans with different molecular weights were purchased from Fluka with characteristics given by the manufacturer: Mw $= 6 \times 10^4$ (designated as D20 throughout) and Mw $= 7 \times 10^4$ (designated as D70 throughout). Cerium (IV) ammonium nitrate (CAN) from Aldrich was used as an initiator. Dextran samples and the ceric salt were used without further purification. N-Isopropylacrylamide (NIPAM) obtained from Aldrich was twice recrystallized from hexane and dried under vacuum at room temperature for 24 h. A cerium ion-induced redox initiation method was previously applied for the synthesis of the branched copolymers dextran-graft-polyacrylamide [11], and it was efficient for obtaining the samples with various graft efficiencies. The number of grafting sites per dextran backbone was predetermined by a molar ratio of acrylamide to cerium ions, and it was equal to 15 and 30. The amount of monomer NIPAM was kept the same for all syntheses during the grafting process to D20 and D70. The samples were designated as D6-g-PNIPAM15, D70-g-PNIPAM15, D6-g-PNIPAM30, and D70-g-PNIPAM30.

The mechanism of Ce(IV) initiation involves the formation of a chelate complex [12–15], which while decomposing generates free radical sites on the polysaccharide backbone. These active free radicals trigger graft growth in the presence of vinyl monomers. The reaction path for grafting PNIPAAm to dextran is described below.

Dextran (D6 or D70) was dissolved in 100 mL of distilled water. This solution was stirred, while removal of the dissolved oxygen was achieved by bubbling a gentle flux of argon for about 20 min. Then the calculated amount of Ce(IV)/HNO_3 initiator (in 0.125 N HNO_3) was injected to obtain a desirable graft number. The NIPAM monomer was added, and the polymerization proceeded at room temperature under an argon atmosphere for 24 h. The synthesized copolymers were precipitated into a mixture of water-methanol, redissolved in water, and finally freeze-dried.

12.2.2 Au NP Synthesis into Polymer Template

Reduction of Au ions was performed in aqueous solutions of D70-g-PNIPAM15. About 0.05 mL of the 0.1 M HAuCl4 aqueous solution was added to 1 mL of polymer solution ($C = 1$ gL^{-1}) and stirred for 20 min at $T = 25$ °C. And then, 0.1 mL of 0.1 M of $NaBH_4$ solution was injected dropwise under stirring. The obtained Au sols were stored under cold and dark conditions. The concentration of Au NPs was

about 0.086 mg/mL. The nanosystems were prepared in polymer solution below the concentration of crossover (Guiner regime) for D70-g-PNIPAM15.

12.2.3 Size-Exclusion Chromatography

Multidetection size-exclusion chromatography (SEC) using a specific SEC line of the Institut Charles Sadron at Strasbourg was used for determining the molecular weight distribution and average molecular weights of the branched PNIPAAm sample. This SEC line involves a usual HPLC part (Shimadzu) and the Malvern's triple detection TDA 302 (Viscotek) incorporating a refractometer, a viscosimeter, and two angles (7 and 90°) of light-scattering apparatus. The fractionation was carried out through three-column PLgel Mixed B with a precolumn arranged in series. The eluent was N-methyl-2-pyrrolidone (NMP) of HPLC grade with 0.1 M of LiBr. Measurements were performed at $T = 60$ °C at a constant flow rate of 0.5 mL/min. PNIPAAm solution at a concentration of 3.33 g/L was filtered on a 0.45-mm membrane prior to injection. A volume of 100 μL of the solution was injected.

12.2.4 Transmission Electron Microscopy

For the sample preparation, 400-mesh Cu grids with plain carbon film were rendered hydrophilic by a glow discharge treatment (Elmo, Cordouan Technologies, Bordeaux, France). A 5-μL drop was deposited and adsorbed for 1 min, and then the excess solution was removed with a piece of filter paper. The observations of the Au NPs were carried on two transmission electron microscopes (TEMs) (Tecnai G2 and CM12 (FEI, Eindhoven, Netherlands)), and the images were acquired with a CCD Eagle camera (Tecnai G2) or a Megaview SIS camera (CM12).

12.2.5 Dynamic Light Scattering

Dynamic light scattering (DLS) measurements were carried out using Zetasizer Nano ZS90 (Malvern Instruments Ltd., UK). The apparatus contains a 4-mW He-Ne laser with a wavelength 632.8 nm, and the scattered light is detected at an angle of 173° (quasiback scattering). For an accurate transition study, correlograms of 0.1 mg/mL aqueous D-g-PNIPAM or Au/D-g-PNIPAM nanosystems were collected with step 1 °C in the temperature range of 25–33 °C and 0.1 °C within the 33–36 °C range. Each temperature point was held for 5 min before measurements to equilibrate the sample. At least ten correlation curves for each temperature

points were treated by CONTIN algorithm [16–18] that is known to be reliable for complicated systems to get hydrodynamic diameter (DH) distributions.

12.2.6 UV-Visible Spectroscopy

Absorption spectra were acquired in the range of 200–700 nm using a double-channel spectrophotometer (Hitachi M 356, Japan) with photomultiplier detection. Quartz cuvettes were used in all spectral measurements of aqueous solution of nanosystems.

12.2.7 Biological Study of D-PNIPAM/Dox Nanocomposite

Dox (doxorubicin hydrochloride; Sigma-Aldrich, USA) was dissolved in saline with a maximum concentration of 0.15 mg mL^{-1}. Aqueous solution of carboxylated single-walled carbon nanotubes (SWCNTs) (Sigma-Aldrich, USA) in a maximum concentration of 0.15 mg mL^{-1} was prepared as described in the previously published papers [9, 10]. GO (Sigma-Aldrich, USA) was dispersed in ultrapure water to prepare stock solution with a maximum concentration of 0.15 mg mL^{-1}. Then this aqueous solution was sonicated for 2 h (40 kHz) [11]. For obtaining an aqueous solution of dextran-PNIPAAm + Dox, the dextran-PNIPAAm and Dox was mixed in a 1:1 volume ratio (0.075:0.075 mg).

12.2.8 Cell Culture

HeLa cells were cultured in Dulbecco's modified eagle medium (DMEM) and supplemented with 10% fetal calf serum (FCS), 100 U mL^{-1} penicillin, and 100 mg mL^{-1} streptomycin at 37 °C in a humidified atmosphere with 5% CO_2. Twelve hours prior to uptake experiments, the cells were trypsinized and seeded in 24-well plates with $5 \cdot 10^4$ cells per well in 0.5 mL DMEM with FCS for HeLa cells.

12.2.9 MTT Assay

The cell viability was analyzed by MTT assay 24 and 48 h after the incubation of cells with the NPs, and so the final concentration of NPs per well after dilution in medium was as follows: 1.5, 3, and 6 mg mL^{-1}. MTT (3-(4.5-dimethylthiazol-2-yl)-2.5-diphenyl-tetrazolium bromide; Sigma, Taufkirchen, Germany) was dissolved in phosphate-buffered saline (PBS) (5 mg/mL) and then diluted to 1 mg mL^{-1}

in the cell culture medium. The cell culture medium of the incubated cells was replaced by 300 μL of the MTT solution and incubated for 1 h at 37 °C under 5% CO_2 in a humidified atmosphere. Three hundred microliters of dimethyl sulfoxide (DMSO) was added to the cells. After 30 min, a 100-μL aliquot was taken for spectrophotometric analysis with a Multiscan FC instrument (Thermo Fisher Scientific, Vantaa, Finland) at $\lambda = 570$ nm. The absorption of incubated cells was normalized to that of control (untreated) cells, thereby indicating the relative level of cell viability.

12.2.10 Statistics

Statistical analysis was performed by conventional methods of variation statistics. Significance of the differences between the control and experimental measurements was estimated within the framework of the Student's t-test using Origin 8.0 software (OriginLab Corporation, USA). The difference between the compared values was considered to be significant at $p < 0.05$.

12.2.11 The Evaluation of Dark Cytotoxicity

The evaluation of dark cytotoxicity of nanoparticles and nanocomposites was carried out by serial dilutions. Calculation of live/dead cells was determined after their staining with trypan blue and cell viability using MTT test. The basis of the method is the ability to convert 3-[4,5-dimethylthiazole-2-1]-2,5 diphenyl tetrazolium bromide – yellow salt – to crystalline MTT-formazan of purple color using the mitochondrial enzymes of the living cell. To this end, 20 μl of MTT solution (Sigma, USA) (stock solution – 5 mg/mL in phosphate buffer) was added to the wells of a 96-well plate with initial and molding resistance and incubated under the same conditions for 3 h. After centrifugation of the plate with cells (1500 rpm, 5 min), the supernatant was removed. To dissolve the formazan crystals in each well, 100 μL of dimethyl sulfoxide (Serva, Germany) was added. The optical absorption of the solution was measured using a multi-spectrophotometer ("STAT FAX 2100") at a wavelength of 540 nm.

12.2.12 Photodynamic Therapy

For photodynamic therapy (PDT), cell suspensions (0.5 × 106 per mL) in Hanks' balanced salt solution (HBSS) were prepared from a culture of the leukemic cell line in the log phase of growth. After 1.5 h of incubation (37 °C) in HBSS with Chlorin e6 alone (0.1 mkg/mL) or with D-g-PNIPAM/Au NPs/Ce6 nanocomposite

containing the same concentration of photosensitizer (Ce6/Au mass ratio 1:10), the cells were washed twice with a tenfold volume of fresh HBSS and were exposed to the red (658 nm) laser light (power density 1.1 mW/cm^2, dose 1 J/cm^2). After irradiation, the cells were transferred to the growth medium and incubated at 37 °C for 18 h to complete the photodynamic-induced apoptosis process. Cell viability was determined by trypan blue dye exclusion test or by MTT test.

12.3 Results and Discussion

The route of synthesis of graft dextran-PNIPAAm copolymer is shown in Fig. 12.2.

Redox system Ce(IV)/HNO_3 has been used for the synthesis of graft polymer. Ce(IV) salt forms a complex with the alcohol groups of polysaccharides. Complex disproportionation determines the rate of redox reaction and therefore kinetics of formation of free radicals on the polysaccharide. There is no common methodology for the synthesis route. The time between initiator addition to the polysaccharide solution and monomer addition to reaction mixture varies from 1 to 10 min [11, 19]. In numerous papers devoted to the synthesis of graft polymers using Ce(IV) salt as the initiator, the precise chromatography analysis of the products of synthesis is absent, that is why the quality of synthesized graft copolymer is not proved. For optimization of the synthesis process, we studied the kinetics of the Ce(IV) to Ce(III) ion transformation in an aqueous solution of dextran using UV-vis spectroscopy [20]. For the analysis, the absorption value at a wavelength of 299 nm has been used. It was established that the transformation of Ce(IV) to Ce(III) ions

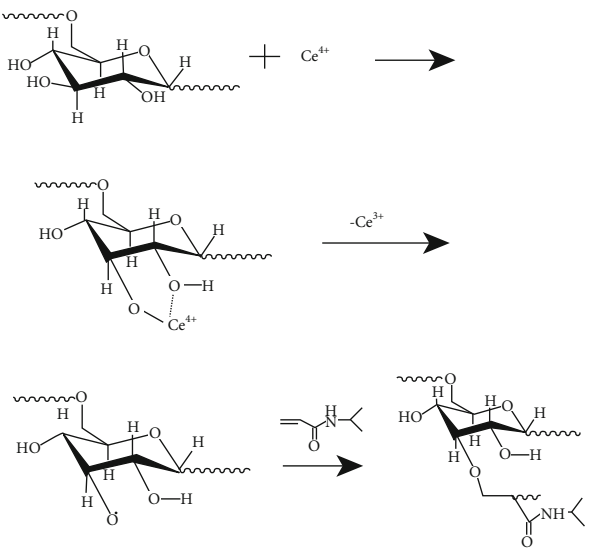

Fig. 12.2 Route of synthesis of graft dextran-PNIPAAm copolymer

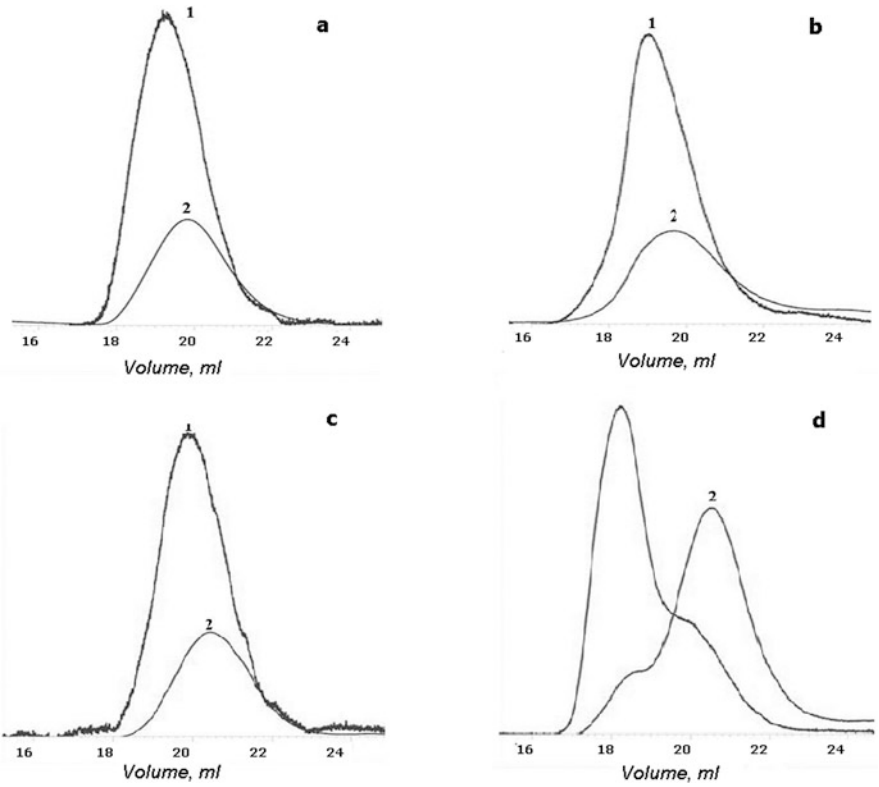

Fig. 12.3 SEC chromatograms for D6-PNIPAAm 15 (**a**), D70-PNIPAAm 15 (**b**), and D70-PNIPAAm 30 (**c**). Detectors: (1) viscometry and (2) refractometry

occurred in two stages. The first stage of the process is a quick process with half life time $\tau 1/2 = 62$ min of the first (or pseudofirst) order for Ce(IV). The second stage is quite a slow process, most likely associated with the reduction of cerium by reacting with free radicals that are formed. Thus it proves the reasonability to add the monomer PNIPAAm to the reaction medium in 20 min (the half-time of the first stage of the oxidation process) after Ce(IV) injection. The chromatograms for both samples synthesized with optimized time for initiator and monomer addition were monomodal (Fig. 12.3a, b). The synthesized copolymers D6-PNIPAAm 15 and D70-PNIPAAm 15 had high molecular weight and low polydispersity (Table 12.1). The next series of copolymers with 30 grafts were synthesized in 10 min between initiator addition to the polysaccharide solution and monomer addition to the reaction mixture. The chromatograms of these samples and their molecular characteristics are represented in Fig. 12.3c, d. It is seen that D6-PNIPAAm 30 samples have relatively low molecular weights, but D70-PNIPAM30 copolymer is polydispersed.

Table 12.1 Molecular parameter of D-PNIPAAm samples

Sample	Mw × 10^{-6}, г/моль	Mn × 10^{-6}, г/моль	Mw/Mn	*n*, % декстр. комп.	τ, min
D6-PNIPAAm 15	0.649	0,453	1.43	0.9	20
D70-PNIPAAm 15	1.03	0.674	1.52	6.8	20
D6-PNIPAAm 30	0.367	0.278	1.32	1.6	10
D70-PNIPAAm 30	1.54	0.419	3.68	4.5	10

The reason of such results can be twofold. First, it was shown [21] that dextran retains the compact coil conformation in the process of copolymerization due to the intermolecular cross-linking caused by Ce(IV) ions. The accessibility of OH groups of dextran macromolecules for Ce(IV) ions is different inside and outside of the polysaccharide macrocoil. Ce(IV) is an initiator of copolymerization and an interrupt agent concurrently. So, the increase of unbounded Ce(IV) twice for the grafting process for samples with 30 grafts in comparison with samples with 15 grafts changes the balance of two opposite radical polymerization processes: growth of the polymer chain and its rupture. Thus, for further characterization of D-g-PNIPAAm behavior, namely, for investigation of the effect of the polymer molecular structure on the peculiarities of polymer behavior in the region of LCST, the copolymers D6-PNIPAAm 15 and D70-PNIPAAm 15 were chosen. The starlike structure of synthesized samples was confirmed [20]. Also, as it was reported for similar systems like dextran-graft-polyacrylamide [13], the distance between grafted chains determines its conformation in starlike copolymers. Depending on graft efficiency, the wormlike or mushroom conformation can be realized (Fig. 12.4). It was shown [20] that the difference in the molecular structure affects the behavior of D-g-PNIPAAm copolymers in the region of LCST (Fig. 12.5). The image of the solution of D-PNIPAAm at 25 and 40 °C is shown in Fig. 12.6. The phase transition is reversible. Figure 12.4 represents the sketch of the swollen and collapsed macromolecule of the starlike D-PNIPAAm copolymer. It is evident that the possible conformational changes of the starlike macromolecule are dependent on the macromolecule internal structure. The close distance between grafts can lead to the steric barrier for PNIPAAm-grafted chains collapse. That is why the changes in size in the region of LCST are more expressed for the D70-PNIPAAm 15 sample with mushroom grafts than for D6-PNIPAAm 15 with wormlike-grafted chains.

For both D70-PNIPAAm 15 and D6-PNIPAAm 15 samples, the decreasing of the hydrodynamic diameter within the temperature interval 32.6–33.4 °C and a sharp aggregation process at 33.7–34.1 °C were observed. Further heating to 36 °C did not cause additional aggregation [20]. The temperature of conformational transition was 2–4 °C higher than the LCST point for a linear PNIPAAm of the similar molecular weight and polydispersity.

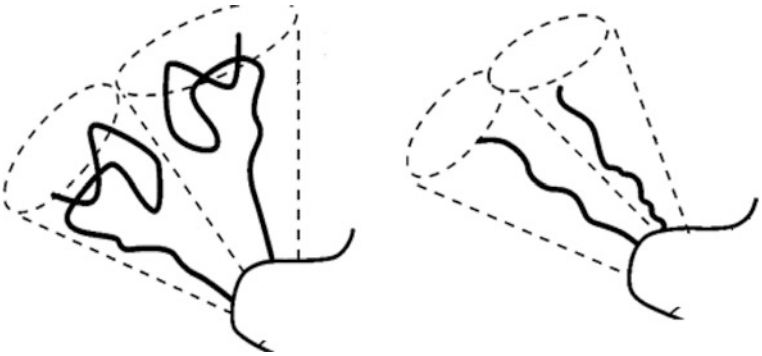

Fig. 12.4 Representation of phase transition in starlike copolymer D-PNIPAAm solution in the region of LCST

12.3.1 Hybrid Nanosystem D70-PNIPAAm 15/Au NPs

The D70-PNIPAAm 15 copolymer as a template has been chosen for in situ preparation of Au NPs. The aim was to analyze the process occurring in the nanosystem within the region of LCTS. The TEM images of polymer/Au NP nanosystem ($T = 25$ °C) are represented in Fig. 12.7.

The main size of Au NPs equals about 7 ± 2 nm (with a standard error of 0.5 nm). The nanoparticles have a spherical shape. Grouping of Au NPs into located assemblies was observed. The sizes of these assemblies are about 20–50 nm that corresponds to the size of an individual molecule of D70-PNIPAAm 15. The behavior of the polymer/Au NP nanosystem was analyzed by using dynamic light scattering in the temperature range of 25–36 °C. The size distribution of the individual D70-PNIPAAm copolymer and polymer/Au NP nanosystems at $T = 25$ °C is shown in Fig. 12.8. A correlation curve analysis has been performed by the CONTIN algorithm for the precise study of the processes occurring in nanosystem within the temperature range of 25–36 °C.

To study the possible influence of Au NPs on the phase transition in D-g-PNIPAAm/Au NPs, the precise analysis of DLS measurements has been made for for D-g-PNIPAAm without Au NPs and for nanosystem D-g-PNIPAAm/Au NPs [13]. The results are presented in Fig. 12.9a, b.

It is seen that at heating in the temperature range from 21 to 32.5 °C, the PNIPAM size decreases slightly from 32 to 26 nm; then in the temperature range of 32.5–33.5 °C, a sharp decrease of the size from 26 to 14 nm occurs. Similar to the D-g-PNIPAAm/Au NP system, it is due to shrinking of the separate macromolecules. However, at temperatures higher than 33.5 °C, the temperature behavior of the size of D-g-PNIPAAm without Au NPs differs drastically from one for D-g-PNIPAAm/Au NPs. Indeed, in the temperature range of 33.5–34.5 °C, the sharp increase of the PNIPAAm size from 14 to 86 nm occurs that reflects the aggregation of PNIPAAm macromolecules. At cooling, the temperature behavior

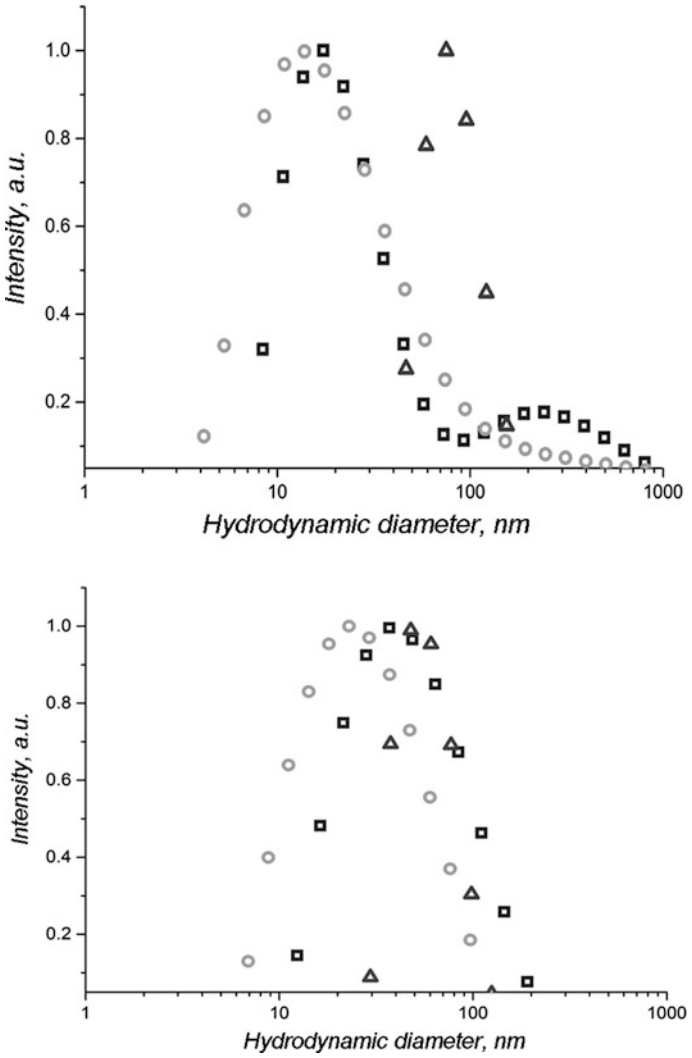

Fig. 12.5 Hydrodynamic diameter distribution for D70-g-PNIPAAm 15 (**a**) and D6-g-PNIPAAm 15 (**b**). Note: 25 °C, squares; 31 °C, circles; and 35 °C, triangles

of the PNIPAAm size is fully reversible, but the temperature of destruction of aggregates (the size decreases) and the temperature of LCST phase transition in the separate macromolecule (the size increases) are lower than the respective temperatures at the heating. So, the usual direct hysteresis is observed for PNIPAAm without Au NPs that is in accordance with reference data [14]. Thus, it proves fully our above assumption of the role of the Au NPs in the change of the sign of the hysteresis at LCST phase transition in D-g-PNIPAAm/Au NP macromolecules. Another conclusion that can be made is that Au NPs counteract the formation of

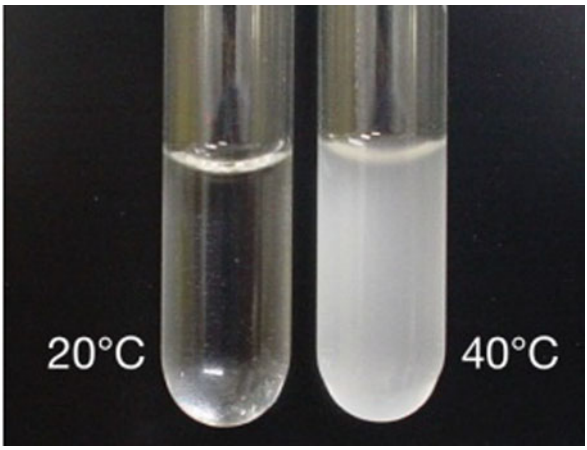

Fig. 12.6 The image of D-PNIPAAm solution below and above LCST

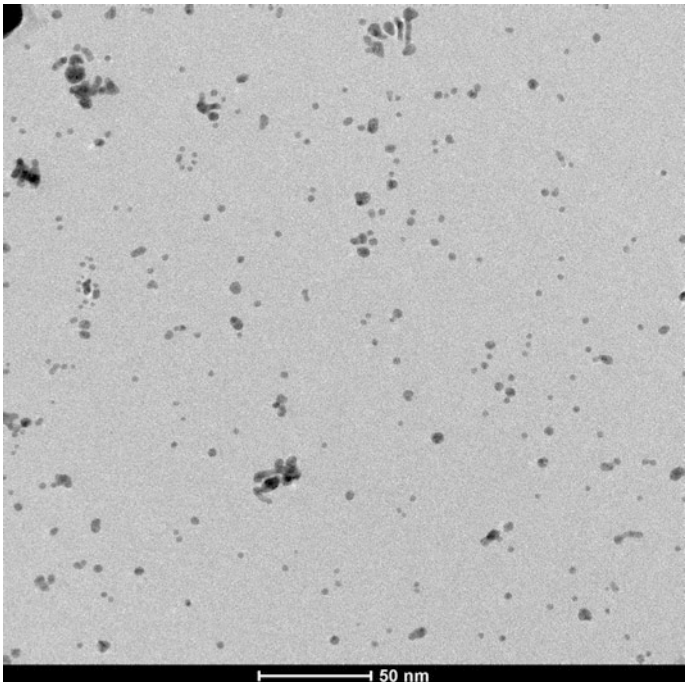

Fig. 12.7 TEM image of the polymer/Au NP nanosystem

aggregates. And lastly, it is important to note that the size of D-g-PNIPAAm/Au NP aggregates at temperatures lower than the LCST point (37 nm) is somewhat larger than the one of the D-g-PNIPAAm aggregates without Au NPs (32 nm)

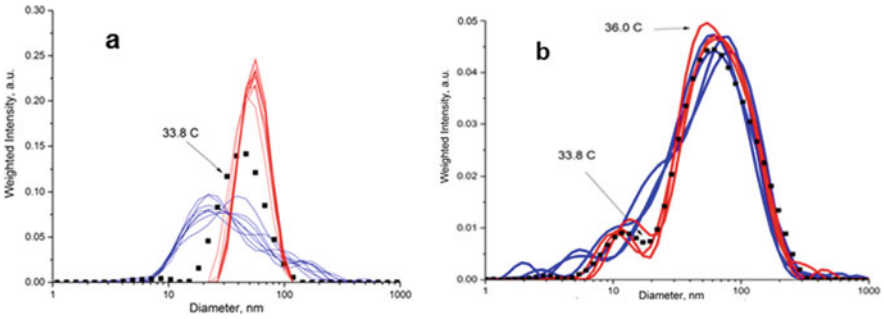

Fig. 12.8 The size distribution in the solution of D70-PNIPAAm (**a**) and polymer/Au NP nanosystems (**b**). Note: $T = 25$ °C (black square), heating from 25 to 37 °C (red curves), and cooling from 37 to 25 °C (blue curves)

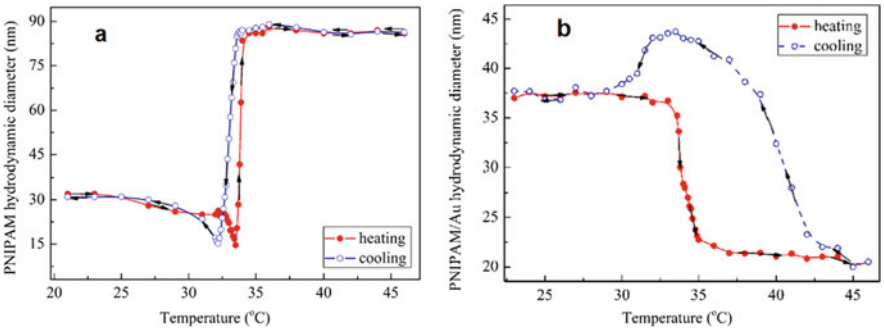

Fig. 12.9 Dependences of the D-g-PNIPAAm hydrodynamic diameter (**a**) and for D-g-PNIPAAm/Au NP hydrodynamic diameter (**a**) on temperature at slow gradual heating and cooling obtained by DLS

(Fig. 12.8a). All these facts confirm our above assumption of the repulsion of the Au NPs in D-g-PNIPAAm/Au NP nanohybrid that differs drastically the character of the temperature-induced phase transformations in the PNIPAM-based system.

12.3.2 Hybrid Nanosystem and Prospects of Their Application for Anticancer Therapy

Since our systems can be used for in vitro and in vivo testing, we compared the behavior of nanocomposites of various compositions in water and in Hanks' balanced salt solution used in cell culture media. UV-vis spectra for individual polymer, dual-system polymer/Au NPs, and triple-system polymer/Au NPs/photosensitizer Chlorin e6 in water (a) and Hanks' solution (b) in the temperature region of 25–40 °C are shown in Figs. 12.10, 12.11, and 12.12, respectively. Dynamic

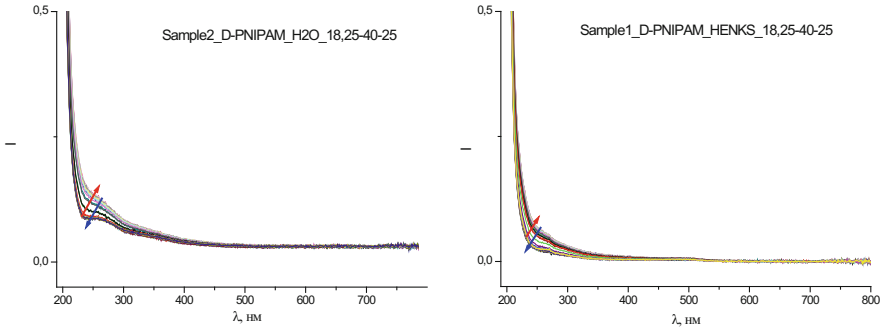

Fig. 12.10 Absorbance spectra for D-g-PNIPAAm in water and Hanks' solution in the temperature range of 25–40 °C within heating-cooling cycles

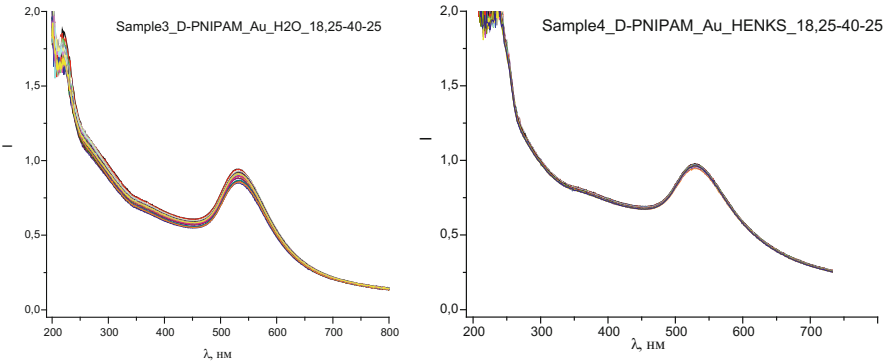

Fig. 12.11 Absorbance spectra for D-g-PNIPAAm/Ag in water and Hanks' solution in the temperature range of 25–40 °C within heating-cooling cycles

light scattering results of solutions of individual polymer and dual nanosystem polymer/Au NPs in water and Hanks' solution as well as a composite consisting of nanocomposite polymer/Au NPs/photosensitizer Chlorin e6 at 25 and 37 °C are represented in Fig. 12.14. Chlorin e6 is a photosensitizer used for photodynamic therapy of malignant cells.

UV-vis spectra of the branched copolymer D70-PNIPAAm 15 in water and in the Hanks' solution, respectively, registered at heating from 18 to 40 °C and then at cooling to 25 °C with a step of 1 °C. Samples were kept for 2 min at each temperature. The intensity of curves increases slowly in the region of absorbance of the C=O group (285 nm) at heating and decreases at the heating process (Fig. 12.10). The character of these changes testifies the presence of conformational changing in macromolecules at heating-cooling cycle. It is evident that these changes are less pronounced for polymers dissolved in Hanks' solution.

Figure 12.11 shows the UV-vis spectra of the Au sols synthesized in situ in the branched copolymer D70-PNIPAAm 15 in water and in the Hanks' solution, respec-

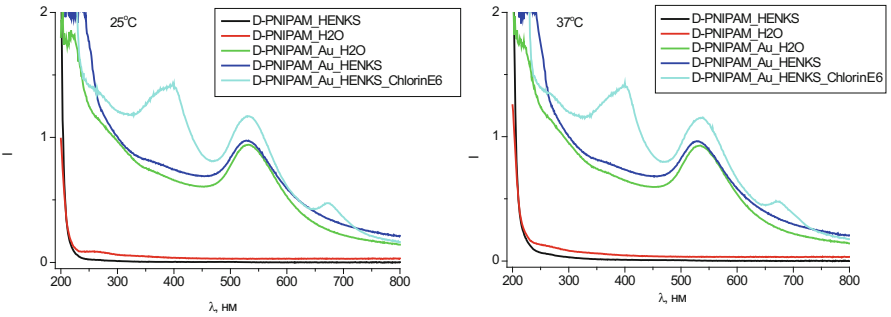

Fig. 12.12 Absorbance spectra for D-g-PNIPAAm, D-g-PNIPAAm/Au, and D-g-PNIPAAm/Au/Chlorin e6 in water and Hanks' solution below (25 °C) and above (37 °C) LCST

tively. The spectra were registered at heating from 18 to 40 °C and subsequently cooling to 25 °C. It is known that the position and shape of the surface plasmon resonance (SPR) depend on the size and shape of the nanoparticles. An intense peak of SPR of Au nanoparticles was registered at 530 nm. The peak position doesn't change at heating and cooling of Au sol. It should be noted that the change in the intensity of this peak with the temperature is much less for Au sols prepared in Hanks' solution than for sols synthesized in the aqueous solution.

Figure 12.12 represents the spectra for nanosystems of hybrid nanosystems polymer/Au NPs/photosensitizer Chlorin e6 registered in the temperature range of 18–40 °C at heating-cooling cycles. The peaks at 530 nm corresponding to Au NPs and peaks at 400 nm and 671 nm corresponding to Chlorin e6 are present at absorbance curves. It was shown that peak positions remain unchanged at heating-cooling. However, the intensity of the peak of Au NP plasmon resonance decreases at heating and subsequent cooling, which may be explained by the formation of some amount of precipitate after measurements. This indicates that after heating, the system cannot be reused, as irreversible changes occur.

The results of dynamic light scattering measured at 25 °C and 37 °C for the studied systems correlate with UV-vis spectroscopy data (Fig. 12.13). The analysis of DLS data for nanosystems prepared in water demonstrates that polymer macromolecules at 25 °C have a size around 40 nm and some asymmetry that reveals in appearance some additional weak expressed peaks (black curve). Au sols contain Au NPs with 10 nm in size and polymer associated with 100 nm in size with incorporated Au NPs inside (red curve). The hybrid multicomponent nanosystem D-g-PNIPAAm/Au/Chlorin e6 (green curve) consists of Au NPs of the size around 10 nm and the aggregates of macromolecules with incorporated Au NPs and Chlorin e6. The addition of Chlorin e6 into polymer/Au NP systems leads to some change in the size distribution of polymer associates. It can be caused by interaction of the photosensitizer with functional groups of polymer and some changes of polymer conformation. Size characteristics of nanosystems at 37 °C differ from the results discussed above. It should be noted that free Au NPs don't

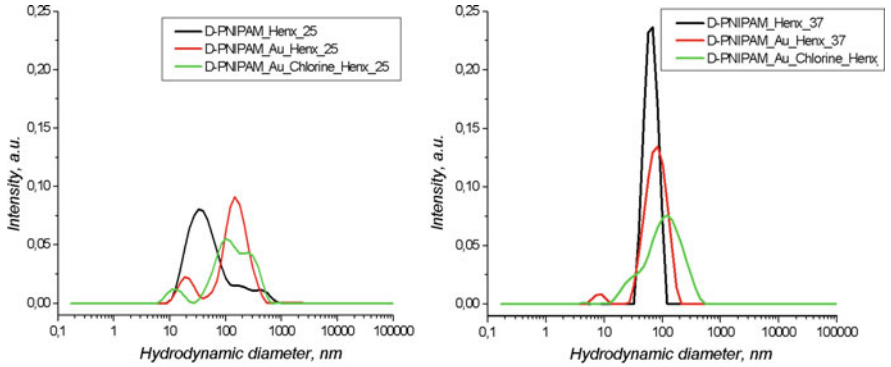

Fig. 12.13 Hydrodynamic diameter distributions for D-g-PNIPAAm (black curve), D-g-PNIPAAm/Au (red curve), and D-g-PNIPAAm/Au/Chlorin e6 (green curve) in water and Hanks' solution below (25 °C) and above (37 °C) LCST

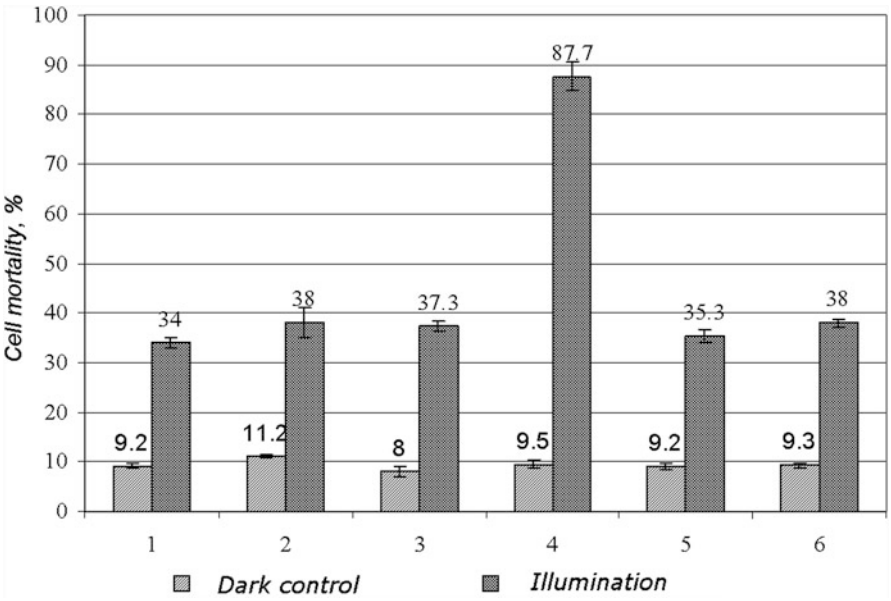

Fig. 12.14 Dark cytotoxicity and photodynamic activity of nanocomposites (Au NP, 1 mkg/mL; Chlorin e6, 0.1 mkg/mL; excitation, 1 J/cm^2 at 658 nm): (1) Chlorin e6, (2) D-PNIPAAm (1:2), (3) D-PNIPAAm (1:4), (4) K1Г4 (1:2), (5) K1Г4 (1:4), and (6) K1Г4 (1:6)

change in size, but drastic changes in polymer size and nanosystem polymer/Au NPs and D-g-PNIPAAm/Au/Chlorin e6 are observed.

Nanocomposite, which contained Au NPs and Chlorin e6 incorporated into D-g-PNIPAM, showed a similar dark toxicity in comparison with individual Chlorin e6 (Fig. 12.14). The photodynamic activity of nanocomposites is only 4% higher than

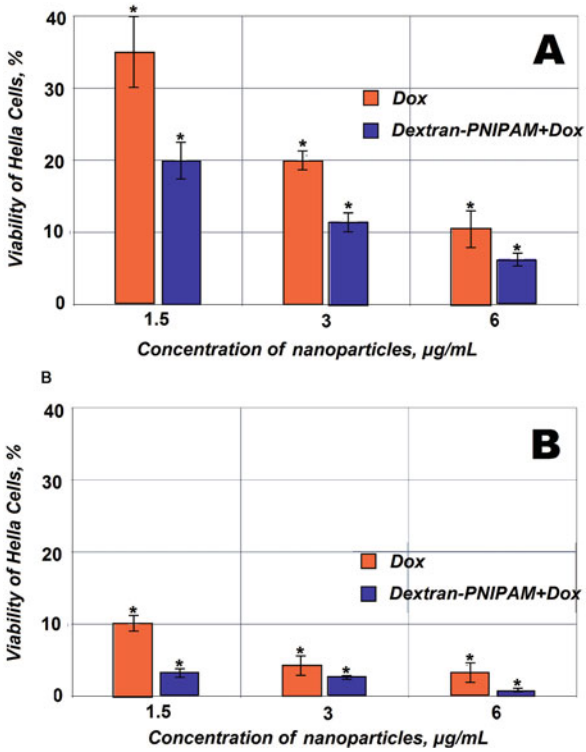

Fig. 12.15 MTT assay on HeLa cells after incubation with studied NPs at different concentrations for 24 h (**a**) and 48 h (**b**). *Significant differences compared to the control (untreated cells) at $p < 0.05$

that for individual Chlorin e6. The increase of $NaBH_4$ concentration during nanoparticle synthesis doesn't influence the photodynamic activity of nanocomposite as for nanosystems synthesized in anionic starlike polymer matrices dextran-g-polyacrylamide (K1Г4) [15].

The next step was to test the efficiency of nanosystems, consisting of D-g-PNIPAAm and doxorubicin [22]. As can be seen from Fig. 12.13a, Dox already kills about 65% of cells for 24 h at the lowest used concentration of 1.5 mg mL^{-1} and D-g-PNIPAAm + Dox at almost 80%. The effectiveness of these therapeutic drugs only increases with increasing concentration (Fig. 12.15a, b). As one can see, the D-g-PNIPAAm + Dox nanofluid shows higher toxicity toward HeLa cells when compared with Dox alone.

Finally, Dox and D-g-PNIPAAm + Dox demonstrated to have even more pronounced treatments and protective effects (about 80–90% cells in both cases), respectively, when incubated with cells for 48 h (Fig. 12.15b). It should be noted that D-g-PNIPAAm aggregates are nontoxic in vitro in the concentration range under study (up to 6 mg mL^{-1}).

It is important to emphasize that the D-g-PNIPAAm copolymer is thermosensitive with a transition temperature from the hydrophilic to the hydrophobic state of the macromolecule in the region of physiological temperatures [20]. Therefore, one

can assume that the anticancer activity of D-g-PNIPAAm + Dox nanofluid sharply increases due to a change in the conformation of the Dg-g-PNIPAAm copolymer, which promotes the release of Dox molecules.

12.4 Conclusions

This study clearly demonstrates that water-soluble nanosystem dextran-g-PNIPAAm) + Dox sharply decreased the viability of HeLa cells at low concentrations (1.5–6 mg mL^{-1}) for 24–48 h. This result indicates the importance of the D-g-PNIPAAm copolymer as a universal platform for drug delivery and, in particular, the huge potential of nanosystem D-g-PNIPAM + Dox as novel anticancer agents for chemotherapy and is less efficient for preparation of nanosystems for photodynamic therapy.

Acknowledgments This research was supported in part by the grant of the Ukrainian State Fund for Fundamental Research, project Ф76/64-2017 "New hybrid nanocomposites for photodynamic chemotherapy of tumor cells."

References

1. Wei M, Gao Y, Lia X, Serpe MJ (2017) Stimuli-responsive polymers and their applications. Polym Chem 8:127–143
2. de Oliveira TE, Mukherji D, Kremer K, Netz PA (2017) Effects of stereochemistry and copolymerization on the LCST of PNIPAm. J Chem Phys 146(3):03490
3. Lima LH, Morales Y, Cabral T (2016) Poly-N-isopropylacrylamide (pNIPAM): a reversible bioadhesive for sclerotomy closure. Int J Retina Vitreous 2:23
4. Fan Y, Boulif N, Picchioni F (2018) Thermo-responsive starch-g-(PAM-co-PNIPAM): controlled synthesis and effect of molecular components on solution rheology. Polymers 10(1):92
5. Lang X, Lenart WR, Sun JEP, Hammouda B, Hore MJA (2017) Interaction and conformation of aqueous poly(N-isopropylacrylamide) (PNIPAM) star polymers below the LCST. Macromolecules 50(5):2145–2154
6. Larsson A, Kuckling D, Schönhoff M (2002) 1H-NMR-investigation of the phase transition of thermo-reversible polymers in solution and at interfaces. In: Fraissard J, Lapina O (eds) Magnetic resonance in colloid and interface science, NATO science series (series II: mathematics, physics and chemistry), vol 76. Springer, Dordrecht
7. Klouda L, Mikos AG (2007) Thermoresponsive hydrogels in biomedical applications. Eur J Pharm Biopharm 68(1):34–45
8. Lanzalaco S, Armelin E (2017) Poly(N-isopropylacrylamide) and copolymers: a review on recent progresses in biomedical applications. Gels 3(4):36
9. Füllbrandt M, Ermilova E, Asadujjaman A, Hölzel R, Bier FF, von Klitzing R, Schönhals A (2014) Dynamics of linear poly(N-isopropylacrylamide) in water around the phase transition investigated by dielectric relaxation spectroscopy. J Phys Chem B 118(13):3750–3759
10. Plunkett KN, Zhu X, Moore JS, Leckband DE (2006) PNIPAM chain collapse depends on the molecular weight and grafting density. Langmuir 22(9):4259–4266
11. Kutsevol NV, Chumachenko VA, Rawiso M, Shkodich VF, Stoyanov OV (2015) Star-like polymers dextran-polyacrylamide: the prospects of application for nanotechnology. J Struct Chem 56(5):1016–1023

12. Kutsevol N, Guenet JM, Melnyk N, Sarazin D, Rochas C (2006) Solution properties of dextran-polyacrylamide graft copolymers. Polymer 47:2061–2068
13. Yeshchenko OA, Naumenko AP, Kutsevol NV, Maskova DO, Harahuts II, Chumachenko VA, Marinin AI (2018) Anomalous inverse hysteresis of phase transition in thermosensitive dextran-graft-PNIPAM copolymer/Au nanoparticles hybrid Nanosystem. J Phys Chem C 122(14):8003–8010
14. Lapworth JW, Hatton PV, Goodchild RL, Rimmer S (2012) Thermally reversible colloidal gels for three-dimensional chondrocyte culture. J R Soc Interface 9:362–375
15. Kutsevol N, Naumenko A, Harahuts Y, Chumachenko V, Shton I, Shishko E, Lukianova N, Chekhun V (2018) New hybrid composites for photodynamic therapy: synthesis, characterization and biological study. Appl Nanosci 36:1–8
16. Provencher S (1982) CONTIN: a general purpose constrained regularization program for inverting noisy linear algebraic and integral equations. Comput Phys Commun 27(3):229–242
17. Scotti A, Liu W, Hyatt JS, Herman ES, Choi HS, Kim JW, Lyon LA, Gasser U, Fernandez-Nieves A (2015) The CONTIN algorithm and its application to determine the size distribution of microgel suspensions. J Chem Phys 142(23):234905
18. Halperin A, Kröger M, Winnik FM (2015) Poly (N-isopropylacrylamide) phase diagrams: fifty years of research. Angew Chem Int Ed 54:5342
19. Kumar D, Pandey J, Raj V, Kumar P (2017) A review on the modification of polysaccharide through graft copolymerization for various potential applications. Open Med Chem J 11:109–126
20. Chumachenko V, Kutsevol N, Harahuts Y, Rawiso M, Marinin A, Bulavin L (2017) Star-like dextran-graft-PNiPAM copolymers. Effect of internal molecular structure on the phase transition. J Mol Liq 235:77–82
21. Kutsevol N, Bezugla T, Bezuglyi M, Rawiso M (2012) Branched dextran-graft-polyacrylamide copolymers as perspective materials for nanotechnology. Macromol Symp 317–318(1):82–90
22. Matvienko T, Sokolova V, Prylutska S, Harahuts Y, Kutsevol N, Kostjukov V, Evstigneev M, Prylutskyy Y, Epple M, Ritter U (2019) In vitro study of the anticancer activity of various doxorubicin-containing dispersions. Bioimpacts 9(1):59–70

Chapter 13
Preparation and Complex Study of Thick Films Based on Nanostructured $Cu_{0.1}Ni_{0.8}Co_{0.2}Mn_{1.9}O_4$ and $Cu_{0.8}Ni_{0.1}Co_{0.2}Mn_{1.9}O_4$ Ceramics

H. Klym, Yu Kostiv, and I. Hadzaman

13.1 Introduction

The problem stabilization of exploitation parameters in functional elements for sensor electronics is of outstanding importance [1, 2]. Often, solid-state media with a highly compact structure are characterized by the ability to resist the influence of various external factors, including higher temperatures, their gradient and time differences, aggressive atmospheric impurities, electromagnetic fields, etc.

For this reason, functional devices prepared using thick-film technology [3–5] are very popular in electronics. Owing to the peculiarities of contact deposition of thick films with subsequent high-temperature sintering of fine-grain substrates with organic binder, it is possible to achieve high density of the final elements with minimal input of post-technological thermal-induced relaxation processes. In particular, in Schmidt et al. [6] it was shown that the $NiMn_2O_4$ thick films obtained have good properties, completeness of the internal structure, high performance of the crystal structure of spinel grains, and defined grain boundaries. Therefore, the electrical characteristics of thick-film elements are not expected to yield to external influences. However, despite the rather stringent regulatory and technical documentation governing the practical use of this type of electronic equipment, this statement was not experimentally verified. Expressed concern becomes particularly important if taking into account that the technological procedure of thermal training is often introduced as a final step to eliminate the spurious drift effects in a number of functional ceramic devices. It is known that spinel ceramic of this composition

H. Klym · Y. Kostiv (✉)
Lviv Polytechnic National University, Lviv, Ukraine

I. Hadzaman
Drohobych State Pedagogical University, Drohobych, Ukraine

O. Fesenko, L. Yatsenko (eds.), *Nanocomposites, Nanostructures, and Their Applications*, Springer Proceedings in Physics 221,
https://doi.org/10.1007/978-3-030-17759-1_13

is widely used as a highly efficient functional medium for temperature-sensitive elements for electronic equipment [7–10]. Thus, the aim of this work is the study of structural, electrical, and thermally induced transformation in the thick-film elements based on mixed transition metal oxymanganites limited by the $NiMn_2O_4$-$CuMn_2O_4$-$MnCo_2O_4$ concentration triangle. Within the specified concentration triangle, a wide range of thermistors (as in bulk and thick-film performance) with different exploitation properties were obtained [11–16]. However, the thermal stability of the thick films of some spinel compounds need to be studied in more detail.

The aim of this work was to prepare and investigate in detail thick films based on temperature-sensitive $Cu_{0.1}Ni_{0.8}Co_{0.2}Mn_{1.9}O_4$ and $Cu_{0.8}Ni_{0.1}Co_{0.2}Mn_{1.9}O_4$ ceramics.

13.2 Sample Preparation

Initial bulk ceramics were prepared via a conventional ceramic processing route using reagent grade copper carbonate hydroxide and nickel (cobalt, manganese) carbonate hydroxide hydrates. The reagents were weighed in the required proportions, wet-milled (in distilled aqueous medium), dried, sieved, and calcinated in air at 700 °C for 4 h. Then, the products were again wet-milled, dried, blended with an organic binder, sieved, and pressed into discs of 11.5 and 25 mm in diameter for disc-type ceramics and thick films respectively [17].

The blanks were sintered in air using two different schedules. Schedule 1 ($Cu_{0.1}Ni_{0.8}Co_{0.2}Mn_{1.9}O_4$ ceramics): heating (+100 °C/h) up to 600 °C, heating (+200 °C/h) up to 1200 °C, isothermal sintering for 1 h at 1200 °C, cooling (−50 °C/h) down to 920 °C, isothermal sintering for 48 h at 920 °C, and rapid cooling at −1000 °C/h down to 100 °C. Schedule 2 (applied for $Cu_{0.8}Ni_{0.1}Co_{0.2}Mn_{1.9}O_4$ ceramics): heating at the rate of +100 °C/h up to 600 °C, heating (+200 °C/h) up to 920 °C, isothermal sintering for 4 h at 920 °C, slow cooling (−50 °C/h) down to 850 °C, and rapid cooling at the rate of −700 °C/h down to 100 °C. After fulfilling schedules 1 and 2, ceramic samples were ejected from the furnaces and finally cooled down to room temperature. The chemical composition of the ceramics under investigation and the main points in their sintering schedules are presented in Table 13.1.

Table 13.1 Chemical composition, temperature and duration of isothermal sintering for the initial ceramics

Chemical composition	Sintering temperature/duration
$Cu_{0.1}Ni_{0.8}Co_{0.2}Mn_{1.9}O_4$	1200 °C/1 h + 920 °C/48 h
$Cu_{0.8}Ni_{0.1}Co_{0.2}Mn_{1.9}O_4$	920 °C/4 h

Table 13.2 Composition of temperature-sensitive pastes

Constituents	Content, % mass
Basic ceramics	75.76
Bi_2O_3	2.30
Glass	3.00
Organic vehicle	18.94

To prepare disc-type ceramic temperature-sensitive elements, the flat surfaces of ceramics were coated with silver paste and the Pt wires were attached. The ohmic contacts were achieved during the metallization process at 850 °C [18].

Experimental thick films were obtained using traditional screen-printing technology from ceramics of similar compositions [19–23]. Temperature-sensitive pastes were prepared by mixing powders of basic ceramics (sintered bulk ceramic discs were preliminary destroyed, wet-milled in isopropyl alcohol medium and dried) with glass powder, Bi_2O_3 (inorganic binder), and an organic vehicle (containing organic binder and organic solvent). Thus, the two pastes based on the $Cu_{0.1}Ni_{0.8}Co_{0.2}Mn_{1.9}O_4$ and $Cu_{0.8}Ni_{0.1}Co_{0.2}Mn_{1.9}O_4$ ceramics under investigation (with constant amounts of constituents) were obtained (Table 13.2).

The prepared pastes were printed onto alumina substrates (Rubalit 708S) with prefired silver electrodes using a manual screen-printing device (DFS 0.1) equipped with a steel screen. To increase the thickness of the thick film, a layer printing procedure was used. Thick films were fired at 850 °C (the temperature–time firing schedule was similar to that applied for the metallization of dick-type temperature-sensitive ceramics). The thickness of the single-layered thick films obtained is 35 μm for $Cu_{0.1}Ni_{0.8}Co_{0.2}Mn_{1.9}O_4$ and 34 μm for $Cu_{0.8}Ni_{0.1}Co_{0.2}Mn_{1.9}O_4$ compositions.

13.3 Results and Discussion

13.3.1 Structural Properties of Ceramics and Thick Films

The phase composition and crystal structure of the phases for bulk $Cu_{0.1}Ni_{0.8}Co_{0.2}Mn_{1.9}O_4$ and $Cu_{0.8}Ni_{0.1}Co_{0.2}Mn_{1.9}O_4$ ceramics and fired thick films were determined by the X-ray diffraction (XRD) powder method. XRD patterns were recorded from ceramic powders and from the surfaces of thick films at room temperature using a powder HZG-4a diffractometer with Fe$K\alpha$ radiation. The measurements were carried out in a step regime (0.05° 2θ, $15.00 \leq 2\theta \leq 140.00$). The profile analysis was performed using the method of approximation of X-ray reflections by the pseudo-Voigt function. The lattice parameters and crystal structure of the phases were refined using the Rietveld method with the program FULLPROF.2 k [24] from WinPLOTR software [25].

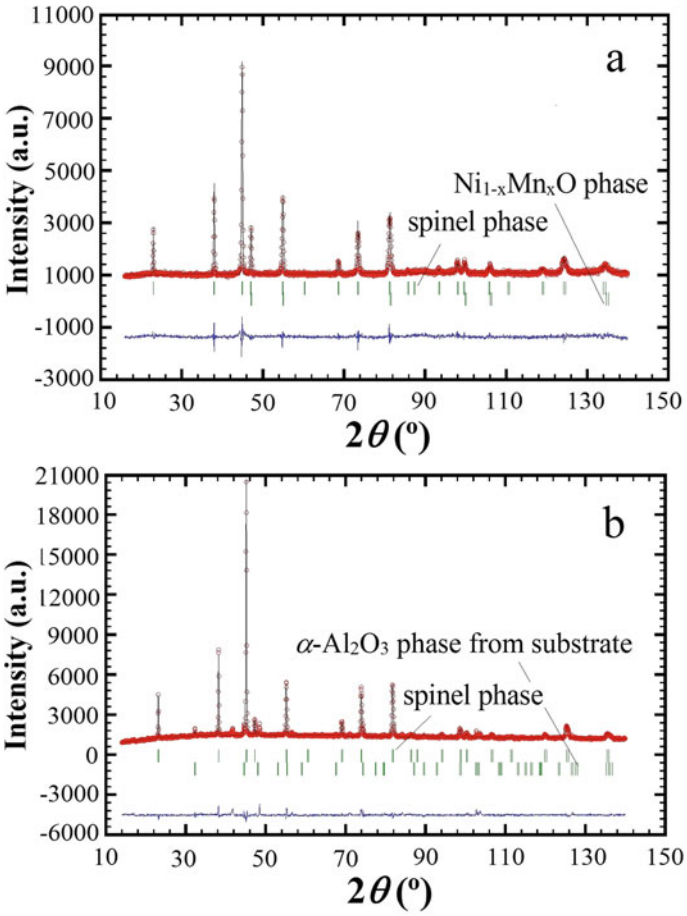

Fig. 13.1 X-ray diffraction results for Ni-enriched $Cu_{0.1}Ni_{0.8}Co_{0.2}Mn_{1.9}O_4$ (**a**) bulk ceramics and (**b**) thick films [28]

The $Cu_{0.1}Ni_{0.8}Co_{0.2}Mn_{1.9}O_4$ ceramics contain two crystalline phases: cubic spinel with $a = 0.84146(4)$ nm, $V = 0.59579(4)$ nm^3 ($R_{Bragg} = 0.0565$, $R_F = 0.0716$, $\chi^2 = 3.17$, $R_p = 0.0259$, $R_{wp} = 0.0333$ for 24 unique reflections and 19 variables) and traces of NiO-based secondary phase with NaCl-type structure (space group $Fm\bar{3}m$; Fig. 13.1,a). Previously, the formation of such NiO-based secondary phase traces was observed in these $Cu_{0.1}Ni_{0.8}Co_{0.2}Mn_{1.9}O_4$ ceramics sintered for 1 h at 1200 °C owing to decomposition reactions [26, 27]. The reverse reactions in ceramics are expected to proceed during the subsequent long-term sintering for 48 h at 920 °C and a single-phase cubic spinel will be obtained. But, as can be seen, the traces of the secondary phase are present in these ceramics after fulfillment of the sintering schedule. Thus, the duration of this additional thermal treatment was insufficient, i.e., the sintering schedule for $Cu_{0.1}Ni_{0.8}Co_{0.2}Mn_{1.9}O_4$

ceramics was not perfect for single-phase material synthesis. However, XRD studies for thick films of these ceramics show the spinel phase with $a = 0.83695(3)$ nm, a pattern of alumina substrate, and do not reveal any traces of the NiO phase (Fig. 13.1,b). It means that the reverse reactions came to an end during the thermal treatment of film firing.

In respect of microstructural investigations using scanning electron microscopy (LEO 982 microscope with the Oxford ISIS system), the thick-film elements under study show quite homogeneous distribution of grains of the main spinel phase in the sample. These grains (gray color, Fig. 13.2a and b for $Cu_{0.1}Ni_{0.8}Co_{0.2}Mn_{1.9}O_4$ and $Cu_{0.8}Ni_{0.1}Co_{0.2}Mn_{1.9}O_4$ thick films respectively) are "enveloped" by a glass phase (white color). In other words, in this case, the glass acts as a binding phase that fills nanovoids formed between the spinel grains during sintering. Thick films of these two compositions were characterized by porosity [17], which could be reduced by

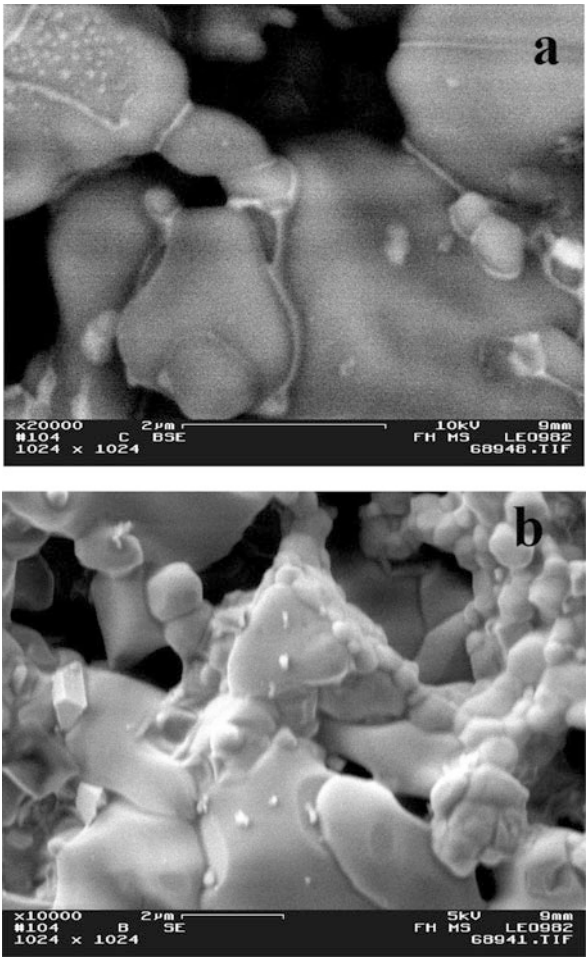

Fig. 13.2 Scanning electron microscopy image for (**a**) $Cu_{0.1}Ni_{0.8}Co_{0.2}Mn_{1.9}O_4$ and (**b**) $Cu_{0.8}Ni_{0.1}Co_{0.2}Mn_{1.9}O_4$ thick films [28]

more uniform distribution of the size of the spinel phase and a small increase in the amount of glasses in the thermistor paste.

13.3.2 Electrical Properties of Thick Films

The electrical resistances of thick films were measured from −30 to +170 °C with precise digital multimeters using temperature chambers MINI SABZERO, model MC-71and HPS 222. The electrical resistivity was calculated from their resistances measured at $T = 25 \pm 0.1$ °C. The main electrical parameters were calculated without taking into account the edge effects according to the formula: $\rho_v = \rho_s \cdot h$ ($\rho_s = R_{25} \cdot w/L$), where ρ_v and ρ_s are volume and sheet resistivity respectively. The geometry characteristics were measured using a Dektak device [27].

The constant $B_{25/85}$ (K) values for both ceramics and thick films were calculated according to the equation: $B_{25/85} = 2.3026 \cdot \log(R_1/R_2) \cdot T_1 \cdot T_2/(T_2 - T_1)$, where R_1 and R_2 were correspondent resistances at $T_1 = 25$ and $T_2 = 85 \pm 0.1$ °C respectively. The values of the temperature resistance coefficient (TRC) α (%/K) at 25 ± 0.1 °C for the samples under investigation were found from the relationship: $-B_{25/85}/T^2$. The current–voltage (I–V) characteristics were measured at $T = 25 \pm 0.1$ °C using a precise digital multimeter.

The main electrical parameters of the fabricated ceramics and thick films based on these ceramics are summarized in Table 13.3.

The resistivities of thick films based on ceramics are approximately 1 order of magnitude larger than those of ceramics. The corresponding value for thick films based on $Cu_{0.8}Ni_{0.1}Co_{0.2}Mn_{1.9}O_4$ ceramics is ~ 2. This result may be explained in terms of the greater microstructure homogeneity of the thick films of $Cu_{0.1}Ni_{0.8}Co_{0.2}Mn_{1.9}O_4$ ceramics in comparison with those of $Cu_{0.8}Ni_{0.1}Co_{0.2}Mn_{1.9}O_4$ ceramics. The more uniform the distribution the constituent phases cause, the better reproducibility of the electrical parameters for thick films based on $Cu_{0.1}Ni_{0.8}Co_{0.2}Mn_{1.9}O_4$ ceramics.

All the thick-film samples studied show the exponential dependences of resistances to temperature (Fig. 13.3). Depending on the chemical composition of ceramics, the values of constant $B_{25/85}$ for thick films range from 2980 to 3690 K

Table 13.3 Electrical parameters of ceramics and thick films based on $Cu_{0.1}Ni_{0.8}Co_{0.2}Mn_{1.9}O_4$ (1) and $Cu_{0.8}Ni_{0.1}Co_{0.2}Mn_{1.9}O_4$ (2) ceramics

	Ceramics		Thick films					
Basic ceramics	ρ_v, Ω·m	$B_{25/85}$, K	Quantity of layers	h, μm	R_{25}, kΩ	ρ_s, kΩ/□	ρ_v, Ω·m	$B_{25/85}$, K
1	2.49	3260	1	35	478	824	28.8	3540
			2	71	268	496	35.2	3560
2	0.03	1680	1	34	24.5	44	1.5	2980
			2	73	34.0	63	4.6	3230

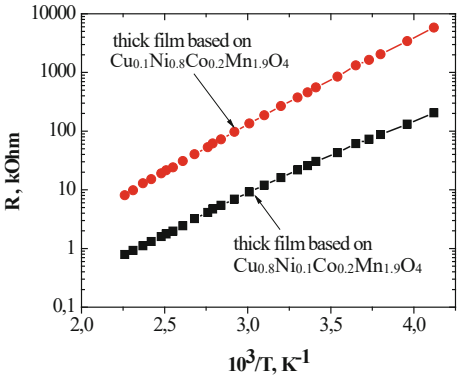

Fig. 13.3 Electrical resistance versus inverse temperature for thick films based on $Cu_{0.1}Ni_{0.8}Co_{0.2}Mn_{1.9}O_4$ and $Cu_{0.8}Ni_{0.1}Co_{0.2}Mn_{1.9}O_4$ ceramics

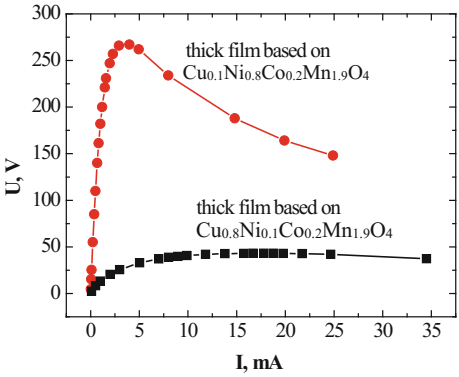

Fig. 13.4 Current voltage characteristics for thick films based on $Cu_{0.1}Ni_{0.8}Co_{0.2}Mn_{1.9}O_4$ and $Cu_{0.8}Ni_{0.1}Co_{0.2}Mn_{1.9}O_4$ ceramics

(corresponding values of TRC at 25 °C are $3.4 \div -4.2\%$/K). Therefore, thick films based on $Cu_{0.1}Ni_{0.8}Co_{0.2}Mn_{1.9}O_4$ ceramics possess a higher temperature sensitivity: the values of TRC $\leq -4.0\%$/K, which are within industrial requirements for these elements [29].

The typical I–V characteristics of double-printed thick-film negative temperature coefficient (NTC) thermistors are presented in Fig. 13.4.

13.3.3 Ageing Process in Thick Films

The ageing tests were performed under conditions of long-term isothermal treatment of samples at 170 °C for study of the thermal stability in the thick films obtained [30, 31]. The duration of the ageing test was 356 h, measurements of electrical resistance R were performed at 25 °C after successive stages of thermal treatment of samples for 64, 104, 144, 198, 251, 304, and 356 h. As a controlled parameter, the relative change (drift) of electrical resistance $\Delta R/R_o$ (R_o is the initial value of

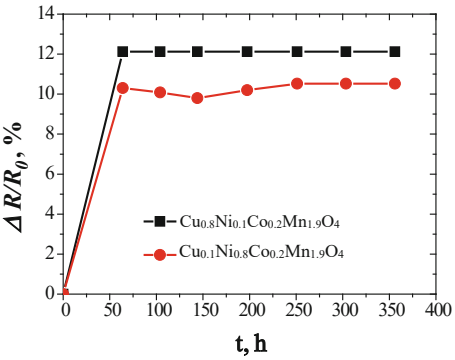

Fig. 13.5 Ageing kinetic characteristics (170 °C) for thick films based on $Cu_{0.8}Ni_{0.1}Co_{0.2}Mn_{1.9}O_4$ and $Cu_{0.1}Ni_{0.8}Co_{0.2}Mn_{1.9}O_4$ ceramics [28]

electrical resistance, ΔR is the absolute change of electrical resistance caused by the degradation test) [11] was selected.

Ageing characteristics for the thick films studied are shown in Fig. 13.5. The results obtained testify that a sharp "disastrous" increase in electrical resistance of thick films or the so-called thermal "shock" effect is shown in the first cycle of thermal exhibition with a duration of 64 h. The value of relative change in electrical resistance, $\Delta R/R_o$, is assumed to be 12% for $Cu_{0.8}Ni_{0.1}Co_{0.2}Mn_{1.9}O_4$ thick films and 10% for $Cu_{0.1}Ni_{0.8}Co_{0.2}Mn_{1.9}O_4$ samples (Fig. 13.5). Electrical resistance is stabilized during the next stages of ageing transformations; there are only minor fluctuations in resistance caused by the apparent accuracy of the measurement.

Similar ageing kinetic characteristics are observed earlier in the investigation of monolithic (bulk) ceramics [32]. In both cases, there is a fairly sharp increase and a gradual saturation of the kinetic characteristics of relative change in electrical resistance, $\Delta R/R_o$, from which the similarity of their nature can be concluded.

It is logical to assume that the ageing processes in monolithic ceramics are longer owing to significant defects in their structure (including porosity) [11]. Typical time constant values are increased by hundreds of hours, causing the curve $\Delta R/R_o = f(t)$ to smooth out to saturation only after 300–500 hours of exposure of samples at high temperature. This process shows a typical stretched exponential dependence on time t according to the known DeBast–Gillard or Williams–Watts relaxation function [33]. In other words, the dispersion of relaxation parameters for thermos-ageing in bulk samples of monolithic oxymanganospinel ceramics determines non-exponential kinetics for the relative drift of electrical resistance.

In contrast to monolithic ceramics, thick films based on these ceramics are distinguished by a relative uniformity of structure; porosity deposits in these materials are substantially offset by the embedding of powdered HT-521-4 glass and Bi_2O_3 oxide. All this leads to a significant reduction in the duration of the observed ageing transformation, i.e., an increase in the typical time constant values. As a result, the process of thermo-induced drift of electrical resistance for thick films assumes saturation after a few tens of hours of ageing tests leading to the observed thermal "shock" effect. Obviously, it is advisable to carry out more transient tests

with a typical duration for individual stages of several hours to establish similar kinetics of ageing processes.

13.4 Conclusions

Thick films based on $Cu_{0.1}Ni_{0.1}Co_{1.6}Mn_{1.2}O_4$ and $Cu_{0.1}Ni_{0.8}Co_{0.2}Mn_{1.9}O_4$ spinel nanostructured ceramics show high density, microstructure homogeneity, good reproducibility of the electrical parameters, high sensitivities, and are suitable for practical uses as accurate temperature sensors. The electrical parameters of thick films can be significantly stabilized using previous isothermal ageing at sufficiently low temperatures (170 °C). This method of heat treatment can be successfully used to stabilize the functional properties of thermo-sensitive elements for electronics in addition to biomedical applications (clinical thermometers, incubators for babies, internal temperature sensors, blood–oxygen equipment, etc.) [34–36].

Acknowledgments H. Klym and Yu. Kostiv thank the Ministry of Education and Science of Ukraine for support. H. Klym thanks Prof. O. Shpotyuk for discussion.

References

1. Guillemet-Fritsch S, Chanel C, Sarrias J, Bayonne S, Rousset A, Alcobe X, Sarriòn MM (2000) Structure, thermal stability and electrical properties of zinc manganites. Solid State Ionics 128(1–4):233–242. https://doi.org/10.1016/S0167-2738(99)00340-9
2. Hosseini M (2000) The effect of cation composition on the electrical properties and aging of Mn-Co-Ni thermistors. Ceram Int 26(3):245–249. https://doi.org/10.1016/S0272-8842(99)00049-8
3. De Torres HB, Rensch C, Fischer M, Schober A, Hoffmann M, Müller J (2010) Thick film flow sensor for biological microsystems. Sensors Actuators A Phys 160(1–2):109–115. https://doi.org/10.1016/j.sna.2010.04.010
4. Gebhardt S, Seffner L, Schlenkrich F, Schönecker A (2007) PZT thick films for sensor and actuator applications. J Eur Ceram Soc 27(13–15):4177–4180. https://doi.org/10.1016/j.jeurceramsoc.2007.02.122
5. Huang J, Hao Y, Lin H, Zhang D, Song J, Zhou D (2003) Preparation and characteristic of the thermistor materials in the thick-film integrated temperature–humidity sensor. Mater Sci Eng B 99(1–3):523–526. https://doi.org/10.1016/S0921-5107(02)00547-0
6. Schmidt R, Basu A, Brinkman AW (2004) Production of NTCR thermistor devices based on NiMn2O4+ δ. J Eur Ceram Soc 24(6):1233–1236. https://doi.org/10.1016/S0955-2219(03)00415-1
7. Jagtap S, Rane S, Mulik U, Amalnerkar D (2007) Thick film NTC thermistor for wide range of temperature sensing. Microelectron Int 24(2):7–13. https://doi.org/10.1108/13565360710745539
8. Feteira A (2009) Negative temperature coefficient resistance (NTCR) ceramic thermistors: an industrial perspective. J Am Ceram Soc 92(5):967–983. https://doi.org/10.1111/j.1551-2916.2009.02990.x

9. Martínez-Cisneros CS, Ibáñez-García N, Valdés F, Alonso J (2007) Miniaturized total analysis systems: integration of electronics and fluidics using low-temperature co-fired ceramics. Anal Chem 79(21):8376–8380. https://doi.org/10.1021/ac0713398
10. Ai L, Jiang J (2010) Influence of annealing temperature on the formation, microstructure and magnetic properties of spinel nanocrystalline cobalt ferrites. Curr Appl Phys 10(1):284–288. https://doi.org/10.1016/j.cap.2009.06.007
11. Shpotyuk O, Balitska V, Brunner M, Hadzaman I, Klym H (2015) Thermally-induced electronic relaxation in structurally-modified $Cu_{0.1}Ni_{0.8}Co_{0.2}Mn_{1.9}O_4$ spinel ceramics. Phys B Condens Matter 459:116–121. https://doi.org/10.1016/j.physb.2014.11.023
12. Klym H, Ingram A, Shpotyuk O, Filipecki J (2010) PALS as characterization tool in application to humidity-sensitive electroceramics. 27th international conference on microelectronics proceedings (MIEL) 239–242. https://doi.org/10.1109/MIEL.2010.5490492
13. Klym H, Hadzaman I, Shpotyuk O (2015) Influence of sintering temperature on pore structure and electrical properties of technologically modified MgO-Al_2O_3 ceramics. Mater Sci 21(1):92–95. https://doi.org/10.5755/j01.ms.21.1.5189
14. Klym H, Ingram A, Shpotyuk O, Hadzaman I, Hotra O, Kostiv Y (2016) Nanostructural free-volume effects in humidity-sensitive MgO-Al_2O_3 ceramics for sensor applications. J Mater Eng Perform 25(3):866–873. https://doi.org/10.1007/s11665-016-1931-9
15. Klym H, Ingram A, Shpotyuk O, Hadzaman I, Solntsev V (2016) Water-vapor sorption processes in nanoporous MgO-Al_2O_3 ceramics: the PAL spectroscopy study. Nanoscale Res Lett 11(1):1. https://doi.org/10.1186/s11671-016-1352-6
16. Klym H, Ingram A, Shpotyuk O, Hadzaman I, Chalyy D (2018) Water-sorption effects near grain boundaries in modified MgO-Al_2O_3 ceramics tested with positron-positronium trapping algorithm. Acta Phys Pol A 133(4):864–868. https://doi.org/10.12693/APhysPolA.133.864
17. Klym H, Ingram A, Shpotyuk O, Hadzaman I, Solntsev V, Hotra O, Popov AI (2016) Positron annihilation characterization of free volume in micro-and macro-modified $Cu_{0.4}Co_{0.4}Ni_{0.4}Mn_{1.8}O_4$ ceramics. Low Temp Phys 42(7):601–605. https://doi.org/10.1063/1.4959021
18. Brunets I, Mrooz O, Shpotyuk O, Altenburg H (2004) Thick-film NTC thermistors based on spinel-type semiconducting electroceramics. 24th International Conference on Microelectronics, (MIEL) 2:503–506. https://doi.org/10.1109/ICMEL.2004.1314873
19. Klym H, Hadzaman I, Ingram A, Shpotyuk O (2013) Multilayer thick-film structures based on spinel ceramics. Can J Phys 92(7/8):822–826. https://doi.org/10.1139/cjp-2013-0597
20. Klym H, Hadzaman I, Shpotyuk O, Brunner M (2014) Integrated thick-film nanostructures based on spinel ceramics. Nanoscale Res Lett 9(1):149. https://doi.org/10.1186/1556-276X-9-149
21. Klym H, Hadzaman I, Shpotyuk O, Fu Q, Luo W, Deng J (2013) Integrated thick-film pi-p+ structures based on spinel ceramics. Solid State Phenom 200:156–161. https://doi.org/10.4028/www.scientific.net/SSP.200.156
22. Vakiv M, Hadzaman I, Klym H, Shpotyuk O, Brunner M (2011) Multifunctional thick-film structures based on spinel ceramics for environment sensors. J Phys Conf Ser 289(1):012011. https://doi.org/10.1088/1742-6596/289/1/012011
23. Hadzaman I, Klym H, Shpotuyk O, Brunner M (2010) Temperature sensitive spinel-type ceramics in thick-film multilayer performance for environment sensors. Acta Phys Pol A 117(1):234–237. http://przyrbwn.icm.edu.pl/APP/PDF/117/a117z148.pdf
24. Rodriguez-Carvajal J (2001) Recent developments of the program FULLPROF, commission on powder diffraction (IUCr). Newsletter 26:12–19
25. Roisnel T, Rodriguez-Carvajal J (2000) WinPLOTR: a windows tool for powder diffraction patterns analysis, materials, science forum. Proc. of the Seventh European Powder Diffraction Conference, Barcelona
26. Mrooz O, Hadzaman I, Vakiv M, Shpotyuk O, Plewa J, Altenburg H, Uphoff H (2002) Aging of copper-nickel-cobalt manganite NTC thermistors. 23rd International Conference on Microelectronics (MIEL) 1:375–378. https://doi.org/10.1109/MIEL.2002.1003215

27. Bodak O, Akselrud L, Demchenko P, Kotur B, Mrooz O, Hadzaman I, Pekhnyo V (2002) Microstructure, crystal structure and electrical properties of $Cu_{0.1}Ni_{0.8}Co_{0.2}Mn_{1.9}O_4$ ceramics obtained at different sintering conditions. J Alloys Compd 347(1–2):14–23. https://doi.org/10.1016/S0925-8388(02)00675-8
28. Klym H (2017) Structural, electrical properties and degradation processes in the Cu-and Ni-enriched thick-film elements for sensor electronics. 37th International Conference on Electronics and Nanotechnology (ELNANO):178–181. https://doi.org/10.1109/ELNANO.2017.7939743
29. Nenov T, Nenova Z (2002) Multifunctional temperature sensor. 23rd International Conference on Microelectronics (MIEL) 1:257–260. https://doi.org/10.1109/MIEL.2002.1003188
30. Klym H, Balitska V, Shpotyuk O, Hadzaman I (2014) Degradation transformation in spinel-type functional thick-film ceramic materials. Microelectron Reliab 54(12):2843–2848. https://doi.org/10.1016/j.microrel.2014.07.137
31. Shpotyuk O, Brunner M, Hadzaman I, Balitska V, Klym H (2016) Analytical description of degradation-relaxation transformations in nanoinhomogeneous spinel ceramics. Nanoscale Res Lett 11(1):499. https://doi.org/10.1186/s11671-016-1722-0
32. Shpotyuk O, Kovalskiy A, Mrooz O, Shpotyuk L, Pechnyo V, Volkov S (2001) Technological modification of spinel-based $Cu_xNi_{1-x-y}Co_{2y}Mn_{2-y}O_4$ ceramics. J Eur Ceram Soc 21(10–11):2067–2070. https://doi.org/10.1016/S0955-2219(01)00173-X
33. De Bast J, Gilard P (1963) Variation of the viscosity of glass and relaxation of stresses during stabilization. Phys Chem Glasses 4:117–128
34. Klym H, Katerynchuk I (2012) High-reliable temperature systems for sensor electronics. International Conference on Modern Problems of Radio Engineering Telecommunications and Computer Science (TCSET):490. https://ieeexplore.ieee.org/abstract/document/6192728
35. Hadzaman I, Klym H, Shpotyuk O (2014) Nanostructured oxyspinel multilayers for novel high-efficient conversion and control. Int J Nanotechnol 11(9–10-11):843–853. https://doi.org/10.1504/IJNT.2014.063793
36. Klym H, Berezko O, Vasylchyshyn I, Kostiv Y (2018) Intelligent cyber-physical computer system and database for microclimate monitoring based on nanostructured sensors. Acta Technica CSAV 63(3):447–458

Chapter 14
Nanoscale Investigation of Porous Structure in Adsorption-Desorption Cycles in the MgO-Al_2O_3 Ceramics

H. Klym, A. Ingram, R. Szatanik, and I. Hadzaman

14.1 Introduction

It is known that among a large number of porous materials used for humidity sensors [1–6], spinel ceramics is one of the best. Functional ceramics, in particular MgO-Al_2O_3 ceramics, are thermally and chemically more stable compared with other types of porous materials with a short reaction time to change humidity [7–9]. In addition, the materials of active elements of humidity sensors based on ceramics do not require additional processes after technological optimization.

As noted in [10–15], the functionality of ceramic materials is determined by the microstructure of their grains, intergranular boundaries, and pores of different sizes and shapes. These elements, in general, depend on the characteristics of sintering ceramics and significantly affect its nanostructure [16–19]. In addition, the operational electrical properties of humidity-sensitive elements depend on the sorption processes, the surface area, and the sufficient amount of nanopore in the material [20–22]. Therefore, it is important to study the processes of nanostructured materials with developed porosity and optimal pore size distribution [19, 23, 24]. It is the void inclusion in ceramic materials that significantly affects their exploitation properties [19, 25].

H. Klym (✉)
Lviv Polytechnic National University, Lviv, Ukraine
e-mail: halyna.i.klym@lpnu.ua

A. Ingram · R. Szatanik
Opole University of Technology, Opole, Poland

I. Hadzaman
Drohobych State Pedagogical University, Drohobych, Ukraine

O. Fesenko, L. Yatsenko (eds.), *Nanocomposites, Nanostructures, and Their Applications*, Springer Proceedings in Physics 221,
https://doi.org/10.1007/978-3-030-17759-1_14

Traditionally, microstructural features of materials are studied using X-ray diffraction, electron microscopy, porosimetric equipment, etc. [26–28]. However, methods for Hg and N_2 porosimetry are limited in use, since it provides information about open nanoscale pores with radius of >5 nm and >2 nm, respectively. It is known that physical processes in ceramics depend not only on the amount and nature of large open pores but also on nanoporous and free-volume vacancies, vacancy clusters, defects, etc. [29]. Therefore, in order to obtain more information about these structural inhomogeneities and their influence on the properties of ceramics MgO-Al_2O_3, it is also helpful to use additional structural research methods that allow studying pores and volumetric inclusion at the nanoscale level. In this case, positron annihilation lifetime (PAL) method is one of the most powerful experimental methods for studying internal structural voids in solids [30–32].

Previously, in studying the structural features of the MgO-Al_2O_3 ceramic by the PAL method, it was shown that two processes can take place in this material: the positron trapping in defects (two components) and ortho-positronium (*o-Ps*) decaying (one component) obtained in the expansion of three components [20–23, 33]. Within the framework of this approach, the short-term component of the PAL spectrum with the lifetime τ_1 reflects the microstructural features of the spinel, the mean component with lifetime τ_2—defects near the intergranular boundaries. The third component with lifetime τ_3 is related to the "pick-off" annihilation of *o-Ps* in intergranular nanoporous filled with adsorbed water [20–22, 33, 34]. Using the lifetime of the third component, it was possible to calculate the radii of nanopores according to the Tao-Eldrup model [35–37]. However, for such a material as humidity-sensitive ceramics MgO-Al_2O_3, there are nanopores of different sizes and different natures [17, 23, 24, 38], the study of which by PAL method requires its modification and optimization.

The aim of this work is nanoscale investigation of pores in adsorption-desorption cycles in the MgO-Al_2O_3 ceramics sintered at 1400 °C for 2 hours using the modified PAL method at four-component spectrum decomposition procedure.

14.2 Experimental Details

The PAL study was performed using the ORTEC spectrometer (full width at half the maximum was 0.27 ns, a separation of 230 ps) at a temperature of 22 °C and an initial relative humidity of 35% [39–41]. Two identical test specimens were placed on both sides of the positron source (^{22}Na isotope, activity ~ 50 kBq) from an aqueous solution of ^{22}NaCl wrapped in a special Kapton® foil with a thickness of 12 μm.

The scheme of the experimental setup for obtaining lifetime spectra is depicted in Fig. 14.1. The signal of an initial 1.27 MeV γ-quantum recorded by the γ-scintillator is converted into an analog electrical pulse in a photomultiplier connected to this scintillator. The signal emitted from the anode of this photomultiplier and gets

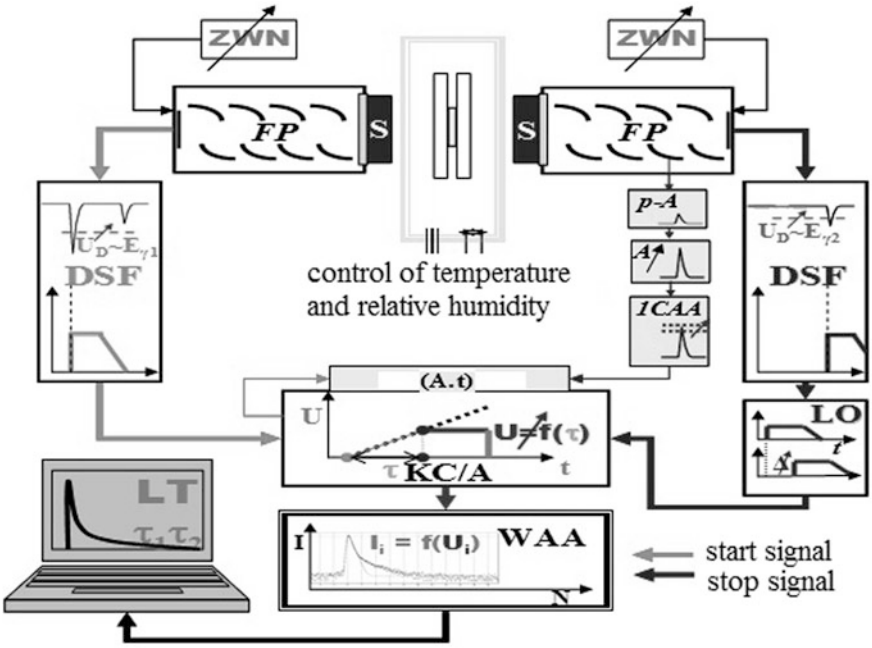

Fig. 14.1 Measuring PAL system based on ORTEC spectrometer [42]

through a constant discriminator serves as the initial signal for the time pulse converter [42].

The second scintillator registers one of two γ-quanta with an energy of 0.511 MeV. The corresponding signal from the photomultiplier anode is compared in a time pulse converter with a signal from the dynode of this photomultiplier, previously processed by the amplifier of the signal, an amplifier, and a one-channel analyzer. When changing the electrical parameters of the delay line, the initial zero-time position of the measured spectrum is selected.

The amplitude of the output signal obtained from the converter is proportional to the difference between the occurrence of the initial and final γ-quanta or the residence time of the positron. Analog-digital signal is recorded in the memory of the multichannel analyzer; the data is fed to a personal computer. Thus, a complete spectrum of the lifetime of a positron is obtained (the dependence of the number of channels or the number of counts from the positron lifetimes).

For statistical surveys with a high number of measurements, investigation was made using the PAL-modified hardware complexity with a modernized digital analog converter KC/A and a multichannel (8000 channels) WAA amplitude analyzer. This is possible to simultaneously register two annihilation spectra: up to 50 ns with a resolution of 6.15 ps and up to 500 ns with a resolution of 61.5 ps [42, 43]. The modified circuit for measuring the PAL spectra is shown in Fig. 14.2.

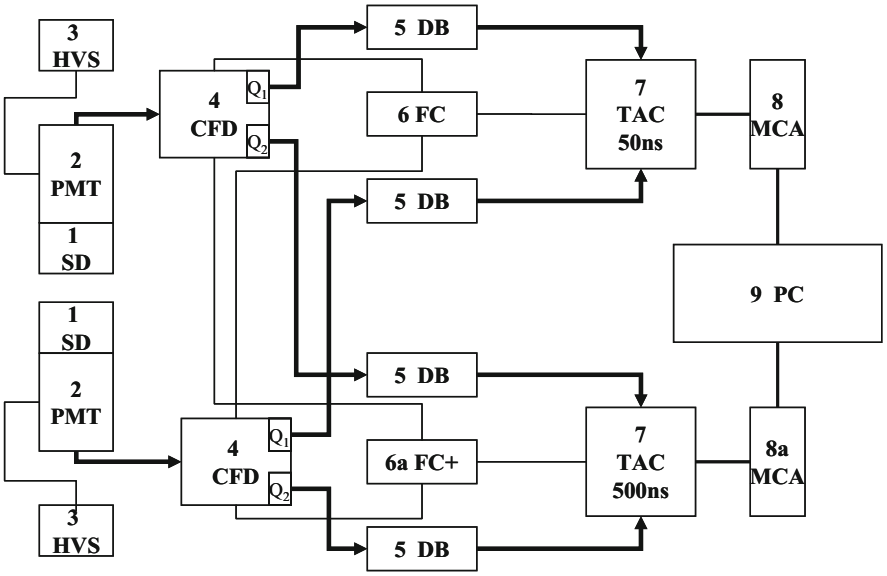

Fig. 14.2 Modified PAL system using ORTEC [43]

Such studies make it possible to obtain information in the expansion of the spectrum into three and four components for a material with advanced nanoporosity (humidity-sensitive $MgO\text{-}Al_2O_3$ ceramics). For the pairs of samples, three measurements of the PAL spectrum were used, which differed in the total number of simple annihilation events [24]. Each spectrum was repeatedly processed due to minor changes in the number of final channels, the background of annihilation, and the time of change in the spectrum. The best results were selected on the basis of the fit, defined as the lowest mean deviation between the experimental points and the theoretical curve [42]:

$$\mathrm{FIT} = \frac{\sum_{k=1}^{N}\left(\frac{T_k - E_k}{\sqrt{E_k}}\right)^2}{N-m} \approx \frac{1}{N}\sum_{k=1}^{N}\left(\frac{T_k - E_k}{\sqrt{E_k}}\right)^2, \tag{14.1}$$

where N is the number of channels (or number of experimental points), E_k experimentally measured number of counts in the kth channel, T_k theoretical number of counts in kth channel, $\sqrt{E_k}$ mean square deviation of the number of counts in the kth channel, m number of fitting parameters.

Thus, in the final result several groups with different numbers of experimental points N were formed in the middle of the chosen procedure of mathematical fitting. Only results with FIT values close to 1 (from 0.95 to 1.1–1.2) were considered to be absolutely relevant. In the next step, these values and the specific characteristics of the PAL were monitored, depending on the annihilation background and the time of

change in the spectrum. It should be noted that the correction for the source and the spectrometer solution function remained constant for the entire spectrum [23, 24, 44].

By working out the PAL spectra by the LT program [45–48], it is possible to obtain the values of the fitting parameters (lifetimes and intensities). Positron trapping parameters in ceramic MgO-Al_2O_3, such as bulk lifetime τ_b, average lifetime τ_{av}, and the rate of positron trapping in defects κ_d, were calculated in accordance with the two-state positron trapping modes [49–51]. The difference $(\tau_2 - \tau_b)$ was evaluated as the size of bulk defects, which occupy positrons.

14.3 Results and Discussion

Since MgO-Al_2O_3 ceramics are humidity-sensitive materials, the main structural component is open nanoscale pores. Using the modified PAL method and performing additional adsorption-desorption procedures [20–22, 42], the processes in nanopores of this material can be studied. So, PAL experiments were carried out in the MgO-Al_2O_3 ceramics sintered at 1400 °C using high-statistical measurements.

Initial measurements were performed in ceramics dried in a vacuum at 120 °C for 4 hours. To study the interconnection of porous structure of ceramics, the same specimens were immersed in water (placed in the distiller, relative humidity was 100%) for 8 hours (1 day) at a temperature of 22 °C. Measurement of the PAL spectra was repeated 7 days after this procedure. At the last stage, samples of ceramics were again dried in vacuum at 120 °C for 4 hours, and measurements by the PAL method were repeated to determine the reversibility of the physical sorption of water molecules [24, 33, 44].

For the maximum estimation of free volume in ceramic samples and calculation of the nanopore size, the PAL spectra were decomposed by the LT program into four components with lifetimes τ_1, τ_2, τ_3, and τ_4, as well as intensities I_1, I_2, I_3, and I_4 [24, 44]. The third and fourth components of the spectrum reflect the annihilation of *o-Ps* through the "pick-off" process, including water-immersed nanopores. The PAL spectrum treatment using four-component treatment due to the application of modified measurement method, which allows to expand the research area, is depicted in Fig. 14.3.

The *o-Ps* lifetime ($\tau_{o\text{-}Ps}$) in ceramic materials (the lifetime of the third and fourth components of PAL spectrum) can be related with average radius of nanopores (R) and calculated by the semiempirical Tao-Eldrup model [36, 37]:

$$\tau_{o-Ps} = \left[2\left(1 - \frac{R}{R+\Delta R} + \frac{1}{2\pi}\sin\left(\frac{2\pi R}{R+\Delta R}\right)\right) + 0.007\right]^{-1}, \qquad (14.2)$$

where ΔR is an empirically determined parameter (in the classical case $\Delta R \approx 0.1656$ nm) which describes the effective thickness of electronic layer responsible for "pick-off" annihilation of *o-Ps* in voids.

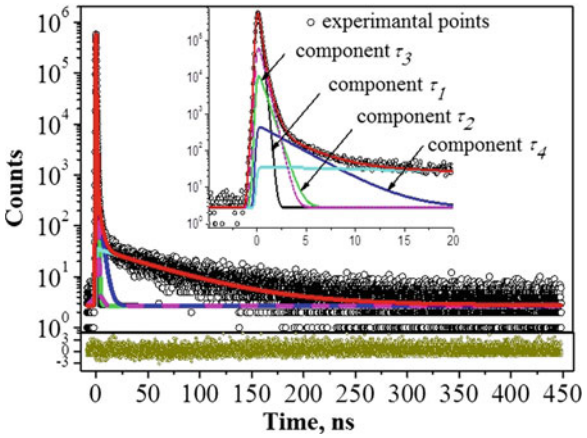

Fig. 14.3 PAL spectra for the MgO-Al_2O_3 ceramics decomposed into four components [42]

Table 14.1 PAL parameters and size of free volumes in the MgO-Al_2O_3 ceramics sintered at 1400 °C in adsorption-desorption cycles: initial ceramics (1), after immersion (2), final dried (3)

	Fitting parameters							
Prehistory	τ_1, ns	I_1, a.u.	τ_2, ns	I_2, a.u.	τ_3, ns	I_3, a.u.	τ_4, ns	I_4, a.u.
1	0.152	0.88	0.388	0.11	2.504	0.007	62.32	0.008
2	0.160	0.77	0.409	0.20	2.562	0.022	57.35	0.006
3	0.154	0.89	0.402	0.10	2.539	0.007	61.85	0.008
Prehistory	Positron trapping modes							
	$\tau_{av.}$, ns		τ_b, ns		κ_d, ns^{-1}		$\tau_2 - \tau_b$, ns	
1	0.178		0.16		0.44		0.23	
2	0.211		0.18		0.78		0.23	
3	0.179		0.16		0.40		0.24	

In addition to the radii of nanopores (R_3 and R_4) calculated from the Tao-Eldrup model, the contribution of the corresponding nanopores by semiempirical relation is determined as [42]:

$$f_v = C \cdot V_f \cdot I_{o-Ps}, \tag{14.3}$$

where $V_f = 4/3 \cdot \pi \cdot R_{o-Ps}$ is free volume calculated using the lifetime of the *o-Ps*-related components in spherical approximation, $I_{o\text{-}Ps}$ is the intensity of the *o-Ps*-related components, and C is an empirical parameter equal to 0.0018.

As can be seen from Table 14.1, after water immersion of the MgO-Al_2O_3 ceramics, the lifetime of the second component τ_2 and the intensity of I_2 increase, which shows the intensification of positron trapping in defects near intergranular boundaries [20–22]. After drying, the intensity values are virtually returned to their initial values, while the lifetime exceeds the initial value. Thus, adsorption processes of water in the MgO-Al_2O_3 ceramics are accompanied by fragmentation of voids and desorption—their agglomeration. The change in the positron capture parameters

correlates with changes in the parameters of the first and second components of PAL spectra.

At water immersion of ceramics, the lifetime of the fourth component τ_4 is accompanied by a decrease in the intensity I_4, while a decrease of lifetime τ_3 leads to an increase in the intensity I_3. In the first case, the decrease of the lifetime τ_4 and the intensity I_4 is due to the arrangement of the layer of water molecules along the walls of the nanopores, which is accompanied by a decrease in the size of the free volume, where the *o-Ps* atoms are captured. In the second case, the *o-Ps* annihilation mechanism is more complicated. The decay of *o-Ps* atoms can occur both in dry nanopores and in the bubbles of water by the "pick-off" process. The last process leads to an increase in the intensity I_3. The contribution of the nanopore with size R_4 is much higher than the pore with radius R_3 (Fig. 14.4). Consequently, the modified multichannel positron annihilation model in the MgO-Al_2O_3 ceramics [44] besides the positron trapping channel contains a decay channel of *o-Ps* atoms, which reflects two different annihilation processes in two types of nanopores: "pick-off" annihilation *o-Ps* in water adsorbed by small nanopores due to "bubble" mechanism and in a free volume of larger nanopores filled by water [52].

Thus, PAL method gives information about nanoscale pores in addition to Hg-porosimetry data [23] (Fig. 14.5).

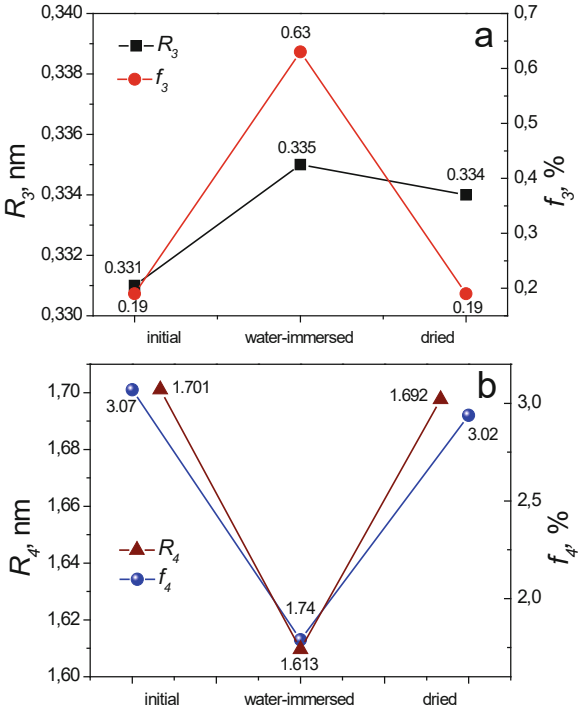

Fig. 14.4 Dependences of the radii of nanopores R_3 and R_4 (**a**) and fraction f_3 and f_4 (**b**) on the conditions of watering and drying

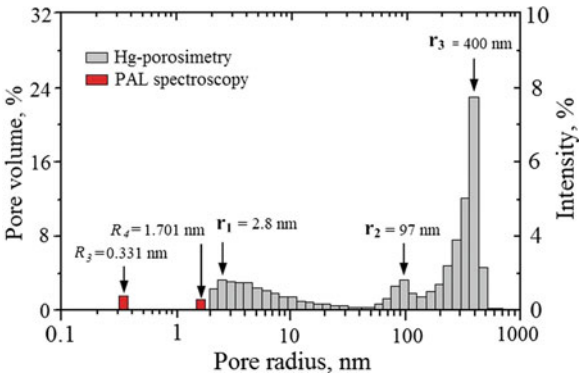

Fig. 14.5 Pore size distributions of MgO-Al_2O_3 ceramics sintered at 1400 °C: Hg-porosimetry [23] and PAL data (for initial ceramics)

In addition, water also affects the parameters of positron trapping in defects near intergranular boundaries (the second component of the PAL spectrum). Changes in the parameters of the second and third components under the influence of water are the same. With regard to the use of the fourth component, two different approaches can be applied. Within the framework of the first one, it is possible to estimate the influence of physically and chemically adsorbed water [22] on the modification of intergranular boundaries in ceramics during immersion. In accordance with the second approach, one can study the patterns of nanostructured MgO-Al_2O_3 ceramics under influence of absorbed water by all nanoporous of ceramics. The second and third components of the PAL spectra are interconnected; for ceramics positronium positrons (the second component) can replace traps (the third component). The fourth component reflects completely different processes in larger nanopores during their immersion. Therefore, in the first approach, we can assume that this component does not affect the positron trapping in defects near intergranular boundaries.

14.4 Conclusions

It is shown that using PAL method for the investigation of nanoscale pores in the MgO-Al_2O_3 ceramic, it is possible to obtain information on size of nanopores of ceramics (according to Tao-Eldrup model) and to study the processes occurring in these ceramics. The spectrum schedule for the four components also allowed modifying the multichannel positron trapping model, which combines two channels: positron trapping channel and decay of the *o-Ps* atoms. The third component describes "pick-off" process of *o-Ps* annihilation in small nanopores and in water, and the fourth component is related to annihilation of *o-Ps* in the volume of larger nanopores not filled by water.

Acknowledgments H. Klym thanks Ministry of Education and Science of Ukraine for support. The authors thank Prof. O. Shpotyuk for discussion.

References

1. Kulwicki BM (1991) Humidity sensors. J Am Ceram Soc 74(4):697–708. https://doi.org/10.1111/j.1151-2916.1991.tb06911.x
2. Chen Z, Lu C (2005) Humidity sensors: a review of materials and mechanisms. Sens Lett 3(4):274–295. https://doi.org/10.1166/sl.2005.045
3. Bearzotti A, Bertolo JM, Innocenzi P, Falcaro P, Traversa E (2004) Humidity sensors based on mesoporous silica thin films synthesised by block copolymers. J Eur Ceram Soc 24(6):1969–1972. https://doi.org/10.1016/S0955-2219(03)00521-1
4. Hadzaman I, Klym H, Shpotuyk O, Brunner M (2010) Temperature sensitive spinel-type ceramics in thick-film multilayer performance for environment sensors. Acta Physica Polonica-Series A 117(1):234–237. http://przyrbwn.icm.edu.pl/APP/PDF/117/a117z148.pdf
5. Rittersma ZM, Splinter A, Bödecker A, Benecke W (2000) A novel surface-micromachined capacitive porous silicon humidity sensor. Sens Actuators B Chem 68(1–3):210–217. https://doi.org/10.1016/S0925-4005(00)00431-7
6. Farahani H, Wagiran R, Hamidon MN (2014) Humidity sensors principle, mechanism, and fabrication technologies: a comprehensive review. Sensors 14(5):7881–7939. https://doi.org/10.3390/s140507881
7. Gusmano G, Montesperelli G, Traversa E (1993) Microstructure and electrical properties of $MgAl_2O_4$ thin film for humidity sensors. J Am Ceram Soc 76:743–750. https://doi.org/10.1111/j.1151-2916.1993.tb03669.x
8. Traversa E (1995) Ceramic sensors for humidity detection: the state-of-the-art and future developments. Sensors Actuators 23:135–156. https://doi.org/10.1016/0925-4005(94)01268-M
9. Gusmano G, Montesperelli G, Nunziante P, Traversa E (1993) Study of the conduction mechanism of $MgAl_2O_4$ at different environmental humidities. Electrochim Acta 38(17):2617–2621. https://doi.org/10.1016/0013-4686(93)80160-2
10. Gleiter H (2000) Nanostructured materials: basic concepts and microstructure. Acta Mater 48(1):1–29. https://doi.org/10.1016/S1359-6454(99)00285-2
11. Li Y, Fu ZY, Su BL (2012) Hierarchically structured porous materials for energy conversion and storage. Adv Funct Mater 22(22):4634–4667. https://doi.org/10.1002/adfm.201200591
12. Dillon SJ, Harmer MP (2007) Multiple grain boundary transitions in ceramics: a case study of alumina. Acta Mater 55(15):5247–5254. https://doi.org/10.1016/j.actamat.2007.04.051
13. Weaver PM, Cain MG, Stewart M, Anson A, Franks J, Lipscomb IP, McBride JP, Zheng D, Swingler J (2012) The effects of porosity, electrode and barrier materials on the conductivity of piezoelectric ceramics in high humidity and dc electric field smart materials and structures. Smart Mater Struct 21(4):045012. https://doi.org/10.1088/0964-1726/21/4/045012
14. Armatas GS, Salmas CE, Louloudi MG, Androutsopoulos P, Pomonis PJ (2003) Relationships among pore size, connectivity, dimensionality of capillary condensation, and pore structure tortuosity of functionalized mesoporous silica. Langmuir 19:3128–3136. https://doi.org/10.1021/la020261h
15. Kashi MA, Ramazani A, Abbasian H, Khayyatian A (2012) Capacitive humidity sensors based on large diameter porous alumina prepared by high current anodization. Sensors Actuators A 174:69–74. https://doi.org/10.1016/j.sna.2011.11.033
16. Vakiv M, Hadzaman I, Klym H, Shpotyuk O, Brunner M (2011) Multifunctional thick-film structures based on spinel ceramics for environment sensors. J Phys Conf Ser 289(1):012011. https://doi.org/10.1088/1742-6596/289/1/012011
17. Klym H, Hadzaman I, Shpotyuk O, Ingram A (2018) Grain porous structure and exploitation properties of humidity-sensitive magnesium aluminate spinel-type ceramics. Springer Proc Phys 214:499–519. https://doi.org/10.1007/978-3-319-92567-7_32

18. Wang W, Fu Z, Wang H, Yuan R (2002) Influence of hot pressing sintering temperature and time on microstructure and mechanical properties of TiB2 ceramics. J Eur Ceram Soc 22(7):1045–1049. https://doi.org/10.1016/S0955-2219(01)00424-1
19. Klym H, Hadzaman I, Shpotyuk O (2015) Influence of sintering temperature on pore structure and electrical properties of technologically modified MgO-Al_2O_3 ceramics. Mater Sci 21(1):92–95. https://doi.org/10.5755/j01.ms.21.1.5189
20. Filipecki J, Ingram A, Klym H, Shpotyuk O, Vakiv M (2007) Water-sensitive positron-trapping modes in nanoporous magnesium aluminate ceramics. J Phys Conf Ser 79(1):012015. https://doi.org/10.1088/1742-6596/79/1/012015
21. Klym H, Ingram A, Shpotyuk O, Hadzaman I, Solntsev V (2016) Water-vapor sorption processes in nanoporous MgO-Al_2O_3 ceramics: the PAL spectroscopy study. Nanoscale Res Lett 11(1):1. https://doi.org/10.1186/s11671-016-1352-6
22. Klym H, Ingram A, Shpotyuk O, Hadzaman I, Chalyy D (2018) Water-sorption effects near grain boundaries in modified MgO-Al_2O_3 ceramics tested with positron-positronium trapping algorithm. Acta Phys Pol A 133(4):864–868. https://doi.org/10.12693/APhysPolA.133.864
23. Klym H, Ingram A, Hadzaman I, Shpotyuk O (2014) Evolution of porous structure and free-volume entities in magnesium aluminate spinel ceramics. Ceram Int 40(6):8561–8567. https://doi.org/10.1016/j.ceramint.2014.01.070
24. Klym H, Ingram A, Shpotyuk O, Hadzaman I, Hotra O, Kostiv Y (2016) Nanostructural free-volume effects in humidity-sensitive MgO-Al_2O_3 ceramics for sensor applications. J Mater Eng Perform 25(3):866–873. https://doi.org/10.1007/s11665-016-1931-9
25. Sommers A, Wang Q, Han X, T'Joen C, Park Y, Jacobi A (2010) Ceramics and ceramic matrix composites for heat exchangers in advanced thermal systems – a review. Appl Therm Eng 30(11-12):1277–1291. https://doi.org/10.1016/j.applthermaleng.2010.02.018
26. Asami K, Mitani S, Fujimori H, Ohnuma S, Masumoto T (1999) Characterization of Co-Al-O magnetic thin films by combined use of XPS, XRD and EPMA. Surf Interface Anal 28:250–253. https://doi.org/10.1002/(SICI)1096-9918(199908)28:1<250::AID-SIA587>3.0.CO;2-T
27. Asami K, Ohnuma T (1998) Masumoto XPS and X-ray diffraction characterization of thin Co-Al-N alloy films prepared by reactive sputtering deposition. Surf Interface Anal 26:659–666. https://doi.org/10.1002/(SICI)1096-9918(199808)26:9<659::AID-SIA412>3.0.CO;2-Z
28. Moreira EA, Coury JR (2004) The influence of structural parameters on the permeability of ceramic foams. Braz J Chem Eng 21(1):23–33. https://doi.org/10.1590/S0104-66322004000100004
29. Ferraris E, Vleugels J, Guo Y, Bourell D, Kruth JP, Lauwers B (2016) Shaping of engineering ceramics by electro, chemical and physical processes. CIRP Ann 65(2):761–784. https://doi.org/10.1016/j.cirp.2016.06.001
30. Chakraverty S, Mitra S, Mandal K, Nambissan PMG, Chattopadhyay S (2005) Positron annihilation studies of some anomalous features of $NiFe_2O_4$ nanocrystals grown in SiO_2. Phys Rev B 71(2):024115. https://doi.org/10.1103/PhysRevB.71.024115
31. Tuomisto F, Makkonen I (2013) Defect identification in semiconductors with positron annihilation: experiment and theory. Rev Mod Phys 85(4):1583. https://doi.org/10.1103/RevModPhys.85.1583
32. Krause-Rehberg R, Leipner HS (1999) Positron annihilation in semiconductors. Defect studies. Springer, Berlin/Heidelberg/New York, p 378
33. Klym H, Ingram A, Shpotyuk O, Hadzaman I (2012) Water-sorption processes in nanostructured ceramics for sensor electronics studied with positron annihilation instruments. 28th international conference on microelectronics (MIEL), p 155–158. https://doi.org/10.1109/MIEL.2012.6222821
34. Klym H, Ingram A, Shpotyuk O, Filipecki J (2010) PALS as characterization tool in application to humidity-sensitive electroceramics. 27th international conference on microelectronics proceedings (MIEL), p 239–242. https://doi.org/10.1109/MIEL.2010.5490492
35. Goworek T (2002) Comments on the relation: positronium lifetime–free volume size parameters of the Tao–Eldrup model. Chem Phys Lett 366(1-2):184–187. https://doi.org/10.1016/S0009-2614(02)01569-5

36. Tao SJ (1972) Positronium annihilation in molecular substance. J Chem Phys 56(11):5499–5510. https://doi.org/10.1063/1.1677067
37. Eldrup M, Lightbody D, Sherwood JN (1981) The temperature dependence of positron lifetimes in solid pivalic acid. Chem Phys 63:51–58. https://doi.org/10.1016/0301-0104(81)80307-2
38. Klym H, Vasylchyshyn I, Hadzaman I, Dunets R (2018) Porous structure and exploitation properties of nanostructured MgO-Al_2O_3 ceramics technologically modified by time-temperature regimes. 38th international conference on Electronics and Nanotechnology (ELNANO), p 142–145. https://doi.org/10.1109/ELNANO.2018.8477514
39. Shpotyuk O, Calvez L, Petracovschi E, Klym H, Ingram A, Demchenko P (2014) Thermally-induced crystallization behaviour of 80$GeSe_2$-20Ga_2Se_3 glass as probed by combined X-ray diffraction and PAL spectroscopy. J Alloys Compd 582:323–327. https://doi.org/10.1016/j.jallcom.2013.07.127
40. Klym H, Ingram A, Shpotyuk O, Calvez L, Petracovschi E, Kulyk B, Serkiz R, Szatanik R (2015) 'Cold' crystallization in nanostructurized 80$GeSe_2$-20Ga_2Se_3 glass. Nanoscale Res Lett 10(1):1–8. https://doi.org/10.1186/s11671-015-0775-9
41. Klym H, Ingram A, Shpotyuk O, Hadzaman I, Solntsev V, Hotra O, Popov AI (2016) Positron annihilation characterization of free volume in micro-and macro-modified $Cu_{0.4}Co_{0.4}Ni_{0.4}Mn_{1.8}O_4$ ceramics. Low Temp Phys 42(7):601–605. https://doi.org/10.1063/1.4959021
42. Klym H, Shpotyuk O, Ingram A, Karbovnyk I (2018) Modified positron annihilation lifetime spectroscopy method for investigation of nanomaterials with advanced porosity. 38th international conference on Electronics and Nanotechnology (ELNANO), p 134–137. https://doi.org/10.1109/ELNANO.2018.8477443
43. Klym HI, Ivanusa AI, Kostiv YM, Chalyy DO, Tkachuk TI, Dunets RB, Vasylchyshyn II (2017) Methodology and algorithm of multicomponent analysis of positron annihilation spectra for nanostructured functional materials. J Nano-Electron Phys 9(3):03037-1–03037-6. https://doi.org/10.21272/jnep.9(3).03037
44. Klym H, Karbovnyk I, Vasylchyshyn I (2016) Multicomponent positronium lifetime modes to nanoporous study of MgO-Al_2O_3 ceramics. 13th international conference on modern problems of radio engineering, Telecommunications and Computer Science (TCSET), p 406–408. https://doi.org/10.1109/TCSET.2016.7452071
45. Giebel D, Kansy J (2011) A new version of LT program for positron lifetime spectra analysis. Mater Sci Forum 666:138–141. https://doi.org/10.4028/www.scientific.net/MSF.666.138
46. Kansy J (2001) Programs for positron lifetime analysis adjusted to the PC windows environment. Mater Sci Forum 363:652–654
47. Kansy J, Consolati G, Dauwe C (2000) Positronium trapping in free volume of polymers. Radiat Phys Chem 58(5-6):427–431. https://doi.org/10.1016/S0969-806X(00)00195-X
48. Kansy J (2000) Positronium trapping in free volume of polymers. Radiat Phys Chem 58:427–431. https://doi.org/10.1016/S0969-806X(00)00195-X
49. Kansy J (1996) Microcomputer program for analysis of positron annihilation lifetime spectra. Nucl Instrum Methods Phys Res, Sect A 374(2):235–244. https://doi.org/10.1016/0168-9002(96)00075-7
50. Ghosh S, Nambissan PMG, Bhattacharya R (2004) Positron annihilation and Mössbauer spectroscopic studies of In^{3+} substitution effects in bulk and nanocrystaline $MgMn_{0.1}Fe_{1.9-x}O_4$. Phys Lett A 325:301–308. https://doi.org/10.1016/j.physleta.2004.03.062. Get rights and content
51. Nambissan PMG, Upadhyay C, Verma HC (2003) Positron lifetime spectroscopic studies of nanocrystalline $ZnFe_2O_4$. J Appl Phys 93:6320. https://doi.org/10.1063/1.1569973
52. Guo Z, Liang X, Pereira T, Scaffaro R, Hahn HT (2007) CuO nanoparticle filled vinyl-ester resin nanocomposites: fabrication, characterization and property analysis. Compos Sci Technol 67(10):2036–2044. https://doi.org/10.1016/j.compscitech.2006.11.017

Chapter 15
Structure, Morphology, and Spectroscopy Studies of $La_{1-x}RE_xVO_4$ Nanoparticles Synthesized by Various Methods

O. V. Chukova, S. Nedilko, S. G. Nedilko, A. A. Slepets, T. A. Voitenko, M. Androulidaki, A. Papadopoulos, and E. I. Stratakis

Abbreviations

IR	Infra Red
PL	Photo Luminescence
RE	Rare Earth
SEM	Scanning Electron Microscopy
UV	Ultra Violet
XRD	X-Rays Diffraction

15.1 Applications of Vanadate Matrices as Efficient Hosts for Luminescent RE^{3+} Ions

Vanadate matrices are well-known hosts for luminescent rare-earth (RE) ions since the middle of the twentieth century, when $YVO_4:Eu^{3+}$ crystals became into mass usage as red phosphor for luminescent lamps, cathodoluminescent tubes, and oscillotrons [1–3]. The main reasons for the application of just vanadate matrix for mentioned purpose were high radiation and temperature hardness of oxides and high efficiency of RE^{3+} luminescence in vanadate matrix [3–6]. Excellent optical characteristics and other interesting structural, electrical, magnetic, and thermal

O. V. Chukova (✉) · S. Nedilko · S. G. Nedilko · A. A. Slepets · T. A. Voitenko
Taras Shevchenko National University of Kyiv, Kyiv, Ukraine
e-mail: chukova@univ.kiev.ua

M. Androulidaki · A. Papadopoulos · E. I. Stratakis
Institute of Electronic Structure & Laser (IESL) of Foundation for Research & Technology Hellas (FORTH), Heraklion, Greece

O. Fesenko, L. Yatsenko (eds.), *Nanocomposites, Nanostructures, and Their Applications*, Springer Proceedings in Physics 221,
https://doi.org/10.1007/978-3-030-17759-1_15

properties of vanadates have attracted wide research attention to development of this class of compounds for the last decades [7–11]. These compounds are chemically stable and nontoxic [12–14]. As a result, vanadate compounds have been considered for applications in many new areas and various technical and research fields involving chemistry and biology, optoelectronics, and renewable energy generation. Usually, each new practical application requires modifications of characteristics of materials due to special needs just of this application. Considering and comparing requirements from various areas of application, we can formulate the main direction for development of new vanadate compositions with improved usage characteristics.

Traditional application of vanadate materials as red phosphors for cathodoluminescent tubes is currently extended to wide area of applications of vanadate-based luminophors for various color imaging and lightening systems. The most promising direction is creation of new materials for converting violet and blue LED emission into white light [15–18]. Such application requires development of new compositions with enhanced efficiency of excitation from violet spectral range around 400 nm, whereas $REVO_4$ matrices usually have only edges of excitation located near 350 nm (Fig. 15.1) [19–21]. Replacement of the RE cations with alkaline earth (AE) cations (Ca^{2+}, Sr^{2+}, Ba^{2+}) in the RE vanadate nanoparticles was proposed recently to achieve arising of excitation effectiveness near 350–450 nm [22–25]. Similar behavior of excitation property was reported previously for several vanadate compounds. In fact, intensity and locations of excitation band of luminescence depend on material composition, concentration, and type of the AE cations. Maxima positions of this band were reported from 380 nm for $Zn_3V_2O_8$ [25], 385 for $Eu_{1-x}Ca_xVO_4$ [23], 389 nm for $Ca_2KZn_2(VO_4)_3$ [24], 393 for $Li_2Ca_2ScV_3O_{12}:Eu^{3+}$ [22] to 405 nm for $La_{1-x-y}Eu_yCa_xVO_4$ [26] (Fig. 15.2).

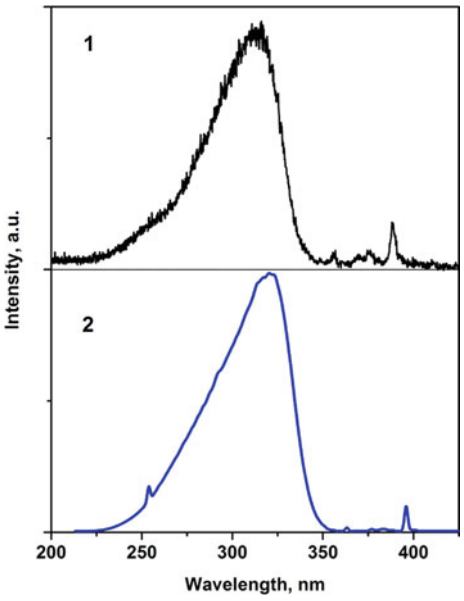

Fig. 15.1 Excitation spectra of the $La_{0.55}Eu_{0.45}VO_4$ (1) and $LaVO_4$:Eu,Li [21] (2) phosphors

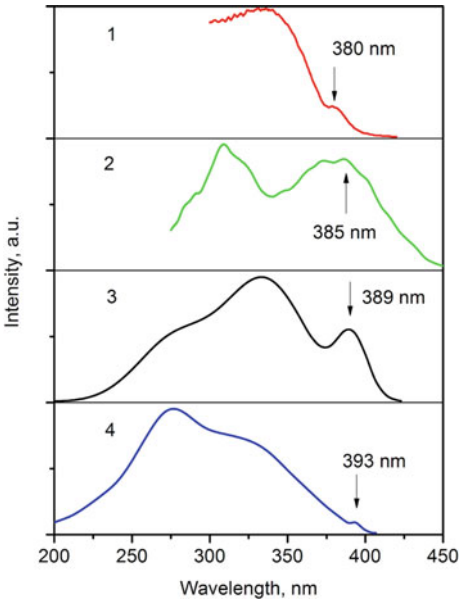

Fig. 15.2 Excitation spectra of the $Zn_3V_2O_8$ [25], $Eu_{1-x}Ca_xVO_4$ [23], $Ca_2KZn_2(VO_4)_3$ [22], and $Li_2Ca_2ScV_3O_{12}:Eu^{3+}$ [24] phosphors

Nature of this excitation band is under discussion. It was ascribed to transitions in the vanadate groups [25], to presence of AE oxide impurity phases [22, 27], and to AE-induced defects [26]. It should be also noted that this excitation band is located in the range of f-f transitions in the Eu^{3+} ions, and sometimes it can be unrecognized in the spectra of the RE-doped vanadates [22]. Thus, additional complex investigation is needed to study AE effect on the RE ions luminescent properties in the vanadate matrices. So, development of new compositions with enhanced efficiency of excitation from violet range is an actual task in creation of vanadate compositions perspective for application in WLED devices.

The range of actual and potential biological applications of vanadates includes fluorescent probes for single molecule tracking, drug delivery and activation, protein detection, fluorescent bio labeling [14, 28, 29]. Some of these applications are used for investigation of living tissues and for therapy of diseases. In particular, singlet oxygen as an effective destroyer of cancer cells is used for the photodynamic therapy of tumors. The singlet oxygen could be produced at the decay of excited electronic states of some oxygen generating molecules, effective excitation of which is possible only from the near infra-red spectral region where absorption of living tissues is low. It is also carried out search of intermediating materials which are effectively excited by soft X-ray and can transfer excitation energy to oxygen generating molecules. Some oxide materials and orthovanadate compounds among them were considered as promising transferring media taking into account their stability in various neighboring and high absorption cross-section.

From the medical and biological points of view, materials for such applications should be safe to human body and have maximally possible high efficiency of energy

transformation in order to decrease X-rays irradiation of patients. As the vanadate compounds are known as nontoxic materials, the main task for development of improved compositions for biological and medical applications is to increase luminescence emission efficiency without incorporation of some toxic agents.

Global demands in energy sector have also attracted attention to possible applications of luminescent nanoparticles in renewable energy sources, in particular, in solar energy. In this connection some vanadates have been proposed for creation of luminescent down-shifting coatings for silicon solar cells [30–33]. Currently, the most sold at the marked commercial silicon-based solar cells have efficiency of solar light to electrical energy conversion about 15%. The large part of the solar energy losses is associated with spectral mismatch of solar cells sensitivity and energy distribution in the solar spectrum. In order to cover this mismatch, "up" (from infrared (IR) to visible (VIS)) and "down" (from ultraviolet (UV) to VIS) conversions of solar photons are applied [34–37]. Considerable research efforts were devoted for the last years to development of materials for effective conversion of solar radiation, in particular dye-sensitization of solar cells that provides a low cost solution [38]. However, dye colors have tendency to degradation under UV irradiation; therefore, UV light is usually blocked by filters, and high-energy photons are not available for down-conversion. Possibility of luminescent absorbers application for adoption of UV light to working range of silicon solar cells was recently considered on the basis of thin inorganic crystalline films doped with RE ions [39, 40]. The RE-doped oxides are perspective candidates for this role due to their excellent thermal, mechanical, and optical properties. Various vanadate compositions such as multi-RE doped YVO_4 and Eu or Sm doped $LaVO_4$ vanadate nanoparticles were considered as promising materials for adaptation of incident solar light to spectral sensitivity of silicon solar cells. Arising of the above-described excitation band around 400 nm is a very desirable feature suitable for this application. Decreasing of cost is also especially important for materials proposed for covering of silicon solar cells.

For the last years, nanosized orthovanadates have been also considered as main perspective photocatalytic material in systems for visible light-driven photocatalytic water splitting. The widely used photocatalyst TiO_2 is active only under ultraviolet light irradiation [41, 42], while bismuth, cerium, and lanthanum orthovanadates are of a special attention as the most promising visible light-driven photocatalysts [43–45].

Summarizing, the wide range of vanadate compounds applications have attracted significant research efforts to development of new vanadate compositions with improved characteristics depending on requirements of various practical tasks. In particular, increase of excitation efficiency under light from near UV and violet spectral ranges is needed for solar energy conversion applications, whereas biological applications require light transformer materials safe to human body with high efficiency of energy transformation in order to decrease X-rays irradiation of living tissues. These goals can be achieved by isovalent and heterovalet doping of the basic $REVO_4$ compositions. In the present work we give overview of our 5-years research activities in these directions together with description and discussion

of new results. The $LaVO_4$ matrix is used as basic for the study in order to achieve desirable cost decrease as the La reagents are among the cheapest RE reagents. Besides, the $LaVO_4$ matrix is characterized by one more unique for the orthovanadate compounds feature that is described in the next paragraph.

15.2 Feature of Lanthanum Vanadate Crystal Matrix Compared to Other Rare-Earth Vanadates

It is known that all the rare-earth orthovanadates ($REVO_4$) crystal compounds crystallize in the so-called zircon structure [46]. This rule has one exception and this exception is lanthanum vanadate ($LaVO_4$), which is dimorphic and can be stabilized in zircon or monazite crystal structures [47].

The zircon crystal structure is characterized by a tetragonal symmetry with space group I41/amd ($Z = 4$). In this structure, the La and V cations are located at high-symmetry positions; those can be described as formed by isolated VO_4 tetrahedral units surrounded by the La atoms forming eight-vertex LaO_8 polyhedrons. Each of V atoms is surrounded by four equivalent oxygen atoms forming the perfect VO_4 tetrahedrons with T_d local symmetry of oxygen surrounding and V–O distances near 1.7 Å (Fig. 15.3). In the LaO_8 dodecahedron, the La atoms are coordinated by eight oxygen atoms with identical four short bond lengths (2.2 Å) and four long bond lengths (2.5 Å) with D_{2d} local symmetry of oxygen surrounding [47–49]. Each VO_4 and LaO_8 polyhedron units are running parallel to the crystallographic c-axis. Each of the chains is joined laterally by edge-sharing LaO_8 dodecahedra.

The monazite structure (space group P21/n, No. 14, $Z = 4$) is another crystal structure adopted by $LaVO_4$ [50]. At ambient conditions this crystal structure is observed only for $LaVO_4$ among the $REVO_4$ family but can be obtained for several $REVO_4$ vanadates at high pressure [51]. In the monazite structure, the V and La atoms are four- and ninefold coordinated, respectively, with C_s local symmetry of oxygen surrounding for both the cations. The distorted VO_4 tetrahedrons only share corners and edges with the LaO_9 polyhedrons (Fig. 15.3).

Dimorphism of the $LaVO_4$ can be an essential advantage in the search of compositions with certain spectroscopy characteristics needed for one of the mentioned purposes, because luminescent properties of the RE^{3+} ions are known to be dependent on symmetry of crystal surrounding [49, 52–54]. It is also important to note here that isolated arrangement of the VO_4 tetrahedrons is a common feature for both the crystal structures which allows description of lattice vibrations as internal and external modes of this unit [55].

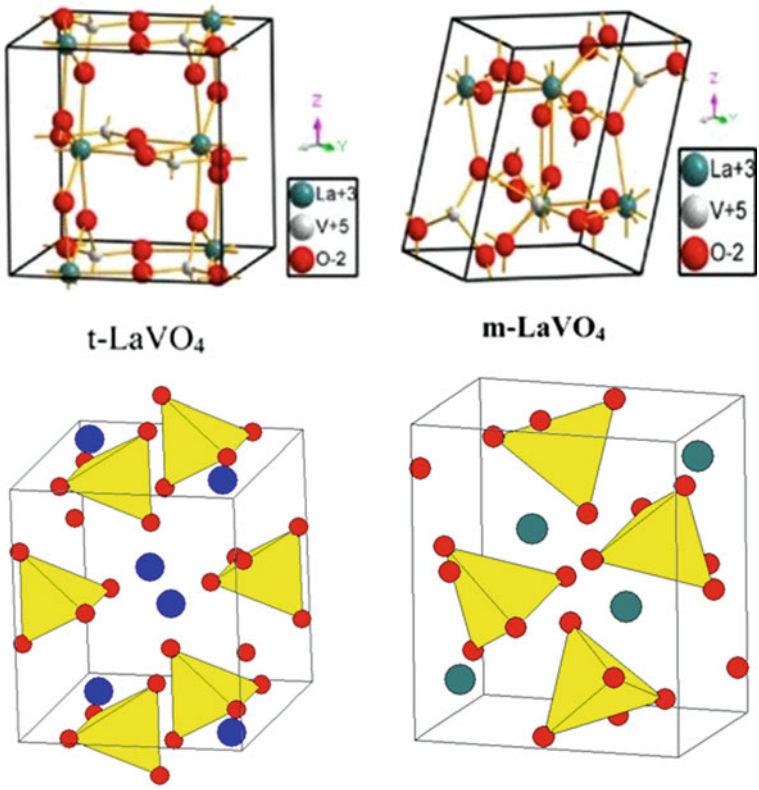

Fig. 15.3 Crystal structures of the $LaVO_4$ in zircon (left) and monoazite (right) phases shown in the form of atoms and bonds (top) and in the form of vanadate tetrahedrons and La atoms (bottom)

15.3 Methods of the Orthovanadate Nanoparticles Synthesis

As methods those could be successfully used for the synthesis of the orthovanadates nanoparticles, several authors have reported solid-state [20, 56], coprecipitation [21, 57], hydrothermal [58], solution combustion [59], and sol-gel synthesis [26, 60]. These methods could satisfy various reactivities of the compounds, homogenization, morphology, and sizes of nanoparticles; therefore, it was important for us to use various methods at the beginning of our work to find those ones that will allow us to achieve the best results in the noted above goals.

15.3.1 Solid-State Method

The La_2O_3 (99.99%), V_2O_5 (99.99%), and Eu_2O_3 (99.99%) powders were selected as the starting materials. For a typical process, all starting materials were weighed in the calculation stoichiometric ratio, and well mixed in the agate mortar. The mixed samples were calcinated using step-by-step heating (the step was 100 °C) up to 680 °C with 1 hour temperature exposure and intermediate grinding for each step. The final products were sintered for 6 hours at 900 °C (Fig. 15.4a).

15.3.2 Coprecipitation Method

The La_2O_3 and Eu_2O_3 starting materials were first dissolved into concentrated nitric acids. The stoichiometric ratios of the rare-earth nitrates solutions were mixed homogenously. After being stirred for half an hour the pH value was adjusted to about 7.0–8.0 with ammonia solution. Simultaneously, the Na_3VO_4 solutions were added into the solutions of $La(NO_3)_3$ and $Eu(NO_3)_3$. After this, the solutions were stirred until they became homogeneous. After being deposited for several days, they were filtered and dried in a drying box and the precursors were achieved. Then, they were thoroughly homogenized and calcinated in a muffle furnace using step-by-step heating up to temperature 680 °C with 1 hour temperature exposure and intermediate grinding for each 100 °C. Then the samples were heat-treated for 6 hours at 900 °C (Fig. 15.4b).

15.3.3 Sol-Gel Synthesis

Stoichiometrically calculated amounts of $La(NO_3)_3$, $Eu(NO_3)_3$, NH_4VO_3, and $Ca(NO_3)_2$ were used as a starting compound. The necessary quantities of the reagents were gradually mixed by 100, 20, 10, and 5 ml pipettes in a 250 ml beaker. The solution system was homogenized using a magnetic stirrer. The content of metal ions in their solutions was estimated out by the trilonometric method: solution of calcium nitrate was established by direct titration with murexide; the concentration of rare-earth ions in their respective nitrate solutions was established by direct titration with xylenol orange [61]. The NH_4VO_3 solution was titrated by using a hydroquinone with sulfuric acid before switching from blue to green and red. Ferroin was used as an indicator. At the next stage, a complexing agent was added to prevent the sedimentation process from the reaction mixture of a similar composition using the deposition method. Then 5 g of citric acid were dissolved in a 100 ml glass by distilled water, in which it was heated and added to the reagents solution. Such a mixture was poured into a graphite cup and placed on a sand bath. The solution gradually evaporated and turned into a gel, and then a powder. The

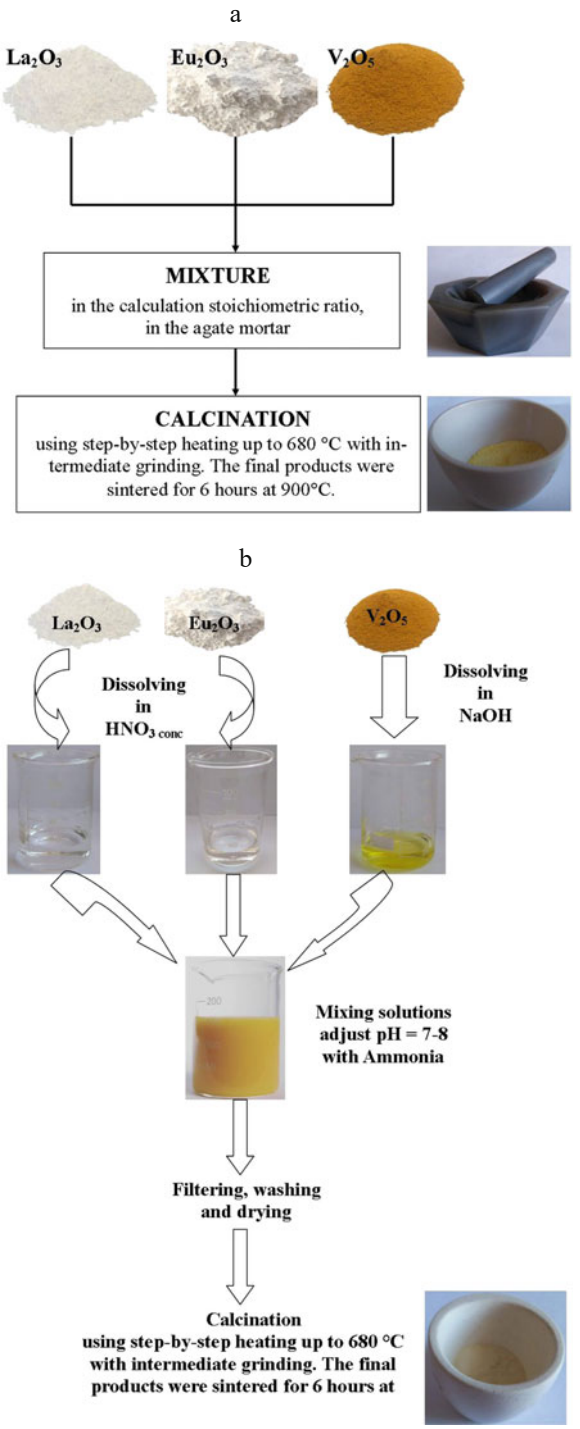

Fig. 15.4 Schematic diagram showing the experimental process for solid-state (**a**), coprecipitation (**b**), and sol-gel [26] (**c**) synthesis of the vanadate nanoparticles

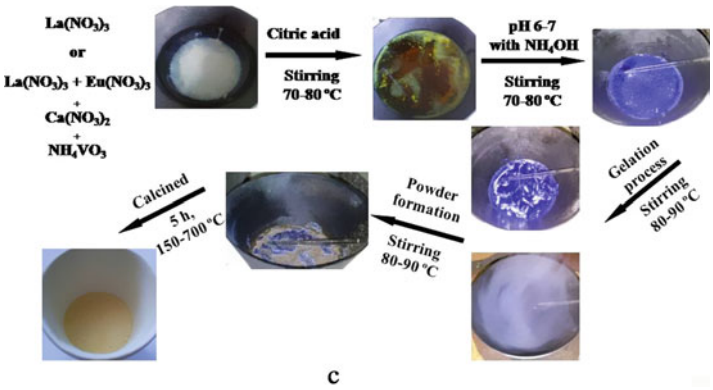

Fig. 15.4 (continued)

fine-grained powder was calcined for 5 hours at a step-by-step heating with 100 °C steps up to 680 °C temperature (Fig. 15.4c).

15.4 Phase Composition of the Synthesized Nanoparticles

Phase compositions and crystal lattice parameters of the synthesized samples were determined using X-ray diffractometer (XRD) DRON-3M ($Cu_{K\alpha}$-radiation with a Ni filter). The diffraction patterns were taken with a 2 deg/min step.

The XRD analysis has shown that all the synthesized samples $La_{1-x}Eu_xVO_4$ are single phase. XRD patterns of synthesized pure $LaVO_4$ are well matched with a standard card of monoclinic $LaVO_4$ (JCPDS PDF2 50-0367) for all the applied methods of synthesis (Fig. 15.5). Thus, crystal structure of pure $LaVO_4$ is monoclinic (space group $P2_1/n$, monazite structure family).

Crystal structure of the $La_{0.95}Eu_{0.05}VO_4$ samples synthesized by the coprecipitation method is also monoclinic. Further increase in the quantities of europium impurities ($x = 0.1$) leads to formation of two phase mixtures (the monoclinic and tetragonal). Finally, the crystal structure of $La_{0.7}Eu_{0.3}VO_4$ sample with a high substitution degree, $x = 0.3$, is tetragonal, belonging to the I41/amd space group. Thus, increasing Eu^{3+} ions concentration in $La_{1-x}Eu_xVO_4$ compositions synthesized by coprecipitation method leads to stabilization of the tetragonal phase. Crystal structures of the $La_{1-x}Eu_xVO_4$ samples with $x \geq 0.1$ are tetragonal (space group I41/amd zircon structure family) for solid-state and sol-gel methods of synthesis. Therefore, presence of europium ions with concentrations from $x \geq 0.1$ leads to change of the crystal structure from monoclinic to tetragonal [20, 21].

The XRD patterns of the $La_{1-x-y}Eu_yCa_xVO_4$ ($x \leq 0.2$, $y \leq 0.2$) samples are shown in Fig. 15.6. The $La_{0.9}Eu_{0.05}Ca_{0.05}VO_4$ sample with low concentration of the Ca^{2+} and Eu^{3+} impurities is also attributed to the monoclinic structure. Proximity

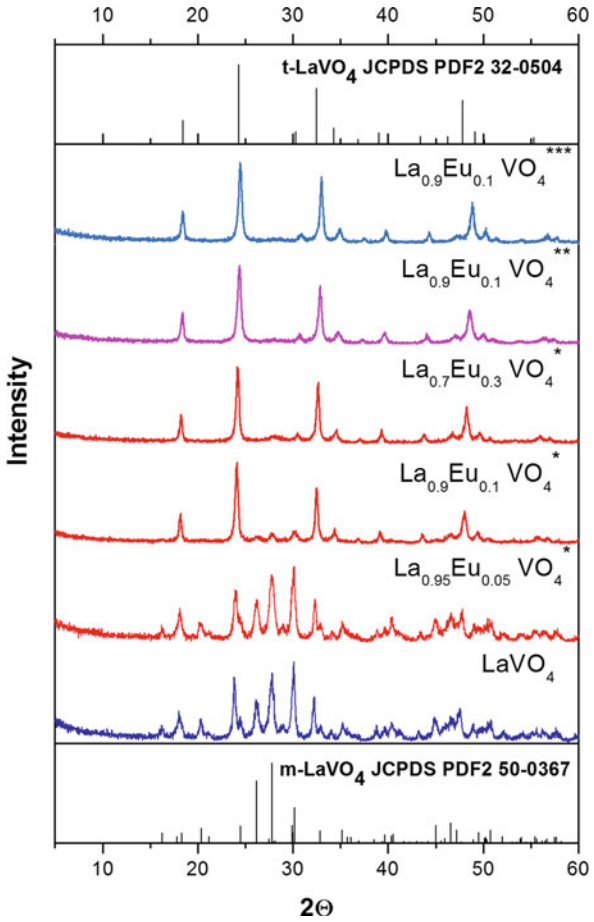

Fig. 15.5 XRD patterns of the La_{1-x} Eu_xVO_4 samples with $0 \leq x \leq 0.3$ synthesized by $_*$, coprecipitation method; $_{**}$, sol-gel method; $_{***}$, solid-state method

of the Ca^{2+} (1.12 nm), La^{3+} (1.16 nm), and Eu^{3+} (1.066 nm) ions radii provides an opportunity for calcium and europium ions incorporation into three plus cation's sites. Besides, we see that small quantities of the Ca^{2+}($x \leq 0.1$) and Eu^{3+} ions ($y \leq 0.05$) can enter into the crystal lattice without change of the monoclinic $LaVO_4$ structure. Increasing concentrations of the $Eu^{3+}$and Ca^{2+}impurities lead to the formation of the monoclinic and tetragonal phase mixture. The $La_{0.6}Eu_{0.2}Ca_{0.2}VO_4$ sample becomes related to tetragonal structure, belonging to the I41/amd space group. This result is in agreement with the standard card of tetragonal $LaVO_4$ (JCPDS PDF2 32-0504) (see Fig. 15.5) [26]. Therefore, increasing the europium and calcium ions concentration in $La_{1-x-y}Eu_yCa_xVO_4$ (x, $y \leq 0.2$) solid solutions leads to the change of the crystal structure with the formation of two phase compositions and subsequent stabilization of the tetragonal at $x = y = 0.2$.

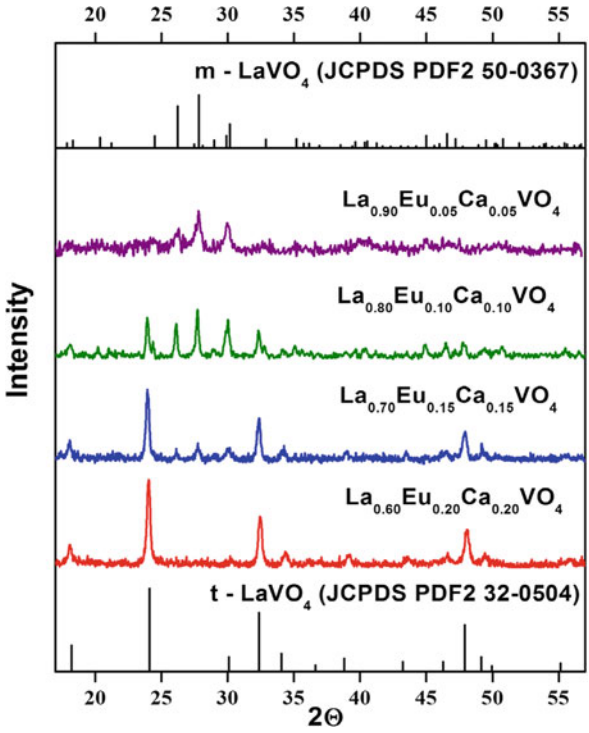

Fig. 15.6 XRD patterns of the $La_{1-x-y}Eu_yCa_xVO_4$ ($x = y = 0.2$) samples

15.5 Chemical Elements Analysis of the Ca-Doped Vanadate Nanoparticles

Chemical elements analysis was performed for the Ca-doped $La_{1-x-y}Eu_yCa_xVO_4$ samples in order to confirm arrangement of the Ca^{2+}cations in vanadate nanoparticles with $LaVO_4$ crystal structure, where cation sites usually have 3+ charge. We have investigated 3–5 various agglomerates or grains for each sample using the EDS tool of MIRA3 TESCAN Scanning Electron Microscope. Monitoring area from which information about content of atoms has been taken was larger than e-beam size, and it was near $(30 - 40) \times (30 - 40)$ μm. We have found that La, Eu, Ca, V, and O are the main components of the samples. The measured contents of the La^{3+} ions in the synthesized samples were quite close to the expected compositions [26]. Total contents of the Eu^{3+} and Ca^{2+} ions are also close to the expected compositions. However, the predicted simultaneous fourfold increase of ions Eu^{3+} and Ca^{2+} content (from 0.05 up to 0.20 at. %) is not implemented for the actual synthesized samples. We have observed that when the content of the Eu^{3+} ions increases by ~10 times, the content of the Ca^{2+} ions increases only by ~ 2–3 times. This is due both to specific of the samples (heterogeneity of sizes, shapes, and thickness of grains of powder, etc.) and features of the method (a significant error for light elements, the effect of electron beam on oxide surfaces, etc.). This result

will be taken into account in the discussion of the synthesized compounds spectral properties.

15.6 Morphology of the Vanadate Nanoparticles Synthesized by Different Methods

Influence of method of synthesis on morphology of the $La_{1-x}Eu_xVO_4$ was studied on comparison of SEM images of nanoparticles synthesized by coprecipitation and sol-gel methods. The images were obtained from MIRA3 TESCAN microscope. SEM images of the samples in Figs. 15.7 and 15.8 show as large areas up to ~ 2 × 2 μm for general view of samples as well as small separated areas up to ~ 0.8 × 0.8 μ.

Coprecipitated samples consist of nanoparticles that are agglomerated in grains of different sizes from tens of nanometers to 1 micron. There are many pores and cavities between nanoparticles in grains. Each of the samples consists of nanoparticles of similar shapes and sizes; the latter are increased with increasing of Eu concentration from 20–40 nm for $x = 0.1$ to 50–70 nm for $x = 0.3$ (Fig. 15.7). The shapes of nanoparticles have slightly distinguished round-polyhedral forms.

Sol-gel samples consist of nanoparticles that are densely agglomerated in solid grains with sizes about 0.5–2.0 microns (Fig. 15.8). Sizes of nanoparticles vary from 40 to 60 nm for samples of all the concentrations. Dependence of morphology on Eu concentration for the sol-gel nanoparticles was not observed. The shapes of nanoparticles cannot be analyzed correctly due to high rate of agglomerization. Thus, we should make a conclusion that coprecipitation allows us to obtain nanoparticles with lower rates of agglomeration and smaller sizes of nanoparticles for the samples with low Eu concentration. Note that the described differences in morphology of the nanoparticles can affect their spectral properties.

The SEM images of the $La_{1-x-y}Eu_yCa_xVO_4$ samples are shown in Fig. 15.9 [26]. The samples are formed by nanoparticles of size from 20 to 100 nm. The $La_{0.9}$ $Eu_{0.05}Ca_{0.05}VO_4$ samples with low concentration of the Eu and Ca impurities consist of grains of 0.1–0.2 μ size; those are formed by nanoparticles of 10–20 nm size (Fig. 15.9c). The nanoparticles of larger size, ~ 100 nm, are characteristic for the samples with higher concentration of dopants, $La_{0.8}Eu_{0.1}Ca_{0.1}VO_4$. Most of them have polyhedral shapes with clearly defined edges and angles between them (Fig. 15.9d). The particles with the observed polyhedral shapes have to be assigned to the crystal system of lower symmetry. Thus, the observed polyhedral shapes can be regarded as a manifestation of the monoclinic phase in the studied samples. The next increase of the Eu^{3+} and Ca^{2+} dopants concentrations also generates particles of ~100 nm sizes (Fig. 15.9e). Despite the poor quality of this image, it is possible to conclude that the shapes of the particles are closer to the cylinders and rods. The same shapes are observed for the samples of the highest dopants concentration, $La_{0.6}Eu_{0.2}Ca_{0.2}VO_4$ (Fig. 15.9f). However, it should be noted that size of the particles is smaller for these samples; it is preferably 30–60 nm.

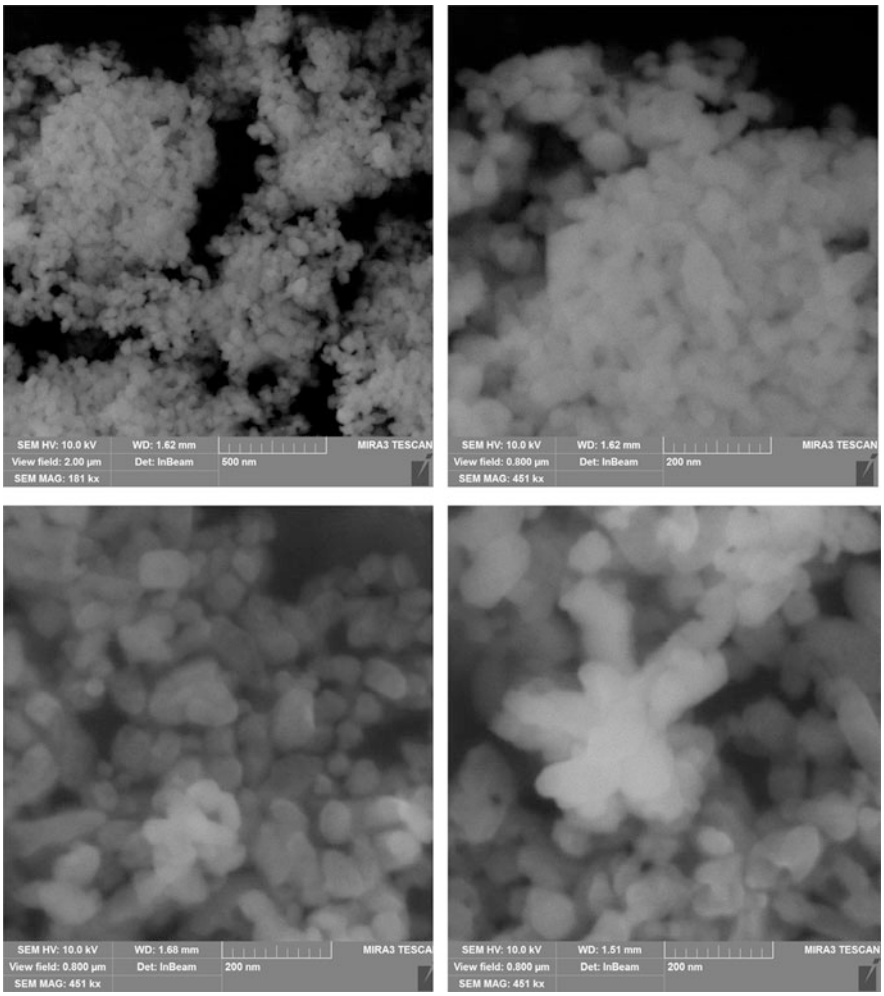

Fig. 15.7 The SEM images of the $La_{1-x}Eu_xVO_4$ nanoparticles synthesized by coprecipitation method $x = 0.1$ (**a**, **b**), 0.2 (**c**), 0.3 (**d**)

Thus, we can say that the change of the powder samples composition is accompanied by the changes in the size and morphology of their constituent particles. These changes are consistent with the XRD data on the structure and phase composition of the samples. Therefore, the SEM data can be interpreted as indicating that the samples of higher dopants concentration are mixtures of monoclinic and tetragonal phases and the content of the latter increases when the content of europium and calcium ions increases.

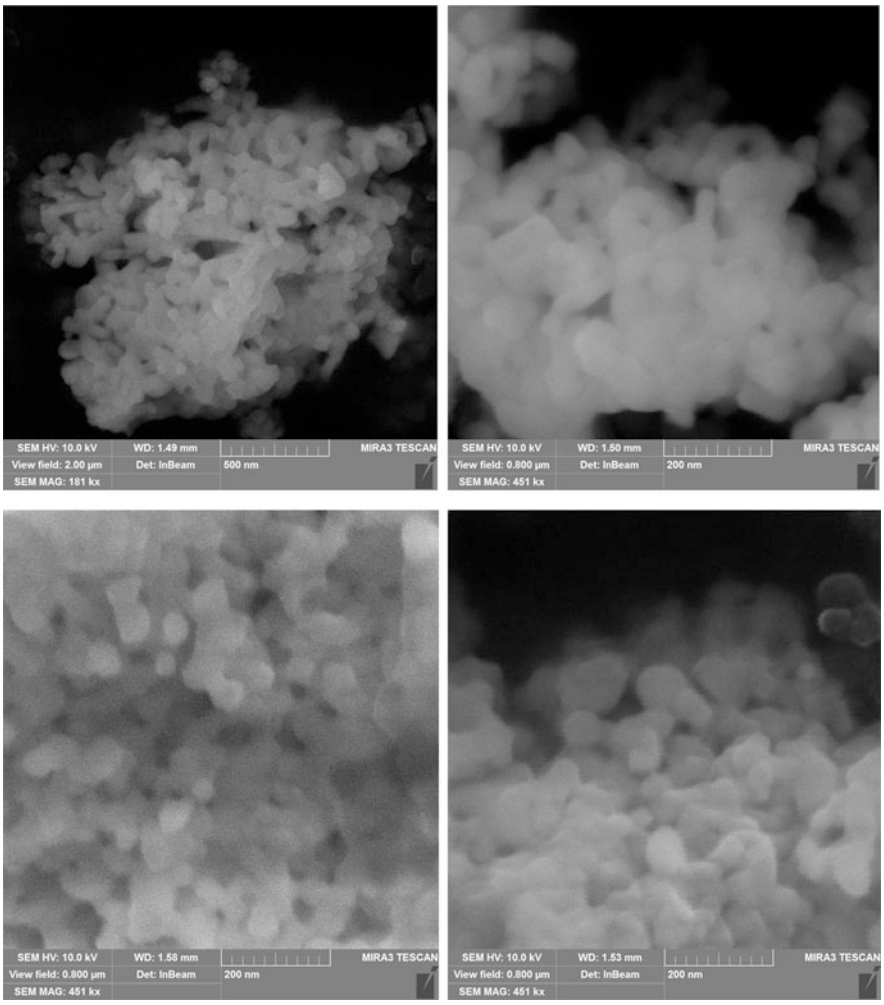

Fig. 15.8 The SEM images of the $La_{1-x}Eu_xVO_4$ nanoparticles synthesized by the sol-gel method $x = 0.1$ (**a**, **b**), 0.2 (**c**), 0.3 (**d**)

15.7 Infrared Spectroscopy

Infrared spectra (IR) of the samples were recorded in the 400–400 cm^{-1} range on Perkin Elmer IR spectrometer using the KBr pellet method.

The view of the IR spectra in the range of 400–1100 cm^{-1} (Fig. 15.10) is typical for the $LaVO_4$ IR- absorption spectra measured previously in this range [62–64].

It is well known that the bending (ν_2 and ν_4) and stretching vibrations (ν_1 and ν_3) of O–V–O bonds of the VO_4^{3-} anion form IR absorption spectra of various orthovanadates in the range 400–700 and 700–1100 cm^{-1}, respectively [65, 66].

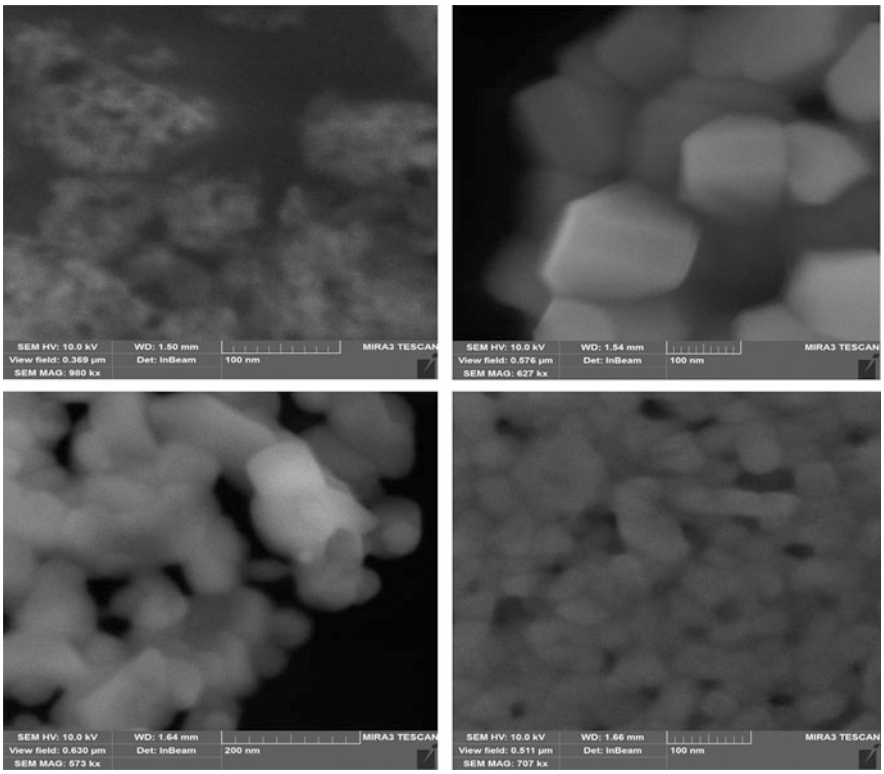

Fig. 15.9 The SEM images of the $La_{1-x-y}Eu_yCa_xVO_4$ synthesized by sol-gel method $x = y = 0.05, 0.1, 0.15, 0.2$

In fact, measured by us spectrum of the un-doped $LaVO_4$ contains separated weak band located in the range 400–700 cm^{-1}, while the main wide band is located in the range 700–1100 cm^{-1} (Figs. 15.10 and 15.11). Sharp peak at 434 cm^{-1} and blurred band centered near 550 cm^{-1} compose IR spectra of this sample in the former range. The main peak at ~ 778 cm^{-1} and three strongly overlapped other ones located at ~ 820, 850, and 880 cm^{-1} form wide band (Fig. 15.11, curve 1). (All the mentioned peaks are marked by arrows close to curve 1 in Fig. 15.11, and their positions are in Table 15.1).

In the spectra of the $La_{1-x}Eu_xVO_4$ samples synthesized by various methods, there are two main strong peaks at 859 and 892 cm^{-1}. This fact is consistent with the results published for the tetragonal $LaVO_4$ [65, 67]. We find that t-$LaVO_4$ has similar vibrational peaks positions with m-$LaVO_4$ (see the table), but as it can be seen from Fig. 15.10, deformation vibrational peaks ν_4 for t-$LaVO_4$ have lower intensity than for the m-$LaVO_4$. Also, increased number of vibrational peaks in the range 750–900 cm^{-1} is observed for m-$LaVO_4$ for all the applied methods of synthesis (see arrows in Figs. 15.10 and 15.11). Thus, six or seven peaks can be

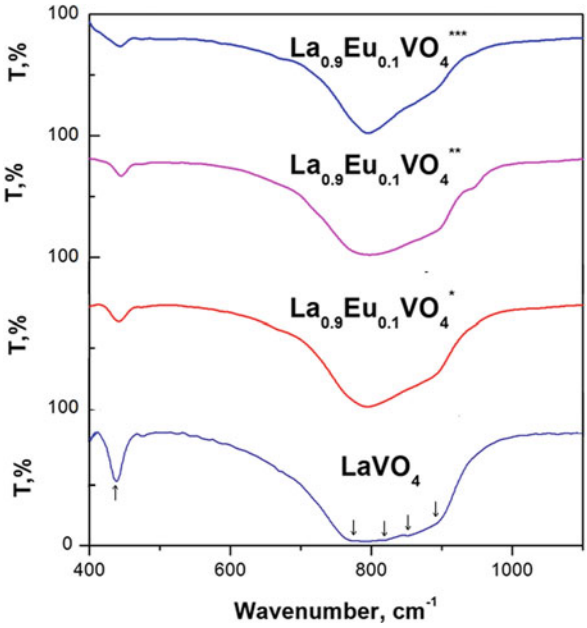

Fig. 15.10 IR absorption spectra of the $La_{0.9}Eu_{0.1}VO_4$ nanoparticles synthesized by $_*$, coprecipitation method; $_{**}$, sol-gel method; $_{***}$, solid-state method; and $LaVO_4$ nanoparticles synthesized by solid-state method

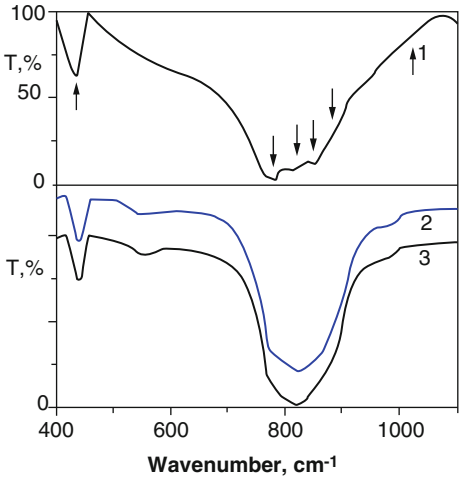

Fig. 15.11 IR absorption spectra of the $LaVO_4$ (1), $La_{0.8}Eu_{0.1}Ca_{0.1}VO_4$ (2), and $La_{0.6}Eu_{0.2}Ca_{0.2}VO_4$ (3) nanoparticles synthesized by sol-gel method

distinguished there, and shape and structure of the band become very similar to the ones previously published on the IR absorption spectra of the $LaVO_4$ [65, 67]. The exact assignment of spectral components to a certain type of modes is difficult, especially that concerning stretching vibration range. Due to the low C_s symmetry of the VO_4^{3-} molecular anion in monoclinic $LaVO_4$, four IR lines lying close to each other can appear in this range of spectra. Our experimental findings are in good agreement with the theoretical prediction noted above. Mentioned fact causes

Table 15.1 IR peaks positions (in cm^{-1}) and their attributions to vibration modes in the VO_4^{3-} vanadate groups

$LaVO_4$	$La_{0.9}Eu_{0.1}VO_4$ Solid state	$La_{0.9}Eu_{0.1}VO_4$ Coprecipitation	$La_{0.9}Eu_{0.1}VO_4$ Sol-gel	$La_{0.8}Eu_{0.1}Ca_{0.1}VO_4$	Vibration modes
434	440	439	440	439	ν_4
				553	
778				783	
820	800	803	801	802, 821	
850	821	820	821	835; 854	ν_3
	858	859	859		
880	889	890	890	875	ν_1
1026	920	922	924	918; 978	

strong overlapping of the lines, that is why they are revealed as one complex wide band.

Doping with calcium ions causes a distortion of certain amount of vanadate groups. As a result, additional peaks near 553 cm^{-1} appear in the spectrum. Besides, as we have shown above all co-doped samples are a mixture of monoclinic and tetragonal $LaVO_4$ phases and contribution of the phases depends on the dopants concentration. The VO_4^{3-} molecular groups possess D_{2d} symmetry in tetragonal $LaVO_4$. So, two lines of E_u and A_{2u} symmetry can be found in the range of stretching vibrations if morphology of the VO_4^{3-} groups corresponds to an ideal tetragonal lattice structure. Really, neighbor environment and symmetry of some VO_4^{3-} groups in tetragonal lattice are also deformed by Ca^{2+} ions and all of VO_4^{3-} internal vibrations can occur in the IR spectra. As previously have been reported the calculated [68] and measured [67] peaks positions of the IR- absorption lines for tetragonal $LaVO_4$ are close to those for monoclinic $LaVO_4$. Thus, the eight lines can form the range of stretching vibrations, we suppose. Change of the phase composition leads to mentioned changes of the shape of the IR bands and their positions. Regarding published theoretical and experimental data a possible assignment of all measured features was made (Table 15.1). Additional studies are necessary in order to clarify the origin of the bands that are in the ranges 500–700 and 900–1000 cm $^{-1}$. We can only note that similar features were previously observed in the IR absorption spectra of some Ca containing orthovanadates [69, 70].

In any cases, we are able to state that observed IR spectra confirm that anionic sublattice of studied vanadates is built by VO_4^{3-} molecular anions.

15.8 Reflectance Spectroscopy

Reflectance spectroscopy of the samples was performed using Perkin Elmer Lambda 950 spectrometer. The powder samples were pressed in a sample holder and then spectra of diffuse reflection were measured. In the used mode, the monochromator

is placed before the samples and all light reflected from the powder samples are collected by photometric sphere. In experimental solution luminescence of the investigated samples could give additional contribution in the recorded spectra and this possibility should be taken into account under analysis of the obtained spectra.

Reflection bands of the undoped $LaVO_4$ nanoparticles are observed in the 250–500 nm spectral range (Fig. 15.12). Maxima of the reflection bands are placed near 300 and 315 nm for the nanoparticles obtained by coprecipitation and sol-gel methods, respectively. The 50% reflection is observed near 340 and 350 nm, respectively. Adding of the Eu^{+} activator ions causes weak narrow peaks at 536, 465, and 395 nm. Also strong decrease of the 300 nm band with increase of the Eu^{3+} concentration is observed. It is accompanied by appearance of the additional peak at 280 nm and increase of the reflection around 250 nm for the samples obtained by all applied methods of synthesis. This effect was also observed for the sol-gel samples co-doped with Ca^{2+} ions. Spectra of the Ca^{2+}-co-doped samples contain also two additional wide reflection bands around 400 and 500 nm. The bands are strong and can achieve at the spectral maxima up to 70–80% reflection compared with the main 300 nm band.

The main band at 300 nm can be attributed to the inner $O^{2-} \rightarrow V^{5+}$ charge transfer transitions in the VO_4^{3-} vanadate groups [71–74]. The narrow peaks at 536, 465, and 395 nm are caused by $^7F_0 \rightarrow {}^5D_{2,3,4}$ *f-f* transitions in the Eu^{3+} ions. The wide bands around 400 and 500 nm that were observed for the Ca^{2+}-co-doped samples should be connected with transitions in Ca-induced defect centers. Their structure will be discussed below together with discussions of luminescence properties. Decrease of the 300 nm band with increase of the Eu^{3+} concentration is obviously connected with contribution of the luminescence emission in the recorded spectra, and it should be discussed together with the analysis of the excitation spectra.

15.9 Luminescent Spectroscopy

15.9.1 Dependencies of Luminescence Properties of the $La_{1-x}Eu_xVO_4$ Nanoparticles on Methods of Synthesis

Luminescence spectra were investigated using ACTONi (500) monochromator with grating 150 grooves/mm (blaze @ 300 nm), slit on 50 micron and liquid N_2 – cooled CCD registration as well as DFS12 monochromator with grating 600 grooves/mm, and slit on 50 micron and FEU-79 photomultiplier registration. Luminescence spectra were excited with 325, 405, 478, and 532 nm diode lasers or powerful Xenon lamp [see for additional details 75, 76].

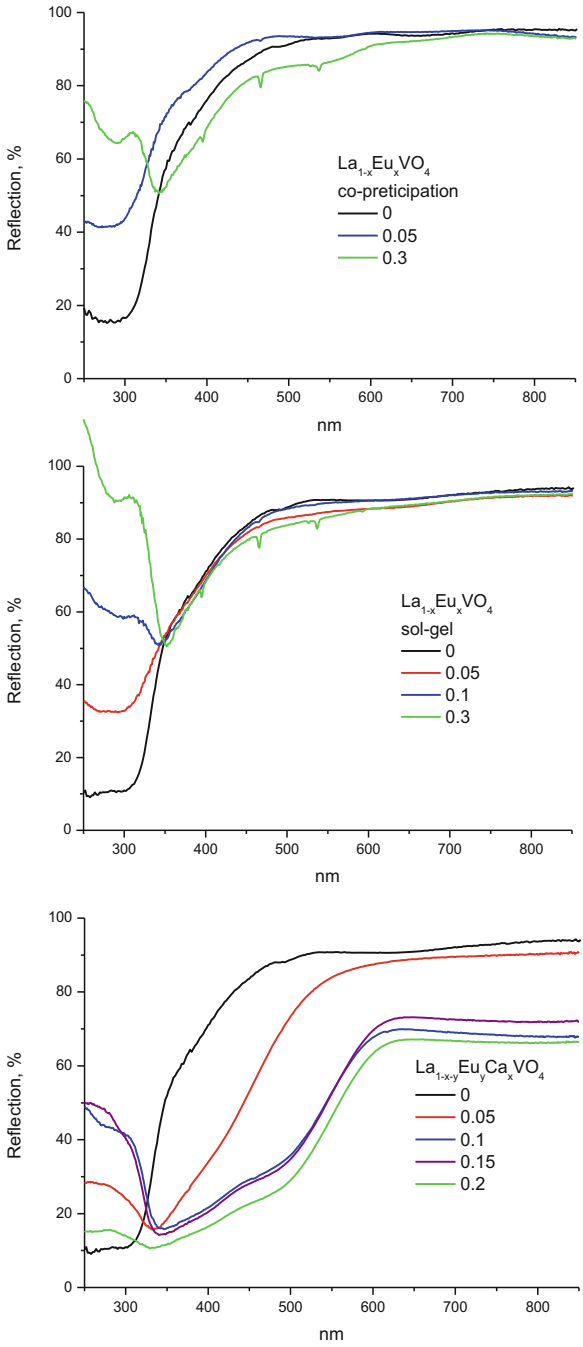

Fig. 15.12 Reflection spectra of the investigated vanadate nanoparticles

Emission of the $La_{1-x-y}Eu_yVO_4$ samples was observed in the 550–730 nm spectral range and they consist of narrow spectral lines (Fig. 15.13). Undoubtedly, those lines are caused by radiation transitions in Eu^{3+} ions. Peculiarities of fine structure of the spectra and their intensities depend on method of synthesis and on the Eu^{3+} concentration. This is clearly demonstrated in Fig. 15.13 using laser excitation with 325 nm. The similar effect was also observed before at synchrotron excitations with shorter wavelengths [20]. At 300 nm excitation, the peaks located at 587, 621, 687, and 698 nm are the best seen for the samples with the lowest Eu concentrations. Then they disappear at $x = 0.1$ for the samples obtained by the solid-state method, whereas these lines are clearly revealed at concentration $x = 0.1$ for the samples obtained by the coprecipitation method (Fig. 15.3b, curve 2). For the samples with $x = 0.3$, the noted lines disappear for the samples obtained by both methods of synthesis. It was also shown previously that structure of emission spectra of the $La_{1-x-y}Eu_yVO_4$ nanoparticles does not essentially depend on excitation wavelength [20].

The observed dependencies can be assigned to transformation from monoclinic phase to tetragonal phase (see XRD analysis Chapter above). Really, the observed luminescence lines in the 580–720 nm spectral range are by the $^5D_0 \rightarrow {}^7F_J$ ($J = 0$, 1, 2, 3, 4) electron radiation transitions in the inner $4f^n$ shell of the Eu^{3+} ions. The

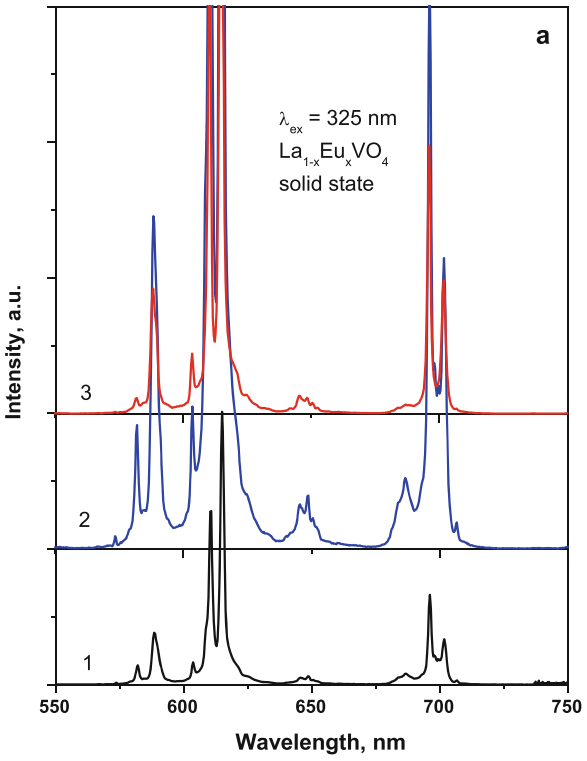

Fig. 15.13 (**a**) Emission spectra of the $La_{1-x}Eu_xVO_4$ nanoparticles synthesized by solid-state method, $\lambda_{ex} = 325$ nm, $x = 0.05$ (1), 0.1 (2) and 0.3 (3). (**b**) Emission spectra of the $La_{1-x}Eu_xVO_4$ nanoparticles synthesized by coprecipitation method, $\lambda_{ex} = 325$ nm, $x = 0.05$ (1), 0.1 (2) and 0.3 (3). (**c**) Emission spectra of the $La_{1-x}Eu_xVO_4$ nanoparticles synthesized by sol-gel method, $\lambda_{ex} = 325$ nm, $x = 0.05$ (1), 0.1 (2) and 0.3 (3)

Fig. 15.13 (continued)

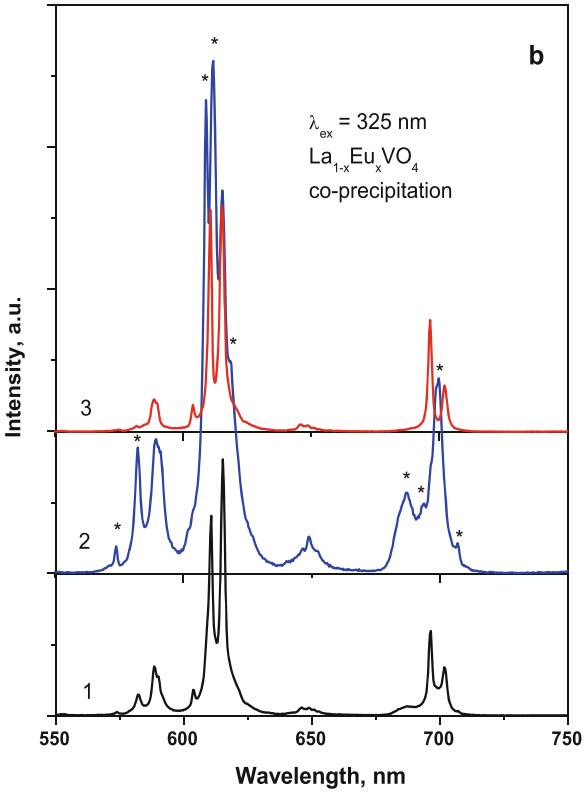

^7F_J energy levels may be split in the crystal field on the $2j + 1$ sub-levels, but some of possible transitions can be forbidden by the symmetry rules [77]. If the Eu^{3+} ions occupy the site of the La^{3+} ions in tetragonal $LaVO_4$ crystal lattice (I41/amd space group), they have D_{2d} site symmetry. In such a case, group theory predicts no luminescence peaks from $^5D_0 \rightarrow {}^7F_0$ transition, two lines from the $^5D_0 \rightarrow {}^7F_1$ and three lines from the $^5D_0 \rightarrow {}^7F_2$ transitions. If the Eu^{3+} ions occupy the site of the La^{3+} ions in monoclinic $LaVO_4$ crystal lattice ($P2_1/n$ space group), they have C_1 site symmetry. In this case, group theory predicts manifestation of all possible transitions: one luminescence peak from the $^5D_0 \rightarrow {}^7F_0$ transition, three lines from $^5D_0 \rightarrow {}^7F_1$, and five lines from the $^5D_0 \rightarrow {}^7F_2$ transitions [48, 49].

It is clearly seen from Fig. 15.13 that noted expectations are exactly realized for the investigated nanoparticles. So, for the samples with low europium content, we have observed three lines in the $J = 1$ range and five lines in the $J = 2$ range (marked by the arrows in Fig. 15.3, curves 1). (Lines in the $J = 3$ range have weak intensity, lines in the $J = 4$ range are strongly overlapped, that is why it is difficult to separate for these ranges all spectral components of emission transitions.) Thus, properties of luminescence spectra for vanadates of the noted composition obtained by both methods reveal monoclinic structure of their lattice. Therefore, for

Fig. 15.13 (continued)

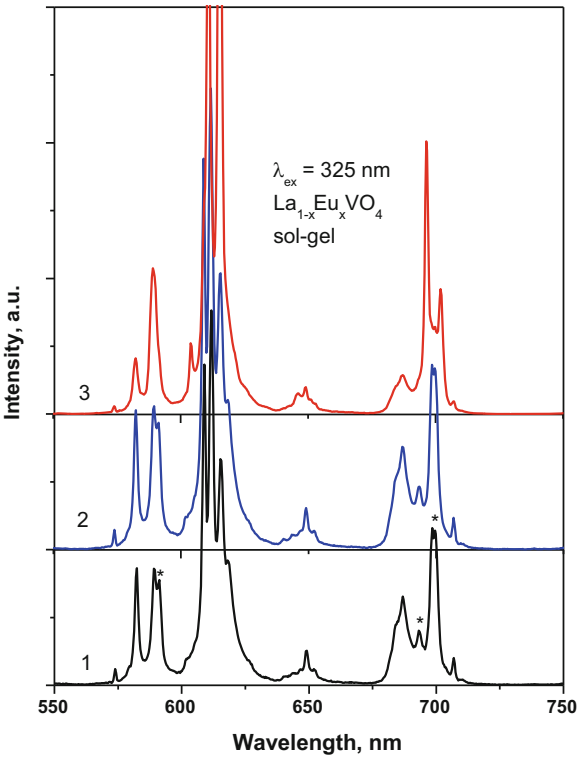

these compositions the Eu^{3+} ions are impurities substituting the La^{3+} ions without changes of crystal lattice. With increasing of the europium content, transformation of crystal lattice structure from monoclinic to tetragonal occurs. This is reflected in transformation of spectra; structure of those at $0.1 \leq x \leq 0.3$ corresponds to high symmetry coordination of the Eu^{3+} ions by oxygen ions.

It has to be emphasized that transformation of the spectra with increasing of the Eu^{3+} concentration takes place with different rates for compounds synthesized by the different methods. For the samples obtained by solid-state method, we have observed at $x = 0.1$ the spectra that completely corresponded to the Eu^{3+} arrangement in tetragonal vanadate structure (Fig. 15.13a), whereas for the same vanadate obtained by coprecipitation and sol-gel methods spectral lines characteristic for monoclinic vanadates remain also at $x = 0.1$ (Fig. 15.13b and c). These effects should be more prominent for the Ca-doped samples, where co-existence of monoclinic and tetragonal phases is observed up to $x = 0.15$ (Fig. 15.5).

15.9.2 *Influence of Ca-Doping on Luminescence Properties of the Sol-Gel $La_{1-x}Eu_xVO_4$ Nanoparticles*

Structure and intensity of the $La_{1-x-y}Eu_yCa_xVO_4$ samples emission depend on impurity concentration (Fig. 15.14) and excitation wavelength (Fig. 15.15 [26]).

For the $La_{0.8}Eu_{0.1}Ca_{0.1}VO_4$ sample, which is just a mixture of monoclinic and tetragonal phases (see Fig. 15.5), the photoluminescence (PL) lines at 586, 592.5, 607, 611, 614, 618, 649, 697, and 702 nm (marked by the arrows in Fig. 15.15, curve 2) are observed at all the applied λ_{ex}. (We call this set of the lines as "first set.") Note also that the ratio of intensity of the lines at 611, 614, and 618 nm changes if λ_{ex} varies. Besides, intensive lines at 580, 590, 591.7, 595.6, 608.7, and 622 and lines near 645, 651, 655, 706, and 708 nm (marked by arrows with asterisk at Fig. 15.15, curve 3) are distinctively observed in the spectra measured at $\lambda_{ex} = 405$ nm. (We call this set of the lines as "second set.") So, the measured emission spectra are the superposition of two sets of luminescence lines. Since we have shown above that the sample $La_{0.8}Eu_{0.1}Ca_{0.1}VO_4$ is just a mixture of two crystalline phases, we have first to suppose that these sets are related to emission

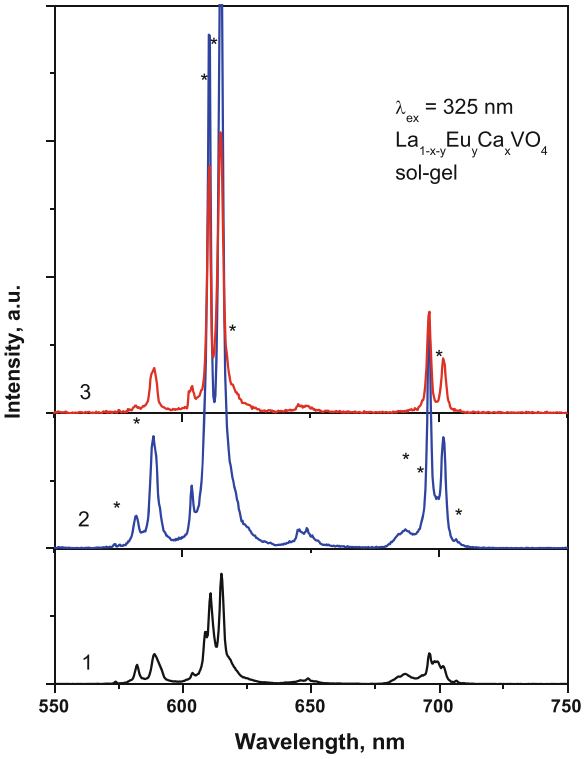

Fig. 15.14 (**a**) Emission spectra of the $La_{1-x-y}Eu_yCa_xVO_4$ nanoparticles synthesized by sol-gel method, $\lambda_{ex} = 325$ nm, $x = y = 0.1$ (1), 0.15 (2) and 0.2 (3). (**b**) Emission spectra of the $La_{1-x-y}Eu_yCa_xVO_4$ nanoparticles synthesized by sol-gel method, $\lambda_{ex} = 405$ nm, $x = y = 0.1$ (1), 0.15 (2) and 0.2 (3)

Fig. 15.14 (continued)

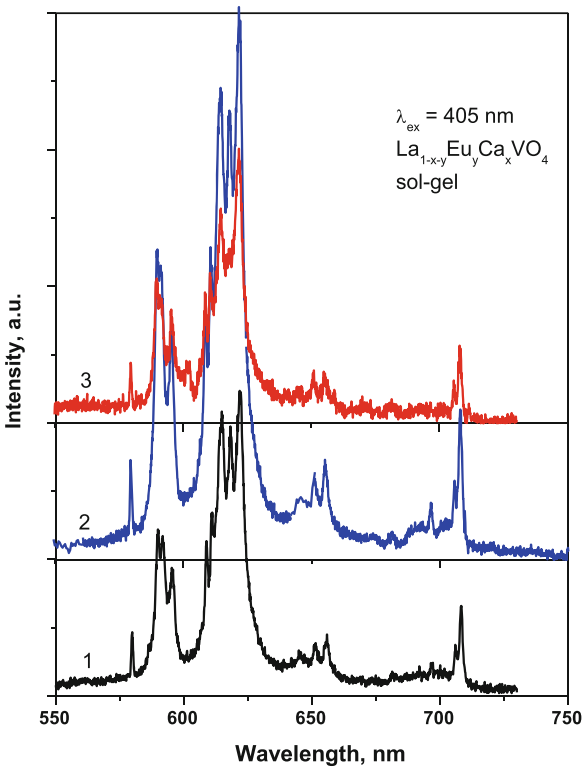

of Eu^{3+} centers in monoclinic and tetragonal phases as it was described above for the Ca-free $La_{1-x}Eu_xVO_4$ nanoparticles.

With the intent to clarify this assumption we performed study of the luminescence spectra dependence on the samples composition at the same excitation wave length, $\lambda_{ex} = 405$ nm (Fig. 15.14b). We found that the emission spectra of the samples where $x = 0.1$ and 0.15 are very close to each other. This finding agrees with the statement that these samples are the mixture of two phases. Tetragonal phase dominates in the $La_{0.6}Eu_{0.2}Ca_{0.2}VO_4$ sample, and we see that "second set" of the luminescence lines also dominates in the spectrum of this sample, but we see also that mentioned before line at 618 nm is vanished in this spectrum. Thus, we concluded that not only competition between content of the crystal phases influences luminescence behavior. Let's discuss this question in more detail.

So, it was not surprising that accounting the spectra in Fig. 15.15 in sum we have found one line for the $^5D_0 \rightarrow {}^7F_0$ (spectral range 570–585 nm), five lines (586, 592.5, 590, 591.7, 595.6 nm) for the $^5D_0 \rightarrow {}^7F_1$ (spectral range 585–600 nm), and seven lines (607, 614, 618, 608.7, 611, 614, 622 nm) for $^5D_0 \rightarrow {}^7F_2$ transitions (spectral range 600–650 nm), as this figure shows the luminescence spectra of the sample which is mixture of the monoclinic and tetragonal phases. This statement also concerns the spectra 1 and 2 in Fig. 15.14b, as they also represent luminescence

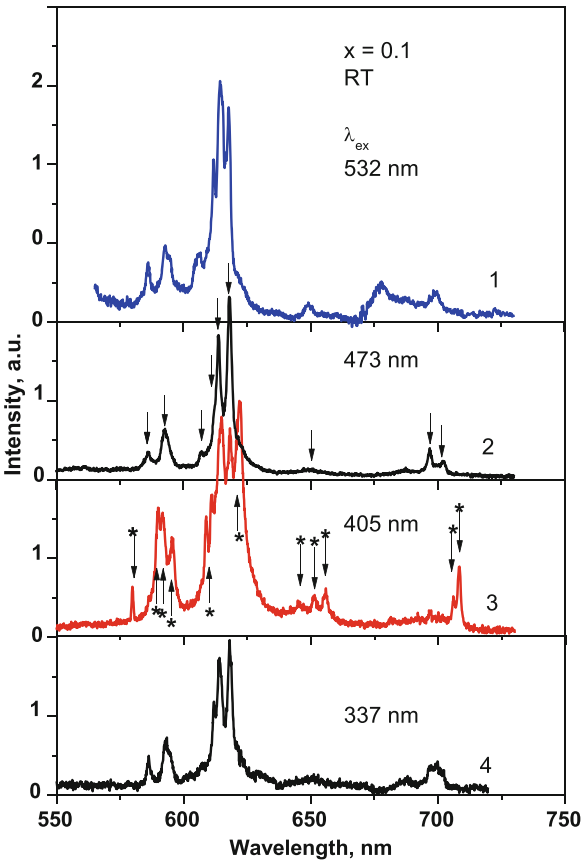

Fig. 15.15 Emission spectra of the $La_{0.8}Eu_{0.1}Ca_{0.1}VO_4$ nanoparticles at $\lambda_{ex} = 532$ (1, 5), 473 (2), 405 (3), and 337 nm (4) [26]

of the mixture, $x = 0.1$ and 0.15, respectively. It was surprising that we see intensive line from the $^5D_0 \rightarrow {}^7F_0$ transition for the $La_{0.6}Eu_{0.2}Ca_{0.2}VO_4$ sample which represents only a tetragonal crystal structure (Fig. 15.14b, curve 3). Thus, we supposed that spectral transformations shown in Figs. 15.14 and 15.15 are related also to role of Ca^{2+} cations, as their concentration increases by 2–3 times when going from $x = 0.1$ to 0.2 (see Sect. 3.2).

In fact, obtained results mean that at least two different types of luminescence centers formed by the ions Eu^{3+} in the sample of tetragonal structure contribute to the PL spectra. We ascribed the above-mentioned spectral lines to emission of type I ("first set" of lines) and type II of the centers ("second set" of lines). Emission line from the $^5D_0 \rightarrow {}^7F_0$ transition (580 nm) was observed only for the type II centers, and the most intensive lines of the $^5D_0 \rightarrow {}^7F_2$ and $^5D_0 \rightarrow {}^7F_4$ transitions for these centers are located at 622 and 708 nm, respectively. For type I centers, the most intensive lines are located at 614 and 697 nm. These spectral features allow us to do assumption that types I and II of centers are characterized by different symmetry of the Eu^{3+} ions environment: the type I centers are characterized by higher site

symmetry and the type II centers are characterized by lower site symmetry in the crystal lattices [77]. We supposed that type I centers are formed by the Eu^{3+} ions in their regular positions in the crystal lattice (D_{2d} symmetry).

As for the type II centers, we suppose that they can be formed by Eu^{3+} ions disturbed by defects generated as a result of Ca^{2+} cations incorporation into $LaVO_4$ crystal lattice. Taking into account that above-noted lines of type II centers (e.g., lines at 622 and 708 nm) were not observed for the Ca^{2+}-free sample (Fig. 15.13), we concluded that the most possible origin of the type II centers is the Eu^{3+} ions disturbed by Ca-induced defects. In the case of the doped with calcium $LaVO_4$ lattice, the Ca^{2+} dopant has to replace the La^{3+} ions. Then, effective "−1" charge arises. Charge compensation of mentioned "−1" charge is needed, as the crystal has to be electroneutral. This compensation can be achieved via the formation of one oxygen vacancy, $[V_O]^{2+}$, on each two Ca^{2+}/La^{3+} replacements. Thus, for the Ca^{2+} dopants arrangement in the $LaVO_4$ crystal lattice, we should expect that some of the Eu^{3+} ions are under effect of both neighbor Ca^{2+} cations and oxygen vacancy. Thus, we can assume that such Eu^{3+} ions are just the type II of the luminescence centers, and their local symmetry is lower if comparing to symmetry of the type I centers. Taking into account that $^5D_0 \rightarrow {}^7F_0$ transition emission line (near 580 nm) is observed in the spectra (Figs. 15.14 and 15.15), the symmetry of type II centers may be C_2 or C_s [47–49]. The C_2 symmetry of the Eu^{3+} surrounding in the I41/amd space group of orthovanadates can be achieved only by equal distortions of two oxygen positions. Therefore, we assume that case of the C_s symmetry of the Eu^{3+} surrounding at the type II centers is more probable.

The observed differences in excitation spectra measured in the emission lines corresponded to different types of centers (614 and 622 nm for type I and II centers, respectively) confirm the made above assumptions [26]. The wide band at 320 nm was more intensive in the excitation spectra of type I centers. The 320 nm band was also observed in the spectra of the $La_{0.9}Eu_{0.1}VO_4$ sample (Fig. 15.16, curve 2). This band is caused by electron transitions in the vanadate VO_4^{3-} groups. Therefore,

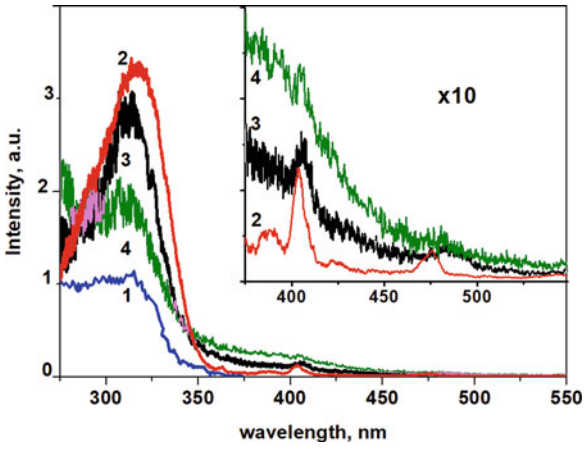

Fig. 15.16 Excitation spectra of the $LaVO_4$ (1), $La_{0.9}Eu_{0.1}VO_4$ (2), and $La_{0.6}Eu_{0.2}Ca_{0.2}VO_4$ (3, 4) sol-gel nanoparticles at $\lambda_{em} = 550$ (1), 614 (2, 3), and 622 nm (4); $T = 77$ K (1), $T =$ RT (2–4)

the type I centers are better excited through the matrix than type II centers, which confirms our assumptions about relation of the type I centers with the Eu^{3+} ions in the regular positions in the crystal lattice.

15.10 Conclusions

The $La_{1-x}Eu_xVO_4$ ($0 \leq x \leq 0.4$) nanoparticles were synthesized by solid-state, coprecipitation, and sol-gel methods. The $La_{1-x-y}Eu_yCa_xVO_4$ ($0 \leq x, y \leq 0.2$) nanoparticles were synthesized by sol-gel method. Phase composition of the sample depends on the x, y values.

Increasing concentration of europium, Eu^{3+}, and calcium ions, Ca^{2+}, in $La_{1-x-y}Eu_yCa_xVO_4$ solid solutions causes changing of the crystal structure from monoclinic to tetragonal.

Phase transformation and especially Ca^{2+} ions influence IR spectroscopy and luminescence behavior of studied compounds, as Ca^{2+} ions impact both VO_4^{3-} molecular groups conformation and La^{3+} and Eu^{3+} ions nearest neighborhood.

Emission of the investigated samples is observed in the 550–730 nm spectral range and it consists of narrow spectral lines. These lines are caused by the $^5D_0 \rightarrow {}^7F_J$ electron transitions in the Eu^{3+} ions.

The Eu^{3+} ions form two types of emission centers in the samples under study. The assumption was made that type I centers are formed by the Eu^{3+} ions in their regular positions in the crystal lattice, while the type II centers have complex structure, and they consist of Eu^{3+} ions, Ca^{2+} cations, and oxygen vacancies.

Acknowledgments This project has received funding from Ministry of Education and Science of Ukraine and from the EU-H2020 research and innovation program under grant agreement No 654360 having benefited from the access provided by Institute of Electronic Structure & Laser (IESL) of Foundation for Research & Technology Hellas (FORTH) in Heraklion, Crete, Greece within the framework of the NFFA-Europe Transnational Access Activity.

References

1. Palilla FC, Levine AK, Rinkevics M (1965) Rare earth activated phosphors based on yttrium orthovanadate and related compounds. J Electrochem Soc 112(8):776
2. Blasse G, Bril A (1969) Luminescence of phosphors based on host lattices ABO4 (A is Sc, In; B is P, V, Nb). J Chem Phys 50:2974
3. Palilla FC, Levine AK (1966) YVO4:Eu: a highly efficient, red-emitting phosphor for high pressure mercury lamps. Appl Opt 5:1467–1468
4. Panayiotakis G, Cavouras D, Kandarakis I, Nomicos C (1996) A study of X-ray luminescence and spectral compatibility of europium-activated yttrium-vanadate (YVO4: Eu) screens for medical imaging applications. Appl Phys A Mater Sci Process 62(5):483–486
5. Krumpel AH, van der Kolk E, Cavalli E, Boutinaud P, Bettinelli M, Dorenbos P (2009) Lanthanide 4f-level location in $AVO_4:Ln^{3+}$ (A = La, Gd, Lu) crystals. J Phys Condens Matter 21:115503–115508

6. Panchal V, Errandonea D, Segura A, Rodríguez-Hernandez P, Muñoz A, Lopez-Moreno S, Bettinelli M (2011) The electronic structure of zircon-type orthovanadates: effects of high-pressure and cation substitution. J Appl Phys 110:043723
7. Kang JH, Im WB, Lee DC, Kim JY, Jeon DY, Kang YC, Jung KY (2005) Correlation of photoluminescence of (Y,Ln)VO_4:Eu^{3+} (Ln = Gd and La) phosphors with their crystal structures. Solid State Commun 133:651–656
8. Wang Q, Zhang Z, Zheng Y, Cai W, Yifei Y (2012) Multiple irradiation triggered the formation of luminescent $LaVO_4$: Ln^{3+} nanorods and in cellulose gels. CrystEngComm 14:4786
9. Xu Z, Li C, Hou Z, Peng C, Lin J (2011) Morphological control and luminescence properties of lanthanide orthovanadate LnVO4 (Ln = La to Lu) nano−/microcrystals via hydrothermal process. CrystEngComm 13:474–482
10. Li K, Van Deun R (2018) Eu^{3+} /Sm^{3+} −doped $Na_2BiMg_2(VO_4)_3$ from substitution of Ca^{2+} by Na^+ and Bi^{3+} in $Ca_2NaMg_2(VO_4)_3$: color-tunable luminescence via efficient energy transfer from $(VO_4)^{3-}$ to Eu^{3+} /Sm^{3+} ions. Dyes Pigments 155:258–264
11. Venkatesan R, Velumani S, Ordon K, Makowska-Janusik M, Corbel G (2018) Nanostructured bismuth vanadate ($BiVO_4$) thin films for efficient visible light photocatalysis. Mater Chem Phys 205:325–333
12. Mialon G, Gohin M, Gacoin T, Boilot J-P (2008) High temperature strategy for oxide nanoparticle synthesis. ACS Nano 2(12):2505–2512
13. Venkataraman BV, Sudha S (2005) Vanadium toxicity. Asian J Exp Sci 19(2):127–134
14. Clark AS, Fagant JM, Mitch WE (1985) Selectivity of the insulin-like actions of vanadate on glucose and protein metabolism in skeletal muscle. Biochem J 232:273–276
15. Biswas P, Kumar V, Padha N, Swart HC (2017) Synthesis, structural and luminescence studies of $LiSrVO_4$:Sm^{3+} nanophosphor to fill amber gap in LEDs under n-UV excitation. J Mater Sci Mater Electron 28:6159–6168
16. Nakajima T, Isobe M, Tsuchiya T, Ueda Y, Kumagai T (2008) Direct fabrication of meta-vanadate phosphor films on organic substrates for white-light-emitting devices. Nat Mater 7:735–740
17. Shinde KN, Singh R, Dhoble SJ (2014) Photoluminescent characteristics of the single-host white-light-emitting $Sr_{3-3x/2}(VO_4)_2$:xEu (0<x<0.3) phosphors for LEDs. J Lumin 146:91–96
18. Lin H-Y, Chang W-F, Chu S-Y (2013) Luminescence of $(Ca,Sr)_3(VO_4)_2$:Pr^{3+},Eu^{3+}phosphor for use in CuPc-based solar cells and white light-emitting diodes. J Lumin 133:194–199
19. Lisiecki R, Ryba-Romanowski W, Cavalli E, Bettinelli M (2010) Optical spectroscopy of Er^{3+}-doped $LaVO_4$ crystal. J Lumin 130:131–136
20. Chukova O, Nedilko S, Nedilko SG, Sherbatsky V, Voitenko T (2013) Comparable structural and luminescent characterization of the $La_{1-x}Eu_xVO_4$ solid solutions synthesized by solid state and co-precipitation methods. Solid State Phenom 200:186–192
21. Park SW, Yang HK, Chung JW, Moon BK, Choi BC, Jeong JH (2010) Enhanced red emission of $LaVO_4$:Eu^{3+} phosphors by Li-doping. J Korean Phys Soc 57:1764–1768
22. Xue C, Xia Z (2013) Luminescence properties of $Li_2Ca_2ScV_3O_{12}$ and $Li_2Ca_2ScV_3O_{12}$:Eu^{3+} synthesized by solid-state reaction method. Opt Mater 35:2736–2739
23. Chukova OV, Nedilko SG, Slepets AA, Nedilko S, Voitenko TA (2018) Synthesis and investigation of La,Ca -doped $EuVO_4$ nanoparticles with enhanced excitation by near violet light. Phys Status Solidi A 215:1700894–1700897
24. Krishna Bharat L, Jeon S-K, Gopi Krishna K, Yu JS (2017) Rare-earth free self-luminescent $Ca_2KZn_2(VO_4)_3$ phosphors for intense white light-emitting diodes. Sci Rep 7:42348
25. Li T, Luo J, Honda Z, Fukuda T, Kamata N (2012) Sintering condition and optical properties of $Zn_3V_2O_8$. Phosphor Adv Mater Phys Chem 2:173–177
26. Chukova OV, Nedilko SG, Slepets AA, Nedilko SA, Voitenko TA (2017) Synthesis and properties of the $La_{1-x-y}Eu_yCa_xVO_4$, ($0 \le x, y \le 0.2$) compounds. Nanoscale Res Lett 12:340–311
27. Bhatkar VB (2013) Synthesis and luminescence properties of yttrium vanadate based phosphors. Int J Eng Sci Innov Technol 2:426–432

28. Yang P, Huang S, Kong D, Lin J, Fu H (2007) Luminescence functionalization of SBA-15 by YVO4:Eu 3+ as a novel drug delivery system. Inorg Chem 46(8):3203–3211
29. Shen J, Sun L-D, Yan C-H (2008) Luminescent rare earth nanomaterials for bioprobe applications. Dalton Trans 42(14):5661–5808
30. Chornii V, Chukova O, Nedilko SG, Nedilko S, Voitenko T (2016) Enhancement of emission intensity of $LaVO_4:RE^{3+}$ luminescent solar light absorbers. Phys Status Solidi C 13(1):40–46
31. Nedilko SG, Chornii V, Chukova O, Degoda V, Bychkov K, Terebilenko K, Slobodyanik M (2016) Luminescence properties of the new complex La,$BiVO_4$: Mo,Eu compounds as materials for down-shifting of VUV–UV radiation. Radiat Meas 90:282–286
32. Van der Ende BM, Aarts L, Meijerink A (2009) Lanthanide ions as spectral converters for solar cells. Phys Chem Chem Phys 11:11081–11095
33. Kumar V, Khan AF, Chawla S (2013) Intense red-emitting multi-rare-earth doped nanoparticles of YVO 4 for spectrum conversion towards improved energy harvesting by solar cells. J Phys D Appl Phys 46:365101–365109
34. Lewis NS, Nocera DG (2006) Powering the planet: chemical challenges in solar energy utilization. Proc Natl Acad Sci U S A 103:15729–15735
35. Morton O (2006) Solar energy: a new day dawning? Silicon Valley sunrise. Nature 443:19–22
36. Van der Zwaan B, Rabl A (2003) Prospects for PV: a learning curve analysis. Sol Energy 74:19–31
37. Goetzberger A, Hebling C, Schock HW (2003) Photovoltaic materials. History, status and outlook. Mater Sci Eng R 40:1–46
38. Huang X, Han S, Huang W, Liu X (2013) Enhancing solar cell efficiency: the search for luminescent materials as spectral converters. Chem Soc Rev 42:173–201
39. Henderson B, Imbusch GF (1989) Optical spectroscopy of inorganic solids. Oxford University Press, Oxford, 657 p
40. Auzel F (2005) Up-conversions in RE-doped solids. In: Liu G, Jacquier B (eds) Spectroscopic properties of rare earths in optical materials. Springer, Berlin, pp 266–319
41. Li W, Li D, Lin Y, Wang P, Chen W, Fu X, Shao Y (2012) Evidence for the active species involved in the photodegradation process of methyl orange on TiO_2. J Phys Chem 116(5):3552–3560
42. Wang D, Li R, Zhu J, Shi J, Han J, Zong X, Li C (2012) Photocatalytic water oxidation on $BiVO_4$ with the electrocatalyst as an oxidation cocatalyst: essential relations between electrocatalyst and photocatalyst. J Phys Chem 116(8):5082–5089
43. Zhang Y, Li G, Yang X, Yang H, Lu Z, Chen R (2013) Monoclinic $BiVO_4$ micro-/nanostructures: microwave and ultrasonic wave combined synthesis and their visible-light photocatalytic activities. J Alloys Compd 551:544–550
44. Sivakumar V, Suresh R, Giribabu K, Narayanan V (2015) $BiVO_4$ nanoparticles: preparation, characterization and photocatalytic activity. Cogent Chem 1:1074647
45. Yang X, Zuo W, Li F, Li T (2015) Surfactant-free and controlled synthesis of hexagonal $CeVO_4$ nanoplates: photocatalytic activity and superhydrophobic property. ChemistryOpen 4:288–294
46. Hazen RM, Finger LW (1979) Crystal structure and compressibility of zircon at high pressure. Am Mineral 64:196–201
47. Errandonea D, Garg AB (2018) Recent progress on the characterization of the high-pressure behaviour of AVO4 orthovanadates. Prog Mater Sci 97:123–169
48. Chukova OV, Nedilko SG, Slepets AA, Nedilko S, Voitenko TA (2017) Crystal field effect on luminescent characteristics of europium doped orthovanadate nanoparticles, proceedings of the 2017 IEEE 7th international conference on nanomaterials: applications and properties. NAP 2017:81903497–81903495
49. Park SW, Yang HK, Chung JW, Chen Y, Moon BK, Cho BC, Jeon JH, Kim JH (2010) Photoluminescent properties of $LaVO_4$ Eu^{3+} by structural transformation. Physica B 405:4040–4044
50. Errandonea D, Pellicer-Porres J, Martinez-Garcia D, Ruiz-Fuertes J, Friedrich A, Morgenroth W, Popescu C, Rodríguez-Hernández P, Muñoz A, Bettinelli M (2016) Phase Stability of Lanthanum Orthovanadate at High Pressure. J Phys Chem C 120:13749–13762

51. Errandonea D, Achary SN, Pellicer-Porres J, Tyagi AK (2013) Pressure-induced transformations in PrVO4 and SmVO4 and isolation of high-pressure metastable phases. Inorg Chem 52:5464–5469
52. Chukova O, Nedilko S, Scherbatskyi V (2012) Effect of annealing on luminescence properties of the undoped and rare earth doped lead tungstate crystals. Opt Mater 34:2071–2075
53. Zorenko Y, Gorbenko V, Voloshinovskii A, Stryganyuk G, Nedilko S, Degoda V, Chukova O (2005) Luminescence of Sc-related centers in single crystalline films of Lu $_3Al_5O_{12}$ garnet. Phys Status Solidi C 2:105–108
54. Malashkevich GE, Chukova OV, Nedilko SG, Shevchenko GP, Bokshyts YV, Kouhar VV (2016) Influence of gold nanoparticles on luminescence of Eu^{3+} ions sensitized by structural defects in germanate films. J Phys Chem C 120:15369–15377
55. Santos CC, Silva EN, Ayala AP, Guedes I, Pizani PS, Loong CK, Boatner LA (2007) Raman investigations of rare earth orthovanadates. J Appl Phys 101:053511
56. Huang Y, Seo H (2013) Structure and luminescence of new red-emitting materials-Eu^{3+-}doped triple orthovanadates $NaALa(VO_4)_2$ (A = Ca, Sr, Ba). J Am Ceram Soc 96:1181–1187
57. Chukova O, Nedilko S, Nedilko SG, Voitenko T, Gomenyuk O, Sheludko V (2015) Study of temperature behavior of luminescence emission of $LaVO_4$ and $La_{1-x}Eu_xVO_4$ powders. Solid State Phenom 230:153–159
58. Xu Z, Li C, Hou Z, Peng C, Lin J (2011) Morphological control and luminescence properties of lanthanide orthovanadate LnVO4 (Ln = La to Lu) nano-/microcrystals via hydrothermal process. CrystEngComm 13:474–482
59. Yoon SJ, Park K (2014) Synthesis and photoluminescent properties of white-emitting $Sr_{2.91}V_2O_8$:0.06:Eu^{3+} phosphors. Opt Mater 36:1305–1310
60. Chumha N, Kittiwachana S, Thongtem T, Thongtem S, Kaowphong S (2014) Synthesis and characterization of $GdVO_4$ nanostructures by a tartaric acid-assisted sol–gel method. Ceram Int 40:16337–16342
61. Chukova OV, Nedilko SG, Slepets AA, Nedilko S, Voitenko TA, Virko SV Influence of Ca^{2+} impurities on structure, morphological and optical characteristics of Eu_xVO_4 and $La_{1-x}Eu_xVO_4$ luminescent nanoparticles, Proceedings of the 2018 IEEE 8th international conference on nanomaterials: applications and properties, NAP 2018, volume, accepted paper
62. Liu J, Li Y (2007) Synthesis and self-assembly of luminescent Ln^{3+}-doped $LaVO_4$ uniform Nanocrystals. Adv Mater 19:1118–1122
63. Liu G, Duan X, Li H, Dong H (2009) Hydrothermal synthesis, characterization and optical properties of novel fishbone-like $LaVO_4$:Eu^{3+} nanocrystals. Mater Chem Phys 115:165–171
64. Escobar Von ME, Baran EJ (1978) Uber die tetragonale Modifikation von Lanthanorthowanadat. Z Anorg Allg Chem 441:273–277
65. Nakamoto K (1963) Infrared spectra of inorganic and coordination compounds. Wiley, New York, p 410
66. Lax M (1974) Symmetry principles in solid state and molecular physics, vol 499. Wiley, New York
67. Fang ZM, Hong Q, Zhou ZH, Dai SJ, Weng WZ, Wan HL (1999) Oxidative dehydrogenation of propane over a series of low-temperature rare earth orthovanadate catalysts prepared by the nitrate method. Catal Lett 61:39–44
68. Sun L, Zhao X, Li Y, Li P, Sun H, Cheng X, Fan W (2010) First-principles studies of electronic, optical and vibrational properties of $LaVO_4$ polymorph. J Appl Phys 108(9):093519
69. Baran EJ (1976) Die Schwingungsspektren von $Ca_3(VO_4)_2$ und $Ca_3(AsO)$. Z Anorg Allg Chem 497:131–136
70. Parhi P, Manivannan V, Kohl S, McCurdy P (2008) Synthesis and characterization of $M_3V_2O_8$ (M = Ca, Sr and Ba) by a solid-state metathesis approach. Bull Mater Sci (India) 31(6):885–890
71. Ardanova LI, Chukova OV, Getman EI, Marchenko VI, Nedilko SG, Scherbatskyi VP (2002) Luminescent properties of the $Ca_5(VO_4)_3OH$ apatites with the heterovalence calcium replacement on alkali and rare-earth elements. Funct Mater 9(2):326–331

72. Sobszyk M, Szymański D (2013) A study of optical properties of Sm^{3+} ions in α-$Na_3Y(VO_4)_2$ single crystals. J Lumin 142:96–102
73. Song D, Guo C, Li T (2015) Luminescence of the self-activated vanadate phosphors $Na_2LnMg_2V_3O_{12}$ (Ln = Y, Gd). Ceram Int 41:6518–6524
74. Tamilmani V, Sreeram KJ, Nair BU (2015) Catechin assisted phase and shape selection for luminescent $LaVO_4$ zircon. RSC Adv 5(100):82513–82523
75. Boyko R, Chukova OV, Gomenyuk OV, Nagornyi PG, Nedilko SG (2005) Origin of red luminescence of sodium titanium phosphate crystals contained chromium and titanium ions. Phys Status Solidi 2(1):712–715
76. Chukova O, Nedilko S, Scherbatskyi V (2010) Luminescent spectroscopy and structure of centers of the impurity Eu^{3+} ions in lead tungstate crystals. J Lumin 130(10):1805–1812
77. Wybourne BG (1965) Spectroscopic properties of ions in crystals. Wiley, New York, p 236

Chapter 16
Investigation of the Conditions of Synthesis of Alumo-Nickel Spinel

L. Frolova and T. Butyrina

16.1 Introduction

Materials based on aluminates of metals are used as magnetic materials, pigments, sensors, and catalysts [1–4].

Pigments are important materials that give colors to paints, plastics, rubber, cosmetics, ceramics, glass, and porcelain enamels, and that is why they are needed in industry. In the process of production, you can adjust the color, chemical and thermal stability. In addition, economic efficiency and environmental safety, corrosion resistance are very important. Organic pigments and dyes are brightly colored, but usually not as light-proof as inorganic pigments. Due to their thermal, chemical, and solar instability, organic coloring materials are limited by short-term applications. Spinel pigments are stable relative to sunlight, heat, and environmental changes [1, 2].

Spinel oxides (the general formula AB_2O_4) belong to the group of mixed metal oxides and are promising for use as pigments [3] because of their characteristic features. Spinels exhibit structural flexibility with respect to cations of chromophore, due to the formation of a continuous series of solid solutions. In addition, oxides exhibit the thermal and chemical resistance required for the application of a pigment [5, 6]. The replacement chromophore ion is introduced into any tetrahedral or octahedral positions for the A^{2+} or B^{3+} ion, which leads to the coloration of the product. The exact correction of the pigment color is possible by choosing a cation-chromophore and the degree of its replacement. Today, the problem of synthesis of materials with given physical and chemical properties is actual. In some cases, these properties are very dependent on the chosen synthesis method, the temperature

L. Frolova (✉) · T. Butyrina
Ukrainian State University of Chemical Technology, Dnipro, Ukraine

O. Fesenko, L. Yatsenko (eds.), *Nanocomposites, Nanostructures, and Their Applications*, Springer Proceedings in Physics 221,
https://doi.org/10.1007/978-3-030-17759-1_16

regime, the atmosphere in which the synthesis is carried out. Nickel pigments represent a large group of brightly colored water-insoluble compounds. For a long time, the production of ceramic pigments was carried out empirically; in this regard, the pigments were a group of colored compounds, the composition of which in most cases was not determined. A fundamental study of the color and crystalline structure of spinel pigments was not conducted.

The formation of $NiAl_2O_4$ by calcination of nickel and aluminum oxides is complicated due to the need to use high temperatures (1300–1500 °C) and low effective because the solubility of cations of chromophore in Al_2O_3 is limited, and the heterogeneous process of spinel formation is quite long. Therefore, as a synthesis, the method of coprecipitation of nickel-aluminum polyhydroxides in the necessary ratios with subsequent heat treatment was chosen. A lot of attention was paid to the study of the mechanism of the formation of hydroxides, oxyhydroxides, and oxides of nickel and aluminum [7, 8]. The process of formation of complex nickel-aluminum hydroxide has been poorly investigated. However, undoubtedly, at the stage of formation of nickel hydroxide and aluminum hydroxide, primary particles are formed that determine the morphology and macro- and microstructure of the particles of the final compound [9–13].

In addition, the size of the particles is an important technological parameter, so for obtaining a fine particle of nickel aluminate, knowledge of the kinetics and mechanism of both the formation of nickel hydroxide and aluminum hydroxide, as well as the influence of the formation of polyhydroxocomplexes, is required.

The main purpose of this paper is to study the process of coprecipitation of polyhydroxocomplexes of nickel and aluminum from solutions of nickel (II) sulfate and aluminum (III) sulfate with sodium hydroxide and study the process of its conversion to nickel aluminate and to check its properties.

16.2 Methodology of the Experiment

For the thermodynamic analysis of the deposition process, the software package MEDUSA was used then based on the calculation of the concentration of compounds in the solution in accordance with the equilibrium constant of their formation reaction [14].

Potentiometric titration was performed on pH-meter-millivoltmetry pH -150. The glass electrode of the marks ESL-15-11 as a measuring electrode was used. Silver-silver chloride electrode marks EVL-1G4 was used as a comparative electrode. The measurement error of the pH value was ±0.02 units. For comparison of results and simplifying interpretation curves, the volume NaOH is added, resulting in the molar ratio $[OH - / (Ni^{2+} + \cdot Al^{3+})]$. The conductivity was measured using the Kolraush bridge. Nickel hydroxide and aluminum hydroxide were prepared by coprecipitation from a mixture of solutions of nickel sulfate and aluminum sulfate with sodium hydroxide with a corresponding ratio of sulfates solutions of 1:2. The concentration of nickel, aluminum, and OH^- ions was determined by standard methods [15].

16.3 Results and Discussion

The pH values of precipitation were selected based on the information obtained with using the MEDUSA software for cations of aluminum and nickel (Fig. 16.1).

Calculations was shown that the formation of aluminum hydroxide occurs through the formation of salt $AlOHSO_4$ at pH = 2–3, with an increase in pH to 7 formed Al $(OH)_3$, at pH = 12 the precipitate is dissolve.

The obtained graph shows that the precipitation of nickel hydroxide begins at pH = 7, complete precipitation is achieved at pH = 8.

It is known that the pH of deposition depends on many factors, and does not coincide with calculated value.

The results of the study of the hydroxide deposition process in the Ni^{2+}-Al^{3+}-SO_4^{2-} -H_2O system carried out by the methods of pH-metric titration and chemical analysis are presented in Figs. 16.2 and 16.3.

The purpose of pH-metric research is the establishment of the laws of precipitation of hydroxides Ni^{2+} and Al^{3+}. On the titration curve of an individual solution of aluminum sulfate after the addition of the first portions of the alkali there is a buffer zone (pH = 2.5–3), which corresponds to the cation hydrolysis. Formation of aluminum hydroxide occurs at pH = 5 and ends at pH = 10. With further addition there is the formation of sodium aluminate, which is reflected on titration curves.

The results of the study of the $NiSO_4$-NaOH-H_2O system by the potentiometric method (Fig. 16.2) show that in the ratio $[OH^-/Ni^{2+}] = 2$, complete precipitation in the form of nickel hydroxide $Ni(OH)_2$ occurs.

On the titration curve of the Ni^{2+} -Al^{3+} solution with a Ni^{2+}: Al^{3+} = 1: 2 ratio corresponding to the spinel, there is one jump that does not coincide with the curve for the individual nickel and aluminum hydroxide. Immediately after the addition of the first drops began alkali buffer zone, which is at a pH ≈ 4.0–4.5 (Fig. 16.2). The buffer zone ends with a jump at $n \approx 2$, which corresponds to a complete transformation into polyhydroxocomplexes of aluminum and nickel.

In determining the final concentrations of Ni^{2+}, Al^{3+}, and OH^- groups, it was found that the addition of alkali undergoes a gradual formation of precipitates, which is accompanied by a decrease in the concentration of initial solutions. At high pH in an individual solution, aluminum hydroxide begins to dissolve, because it has an amphoteric nature.

Therefore, to the value $n \approx 1.5$–2, precipitates are formed and the electrical conductivity decreases, and at $n \approx 2.5$–3, the precipitates begin to dissolve intensively. As can be seen from the curve, at the dissolution of the precipitate, the concentration of Al^{3+} ions increases, and, accordingly, the electrical conductivity increases (Fig. 16.4). The dissolution of the precipitate is clearly noticeable on the curves of residual concentrations of Ni^{2+}, Al^{3+}, and OH^- ions, as the concentration of Al^{3+} ions increases with the dissolution of aluminum hydroxide (Fig. 16.3).

The optimal range of values of pH, in which the almost complete precipitation of Ni^{2+} and Al^{3+} occurs, is 8–9, which corresponds to jump on the titration curve (Fig. 16.2).

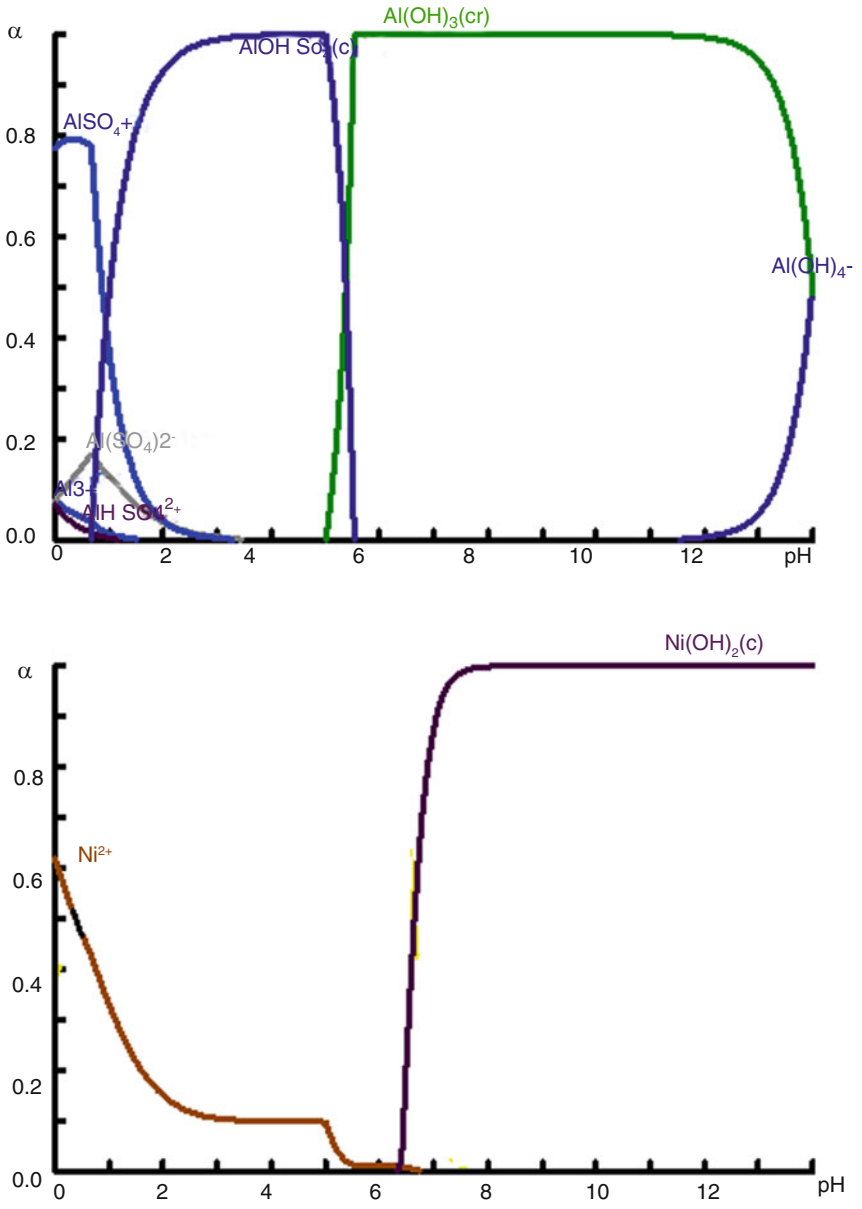

Fig. 16.1 Diagram of distribution of molar particles of hydroxocomplexes of aluminum (III) (**a**) and nickel (II) (**b**) at different pH of the solution (temperature 25 °C, $C\text{к} = 0.5\text{M}$)

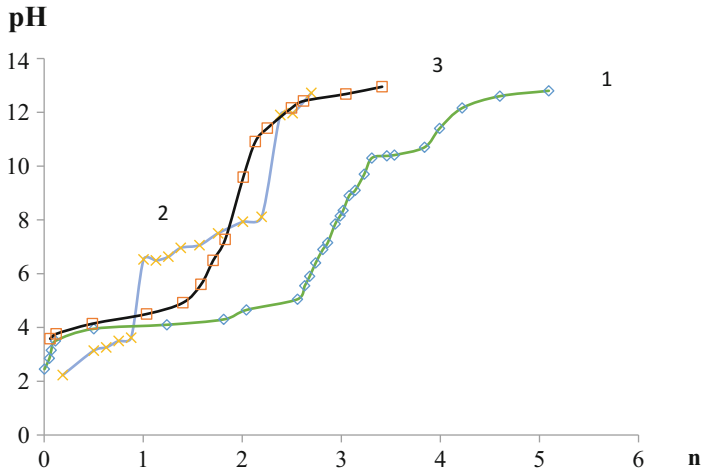

Fig. 16.2 Curves of pH-metric titration of solutions: 1, nickel sulfate; 2, aluminum sulfate; 3, nickel sulfate and aluminum sulfate

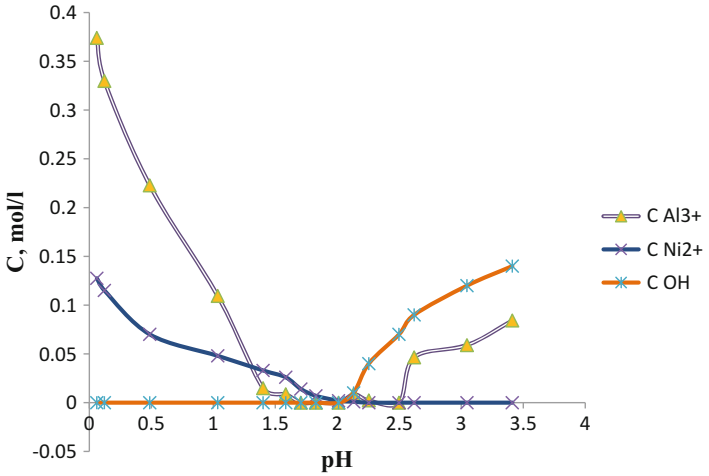

Fig. 16.3 Curves of dependence of residual concentrations of Ni^{2+}, Al^{3+}, and OH^{-} groups ions

Thermogravimetric analysis showed that during heat treatment up to 1000 °C the mass loss of the samples synthesized under the indicated optimum conditions is 40.00–43.07%. The process of mass loss completes at lower temperatures compared with other data, especially for precipitates obtained from solutions (950°C instead of 1300–1500°C).

The results of this research allow us to develop the scientific basis for the synthesis of $NiAl_2O_4$ spinel from chemically precipitated mixtures, which will ensure that it is obtained in a highly dispersed state at high output of the finished

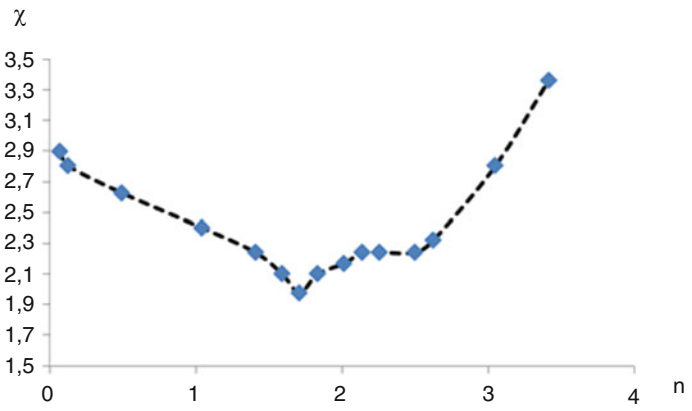

Fig. 16.4 Curves of dependence of electrical conductivity on the ratio of OH/Mn

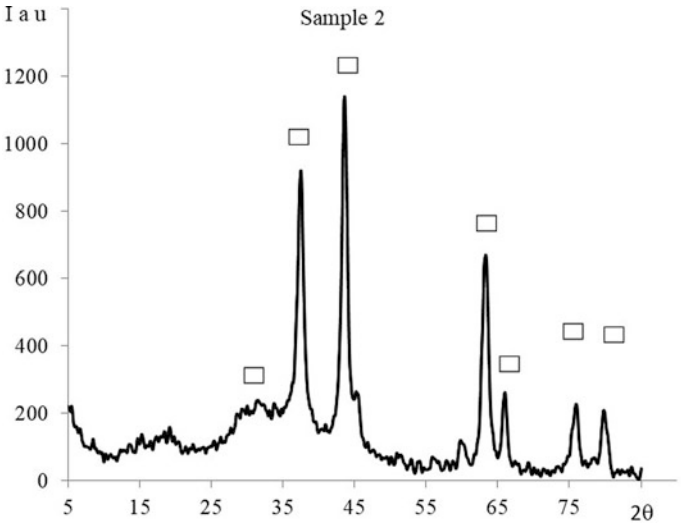

Fig. 16.5 X-ray pattern of the sample □ -$NiAl_2O_4$

product and the possibility of lowering the temperature of the next sintering of materials on its basis.

A combination of independent methods of research has established the optimal range of pH values for the preparation of precipitates – the synthesis of alumo-nickel spinel. It is shown that from the precipitates obtained under optimum conditions, in the following process of heat treatment, a single phase – an alumo-nickel spinel is formed. X-ray pattern of pigment is presented in Fig. 16.5.

With the spectrophotometric method were obtained color characteristics of pigment.

Table 16.1 Color pigment characteristics

№ з/п	*X*	*Y*	*Z*	*X*	*Y*	λ, nm	*P*, %	*A*, nm	*D*, sm^{-2}
2	16.76	15.88	6.053	0.4331	0.4104	499	5	27.5	$72.5*10^{10}$

The results are shown in Table 16.1 (*X*, *Y*, *Z*, color coordinates; *x*, *y*, the chromaticity coordinates; λ, wavelength nm; *P*, the color purity%).

Color of pigment after calcination characteristics are shown in Table 16.1, stoichiometric composition corresponds to a wavelength of blue color spectrum of electromagnetic radiation. It should be borne in mind that with increasing purity of color reflectance increases.

16.4 Conclusion

Using a set of independent research methods were set optimal range of pH values to produce precipitation, which are the precursor for synthesis alumino-nickel spinel.

The results of the research allow us to develop the scientific basis for the synthesis of alumino-nickel spinel from chemically precipitated mixtures, which will ensure its obtaining in a dispersed state at a high degree of conversion and the possibility of a sharp decrease in the temperature of sintering of materials on its basis.

It is shown that from the precipitates obtained under optimum conditions in the course of further heat treatment, nickel aluminate is obtained.

References

1. Kalendová A (2000) Application of spinel pigments in anticorrosive heat-resistant coatings. Pigm Resin Technol 29(3):164–172
2. Zhang G-Y, Guo B, Chen J (2006) MCo_2O_4 (M= Ni, Cu, Zn) nanotubes: template synthesis and application in gas sensors. Sensors Actuators B Chem 114(1):402–409
3. PalDey S et al (2005) Evaluation of a spinel based pigment system as a CO oxidation catalyst. Appl Catal B Environ 56(3):241–250.
4. Gil-Calvo M et al (2017). Effect of Ni/Al molar ratio on the performance of substoichiometric $NiAl_2O_4$ spinel-based catalysts for partial oxidation of methane. Appl Catal B Environ 209:128–138.
5. Dawoud HA (2017) Synthetize and magnetic properties of Al substituted Ni spinel ferrites prepared by conventional method. IUG J Nat Stud 25(2):244–249
6. Han M et al (2018) Physical properties of $MgAl_2O_4$, $CoAl_2O_4$, $NiAl_2O_4$, $CuAl_2O_4$, and $ZnAl_2O_4$ spinels synthesized by a solution combustion method. Mater Chem Phys 215:251–258
7. Souza ADV et al (2015) Characterization of aluminum hydroxide (Al (OH) 3) for use as a porogenic agent in castable ceramics. J Eur Ceram Soc 35(2):803–812

8. Salunkhe RR et al (2015) Large-scale synthesis of coaxial carbon nanotube/Ni (OH) 2 composites for asymmetric supercapacitor application. Nano Energy 11:211–218
9. Frolova L, Pivovarov A, Tsepich E (2016) Ultrasound ferritization. J Chem Technol Metallurgy 51(2):163–167
10. Maskani N et al (2017) Synthesis of al2o3-ni composite powders by co-precipitation method. Iran J Mater Sci Eng 14(1):31–37
11. Frolova L, Pivovarov A, Butyrina T (2017) Synthesis of pigments in Fe_2O_3-Al_2O_3-CoO by co-precipitation method. Pigm Resin Technol 46(5):356–361
12. Wang CY et al (2002) Structural study of Al-substituted nickel hydroxide. Solid State Ionics 148(3–4):503–508
13. Zhao YL et al (2004) Al-substituted α-nickel hydroxide prepared by homogeneous precipitation method with urea. Int J Hydrog Energy 29(8):889–896
14. Puigdomènech I (2002) MEDUSA (make equilibrium diagrams using sophisticated algorithms) windows interface to the MS-DOS versions of INPUT, SED and PREDOM (FORTRAN programs drawing chemical equilibrium diagrams) Vers. 31 July. 2002. Royal Institute of Technology, Stockholm
15. Vogel AIA (2013) Text-bok of quantitative inorganic analysis-theory and practice. Longmans, Green And Co., London/New York/Toronto

Chapter 17
IV–VIB Group Metal Boride and Carbide Nanopowder Corrosion Resistance in Nickeling Electrolytes

Oleksandr Goretskiy, Dmytro Shakhnin, Viktor Malyshev, and Tetiana Lukashenko

17.1 Introduction

The corrosion resistance of powder materials used as reinforcing phases in composite electrochemical coatings (CEP) is an important characteristic defining the fundamental possibility of their obtaining. Dissolution of powders in electrolytes solutions leads to deterioration of the electrolysis conditions which imposes significant process limitation on the use of each specific material for the CEP obtaining [1–3]. Analysis of available data shows that a number of studies in which no dissolution of hardening phases (borides) was taken into account contain inaccuracies, and the neglecting of this fact led to excessively wide advertising of dispersion hardening processes realized in chroming electrolytes containing zirconium diboride. Therefore, the study of corrosion resistance of powders of refractory compounds is an important task and of their nanostates—a scientific problem as well. Urgent need for such research is also due to the lack of information on this subject. Only in [4], there is evidence of stability in acid solutions of nanostructured nitride-boride composites of titanium and zirconium.

This paper is devoted to the investigation of the corrosion resistance of nanopowders of borides and carbides of zirconium, titanium, vanadium, chromium, molybdenum, and tungsten in the nickeling electrolytes depending on the acidity of the electrolyte, temperature, and duration of the interaction.

O. Goretskiy (✉) · D. Shakhnin · V. Malyshev · T. Lukashenko
Institute for Engineering & Technology, University “Ukraine”, Kyiv, Ukraine

O. Fesenko, L. Yatsenko (eds.), *Nanocomposites, Nanostructures, and Their Applications*, Springer Proceedings in Physics 221,
https://doi.org/10.1007/978-3-030-17759-1_17

17.2 Materials and Methods

The test objects were nanopowders of borides and carbides of zirconium, titanium, vanadium, chromium, molybdenum, and tungsten and also silicon carbide, obtained by plasmochemical and by high-temperature electrochemical synthesis methods, main characteristics of which are shown in Table 17.1. Conditions of their obtaining were systematized in [5, 6]. A study of resistance of nanopowders of refractory metals borides and carbides was performed in standard nickeling electrolytes (Table 17.2).

The acidity of the electrolyte was adjusted by adding concentrated sulfuric acid. Concentration of powders of carbides and borides was in all experiments 10 kg/m^3. Prior to treatment in the electrolyte, powders were subjected to repeated refinement, thus reducing the content of nanoscale graphite and boron down to 0.1–0.3% (by weight), and to vacuum thermal stresses to prevent coagulation of the particles. Nanopowders corrosion resistance was evaluated depending on the acidity of the electrolyte, temperature, and duration of the interaction. Dissolution rate was calculated by the insoluble residue mass and by the concentration of ions of carbide(boride)-forming element in the electrolyte determined by the magnetometric method [7, 8].

Table 17.1 Main characteristics of nanopowders of borides and carbides

Compound	Contents[a] of main phase, %	Avg. particle size, nm	30–70 nm fraction content, %
ZrB_2	91.6	41	85.1
TiB_2	92.1	39	77.3
VB_2	93.3	38	79.0
CrB_2	96.8	41	82.0
MoB_4	91.8	62	81.6
WB_4	97.6	68	82.3
$ZrC_{0.90}N_{0.06}$	94.4	41	78.0
$TiC_{0.90}N_{0.06}$	91.7	58	81.0
$VC_{0.85}N_{0.05}$	94.8	45	76.0
$Cr_3(C_{0.80}N_{0.20})_2$	95.6	42	80.0
Mo_2C	97.2	78	79.6
WC	97.1	76	82.4
$SiC_{0.95}N_{0.05}$	96.3	62	75.0

[a]After enrichment

Table 17.2 Compositions of electrolytes, kg/m^3

Electrolyte	$NiSO_4 \cdot 7H_2O$	H_3BO_3	NaCl	NaF	$NiCl_2 \cdot 6H_2O$	pH
1	245	30	20	6	–	4.0–5.5
2	300	30	–	–	60	2.0–4.0

17.3 Results and Discussion

The study results for nanopowders of borides and carbides are shown in Figs. 17.1 and 17.2. It was noted that, in both groups of compounds, corrosion resistance of materials was comparable and attributable primarily to the electrolyte acidity.

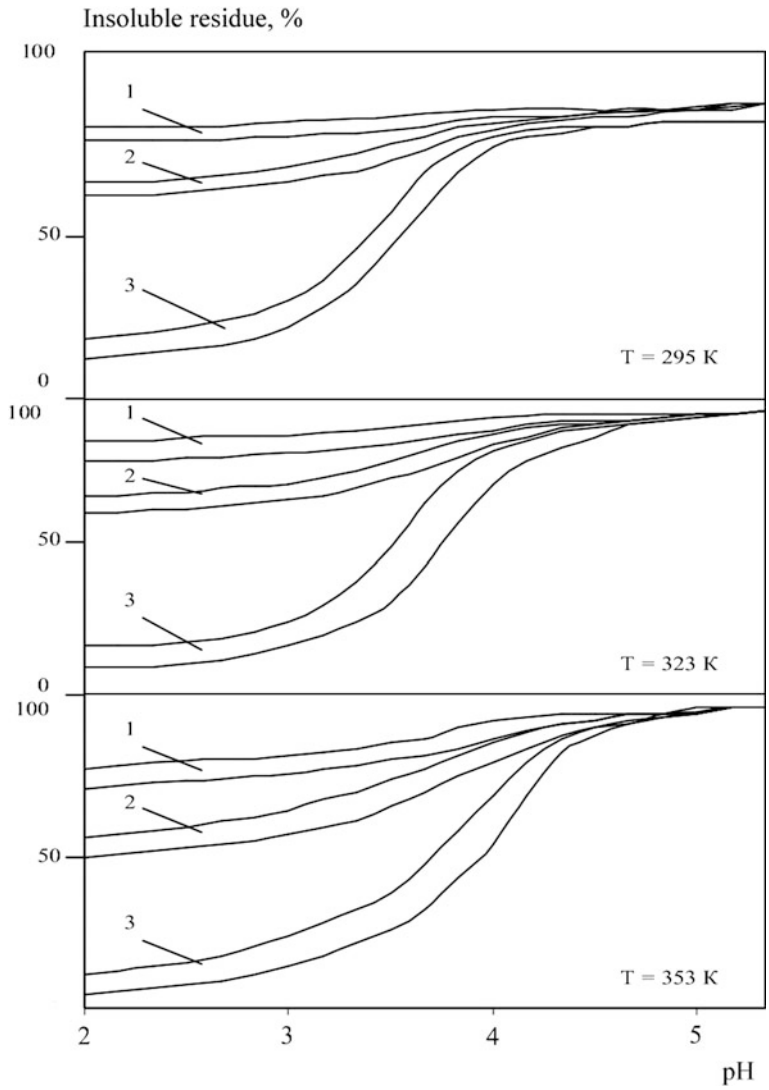

Fig. 17.1 Corrosion resistance of nanopowders of borides of zirconium, titanium, vanadium, chromium, molybdenum, and tungsten in electrolytes solutions of different acidity depending on the temperature and exposure time: 1 –τ = 3 h, 2–24 h, 3–240 h

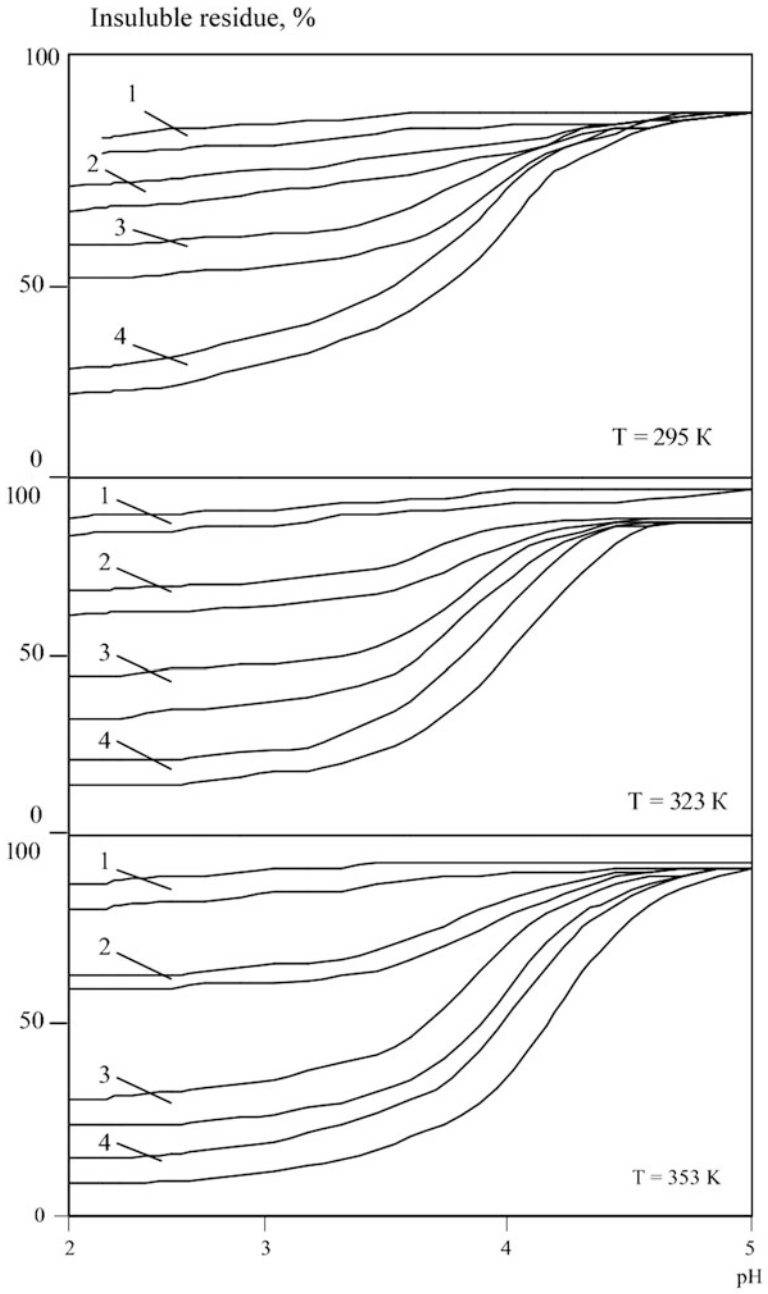

Fig. 17.2 Corrosion resistance of nanopowders of carbides of silicon, zirconium, titanium, vanadium, chromium, molybdenum, and tungsten in electrolytes solutions of different acidity depending on exposure time and temperature: 1 – τ = 3 h, 2–24 h, 3–120 h, 4–360 h

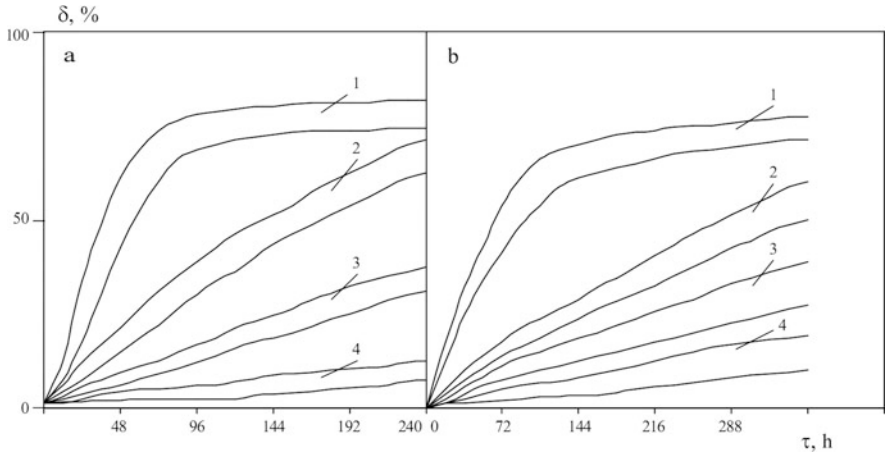

Fig. 17.3 Kinetic curves of dissolution of nanopowders of borides (**a**) and carbides (**b**) of zirconium, titanium, vanadium, chromium, molybdenum, and tungsten in electrolytes solutions: $T = 323$ K; electrolyte pH value – 2.5 (1), 3.0 (2), 3.5 (3), and 5.0 (4)

In acid electrolytes (pH = 2.0–3.0), nanopowders were quickly dissolved. Thus, after 3 h at $T = 323$ K, borides dissolution degree was 15.6–9.5%, after 24 h – 38.2–31.0%, and after 240 h – 89.9–75.1%. Nanopowders of metallike carbides have a higher corrosion resistance: similar to borides, dissolution degrees were achieved, respectively, after 24, 120, and 360 h. All the materials exhibit corrosion resistance decrease with temperature increase and increase of the specific surface area during the dissolution which, while maintaining the particle shape, is equal to 2000–10,000 m^2/kg, showing mainly layered nature of the dissolution process. The only exception is silicon carbide nanopowder whose degree of dissolution in the whole studied pH and temperature range did not exceed 7–10%.

Kinetic curves of dissolution of borides and carbides calculated from change of concentrations of ions of boride(carbide)-forming metals are shown in Fig. 17.3. Calculations from the results give induction periods, i.e. times in which half of the original particulate material is dissolved. In electrolytes with pH 2.5, these values for borides were 32–49 h, and for carbides – 68–88 h; in electrolytes with pH = 3.0, these values were 92–112 and 138–167, respectively; and with pH = 5.0, these times were practically unlimited. Comparison of kinetic parameters with known data for the coarse powders shows that the dissolution rate of nanopowders is 3–5 times higher.

Thus, corrosion resistance of borides and carbides of zirconium, titanium, vanadium, chromium, molybdenum, and tungsten in the electrolytic solutions within each group of compounds is similar and mainly determined by the acidity of the medium, wherein the nanopowder dissolution rate is significantly higher than that for coarse-grained materials [9, 10], which can be considered as one of the manifestations of the size effect. To a lesser extent the latter is manifested during dissolution of silicon carbide nanopowder resistant within almost all the investigated

pH range. Consequently, nanopowders of borides and metallike carbides may be used in processes of the composite reinforcement with weakly acid or alkaline electrolytes and of silicon carbide—in processes involving electrolytes of any acidity.

17.4 Conclusions

1. The solubility of nanopowders of borides and carbides of zirconium, titanium, vanadium, chromium, molybdenum and tungsten, as well as of silicon carbide, was studied in standard nickel plating electrolytes depending on the acidity of the electrolyte, temperature, and duration of the interaction. It was established that, in both groups of compounds, the materials corrosion resistance is comparable and determined primarily by the electrolyte acidity. Rather quick nanopowders dissolution is noted in acidic electrolytes (pH = 2.0–3.0), reaching 75–90% after 240 h and accelerating with temperature increase.
2. Silicon carbide nanopowder is rather corrosion resistant; its dissolution degree within the whole studied range of pH (2.0–5.0) and temperature (295–353 K) values does not exceed 8–12%.
3. The present study results are recommended to use for the development of new compositions of suspension electrolytes for composite hardening of tools and accessories with a particularly complex microrelief of working surfaces.

References

1. Boda M, Phand RV, Kotali AC (2017) Metal and nonmetal composite materials a new alternative for materials: Review. Int J Sci Develop Res 2(4):236–239
2. Haghshenas M (2015) Metal–matrix composites. Ref Mod Mater Sci Mater Eng. https://doi.org/10.1016/B978-0-12-803581-8.03950-3
3. Steinhauser S, Wielage B (1997) Composite coatings: manufacture, properties, and applications. Surf Eng 13(4):289–294
4. Rawal S (2001) Metal-matrix composites for space applications. JOM 53(4):14–17
5. Malyshev VV, Kushkov HB, Shapoval VI (2002) High-temperature electrochemical synthesis of carbides, silicides and borides of VI-A group metals in ionic melts. J Appl Electrochemistry 32(5):573–579
6. Malyshev V, Shakhnin D, Gab A, Astrelin I, Molotovska L, Soare V, Donath C, Constantin V, Popescu AM (2016) Electrochemical synthesis of borides and silicides of chromium, molybdenum and tungsten in molten salts. Rev Chim 67(12):2490–2500
7. Nickel KG, Quirmbach P, Potschke J (2010) High temperature corrosion of ceramics and refractory materials, vol 1. Sheir's Corrosion, Elsevier, pp 668–690
8. Uhlig HH (2011) Uhlig's corrosion handbook. Ed. by R. Winston Revie – 3rd ed. John Wiley & Sons, Inc., Hoboken, New Jersey, USA. 1253 p. ISBN 978-0-470-87285-7
9. Samsonov G (1980) Handbook of refractory compounds. Springer, New York, NY, USA. 556 p. ISBN 978-1-4684-6101-5
10. Andrievski RA (1994) The synthesis and properties of nanocrystalline refractory compounds. Russ Chem Rev 63(5):411–427

Chapter 18
Hydrodynamic and Thermodynamic Conditions for Obtaining a Nanoporous Structure of Ammonium Nitrate Granules in Vortex Granulators

A. V. Ivaniia, A. Y. Artyukhov, and A. I. Olkhovyk

18.1 Introduction

Formation of the developed nanoporous structure on the surface and inside granules of customary ammonium nitrate (used as mineral fertilizers) expands the areas of its application due to the peculiar properties obtained. Customary and multilayer granules of porous ammonium nitrate (PAN) are used as a main component of the industrial explosive ANFO [1]. Ammonium nitrate granules with a nanoporous organic membrane are successfully applied in agriculture [2, 3].

Based on the analysis of advantages and disadvantages of the existing methods for obtaining porous ammonium nitrate (PAN), this paper introduces a method of the combined moisturizing and thermal processing in the two-phase flow using an active hydrodynamic regime [4–6]. In such a case, a nanoporous structure of ammonium nitrate granules is formed due to moisturizing by water or special water solutions and further thermal processing in a vortex fluidized bed, as described in the works [7–9].

The aim of this work is to model the optimal conditions for forming a nanoporous structure on the surface and inside a PAN granule. Herewith, it must be considered that the presence of a nanoporous structure itself does not guarantee the quality of PAN. It is important to ensure special characteristics of the granules if ammonium nitrate is applied as a component of the ANFO explosive. These characteristic features are the absorbing and the binding abilities of granules. Figure 18.1 depicts the optimal structure of the PAN granule, obtained in a vortex heat-transfer flow by the methods [10, 11]. The macropores on the surface layer of the granules (Fig.

A. V. Ivaniia (✉) · A. Y. Artyukhov · A. I. Olkhovyk
Processes and Equipment of Chemical and Petroleum-Refineries Department, Sumy State University, Sumy, Ukraine
e-mail: a.ivaniya@pohnp.sumdu.edu.ua

O. Fesenko, L. Yatsenko (eds.), *Nanocomposites, Nanostructures, and Their Applications*, Springer Proceedings in Physics 221,
https://doi.org/10.1007/978-3-030-17759-1_18

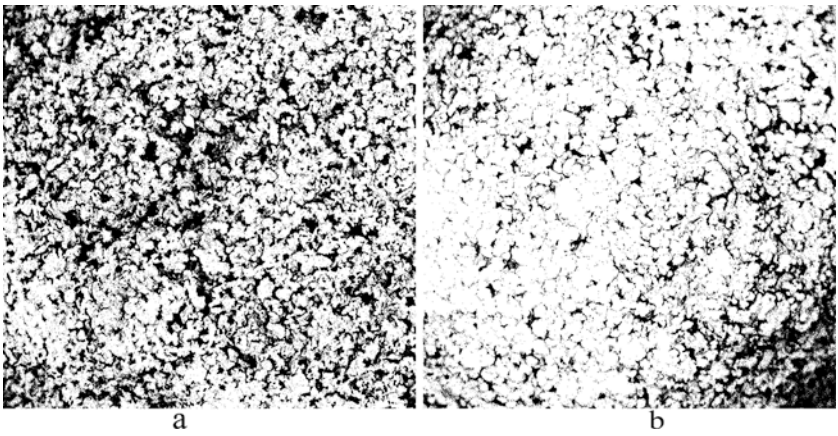

Fig. 18.1 A structure of: (**a**) a surface layer of PAN granules with macropores; (**b**) inner layers of PAN granules with meso- and micropores

18.1a) allow diesel fuel to penetrate the inner layers and, thus, increase an absorbing ability of granules [12, 13]. The structure of the inner layers of granules (Fig. 18.1b) mostly consists of the material with meso- and micropores, which increases the binding ability of granules due to the capillary forces, arising in these pores [14, 15]. Therefore, a promising area for studies lies in the process of consecutive obtaining of individual layers with the given properties on the customary ammonium nitrate granules.

Within the objective of this work, we will present the results of the study on the following:

- the hydrodynamic characteristics of the two-phase flow motion;
- thermodynamic operational parameters of a vortex granulator;
- an influence of the type of a moisturizer on a nanoporous structure of a granule.

The multilayer granules with nanoporous layers can be obtained due to the use of apparatuses with different organizations of the flows motion [16]:

- single-stage granulation units, the number of which is equal to the necessary number of layers on a customary ammonium nitrate granule;
- multistage and multifunctional granulation units.

This paper proposes an application of the multistage vortex granulator with a height-variable section of the workspace (Fig. 18.2) [17].

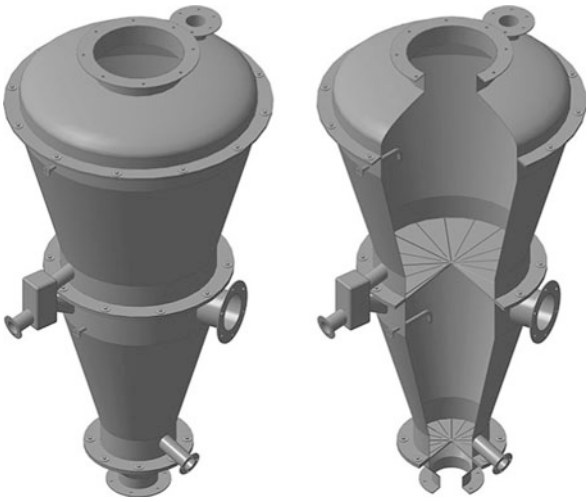

Fig. 18.2 A model of the two-section vortex granulator

18.2 Hydrodynamic Conditions for Obtaining a Nanoporous Structure

In the frames of this work, we conducted a series of experimental studies on the influence of the constrained flow and a construction of a swirler on the fluidized bed structure. The quality of the PAN nanoporous structure when using each type of a swirler is evaluated. An optimal thermodynamic mode is preliminarily considered a "mild" regime, described in the work [9].

The analysis of the granules' trajectory (an average content of the disperse phase in the two-phase system $\psi = 0.15$) and a diagram of the velocity components of the gas flow for each of the considered gas distribution devices (Figs. 18.3, 18.4, 18.5, 18.6, and 18.7) allowed us to define their operational peculiarities and to recommend each of the devices for the application in certain conditions.

It should be noted that an increase in the average content of the disperse phase in the two-phase system impairs the stability of a vortex fluidized bed in all the types of the gas distribution devices, yet the range of operational sustainability of the devices varies.

Gas distribution devices with slots and the ones of a combined type are recommended for the application in the low power apparatuses with a value of ψ up to 0.2. A higher average content of the disperse phase destructs the structure of the stable vortex fluidized bed and evokes spontaneous pulsating zones of the granules. A peculiar feature of the fluidized bed, which is formed in the apparatus with such a gas-distribution device, is an intensive side mix of granules in the so-called "active" zone of a granulator directly above the gas-distribution device. Vertical holes in the central part of the gas-distribution device provide a vertical circulation of granules with low intensity. Such a gas-distribution device combines the advantages of a vortex fluidized bed and a possibility to keep the strength of materials with its small value.

Fig. 18.3 A trajectory of the granules' motion in the application of a gas distribution device with tilted holes

Fig. 18.4 A trajectory of the granules' motion in the application of a gas distribution device with central vertical and periphery tilted holes

A slit-type gas distribution device, as depicted in Fig. 18.8, is characterized by a stable vortex structure with the power almost twice as high as the disperse phase. Such a gas distribution device is recommended as optimal due to a wide range of power in the disperse phase ($\psi = 0.1$–0.3) while maintaining a stable vortex flow of granules.

Fig. 18.5 A trajectory of the granules' motion in the application of a gas distribution device with central tilted and periphery vertical holes

Fig. 18.6 A trajectory of the granules' motion in the application of a gas distribution device with slots

Fig. 18.7 A trajectory of the granules' motion in the application of a combined gas distribution device (slots and holes within the whole space)

Fig. 18.8 A trajectory of the granules' motion in the application of a slit-type gas distribution device

The above-mentioned constructions of the gas distribution devices are widely recognized for applications in the low power apparatuses with a value of ψ up to 0.3. Higher power and higher relative content of the disperse phase require an application of the gas distribution devices of other types.

18.3 Thermodynamic Conditions for Obtaining a Nanoporous Structure

A distribution pattern of the temperature field of the drying agent in the workspace of the vortex granulator depends on:

- the intensity of the drying agent vortex flow;
- a warm-up time of the apparatus;
- a warm-up regime of the apparatus (simultaneously with granules or during the inlet of granules after the drying agent acquires the necessary temperature characteristics).

It should be mentioned that a nanoporous structure of the PAN granules is formed mostly in the "active" zone of the granulator (directly above the swirler and in a zone of an active vortex motion of the two-phase system). Herewith, an increase in the height of the workspace in the granulator's upper part (resulted from damping of an active vortex motion of the fluidized bed) leads to the decreased uniformity of the nanoporous structure formation. Figure 18.9 shows an example of the thermogram of the vortex granulator's workspace (one of the sections in a multisection apparatus) with various intensity (an initial velocity) of the drying

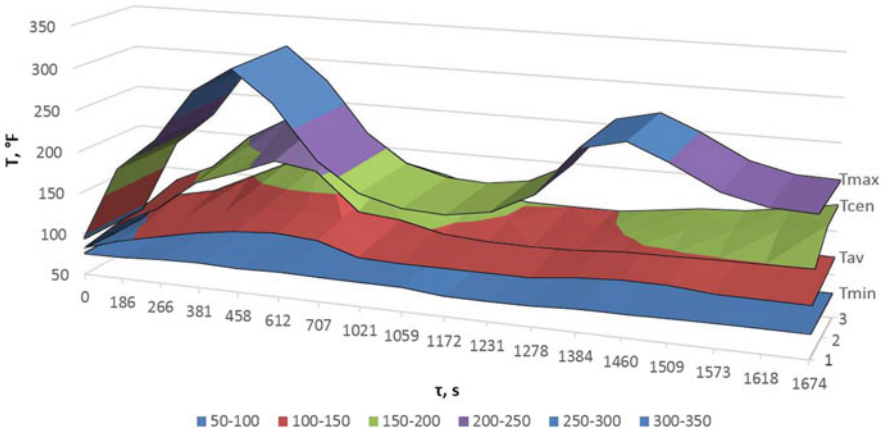

Fig. 18.9 Thermograms of the workspace in the vortex granulator's section and a nanoporous structure of PAN granules: (**a**) low intensity of the drying agent vortex motion; (**b**) an optimal velocity of the drying agent vortex motion; (**c**) high intensity of the drying agent vortex motion

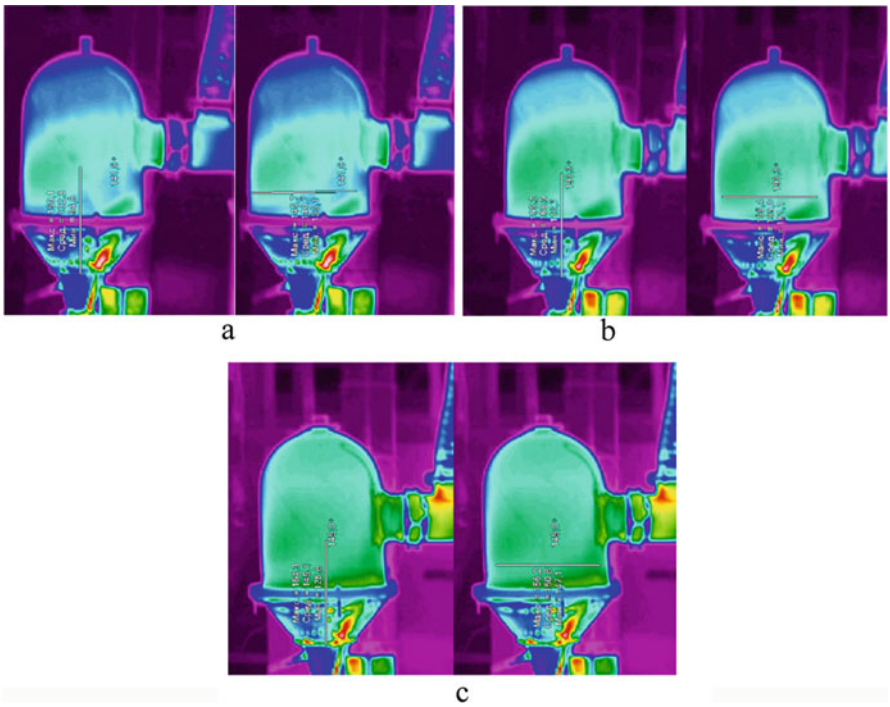

Fig. 18.10 An influence of the vortex gas flow velocity on the distribution pattern of the temperature field in the vortex granulator's section: (**a**) fluidized bed with partial twisting; (**b**) developed vortex fluidized bed (strat of the regime); (**c**) developed vortex fluidized bed (end of the regime)

agent vortex flow and the nanoporous structure of granules, which corresponds to this thermodynamic condition. A nonuniform contact of a granule with a drying agent results in the formation of zones without a developed network of pores. Under a very high vortex motion of the drying agent and over-heating of the granule, its structure receives mechanical cracks that can increase the absorbency of the granule. However, these cracks do not influence a binding ability of the granule and reduce its strength.

Therefore, it is necessary to achieve the optimal intensity of the drying agent, which allows balancing of the temperature field in the workspace of the vortex granulator. Figure 18.10 presents the data of the experimental investigations on determining the relationship between the intensity of the vortex gas flow and the uniform warm-up of the granulator's workspace.

According to the results of the experimental investigations, it is possible to select the optimal velocity of the drying agent vortex flow in the given construction of the vortex granulator.

18.4 An Influence of the Moisture Intensity on the PAN Granules' Structure

The results of the experimental investigations allowed us to define the main patterns of how a nanoporous structure of granules is formed in relation to the intensity of moisturizing of the granule's surface. The maximum amount of the moisturizer was determined taking into account the previously calculated velocities of the gas flow, corresponding to the range between the initial formation of the vortex fluidized bed of granules and their removal from the workspace of the apparatus (critical velocities of fluidization for a vortex flow). A change of the granules' mass under the uniform liquid filming was also considered in the calculations. An optimal temperature of the drying agent was determined on the basis of the conducted investigations on the thermodynamic conditions for obtaining a porous structure of the granules [18]. The process of moisturization was completed after the vortex fluidized bed had lost its stability (a significant reduction of swirling had occurred, and the fluidized bed had lost its vortex characteristics).

With minimal moisturization, only the surface layers of granules are modified, and a small amount of micropores appears after the thermal processing (Fig. 18.11). With the optimal moisturization, the structure of PAN granules is characterized by a considerable amount of macropores on the surface layers of granules, as well as deep micro- and mesopores (Fig. 18.12). The maximum moisturization of the granule's layer results in the developed porous structure of the granules within its whole depths and the reduced strengths of the core due to high temperature stresses during the evaporation of moisture (Fig. 18.13).

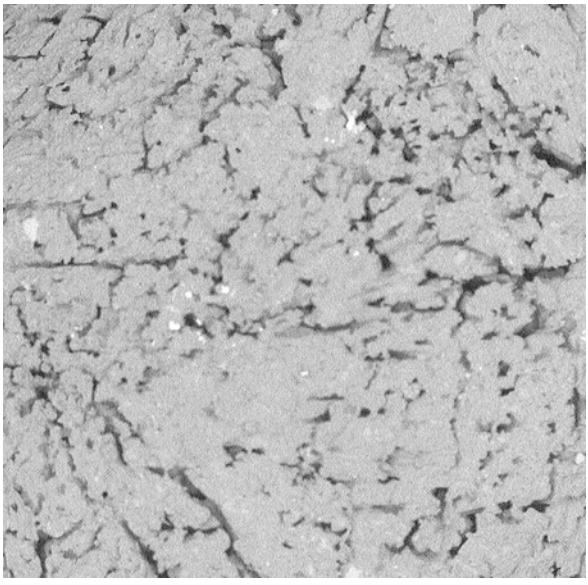

Fig. 18.11 The granules' structure with minimal moisturization

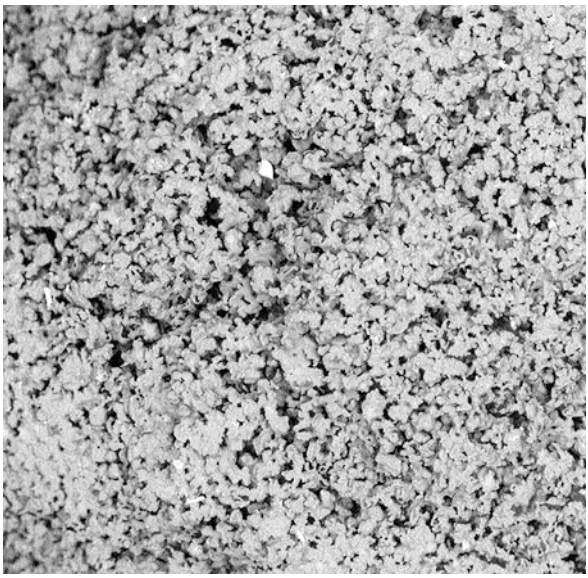

Fig. 18.12 The granules' structure with optimal moisturization

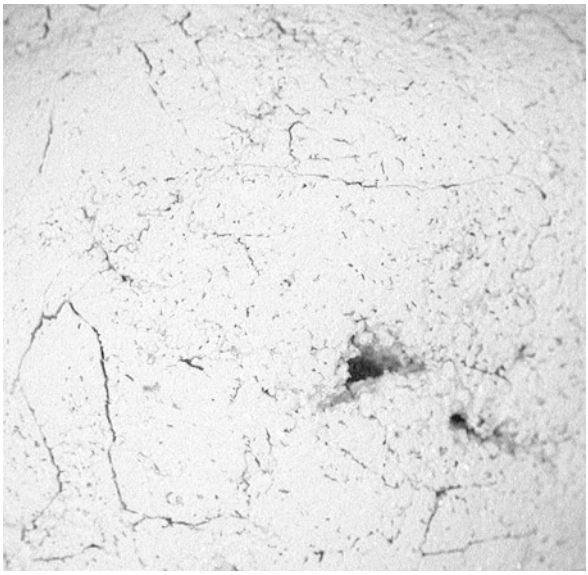

Fig. 18.13 The granules' structure with maximum moisturization

18.5 Conclusions

The results of the investigations, described in this paper, allow us to select the optimal processing regime of the vortex granulator, used for the production of PAN granules. This regime will be optimized according to the following indicators:

- The minimal velocity of the drying agent vortex flow, which is necessary for the formation of the developed nanoporous structure

- The minimal temperature potential of the drying agent for the successful dehydration of granules
- The minimal consumption of the moisturizer for the uniform filming

In this regard, further investigations on the following processes are required:

- An influence of several cycles of moisturization and heat processing on the structure of the previous nanoporous layers
- A complex assessment of the mutual influence of the temperature-moisture characteristics of the flow and the moisturizing pattern (the intensity, type of moisturizer, the consumption of the moisturizer) during the formation of the nanoporous structure of granules

References

1. Erode GM (2013) Ammonium nitrate explosives for civil applications: slurries, emulsions and ammonium nitrate fuel oils. Wiley-VCH Verlag & Co, Weinheim
2. Scialabbe N, Muller-Lindenlauf M (2010) Organic agriculture and climate change. Renew Agri Food Syst 25(2):158–169
2. Kornienko Y et al (2009) Mathematical modeling of continuous formation of multilayer humic-mineral solid composites. Ch&ChT 3(4):335–338
4. Artyukhov A et al (2016) Application software products for calculation trajectories of granules movement in vortex granulator. CEUR Workshop Proceedings 1761:363–373
5. Artyukhov A et al (2016) Software for calculation of vortex type granulation devices. CEUR Workshop Proceedings 1761:374–385
6. Artyukhov AE, Sklabinskyi VI (2013) Experimental and industrial implementation of porous ammonium nitrate producing process in vortex granulators. Nauk Visnyk Nats Hirnychoho Univ (6):42–48
7. Artyukhov AE, Sklabinskyi VI (2016) 3D nanostructured porous layer of ammonium nitrate: influence of the moisturizing method on the layer's structure. J Nano- Elect Phys 8(4):04051–1–04051–5
8. Artyukhov AE, Sklabinskyi VI (2016) Thermodynamic conditions for obtaining 3D nanostructured porous surface layer on the granules of ammonium nitrate. J Nano- Elect Phys 8(4):04083–1–04083–5
9. Artyukhov AE, Sklabinskyi VI (2017) Investigation of the temperature field of coolant in the installations for obtaining 3D nanostructured porous surface layer on the granules of ammonium nitrate. J Nano- Elect Phys 9(1):01015–1–01015–4
10. Artyukhov AE, Voznyi AA (2016) Thermodynamics of the vortex granulator's workspace: the impact on the structure of porous ammonium nitrate. Abstracts of the 6th International Conference Nanomaterials: Application & Properties (NAP-2016) 5(2):02NEA01
11. Artyukhov AE (2016) Kinetics of heating and drying of porous ammonium nitrate granules in the vortex granulator. Abstracts of the 6th International Conference Nanomaterials: Application & Properties (NAP-2016) 5(2):02NEA02
12. Lipinska K, Lipinski M, Maranda A (2005) Demilitarized propellants as ingredients in commercial explosives. European Federation of Explosives Engineers: Brighton conference proceedings, Brighton, pp 493–498
13. Weber PW et al (2015) Numerical simulation of a 100-ton ANFO detonation. Shock Waves 25(2):127–140
14. Artyukhova NO (2018) Multistage finish drying of the N_4HNO_3 porous granules as a factor for nanoporous structure quality improvement. J Nano- Elect Phys 10(3)03030–1–5, 03030-1

15. Artyukhov AE, Ivaniia AV (2017) Obtaining porous ammonium nitrate in multistage and multifunctional vortex granulators. Naukovyi Visnyk Natsionalnoho Hirnychoho Universytetu (6):68–75
16. Artyukhov AE, Sklabinskyi VI (2015) Hydrodynamics of gas flow in small-sized vortex granulators in the production of nitrogen fertilizers. Ch&ChT 9(3):337–342
17. Artyukhov AE, Ivaniia AV (2016) Vykhrovyi hranuliator (the vortex granulator). UA patent 112021, 25 Nov 2016
18. Artyukhov A et al (2017) Multilayer modified NH_4NO_3 granules with 3D nanoporous structure: effect of the heat treatment regime on the structure of macro- and mezopores. In: Abstracts of the IEEE international young scientists forum on applied physics and engineering (YSF-2017), pp 315–318

Chapter 19
Nanostructured Mixed Oxide Coatings on Silumin Incorporated by Cobalt

Ann. V. Karakurkchi, Nikolay D. Sakhnenko, Maryna V. Ved', and Maryna V. Mayba

The alloys of aluminum with silicon (silumins) are demanded construction materials. They are widely used in various industries: motor engineering and automotive, water and heating supply systems, consumer goods. Silumins have the unique physical-mechanical properties and high treatment manufacturability. High silicon content provides silumins with enhanced casting properties, higher corrosion resistance, strength, and durability [1].

At the same time, coarse-needle eutectics and primary deposition of silicon in the structure of these alloys cause embrittlement of the material [2]. This undesirable phenomenon strengthens with an increase in the content of silicon in alloy composition. That is why, in order to ensure a high level of mechanical properties, it is required to use additional methods for the surface modification of such materials.

Electrochemical technologies are widely employed for the modification of surfaces of metals and alloys by forming coatings with different composition and purpose [3, 4]. One of the approaches is to create on the material's surface ceramic-like oxide coatings by the method of plasma-electrolytic oxidizing (PEO) [5, 6]. The technique involves the oxidizing of surface in aqueous electrolytes at high voltage under the action of short-lived electrical discharges. Under such high-energy modes, due to the implementation of electrochemical and thermochemical reactions, the highly developed oxide matrix of the base metal incorporated with the electrolyte components forms [3, 5]. The advantages of a given technique of surface modification include simplicity of the equipment used, nontoxic working solutions, absence of the stage for preliminary preparation of a part, and the possibility of efficient treatment of complex-shaped products. The indicated factors characterize PEO process as economical, eco-friendly, and resource-saving [7].

A. V. Karakurkchi (✉) · N. D. Sakhnenko · M. V. Ved' · M. V. Mayba
National Technical University "Kharkiv Polytechnic Institute", Kharkiv, Ukraine

O. Fesenko, L. Yatsenko (eds.), *Nanocomposites, Nanostructures, and Their Applications*, Springer Proceedings in Physics 221,
https://doi.org/10.1007/978-3-030-17759-1_19

PEO of valve metals is traditionally carried out in homogeneous electrolytes, which are characterized by high stability and easy adjustment during operation and make it possible to change qualitative and quantitative composition in a wide range [8]. Using the electrolytes of a given type allows efficient treatment of alloys with different chemical composition and creation of oxide coatings doped with one or more components [6, 9].

The type of the electrolyte used and the nature of doping components predetermine the composition and properties of the formed oxide layer [10, 11]. Electrolytes with different compositions are used for obtaining oxide coatings on silumins. Plasma-electrolytic treatment of aluminum in borate and silicate electrolytes allows obtaining oxide coatings with high micro-hardness [12, 13]. Al-Si alloys oxidation in alkali silicate electrolytes is most common. It is proved by the significant number of studies on formation of PEO coatings on silumins in electrolytes of this type [13–16]. But it should be noted that silicon particles in alloys composition and Si-containing phases inhibit aluminum oxidation and affect morphology and composition of obtained coatings. To form oxide coatings with enhanced chemical and thermal resistance, surface layers of aluminum alloys are doped with nickel and iron from the solutions of polyphosphates [17, 18]. The introduction of transition metals to the composition of surface oxide layers considerably improves catalytic properties of PEO coatings in the reactions of decomposition of toxic components [3, 4, 19]. Electrolyte suspensions that consist of the base homogeneous electrolyte and additives from powders of different nature and dispersion degree have also been used [20, 21]. In this case, in addition to electrochemical and thermochemical transformations, the growth of coating occurs due to mechanical capture of particles from a working solution. At the same time, using the complex electrolytes particularly helps to improve the stability and operational lifecycle of working solutions [11, 18], and contributes as well to a more uniform distribution of doping components on the surface of the treated material.

At the same time, still unresolved are the issues of control over composition and morphology of the formed coatings on alloys with a high content of impurities (alloying components). Surface heterogeneity of such materials and, as a consequence, different conductivity of alloy components' oxides requires correction of the used electrolyte composition, and of technological process of oxidizing.

Oxide coatings on silumins can be obtained under galvanostatic mode [18, 22] and at polarization by pulse current [3]. In this case, the mode of d.c. current leads to the "healing" of defects in oxide coatings and the formation of surface with a more uniform morphology [23].

That is why studying the processes of targeted modification of surface through the formation of oxide PEO coatings on aluminum alloys is an important practical task. Solving it would enable improvement in the operational properties of silumins and would broaden the scope of their application.

19.1 Experimental

Oxide coatings were formed on rectangular samples of aluminum cast alloy AK12M2MgN (AL25). The chemical composition of the silumin, (GOST 1583), wt. %: мас. %: Si – 11,5 – 13,0; Cu – 1,5 – 3,0; Ni – 0,8 – 1,3; Mg – 0,8 – 1,3; Mn – 0,3 – 0,6; Fe < 0,8; Zn < 0,5; Ti < 0,2; Pb < 0,1; Sn < 0,02; Cr < 0,2. Working area for the formation of oxide coatings was 0.2 dm^2. The surface of samples for coatings application was prepared by grinding with subsequent degreasing, washed with water, and dried at a temperature of 30 °C.

PEO was conducted in the galvanostatic mode. The laboratory setup was used to form coatings. It included the industrial stabilized power source B5–50 (Ukraine), an electrolytic cell with forced cooling and stirring, an ammeter, and a voltmeter. PEO stages were controlled visually and recorded according to the readings of the devices.

Oxidizing was carried out in alkaline pyrophosphates electrolytes with additions of $CoSO_4$. Working solutions for research were prepared using certified "chemically pure" reagents and distilled water. The composition of the working electrolytes and the parameters of oxidizing are given in Table 19.1. The temperature of the electrolyte was maintained within 20–25 °C.

The chemical composition of the oxide coatings was determined using the energy-dispersion spectrometer Oxford INCA Energy 350 with the integrated programming environment SmartSEM. The X-rays were excited by exposure of the samples to a beam of 15 keV electrons. The surface morphology of the obtained oxide coatings was investigated using the scanning electron microscope ZEISS EVO 40XVP. SEM-images were recorded by the registration of secondary electrons via scanning with an electron beam; this mode made it possible to study the morphology with a high resolution and contrast ratio.

The topography of the coating surface was studied by the method of atomic-force microscopy using the microscope NT-206, the probe CSC-37. Scanning was performed by using the contact probe CSC-37 with a cantilever lateral resolution of 3 nm [24]. The scan area size was 5.0 × 5.0 μm, and the height of the surface relief was recorded at the resolution of 256 × 256 pixels. In order to analyze the AFM images, all image data were converted into Surface Explorer software.

The structure of the deposits was examined by X-ray diffraction analysis using a diffractometer DRON-2.0 in monochromatic Co-Kα radiation (λ = 17902A). The

Table 19.1 Electrolytes composition and the parameters of PEO

	Composition, mol/dm^3				
Electrolyte number	$K_4P_2O_7$	$CoSO_4$	Current density, A/dm^2	Voltage, V	Time of PEO, min
№1	0.4	0.05	3 . . . 10	110 . . . 160	2 . . . 60
№2	0.4	0.1			
№3	0.6	0.2			

phase identification was carried out by comparing the distance between the planes (d, A) and the relative intensities of the experimental curve with the data of the electronic file system PCPDFWIN.

The corrosion properties of the synthesized systems were determined by methods of polarization resistance and impedance measurement [25]. The spectra of electrochemical impedance were measured by a two-electrode scheme with coplanar electrodes in the area of 1 cm^2, located at a distance of 1 cm, on the Autolab-30 electrochemical module PGSTAT301N Metrohm Autolab, equipped with the FRA-2 (Frequency Response Analyzer), in the frequency range $10^{-2} \ldots 10^{6}$ Hz. The module was managed using the Autolab 4.9 program in a standard procedure followed by a package processing Zview 2.0. Modeling of the structure of the interphase boundary was carried out by the method of equivalent circuits. The parameters were analyzed with an error of simulation of the equivalent circle not higher than 10%.

The catalytic properties of the oxide systems were studied in the oxidation of carbon (II) oxide to carbon (IV) oxide [19]. The studies were conducted on a laboratory bench in a tubular flow reactor made of silica glass with a coaxially wound heating coil. The initial mixture of air and carbon (II) oxide with a concentration of 1.0 vol % was fed to a reactor with a volume of 1.5×10^{-2} dm^3 at a rate of 1.5 dm^3/h. The reactor temperature was gradually increased from 20 to 450 °C at a rate of 1 °C/s. The CO concentration at the inlet and outlet of the reactor was recorded using Dozor signaling-analyzing devices. The catalytic activity was evaluated by the following parameters: the initial temperature of the oxidation process (the ignition temperature, T_i) and the conversion extent (X, %). The extent of conversion was calculated by the following equation:

$$X = \frac{c(\mathrm{CO})_i - c(\mathrm{CO})_f}{c(\mathrm{CO})_i} \ 100\%,$$

where $c(\mathrm{CO})_i$ and $c(\mathrm{CO})_f$ are the initial and the final concentrations of carbon (II) oxide, %.

19.1.1 Effect of Electrolyte Composition

The formation of an oxide layer on the silumin AK12M2MgN in pyrophosphate electrolytes, in accordance with contemporary views on the mechanism of PEO, occurs at sequential implementation of the following stages: formation of the dielectric phase oxide Al_2O_3 in line with the electrochemical mechanism (a pre-spark mode); breakdown of Al_2O_3 film (start of sparking); gaseous-phase and thermochemical reactions involving the oxide of base metal and electrolyte components (a micro-arc mode); polymorphic transformations of oxide phases (an arc mode).

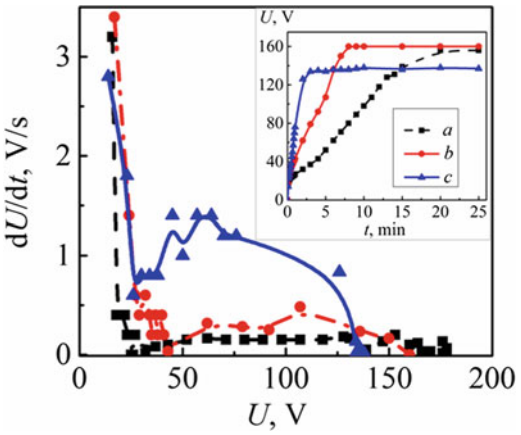

Fig. 19.1 Chronograms of forming voltage and rate of voltage change during PEO in electrolytes, mol/dm^3: 0.4 $K_4P_2O_7$, 0.05 $CoSO_4$ (**a**); 0.4 $K_4P_2O_7$, 0.1 $CoSO_4$ (**b**); 0.6 $K_4P_2O_7$, 0.2 $CoSO_4$ (**c**)

Chronograms of the forming voltage of cobalt-containing oxide coatings in electrolytes with a varied composition take the classical form, divided into characteristic regions (Fig. 19.1).

U-t dependence sections in a pre-spark area are almost linear, which is explained by an increase in the aluminum oxide film thickness and its enhanced resistance. Time to the sparking regime for the examined electrolytes increases from 2 to 11 minutes in proportion to a decrease in $CoSO_4$ content in the solution from 0.2 to 0.05 mol/dm^3. The sparking voltage in this case is 115–120 V, and the resulting forming voltage is 140–160 V.

The dependence of rate of voltage change dU/dt on forming voltage U (Fig. 19.1) reflects the formation kinetics and allows us to more accurately determine the voltage of sparking start 45–50 V. In addition, it becomes apparent that in the solutions containing 0.4 mol/dm^3 of potassium pyrophosphate the fluctuations on $dU/dt-U$ dependences are significantly lower compared to the more concentrated solution.

At the early stages of oxidizing, there occurs, in the alkaline pyrophosphate electrolyte, the anodic dissolution of alloying components from the surface with the formation of oxoanions (SiO_3^{2-}) or sufficiently strong complexes $[MP_2O_7]^{x-}$ (M is the alloying metal). The result is the homogenization of surface of the treated alloy when the preconditions are created for the incorporation of cobalt to the composition of the formed oxide layer [26].

An analysis of the oxide coatings composition, averaged by the surface, indicates that the aluminum oxide matrix includes cobalt oxides and remelted electrolyte components (Fig. 19.2).

It was established that an increase in the $CoSO_4$ concentration in the electrolyte contributes to the enrichment of surface layers with cobalt with a simultaneous decrease in the content of silicon in them. Coatings with the highest cobalt content were obtained from solution with a $CoSO_4$ concentration at 0.1 mol/dm^3. The content of silicon in this case is minimal and is only 2.1 at. %.

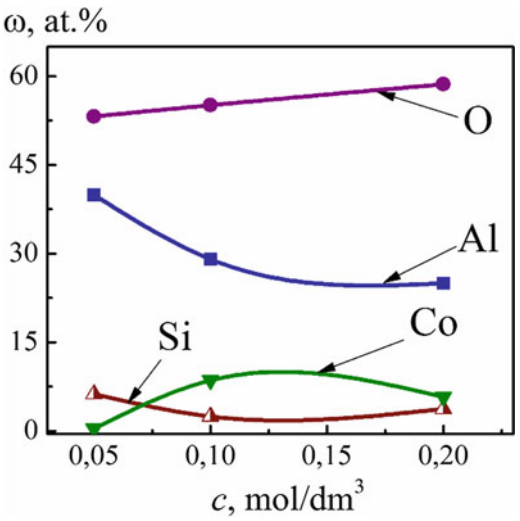

Fig. 19.2 Dependence of gross composition of PEO coatings on silumin on the concentration of $CoSO_4$ in a working electrolyte

During treatment of samples in electrolyte 1 (Table 19.1) whose ratio between concentrations of ligand and cobalt is 8:1, entering a sparking mode occurs only on minute 11. A sloping forming dependence and low rate of voltage change at $U > 115$ V (Fig. 19.1a) indicate the competition between processes of aluminum oxide formation/dissolution and weak intensity of thermo-chemical reactions. That is why the incorporation of cobalt to the composition of the formed oxide layer is insignificant, its content does not exceed 2 at. %, and a large amount of silicon remains in the composition of a surface layer (Fig. 19.2).

With an increase in the $CoSO_4$ content in a working solution to 0.1 mol/dm^3 (electrolyte 2, concentration ratio $K_4P_2O_7$:$CoSO_4$ is 4:1), duration of entering a sparking mode is reduced by 2 times while maintaining high working formation voltage (Fig. 19.1b). The presence of fluctuations on $dU/dt - U$ dependences indicates the formation on the surface oxides with different specific resistance and thermal stability, as well as the intensification of thermo-chemical reactions [27]. This makes it possible to obtain coatings with a high content of dopants and lower amount of silicon (Fig. 19.2).

The process of sample oxidizing in electrolyte 3 (ratio of concentrations between ligand and cations of cobalt is 3:1) is characterized by the rapid formation of a barrier aluminum oxide. Entering a sparking mode occurs on minute 2 of the treatment (Fig. 19.1c); however, the voltage of a micro-arc mode does not exceed 140 V. Dependence $dU/dt - U$ differs from the previous ones by the existence of significant fluctuations and sharp decline in dU/dt when voltage reaches a micro-arc mode. Obviously, at a high concentration of pyrophosphate, there is a competition between the reactions of formation/dissolution of mixed oxides, as well as the accumulation of insoluble salts in a near-electrode layer, which reduces process stability [28]. Cobalt is included in the generated oxide coating in the amount of 15 at. %, but the content of silicon in the surface layer remains significant.

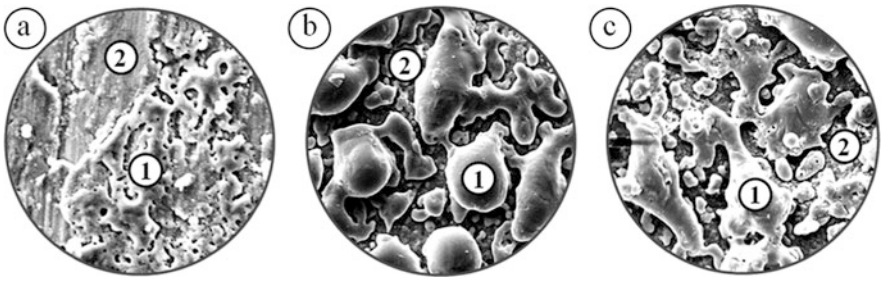

Fig. 19.3 Surface morphology of oxide coatings on AK12M2MgN, formed on electrolytes, mol/dm^3: 0.4 $K_4P_2O_7$, 0.05 $CoSO_4$ (**a**); 0.4 $K_4P_2O_7$, 0.1 $CoSO_4$ (**b**); 0.6 $K_4P_2O_7$, 0.2 $CoSO_4$ (**c**). Magnification ×1000

The incorporation of dopants to the generated oxide coating affects the surface layer morphology (Fig. 19.3). As a result of plasma-electrolytic treatment of AK12M2MgN samples in the alkaline cobalt-pyrophosphate solutions, we obtained oxide layers with high adhesion to the base metal. The incorporation of cobalt to the coating composition leads to the formation of blue-purple color spheroids (globules) on the surface. At a sufficiently big quantity, they merge and form mosaic structures, which cover almost the entire surface of a sample [27].

The surface morphology of the samples treated in electrolyte 1 (Fig. 19.3a) matches the structure of a barrier aluminum oxide with the initial stage of the island incorporation of cobalt. Oxidizing in electrolyte 2 ensures the formation of a highly developed surface with a mosaic structure (Fig. 19.3b). During plasma-electrolytic treatment in electrolyte 3, oxide coatings are formed with large spheroids (Fig. 19.3c). This is confirmed by the results of chemical composition analysis on the plots with different topography.

SEM images of the examined coatings (Fig. 19.3) visualize plots with varying topography. Plot 1 is defined as a protrusion of the mixed oxide coating, or a globule. Plot 2 is positioned as a plateau and corresponds to the matrix of oxides of the treated material. These are the plots that are selected for a comparative analysis of composition of the obtained coatings (Fig. 19.4).

During oxidizing in electrolyte 1 the incorporation of cobalt to the composition of the formed oxide layer is insignificant, its content does not exceed 2 at. %, and a large amount of silicon remains in the composition of a surface layer (Fig. 19.4a). PEO silumin in electrolyte 2 makes it possible to obtain coatings with a high content of dopants and lower amount of silicon (Fig. 19.4b). Cobalt is included in the generated oxide coating in the amount of 15 at. % during oxidizing in electrolyte 3, but the content of silicon in the surface layer remains significant (Fig. 19.4c).

The results obtained indicate that the cobalt content on the protrusions of coatings is higher than that on the plateau, and ranges from 1.2 to 23.3 at. % depending on the composition of an electrolyte. Inverse dependence is observed in aluminum and silicon distribution on the surface. Thus, on the surface of globules silicon content

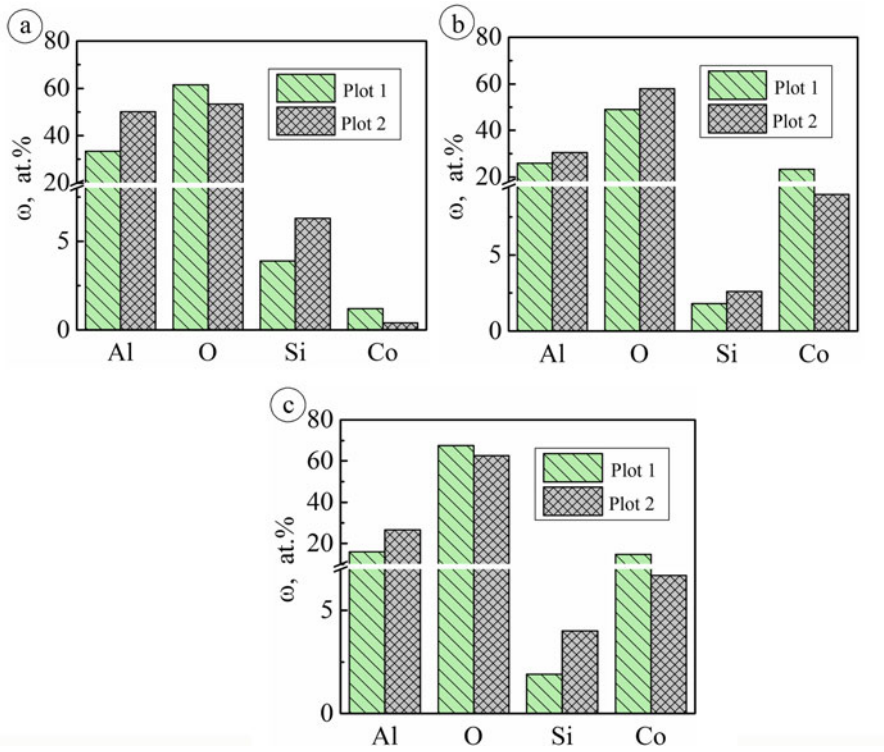

Fig. 19.4 Chemical composition of plots 1 and 2 (Fig. 19.3) on oxide coatings obtained in electrolytes of following composition, mol/dm^3: 0.4 $K_4P_2O_7$, 0.05 $CoSO_4$ (**a**); 0.4 $K_4P_2O_7$, 0.1 $CoSO_4$ (**b**); (**c**) 0.6 $K_4P_2O_7$, 0.2 $CoSO_4$

is 1.8–3.9, aluminum − 15.9−33.4 at. %; silicon concentration on the plateau is 2.6–6.3, aluminum − 26.7−40.0 at. %. The content of oxygen on all plots reflects the formation of nonstoichiometric cobalt oxides. Sphere-like globules are almost evenly distributed across the sample surface with the concentration of cobalt not exceeding 20 at. %. At the same time, the content of catalytically active component on plateau is 2.5 times lower and is only 9 at. %.

Based on the research performed for the purpose of obtaining mixed oxide layers, on silumin AK12M2MgN, under PEO mode, with a high content of cobalt and a developed surface, we recommended using the electrolyte of the composition, mol/dm^3: 0.4 $K_4P_2O_7$, 0.1 $CoSO_4$. This electrolyte composition was selected for further research.

19.1.2 Effect of Oxidizing Regime

The studies demonstrate that chronograms of formation voltage of oxide coatings on silumin in electrolyte 0.4 mol/dm^3 $K_4P_2O_7$, 0.1 mol/dm^3 $CoSO_4$ at different current densities have classic form too (Fig. 19.5).

In the pre-spark area, the process is characterized by formation of a barrier layer of aluminum oxide. Angle of slope of formation chronogram in the initial section reflects oxidation rate, which increases at an increase in current density from 3 to 10 A/dm^2. It should be noted that chronograms at i = 3–5 A/dm^2 are characterized by existence of a kink in the pre-sparking area in the time interval of 1–2 minutes, and in this case, a kink is more pronounced at lower current density (Fig. 19.5a).

Time of entering the sparking mode decreases from 6 to 1 minutes at an increase in current density i at the studied interval. Sparking voltage in all cases is 120–125 V. Sparking intensity in the oxidation process is quite high.

The final formation voltage depends on initial current density of PEO. For i 3–5 A/dm^2 U_i is 160–170 V and enables conducting the process of PEO treatment within 15 minutes or longer. At the initial current density of 10 A/dm^2, this indicator does not exceed 160 V. The oxidation process rapidly goes through all stages and from the 4th minute enters the arc mode. In this case, PEO of the alloy after 8 minutes is impractical; the formed coating is destroyed under the influence of arc discharges.

The influence of current density is sufficiently evident in the change of surface morphology of oxide coatings obtained during 15 minutes (Fig. 19.6).

In the PEO process, cobalt incorporation into the composition of oxide layers occurs in the form of drop-shaped and spherical inclusions of blue-purple color. With an increase in oxidation current density from 3 to 5 A/dm^2, their number increases, they form mosaic structures and evenly cover the entire surface of the sample. The resulting ceramic-like coating has high adhesion to the substrate. Oxidation of samples at i of 10 A/dm^2 leads to cobalt incorporation in the form

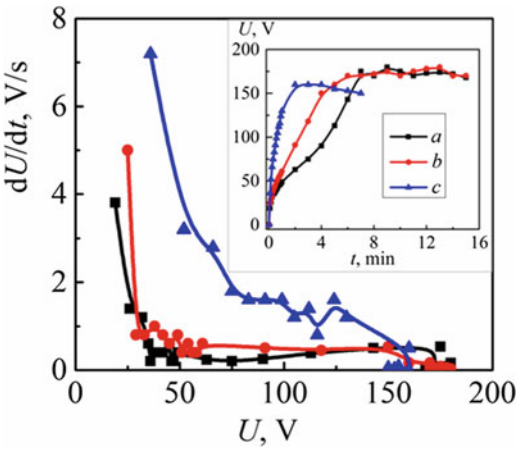

Fig. 19.5 Chronograms of forming voltage and rate of voltage change during PEO at different current densities, A/dm^2: 3 (**a**); 5 (**b**); 10 (**c**)

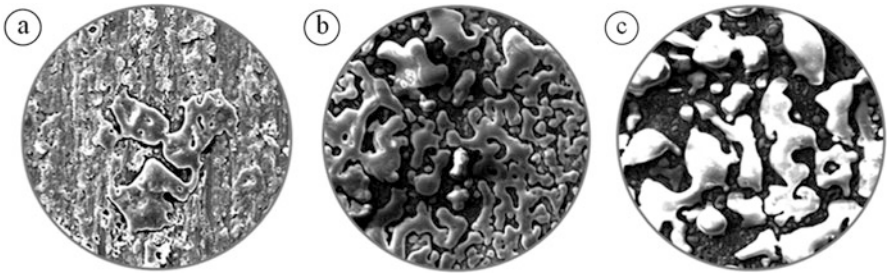

Fig. 19.6 Surface morphology of $Al_2O_3{\cdot}CoO_x$ coatings, obtained at different current densities, A/dm^2: 3 (**a**); 5 (**b**); 10 (**c**). Magnification ×500

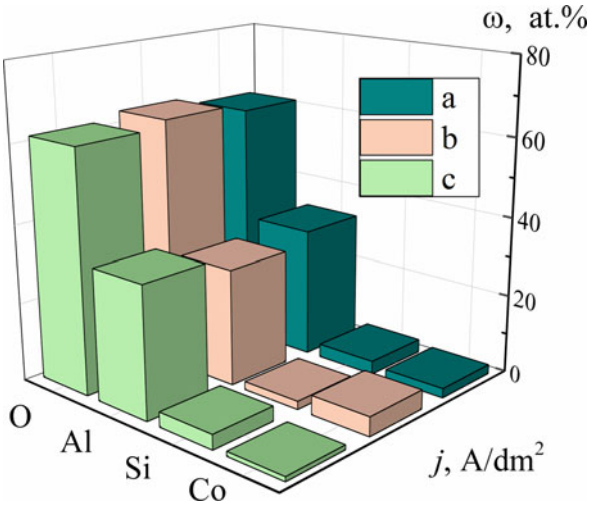

Fig. 19.7 Composition of $Al_2O_3 \cdot CoO_x$ coatings (Fig. 19.2), formed at different current densities, A/dm^2: 3 (**a**); 5 (**b**); 10 (**c**)

of voluminous islet structures. Given a quite rapid transition of PEO into the arc mode, there is a tendency to these inclusions peeling off from the basis.

Homogenization of the surface of the treated alloy and formation of uniformed oxide coatings, doped with cobalt is achieved by selection of optimal PEO mode [18]. As a result of PEO, aluminum oxide matrix with incorporated remelts of the components of electrolyte and the alloy itself is formed (Fig. 19.7).

The oxidizing of silumin at current density of 3 A/dm^2 occurs at a low rate. Kink appearance at the formation dependence (Fig. 19.1a) indicates the competition processes of Al_2O_3 formation and dissolution of alloying components. Under specified conditions in general, prerequisites for cobalt incorporation in the composition of the formed oxide coating are created; however, average concentration of cobalt is low and is a little higher than 2 at. %. Due to low formation rate, quite a lot of silicon (up to 4 at. %) remains on the surface (Fig. 19.7a). For the same reason,

a large number of pores remain on the surface in the discharges glow areas (Fig. 19.6a), although separate areas are formed which include electrolyte component remeltings.

An increase in current density of PEO up to 5 A/dm^2 contributes to intensification of the oxidation process and stabilization of the glow of microarc discharges. The kink on the dependence is not pronounced as much, which indicates faster dissolution of silicon from surface layers and homogenization of their composition. Formation of oxides of aluminum and cobalt with highly specific resistance makes it possible to carry out the PEO process for a sufficiently long time interval and to obtain oxide layers, enriched with the doping component. This is proved by the results of the study of morphology (Fig. 19.6b) and chemical composition of the surface layer (Fig. 19.7c). Volumetric mosaic structures cover the treated surface and contain up to 5 at. % of cobalt; and silicon concentration is not more than 2 at. %.

PEO at an initial current density of 10 A/dm^2 leads to a rapid formation of a barrier layer of Al_2O_3 by the end of min 1 of treatment. However, the oxidation process is unstable and rather quickly enters the arc mode. Formation voltage after 4 minutes of PEO drops to the level of 145–150 V. Large arc discharges, destroying the formed oxide layer, are visualized on the sample's surface. In this case, it is not possible to obtain the coating of the sufficient quality. Morphology of the surface layer (Fig. 19.6b) is characterized by islet structures with a considerable content of dopants. At the same time, the surface cobalt content is negligible and does not exceed 1.5 at. % (Fig. 19.7c).

An increase in oxidizing current density was found to contribute decreasing in silicon content in the surface layers of formed oxide coatings by 3–5 times compared to the untreated alloy. Mass fraction of silicon ω(Si) for the treated samples does not exceed 4 at. %. In this case, the content of aluminum and oxygen in coatings at current density varying changes only in the range of 2–3 at. %. Content of catalytically active component is an important characteristic for processing properties of PEO-based systems. The coating with the highest cobalt content was obtained at current density of 5 A/dm^2. It also contains the least amount of silicon of 2.1 at. %. Minimal cobalt incorporation is ensured in the oxidation process at $i = 10$ A/dm^2.

Thus, the rational parameters for obtaining coatings with high cobalt content and low concentration of impurities (Si) are to enter the sparking mode within 4–5 minutes and voltage of the micro-arc mode of up to 160–170 V. The optimal combination of the technological parameters of treatment and characteristic properties of the formed coating is achieved at PEO within the range of current densities of 3–5 A/dm^2.

It was also established that PEO must be performed in the incident power mode. Initial current density is higher for forming barrier aluminum oxide film on the AK12M2MgN substrate, which is accompanied by oxidation of the alloying components and particularly silicon with forming soluble substances and promotes homogenization of the alloy surface. After the process enters a mode of stable arcing current density for the following stages is reduced to ensure a formation of the mixed

oxide layer. The current density for the first PEO stage does not exceed the interval 5–10 A/dm, while the second stage is advisable to hold at current density of 2.0–4.0 A/dm.

19.1.3 Effect of Plasma-Electrolytic Oxidizing Time

The dynamics of morphology of surface layers and the content of major components in them can be traced at varying the oxidation time within the specified interval of current densities.

During PEO, a certain amount of anode current at the initial stage of oxidation is spent on the homogenization of the alloy surface [22]. The reflection of this is the change in the chemical composition and morphology of the sample surface (Fig. 19.8) at different sections of the characteristic curve (Figs. 19.1 and 19.5).

In the pre-spark mode the process runs over the classical anodizing: a layer of barrier alumina is formed. The process is visualized by a significant gas evolution

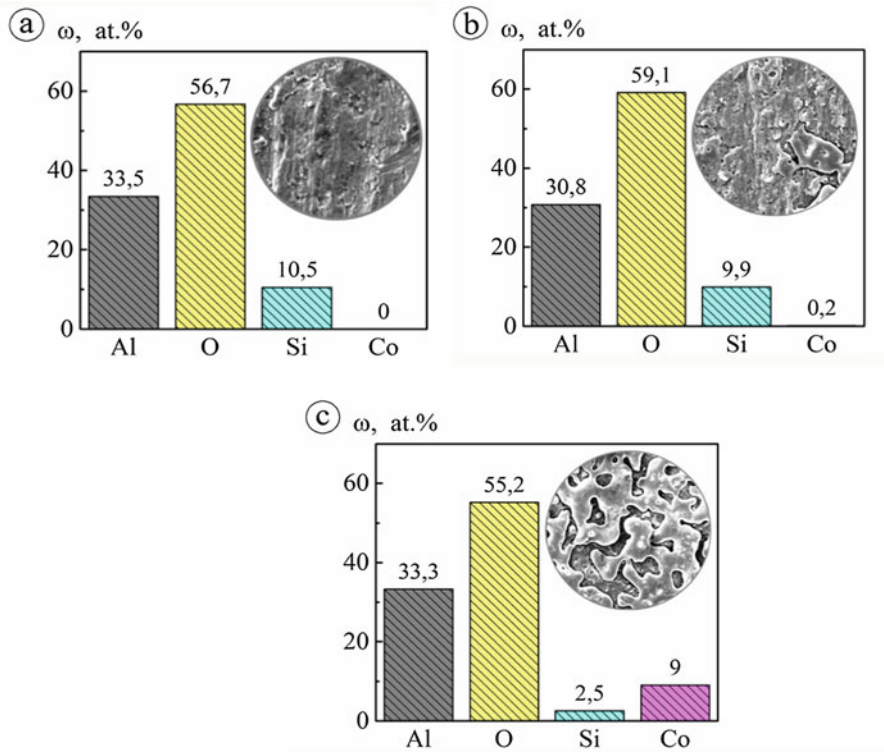

Fig. 19.8 Morphology and chemical composition of the surface (at.%) at the sections of the characteristic curve: pre-spark mode (**a**); spark mode (**b**); micro-arc mode 40 (**c**)

on the treated surface. The duration of this stage depends on the starting current density of oxidizing and for the studied conditions is 2–6 minutes.

Due to the simultaneous flow of partial reactions, there is a local dissolution of the alloying components, in particular, the silicon content at this stage is reduced by 3–5 at.%. There is a transition from the juvenile surface to the formation of a developed structure of Al_2O_3 with a large number of inclusions of irregular shape (Fig. 19.8a). At this stage, there is almost no cobalt incorporation into the oxide layer.

With the onset of sparkling (luminescence), a number of small sparks are visualized that cover the entire surface of the treated sample evenly. It characterizes the beginning of thermochemical reactions and the incorporation of products of high-temperature transformation of electrolyte components into the surface layers (Fig. 19.8b). On SEM images it is possible to identify a significant number of crater-like small openings with fused edges, which indicates the beginning of the formation of ceramic-like layer. The content of silicon in the surface layer is reduced by almost twice and is not more than 5 at. %. At the same time, the content of cobalt is gradually increasing to 3.5 at. %.

In micro-arc mode there is an increase in size sparks with a decrease in their number; the burning of micro-arc discharges occurs at the corners (projections) of the sample and is accompanied by a characteristic cracking due to the "collapse" of gas vapors in micro-discharge channels. In the places of burning sparks there are spheroid islands of cobalt oxides. During processing, the number of such island structures is significantly increased; they are combined and agglomerated and form mosaic structures (Fig. 19.8c).

Summary results of changing the chemical composition of oxide coatings $Al_2O_3 \cdot CoO_x$, formed for 10–60 minutes, are shown in Fig. 19.9.

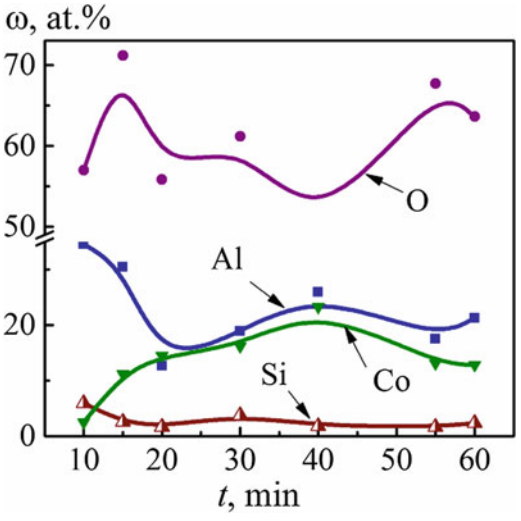

Fig. 19.9 Changes in the chemical composition of coatings $Al_2O_3 \cdot CoO_x$ vs the time of PEO

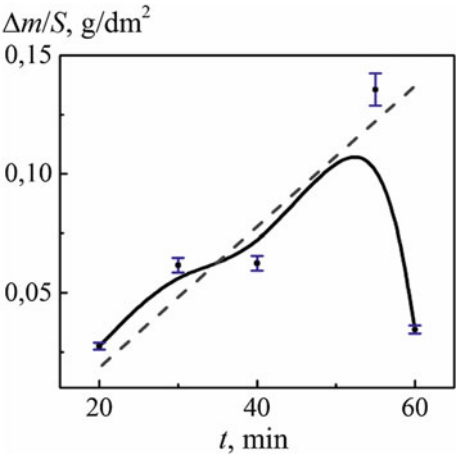

Fig. 19.10 Chronogram of the formation rate for oxide $Al_2O_3 \cdot CoO_y$ on silumin. Dotted line – process trend

Analysis of oxide systems indicates a non-stoichiometric ratio of cobalt and oxygen, which is favorable for the implementation of catalytic processes involving oxygen.

Investigation of the quantitative indexes of the formation of oxide coating showed that the growth of the relative mass of the formed mixed oxides layer is a function of time (Fig. 19.10). The obtained dependence reflects the peculiarity of the formation of PEO-covers on each of the steps of the characteristic curve (Figs. 19.1 and 19.5).

The actual increase in the mass of the oxide layer is observed only in the micro-arc mode with a gradual increase and a maximum of 55 minutes of processing. The optimal time interval, based on the results obtained, is the oxidizing of silumin within 30–55 minutes.

It should be noted that the change in the chemical composition of the oxide coatings can be traced in the morphology change of the surface layers in the variation of PEO processing time. The incorporation of cobalt into the surface layers substantially changes their morphology and causes the formation of bulk structures with a high specific surface.

The coating surface changes from unevenly rough (Fig. 19.11a) to uniformed mosaic (Fig. 19.11b) and then to globular-mosaic (Fig. 19.11c–e) at an increase in oxidizing time from 10 to 55 minutes. Oxidizing within 60 minutes or more leads to "overgrowing" of the voluminous structure and its visual alignment (Fig. 19.11f).

Plots of different topography (Fig. 19.12a–d) are selected for comparative analysis of the formed oxide coatings.

Analysis of the chemical composition of the obtained oxide structures in the areas of different topography indicates enrichment of the surface layer with cobalt at an increasing PEO time. At that, in all cases, its concentration on projections of the coating is 2–3 times higher in comparison with the content on the basic surface (Fig. 19.13).

The lowest cobalt content in the coating (up to 0.6 at. %) was obtained at oxidation of samples within 10 minutes (Fig. 19.13a). The highest concentration of

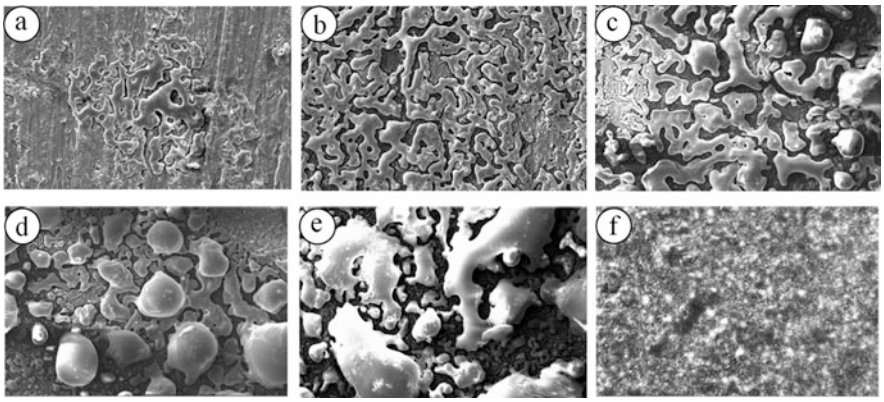

Fig. 19.11 Morphology of surface of $Al_2O_3 \cdot CoO_x$ coating on silumin, obtained in pyrophosphate electrolyte at different oxidation times, min: 15 (**a**); 20 (**b**); 30 (**c**); 40 (**d**); 55 (**e**); 60 (**f**). Magnification ×500

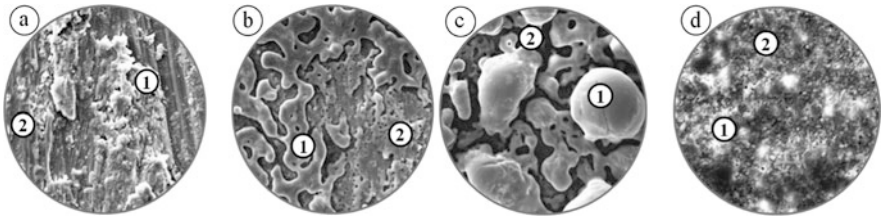

Fig. 19.12 Morphology of surface of $Al_2O_3 \cdot CoO_x$ coating for chemical analysis, obtained at different oxidation times, min: 10 (**a**); 20 (**b**); 40 (**c**); 60 (**d**). Magnification ×1000

the dopant (up to 23 at. %) is observed in ceramic-like globules of the coating (Fig. 19.13c) at PEO within 40 minutes. In other cases, cobalt content on the projections is 15–20 at. % and on the plateau of the coating, it is 2–2.5 at. % (Fig. 19.13b, d). This distribution of the dopant on the surface is explained by peculiarities of the PEO, in which cobalt transport to projections of the sample surface is facilitated, while its transport to pores is complicated. Bearing in mind the possibility of thermolysis of water and release of oxygen on the anode, one may assume that released gases carry the dopant salts out of pores [19].

The inverse dependence is observed for silicon content in surface layers: its concentration decreases at an increase in treatment time. The most effective Si removal from the surface layer is achieved when PEO lasts more than 20 minutes (Fig. 19.13a–d). It is explained by chemical instability of silicon oxides in the alkaline medium and at high temperatures in sparking region.

The obtained results are in full accordance with the kinetic laws and allow determining the rational time of PEO for obtaining oxide coatings of the specified composition and morphology.

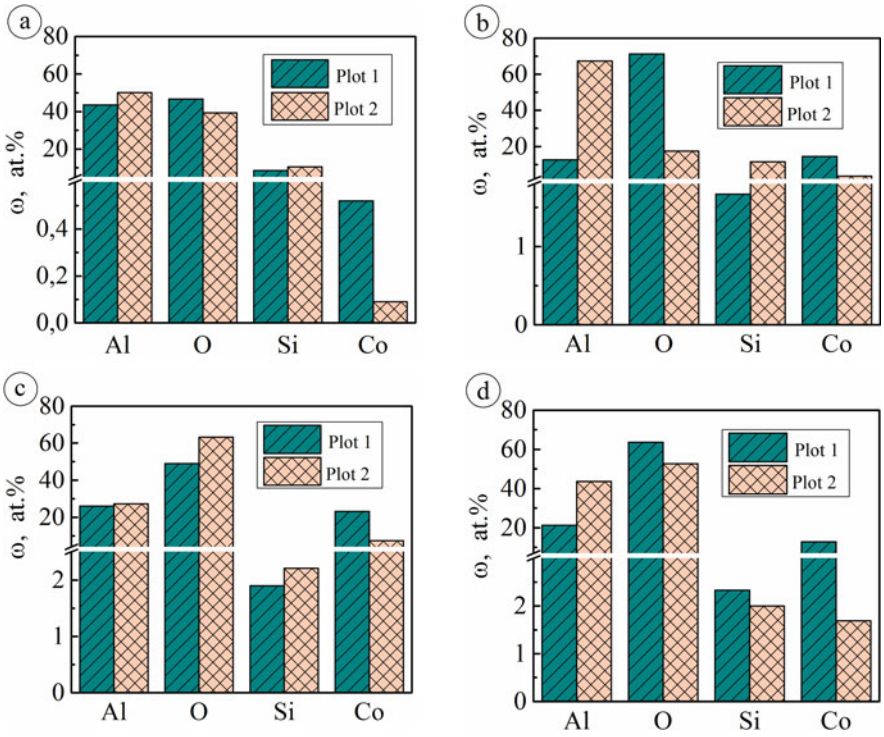

Fig. 19.13 Chemical composition of plots 1 and 2 (Fig. 19.12) of $Al_2O_3 \cdot CoO_x$ coatings on silumin oxidized within different times, min: 10 (**a**); 20 (**b**); 40 (**c**); 60 (**d**)

Table 19.2 Recommended parameters of plasma-electrolytic treatment of silumin AK12M2MgN and the formation of mixed oxide incorporated by cobalt

Parameter	Coating $Al_2O_3 \cdot CoO_x$
Electrolyte composition, mol/dm^3	$CoSO_4$–0.1, $K_4P_2O_7$–0.4
Temperature, °C	20 . . . 25
Treatment mode	galvanostatic, incident power
Current density, A/dm^2	3 . . . 5
Voltage, V	115 . . . 160
Treatment time, min	20 . . . 40
Content, at. %cobaltsilicon	up to 24.0up to 2.0

Thus, the results of the carried out studies take into account the influence of the electrolyte composition and PEO parameters on the chemical composition and morphology of the surface of cobalt-containing oxide coatings on the AK12M2MgN. Proceeding from this, the following technological parameters of the silumin treatment can be recommended to incorporate the catalytically active component and minimize the silicon content in the surface layers (Table 19.2).

Based on the research results analysis, optimal parameters of plasma electrolytic oxidizing of silumin AK12M2MgN are determined, under which effective treatment of the alloy with formation of oxide coating incorporated by cobalt is provided.

19.1.4 Topography and Phase Composition of PEO Cobalt-Containing Coatings

The study of morphology and chemical composition of the surface layers makes it possible to conclude that PEO treatment of high-silicon silumin in pyrophosphate electrolyte with addition of cobalt sulfate leads to formation of a sufficiently developed voluminous structure.

A high degree of surface development of mixed $Al_2O_3 \cdot CoO_x$ coatings is proved by the results of atomic-force microscopy (Fig. 19.14). For comparative analysis samples with different dopant content were taken. It was established that the cobalt incorporation leads to an increase in roughness oxide layers compared to the Al | Al_2O_3.

The oxide coating with 1.0 at.% of cobalt (Fig. 19.14a) consists of a number of conglomerates of spherical structures with an average size of 1.5–2 um which gather and form the parts of smooth surface. The surface roughness may be characterized with the spread of conglomerate size on the cross section between markers 1–2. In addition, indicators of roughness these coatings R_a and R_q are in the range of 160–190 nm.

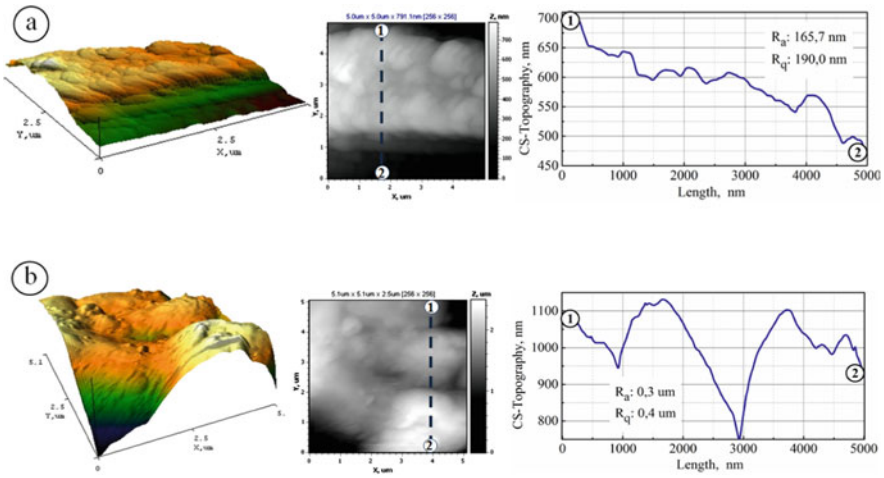

Fig. 19.14 3D and 2D surface maps and cross-sectional profile of Al|Al_2O_3 CoO_x coating with different cobalt containing at.%: 1.0 (**a**); 10.0 (**b**). Scanning area 5 × 5 μm

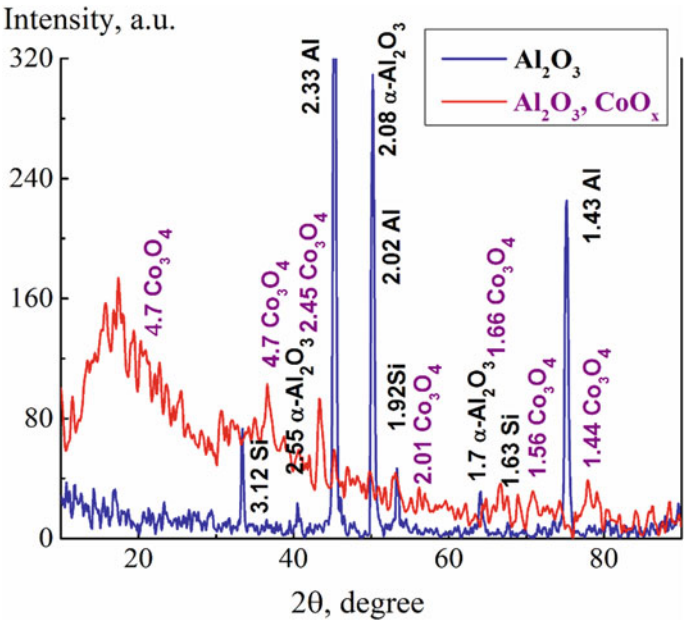

Fig. 19.15 X-ray diffraction patterns for systems Al_2O_3 and Al_2O_3, CoO_x

An increase in cobalt content up to 10.0 at.% (Fig. 19.14b) leads to formation of a voluminous mosaic structure. Taking into consideration the resolution capability of the probe, it is possible to scan effectively its most projected part [29]. The studied ceramic-like structure is a conglomerate and consists of a number of small spherical components, forming a smooth globular surface. Indicators of roughness of obtained coatings R_a and R_q are in the range of 0.3–0.4 um in the studied scan area.

Figure 19.15 shows X-ray diffraction patterns for oxide systems $Al|Al_2O_3$ (blue line) and $Al|Al_2O_3 \cdot CoO_x$ (red line) obtained in pyrophosphate electrolytes.

The X-ray diffraction pattern $Al|Al_2O_3$ (Fig. 19.15, *blue line*) contains peaks of the components of the substrate material (aluminum, silicon) and aluminum oxide which indicates the formation of α-$Al|Al_2O_3$ during oxidizing.

The addition of cobalt sulfate to the working electrolyte leads to the incorporation of cobalt oxides in the aluminum oxide matrix and formation of mixed $Al|Al_2O_3 \cdot CoO_x$ which reflects by X-ray diffraction patterns (Fig. 19.15, *red line*). It is interesting that aluminum and silicon lines disappear and the lines corresponding to the mixed oxide (Co_3O_4) are manifested. No any line of silicon at the diffraction patterns reflects the effective silumin surface-treatment in the complex cobalt-pyrophosphate electrolyte. On X-ray diffraction pattern also revealed an amorphous halo at angles 2θ–20°, due to the peculiarities of formation of an oxide PEO structure under non-equilibrium conditions.

In general, the obtained results both AFM and X-ray analysis correlate with data for oxide PEO systems on aluminum alloys and other valve metals [18, 30].

19.1.5 Corrosion Behavior of Cobalt-Containing Coatings on Silumin

Corrosion properties of cobalt-containing oxide coatings, synthesized in PEO mode, were determined by the results of potentiometry and impedance measurement of electrodes exposed in medium of varying acidity. The dynamics of the chemical resistance reflect the chronograms of the corrosion potentials, as well as the significance of the elements of equivalent circuits, which visualize the information responses of individual states of the electrochemical systems to external polarization. The geometry of the hodographs for the impedance of multicomponent cobalt-containing oxide systems reflects the generalized Voit model. According to this model, an equivalent circuit of an electrode can be given by the sequence R–C chains (Fig. 19.16). The latter are distinguished by the nature of physical and chemical processes and phenomena, which correspond individual elements and, significantly, the R–C chains of different time constants. The first chain reflects the

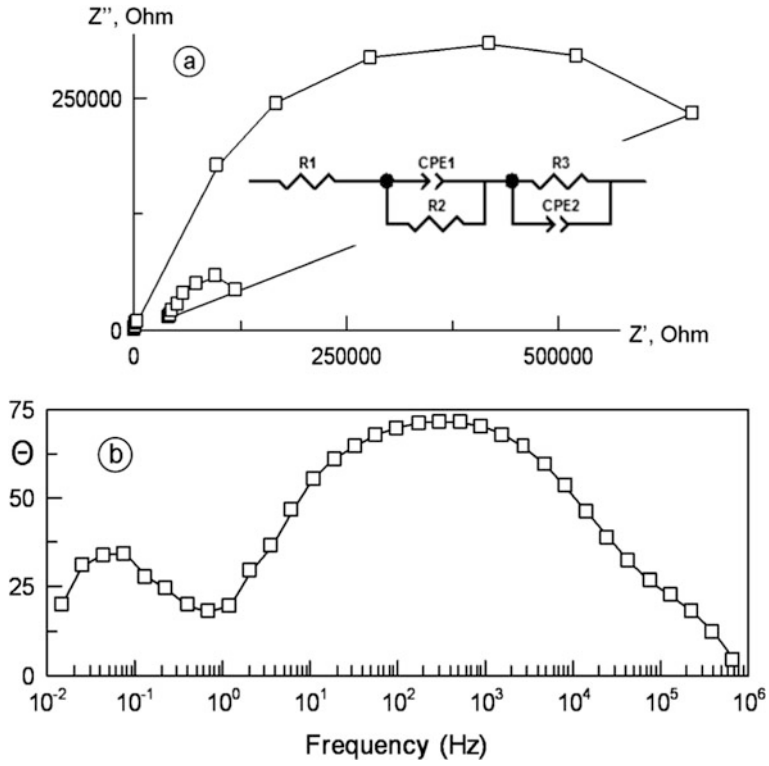

Fig. 19.16 The Nyquist plots (**a**) and frequency dependence of phase angle (**b**) for system $Al|Al_2O_3, CoO_x$

Table 19.3 Corrosion indicators of heteroxide PEO coatings

Corrosion medium	Coating	Current index, $j_c \cdot 10^6$, A/cm^2		Deep index, $k_h \cdot 10^3$, mm/year	
		1 day	30 days	1 day	30 days
0,1 M Na_2SO_4	$Al\|Al_2O_3$[a]	3.40	0.39	37.03	4.25
	$Al\|Al_2O_3, CoO_x$	0.04	0.004	0.44	0.04
0,01 M NaOH	$Al\|Al_2O_3$[a]	3.54	10.36	38.55	112.8
	$Al\|Al_2O_3, CoO_x$	1.93	0.70	21.02	7.62

[a]Oxide coating obtained from an electrolyte based on sulfate acid

Table 19.4 Characteristics of the CO conversion to CO_2

Material	Active metal content, at %	Ignition temperature T_i, K	Complete conversion temperature T_c, K
Pt	100	490	570
$Al\|Al_2O_3$	30.8	595	670
$Al\|Al_2O_3 \cdot CoO_x$	8.7	505	580

properties of the oxide coating, and the second one is associated with the kinetics of corrosion process.

Corrosion indexes of heteroxide systems (deep corrosion rate and corrosion current) (Table 19.3) are calculated using the equivalent circuit parameter R3 on 2–3 orders of magnitude smaller than for the traditionally oxidized in sulfate acid mono-oxide systems. Corrosion potentials of samples with complex oxide coatings are much more positive than ones for samples oxidized by classical technology. Corrosion inhibition by heteroxide systems with the increase of the exposure time in freely aerated media (Table 19.3) is due to the insignificant porosity of the formed oxides which does not exceed 5%.

19.1.6 Catalytic Activity of $Al_2O_3 \cdot CoO_x$ Coatings

The peculiarities of the phase structure obtained oxide coatings in combination with a developed surface, and a high content of cobalt is a prerequisite for their high catalytic properties.

Testing of oxide system in the model reaction of carbon (II) oxide conversion to CO_2 showed (Table 19.4) that their activity (both ignition and complete conversion temperature) is close to platinum catalyst.

This can be attributed to several factors: first due to a high affinity of non-stoichiometric cobalt oxides to oxygen and the corresponding decrease in the activation energy of double bonds O=O destruction [7, 31]. Secondly, the developed micro-globular surface of oxide systems is characterized by a large number of catalytic centers and provides an increase in the number of elementary collisions and interactions.

Pilot tests of mixed oxides deposited on the surface of combustion chambers piston of the ICE showed that the coating of $Al_2O_3 \cdot CoO_x$ allows to reduce NO_x emissions within 10% and CO 15–18% at forced diesel engine operating modes. This is due to lower ignition temperature of the air-fuel mixture on the surface of $Al \mid Al_2O_3 \cdot CoO_x$ catalyst composed of mixed oxides with developed surface [32].

19.2 Conclusions

The regularities of influence of the electrolyte content and parameters of plasma-electrolytic oxidizing of silumin AK12M2MgN in pyrophosphate cobalt-containing electrolyte were studied.

It was established that the formation of PEO coatings on high-silicon silumin with a maximum content of cobalt at minimizing the impurities is expedient to carry out from the electrolyte with a composition of 0.4 mol/dm^3 $K_4P_2O_7$, 0.1 mol/dm^3 $CoSO_4$.

Also it was found that a change of the working current density and the time of PEO enable us to control the process of cobalt incorporation in matrix of basic metal oxide. It was found that PEO must be performed in the incident power mode. The current density for the first PEO stage does not exceed the interval 5–10 A/dm, while the second stage is advisable to hold at current density of 2.0–4.0 A/dm. It is advisable to conduct formation of PEO coatings on silumin within 20–40 minutes to obtain the developed surface and cobalt content up to 23 at. % and minimizing silicon content at the level of 3 at. %.

Cobalt incorporation in the surface oxide layers leads to a change in surface morphology and topography. Obtained oxide systems have a high degree of surface development and consist of nanostructured spherical conglomerates.

Oxide coatings on silumin incorporated by cobalt possess the increased corrosion resistance and catalytic activity in comparison with pure aluminum oxide. These systems can find application in ecological catalysis.

References

1. Glazoff MV, Zolotorevsky VS, Belov NA (2007) Casting aluminum alloys. Elsiever, Oxford, p 544
2. Dong H (2010) Surface engineering of light alloys: aluminium, magnesium and titanium alloys. Woodhead Publishing Limited, Oxford, Cambridge, New Delhi, p 680
3. Rudnev VS, Lukiyanchuk IV, Vasilyeva MS, Medkov MA, Adigamova MV, Sergienko VI (2016) Aluminum- and titanium-supported plasma electrolytic multicomponent coatings with magnetic, catalytic, biocide or biocompatible properties. Surf Coat Technol 307 (Part C) 307:1219–1235
4. Karakurkchi A, Sakhnenko M, Ved M, Galak A, Petrukhin S (2017) Application of oxide-metallic catalysts on valve metals for ecological catalysis. East Eur J Enterp Technol 5/10(89):12–18

5. Gupta P, Tenhundfeld G, Daigle EO, Ryabkov D (2007) Electrolytic plasma technology: science and engineering – An overview. Surf Coat Technol 201(21):8746–8760
6. Rakoch AG, Khokhlov VV, Bautin VA, Lebedeva NA, Magurova YV, Bardin IV (2006) Model concepts on the mechanism of microarc oxidation of metal materials and the control over this process. Prot Met 42(2):158–169
7. Sakhnenko N, Ved M, Karakurkchi A, Galak A (2016) A study of synthesis and properties of manganese-containing oxide coatings on alloy VT1−0. East Eur J Enterp Technol 3/5(81):37–43
8. Bykanova VV, Sakhnenko ND, Ved' MV (2015) Synthesis and photocatalytic activity of coatings based on the $Ti_xZn_yO_z$ system. Surf Eng Appl Electrochem 51(3):276–282
9. Lukiyanchuk IV, Rudnev VS, Tyrina LM (2016) Plasma electrolytic oxide layers as promising systems for catalysis. Surf Coat Technol 307 (Part C) 307:1183–1193
10. Sakhnenko M, Karakurkchi A, Galak A, Menshov S, Matykin O (2017) Examining the formation and properties of TiO_2 oxide coatings with metals of iron triad. East Eur J Enterp Technol 2(11/86):4–10
11. Rogov AB, Slonova AI, Shayapov VR (2012) Peculiarities of iron-containing microplasma coating deposition on aluminum in homogeneous electrolyte. Appl Surf Sci 261:647–652
12. Rudnev VS, Yarovaya TP, Nedozorov PM, Mansurov YN (2017) Wear-resistant oxide coatings on aluminum alloy formed in borate and silicate aqueous electrolytes by plasma electrolytic oxidation. Prot Met Phys Chem Surf 53:466
13. Rogov AB (2015) Plasma electrolytic oxidation of A1050 aluminium alloy in homogeneous silicate-alkaline electrolytes with edta4-complexes of Fe, Co, Ni, Cu, La and Ba under alternating polarization conditions. Mater Chem Phys 167:136–144
14. Dudareva NY, Abramova MM (2016) The structure of plasma-electrolytic coating formed on Al–Si alloys by the micro-arc oxidation method. Prot Met Phys Chem Surf 52(1):128–132
15. Wang P, Li JP, Guo YC, Yang Z, Wang JL (2016) Ceramic coating formation on high Si containing Al alloy by PEO process. Surf Eng 32(6):428–434
16. Ayday A, Durman M (2015) Growth characteristics of plasma electrolytic oxidation coatings on aluminum alloys. Acta Phys Pol A 127(4):886–887
17. Boguta DL, Rudnev VS, Yarovaya TP, Kaidalova TA, Gordienko PS (2002) On composition of anodic-spark coatings formed on aluminum alloys in electrolytes with polyphosphate complexes of metals. Russ J Appl Chem 75(10):1605–1608
18. Sakhnenko ND, Ved MV, Karakurkchi AV (2017) Nanoscale oxide PEO coatings forming from diphosphate electrolytes. In: Fesenko O, Yatsenko L (eds) Nanophysics, nanomaterials, interface studies, and applications. NANO 2016. Springer proceedings in physics 195. Springer, Cham, pp 159–184
19. Ved' MV, Sakhnenko ND, Karakurkchi AV, Myrna TY (2017) Functional mixed cobalt and aluminum oxide coatings for environmental safety. Funct Mater 24(2):303–310
20. Borisov AM, Borisov AM, Krit BL, Lyudin VB, Morozova NV, Suminov IV, Apelfeld AV (2016) Microarc oxidation in slurry electrolytes: a review. Surf Eng Appl Electrochem 52(1):50–78
21. Malyshev VN, Zorin KM (2007) Features of microarc oxidation coatings formation technology in slurry electrolytes. Appl Surf Sci 254(5):1511–1516
22. Sakhnenko ND, Ved' MV, Androshchuk DS, Korniy SA (2016) Formation of coatings of mixed aluminum and manganese oxides on the AL25 alloy. Surf Eng Appl Electrochem 52(2):145–151
23. Dai L, Li W, Zhang G, Fu N, Duan Q (2017) Anti-corrosion and wear properties of plasma electrolytic oxidation coating formed on high Si content Al alloy by sectionalized oxidation mode. IOP Conf Ser Mater Sci Eng 167:012063
24. Labardi M, Allegrini M, Salerno M, Fredriani C, Ascoli C (1994) Dynamical friction coefficient map using a scanning force and friction force microscope. Appl Phys 59:3
25. Arbizzani C, Borghini M, Mastragostino M, Meneghello L, Zanelli A (1994) Impedance spectroscopy in electrode/electrolyte interface investigations. Solid State Ion 72(2):115–121. https://doi.org/10.1016/0167-2738(94)90134-1

26. Ved' MV, Sakhnenko MD, Bohoyavlens'ka OV, Nenastina TO (2008) Modeling of the surface treatment of passive metals. Mater Sci 44(1):79–86
27. Yar-Mukhamedova GS, Ved MV, Karakurkchi AV, Sakhnenko ND (2017) Mixed alumina and cobalt containing plasma electrolytic oxide coatings. IOP Conf Ser Mater Sci Eng 213:012020
28. Cho JY, Hwang DY, Lee DH, Yoo B, Shin DH (2009) Influence of potassium pyrophosphate in electrolyte on coated layer of AZ91 Mg alloy formed by plasma electrolytic oxidation. Trans Nonferrous Met Soc Chin 19:824–828
29. Senesi GS, Massaro A (2016) AFM applications to the analysis of plasma-treated surface growth and nanocomposite materials. Curr Nanosci 12(2):202–206
30. Serdechnova M, Mohedano M, Bouali AC, Höche D, Kuznetsov B, Karpushenkov S, Blawert C, Zheludkevich ML (2017) Role of phase composition of PEO coatings on AA2024 for in-situ LDH growth. Coatings 7:190
31. Snytnikov PV, Belyaev VD, Sobyanin VA (2007) Kinetic model and mechanism of the selective oxidation of CO in the presence of hydrogen on platinum catalysts. Kinet Catal 48(1):93–102
32. Parsadanov IV, Sakhnenko ND, Ved' MV, Rykova IV, Khyzhniak VA, Karakurkchi AV, Gorokhivskiy AS (2017) Increasing the efficiency of intra-cylinder catalysis in diesel engines. Vopr Khim Khim Tekhnol 6:75–81

Chapter 20
Effect of Carbon Nanofillers on Processes of Structural Relaxation in the Polymer Matrixes

T. G. Avramenko, N. V. Khutoryanskaya, S. M. Naumenko, K. O. Ivanenko, S. Hamamda, and S. L. Revo

20.1 Introduction

Nanocomposite materials (NCMs) are an important group of engineering materials that contain a combination of two or more different materials with a clear interface between them. Such structural features of NCMs as nanosized elements and their morphology and interfacial boundaries provide the unique complex of physical properties of these materials that is quite interesting not only in the context of their application but also toward developing our knowledge on materials science.

Besides one of the most important tasks of appliance manufacturing is the creation of reliable and sustainable parts and elements of structures. This can be successfully solved with the use of materials with high and stable physical-mechanical, electrophysical, and chemical characteristics. Formation and development of scientifically principles of obtaining lighter, stronger and more resistant to external influences NCM in comparison with traditional ones is relevant for today [1, 2]. Increasing scientific interest in the creation and research of new polymer-carbon NCMs is associated with a significant expansion of the areas of use of these materials. At the same time, PE - thermoplastic polymer, one of the main disadvantages of which are low thermal conductivity, resistance to ultraviolet radiation, fluidity, which begins at low relative deformations and, accordingly, a high tendency to deformation under prolonged static loads. With the use of nanosized fillers, these shortcomings can be partially eliminated or materials with new improved characteristics can be obtained. For example, the use of carbon

T. G. Avramenko · N. V. Khutoryanskaya · S. M. Naumenko · K. O. Ivanenko · S. L. Revo (✉)
Taras Shevchenko National University of Kyiv, Kyiv, Ukraine

S. Hamamda
Laboratory of Thermodynamics and Surface Treatment of Materials, University of Frères Mentouri Constantine 1, Constantine, Algeria

O. Fesenko, L. Yatsenko (eds.), *Nanocomposites, Nanostructures, and Their Applications*, Springer Proceedings in Physics 221,
https://doi.org/10.1007/978-3-030-17759-1_20

nanotubes as filler, which have a high specific strength, makes it possible to improve the mechanical properties and electrical conductivity of NCM (at concentrations of CNTs exceeding the percolation threshold) [3, 4].

Another promising representative of carbon nanofiller is expanded graphite (EG). Its particles consist of graphene blocks separated of air gaps. EG has high compactability and anisotropy of physical properties. In spite of a great number of studies aimed at creating and investigating polymer NCM with carbon nanofillers, there are no thorough results about how EG morphology and dispersion of its particles affect structural relaxation of polymer. In our case it is fluoroplastic (FP) (polychlorotrifluoroethylene) matrix.

Therefore, the study on the effect of carbon nanofiller, its morphology and concentration on processes of structural relaxation in polymer matrixes is the main goal of present work.

20.2 Methods

Low-density PE and FP as matrixes and MWCNTs and grinded EG as fillers were chosen for preparation of NCM samples for testing. Low-density PE is a moisture- and corrosion-resistant and price-accessible raw material. Among all types of polyethylene, this material has the highest physical and chemical performance. MWCNT were purified in a traditional way in a solution of hydrofluoric hydrochloric acid, after which they were washedobtained by the CVD method in a rotating reactor [5, 6]. As a catalyst, oxides of the type Al_2O_3-MoO_3-Fe_2O_3 were used. The source of carbon was propylene, obtained by dehydration of isopropyl alcohol. MWCNT were purified in a traditional way - in a solution of hydrofluoric hydrochloric acid, after which they were washed. Parameters of nanotubes were as follows: average diameter of 10–20 nm, specific surface area (determined by argon desorption method) of 200–400 m^2/g, and poured bulk density varying from 20 to 40 g/dm^3. The concentration (C) of nanotubes in the NCM was changed in the range of 0.3–5 vol.%. Polyethylene and carbon nanotubes-based powder mixtures were mechanically milled in a drum mixer. A special vacuum mold with a spinner was used to make the samples by extruding the NCM molten mixture.

FP powder of B3 grades and EG, obtained by thermolysis of oxidized graphite in an ascending stream furnace, were used for the preparation of NCM on the basis of FP. The initial EG was mechanically grinded in a two-piston disintegrator. After shredding, the EG particles were separated by different fractions using a set of sieves. As a result, the following fractions of particles were obtained: <60 μm, 60–100 μm, 100–160 μm, 160–200 μm, and 200–315 μm. After mixing the FP and dispersed EG powders in a rotary stirrer of a revolving type, the mixture was compressed at a load of 1000 kg/cm^2 and sintered at a temperature of 215 °C.

Photographs of the microstructure of the materials were obtained using a transmission electron microscope manufactured by SELMI [7] at an accelerating voltage of 100 kV and the optical microscope AXIO Observer A1m production

of the new generation (CarlZeiss), the maximum increase of which is 1000x [8]. Samples for research by the method of transmission electron microscopy were prepared in an agate mortar with water. The resulting suspensions were applied to a copper mesh coated with a carbon film. The grid was dried in vacuum for 5 h at a temperature of 150 °C.

The structural characteristics of the samples were determined using diffractograms obtained on an automated diffractometer DRON-4 M with CuKα radiation (0.154 nm). The original software package elaborated for the automated DRON equipments and including full complex of the Rietveld refinement procedure was used [9].

Measurement of the ADIF was carried out through the inverted torsion pendulum method [10].

Tensile strength (for nonbreakable samples) was determined by computerized equipment of type). The device can measure changes of tension depending on the strain $\sigma = f(\varepsilon)$ and time $\sigma = f(t)$ degree. The rate of bursting machine is 2.5–25 mm/min. The maximum load on the sample is 200 kg. The sample studied had a working area of 20–25 mm. Stretching speed was 5 mm/min. Average tensile strength was measured on ten samples at room temperature. Stress relaxation was studied by a step change in the load. After each load, the sample was left in a stressed state for 80 min until the saturation curves were released. After that, stress relieving and further loading were carried out.

20.3 Results and Discussion

Image of MWCNTs (Fig. 20.1a), obtained by the transmission electron microscopy, demonstrates the presence of agglomerates, which is natural for this material. This always creates technological difficulties at the production of compositions with a uniform distribution of MWCNTs. In the case of EG at low concentration in the polymer matrix, it is possible to achieve an isotropic distribution of particles. But when EG concentration is higher than 5 vol.%, the NCM structure becomes more anisotropic and layered (Fig. 20.1b).

During samples sintering, EG flakes line up in planes perpendicular to the pressure direction. At the same time, with the decrease of dispersity, the average thickness of the carbon layers grows. For example, for NCM FP-EG with EG concentrations of $C = 10$ vol.% and particles dispersity (an average particle size) of $s = 80$ μm an average layer thickness ≈ 8 μm. But for NCM with EG dispersity of $s = 180$ μm it is ≈ 12 μm. Increasing of EG concentrations causes the conglomeration of individual particles aggregates. The thickness of filler layers increases and varies in the range of 8–20 μm. Both main channels of the EG and separate graphite flakes can be clearly observing (Fig. 20.1b).

The analytical calculation of structural anisotropy of FP-EG samples was made on the basis of their microstructure analysis. In particular, the ratio between the carbon component and the total composition area was determined. The structural

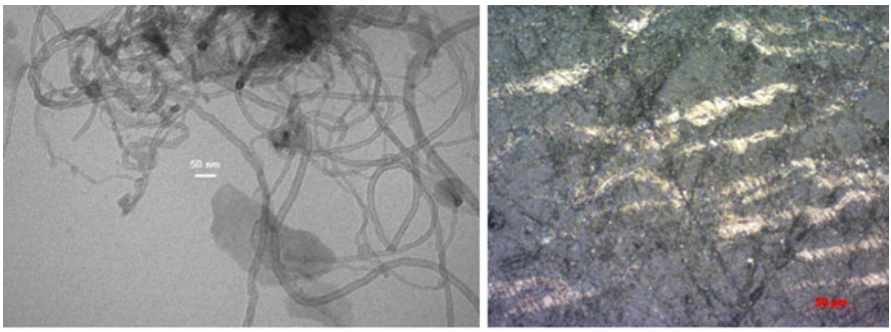

Fig. 20.1 TEM image of MWCNTs (**a**) and optical image of FP-EG sample cut (**b**) with $s(\mathrm{EG}) = 180$ μm and $C(\mathrm{EG}) = 15$ vol.%

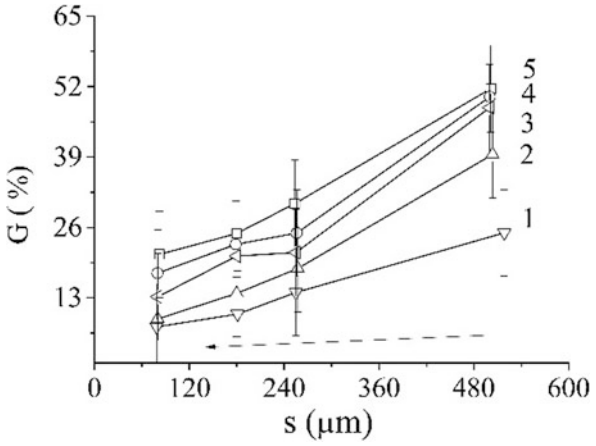

Fig. 20.2 Dependence of the structure anisotropy parameter for the FP-EG NCM with the EG concentration of 5 (1); 7 (2); 10 (3); 15 (4); 20 (5) vol.% vs filler dispersity

anisotropy parameter (G) was calculated by the formula:

$$G = \frac{S_{\mathrm{EG}}}{S_{\mathrm{EG}} + S_{\mathrm{FP}}} \cdot 100\%, \tag{20.1}$$

where S_{EG} –is the area occupied by EG particles and S_{FP} by FP.

The dependences of structural anisotropy parameter vs the average EG particle size are presented in Fig. 20.2. Parameter G gives us an opportunity to estimate the distribution of the filler on the sample cut.

The value of G decreases with increasing dispersity of filler particles and increases with increasing concentration in the polymer matrix. For example, G decreases from 20% to 9% with an increase in dispersity for NCM with C

(EG) = 5 vol.%, whereas the structure anisotropy parameter decreases by almost 2.5 times for C (EG) = 20 vol.%.

On the diffractograms of the samples, the Bragg maxima were observed in the region of 2θ – 21° and 24° corresponding to the crystalline phase for the PE and the diffuse halo with maximum of 19°50′. These data are consistent with literature. Three peaks with centers at 2θ = 28, 50, and 63 degrees were fixed for carbon nanotubes. The Bragg's diffraction has shown that PE has an amorphous and crystalline structure. Similarly, this was found for FP matrix. The ratio of the integral intensities of the Braggs peaks, corresponding to the crystalline and amorphous phases, was chosen to determine the degree of crystallinity for polymers. The degree of crystallinity (χ) does not show the actual content of the crystalline phase, but it is indirectly related to the content of crystallites in the material. The value of χ was determined using the equation:

$$\chi = \frac{I_c}{I_c + I_a} \tag{20.2}$$

where I_c is the area under the crystalline peaks and I_a is the area under the amorphous peaks.

The resulting triplet of PE was investigated to determine the degree of crystallinity of the NCM matrix. The installation background was taken away from the original data and multiplet was divided into individual peaks. The degree of crystallinity was determined as the ratio of the area of the two crystal peaks in the total area under the triplet, which was observed (Eq. 20.2).

The literature indicates that the use of carbon nanotubes as a filler leads to an increase in the degree of crystallinity of the matrix [11, 12]. But this is not always the case. The main factors affecting this parameter are the spatial distribution of components, their dimensions, and adhesion. Due to nature (large specific surface), carbon nanotubes tend to form agglomerates and are held together by van der Waals forces. One of the most important tasks of the researchers is to ensure a good distribution of dispersed nanotubes in the matrix and to select an appropriate method of sample production [13, 14]. The formation of supramolecular structures in polymers is a complex and multistage process that is determined by the chemistry of the polymers and the parameters of the manufacturing process such as temperature, molding pressure, holding time under specified conditions, cooling rate of the material, etc.

The dependence of the crystallinity degree of the matrix on nanotubes concentration is shown in Fig. 20.3. Both the content of MWCNTs in the composite and the conditions of its production influence on the formation process of the crystalline structure of PE. For this, sintered and extruded specimens of polymer NCMs were investigated.

For PE-MWCNTs NCM obtained by vacuum sintering under the pressure of 20 MPa at a temperature of 120 °C, the degree of crystallinity monotonically decreases with increasing concentration of MWCNTs. The degree of crystallinity of unfilled PE – 86%. With the increase of the content of the carbon component

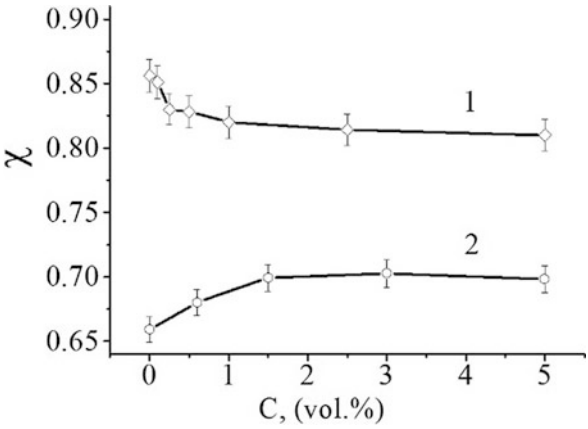

Fig. 20.3 Dependences of the degree of crystallinity of the polymer matrix on the concentration of carbon nanotubes for PE-MWCNTs samples obtained by hot vacuum sintering (1) and extrusion (2)

in the composition to 5 vol.%, degree of crystallinity decreases to 80%. This can be explained by blocking formation of an ordered globular-lamellar structure of the matrix by nanotubes.

For PE-MWCNTs composite obtained by extrusion, the degree of crystallinity of the matrix is significantly decreased, and another influence of the concentration of nanotubes on the degree of crystallinity is observed. With the increase in the content of carbon filler, the value of χ increases. In this case, the carbon component acts as a catalyst for the formation of crystallites [14].

The results have shown that the manufacturing method of NCM influences on the degree of crystallinity of the PE matrix. The mechanism of structuring of the polymer matrix occurs under composition cooling. When a polyethylene melt solidifies, particles of MWCNTs act as centers of nucleation of the crystalline phase. At the same time the size of the crystalline formations is strongly influenced by the cooling rate of the polymer and the temperature of the melt in the process. Cooling rate is higher for extrusion. The time for the molecule's rearrangement is not enough and crystallization ends in the intermediate phase. So, small crystalline structures are formed in material.

The degree of crystallinity of the FP matrix filled with carbon nanofillers also changes. Both the concentration of EG and its particle's morphology effect on the structure of the polymer.

The initial TEG particles had a specific wormlike shape. Previous studies [15] have demonstrated that each EG particle is a laminated package of graphite plates, whose thickness varies from unity to several hundreds of nanometers with the spacing between 10 nm and 10 μm. It was also found [16, 17] that the morphology of the grinded EG particles changes. Mechanical grinding causes break of the framework of EG worms and its particles fragmentize into platelets. Here, particles of greater size (260 μm) were observed as separate EG elements or shapeless plates with ragged edges, whereas particles of higher dispersity (~40 μm) are similar to microdisks, which shape tends to equiaxial.

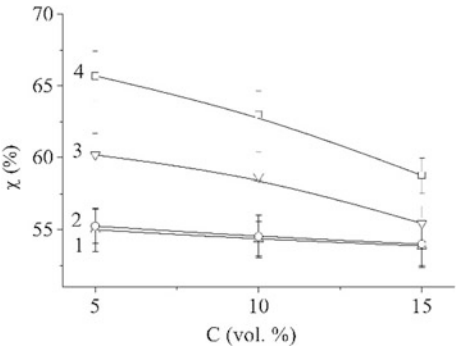

Fig. 20.4 Concentration dependences of the degree of crystallinity of the matrix for FP-EG samples with an average particle size of EG: 40 (1), 80 (2), 180 (3), 260 (4) μm

Changes of the degree of crystallinity are presented in Fig. 20.4. It demonstrates that with decreasing of EG dispersity, the degree of crystallinity of the matrix increases. This can be related to both the change in the morphology of the filler particles and the specifics of their distribution in the polymer. It is known that mobility of macromolecules near the contact surface of the filler particles decreases. This creates favorable conditions for the formation of nuclei of crystallization [18] in the polymer. As nanoclay [19, 20], EG particles delaminate in the FP matrix, and, as a result, the total active surface of the filler increases, and the number of nucleating centers increases. Besides EG with higher irregularities of particle morphology demonstrates better delamination ability. Therefore, with an increase in the average size of EG particles, the degree of crystallinity of the FP phase increases. So, for NCM FP-EG with C (EG) = 5 vol.% and the average particle size of $s = 40$ μm, $\chi \approx 55\%$. When s (EG) = 260 μm, the value of χ is 65.7%.

When the concentration of carbon filler increases, the process of particles aggregation occurs. At the same time, the heterogeneity of the system reduces, and the degree of crystallinity decreases. The reducing intensity of the degree of crystallinity with the increase in the filler content can be associated with the influence of the size of polymer crystals, which are formed during NCMs sintering. In addition, the supramolecular structure, which is characterized by the formation of small in form and size spherulites, which are distributed in the volume of matrix, is also influenced on this [21]. This is due to increased structurally active part of the EG surface, on which crystallization processes are proceed. Besides, the volume fraction of the boundary layer increases at the matrix-filler interface, which contributes to the amorphous phase of the composition.

It is known that PE behaves inelastically and nonlinearly at the low deformation amplitudes. At deformation of this polymer two basic types of interactions internally molecular and intermolecular are realized in its structure. The first type is covalent or ionic-covalent. The second one is the forces of van der Waals. The nature of the relaxation processes depends considerably on the content of the crystalline and amorphous phases in material.

Figure 20.5 demonstrates ADIF for samples of PE (curve 1) and NCM with different concentrations of MWCNTs (curves 2–4).

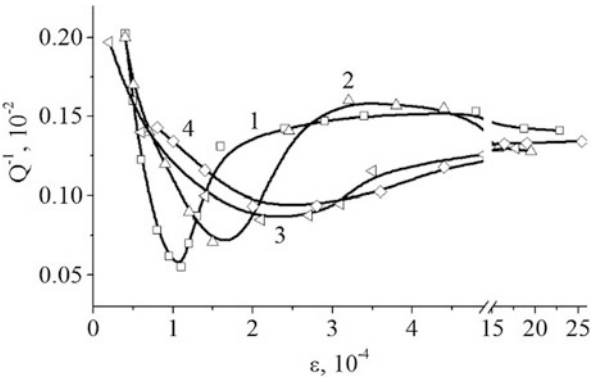

Fig. 20.5 Amplitude dependences of internal friction for initial samples of PE (1) and for PE-MWCNTs composite with concentration of MWCNTs: 0.6 (2); 1.5 (3); 5 (4) vol.%

Figure 20.5 shows that the ADIF have a minimum in the region of relative deformations $\varepsilon = (0.5 \ldots 2) \times 10^{-4}$. The presence of these minima indicates that an interaction between structural elements of the NCM occurs at some point of load. This interaction is less pronounced at deformations of $\varepsilon = 10^{-5}$ and $\varepsilon = (3–20) \times 10^{-4}$.

When the concentration of MWCNTs increases, the depth of the minima gradually decreases. More rapid decline was observed to 3 vol.% of MWCNTs than at higher concentrations. With increasing filler concentration, the minimum on the ADIF shifts toward higher values of relative deformations.

For NCM with low concentrations (<4 vol.%) at relative deformations of $\varepsilon \approx (0.5–5) \times 10^{-4}$, there is a reorganization of material structure. At some deformation stage (up to $\varepsilon = \varepsilon_m$) the interaction of the molecular segments of PE occurs. They are first fixed and then freed at $\varepsilon > \varepsilon_m$.

Changes in the total area, which is swiped by molecular segments during torsional oscillations of samples, cause the formation of a minimum on ADIF. The production of NCM on the base of PE with MWCNTs causes the structuring of the matrix and the relative stabilization of the segmental mobility of the molecular chains of PE and the value of internal friction at $C > 4$ vol.%.

Experimental results of stresses relaxation during samples stretching and their step load (Fig. 20.6) can be described by the following equation:

$$\sigma = \sigma_{0_i} \tau^k, \tag{20.3}$$

where τ is the relaxation time and k is the critical index that characterizes the relaxation rate.

The dependences on Fig. 20.6 demonstrate that with increasing initial load ($\sigma = \sigma_{0i}$) the inclination of curves $\sigma(\tau)$ increases, and relaxation rate is stabilized. With increasing initial load, the relaxation rate increases. It can be observed on the next figure, which demonstrates the dependencies of the critical index on the load (Fig. 20.7).

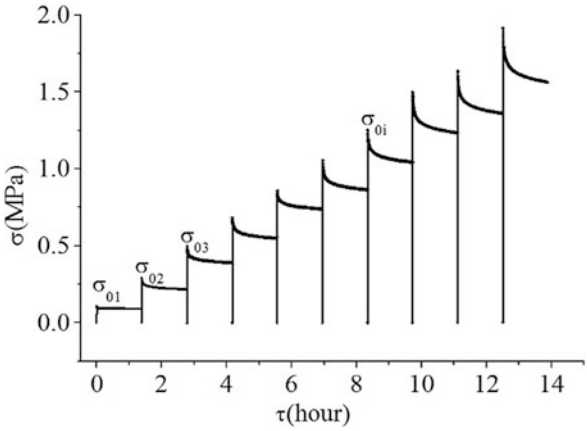

Fig. 20.6 Stresses relaxation in PE-MWCNTs ($C = 3$ vol.%) samples under their step stretching

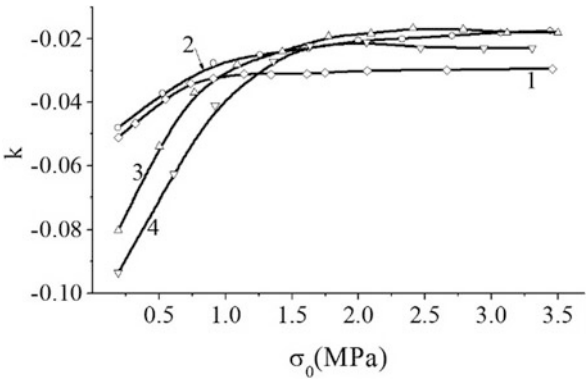

Fig. 20.7 Dependence of the critical index for PE (1) and PE-MWCNTs NCM (2–4) with the concentration of MWCNTs: 1.5 (2), 3 (3), and 5 (4) vol.%

All NCM samples in the vicinity of $\sigma_{0i} = 1.2$ MPa have the equilibrium value of k. A similar behavior of the critical index is observed for pure PE but at load of 0.75 MPa. With increasing of σ_0 from 0.2 to 3.5 MPa the change in the critical index for PE is $\Delta k = 0.02$. For NCM the value of k decreases more significantly in a similar zone of loads. It also increases with an increase in the concentration of MWCNTs. For $C = 1.5$ vol.%, the value of $\Delta k = 0.03$, and for $C = 5$ vol.%, it is equal 0.72. Thus, the relaxation rate increases with increasing filler concentration owing to increase in the hardness of NCM due to the hardness of the carbon component.

Similarly, stress relaxation was investigated with a stepwise increase in the output load for NCM FP-EG. The obtained experimental results had shown that both the concentration and the dispersity of filler particles affect the relaxation processes of the NCM. Figure 20.8 demonstrates the dependences of the degree of stresses relaxation in NCM samples with different concentration and average EG particle size.

Relaxation phenomena in polymers occur due to their restructuring as a result of the supramolecular elements movement. Analysis of the obtained results had

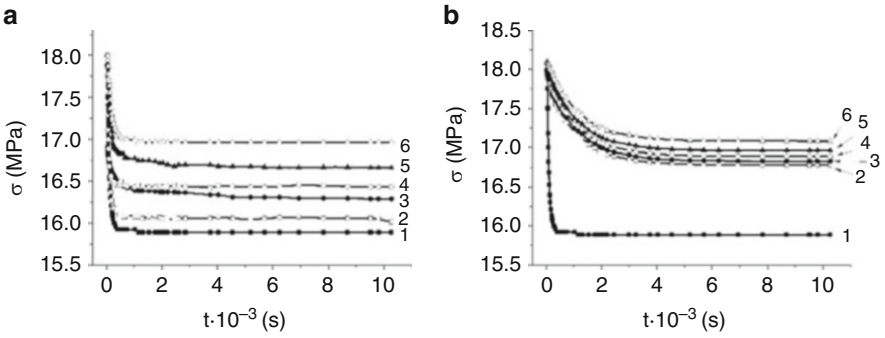

Fig. 20.8 Stresses relaxation in samples of FP (1) and NCM FP-EG with EG dispersity of 40 (2), 80 (3), 130 (4), 180 (5), and 260 (6) μm and its concentration of 1 vol.% (**a**) and 5 vol.% (**b**)

shown that the rearrangement of the macromolecular segments from more twisted to more stretched under the action of a constant load occurs differently for NCM with different content and size of EG particles.

The supramolecular restructuring occurs more rapidly for a pure FP (curve 1, Fig. 20.8a, b). With an increase in the average size of EG particles up to 260 μm, the time of stresses relaxation increases. Thus, for a composition with a minimum particle size of 40 μm under the load of 18 MPa the stress relaxation time is 1290 s. At the same time for NCM with a maximum particle size of 260 μm, the relaxation time is 1500 s, which is 17% higher than the corresponding value for the first compositions. With the decrease of filler dispersity, the value of the equilibrium stress ($\sigma\infty$) increases. For a composition with s (EG) = 40 μm, the $\sigma\infty$ value is 15.8 MPa and increases to 17 MPa for NCM with s (EG) = 260 μm. Consequently, the presence of EG prevents the maximum possible unwinding of macromolecule chains, and for larger filler particles the processes of stresses relaxation proceeds slower.

With an increase in the volume content of EG to 5%, the relaxation curves shift to the region of high stress values (Fig. 20.8b). The effect of the dispersity of EG particles on relaxation processes becomes less noticeable, but relaxation time increases. So, for samples with C (EG) = 5 vol.% and particle size of 40 μm and 260 μm relaxation time is 1870 s and 2103 s, respectively. Thus, when the concentration of the filler increases, the spatial distribution of polymer macromolecules changes. Structuring of polymer occurs, which affects the spinning dynamics of macromolecule chains, and, as a result, relaxation processes occur in wider time intervals.

Attention has been also focused on the effects of nanoparticles on the NCM creep response. Our investigation was performed in order to understand the respective role of the nanoparticles volume fraction, size, and distribution and also the interphase on the creep behavior. Figure 20.9 displays the creep strain of PE at different EG concentration and average particles size.

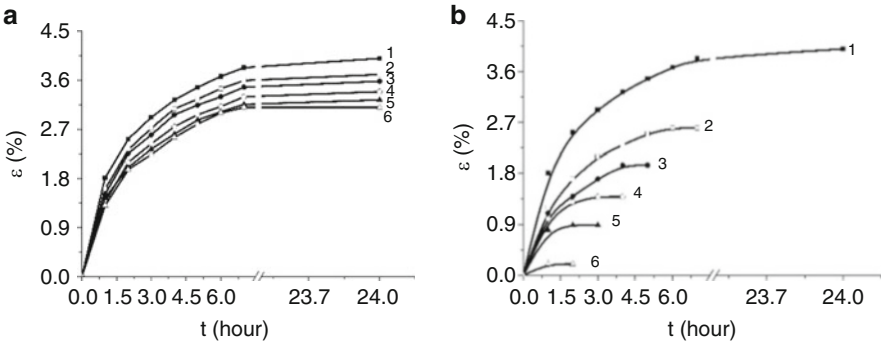

Fig. 20.9 Creep behavior of FP (1) and compositions of FP-EG, with different dispersity of EG particles (40 (2); 80 (3); 130 (4); 180 (5); 260 (6) μm) and its content in the composition (1 vol.% (**a**), 2.5 vol.% (**b**)) under a load of 12 MPa

As the first founding, the creep strain of FP nanocomposite containing 1 vol.% of EG is lower than that of the pure polymer matrix implying that the creep behavior is improved by adding a small volume fraction of the nanoparticles. It is due to the fact that the EG particles have a stiffing effect on the NCM that reduce the overall creep of the polymer. With an increase in the average size of the EG particles, the creep of NCM decreases. At this case interphase and particle aggregation play an important role. The surface-to-volume ratio of the smaller particles would be considerably higher than that of greater ones. It can greatly enhance the interfacial reactivity between the filler particles and polymer matrix. Besides larger EG particles can be viewed as aggregates of smaller ones, which also influences on the filler/polymer boundaries and formation of interphase.

However, as the filler doping level increased the fatigue life of materials can be significantly decreased [22]. It can be also observed for NCM studied. In the cases of 2.5 vol.% of EG (Fig. 20.9b) the creep response of the nanocomposite was found to be significantly dependent on the nanoparticle aggregation degree. As a result, creep strain and time for samples destruction reduce. Another noteworthy point is that with increasing volume fraction, the reduction of the creep with EG particles of 260 μm is much more significant than that of the creep strain with EG particles of 40 μm. This can be associated with different degrees of particle aggregation for EG of different dispersity.

20.4 Conclusions

It was shown that not only concentration and structural, physical, and chemical characteristics of the filler but also the conditions for the production of samples are important for the creation of nanocomposite material based on PE and MWCNTs. The conditions of creation effect on the structuring of the matrix, which leads to

stabilizing its characteristics and controlling the damping parameters of the material. The addition of carbon nanotubes in 4–5 vol.% to the polyethylene matrix allows to obtain not only the conductive composite but also to increase the stiffness of the material.

The EG particles morphology and their distribution in the polymer matrix play an important role in the nanocomposite effective properties. For NCM with a fluoroplastic matrix and EG filler, the degree of crystallinity of the matrix increases from 55 to 65.7% with an increase in the average particle size of the EG particles from 40 to 260 μm. It also decreases with increasing concentration of the carbon phase due to a change in the structurally active part of filler surface, where processes of crystallization of phase transition occur.

The degree and time of structural relaxation of nanocomposite FP-EG depend on the size of the filler particles: with an increase in the size from 40 to 260 μm, the relaxation rate reduces by 25%; with an increase in concentration from 1 to 5 vol. % the relaxation time increases almost twice. Also, it was concluded that the nanoparticle/polymer interphase region plays a significant role in the nanocomposite properties and its creep behavior. Besides, the interphase effect is found to be more significant on the MNC creep resistance with larger particles and their aggregations as compared with that of NCM creep response with smaller ones.

References

1. Müller K, Bugnicourt E, Latorre M, Jorda M, Echegoyen Sanz Y, Lagaron JM et al (2017) Review on the processing and properties of polymer nanocomposites and nanocoatings and their applications in the packaging, automotive and solar energy fields. J Nanomater 7:74. https://doi.org/10.3390/nano7040074
2. Wang J, Chowdhury S, Wu D, Bohnstedt B, Liu Y et al (2017) Carbon nanotube enhanced shape memory polymer nanocomposites for development of biomedical devices. J Nanomed Res 6(1):00141. https://doi.org/10.15406/jnmr.2017.06.00141
3. Sabet M, Soleimani H (2014) Mechanical and electrical properties of low density polyethylene filled with carbon nanotubes. IOP Conf Series: Mater Sci Eng 64:012001. https://doi.org/10.1088/1757-899X/64/1/012001
4. Du J, Zhao L, Zeng Y, Zhang L, Li F, Liu P, Liu C (2011) Comparison of electrical properties between multi-walled carbon nanotube and graphene nanosheet/high density polyethylene composites with a segregated network structure. Carbon 49:1094–1100. https://doi.org/10.1016/j.carbon.2010.11.013
5. Carbon nanotubes: TC U 24.1–03291669-009:2009. № 02568182/095617 from 01.09.2009. Authors: Sementsov YuI, Melezhik OV, http://nabivka.com/ru/nanouglerodnie_materiali.html. (in Ukrainian)
6. Yanchenko VV, Sementsov Yu I, Melezhyk OV. Patent Ukraine 17387. 15 Sept 2006
7. TEM: Sumy. http://selmi.sumy.ua/microscopes.html. Accessed 10.10.2013
8. Axio Observer (Zeiss, Germany). http://www.zeiss.com/microscopy/en_de/products/light-microscopes/axio-observer-for-materials.html. Accessed 14.10.2016
9. Markiv V, Belyavina N (1997) Proceedings of the Second International EFM'97, Lviv, p 260
10. Mccrum NG (1959) An Internal Friction Study of Polytetrafluoroethylene. J Polymer Sci 34:355–369

11. Dassios KG, Galiotis C (2012) Polymer–nanotube interaction in MWCNT/poly(vinyl alcohol) composite mats. Carbon 50:4291–4301. https://doi.org/10.1016/j.carbon.2012.04.042
12. Youssefi M, Safaie B (2013) Effect of multi walled carbon nanotube on the crystalline structure of polypropylene fibers. J Fibers Polymers 14:1602–1607. https://doi.org/10.1007/s12221-013-1602-5
13. Coleman JN, Khan U, Blau WJ, Gun'ko YK (2006) Small but strong: A review of the mechanical properties of carbon nanotube–polymer composites. Carbon 44:1624–1652. https://doi.org/10.1016/j.carbon.2006.02.038
14. Xiang D, Harkin-Jones E, Linton D (2015) Effect of cooling rate on the properties of high density polyethylene/multi-walled carbon nanotube composites. AIP Conf Proc 1664:070001–070005. https://doi.org/10.1063/1.4918440
15. Dovbesko GI, Konan' VS, Revo SL et al (2005) Nanodimentional Structure of Expholiated Graphite. J Metallofiz Noveishie Tekhnol 27(3):1001–1010
16. Revo S, Avramenko T, Melnichenko M, Ivanenko K, Teselko P (2017) Morphological structure and microhardness of ground thermally expanded graphite. IEEE 7th Intern Conf NAP. https://doi.org/10.1109/NAP.2017.8190227
17. Avramenko TG, Maksimova GA, Ivanenko EA et al (2015) Effect of structural and morphological features of a nanocarbon component on electrophysical properties of fluoroplastic composite materials. Surf Engin Appl Electrochem 51(6):509–516. https://doi.org/10.3103/S1068375515060034
18. Maiand Y-W, Yu Z-Z (eds) (2006) Polymer nanocomposites. Woodhead Publishing Limited/CRC Press LLC, Cambridge
19. Wu D, Zhou C, Fan X et al (2006) Nonisothermal crystallization kinetics of poly(butylene terephthalate)/montmorillonite nanocomposites. J Appl Polym Sci 99:3257–3265. https://doi.org/10.1002/app.22782
20. Huang JW (2008) Poly(butylene terephthalate)/clay nanocomposite compatibilized with poly(ethylene-co-glycidyl methacrylate). II. Nonisothermal crystallization. J Polym Sci B Polym Phys 46(6):564–576. https://doi.org/10.1002/polb.21392
21. Okhlopkova AA, Parnikova AG (2011) Study of the properties of nanocomposite materials based on PTFE. Izvestia Samar. Sci Center Sci 13(1(2)):394–396. (in Russian)
22. Wang ZD, Zhao XX (2008) Creep resistance of PI/SiO2 hybrid thin films under constant and fatigue loading. Compos Part A 39:439–447. https://doi.org/10.1016/j.com

Chapter 21
Simulation of Tunneling Conductivity and Controlled Percolation In 3D Nanotube-Insulator Composite System

I. Karbovnyk, Yu. Olenych, D. Chalyy, D. Lukashevych, H. Klym, and A. Stelmashchuk

21.1 Introduction

Nanocomposites that are obtained by introducing different nanofillers into insulating matrices have been proven to exhibit outstanding mechanical and electrical properties and therefore attract much attention of the researchers [1–11]. Nanotubes randomly dispersed in dielectric medium (typically polymer) can form conductive network that defines electrical properties of such a composite system. Usually, very low concentration of nanofiller is needed to make such system conductive as the aspect ratio for nanotubes is very high. When percolation threshold is reached, conductive paths that appear inside the insulating host matrix allow electrons to transfer along the nanotubes that form the network. Individual nanotubes are known to have remarkable current-carrying capacity with orders of magnitude higher than conventional metals. After summing up the aforementioned information, one can conclude that many opportunities to exploit features of nanotube-based composites in electronic applications arise [7].

Widespread use of the percolation theory in the modeling and analysis of various systems is due to the influence of geometric characteristics of system components on involved processes. The development of novel algorithms that rely on the ideas of geometry and discrete mathematics is a crucial challenge for the effective

I. Karbovnyk (✉) · Y. Olenych · A. Stelmashchuk
Ivan Franko National University of Lviv, Lviv, Ukraine

D. Chalyy
Lviv State University of Life Safety, Lviv, Ukraine

D. Lukashevych · H. Klym
Lviv Polytechnic National University, Lviv, Ukraine

O. Fesenko, L. Yatsenko (eds.), *Nanocomposites, Nanostructures, and Their Applications*, Springer Proceedings in Physics 221,
https://doi.org/10.1007/978-3-030-17759-1_21

application of the percolation theory in complex systems with a large number of elements.

The theory of percolation considers the connectivity of a large number of elements, provided that the connection between adjacent elements is completely random in nature [12, 13]. To give an example, such systems can be crystalline semiconductors with impurities [14], composites consisting of conductor, and dielectric or security systems of computer networks.

One notable application of the percolation theory is the study of electrical properties of disordered systems [15], which comprise the components with different electrical properties, in particular, insulators and conducting elements [5, 16]. Such systems include nanocomposites based on metallic nanotubes dispersed in a dielectric matrix [17, 18]. Composites have a number of advantages over traditional electronic materials and as of today are intensively investigated experimentally and theoretically [3, 19]. In particular, computer simulation of charge transfer processes into such functional materials within the percolation theory is of great practical importance.

The study of percolation phenomena at the nanoscale in systems based on carbon nanotubes shows a significant influence of the anisotropy level of the material on the percolation threshold [20]. Moreover, of specific practical importance is the possibility of controlled manipulation of carbon nanotubes aiming to create a conductive path. In particular, in [21], the authors report thin film composites that are based on carbon nanotubes suspended in liquid crystal, the morphology of which can be changed by applying an electric field. The nanotubes act as a conductive network, with the liquid crystal providing a host medium to allow the conductive network to rearrange under voltage. As a result, nanotubes adapt a prevailing orientation along the direction of the field.

Therefore, the study of the influence of the nanotubes predominant orientation on the percolation network formation by computer modeling is an important task as it shines light on macroscopic electrical parameters of a nanocomposite [22, 23]. In this work, an analysis of percolation phenomena in a three-dimensional system of nanotubes and modeling of tunneling conductivity in nanotubes are carried out. Particular attention was paid to exploring the influence of geometric sizes of nanotubes and their spatial orientation on the probability of percolation cluster formation.

21.2 Nanocomposite Conductivity Simulation Method

21.2.1 Model of Nanotube Dielectric Composite

Nanotube/dielectric composite can be described as 3D volume box also known as representative volume element (RVE) [1] filled with randomly dispersed conductive carbon nanotubes. Electrodes attached to the two opposite sides of RVE act as

the entry points of the external electric circuit. In the simplest model, CNTs can penetrate each other. In our case, we are using "hard core" model in which CNTs cannot overlap by its volumes. In the "hard core" model, an electric contact between nanotubes is provided by tunneling effect which usually exists among nanoscale objects. In papers [2, 24], it is mentioned that tunneling conductivity has more significant impact on the resulting conductivity of the RVE than the resistance of the nanotubes themselves. So, it is crucial that the effect of tunneling conductivity is not neglected when computer simulations of nanotube composite are performed.

21.2.2 Simulation Model

In our model, CNT is represented as a cylinder with spherical faces. The axis of this cylinder starts at point A with coordinates (x_1, y_1, z_1) and ends at point B (x_2, y_2, z_2). The process of generating and placing nanotube in RVE consists of several phases. First, the coordinates of starting point are calculated as [19]:

$$x_1 = \text{rand} \times L_x \tag{21.1}$$

$$y_1 = \text{rand} \times L_y \tag{21.2}$$

$$z_1 = \text{rand} \times L_z \tag{21.3}$$

where rand is a random floating point value from [0, 1] range. Then the random direction in space is described by two angles α and β:

$$\alpha = 2\pi \times \text{rand}_1 \tag{21.4}$$

$$\beta = 2\pi \times \text{rand}_2 \tag{21.5}$$

Using this direction, the position of the end point B is defined as:

$$x_2 = x_1 + \text{length} \times \cos(\alpha)\cos(\beta) \tag{21.6}$$

$$y_2 = y_1 + \text{length} \times \sin(\alpha)\cos(\beta) \tag{21.7}$$

$$z_2 = z_1 + \text{length} \times \sin(\beta) \tag{21.8}$$

If the obtained by aforementioned procedure point B is located outside of the boundaries of RVE, then the exceeding part of the newly generated CNT is cut off, so we are sure that our CNT lies within RVE.

In the "hard core" model, we have to guarantee that there are no collisions between nanotubes after adding new CNTs to the system. In order to achieve this, we check the distances between the newly generated nanotube and all the other

nanotubes already placed inside RVE. If the shortest distance between the axes of the pair of the tubes being checked is less than CNT diameter d, it means that tubes are penetrating each other. In this case, the newly generated tube is rejected and not placed into the RVE. The process continues up to the point the desired volume fraction of CNTs inside RVE is reached. This evaluation process requires additional computational costs since a significant amount of the nanotubes is thrown away, especially at high-volume fraction ratios.

Electrical connection between CNTs is assumed to exist if the shortest distance D between them is smaller than the tunneling cutoff distance.

In order to find conducting (or percolative) cluster between electrodes, we have implemented the weighted union-find algorithm with the pass compression. This cluster consists of all the nanotubes which have conductive path to both electrodes. It is important to take into account that there can be several parallel conductive clusters.

21.2.3 Resistor Network Formation

We use random resistor network approach described in [25] to simulate the equivalent conductivity of the CNTs system. In order to convert the set of connected nanotubes into such a type of representative resistor network, locations of all connections between CNTs must be found. To illustrate the technique we utilize, an example of a possible connection pattern is shown in Fig. 21.1. Each contact place between two CNTs is represented as a pair of "junction" points: one on the axis of the first CNT and the other one on the axis of the second CNT. At the same time a pair of "junction" points located at the same nanotube defines the part of this nanotube as the segment with length l_s (see Fig. 21.1), which the electric current will be run through.

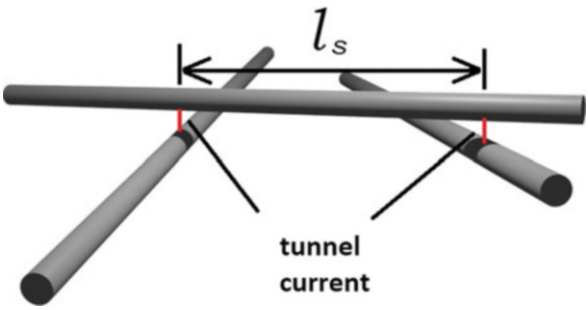

Fig. 21.1 Possible connection pattern between CNTs

Let us describe the process which allows us to find both the shortest distance between CNTs and the actual coordinates of these "junction" points. The coordinates of the point on the CNT axis can be described by the following expression:

$$p + \alpha \cdot \overrightarrow{d}, \tag{21.9}$$

where p is the point of the start of the CNT, $\overrightarrow{d}$ is the directional vector of the CNT, and $\alpha$is a variable coefficient ($\alpha \in [0, 1]$), whose concrete values define the points located on the CNT axis.

Let $p_1 + \alpha \cdot \overrightarrow{d}_1$ and $p_2 + \beta \cdot \overrightarrow{d}_2$ be the arbitrary points on the first and second CNTs, respectively, and the distance between these segments is to be found. Then $\left(p_1 + \alpha \cdot \overrightarrow{d}_1\right) - \left(p_2 + \beta \cdot \overrightarrow{d}_2\right)$ is the vector, which connects these two points. The minimal distance between CNTs can be obtained as the norm of this aforementioned vector:

$$D = \left\| \left(p_1 + \alpha \cdot \overrightarrow{d}_1\right) - \left(p_2 + \beta \cdot \overrightarrow{d}_2\right) \right\|^2. \tag{21.10}$$

Taking into account the property of scalar product $\left(\overrightarrow{a}, \overrightarrow{a}\right) = \left\| \overrightarrow{a} \right\|^2$ we can conclude that to find the values of coefficients α and β, we have to find the values which provide the minimal scalar product of the vector with itself. So, after some transformations, we obtain the following expressions for finding coefficients α and β.

Auxiliary notations:

$$\begin{aligned}
A_1 &= \left(\overrightarrow{d}_1, \overrightarrow{d}_1\right), \quad A_2 = \left(\overrightarrow{d}_1, \overrightarrow{d}_2\right), \\
B_1 &= \left(\overrightarrow{d}_2, \overrightarrow{d}_1\right), \quad B_2 = \left(\overrightarrow{d}_2, \overrightarrow{d}_2\right), \\
C_1 &= \left(\overrightarrow{p_2 - p_1}, \overrightarrow{d}_1\right), \\
C_1 &= \left(\overrightarrow{p_2 - p_1}, \overrightarrow{d}_2\right), \\
D &= (A_1 \cdot B_2 - B_1 \cdot A_2).
\end{aligned} \tag{21.11}$$

The values of the unknown coefficients:

$$\begin{aligned}
\alpha &= \frac{(C_1 \cdot B_2 - B_1 \cdot C_2)}{D}, \\
\beta &= \frac{(C_2 \cdot A_1 - C_1 \cdot A_2)}{D}.
\end{aligned} \tag{21.12}$$

If the found values of coefficients α and β do not belong to the interval $[0, 1]$, then their values should be adjusted to nearest admissible values.

21.2.4 CNT and Contact Conductivities

In our model, we are considering two types of conductivity: tunneling conductivity between CNTs and CNT intrinsic conductivity. Two CNTs are treated as the connected ones, when the shortest distance between them is shorter than some preset value of the cutoff distance d_{cutoff}.

Let us define a part of CNT by a pair of points located on its axis. Suppose the length of this segment is l_s (Fig. 21.1). Then the intrinsic resistance of this part of CNT can be calculated according to the formula [19, 24]:

$$R_{\text{intrinsic}} = \frac{4l_s}{\pi \sigma_{\text{CNT}} d^2}, \tag{21.13}$$

where σ_{CNT} is the intrinsic electrical conductivity of the CNT and d is the diameter of the CNT.

The contact resistance between a pair of nanotubes is caused by a tunneling effect at the "junction" points. Suppose the shortest distance between a pair of nanotubes is d_{kp}, where d_{kp} is shorter than d_{cutoff}. Then the contact resistance can be estimated using Landauer-Büttiker formalism as [26–30]:

$$R_{\text{contact}} = \frac{h}{2e^2} \frac{1}{NP}, \tag{21.14}$$

$$P = \begin{cases} \exp\left(-\frac{d_{\text{vdw}}}{d_{\text{tunnel}}}\right) & \text{for } 0 \le d_{\text{kp}} \le d + d_{\text{vdw}} \\ \exp\left(-\frac{d_{\text{kp}} - d}{d_{\text{tunnel}}}\right) & \text{for } d + d_{\text{vdw}} \le d_{\text{kp}} \le d + d_{\text{cutoff}} \end{cases}, \tag{21.15}$$

$$d_{\text{tunnel}} = \frac{h}{2\pi} \frac{1}{\sqrt{2m_e \Delta E}}, \tag{21.16}$$

where h is Planck's constant; P is the transmission probability for electron tunneling between CNTs; N is the number of conduction channels, which is dimensionless and related to diameter of a CNT [31]; e is the charge of an electron; d_{vdw} is the van der Waals separation distance [32, 33], which limits the minimum distance between a pair of CNTs; d_{tunnel} is the tunneling characteristic length; m_e is the mass of an electron; and ΔE is the height of energy barrier [34].

In our simulations, a random resistor network is represented as the matrix of conductivities between all "junction" points. After applying Kirchhoff's current law, the system of linear equations is created. Since a "junction" point has only few connections to the other points, the resulting matrix is sparse. That is why we use a specific sparse solver to achieve good simulation performance. SuperLU [35–37] library is used to solve this system of linear algebraic equations and obtain the values of electric potential at all the "junction" points. After that the equivalent conductivity of random resistance network is calculated.

21.3 Simulation of Tunneling Conductivity

We have developed software for simulation of nanotube-dielectric composite conductivity using "hard core" model described in the previous chapter. The main role of simulations was to explore how tunneling effect influences the total conductivity of nanocomposite described by CNTs hard core model. For the purpose of comparison, "soft core" model was also implemented.

The very first challenge we encounter is, obviously, to compare our computer simulation results with experimental measurements, which are available, for example, in [19]. To accomplish this goal, we set up the parameters of the system under simulation as follows in Table 21.1 [38].

The results of the simulations for various CNTs volume fractions are shown in Fig. 21.2.

The data shown on "hard core" part of Fig. 21.3 coincides with experimental results [15] both qualitatively and quantitatively. Also, one can notice the difference in actual values of the simulation results between "soft core" and "hard core" models, but the behavior of both models develops in the same way as volume fraction changes.

Table 21.1 Parameters of simulated composite

Parameter name	Value
RVE size	1000 nm 1000 nm 100 nm
CNT length	200 nm
CNT diameter	2 nm
CNT aspect ratio	100
CNT intrinsic conductivity	10^4 S/m
Tunnel cut off distance	1.9 nm

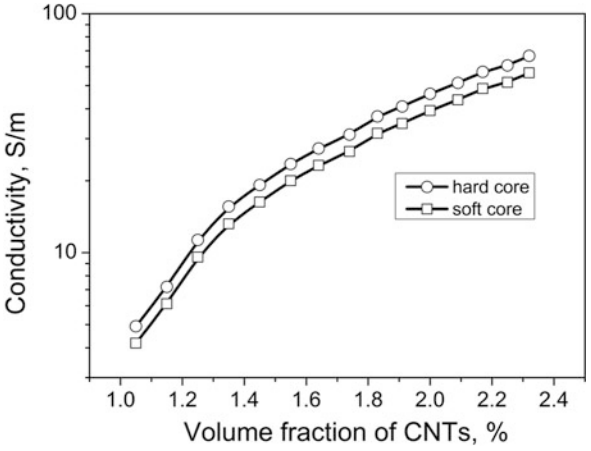

Fig. 21.2 Composite conductivity both for soft core and hard core models [38]

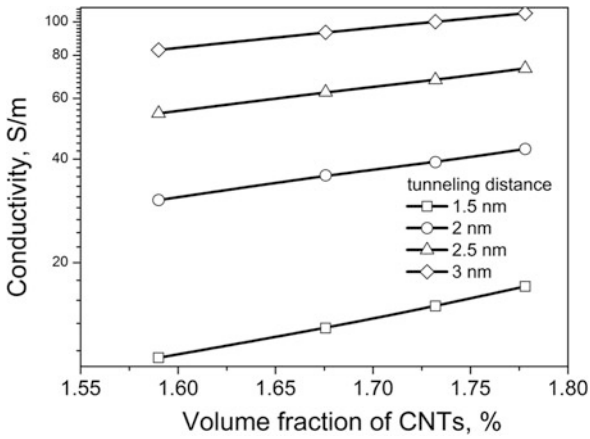

Fig. 21.3 Dependency of composite conductivity on tunneling cutoff distance [38]

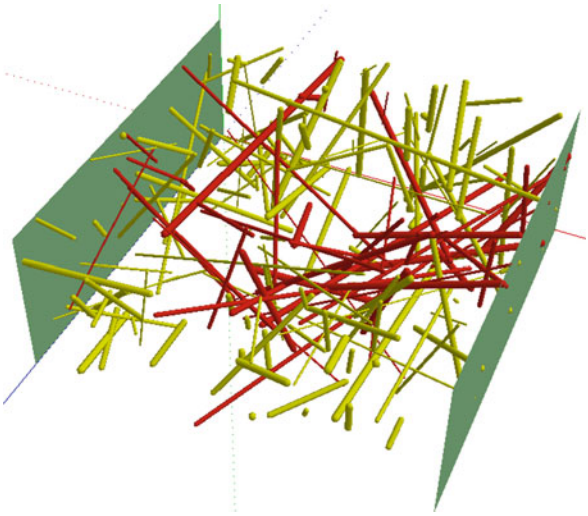

Fig. 21.4 Model of nanotubes system with a highlighted conductive path between two opposite sides of parallelepiped [41]

Looking at Fig. 21.4 we can conclude that tunneling cutoff distance does not affect significantly the character of the system's behavior depending on volume fraction changes. On the other hand, the tunneling cutoff distance does influence on the actual values of the electric conductivity of the system [38–40].

21.4 Model and Methods for Implementing the Algorithm

In the proposed model, the nanotube system is represented as a volume element in the form of a rectangular parallelepiped, in which nanotubes are located chaotically (Fig. 21.4). Nanotubes are considered as hollow cylinders with length L and

diameter D to simplify the description of the system. In terms of representation, an individual nanotube is built of three primitive constituent elements: two hemispheres at the ends of the tube, and a cylinder between these hemispheres. The spatial position of each nanotube is determined by the coordinates of two boundary points on the opposite ends of the tube. During the process of the generation of the nanotubes system, the number of elements in this volume is calculated according to the concentration and geometric sizes. Nanotubes can be either isolated or in direct contact with each other.

The simulation of percolation of the tube system is provided by alternating checking of distances between all nanotubes. The contact of two tubes is determined by the condition that the distance between them does not exceed the diameter of the nanotubes. Since the position of the nanotubes is random, the presence or absence of a connection between two specific tubes is also an accidental event. However, for many objects set, the system parameters are no longer random variables but depend on the concentration and geometric dimensions of the nanotubes.

In the simulation of the electrical properties of the system, the solution of the percolation problem requires finding the paths of current flowing through the connected electrically conductive nanotubes between the two opposing sides of the rectangular parallelepiped (see Fig. 21.4). The flow of current between these electrodes depends on such parameters of the investigated system as the density of filling, the ratio of conducting and nonconducting nanotubes, their orientation, length, and diameter (or aspect ratio).

To find the conductive cluster in a nanotube system between two electrodes and to calculate the probability of percolation, an algorithm based on the graph theory is used. According to the algorithm, all tubes of the system are represented as vertices of a simple graph, edges of which correspond to the connections between the tubes. Nanotubes that are in contact with the opposite sides of the parallelepiped form two subsets corresponding to the electrode. At the next stage, a component that combines these subsets is sought by means of the union-find algorithm. Thus, a conductive path in the nanotubes system is formed.

For the implementation of the algorithm for modeling percolation phenomena in the nanotubes system, a high-level programming language C++ and a Qt cross-platform toolkit were used. To reduce the computing time, multithreaded implementation of algorithms is used. The 3D visualization of the model of a nanotubes system was performed by means of OpenGL using a virtual camera that generates a raster image of an object on a flat surface using special procedures for drawing graphics. As a result, for each image pixel, the color and intensity reflected from the object of light are determined for each image pixel. These visualization tools were used for model testing and displaying of the conductive path between two electrodes.

21.5 Simulation of Field-Controlled Percolation in 3D System

The analysis of percolation phenomena in a system of nanotubes was carried out with the help of the developed program for finding the percolation probability. The program interface allows changing the model parameters that affect the percolation threshold value. From multiple numerical experiments, dependencies of the probability of percolation on the concentration and geometric sizes of nanotubes and their spatial orientation were found. The nanotubes percolation probability is the percentage of positive results of the calculation, which are the calculations when a conductive path is established. Based on performed calculations, the influence of applied voltage on the probability of the formation of conductive network from straight nanotubes was studied.

The dependence of the percolation probability on the concentration and geometric dimensions of nanotubes under the conditions of their uniform and isotropic distribution in 3D space is shown in Fig. 21.5. Analysis of the obtained dependences indicates a reduction in the percolation threshold due to an increase in the length of nanotubes from 0.5 to 2.5 microns. The minimal concentration of nanotubes that ensure the formation of the conductive cluster decreases from 9% to 2.5%. The increase in the radius of nanotubes from 20 to 110 nm leads to the respective increase in the percolation threshold. It may be related to the decreased number of nanotubes in a given volume and the increase in their diameter for constant volumetric concentrations.

Anisotropy was introduced by limiting the angles α and β between the nanotube axis and the normal to the electrodes as shown in Fig. 21.6. The goal was to study the influence of nanotubes orientation on the percolation probability in the 3D model of the system. For a completely anisotropic system, all nanotubes are oriented along the normal and $\alpha = \beta = 0$. The isotropic distribution of nanotubes corresponds

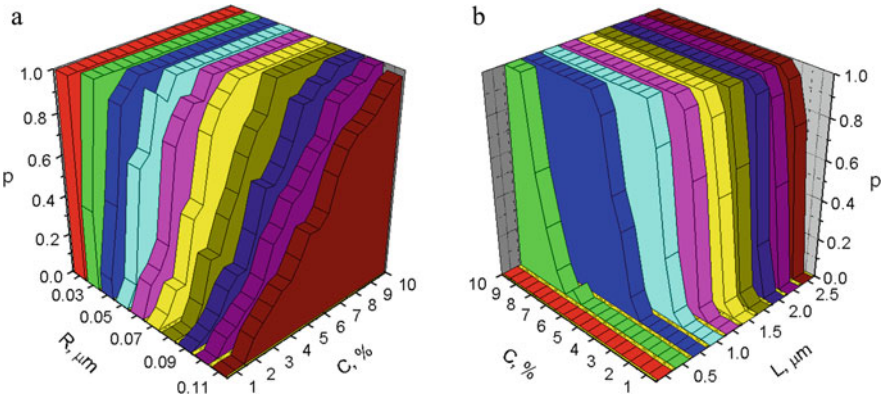

Fig. 21.5 Dependence of the percolation probability on the concentration and length of nanotubes (**a**), on the concentration and radius of nanotubes (**b**) [41]

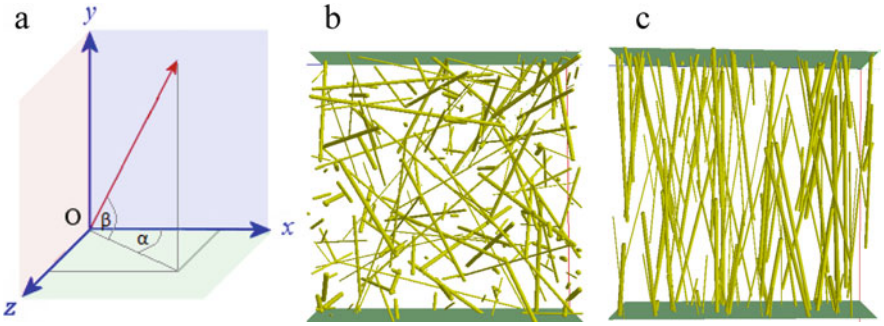

Fig. 21.6 Determination of the nanotube orientation in 3D space (**a**) and the isotropic (**b**) and anisotropic (**c**) nanotubes distribution with the following angular dispersion limitation: $-90^o < \alpha < 90^o$, $-90^o < \beta < 90^o$ (**b**); $-15^o < \alpha < 15^o$, $-15^o < \beta < 15^o$ (**c**) [41]

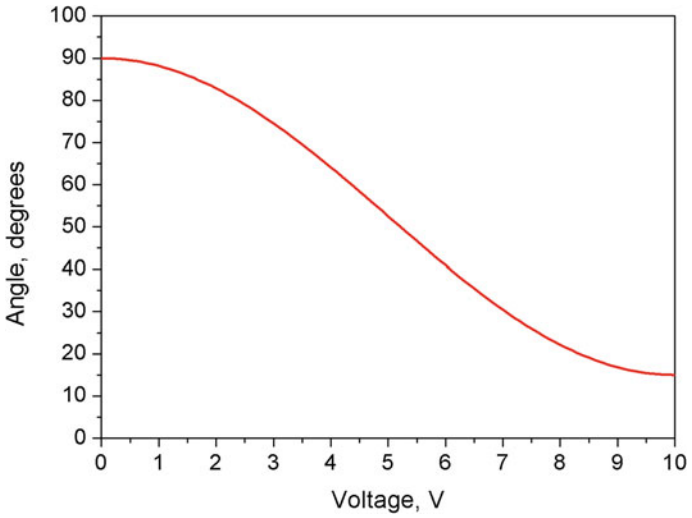

Fig. 21.7 Dependence of the orientation limitation angle of nanotubes on the applied voltage

to a limit of $-90^o < \alpha < 90^o$, $-90^o < \beta < 90^o$. No restrictions on the orientation of nanotubes correspond to the case, when applied voltage is 0. In the case where $\alpha = 0$ or $\beta = 0$ and an arbitrary dispersion of the other angle, a 2D model of the percolation system can be obtained.

In order to observe field-controlled percolation in 3D system of straight carbon nanotubes, the dependence of the orientation limitation angle on the applied voltage U shown in Fig. 21.7 was used. Distribution of the nanotubes in disordered system at $U = 0$ corresponds to the angular dispersion limitation: $-90^o < \alpha < 90^o$ and $-90^o < \beta < 90^o$. With the increase of the voltage applied to the percolation system, the orientation limitation angle decreases nonlinearly. At $U = 10$ V nanotubes orientation is limited by about 15^o angle. Boundary conditions of the dependence

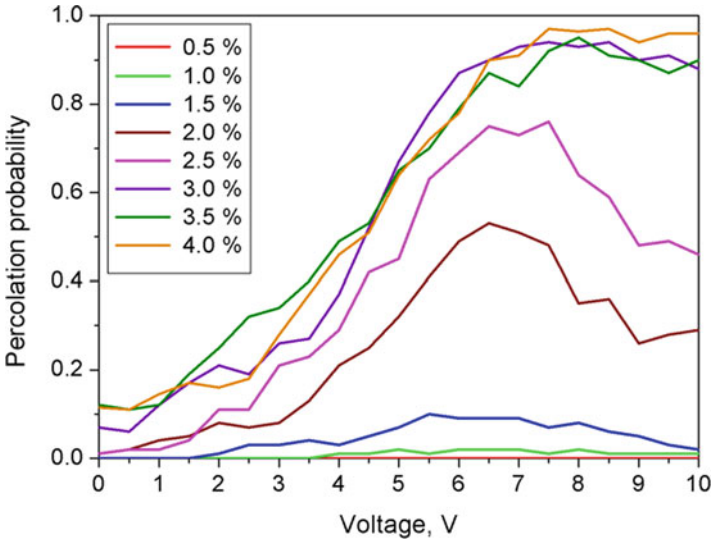

Fig. 21.8 Dependences of the percolation probability on the applied voltage for different nanotubes lengths (nanotubes concentration C equal to 3%) [41]

of the orientation limitation angle on the applied voltage are based on experimental results of field-controlled nanocomposite morphology change [42]. Figure 21.7c illustrates the isotropic and anisotropic distributions of nanotubes with angular dispersion of 15°.

The simulation results show that the percolation probability significantly depends not only on the concentration and geometric sizes of nanotubes but also on their prevailing orientation, which can be controlled by electric field. Figure 21.8 shows dependences of the percolation probability on the applied voltage for different nanotubes lengths. Calculations were performed for the fixed concentration of nanotubes in the composite which was set to 3%.

If the field is not applied at $\alpha = \beta = 90^{o}$, the probability of percolation of nanotubes with the length up to 3 nm is close to zero. Increasing the applied voltage leads to the decrease of the orientation limitation angles and, consequently, to the increase of the percolation probability. The obtained results are in good agreement with the data of the studies of the carbon nanotubes system in the 2D model [43]. For nanotubes with 3–4 nm length, the percolation probability reaches values as high as (0.8–1.0) under the voltage of 5 V. One has to note that at 3% concentration nanotubes longer than 3 нм can form conductive network even without applied electric field. On the other hand, the efficiency of conductive cluster formation in the system of nanotubes of 0,5–1,5 nm length is low for random orientation. Therefore, optimal length of nanotubes for an electrically controlled percolating system is 3 nm.

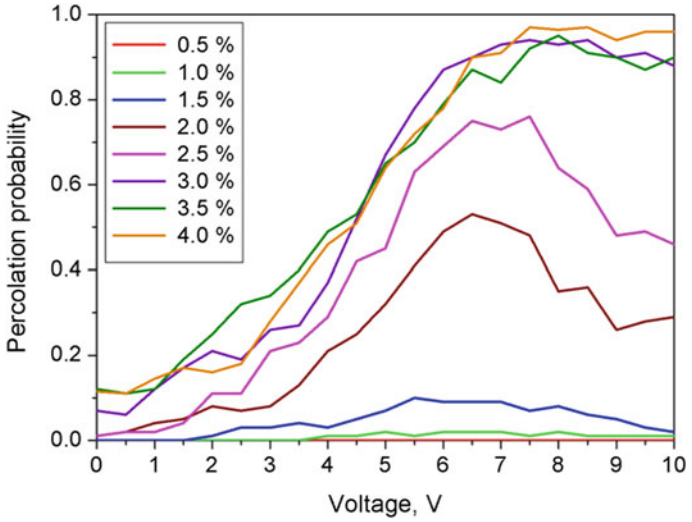

Fig. 21.9 Percolation probability as the function of the applied voltage for different nanotubes concentrations (nanotubes length $L = 3$ nm) [41]

The results of the calculations of percolation probability dependence on voltage for different concentrations of filling nanotubes of fixed length (3 nm) are depicted in Fig. 21.9 Based on the analysis of the obtained results, weak dependence of the percolation in the system of straight nanotubes on the distribution anisotropy level was established for the concentration of nanotubes in the 0.5–1.5% range. Efficient switching of the percolating system to conductive regime under applied voltage above 5 V is granted in nanocomposites with nanotubes loadings of about 3–4% [41, 44].

21.6 Conclusions

In this paper, the analysis of percolation phenomena in a three-dimensional system of straight nanotubes is carried out. The influence of geometric size and spatial orientation of nanotubes on the probability of conductive cluster formation is studied using the model environment. The possibility of controlling the nanotubes orientation by applying electric field was investigated. Performed simulations indicate the variation of the percolation probability of nanotubes depending on the parameters of the system, such as angular dispersion limits. Optimal values of the length and concentration of the nanotubes were determined for the efficient field control over the states of the percolating system.

The influence of tunneling distance parameter of the system conductivity was investigated. The results of the simulations coincide with experimental data obtained

by other researchers and also indicate the difference for the cases of overlapping nanotubes ("soft core" model) and nonoverlapping nanotubes ("hard core" model). The comparison with measured results shows that "hard core" model can be effectively used for predicting the parameters of fabricated composite being an important step toward the creation of the material with desired properties.

Acknowledgments The authors thank the Ministry of Education and Science of Ukraine for support.

References

1. Bao WS, Meguid SA, Zhu ZH, Meguid MJ (2011) Modeling electrical conductivities of nanocomposites with aligned carbon nanotubes. Nanotechnology 22(48):485704. https://doi.org/10.1088/0957-4484/22/48/485704
2. Yu Y, Song G, Sun L (2010) Determinant role of tunneling resistance in electrical conductivity of polymer composites reinforced by well dispersed carbon nanotubes. J Appl Phys 108:084319. https://doi.org/10.1063/1.3499628
3. Karbovnyk I, Olenych I, Aksimentyeva O, Klym H, Dzendzelyuk O, Olenych Y, Hrushetska O (2016) Effect of radiation on the electrical properties of PEDOT-based nanocomposites. Nanoscale Res Lett 11(1):84. https://doi.org/10.1186/s11671-016-1293-0
4. Klym H, Hadzaman I, Shpotyuk O (2015) Influence of sintering temperature on pore structure and electrical properties of technologically modified MgO-Al_2O_3 ceramics. Mater Sci 21(1):92–95. https://doi.org/10.5755/j01.ms.21.1.5189
5. Karbovnyk I, Collins J, Bolesta I, Stelmashchuk A, Kolkevych A, Velupillai S, Klym H, Fedyshyn O, Tymoshuk S, Kolych I (2015) Random nanostructured metallic films for environmental monitoring and optical sensing: experimental and computational studies. Nanoscale Res Lett 10:151. https://doi.org/10.1186/s11671-015-0855-x
6. Klym H, Ingram A, Shpotyuk O, Hadzaman I, Hotra O, Kostiv Y (2016) Nanostructural free-volume effects in humidity-sensitive MgO-Al_2O_3 ceramics for sensor applications. J Mater Eng Perform 25(3):866–873. https://doi.org/10.1007/s11665-016-1931-9
7. Klym H, Balitska V, Shpotyuk O, Hadzaman I (2014) Degradation transformation in spinel-type functional thick-film ceramic materials. Microelectron Reliab 54(12):2843–2848. https://doi.org/10.1016/j.microrel.2014.07.137
8. Vakiv M, Hadzaman I, Klym H, Shpotyuk O, Brunner M (2011) Multifunctional thick-film structures based on spinel ceramics for environment sensors. J Phys Conf Ser 289(1):012011. https://doi.org/10.1088/1742-6596/289/1/012011
9. Klym H, Hadzaman I, Shpotyuk O, Brunner M (2014) Integrated thick-film nanostructures based on spinel ceramics. Nanoscale Res Lett 9(1):149. https://doi.org/10.1186/1556-276X-9-149
10. Klym H, Ingram A, Shpotyuk O, Filipecki J (2010) PALS as characterization tool in application to humidity-sensitive electroceramics. 27th Int Conf Microelectron Proc (MIEL):239–242. https://doi.org/10.1109/MIEL.2010.5490492
11. Olenych IB, Aksimentyeva OI, Karbovnyk ID, Olenych YI, Yarytska LI (2014) Preparation and properties of hybrid poly (3,4-ethylenedioxythiophene)–carbon nanotubes composites. Proc Int Conf Nanomater Appl Prop 3(2):02NNSA13-1 13-3
12. Tarasevich YY (2002) Percolation: theory, applications, algorithms. Editorial URSS (in Russian), Moscow
13. Sahimi M (1994) Applications of percolation theory. Taylor & Francis, London

14. Bellucci S, Bolesta I, Cestelli Guidi M, Karbovnyk I, Lesivciv V, Micciulla F, Pastore R, Popov AI, Velgosh S (2007) Cadmium clusters in CdI_2 layered crystals: the influence on the optical properties. J Phys Condens Matter 19(39):395015. https://doi.org/10.1088/0953-8984/19/39/395015
15. Hadzaman I, Klym H, Shpotyuk O (2014) Nanostructured oxyspinel multilayers for novel high-efficient conversion and control. Int J Nanotechnol 11(9-10-11):843–853. https://doi.org/10.1504/IJNT.2014.063793
16. Berhan L, Sastry AM (2007) Modeling percolation in high-aspect-ratio fiber systems. I. Soft-core versus hard-core models. Phys Rev E 75(4):041120. https://doi.org/10.1103/PhysRevE.75.041120
17. Bauhofer W, Kovacs JZ (2009) A review and analysis of electrical percolation in carbon nanotube polymer composites. Compos Sci Technol 69(10):1486–1498. https://doi.org/10.1016/j.compscitech.2008.06.018
18. Lu W, Chou TW, Thostenson ET (2010) A three-dimensional model of electrical percolation thresholds in carbon nanotube-based composites. Appl Phys Lett 96(22):223106. https://doi.org/10.1063/1.3443731
19. Hu N, Masuda Z, Yan C, Yamamoto G, Fukunaga H, Hashida T (2008) The electrical properties of polymer nanocomposites with carbon nanotube fillers. Nanotechnology 19(21):215701. https://doi.org/10.1088/0957-4484/19/21/215701
20. Du F, Fischer JE, Winey KI (2005) Effect of nanotube alignment on percolation conductivity in carbon nanotube/polymer composites. Phys Rev B 72(12):121404. https://doi.org/10.1103/PhysRevB.72.121404
21. Massey MK, Kotsialos A, Volpati D, Vissol-Gaudin E, Pearson C, Bowen L, Obara B, Zeze DA, Groves C, Petty MC (2016) Evolution of electronic circuits using carbon nanotube composites. Sci Rep 6:32197. https://doi.org/10.1038/srep32197
22. Stelmashchuk A, Karbovnyk I, Klym H, Berezko O, Kostiv Y, Lys R (2017) Modeling and quantitative analysis of connectivity and conductivity in random networks of nanotubes. EastEur J Enterp Technol 5(12 (89)):4–12. https://doi.org/10.15587/1729-4061.2017.112037
23. Karbovnyk I, Olenych Y, Lukashevych D, Chalyy D, Girnyk I, Rudko M, Klym H (2018) Low temperature electrical behavior of CNT-based nanocomposites. Proceedings of the 2018 IEEE 8th international conference on nanomateroals applications & properties (NAP-2018):01SPN80-1-4
24. Bao WS, Meguid SA, Zhu ZH, Weng GJ (2012) Tunneling resistance and its effect on the electrical conductivity of carbon nanotube nanocomposites. J Appl Phys 111(9):093726. https://doi.org/10.1063/1.4716010
25. Fang W, Jang HW, Leung SN (2015) Evaluation and modelling of electrically conductive polymer nanocomposites with carbon nanotube networks. Compos Part B 83:184–193. https://doi.org/10.1016/j.compositesb.2015.08.047
26. Büttiker M, Imry Y, Landauer R, Pinhas S (1985) Generalized many-channel conductance formula with application to small rings. Phys Rev B 31(10):6207. https://doi.org/10.1103/PhysRevB.31.6207
27. Tamura R, Tsukada M (1997) Electronic transport in carbon nanotube junctions. Solid State Commun 101(8):601–605. https://doi.org/10.1016/S0038-1098(96)00761-2
28. Saito R, Dresselhaus G, Dresselhaus MS (1998) Physical properties of carbon nanotubes, vol 3. Imperial College Press, London
29. Imry Y, Landauer R (1999) Conductance viewed as transmission. Rev Mod Phys 71(2):S306. https://doi.org/10.1103/RevModPhys.71.S306
30. Buldum A, Lu JP (2001) Contact resistance between carbon nanotubes. Phys Rev B 63(16):161403. https://doi.org/10.1103/PhysRevB.63.161403
31. Naeemi A, Meindl ID (2009) Performance modeling for carbon nanotube interconnects. In: Carbon nanotube electronics. Springer, New York, pp 163–190
32. Hertel T, Walkup RE, Avouris P (1998) Deformation of carbon nanotubes by surface van der Waals forces. Phys Rev B 58(20):13870. https://doi.org/10.1103/PhysRevB.58.13870

33. Girifalco LA, Hodak M, Lee RS (2000) Carbon nanotubes, buckyballs, ropes, and a universal graphitic potential. Phys Rev B 62(19):13104. https://doi.org/10.1103/PhysRevB.62.13104
34. Simmons JG (1963) Generalized formula for the electric tunnel effect between similar electrodes separated by a thin insulating film. J Appl Phys 34(6):1793–1803. https://doi.org/10.1063/1.170268
35. Li XS (2005) An overview of SuperLU: algorithms, implementation, and user interface. ACM Trans Math Softw 31(3):302–325. https://doi.org/10.1145/1089014.1089017
36. Li XS, Demmel JW, Gilbert IR, Grigori L, Shao M, Yamazaki I (1999) SuperLU users' guide. Lawrence Berkeley National Laboratory, Berkeley
37. Demmel JW, Eisenstat SC, Gilbert JR, Li XS, Liu JW (1999) A supernodal approach to sparse partial pivoting. SIAM J Matrix Anal Appl 20(3):720–755. https://doi.org/10.1137/S0895479895291765
38. Stelmashchuk A, Karbovnyk I, Klym H, Lukashevych D, Chalyy D (2017) Simulation of the tunelling conductivity in nanotube/dielectric composite. 37th international conference on electronics and nanotechnology (ELNANO):209–212. https://doi.org/10.1109/ELNANO.2017.7939751
39. Stelmashchuk A, Karbovnyk I, Klym H (2016) Computer simulations of nanotube networks in dielectric matrix. 13th international conference on modern problems of radio engineering telecommunications and computer science (TCSET): 415–417. https://doi.org/10.1109/TCSET.2016.7452074
40. Stelmashchuk A, Karbovnyk I, Chalyy D, Lukashevych D, Klym H (2017) Parametric modeling of conductivity in percolating nanotube network. First Ukraine conference on electrical and computer engineering (UKRCON):740–743. https://doi.org/10.1109/UKRCON.2017.8100343
41. Olenych Y, Karbovnyk I, Klym H (2018) Computer simulation of field-controlled percolation in 3D system of straight nanotubes. XIV-th international conference on perspective technologies and methods in MEMS design (MEMSTECH):48–51. https://doi.org/10.1109/MEMSTECH.2018.8365699
42. Li C, Thostenson ET, Chou TW (2008) Sensors and actuators based on carbon nanotubes and their composites: a review. Compos Sci Technol 68(6):1227–1249. https://doi.org/10.1016/j.compscitech.2008.01.006
43. Zeng X, Xu X, Shenai PM, Kovalev E, Baudot C, Mathews N, Zhao Y (2011) Characteristics of the electrical percolation in carbon nanotubes/polymer nanocomposites. J Phys Chem C 115(44):21685–21690. https://doi.org/10.1021/jp207388n
44. Olenych Y, Karbovnyk I, Shmygelsky Y, Klym H (2018) Modeling of percolation phenomena in 3D nanotube system. Electron Inf Technol 9:40–47. http://elit.lnu.edu.ua/pdf/9_4.pdf

Chapter 22
Radiation-Stimulated Formation of Polyene Structures in Polyethylene Nanocomposites with Multi-walled Carbon Nanotubes

M. A. Alieksandrov, T. M. Pinchuk-Rugal, O. P. Dmytrenko, M. P. Kulish, V. V. Shlapatska, and V. M. Tkach

22.1 Introduction

High-molecular compounds (polymers) are important technological materials. At the same time, they are characterized by low physical and mechanical properties and high dielectric properties, which leads to their limited application. Such restrictions are inherent to polyethylene (PE). To improve these properties, polymeric composites are preferably used, the physical and mechanical characteristics of which can vary widely, depending on the formulated purpose. The change of properties essentially depends on the introduction of certain modifiers and fillers, their concentration, dispersion distribution, and the methods of manufacturing and processing introduced into the polymer matrix of a certain density. One of the unique fillers that can significantly improve the physical and mechanical properties of composites is carbon, including multi-walled carbon nanotubes (MWCNTs) [1–7]. The latter belong to one of the varieties of π-conjugate systems, for which the characteristic feature is the presence of delocalized π-electrons. The same structures include polyenes that are formed in polymers under thermal degradation. Such polymers include PVC, which already has a developed polyene structure modified by ionization irradiation during the production of samples by melting [8]. PE is belongs to a group of polymers that are effectively cross-linked owing to the appearance of double bonds between macromolecules in radiation treatment with

M. A. Alieksandrov (✉) · T. M. Pinchuk-Rugal · O. P. Dmytrenko · M. P. Kulish
Taras Shevchenko National University of Kyiv, Kyiv, Ukraine

V. V. Shlapatska
L.V. Pisarghevskiy Institute of Physical Chemistry NAS of Ukraine, Kyiv, Ukraine

V. M. Tkach
V. Bakul Institute for Superhard Materials NAS of Ukraine, Kyiv, Ukraine

O. Fesenko, L. Yatsenko (eds.), *Nanocomposites, Nanostructures, and Their Applications*, Springer Proceedings in Physics 221,
https://doi.org/10.1007/978-3-030-17759-1_22

high-energy bombarding particles, including γ-photons and electrons. Formation of polyene structures, as defects in the internal structure, has been insufficiently studied in PE.

22.2 Experimental Studies

To prepare samples of PE and its nanocomposites with multi-walled carbon nanotubes (PE-MWCNTs) a powder of low-density PE was used. As a conductive filler, MWCNTs measuring 9.5 nm in diameter and 1.3 μm in length produced by NANOCYL (Sambreville, Belgium) were used. At the first stage, a blend of PE powder with an appropriate content of MWCNTs (0.5, 1.0, 1.25, 1.5, 1.75, 2.0, and 3.0 vol.%) was thoroughly mechanically mixed by grinding in porcelain mortar. Next, the obtained mixture was mixed with a two-screw mini-extruder at 190 °C with a rotation speed of 80 rpm for 15 min. In the next stage, the nanocomposite was placed into steel mold heated to 170 °C and hot-compacted with pressure of 12 MPa for 10 min. After that, samples were cooled to room temperature at a speed of 15 °C per minute. Samples with a diameter of 12 mm and a thickness of 1.0 mm were prepared.

The structure of PE and nanocomposites of PE-MWCNTs was determined using a transmission electron microscope (JEM 100C; JEOL, Tokyo, Japan), scanning electron microscope (Zeiss EVO 60) and X-ray diffractometer DRON-3 M ($\lambda = 0.154178$ nm). Measurements were made with the use of LiF (002) flat crystals and Bragg–Brentano-type geometry.

Investigation of infrared (IR) spectra was carried out using the Fourier transform IR Nicolet iS10 spectrometer within the frequency range 400–8000 cm^{-1}. Photoluminescence (PL) spectra were measured using the reflective geometry method at the room temperature by means of a triple spectrometer (HORIBA Jobin Yvon T64000, Japan), provided with a cooled charge coupled device (CCD) detector. The PL spectra were excited using the lines of continuous He-Cd laser with the wavelength $\lambda_L = 325$ nm. Exciting irradiation with 1–2 MW of power was focused on the specimen to a spot of 1 μm in diameter.

Specimens were irradiated with electrons by means of a linear electron accelerator (ILU-6, Russia). The energy of the electrons was *E*e 1.8 MeV, whereas the dosage was equal to 0.01, 0.05, 0.2, 0.7, 2, and 4.72 MGy. During the course of their irradiation the temperature of the specimens did not exceed 333 K.

22.3 Results and Discussion

The state of polymeric nanocomposites is influenced not only by the conditions of their production, but also by radiation modification. The morphology of nanocomposites PE/MWCNT should vary at different concentrations of the filler, and as a

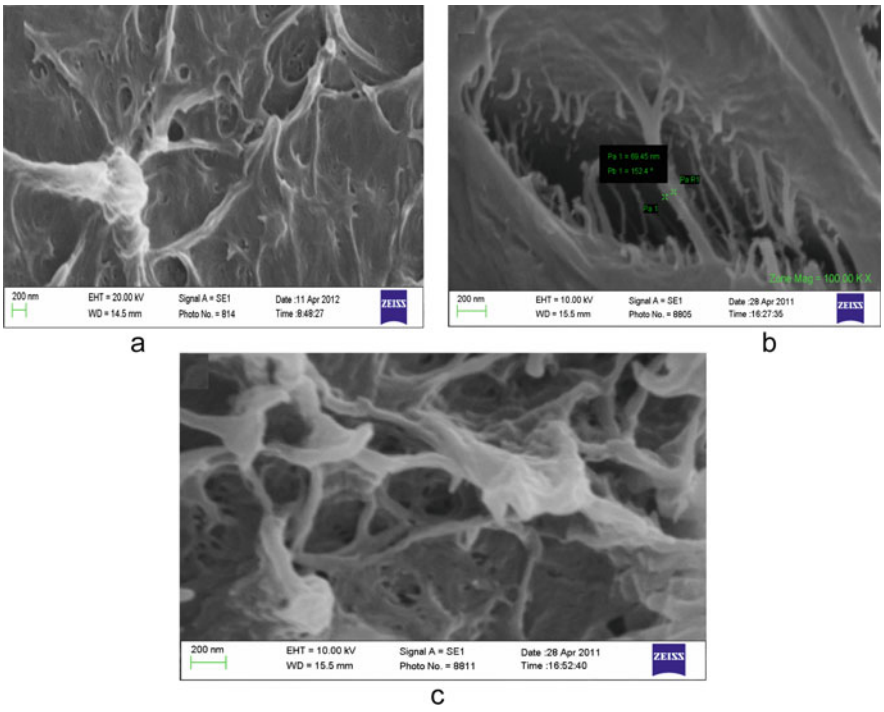

Fig. 22.1 Scanning electron microscopy (SEM) images of (**a**) pure PE and nanocomposites multi-walled carbon nanotubes (PE/MWCNTs) with (**b**) 1.0 and (**c**) 2.0 vol.% MWCNTs

result of irradiation. In Fig. 22.1, scanning electron microscopy (SEM) images of pure PE and nanocomposites PE-MWCNT with 1.0 and 2.0 vol.% MWCNT are shown.

It is evident that there is a homogeneous spherulite structure of crystals with lamellae varying within the range 1.0–5.0 μm. The crystallites of the polymer are isotropically oriented and differ in shape. Spherulite lamellar structure of pure PE is maintained at absorption doses of 0.01–4.72 MGy (Fig. 22.2). In the case of an increase in the absorption dose to 2.0 MGy, there is a destruction of the structure as a consequence of the growth of degradation of the macromolecules of PE (Fig. 22.2b).

Figure 22.3 shows the X-ray diffraction pattern of pure PE. A structural maxima indicates that the PE forms an orthorhombic crystalline phase; the parameters of the crystalline lattice are $a = 0.7520$ nm, $b = 0.44974$ nm, $c = 0.2550$ nm. For the reflex (110), using the Scherrer equation, a typical crystallite size was obtained, which is equal to 14 nm [9–11].

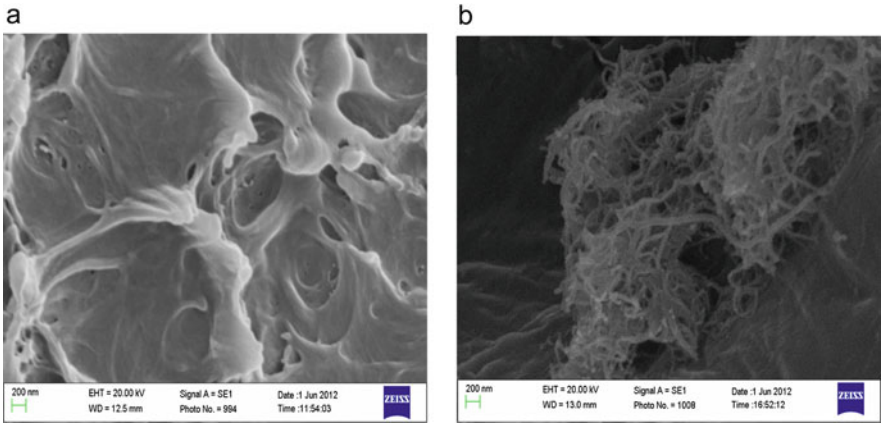

Fig. 22.2 SEM images of (**a**) pure polyethylene (PE) and nanocomposite PE/MWCNTs with 1.0 vol.% MWCNT after electron irradiation (**b**) with the absorption dose 2.0 MGy ($E_e = 1.8$ MeV), $T = 293$ K

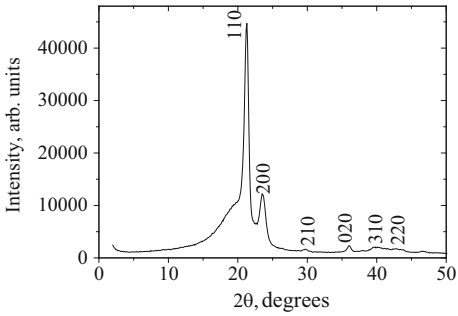

Fig. 22.3 X-ray diffraction pattern from pure PE. ($\lambda_{CuK\alpha 1.2} = 0.154178$нм)

At a low concentration of nanotubes, under 1.0 vol.%, the degree of crystallinity falls because of the mechanochemical destruction of ordered macromolecular chains in crystalline regions. At a further increase in nanotube concentration, the degree of crystallinity rises, as the role of nanotubes as centers of nucleation begin to prevail. At the same time, the degree of crystallinity changes slightly as it is determined by a low value of initial PE density (Fig. 22.4).

The orthorhombic structure of the crystalline phase also preserves PE and its nanocomposites in the case of high-energy electron irradiation with different doses (Fig. 22.5).

Figure 22.6 shows the degree of crystallinity after electron irradiation for pure PE and nanocomposites PE-MWCNTs with 1.0 and 2.0 vol.% MWCNT. It is seen that in the case of lower doses (0.05 and 0.2 MGy) the degree of crystallinity falls, reaching a minimum of 0.2 MGy. At a high dose of 4.72 MGy, the degree of crystallinity for all samples falls drastically.

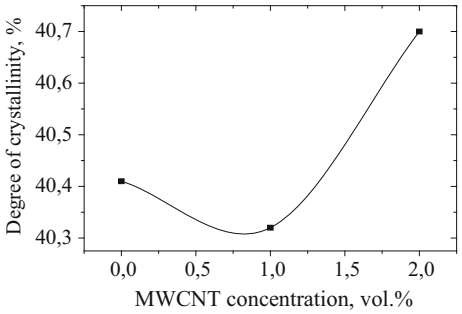

Fig. 22.4 Degree of crystallinity of PE-MWCNT nanocomposites as a function of MWCNT content

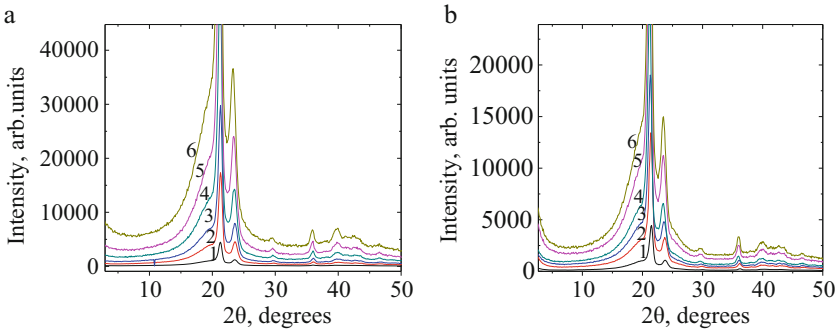

Fig. 22.5 3 X-ray diffraction pattern from (**a**) pure PE and (**b**) PE-MWCNT nanocomposites with 2.0 vol.% MWCNT after electron irradiation with the absorption doses 0 (1); 0.05 (2); 0.2 (3); 0.7 (4); 2.0 (5) 4.72 MGy (6) ($E_e = 1.8$ MeV)

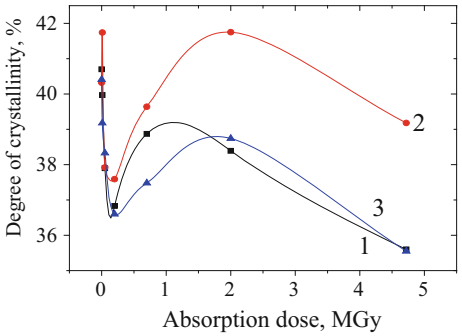

Fig. 22.6 Degree of crystallinity of pure PE (1) and PE-MWCNT nanocomposites with 1.0 (2) and 2.0 (3) vol.% MWCNT as a function of electron irradiation ($E_e = 1.8$ MeV)

The process of macromolecular chain destruction within crystalline regions prevails at low doses. It is worth noting that the destruction process takes place simultaneously with molecular chains crosslinking, which occurs mainly in amorphous regions. It is possible that intramolecular crosslinking within crystalline regions leads to a decrease in the degree of crystallinity. For LDPE, there exists destruction not only of the main macromolecular chain, but also their side branches or parts. Cleavage of side branches can be assumed to occur at higher doses of 0.2 to 2.0 MGy and accompanied by an increase in the degree of crystallinity. It is worth noting that high-density PE, as it lacks side branches, only has a reduced degree of crystallinity when there is an increase in irradiation dose. At a low concentration of nanotubes, when the homogeneity of their distribution in the polymer matrix is higher, the degree of crystallinity changes owing to the nucleation role of nanotubes.

Figure 22.7 shows the IR transmission spectra within a wide frequency range of 500–8000 cm^{-1} for pure PE and PE after electron irradiation with absorption doses of 0.05, 2.0, and 4.72 MGy.

It is evident that there are various absorption bands in valence and deformation oscillatory modes in single-, double-phonon, and higher frequency bands. Thus, the presence of the absorption band $B_{2u} \approx 746$ cm^{-1} is observed, which corresponds to deformation oscillations of the methylene group CH_2 in amorphous ($\approx$720 cm^{-1}) and crystalline ($\approx$730 cm^{-1}) phases. There is a set of bands within the frequency range 1300–1400 cm^{-1} owing to the oscillatory modes of the torsion of the groups CH_2 in amorphous ($\approx$303 cm^{-1}), the "fan" modes in amorphous (1353 cm^{-1}) and crystalline (1369 cm^{-1}) phases. In the IR absorption spectrum, a broad maximum of $\approx$1480 cm^{-1} associated with asymmetric deformation oscillations in the bend of the methylene groups of CH_2 (δas $\approx$ 1460 cm^{-1}) A bands within the range 1500–2500 cm^{-1} is observed, belonging to the carbonyl groups C=O ($\approx$1715 cm^{-1}), composed of oscillating mode $\approx$1904 cm^{-1}, which manifests only in the crystalline phase, and a band of $\approx$2037 cm^{-1}, which takes place for both phases. The broad IR absorption peak is within the range 2664–3026 cm^{-1}, which corresponds to a set of valence symmetrical 2853 and 2874 cm^{-1} and asymmetric 2926 and 2959 cm^{-1} oscillating modes, characteristic of methylene CH_2 and methyl CH_3 groups respectively [12].

Owing to the effect of ionizing radiation, changes in the spectra of IR absorption are already taking place at low absorption doses. In the case of an absorption dose of 0.05 MGy, the restructuring of the IR absorption spectrum is insignificant. At the same time, there is a shift of individual bands and a change in their relative intensities (Fig. 22.7b). It is more noticeable to reconstruct IR absorption spectra in the case of significant absorption doses of 2.0 and 4.72 MGy (Fig. 22.7c, d). It can be seen that there is a significant drop in transmission across the frequency range of 500–4500 cm^{-1} and it is particularly noticeable in the range up to 1450 cm^{-1}. At the absorption dose of 2.0 MGy, in addition to a sharp decrease in the transmission, there is already a shift of the individual strains of deformation oscillations. Thus, the band $\approx$746 cm^{-1} shifts to a position of 724 cm^{-1}. The band near 1391 cm^{-1} shifts to a frequency of 1360 cm^{-1}. Similarly, the displacement of the band is $\approx$1487 cm^{-1} to a new position of 1450 cm^{-1}. Such softening of oscillating modes

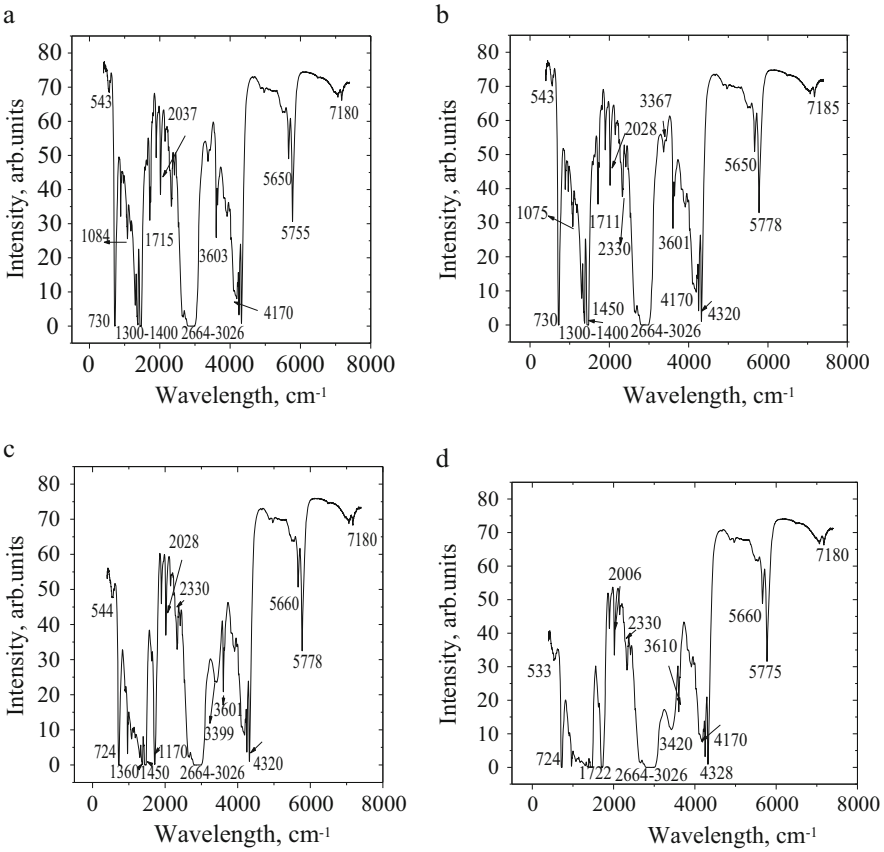

Fig. 22.7 Infrared transmission spectra within a wide frequency range of 500–8000 cm^{-1} for pure (**a**) PE and PE after electron irradiation with absorption doses of (**b**) 0.05, (**c**) 2.0, and (**d**) 4.72 MGy. ($E_e = 1.8$ MeV)

indicates a significant restructuring of PE. Peaks in the frequency range up to 1500 cm^{-1} show a sharp decrease. Even more significant is the change in absorption spectrum at an absorption dose of 4.72 MGy. If the intensity of the absorption peak from the carbonyl groups continues to grow, then the maxima in the interval 800–1500 cm^{-1} almost disappear. It can be assumed that such complex transformations of the IR absorption spectra are due to the radiation-stimulated restructuring of PE, which includes the destruction of the main and side chains, the cross-linking of the macronutrients, and the creation of π-conjugated polyene sequences.

Figure 22.8 shows the PL spectra of PE (1) and PE-MWCNT nanocomposites with 1.0 (2) and 2.0 (3) vol.% MWCNT in a non-irradiated state (a) and after electron irradiation with 4.72 MGy (b).

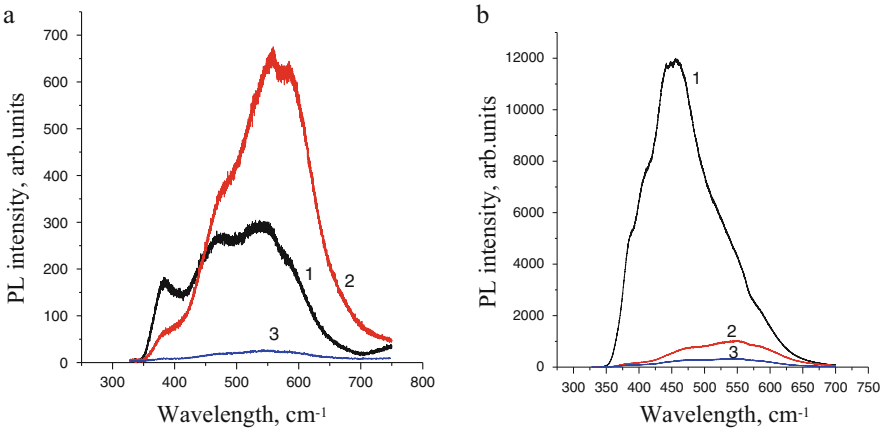

Fig. 22.8 Photoluminescence spectra of PE (1) and PE-MWCNT nanocomposites with 1.0 (2) and 2.0 (3) vol.% MWCNT in (**a**) a non-irradiated state and (**b**) after electron irradiation with 4.72 MGy

The inability to observe fluorescence for defect-free polymers is explained by the absence of optical absorption within the 200–800 nm spectra range [13–16]. Owing to the emergence of radicals, a sequence of radical transformations, polyenic structures $–CR_2(CR = CR)_nCR_2–$ containing π-conjugated bonds appears in polymers [13], where R is the hydrogen atom [17]. Defects cause the appearance of localized defective energetic levels set within an energy gap, which results in the emergence of PL bands. For study samples in Fig. 22.8, it can be seen that there is a bright structured fluorescence band located within the 350–700 nm range with a maximum close to 500 nm. More intensive PL, which is observed for PE filled with 1.0 vol.% of MWCNT compared with pure PE, suggests that nanotubes might play a destructive role in polymer, generating an excessive concentration of emission centers. A further increase in MWCNT concentration to 2.0 vol.% leads to a decrease in the intensity of PL. Structural defects responsible for PL within the visible range were obtained because of the recombination of ruptured C–C bonds which result in the appearance of π-conjugated polyenic chains. PL spectra have several components according to the number of carbon atoms constituting this chain. Irradiation treatment of PE leads to an increase in PL intensity of a pure sample compared with a sample filled with MWCNT (Fig. 22.8b). After irradiation with a dose of 4.72 MGy, the higher MWCNT content corresponds to a lower intensity of PL, as it should be because of the mechanism of charge carrier separation. For pure irradiated PE, components are located at 390, 423, 457, and 507 nm for polyenic chains with $n = 4$, 5, 6, and 7 respectively. PE with 1.0 vol.% nanotube content has very different components of irradiation. A band located at 391 nm corresponds to $n = 4$, but the next component is located at 476 nm, which is due to a polyenic chain with $n = 6$. Emission of the polyenic chain with $n = 5$ is unobservable. The following band is positioned at 536 nm, corresponding to $n = 7$. The band at a

wavelength of 577 nm is provided by the emission center, which is a polyenic chain with $n = 8$. An increase in the MWCNT concentration to 2.0 vol.% at the same irradiation dose of 4.72 MGy gives the same set of PL components, but compared with 1.0 vol.%, the first three components shift toward shorter wavelengths (390, 466, and 536 nm corresponding to $n = 4$, 6, and 7 respectively), whereas the component for $n = 8$ shifts to 584 nm.

22.4 Conclusion

1. Investigation of morphology for PE nanocomposites with MWCNs 0.1 1 10–12 10–11 10–10 10–9 10–8 10–7 2 σ, S/cm irradiation dose, MGy 1 (MWCTN) indicate good wetting of samples between constituents, and therefore enough adsorption and probably a chemical interaction on the boundary of phases. The orthorhombic structure of PE under filling with nanotubes and electron irradiation is maintained and the degree of crystallinity changes slightly.
2. Ionization irradiation is already at low doses of absorption (0.05 MGy) leading to simultaneous processes of the formation of polyene sequences, the destruction of the main circuit and lateral branches, in addition to the cross-linking of macromolecules PE, which manifests in general the growth of IR absorption within the range of deformation fluctuations of methylene CH_2 and CH_3 groups, C=C bonds, and valence oscillations C–C and C=C. In addition, the depth of these bands change in IR spectra.
3. Filling the polymer with MWCNT leads to the redistribution of contributions from different emission centers. On the other hand, the type of defects is preserved. The quenching of PL with an increase in MWCNT concentration is observed. Although nanotubes play a destructive role, creating more defects, the mechanism of charge separation due to interaction between nanotubes and polyenic chains, which are conjugated systems, determines the behavior of PL. Because of these two opposing roles of nanotubes with respect to PL spectra, for PE there is a crossover of PL intensity between pure PE and PE filled with nanotubes. Without irradiation, the destructive role of MWCNT in the polymer matrix for PE prevails, whereas after irradiation, charge separation becomes more efficient than the creation of new defects by nanotubes. Thus, the concentration of polyene chains created by irradiation is much higher than the impact of nanotubes alone.

References

1. Bhattachargya AR, Sreekumar TV (2003) Crystallization and orientation studies in polypropylene/single wall carbon nanotube composite. Polymer 44:2373–2377
2. Mierczynska A, Friedrich J (2004) Segregated network polymer/carbon nanotubes composites. Cent Eur J Chem 2(2):363–370
3. Olasz L, Gudmundson P (2006) Viscoelastic model of crosslinked polyethylene including effects of temperature and crystallinity. Mech Time Depend Mater 9:225–246
4. Myasnikova L, Blashenkov N, Boiko Y (2006) Relaxation processes in polymer surface layers. Micromol Symp 242:182–192
5. Valentinoa O, Sarnoad M, Rainone N (2008) Influence of the polymer structure and nanotube concentration on the conductivity and rheological properties of polyethylene/CNT composites. Phys E 40:2440–2445
6. Bystrzejewski M, Rümmeli MH, Gemming T (2009) Functionalizing single-wall carbon nanotubes in hollow cathode glow discharges. Plasma Chem Plasma Process 29:79–90
7. Gorrasi G, Di Lieto R, Patimo G (2011) Structure-property relationships on uniaxially oriented carbon nanotube/polyethylene composites. Polymer 52:1124–1132
8. Pinchuk-Rugal TM, Dmytrenko OP, Kulish MP, Prylutskyy YI, Nychyporenko OS, Shut MI, Tkach VM, Shlapatska VV (2016) The electron radiation effect of polyvinylchloride (PVC) nanocomposites with multiwalled carbon nanotubes. Nanophysics, nanomaterials, interface studies and applications. Springer Proc Phy 195:757–770
9. Mo Z (1995) The degree of crystallinity in polymers by wide-angle X-ray diffraction (WAXD). Macromol Chem Phys 35(4):555–580
10. Pinchuk-Rugal TM, Nychyporenko OS, Dmytrenko OP, Kulish MP, Grabovskyy YY, Zabolotnyy MA, Rugal OG, Mamunya YP, Levchenko VV, Shlapatskaya VV, Tkach VM (2013) Morphology and structure of high-pressure polyethylene nanocomposites with multi-walled carbon nanotubes under irradiation. Probl At Sci Technol 5(87):173–177
11. Pinchuk-Rugal TM, Nychyporenko OS, Dmytrenko OP, Kulish MP, Grabovskyy YY, Zabolotnyy MA, Mamunya YP, Levchenko VV, Shlapatskaya VV, Strelchuk VV, Tkach VM (2016) Radiation-stimulated alternation of electrical conductivity of nanocomposite of polyethylene with multi-wall carbon nanotubes. Probl Atom Sci Tech 102(2):99–106
12. Krimm S, Liang CY, Sutherland GB (1956) Infrared spectra of high polymers. II. Polyethylene. J Chem Phys 25:549–562
13. Khatipov SA, Nurmukhametov NR, Seliverstov ID, Sergeev AM (2006) Spectrophotometric and luminescent analysis of polytetrafluoroethylene treated by γ-irradiation near the melting point. Polym Sci Ser A 48(2):263–270
14. Oshima A, Ikeda S, Kator E, Tabata Y (2001) Chemical structure and physical properties of radiation-induced crosslinking of polytetrafluoroethylene. Radiat Phys Chem 62(1):39–45
15. Konova ME, Sakhno YE, Khatipov AS et al (2011) Mechanical and optical properties of polytetrafluoroethylene treated by γ-irradiation near the melting point. Phys Chem Solid State 12(4):1013–1017
16. Chatipov AS, Artamonov AN (2008) Creating a new sealing and antifriction material based on radiation-modified polytetrafluoroethylene. Ros Chim J LII(3):89–97
17. Pikaev KA (1987) Modern radiation chemistry. Solid body and polymers. Applied aspects. Nauka, Moscow

Chapter 23
Theoretical Analysis of Metal Salt Crystallization Process on the Thermoexfoliated and Disperse Graphite Surface

Luidmila Yu. Matsui, Luidmila L. Vovchenko, Iryna V. Ovsiienko, Tatiana L. Tsaregradskaya, and Galina V. Saenko

23.1 Introduction

The investigations of nanocomposite systems are the objective for new branches of science, which are intensively developed and their achievements are highly associated with the development of the synthesis methods. The set of methods being used for producing of nanocomposite materials is quite wide [1]. It is possible to eliminate two principal approaches for solving the problem of nanocomposite materials producing, namely, physical and chemical approaches. The deposition methods are the most spread ones among the physical technologies. The method of metal reduction from the salt solution is a commonly used chemical method. The using of chemical modifying of the developed surface of graphite supporter in order to deposit the metals or their compound in nanocrystalline state seems to be highly prospective [2]. Investigations showed the formation of nanoscaled component on the surface of graphite supporter to be the multistage process, each stage of it being determined by a variety of factors. These factors, in term, determine the structure and phase composition of final product. Evidently, the creation of theoretical background for the description of the principal mechanisms of metal component formation on the different types of graphite supporter is necessary for the further development of synthesis of nanocomposite materials with the predetermined set of structural, physical, and chemical properties.

L. Yu. Matsui · L. L. Vovchenko · I. V. Ovsiienko · T. L. Tsaregradskaya (✉) · G. V. Saenko
Departments of Physics, Taras Shevchenko National University of Kyiv, Kyiv, Ukraine

O. Fesenko, L. Yatsenko (eds.), *Nanocomposites, Nanostructures, and Their Applications*, Springer Proceedings in Physics 221,
https://doi.org/10.1007/978-3-030-17759-1_23

23.2 The Kinetics of Impregnation of the Thermoexfoliated Graphite by Water-Salt Solutions

Thermoexfoliated graphite (TEG) with a peculiar morphology of particles is the one among the graphite materials that are used for composite materials production. The first stage of composite materials (CM) production – the TEG impregnation with water-salt solution will be considered in detail below.

TEG particles by their geometry are the openwork structures formed by thin (~ 10 nm) graphite planes, which bound the pores. The characteristic linear dimensions of pores are equal to: $d = (7 \pm 2) \cdot 10^3$nm for effective cross section diameter, l_0~($0.1 \div 0.2$)mm for the length. There are two possible groups of pores existing in TEG. The "open" pores exhausting onto TEG surface belong to the first group. Those pores forming the closed volumes inside TEG particles ("closed" pores) belong to the second group. High values of TEG-specific free surface certify that vast majority of pores in TEG are of the first group.

Penetration of salt-water solution into the pores due to the surface tension and accompanied by locking of air bubble in the pore (it is necessary to note that the wetting of TEG surface by salt solution is provided by preliminary chemical treatment of TEG) is observed under TEG particles sinking into solution. To fill pore completely by salt solution air should be removed.

Two principle mechanisms of liquid penetration into the pores have been proposed in Refs [3, 4], namely, diffusive removal of gas (a) and liquid transport onto the pore's surface within the bubble by the vapor condensation (b). Evidently, the pore will be filled by pure solvent (water) rather than salt solution in a case of mechanism (b). The performed studies have shown that just the salt solution penetrates into the pores. This fact permits to consider mechanism (a) being dominant.

The process of diffusive removal of gas from TEG pores is qualitatively looking as follows. The air pressure over meniscus $P = P_0 + P_c$ is higher than the pressure on the open end of pore P_0 by capillary pressure P_c due to capillary effect. This leads to the excess dissolving of air (i.e., to the increasing of dissolved air content) in liquid layer directly adjacent to meniscus. The content of dissolved air at the open end of the pore is determined by the extreme dissolving at ambient conditions (this is easy to obtain by simple mixing of "salt solution – TEG" mixture). Hence, the concentration gradient arises in the filled part of the pore that provides the diffusive flow directed from meniscus to the open end of pore.

Let us begin the quantitative description of diffusive removal of gas from TEG pore by the formulation of the approaching being used.

In a sense of geometry, the pore in TEG looks as a cylindrical channel of the length l_0 and diameter d; a part of the pore of the length l is filled by salt solution (Fig. 23.1).

The content of the diluted air in the thin layer of liquid adjacent to meniscus is propartal to the air pressure over meniscus.

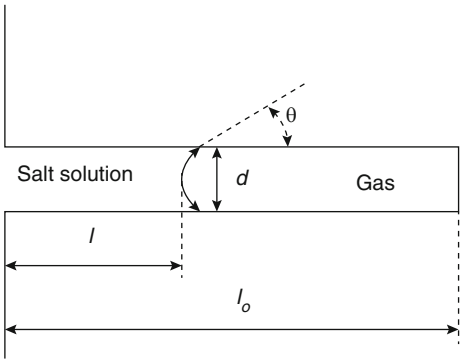

Fig. 23.1 Scheme of the pore in TEG

The content of air diluted in liquid is the linear function of the distance to the open end of the pore. State of air in the bubble could be described sufficiently by the Mendeleev-Clapeyron equation. The process of air solution in liquid and diffusion are described by effective parameters: solubility and diffusion coefficient reduced to the standard composition of air.

With respect to specific character of the problem under consideration, it is convenient to present the first Fick law in a form:

$$\vec{j}_{\mathrm{m}} = -D\,\vec{\nabla}\rho, \tag{23.1}$$

where $\vec{j}_{\mathrm{m}}$ is the mass flow of the diffusing air, ρ is the density of dissolved air, and D is the effective coefficient of air diffusion in salt solution.

The density gradient could be written as

$$\vec{\nabla}\rho = \frac{\rho - \rho_0}{l} = \frac{\Delta\,\rho}{l}, \tag{23.2}$$

where ρ is the density of dissolved air just under meniscus and ρ_0 is the density of dissolved air at the open end of the pore.

Evidently, diffusive removal of air from the bubble is accompanied by the meniscus motion:

$$\frac{\mathrm{d}l}{\mathrm{d}t} = \frac{j_{\mathrm{m}}}{\rho} = \gamma\frac{D\,\Delta\rho}{\rho l}. \tag{23.3}$$

where γ is the propartality factor between gas densities in the bubble ρ_{b} and in the solution ρ: $\rho = \gamma\rho_{\mathrm{b}}$.

Differential Eq. (23.3) is the equation of meniscus motion at air diffusive removal from the pore. Its solution could be represented as

$$l(t) = \sqrt{\frac{2\gamma D\Delta\rho}{\rho}t + l^2(0)}, \tag{23.4}$$

where $l(0)$ is the depth of capillary retraction of meniscus into the pore at the instant TEG is sinking into the salt solution.

Let us calculate ρ, $\Delta\rho$ and $l(0)$ parameters of Eq. (23.4):

$$\rho_0 = \gamma\frac{P_0\langle M\rangle}{RT};\quad \rho = \gamma\frac{(P_0 + P_c)\langle M\rangle}{RT};\quad \Delta\rho = \gamma\frac{P_c\langle M\rangle}{RT}, \tag{23.5}$$

where $\langle M \rangle$ is the molar mass of air, P_o is the pressure at the open end of the pore, and P_c is the capillary pressure. The known Stokes formula

$$P_c = \frac{4\sigma\cos\theta}{d}, \tag{23.6}$$

where σ is the index of surface tension and θ is the edge angle, was used to determine capillary pressure.

Parameter $l(0)$ is determined from the condition of meniscus equilibrium at zero time:

$$l(0) = l_0\frac{4\sigma\cos\theta}{P_0 d + 4\sigma\cos\theta}. \tag{23.7}$$

If we substitute Eqs. (23.6) and (23.7) to Eq. (23.4), we finally obtain

$$l(t) = \sqrt{8\frac{\sigma\cos\theta\left\{dDP_0\gamma t + 2\left(l_0^2 + 2Dt\gamma\right)\sigma\cos\theta\right\}}{(P_0 d + 4\sigma\cos\theta)^2}}. \tag{23.8}$$

Equation (23.8) is just the desired equation, which describes the kinetics of TEG pore filling by salt solution.

Time t_0 of total filling of the pore could be easily derived from Eq. (23.8):

$$t_0 = \frac{dl_0^2 P_0}{8D\gamma\sigma\cos\theta}\frac{(8\sigma\cos\theta + dP_0)}{(dP_0 + 4\sigma\cos\theta)}. \tag{23.9}$$

Equation (23.9) is used to calculate the exposure time of the TEG in the salt solution needed to completely fill the pores.

23.3 The Factors Determining Kinetics of the Pores Filling by Salt Solution

The factors, which determine the passing of TEG pore filling by salt solution, could be divided into three groups.

Parameters of salt solution interaction with the chemically activated TEG surface: These parameters determine the value of $\sigma \cos \theta$ product in formulas (23.8) and (23.9). Naturally, the parameters relevant to this group depend on the state of TEG surface, type of salt, solution composition, and, presumably, temperature. The kind of Eqs. (23.8) and (23.9) as well as the results of calculations that will be presented below show the impregnation rate being increased with $\sigma \cos \theta$ value. This is provided by activation of TEG surface enhancing its interaction with salt solution.

Geometric parameters of pores: effective diameter and length. The increasing of both the length and effective diameter results in reducing of impregnation rate.

Parameters determining the diffusive flow of air through the salt solution: index γ and diffusion coefficient D. Both these parameters depend essentially on temperature: diffusion coefficient increases with temperature, while index γ reduces. Parameters γ and D are presented in formulas (23.8) and (23.9) as a product, which is almost temperature independent due to competitive character of multipliers' changing with temperature.

We performed calculation of (23.8) and (23.9) dependences for different values of "interaction parameter" $\sigma \cos \theta$, geometric parameters d and l_0, and also quantitatively analyzed the dependence of γD on temperature.

Numerical analysis of the parametric dependencies $l(t; \sigma \cos \theta, d, l_0)$ and $t_0(\sigma \cos \theta, d, l_0)$ allows: to make complete view on the influence of parameters of impregnation process on its kinetics; to estimate the required impregnation time; to determine the possibilities of impregnation process optimizing.

To simplify the calculation data interpretation the one-parametric analysis of $l(t; \sigma \cos \theta, d, l_0)$and $t_0(\sigma \cos \theta, d, l_0)$ dependences has been performed. Here, the values of all parameters except for varying one were considered to be equal to its typical values.

The typical values of the parameters determining kinetics of TEG pores impregnation by salt solution are listed below. Some values of these parameters are available in appropriate references and other ones were obtained at performed studies: $D_{\text{eff}} = 1.87 \cdot 10^{-9} \frac{\text{m}^2}{\text{s}}$ [5], $\gamma = 0.02$ [6], $\sigma \cos\theta = 0.03 \frac{N}{\text{m}}$ [7], $T = 300\,\text{K}$, $P_0 = 10^5$ Pa, $d = 7 \cdot 10^3$nm, $l_0 = 0.15$ mm.

The data of $l(t; d)$ dependencies calculations are presented in Fig. 23.2 in a graphic mode for three values of the effective diameter of pore: $d_1 = 10^{-6}$ vbgm (curve 1), $d_2 = 5 \cdot 10^{-6}$ m (curve 2), and $d_3 = 10^{-5}$m (curve 3).

The curves presented in Fig. 23.2 are of a root dependence character.

Rate of impregnation increases at decreasing of the effective pore's diameter. The depth of initial impregnation $l(0)$ also increases. The time of filling the pore

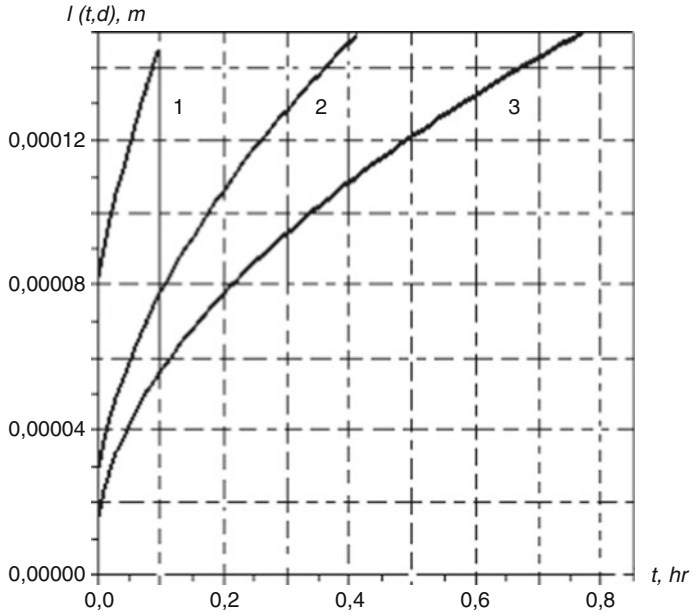

Fig. 23.2 Calculated dependence $l(t, d)$ for different values of effective pore diameters $d_1 = 10^{-6}$ m (curve 1), $d_2 = 5{\cdot}10^{-6}$ m (curve 2), $d_3 = 10^5$ m (curve 3)

ranges from 6 to 48 min for the considered interval of the effective diameter of pore. Evidently, the actual time of impregnation should be some higher in order to provide the filling of pores that are characterized by high values of diameter and length. Figure 23.3 presents $l(t; l_0)$ dependences calculated for the following values of l_0: $l_{01} = 0.2 \cdot 10^{-3}$m (curve 1), $l_{02} = 0.15 \cdot 10^{-3}$m (curve 2), and $l_{03} = 0.1 \cdot 10^{-3}$m (curve 3). The character feature of the curves presented in Fig. 23.4 is their closeness except for interval of low time of impregnation. Such behavior of $l(t; l_0)$ dependences could be easily explained: the diffusive flow of exhausting air is defined by the initial value of $l(0)$~l_0 at low times; as the time of impregnation increases, the contribution of $l(0)$ to the total length of filling $l(t)$ reduces.

Now let us analyze the influence of "interaction parameter" $\sigma \cos \theta$. The data of simulation illustrating the parametric dependence of $l(t)$ vs. $\sigma \cos \theta$ are plotted in Fig. 23.4.

The parametric dependence of $l(t)$ function vs. "interaction parameter" $\sigma \cos \theta$ occurs to be significant and shows the importance of the chemical activation of the surface of TEG pores before the impregnation. Figures 23.5–23.8 present the dependences of $t_0(d)$, $t_0(l_0)$, and $t_0(\sigma \cos \theta)$, respectively. The dependence $t_0(d)$ (Fig. 23.5) is convenient to determine the time of filling of the pore of the certain diameter. The dependence $t_0(l_0)$ (Fig. 23.6) is quadratic in l_0, the dependence $t_0(\sigma \cos \theta)$ (Fig. 23.6) is close to hyperbolic.

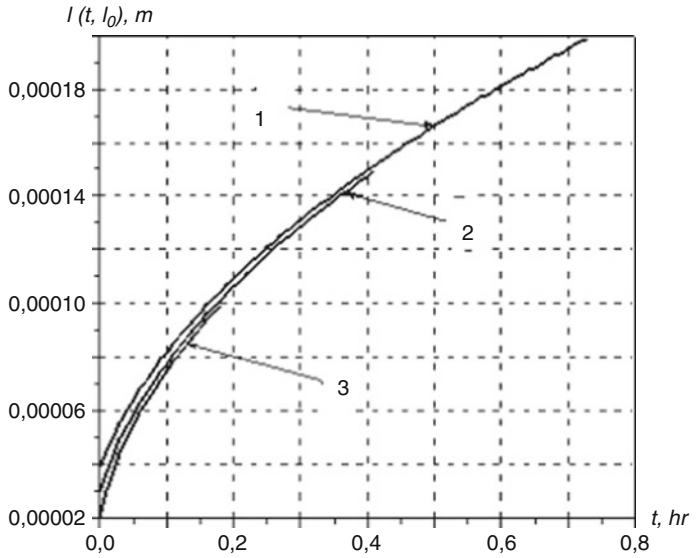

Fig. 23.3 Calculated dependence $l(t,\ l_0)$ for different values of parameter l_0. $l_{01} = 0.2{\cdot}10^{-3}$ m (curve 1), $l_{02} = 0.15{\cdot}10^{-3}$ m (curve 2), and $l_{03} = 0.1{\cdot}10^{-3}$ m (curve 3)

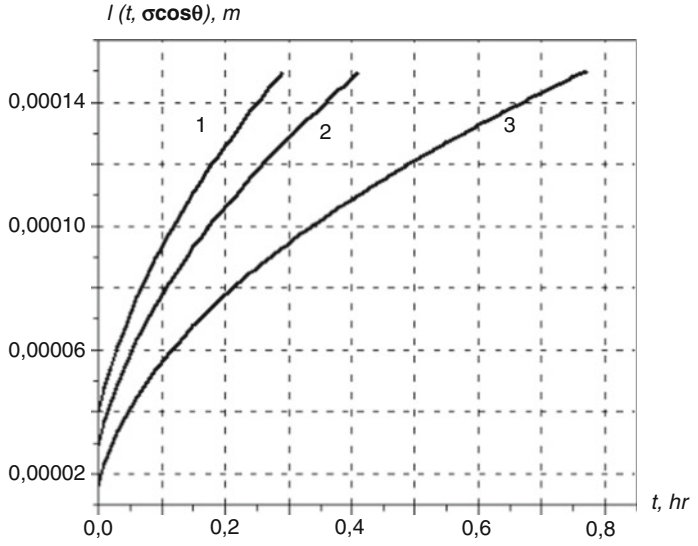

Fig. 23.4 Calculated dependence $l(t,\ \sigma\cos(\theta))$ for different values of $\sigma\cos(\theta)$ parameter: 1, $\sigma\cos(\theta) = 0.045$ N/m; 2, $\sigma\cos(\theta) = 0.03$ N/m; 3, $\sigma\cos(\theta) = 0.015$ N/m

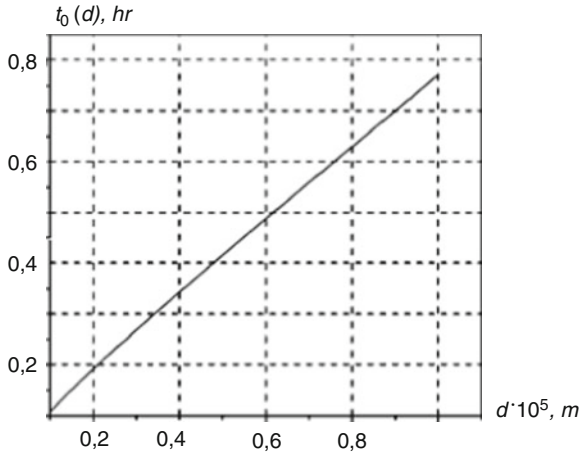

Fig. 23.5 Calculated dependence $t_0(d)$

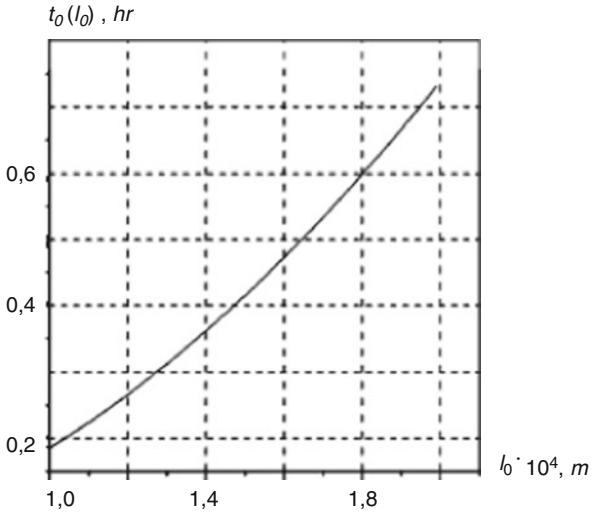

Fig. 23.6 Calculated dependence $t_0(l_0)$

Finally, let us analyze the temperature dependence of γD product that determines the diffusive removal of air from the pore.

Temperature dependence of the diffusion coefficient D is known to be determined by the expression $D(T) = D_0 \exp\left[-\frac{E_D}{kT}\right]$.

Hence, the temperature dependence of γ could be expressed as $\gamma(T) = \gamma_0 \exp\left[\frac{E_\gamma}{kT}\right]$, where $\frac{E_\gamma}{k} = 1.717 \cdot 10^3\ K^{-1}$ that is close to $\frac{E_D}{k}$ calculated by the data presented in Ref. [3].

So, the product $\gamma(T)D(T) = \gamma_0 D_0 \exp\left[\frac{E_\gamma - E_D}{kT}\right]$ exhibits weak dependence on temperature.

Thus, the theoretical investigations of TEG impregnation with salt solution have shown that kinetics of impregnation process is determined by many factors. The rate

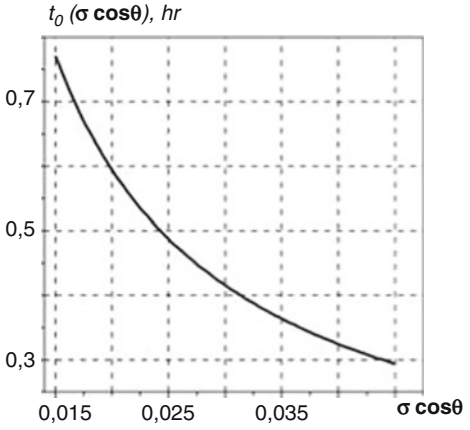

Fig. 23.7 Calculated dependence $t_0(\sigma \cos \theta)$

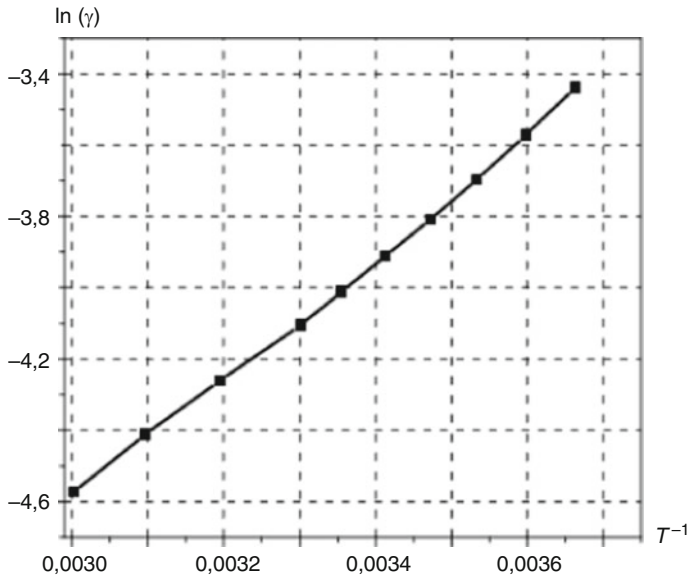

Fig. 23.8 Calculated dependence $\ln(\gamma)(1/T)$ based on experimental data [4]

of TEG salt solution impregnation depends on state of graphite surface, type of salt, and their concentration in solution, i.e., on interaction of salt solution with TEG surface. The activation of TEG surface leads to the enhancement of TEG surface-salt solution interaction and decrease in the impregnation duration. The geometrical parameters of TEG pores also influence the impregnation rate: the decrease in pore's length and their diameter causes the increase in impregnation rate.

23.4 Crystallization of Metal Salt on the Surface of Different Types of Graphite

The next stage of multistage process metal-graphite CM production by method of metal reduction in water-salt solution is the formation of crystalline salt film on graphite surface. While thin films of salt form on the surface of the solid phase, it is necessary to control a number of parameters such as the type and structure of the substrate, the state of its surface, temperature, the degree of supersaturation of the solution and its temporary change, diffusion coefficients, the intensity c of which the solution enters the nuclei of new phase. Usually, these parameters are selected empirically, but this way does not result in obtaining the necessary properties, structure, thickness, and other characteristics of the produced films. To reach this aim, it is necessary to analyze complicated physical phenomenon taking place at film's growing.

The fundamental studies of the kinetics of first-order phase transitions [8] showed this process to be multistage accompanied by the different nonlinear phenomena, such as nucleation, separated growing of new phase nuclei, coalescence, and, finally, Ostwald ripening. During last stage the growing of larger nuclei is realized through smaller nuclei decomposition. Mentioned processes are absolutely different in time consuming. The fastest is nucleation stage, the stage of separated growing is next, etc. Such time hierarchy means that the faster processes appear to be slaved of slow processes. The solution of the equation for the fast processes gives the initial conditions for the equations describing slow processes. It was shown that the solution obtained by Ya.B. Zeldovitch is valid for nucleation stage and, in a certain approach, for the stage of separated growing.

For late stages it is necessary to take into account the equation of substance conservation in the system and to solve the appropriate nonlinear problems. The stated above allows to conclude the impossibility of solving this problem in the general case.

However, it should be noted that the whole information on each stage of new phase formation on substrate is required only for some technological tasks. For example, it appears to be possible to consider just two-stage process (nucleation and separated growing stages) in a case of obtaining of nanocrystalline phase on solid substrate. Here, the solution of Kholmogorov-Zeldovitch equations is quite enough.

At this stage the problem of the formation of nanocrystalline metals on graphite surface is considered through the formation of crystalline films of metal salts on its surface, their transformation into metal oxide, and subsequent reduction of oxide to nanocrystalline metal. Two types of graphite, namely, thermoexfoliated and natural disperse graphites differing by the morphology of surface, were used as a graphite supporter.

An important feature of heterogeneous nucleation of new phase on the substrate surface as compared to homogeneous bulk nucleation is the fact that substrate con-

tains different imperfections. Even an ideal substrate contains such imperfections as Tamm's echelons formed by the abruption of crystalline planes.

It is quite natural that presence of all imperfections is inherent to substrates both of thermoexfoliated graphite, which is characterized by extremely high specific surface (~50 m^2/g), and of oxidized graphite obtained through thermal shock. The performed experiments prove that thermoexfoliated graphite essentially differs from granular. This fact we will use later to determine the surface roughness.

The strict theory of heterogeneous nucleation of new phase on the surface is not developed yet. The known theories of this process are based either on classical theory of nucleation [9] modified for two-dimensional case considering possible role of imperfections or Walton-Rosin atomistic model [10].

Cahn, Jackson, Temken, and some other model [11, 12] are usually used to calculate surface parameters in liquid-solid system. As it follows from the Jackson model, the interface is atom-scale rough if $q/kT < 2$ (q is latent heat of phase transition per particle) and if $q/kT > 5$, the surface becomes smooth.

The nucleation of new phase according to the heterogeneous theory occurs on the "ready centers" including solid substrates in contrast to the theory of homogeneous nucleation when new phase formation takes place through fluctuations arising in liquid. Wetting of the substrate surface by crystallizing liquid is the key factor of the heterogeneous crystallization. The wetting angle θ is introduced to characterize the wetting process. Its value is ranging from 0 (complete wetting) up to π (complete nonwetting). It is evident to assume that θ value is determined by substrate surface state. Let us consider θ as a function of surface roughness η, i.e., $\theta = f(\sigma)$.

The function considering changes of wetting angle while heterogeneous nucleation is as follows [9]:

$$\psi(\theta_i) = \frac{1}{4}(1 - \cos\theta_i)^2 (2 + \cos\theta_i), \tag{23.10}$$

where θ_i is the limiting wetting angle on the substrate surface of i order.

The equation to calculate the work of the critical size nucleus formation is as follows:

$$A_k = \frac{16}{3}\pi \frac{\sigma^3 V^2 \psi(\theta_i)}{\left(\Delta G^{\alpha-\beta}\right)^2}, \tag{23.11}$$

where $\sigma = \frac{\sum_{i=1}^{N} \sigma_i \Delta S_i}{(4\pi r^2)}$ is an effective surface tension; i – index – determines corresponding facet; r is the radius of sphere, whose volume is equal to that of equilibrium crystal with the surface of $S_0 = \sum_i S_i$; $\Delta G^{\alpha-\beta}$ is the Gibbs free energy changing upon transformation of salt from solution (α-phase) to crystal (β-phase); and V is the molar volume of crystalline salt.

The expression for $\Delta G^{\alpha-\beta}$ in a case of water-salt solutions could be written as [9].

$$\Delta G^{\alpha-\beta} = \frac{[T_{\mathrm{L}}(C_{\mathrm{C}}) - T]}{T_{\mathrm{L}}} \Delta H, \tag{23.12}$$

where $T_{\mathrm{L}}(C_{\mathrm{C}})$ is the temperature of salt limiting dissolving in the water, C_{C} is the salt content in water solution, ΔH is the enthalpy change at salt transition from solution to the crystalline phase.

As it follows from the analysis of Eq. (23.12) the quantity $\Delta G^{\alpha-\beta}$, which is often denominated as the motive force of crystallization, depends on the value of liquid supercooling $[T_{\mathrm{L}}(C_{\mathrm{C}})–T]$. This value, in turn, is determined by the salt content in the solution (just this parameter determines $T_{\mathrm{L}}(C_{\mathrm{C}})$) and by the temperature. When $\Delta G^{\alpha-\beta} = 0$ this means that liquid and crystalline phases are in a state of thermodynamic equilibrium. Crystallization is impossible if $\Delta G^{\alpha-\beta} < 0$. The quantity ΔH does not depend on the salt content in the solution and, hence, is constant for the given salt type.

The principal functions characterizing the process of heterogeneous nucleation are nucleation frequency (I), the linear rate of crystal growth (U), and the volume part of crystalline phase:

$$X = 1 - \exp\left[-\frac{\pi}{3} I U^3 t^4\right]. \tag{23.13}$$

The functions I and U could be expressed as

$$I_{\Gamma\mathrm{eT}} = \sum_{i=1}^{N} N_i \frac{D}{a^2} \exp\left[-\frac{A_k \psi(\theta_i)}{kT}\right], \tag{23.14}$$

$$U = \frac{D}{a}\left[1 - \exp\left(\frac{\Delta G^{\alpha-\beta}}{RT}\right)\right], \tag{23.15}$$

where N_i is the amount of atoms per unit volume on the area of surface where crystalline nuclei are formed at wetting angle θ_i, D is the diffusion coefficient, and a is the salt molecule cross section.

The function $\psi(\theta_i)$ in Eq. (23.14) is marked as multiplier and A_{k} could be expressed as

$$A_{\mathrm{k}} = \frac{16}{3}\pi \frac{\sigma^3 V^2}{\left(\Delta G^{\alpha-\beta}\right)^2}. \tag{23.16}$$

As far as only two initial stages (nucleation and separate growth) which are characterized by typical time 10^{-4} s, Eq. (23.13) can be expanded. As a result one may obtain the following:

$$X = \frac{\pi}{3} I U^3 t^4. \tag{23.17}$$

Thus, the nucleation frequency, linear rate of crystal growth, and time determine the size of crystallized salt particle. Let us analyze separately each of these functions.

According to Eqs. (23.15) and (23.12), the linear rate of crystal growth U is determined only by the characteristics of water-salt solution: diffusion coefficient D, the temperature of limiting dissolving T_L (C_C), the value of enthalpy change ΔH at salt transition from solution to crystalline phase. So, one can control the thickness of the crystalline coating on the substrate surface through the selection of the appropriate water-salt solution, for example, either metal acetate or metal nitrate, or even by changing salt content in the solution of the same type.

Let us put an attention to Eqs. (23.14) and (23.11) and define what parameters influence the frequency of nucleation of the "future" salt crystals on the substrate surface. The value of I in this case is influenced by the following parameters: salt solution parameters (diffusion coefficient, salt content in the solution, the enthalpy of salt transition from solution to crystalline phase ΔH, molar volume of salt crystalline phase) and substrate parameters (the state of surface, i.e., its roughness introduced indirectly through limiting wetting angle θ; the effective surface tension (specific surface energy) at the salt solution-salt crystal boundary).

Let us consider in more detail what factors determine the wetting angle θ and surface tension. Figure 23.9 presents in diagram form crystalline nucleus on graphite surface. The equilibrium value of wetting angle (Fig. 23.9) is determined by the ratio of surface energies for solution-crystal (σ_{sc}), solution-substrate (σ_{ss}), and crystal-substrate (σ_{cs}) boundaries if crystalline nucleus is approximated by sphere.

Moreover, reasoning from the equilibrium of the arisen forces, one could write.

$$\sigma_{sc}\cos\theta = \sigma_{ss} - \sigma_{cs}, \tag{23.18}$$

Several conclusions follow from Eq. (23.18). Let us express them as follows: the value of σ_{sc} (hereinafter it will be denoted as σ) is the constant and does not depend both on type of substrate and the state of its surface and is determined exclusively by the type of salt in a certain solution and limiting wetting angle is determined by

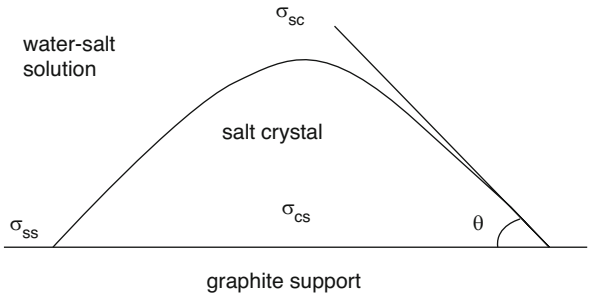

Fig. 23.9 Crystalline nucleus on graphite surface

the ratio of σ_{ss} and σ_{cs}, which, in turn, are determined by the nature of coexisting phases (salt solution-graphite surface and salt crystal-graphite surface in a case under consideration), i.e., depends on the roughness and activation of surface.

The stated above gives the possibility to use the same value of σ in order to calculate the work of critical nucleus formation at heterogeneous nucleation from certain water solution for substrates of different state of surface (thermoexfoliated, disperse, activated graphite, etc.). The state of the substrate surface is taken into account using the function $\psi(\theta_i)$. The limiting wetting angle (Fig. 23.9) could vary from 0 (complete wetting) up to π (complete nonwetting). Thus, $\psi(\theta_i)$ function according to Eq. (23.10) could vary from 0 if $\theta_i = 0$ to 1 if $\theta_i = \pi$.

In keeping with Eqs. (23.12), (23.14), and (23.17), the maximal value of X is reached at $\psi(\theta_i) = 0$. This may be easily tested experimentally, if thermoexfoliated, disperse, and activated graphites are selected as substrates. The treatment of such experimental data may be realized within the following equations.

Let us consider the relationship

$$\frac{X_1\,(t_1\theta_1)}{X_2\,(t_2\theta_2)} = \frac{J_1 {U_1}^3 {t_1}^4}{J_2 {U_2}^3 {t_2}^4}. \tag{23.19}$$

According to the performed analysis, the linear rate of crystal growth does not depend on type of substrate and is the same for a certain solution. So, Eq. (23.19) may be expressed as

$$\frac{X_1}{X_2} = \frac{J_1}{J_2} = \exp\left(\frac{A_k}{kT}\left[\psi_2\,(\theta_2) - \psi_1\,(\theta_1)\right]\right). \tag{23.20}$$

Finding a logarithm of Eq. (23.20) results in

$$\ln\frac{X_1}{X_2} = \frac{A_k}{kT}\left[\psi_2\,(\theta_2) - \psi_1\,(\theta_1)\right] = \frac{A_k}{kT}\varphi\,(\theta_{12})\,, \tag{23.21}$$

where the function $\varphi(\theta_{12}) = \psi_2(\theta_2) - \psi_1(\theta_1)$ varies within [0,1]. $\ln\frac{X_1}{X_2} = \frac{A_k}{kT}$ in a limiting case of $\varphi = 1$ (i.e., if one of the substrates is completely wetted ($\theta_2 = \pi$) and the other is completely non-wetted ($\theta_2 = 0$)). Thus, it becomes possible to determine the work of critical nucleus formation experimentally.

Using the experimental X data for graphite substrates of different roughness allows us to determine the wetting function $\varphi(\theta_1)$ by Eq. (23.21), since A_k is calculated directly from Eq. (23.16) and tabulated data for G, V, ΔH.

Now let us analyze the main conclusions of the presented theory and calculate the limiting wetting angles for different substrates using the experimental data on crystallization of water solutions of cobalt acetate at thermoexfoliated graphite, disperse natural graphite, and disperse natural graphite activated by sulfur acid.

To calculate $A_к$ in Eq. (23.21), the following tabulated data were used [5, 7]: $T = 348$ K, $\Delta T = 55$ K, $\Delta H = 26.8$ kJ/mole, $G = 0.03$ J/m^2, $V = 40{\cdot}10^{-6}$ m^3/mole. As a result $A_к = 4{\cdot}10^{-20}$ J.

Since $A_к/\kappa T \approx 10$ at $T = 293$ K, Eq. (23.21) transforms to

$$\ln \frac{X_1}{X_2} = 10\left[\psi_2(\theta_2) - \psi_1(\theta_1)\right]. \tag{23.22}$$

The weight increase at salt crystallization on the TEG surface is equal to $\Delta m_{TRG} = 6$ g (let us denominate it as X_1), in a case of natural graphite $\Delta m_{nat} = 0.3$ g (X_2), and in a case of natural graphite activated by sulfur acid $\Delta m_A = 0.7$ g (X_3). Then the ratios of weight increases for different types of graphite are equal to $X_1/X_2 = 20$, $X_1/X_3 = 8.5$, and $X_3/X_2 = 2.3$.

This permits us to express Eq. (23.22) as three relationships

$$\begin{aligned} \psi_2(\theta_2) - \psi_1(\theta_1) &= 0.3, \\ \psi_3(\theta_3) - \psi_1(\theta_1) &= 0.22, \\ \psi_2(\theta_2) - \psi_3(\theta_3) &= 0.08. \end{aligned} \tag{23.23}$$

According to the estimations performed in Ref. [7], the value of limiting wetting angle is approximately equal to $\theta = 2/3\pi$ for the Ceylon graphite, which is poorly wetted. Besides, natural graphite is almost the same as the Ceylon one by the surface structure of particles. That's why let us consider that among all used substrates natural graphite is the most weakly wetted. So, $\theta_2 = 2/3\pi$, and then $\psi_2(\theta_2) = 0.843$. In keeping with Eq. (23.23), one can obtain $\psi_1(\theta_1) = 0.543$, $\theta_1 = 0.52\pi$, $\psi_3(\theta_3) = 0.763$, and $\theta_3 = 0.62\pi$.

Thus, TEG substrate possesses the smallest limiting wetting angle and, consequently, the highest roughness. The performed theoretical speculations and experimental investigations assumed just this. The activation of surface natural graphite by sulfur acid leads to an essential increase (almost by 2.5 times) of crystalline phase on its surface as compared to natural graphite.

23.5 Conclusion

The kinetics of impregnation of micro- and meso-porous graphite materials (TEG) by water-salt solutions has been described theoretically. This process was shown to depend on the structural peculiarities of graphite supporter and has diffusive character.

The equation to estimate the time of graphite materials impregnation by water-salt solutions has been derived. This parameter was shown to be determined by the state of surface, geometry structure of pores, type of salt and its solution concentration as well as by the parameters of air diffusion through salt solution. The activation of graphite material surface results in the enhancement of the interaction between its surface and salt solution that causes the reducing of TEG impregnation time.

The process of salt crystallization on the surface of graphite materials has been analyzed theoretically. The equilibrium value of wetting angle (i.e., the state of graphite surface) was revealed to be the main parameter determining this process. The dependence between part of crystalline salt phase on the surface of graphite material and wetting angle has been derived. The chemical activation of graphite material surface results in the reducing of wetting angle and, respectively, to the increasing of the part of crystalline salt phase.

References

1. Borovij MO, Kunic'kij YUA, Kalenyk OO, Ovsiienko IV, Tsaregradskaya TL (2015) Nanomateriali, nanotekhnologi, nanopristro. Interservis. Kyiv:350
2. Matsuy LY, Ovsiienko IV, Fedorov VE (2006) Modeling of the formation processes of nanocomposite material graphite - metal oxide. Metallofiz Noveishie Tekhnol 28(4):521–533
3. Lykov AV (1954) Transport phenomena in capillary-porous solids. GITTL, Moskva, p 298
4. Reshetin OL, Orlov SU (1998) Theory of heat and moisture transport in capillary-porous solids. J Techn phys 68(2):140–142
5. Physical encyclopedia (1988) Nauka, Moskva, p 708
6. Reference book on solubility (1961) Academy of Sciences of the USSR, M.-L. p.970
7. http://www.msm.cam.ac.uk/phase-trans/mtdata/mtdata.html
8. Kukushkin SA, Osipov AV (1998) Condensation of thin films. UPN 168(10):1083–1116
9. Shpak AP, Lysov VI, Kunitskij YA, Tsaregradskaya TL (2002) Crystallization and amorphization of metallic systems Akademperiodika. Kyiv 207. (in Ukrainian)
10. Walton LJ (1962) Chem.Phys. 37:2182–2189
11. Jekson K, Ulman D, Hant J (1968) Problems of crystals growth Mir, Moskva, p 293
12. Temnin DE in collect (1964) Mechanism and kinetics of crystallization Nauka i tekhnika. Minsk:250

Chapter 24
Modeling of Dielectric Permittivity of Polymer Composites with Mixed Fillers

Luidmila L. Vovchenko, Oleg V. Lozitsky, Luidmila Yu. Matsui, Olena S. Yakovenko, Viktor V. Oliynyk, and Volodymyr V. Zagorodnii

24.1 Introduction

Today it is promising to use the polymer-filled composites at the designing of new materials for various applications since the dielectric/electric properties of such composites can be varied within the wide range depending on the type and concentration of filler [1]. In addition, the polymers filled with comparatively low content of carbon or dielectric particles are corrosion-stable, light, easily workable, and cheaper compared to traditional materials. So, the nanocomposites with fillers based on $BaTiO_3$ and TiO_2 [2, 3] showed high permittivity values (ε_r'=10–30) and relatively low dielectric loss in the frequency range 8–18 GHz. The sufficiently high dielectric constant ε_r' was observed for polymer CM filled with nanocarbon fillers, carbon nanotubes (CNTs), and graphite nanoplatelets (GNPs) [4–6] at relatively low filler content due to high aspect ratio of nanocarbon particles and the large contribution of interfacial polarization. As it was shown in our previous papers [7–9], the permittivity ε_r' of epoxy composites filled with GNPs and CNTs may range within 4–50 depending on the filler content and slightly decreases with the frequency in the range 26–54 GHz, while the dielectric loss tangent $\tan\delta = \varepsilon_r''/\varepsilon_r'$ for such CMs is 0.02–0.3. The main obstacle for reaching the high permittivity in CMs, filled with conductive nanocarbon particles, is that a significant increase in the dielectric permittivity ε_r' of these composites with increasing nanocarbon content occurs in a relatively narrow concentration range, limited by low percolation

L. L. Vovchenko (✉) · O. V. Lozitsky · L. Y. Matsui · O. S. Yakovenko
Department of Physics, Taras Shevchenko National University of Kyiv, Kyiv, Ukraine
e-mail: vovch@univ.kiev.ua

V. V. Oliynyk · V. V. Zagorodnii
Department of Radiophysics, Electronics, and Computer Systems, Taras Shevchenko National University of Kyiv, Kyiv, Ukraine

O. Fesenko, L. Yatsenko (eds.), *Nanocomposites, Nanostructures, and Their Applications*, Springer Proceedings in Physics 221,
https://doi.org/10.1007/978-3-030-17759-1_24

threshold for such systems, since after percolation the transition to through-conduction and substantial electric losses occur.

Recently, some ways to increase the content of isolated anisotropic conductive filler particles, which act as "artificial dipoles" and significantly increase the permittivity of the CMs, have been proposed. So, along with the carbon filler, the use of second dielectric filler will prevent the formation of conductive carbon network [10, 11], and on the other hand, the additional increase of interfacial regions enhances the role of interfacial polarization in the formation of effective permittivity of CM. The high dielectric constant of dielectric particles with dominant dipolar polarization also can lead to greater shielding effectiveness due to an absorption of electromagnetic waves. Variation of geometrical parameters of carbon particles and the inorganic nanoparticles and their relative concentrations allows tuning the electromagnetic response of the hybrid material over a very wide range: from metallic to a high dielectric constant material. Another way to increase a permittivity of CMs consists in the formation of an insulating polymer layer on the surface of conductive filler before introducing them into the polymer matrix at CM fabrication [12]. The use of hybrid conductive filler with a special particle morphology such as GNP synthesized on their surface CNTs also leads to enhancement of CM permittivity [13]. The task of the prediction of the material parameters is very important since when these parameters are determined, in particular, the complex permittivity and its dependence on the content, morphology of the fillers, and the frequency of the EMR, it is easy to fabricate the composites with controllable properties for various applications, such as high energy-density capacitors and electric field grading materials, electromagnetic wave absorbers, leakage current controllers, etc.

The aim of this paper is the modeling of dielectric permittivity of composite materials filled with randomly oriented and spatially distributed conducting particles of various morphologies. The Maxwell-Garnett model for the effective medium was used for analytically predicting the effective complex permittivity of CMs with fillers concentration below the percolation threshold. We also modeled the permittivity of polymer composite filled with mixed conductive/dielectric filler and analyzed the changes of permittivity depending on ratio conductive/dielectric filler content.

24.2 Maxwell-Garnett Model for Dielectric Permittivity of Polymer Composites Filled with Mixed Fillers

In a case of polymer composites filled with electrically conductive particles characterized by a high aspect ratio AR (carbon nanotubes CNTs, graphite nanoplatelets GNP, carbon fibers CF), the Maxwell-Garnett model is the most appropriate to describe the effective permittivity [14, 15] at fillers concentration below the percolation threshold ($\varphi \leq \varphi_c$, throughout conductivity is not set yet). This model

takes into account the permittivity of CM components, the volume fraction, and the shape of the filler particles (depolarization factor related to morphology and aspect ratio of filler particles). The effective permittivity of CM with randomly distributed filler particles may be described by the following expression [15]:

$$\varepsilon_{\text{eff}} = \varepsilon_{\text{p}} + \frac{\frac{1}{3}\sum_{i=1}^{n} \varphi_i \left(\varepsilon_i - \varepsilon_{\text{p}}\right) \cdot \sum_{j=x,y,z} \frac{\varepsilon_{\text{p}}}{\varepsilon_{\text{p}} + N_{ij}\left(\varepsilon_i - \varepsilon_{\text{p}}\right)}}{1 - \frac{1}{3}\sum_{i=1}^{n} \varphi_i \left(\varepsilon_i - \varepsilon_{\text{p}}\right) \cdot \sum_{j=x,y,z} \frac{N_{ij}}{\varepsilon_{\text{p}} + N_{ij}\left(\varepsilon_i - \varepsilon_{\text{p}}\right)}}, \tag{24.1}$$

where ε_{eff} is the permittivity of the composite; ε_i and ε_{p} are the permittivities of the fillers and matrix, respectively; φ_i is the volume fraction of i-filler; and N_{ij} is the depolarization factor for the ellipsoid particles along j-axis. The sum of the depolarization factors satisfies the condition $N_{i1} + N_{i2} + N_{i3} = 1$.

The depolarization factors for elongated ellipsoids (carbon fibers CF, carbon nanotubes CNTs) are described by the following expressions:

$$N_x = \frac{\left(1 - e^2\right)}{2e^3} \cdot \left(\ln \frac{(1+e)}{(1-e)} - 2e\right), \quad N_y = N_z = \frac{(1 - N_x)}{2}, \quad e = \sqrt{1 - a_y^2/a_x^2}, \tag{24.2}$$

where a_x, a_y, and a_z are the ellipsoid semiaxes, $a_x > a_y = a_z$.

In a case of disk-like filler particles of diameter D and thickness h, the depolarization factors can be expressed as:

$$N_x = \frac{\left(1 + e^2\right)}{e^3} \cdot \left(e - \text{Arctg}(e)\right), \quad N_y = N_z = \frac{(1 - N_x)}{2}, \quad e = \sqrt{D^2/h^2 - 1}. \tag{24.3}$$

Dielectric properties of conductive filler ε_i are determined by the complex permittivity which may be presented as

$$\varepsilon_i = \varepsilon' - i \cdot \frac{\sigma_i}{\omega \cdot \varepsilon_0}, \tag{24.4}$$

where σ_i is the electrical conductivity of individual filler particle, ω is the angular frequency, and real part of permittivity ε_r' is much lower than imaginary part ε_r''.

Using Eqs. (24.1, 24.2, 24.3, and 24.4) and the known parameters of composite's constituents, it is possible to calculate the effective permittivity for a given concentration of the composite filler below the percolation threshold. In this case, the filler particles are isolated, and the Maxwell-Wagner-Sillars polarization effect in the electric field is very pronounced [16–18]. The abovementioned effect results in high values of permittivity for such CMs. The essence of the effect for binary CMs with attributes $\varepsilon_1' \cdot \sigma_2 \neq \varepsilon_2' \cdot \sigma_1$is a gradual charge accumulation at the interphase

boundaries under the applied electric field. So, the isolated conductive particles of the filler can be considered as "artificial dipoles" which are polarized in the electric field. As it was shown in Refs. [19, 20], the permittivity value of CM depends both on the content of the conductive filler and on the depolarization factors of the filler particles.

In a case of dielectric filler particles (e.g., $BaTiO_3$, TiO_2, etc.) permittivity is described by Debye formulas as:

$$\varepsilon = \varepsilon_\infty + \frac{\varepsilon_s - \varepsilon_\infty}{1 - i\omega\tau}, \tag{24.5}$$

where ε_∞ and ε_s are the static and optical permittivities of the dielectric particles and τ is the Debye time of relaxation.

In our calculation of the permittivity, we assume that all the filler particles are of the same form for a single type of inclusions.

24.3 Results and Discussion

We have modeled the permittivity within the Maxwell-Garnet approximation for composites filled with 1D, 2D, and mixed 1D/2D electroconductive fillers and also for the polymer composites filled with mixed electroconductive 1D (or 2D) and spherical 3D dielectric filler particles. The multiwalled carbon nanotubes were used as 1D conductive filler, while graphite nanoplatelets were used as 2D conductive filler. In a case of polymer composite with mixed nanocarbon/dielectric, the ceramic $BaTiO_3$ ultra-disperse particles were used.

Table 24.1 summarizes the data on the size and morphology of filler particles.

Figure 24.1 schematically presents the various types of considered polymer-filled composites.

The electrical conductivity of carbon fillers is relatively high and can vary widely for fillers such as GNP and carbon nanotubes, from 10^3 to 10^6 S/m, depending on the defects and state of the carbon nanoparticle surface [21]. In our calculations, we constrain the values of conductivity to 10^4–10^5 S/m.

Table 24.1 Morphology of the polymer composite fillers

	GNPs	CNTs	$BaTiO_3$
Shape of particles	Plates	Cylinders	Spherical particles
Length of particles		10–30 μm	
Diameter	0.2–30 μm	10–30 nm	400–700 nm
Thickness	5–65 nm		
Aspect ratio, AR	300–500	1000	~1.5
Packing factor *F*	0.05	0.06	
Electrical conductivity, S/m	10^4	10^4–10^5	

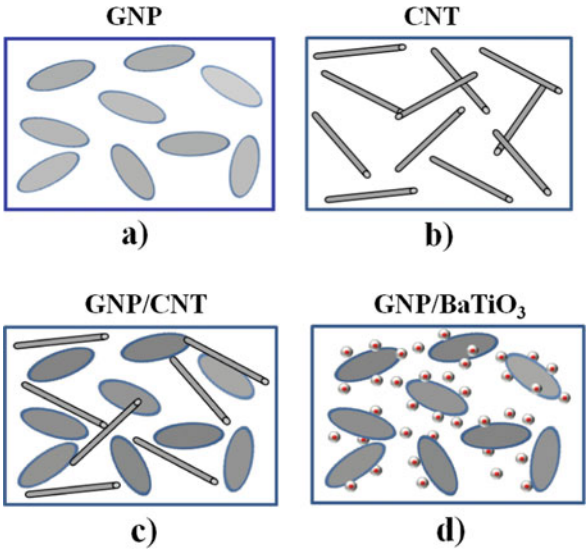

Fig. 24.1 Schematic presentation of polymer composites: filled with (**a**) GNP, (**b**) CNT and (**c**), (**d**) mixed GNP/CNT and GNP/BT fillers

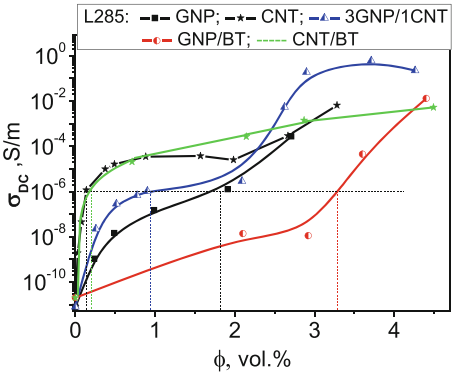

Fig. 24.2 DC conductivity data for nanocarbon/epoxy and nanocarbon/$BaTiO_3$/epoxy CMs versus content of nanocarbon; dashed lines indicate the percolation threshold

24.3.1 1D Conductive Nanofiller in Polymer Matrix Before Percolation Threshold

Let us consider the composites filled with 1D multiwalled carbon nanotubes. As it was presented in the literature [22, 23], the percolation threshold for CNT-filled composites is sufficiently low due to high aspect ratio AR of CNTs (from 200 to 1000) and can be varied within 0.002–1.0 vol.% depending on the type of polymer matrix, CNT perfection, and preparing method. For example, as it was shown in our previous paper [24, 25] in CMs based on epoxy resin L285 filled with multiwalled carbon nanotubes, the percolation threshold is equal to 0.13 vol.%. Data is presented in Fig. 24.2.

The depolarization factors for elongated ellipsoids (1D particles such as nanofibers NCF, nanotubes CNTs) are described, as noted early, by Eq. (24.2).

In our calculation we used the average values of aspect ratio AR = 200, 400, 500, $\sigma = 10^4$–10^5 S/m, and filler concentration $\phi = 0.1$–0.5 vol.%. The content of CNT in 0.3–0.5 vol.% is higher than the percolation threshold, but, as shown in many studies [26–28], the contact between CNT and agglomerates of CNT (even at contents higher than the percolation threshold) in formed conductive chains occurs through thin polymeric layers (or gaps), and tunneling mechanism of electrical conductivity is dominant. In this case, in the first approximation, CNTs (or agglomerates of CNTs) can still be considered as isolated, and Maxwell-Garnett model for permittivity calculations can be used.

Figures 24.3 and 24.4 present the modeling results for dielectric permittivity of polymer CMs filled with CNTs.

As can be seen from the above data, an increase in aspect ratio of CNTs and their content in the CM leads to a significant increase in both real ε_r' and imaginary ε_r'' parts of permittivity. With an increase of CNT content by five times, the permittivity

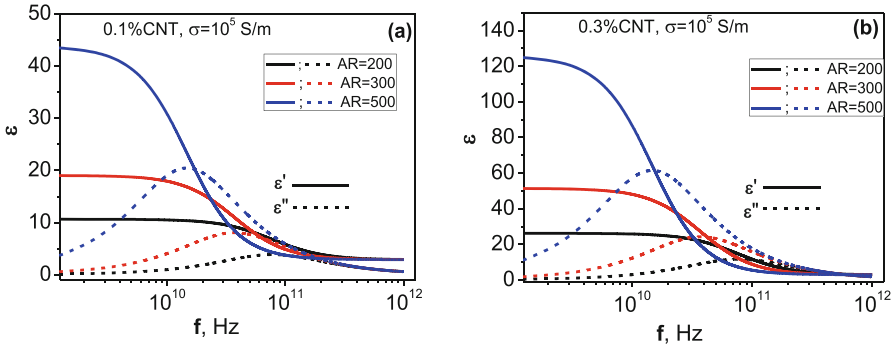

Fig. 24.3 Real and imaginary parts of dielectric permittivity of polymer composites filled with 1D CNT with various aspect ratios, electrical conductivity of CNT particles 10^5 S/m, and filler content before (**a**) and close to (**b**) the percolation threshold (filler content in vol.%)

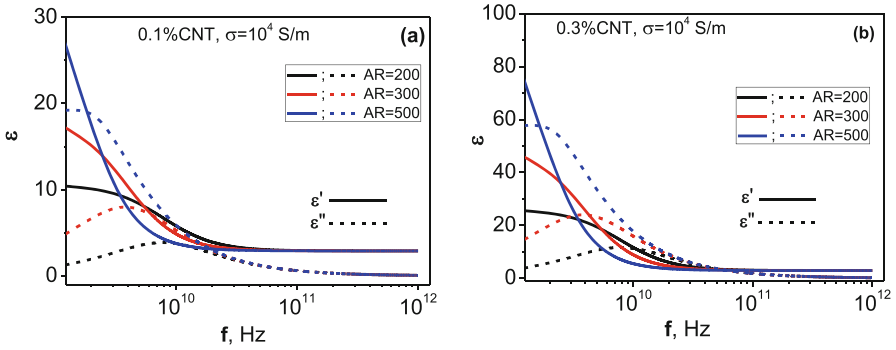

Fig. 24.4 Real and imaginary parts of dielectric permittivity of polymer composites filled with 1D CNT with various aspect ratios, electrical conductivity of CNT particles 10^4 S/m, and 1D filler content before (**a**) and close to (**b**) the percolation threshold (filler content in vol.%)

increases by 5 times, while the increase in the aspect ratio AR of 300–500 leads to a more significant increase in both the real and the imaginary parts of the permittivity. With the increase of the AR of the nanotubes, there is also a shift of the ε_r'' maximum to lower frequencies, while an increase in the content of CNT (which does not exceed the threshold of percolation) does not affect the position of this maximum. As can be seen from the data shown in Fig. 24.4, the decrease in the electrical conductivity of the nanotubes themselves by an order of magnitude (up to 10^4 S/m) leads only to the shift of the frequency dependences of the dielectric permittivity and, accordingly, to shift of the maximum of dielectric losses, to lower frequencies.

24.3.2 2D Carbon Nanofiller in Polymer Matrix Before Percolation Threshold

In a case of disk-like filler particles of diameter D and thickness h, the depolarization factors described by Eq. (24.3) and imaginary part of permittivity of GNP filler are determined by electrical conductivity of GNP via Eq. (24.4). For composites filled with 2D GNP particles, the percolation threshold is sufficiently higher than for CMs filled with 1D CNTs, and, for example, as it was shown in our previous papers for GNP/epoxy CMs, ϕ_c lies within 1.75–2.5 vol.% [8, 9]. Figures 24.5 and 24.6 show the calculated data for ε_r' and ε_r'' for composites filled with graphite nanoplatelets with the various aspect ratios and electrical conductivity as for CNTs. The filler content of GNP is selected as 1 and 2 vol.%, which is higher as compared with CNT-based CMs since the percolation threshold for GNP-based CMs is sufficiently higher.

As it is seen from Fig. 24.5a, b, the composites with GNPs are characterized by lower values of permittivity and dielectric loss in comparison with CMs filled with

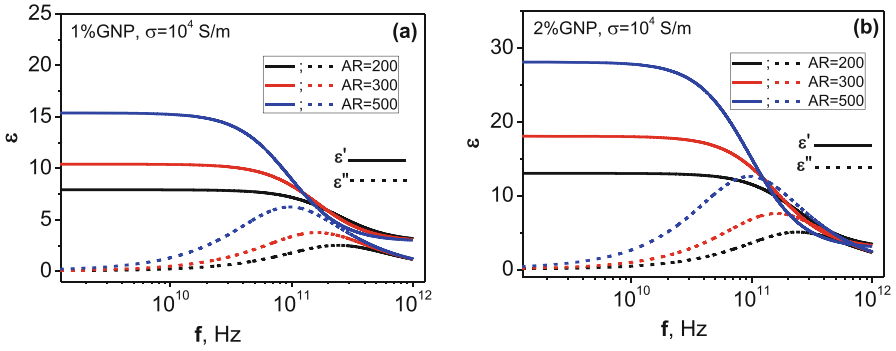

Fig. 24.5 Real and imaginary parts of dielectric permittivity of polymer composites filled with 2D GNP with various aspect ratios, electrical conductivity of GNP particles 10^4 S/m, and filler content below (**a**) and close to (**b**) the percolation threshold (filler content in vol.%)

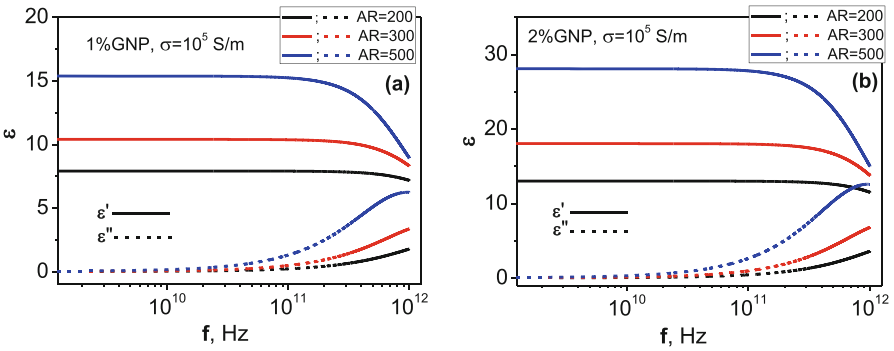

Fig. 24.6 Real and imaginary parts of dielectric permittivity of polymer composites filled with 2D GNP with various aspect ratios, electrical conductivity of GNP particles 10^5 S/m, and filler content before percolation threshold (filler content in vol.%)

CNTs despite the higher GNP content in CMs. In addition, the plateau on $\varepsilon_r'(f)$ dependence is extended, and the maximum of ε_r'' is shifted to higher frequencies. The increase of content by two times nearly doubles the ε_r' and maximum ε_r'', while increasing aspect ratio from 300 to 500 increases ε_r' and ε_r'' much less than in a case with CNT.

As it is seen from Fig. 24.6, the increase of electrical conductivity of GNP particles by an order of magnitude (up to a 10^5 S/m) causes the shift of frequency dependencies of permittivity to higher frequencies and, thus, to the shift of ε_r'' maximum.

Thus, it may be concluded that cylindrical CNT particles promote a more effective increase of complex dielectric permittivity of CMs as compared with disk-like particles with the same aspect ratio (AR). However, the effective increase of permittivity with CNT content (number of "artificial dipoles") is restricted by the narrow concentration range due to low percolation threshold in CNT-filled CMs and occurrence of the leakage current. Finally, the predictions of the performed modeling of the effective permittivity of the polymer filled with anisometric conductive nanoparticles are the following:

1. The increase of aspect ratio (AR) of filler particles as well as the filler content promotes the increase of the permittivity.
2. The increase of electrical conductivity of filler particles shifts the fall of permittivity ε_r' and maximum of dielectric loss ε_r'' into the higher frequency range.
3. The 1D CNT particles lead to more effective increase of complex dielectric permittivity of CMs as compared to 2D GNP disk-like particles with the same aspect ratio (AR).

Let us consider the influence of combination of carbon fillers of various morphology (1D and 2D) on the behavior of complex dielectric permittivity versus EMR frequency *f*.

24.3.3 1D/2D Mixed Carbon Nanofiller in Polymer Matrix Before Percolation Threshold

As it was shown in our previous paper [29], the addition of part of CNT instead of GNP particles into epoxy CMs leads to the decrease of percolation threshold compared to composite with single GNP filler. On the other hand, as we show above, the use of CNT is more perspective for sufficient enhancement of permittivity due to the high aspect ratio of CNT and its 1D morphology. We can assume that addition of a small content of CNT (lower than percolation threshold for CNT/polymer CM) along with GNP content that also is lower than percolation threshold for GNP/polymer CMs can lead to increase of dielectric permittivity of CMs with mixed CNT/GNP filler. We have modeled the permittivity of such CMs with various total filler contents and ratios between CNT and GNP. Since GNP particles are more defective compared to CNTs we used only one value of GNP conductivity, namely, 10^4 S/m for permittivity calculation, while for CNT σ was equal to 10^4–10^5 S/m in our calculations. As concerning to aspect ratio of filler particles, we choose the realistic values, AR = 300 for GNP particles and AR = 300 for CNT particles (taking into account the high level of CNT entanglement).

Figure 24.7 presents the calculated permittivity of polymer composites filled with mixed 1D/2D nanocarbon filler (CNT/GNP).

As it is seen from Fig. 24.6a, the adding of a small part of CNT (0.1 vol.%) along with 0.5 vol.% GNP particles (much lower than percolation threshold in CMs with single filler GNP) with $\sigma_{GNP/CNT} = 10^4$ S/m and aspect ratio AR = 300 leads to a small increase of permittivity in such composite. The increase of GNP content up to 1.75 vol.% along with 0.1 vol.% CNT (see Fig. 24.7b) leads to a more significant increase of permittivity and extends the frequency range of dielectric loss (broad maximum of ε_r'' is observed). Figures 24.7c, d show that the increase of electrical conductivity of CNT up to 10^5 S/m and their content in mixed filler GNP/CNT results in sufficient increase of permittivity, extending the plateau on $\varepsilon_r'(f)$ before falling, and shifts the maximum of ε_r'' into higher frequency range.

On the basis of the comparative analysis of calculated dielectric permittivity for polymer composites filled with various electroconductive single (1D or 2D) fillers, it was found that the frequency dependence of the effective composite permittivity is described satisfactorily within Debye model that is commonly used for polymer material permittivity. Debye expression [30] for the effective permittivity of CM-filled electroconductive particles is given by

$$\varepsilon_{\text{eff}} = \varepsilon_{\text{eff}\infty} + \frac{\varepsilon_{\text{effs}} - \varepsilon_{\text{eff}\infty}}{1 - i\omega\tau_{\text{eff}}}, \tag{24.6}$$

where $\varepsilon_{\text{eff}\infty}$ and $\varepsilon_{\text{effs}}$ are the static and optical permittivities of the composite and τ_{eff} is Debye time of relaxation, which is inversely proportional to the electrical conductivity of the filler ($\tau_{\text{eff}} \sim 1/\sigma_i$). Thereafter, the frequency dependences of real and imaginary parts of the composite permittivity are given by

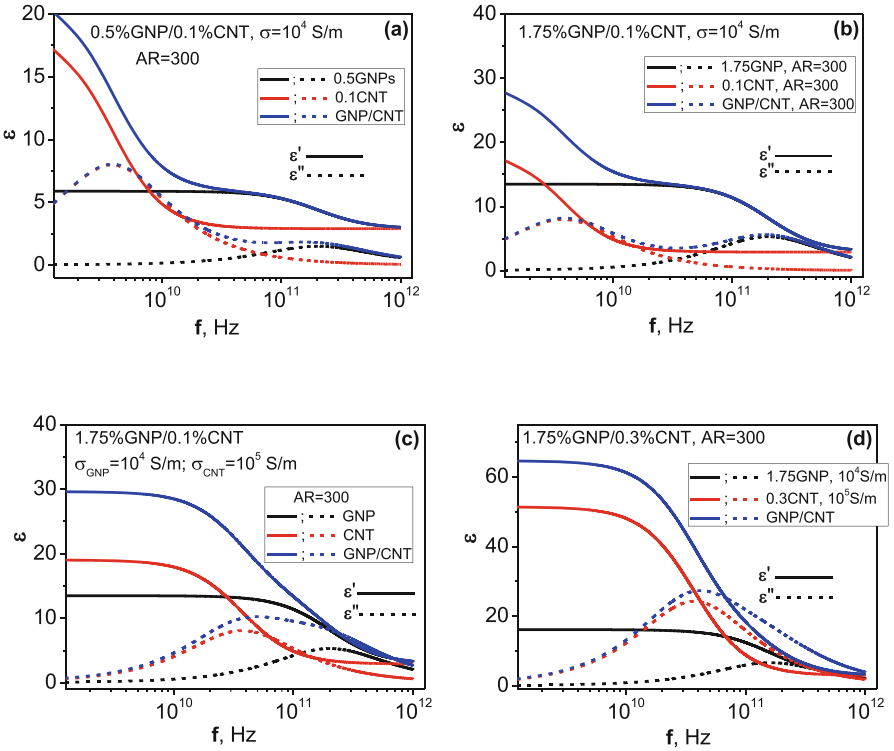

Fig. 24.7 Real and imaginary parts of dielectric permittivity of polymer composites with various mixed filler GNP/CNT versus EMR frequency: (**a**) 0.5%GNP/0.1%CNT, electrical conductivity of GNP, and CNT particles 10^4 S/m; (**b**) 1.75%GNP/0.1%CNT, electrical conductivity σ of GNP, and CNT particles 10^4 S/m; (**c**) 1.75%GNP/0.1%CNT, $\sigma_{GNP} = 10^4$ S/m, $\sigma_{CNT} = 10^5$ S/m; (**d**) 1.75%GNP/0.3%CNT, $\sigma_{GNP} = 10^4$ S/m, $\sigma_{CNT} = 10^5$ S/m (filler content in vol.%)

$$\varepsilon'_{\text{eff}}(T) = \varepsilon_{\text{eff}\infty} + \frac{\varepsilon_{\text{effs}} - \varepsilon_{\text{eff}\infty}}{1 + (\omega\tau_{\text{eff}})^2}, \quad \varepsilon''_{\text{eff}}(T) = \frac{\varepsilon_{\text{effs}} - \varepsilon_{\text{eff}\infty}}{1 + (\omega\tau_{\text{eff}})^2}\omega\tau_{\text{eff}}, \tag{24.7}$$

The Debye-like behavior of composites containing conducting 1D (or 2D) particles may be explained by the polarization of the induced dipoles in the filler particles embedded in a polymer matrix. The polarizability of an individual filler particle increases with the increase of its aspect ratio and bulk conductivity.

This equivalent Debye model depends upon the original electromagnetic characteristics of the host and inclusions. So, as it was discussed above, the higher electrical conductivity of filler leads to the shift of $\varepsilon''_{\text{eff}}$ maximum into higher range of EMR frequency, while the values of $\varepsilon_{\text{effs}}$ and $\varepsilon_{\text{eff}\infty}$ are determined only by the morphology of conductive particles (their depolarization factor related to the aspect ratio), their content and distribution in polymer composite, and the type of polymer matrix.

In the case of mixed 1D/2D electroconductive filler, the dielectric spectra deviate from Debye-like behavior, and at equal aspect ratios and electrical conductivity of 1D and 2D particles (see Figs. 24.6a, b), they are the superposition of Debye curves for 1D and 2D filled CMs. For this case ε_r' is characterized by two plateau and two falls, corresponding to 1D and 2D fillers. As concerning ε_r'' we can observe the two maximums or one broad maximum. That is, the use of two types of the electroconductive fillers allows extending the range of dielectric loss.

The main disadvantage of the real multiwalled CNTs that are used in the fabrication of polymer-filled composites is the high level of CNT deformation and entanglement. Consequently, the CNTs are not individually separated cylindrical particles, and modeling of permittivity for such multiwalled CNT as fillers in polymer matrix is very approximate since the interaction and mutual influence between CNT particles may be sufficient. Contrarily, graphite nanoplatelets are separate disk-like particles, and in the case of good dispersion in polymer matrix, dielectric permittivity may be more accurately simulated, and satisfactory agreement between experimental and modeled values of dielectric permittivity may be expected.

Another disadvantage of polymer composites filled with nanocarbon particles is that a significant increase in the dielectric permittivity ε_r' of these composites with increasing content of highly anisometric nanocarbon conductive particles occurs in a narrow concentration range, limited by low percolation threshold for such a system since after percolation, the transition to through-conduction and substantial electric losses occur. Recently, in some publications the few ways to increase the content of isolated anisotropic conductive filler particles, which act as "artificial dipoles" and significantly increase the permittivity of the CMs, have been proposed [31–33]. For example, along with the carbon filler, the use of second dielectric filler will prevent the formation of conductive carbon network, and on the other hand, the additional increase of interfacial regions enhances the role of interfacial polarization in the formation of effective permittivity of CM. The formation of an insulating polymer layer on the surface of conductive filler before introducing them into the polymer matrix at CMs fabrication also is an effective method for increase of permittivity of CMs [34].

In the next part, the results of permittivity modeling for composites with a mixture of electroconductive and dielectric particles will be presented. In our calculation as conductive filler, we used only GNP particles as more able for higher dispersing in the polymer matrix.

24.3.4 2D Nanocarbon/Dielectric Particle Mixed Filler in Polymer Matrix Before Percolation Threshold

As it was mentioned above, in order to increase the permittivity of polymer composites, the various combinations of electrical and dielectric particles are used, including the simple mixture of filler or more complicated hybridized filler particles.

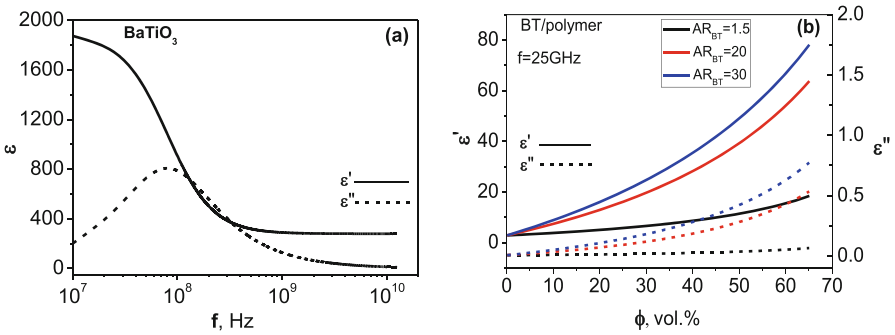

Fig. 24.8 Real and imaginary parts of dielectric permittivity for BaTiO3 versus frequency (**a**) and for BT/polymer composites versus content of plate-like BT particles with various aspect ratios (**b**)

In this part, we present the modeling of the permittivity of polymer composites filled with the mixture of electroconductive 2D GNP particles and highly dielectric ceramic particles of $BaTiO_3$ (BT). 2D GNP particles were chosen as more able for higher dispersing in polymer matrix.

In our calculation for the permittivity of $BaTiO_3$, we have used the relation $\varepsilon_r = 280 + (1900 - 280)/(1 + i \cdot 2\pi f \cdot 2 \cdot 10^{-9})$ [35], and dielectric spectrum is presented in Fig. 24.8a.

As can be seen from the data given, the dielectric constant, starting at a frequency of 10^7 Hz, decreases and goes to a constant value of ε_r=280 and has a maximum in the frequency region of 10^8 Hz.

Figure 24.8b shows the calculated concentration dependences of dielectric constant (at 25 GHz) for polymer composites filled with high dielectric particles BT of various morphologies. During the calculations, it was considered that for spherical-like shape $BaTiO_3$ particles [36], the aspect ratio AR is equal to 1.5. As can be seen from the data presented, with an increase of AR of BT particles there is a sharp increase in the permittivity of composites with BT particles. Such an increase of ε_r' and ε_r'' with the increase of the AR of BT particles is consistent with the experimental results of the investigation of the permittivity of $BaTiO_3$ fibers [37, 38] and $BaTiO_3$ flake nanoparticles [2] based on different polymer matrices, and with the predictions of the Maxwell-Garnett model (see Eq. 24.1, 24.2, and 24.3), which takes into account the morphology of the particles of the filler through the parameters of the depolarization of the particles N_{ij}.

Figure 24.9 shows the calculated dielectric spectra for composites with a mixture of fillers GNP/BT at various weight ratios between GNP and BT.

As can be seen from the calculated data presented in Fig. 24.9a, the addition of 10% BT along with 1.75% GNP leads to a slight increase in the permittivity of the composite compared to the composite with GNP filler only. But, as shown in our previous work, the addition of dielectric particles of BT leads to a shift in the percolation threshold in the electrical conductivity to the region of higher volumetric concentrations of GNP, from 1.75 to 3.26 vol.% (see data in Fig. 24.2),

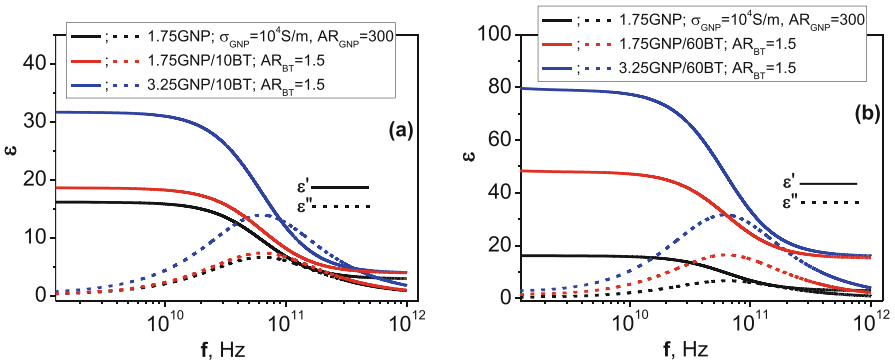

Fig. 24.9 Real and imaginary parts of dielectric permittivity of polymer composites with various mixed filler GNP/$BaTiO_3$ versus EMR frequency: (**a**) 1.75%GNP/0%BT, 1.75%GNP/10%BT and 3.25%GNP/10%BT; (**b**) 1.75%GNP/0%BT, 1.75%GNP/60%BT and 3.25%GNP/60%BT; electrical conductivity of GNP particles 10^4 S/m, $AR_{GNP} = 300$, $AR_{BT} = 1.5$ (filler content in vol.%)

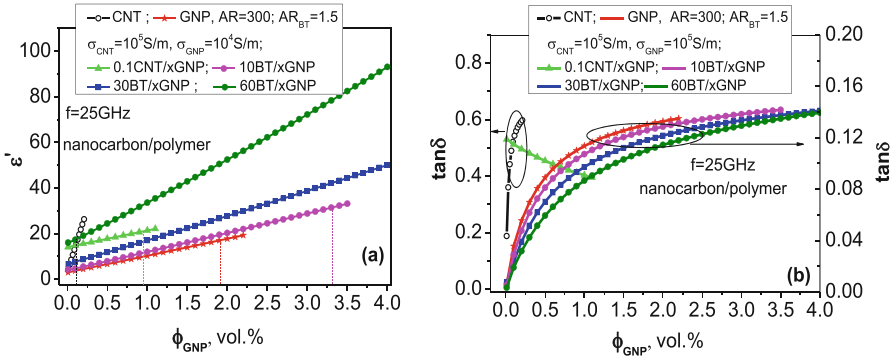

Fig. 24.10 Real part of dielectric permittivity (**a**) and dielectric loss tangent tand (**b**) of polymer composites with various mixed fillers versus GNP content

since the number of particles of GNP in composite volume increases when adding high-density BT. The calculation of permittivity at a concentration of 3.25 vol.% of GNP and 10 vol.% of BT showed a significant increase in the values of ε_r' and ε_r'' for this composite. Obviously, an increase in the BT concentration in the composite with mixed filler GNP/BT will lead to a significant increase in permittivity, and the result of the simulation of such composites is presented in Fig. 24.9b for concentrations of BT in 60 vol.%. Figure 24.10 shows the calculated concentration dependences of permittivity and dielectric loss tangent $\tan\delta = \varepsilon_r''/\varepsilon'$ for polymer composites with a mixture of fillers: 1D conductive/2D conductive and 2D conductive/3D dielectric. For comparison, data for a single nanocarbon filler (1D or 2D) is also provided. Calculations were made for the same values of AR = 300 of GNP particles and CNT and in the range of concentrations of up to the percolation threshold of CM. As an

example, the CMs based on the L285 epoxy resin are considered, and the dashed vertical lines indicate the percolation thresholds for each type of CM. The data presented in Fig. 24.10 shows that the greatest increase of ε_r' and tanδ is observed for composites with 1D conductive filler (CNT), but the content range before the percolation threshold (transition to the conductive state and the occurrence of high electrical losses) is rather narrow (0–0.15 vol.%).

For the case of composites with 2D conductive filler (GNP), permittivity increases slower, but a range of concentrations before the percolation threshold is wider (0–1.75) vol.%. In composites containing 0.1 vol.% of CNT and x vol.% of GNP, permittivity is much higher than in the case of CM with GNP only. Such increase of ε_r' and ε_r'' is due to the presence of 1D CNT, although the percolation threshold is slightly lowered, compared to CM GNP/polymer.

For a CM with a mixture of 2D conductive/3D dielectric (GNP/BT) fillers, with 10 vol.% content of BT, the concentration curve $\varepsilon_r'(f)$ is slightly higher than for a CM with a GNP, but a range of GNP concentrations up to the percolation threshold is significantly expanded: more GNP particles in the volume of the composite and accordingly higher permittivity. A significant increase in the BT content (up to 60 vol.%) leads to a significant increase in permittivity. However, it should be noted that, with the high content of BT particles, permittivity calculations may not give correct results, since the interaction between particles is not taken into account. As to tanδ value in CMs with GNP/BT, it increases with increasing GNP content and is smaller compared to GNP/polymer CMs.

Thus, the presented numerical modeling of electromagnetic properties for microwave range of polymer-filled composites based on material parameters of composite constituents and its content will expedite the process of engineering electromagnetic materials with frequency dependences of electromagnetic parameters desirable for practical applications.

24.4 Conclusion

The complex permittivity of the nanocomposites with randomly distributed 1D and 2D conductive filler is predicted using the Maxwell-Garnett model. The performed analysis showed the increase of effective permittivity with the increase of the aspect ratio (AR), electrical conductivity, and content (lower than the percolation threshold) of electroconductive inclusions in a composite. It was found that the composites filled with 1D conductive particles (CNTs) with high aspect ratio (AR) were closer to percolative state and showed the large enhancement of effective permittivity (including increased dielectric loss) for narrow CNT concentration range before percolation threshold compared to composites with 2D conductive particles (GNPs) with much higher percolation threshold. The mixing of 1D/2D conductive fillers in polymer matrix allows obtaining of composite materials with tunable dielectric properties, depending on weight ratio between 1D and 2D fillers, its aspect ratio, electrical conductivity, and content in a composite. The addition of spherical highly

dielectric disperse particles (e.g., $BaTiO_3$) into CMs with 2D conductive filler increases the permittivity of such three-phase composites proportionally $BaTiO_3$ content. It was found that addition of 10 vol.% of spherical BT particles only slightly increases the effective permittivity for the same GNP volume content. On the other hand, the shift of the percolation threshold into higher 2D GNP filler concentration was observed, so the larger number of conductive particles may be inserted into polymer matrix before percolation, and higher permittivity may be achieved. It was shown that the use of plate-like or fibrous $BaTiO_3$ particles as fillers in polymer composites promotes the more essential increase of effective permittivity compared with spherical BT particles. The prediction of the permittivity of polymer filled with electric and/or dielectric particles of various morphologies allows the designing of the new materials with controllable properties for various applications.

References

1. Nakagawa T, Kageyama K, Takagi H, Sakabe Y, Kirihara S, Miyamoto Y (2008) Stereolithographic fabrication and microwave properties of 1D tunable photonic crystals composed of YIG and alumina plates in resin. J Am Ceram Soc 91:2195–2200
2. Jain R-K, Dubey A, Soni A, Gupta S-K, Shami TC (2013) Barium titanate flakes based composites for microwave absorbing applications. Proc Appl Ceram 7:189–193
3. Xu N, Hu L, Zhang Q, Xiao X, Yang H, Yu E (2015) Significantly enhanced dielectric performance of poly(vinylidene fluoride-co-hexafluoropylene)-based composites filled with hierarchical flower-like TiO_2 particles. ACS Appl Mater Interfaces 7:27373–27381
4. Wang F, Wang J-W, Li S, Xiao J (2009) Dielectric properties of epoxy composites with modified multiwalled carbon nanotubes. Polym Bull 63:101–110
5. Min C, Yu D, Cao J, Wang G, Feng L (2013) A graphite nanoplatelet/epoxy composite with high dielectric constant and high thermal conductivity. Carbon 55:116–125
6. Wang Z, Luo J, Zhao G-L (2014) Dielectric and microwave attenuation properties of graphene nanoplatelet–epoxy composites. AIP Adv 4:017139–017139
7. Vovchenko L, Matsui l OV, Launetz V, Lazarenko A (2008) Nanocarbon-epoxy composites as electromagnetic shielding materials. Mol Cryst Liq Crys 497:46/[378]–54/[386]
8. Vovchenko L, Matsui L, Oliynyk V, Launetz V (2010) Attenuation of electromagnetic radiation by graphite-epoxy composites. Phys Status Solidi C 7:1260–1263
9. Vovchenko L, Matsui L, Oliynyk V, Launetz V, Zhuravkov O (2013) Electrical and shielding properties of epoxy composites containing hybrid carbon fillers. Mat-wiss u Werkstofftech 44:249–253
10. Zhang X, Ma Y, Zhao C, Yang V (2015) High dielectric performance composites with a hybrid $BaTiO_3$/graphene as filler and poly(vinylidene fluoride) as matrix. ECS J Solid State Sci Technol 4:N47–N54
11. Xiao Y, Wang W, Lin T, Chen X, Zhang Y, Yang J, Wang Y, Zhou Z (2016) Largely enhanced thermal conductivity and high dielectric constant of poly(vinylidene fluoride)/boron nitride composites achieved by adding a few carbon nanotubes. J Phys Chem C 120:6344–6355
12. Li C, Yu S, Luo S, Yang W, Ge Z, Huang H, Sun R, Wong C-P (2016) Enhancement of dielectric performance up to GHz of the composites with polymer encapsulated hybrid BaTiO3–Cu as fillers: multiple interfacial polarizations playing a key role. RSC Adv 6:36450–36458
13. Zhao H, Yang M-H, He D, Bai J (2016) Enhanced dielectric performance of polyvinylidene fluoride composites with all-carbon hybrid architecture: vertically aligned carbon nanotube arrays on graphite nanoplatelets. J Mater Chem C 4:8911–8919

14. Kuzhir P, Paddubskaya A, Bychanok D, Nemilentsau A, Shuba M, Plusch A, Maksimenko S, Bellucci S, Coderoni L, Micciulla F (2011) Microwave probing of nanocarbon based epoxy resin composite films: toward electromagnetic shielding. Thin Solid Films 519:4114–4118
15. Koledintseva MY, Chandra SKR, DuBroff RE, Schwartz RW (2006) Modeling of dielectric mixture containing conducting inclusions with statically distributed aspect ratio. Prog Electromag Res, PIER 66:213–228
16. Sun LL, Li B, Mitchell G, Zhong WH (2010) Structure-induced high dielectric constant and low loss of CNF/PVDF composites with heterogeneous CNF distribution. Nanotechnology 21(8):305702
17. Nan C-W, Shen Y, Ma J (2010) Physical properties of composites near percolation. Annu Rev Mater Res 40:131–151
18. Clayton LM, Knudsen B, Cinke M, Meyyappan M, Harmon JP (2007) DC conductivity and interfacial polarization in PMMA/nanotube and PMMA/soot composites. J Nanosci Nanotechnol 7:3572–3579
19. Koledintseva MY, DuBroff RE, Schwartz RW, Drewniak JL (2007) Double statistical distribution of conductivity and aspect ratio of inclusions in dielectric mixtures at microwave frequencies. Progress In Electromagnetics Research, PIER 77:193–214
20. Nisanci MH, Paulis F, Koledintseva MY, Drewniak JL, Orlandi A (2012) From Maxwell Garnett to Debye model for electromagnetic simulation of composite dielectrics—Part II: random cylindrical inclusions. IEEE Trans Electromagn Compat 54:280–289
21. Bandaru PR (2007) Electrical properties and applications of carbon nanotube structures. J Nanosci Nanotechnol 7:1239–1267
22. Sandler JKW, Kirk JE, Kinloch IA, Shaffer MSP, Windle AH (2003) Ultra-low electrical percolation threshold in carbon-nanotube-epoxy composites. Polymer 44:5893–5899
23. Spitalsky Z, Tasis D, Papagelis K, Galiotis C (2010) Carbon nanotube-polymer composites: Chemistry, processing, mechanical and electrical properties. Prog Polym Sci 35:357–401
24. Perets Y, Aleksandrovych L, Melnychenko M, Lazarenko O, Vovchenko L, Matsui L (2017) The electrical properties of hybrid composites based on multiwall carbon nanotubes with graphite nanoplatelets. Nanoscale Res Lett 12(406):406
25. Vovchenko L, Matsui L, Perets Y, Sagalianov I, Yakovenko O (2018) Electrical and thermal conductivity of epoxy nanocomposites with hybrid fillers. In: Bartul Z, Trenor J (eds) Advances in nanotechnology, vol 21. Nova Science Publishers, New York, pp 1–85
26. Hu N, Karube YI, Arai M, Watanabe T, Yan C, Li Y, Liu Y, Fukunaga H (2010) Investigation on sensitivity of a polymer/carbon nanotube composite strain sensor. Carbon 48:680–687
27. Brown M, Jagannadham K (2013) Interfacial effects in the electrical conductivity and viscous deformation of multiwall carbon nanotube–epoxy composites prepared by sonication. J Compos Mater 47:3413–3420
28. Zare Y, Rhee KY (2017) A simple methodology to predict the tunneling conductivity of polymer/CNT nanocomposites by the roles of tunneling distance, interphase and CNT waviness. RSC Adv 7:34912–34921
29. Vovchenko LL, Matsui LY, Perets YS, Milovanov YS (2018) Chapter 24 Dielectric properties and AC conductivity of epoxy/hybrid nanocarbon filler composites. Springer Proceedings in Physics 214:377–393
30. Von Hippel A (1995) Dielectrics and waves. Artech House, Boston/London
31. Zhang X, Ma Y, Zhao C, Yang V (2015) High dielectric performance composites with a hybrid BaTiO3/graphene as filler and poly(vinylidene fluoride) as matrix. ECS J Solid State Sci Technol 4:N47–N54
32. Xiao Y, Wang W, Lin T, Chen X, Zhang Y, Yang J, Wang Y, Zhou Z (2016) Largely enhanced thermal conductivity and high dielectric constant of poly(vinylidene fluoride)/boron nitride composites achieved by adding a few carbon nanotubes. J Phys Chem C 120:6344–6355
33. Zhao H, Yang M-H, He D, Bai J (2016) Enhanced dielectric performance of polyvinylidene fluoride composites with all-carbon hybrid architecture: vertically aligned carbon nanotube arrays on graphite nanoplatelets. J Mater Chem C 4:8911–8919

34. Li C, Yu S, Luo S, Yang W, Ge Z, Huang H, Sun R, Wong C-P (2016) Enhancement of dielectric performance up to GHz of the composites with polymer encapsulated hybrid $BaTiO_3$–Cu as fillers: multiple interfacial polarizations playing a key role. RSC Adv 6:36450–36458
35. Paulis F, Nisanci MH, Koledintseva MY, Drewniak J, Orlandi A (2011) From Maxwell Garnett to Debye model for electromagnetic simulation of composite dielectrics part I: random spherical inclusions. IEEE Trans Electromagn Compat 53:933–942
36. Lozitsky O, Vovchenko L, Matsui L et al. (2017) Electromagnetic shielding properties of epoxy composites with hybrid filler nanocarbon/$BaTiO_3$. In Abstract Book International research and practice conference Nanotechnology and Nanomaterials NANO-2017, 23-26 August 2017, Chernivtsi, Ukraine. P.197
37. Zepu Wang Z, Nelson JK, Miao J, Linhardt RJ, Schadler LS (2012) Effect of high aspect ratio filler on dielectric properties of polymer composites: a study on barium titanate fibers and graphene platelets. IEEE Trans Dielectr Electr Insul 19:960–967
38. Ávila HA, Reboredo MM, Parra R, Castro MS (2015) Dielectric permittivity calculation of composites based on electrospun barium titanate fibers. Mater Res Exp 2:045302

Chapter 25
Nanostructural Effects in Iron Oxide Silicate Materials of the Earth's Crust

A. V. Panko, I. G. Kovzun, O. M. Nikipelova, V. A. Prokopenko, O. A. Tsyganovich, and V. O. Oliinyk

25.1 Introduction

Solving important tasks concerning the modern sciences of the Earth's crust and its surface properties include crucial studies of complex nanostructural effects depending on geomechanical, biocolloid, and nanochemical factors. Such effects and processes have not been yet systematically considered with the help of colloid and biocolloid science, and with physicochemical geomechanics (PCGM) [1–7]. It was taken into account that up to 90% of the rocks of the Earth's crust belong to fine-grained polymineral, commonly nanostructured, disperse iron aluminum silicate systems and materials (IASSMs). Those are being presented both by dense nano- and fine-grained, and by fine-dispersed rocks, iron oolite and polymetallic ores, pelitic clay-containing and other sediments from aqueous basins, basically of marine origin. Thus, investigations of such scientifically and practically extensively used materials in assigned task bounds, especially of little-studied microorganism- and nanostructure-aided biocolloid and geomechanical deformations in IASSMs are current. That is why such problems are considered in this paper with the aid of various physicochemical methods and highly concentrated viscous disperse system rheology. The main attention here was given to defining the mechanism of

A. V. Panko (✉) · I. G. Kovzun · V. O. Oliinyk
F.D. Ovcharenko Institute of Biocolloid Chemistry of NAS of Ukraine, Kyiv, Ukraine

O. M. Nikipelova
SA "Ukrainian Research Institute of Medical Rehabilitation and Balneology, Ministry of Health of Ukraine", Odessa, Ukraine

V. A. Prokopenko · O. A. Tsyganovich
F.D. Ovcharenko Institute of Biocolloid Chemistry of NAS of Ukraine, Kyiv, Ukraine

National Technical University of Ukraine "KPI", Kyiv, Ukraine

O. Fesenko, L. Yatsenko (eds.), *Nanocomposites, Nanostructures, and Their Applications*, Springer Proceedings in Physics 221,
https://doi.org/10.1007/978-3-030-17759-1_25

nanostructural–nanochemical effects on IASSMs aided by biogeocenosis and analysis of its influence on geomechanical stress phenomena occurring with dispersing deformations in IASSMs of the Earth's crust.

25.2 Materials and Methods

Iron-aluminum-silicate systems and materials electron microscopy images were taken on a SELMI electron microscope in light field mode and their morphology was studied on a JEOL scanning electron microscope JSM6490LV. X-ray diffraction (XRD) was obtained on DRON-UM1 with two Soller slits and filtered CuKα emission. Rheological investigations were conducted on a Rheotest-2 connected to a PC to collect data. Chemical composition was defined by chemical and X-ray fluorescence analysis. Physico-geomechanical and nanochemical transformation processes of IASSMs under natural and technogenic conditions were modeled using methods of PCGM [6, 7]. Microbiological tests of IASSM suspension were performed using methods from Oleinik et al., Panko et al., and Nikipelova [8–10]. Iron-containing aluminosilicate systems (generally pelitic marine sediments and clays) were investigated in the same specimen series that were used in Panko et al. [11], where their electromagnetic interference, XRD, thermic, adsorption, and rheological properties are described.

25.3 Experiment and Discussion

25.3.1 Analysis of Nanostructure Phenomena in the Earth's Surface IASSMs Occurred with Geomechanical, Nanochemical, and Biocolloid Processes

25.3.1.1 Geochemical and Nanochemical Processes

Thanks to advances in physicochemical mechanics as part of colloid chemistry, the geological and geochemical lines of development in areas of mechanical, microbiological, and nanochemical interphase contact interactions in natural and technogenic materials were recently defined as PCGM of rocks and disperse materials [5, 6, 12, 13]. This standalone branch of colloid science analyses geological and geochemical structural and nanostructural factors, mainly ascertaining mechanical, physicochemical, colloid–chemical, biocolloid, and nanochemical influence on geomechanochemical properties of the Earth's crust solids in a contact phase boundary.

The most valuable achievement of PCGM at the time of its conception should be named the development of fundamental investigations concerning the influence

of water on geomechanochemical properties, disperse structure, and the dispersion of rocks [6, 12–17]. Although concepts about the special role of water in natural processes were formed in olden times, its geological impact was discovered only at the end of the twentieth century from two points of view – chemical (geochemistry) and mechanical (rock mechanics) [5, 17]. The formality of such a division is obvious. Until the end of the twentieth century, mechanical properties were considered without the influence of a physicochemical medium (i.e., nanochemical, colloid, and biocolloid processes). Their integration into earth science [5, 7] and the advances of other natural sciences occurred step by step – limited by the development of fundamental basics of such sciences connected with geomechanical processes in the materials of the Earth's crust [6].

As long as water is a usual component in dense and microdispersed rocks that are, in general, in a polydisperse nano- and micrograin state and that are being sustained to a common impact of mechanical strain and liquid medium, the influence of water on such processes is by far essential. Besides, neither the high solubility of rock-forming minerals, nor considerable amounts of liquid medium is not obligatory for the mechanical effects appearance owing to nanochemical and nanostructural processes whereas water interacts with rock surfaces [17]. The required condition lies in the availability of a developed contact surface between nano- and micrograins of polymineral structure and its connected high rock contact surface formed by internal micro- and nanosized interphase boundaries of various mineral compositions [6, 13–17].

These principles substantially broaden a variety of geological and geochemical phenomena where water can be the active component of dispersion processes. For example, they include many deformation processes and fracturing of the usual IASSMs of the Earth's crust, containing water traces in grain boundary layers. Therefore, effective water concentration, i.e., its thermodynamic activity, is substantially dependent both on the quantity and on the chemical nature of components dissolved in it. Thus, in our recent [18, 19] works it was shown that a low quantity (0.05–0.1%) of alkali silicate nanoclusters dissolved in water can increase the dispersion water activity few degrees higher for rock materials of a different nature, particularly for aluminum and iron oxide silicate ones – it happens owing to both mechanical external strains and by self-dispersion (internal strains).

Hydrolytic breaking of siloxane bonds [18–20] was the basis of the mechanochemical and nanochemical water-aided self-dispersion of rocks:

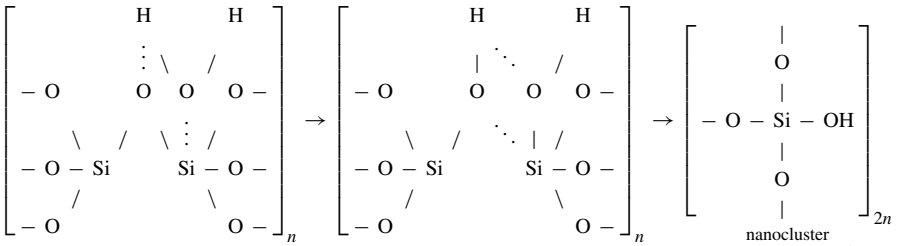

(25.1)

where n is the quantity of siloxane structures in nanoparticles or nanoclusters.

The reaction (25.1) rises steeply under the influence of mechanical forces [18, 19], which in turn eases the process of fracturing nanocrack development in silicate rock even with only traces of water. The frequency of bond breaking on the top of the crack and its enlargement velocity (V) depends on added mechanical strain in the following way [6]:

$$V = V_0 \cdot e^{-(U_0 - \gamma P)/RT};\ V_0 = \upsilon b \tag{25.2}$$

where υ is the Debye frequency; γ is the active volume with included overstrain factor $(c/b)^{1/2}$; c is the crack size; b is the crystal lattice parameter; U_0 is the activation energy of the process at $P = 0$.

Study of this fracturing rock mechanism with the presence of water and aqueous solutions is essential because it describes the rock dispersion processes of many solids in zones of metamorphism, hypergenesis, in addition to the physical chemistry and mechanochemistry of complex stress and tectonic phenomena, for example, creeping sediment under earthquake conditions [2]. Thus, it was experimentally shown in the work by Ivanova [21] with the example of compressed granodiorite, that in a month its dispersion was almost 10%. Thus, nanocracks with initial sizes of 10–100 nm were increased to cracks with sizes between micrometer up to a part of millimeter, with a maximum of 200 μm.

At first, the fracturing mechanism of hydrolytic siloxane bonds of silicate materials was considered to be much more characteristic chiefly for rocks containing quartz. However, recently it was shown that reaction (25.1) and other nanochemical reactions aided by water play an essential role in chemical processes in rocks and IASSMs in particular [18, 19]. Thus, one of the general ways of fracturing a rock mechanism aided by the presence of water and aqueous solutions is the mechanism of liquid phase penetration by a grain nanoboundary. This process is considered one of the most important ways of dispersing most rocks with an IASSM matrix, and other minerals [20]. In addition, energy gain is the reason why the liquid spontaneously forces its way the through almost nonporous dense rocks in metamorphism or weathering processes in the case of grain boundary replacement with a liquid nanolayer. This conclusion was then specified [18, 19] by the development of nanochemistry [22] and understanding the role of nanoparticles in kinetics of contact interactions in disperse polymineral rocks. It was shown that for almost every mechanical rock fracturing mechanism started, the chemical interaction of water with silicate rocks on a nanolevel is required, in particular, the reaction (25.1). Thus, at initial stages, the rock mechanical dispersion mechanism starts from the above-mentioned hydrolytic siloxane bond breaking and formation of nanocracks at least, according to reaction (25.2). Then, according to the Gibbs–Smith condition [17, 20], grain boundaries between A and B crystals are being replaced by liquid C:

$$\sigma_{AB} > \sigma_{AC} + \sigma_{BC}. \tag{25.3}$$

Thus, grain boundary energy appears to be higher than the sum of surface energies on crystal boundaries with a liquid phase (in our case, with water or aqueous solutions). As a result, the process of surface reconstruction is due to chemical reactions, shown generally in Panko et al. [6, 11], and at the same time growing facets, being thrust on neighboring grains, breaking the material on the grain boundary. Thus, the crack on the grain boundary widens by a stepwise nanochemical mechanism [19, 23], and if the average number of penetrated boundaries exceeds 1/3 then the process will proceed continuously and it will obey the linear parabolic equation:

$$\mathrm{AL} + \mathrm{BL}^2 = t, \tag{25.4}$$

where t is the time needed for the liquid penetration front to drift away from the liquid source at distance L deep into the polycrystalline rock [16, 17]. The linear part of Eq. (25.4) is defined by crystallization pressure P_{cr} kinetics:

$$A = \delta RT / D_{\mathrm{SL}} C_0 P_{\mathrm{cr}} \omega, \tag{25.5}$$

where δ is the average grain size; R is the gas constant; T is the temperature; D_{SL} is the diffusion coefficient of grain matter in liquid; C_0 is the liquid mole concentration; ω is the mole volume.

Part of the parabolic equation (25.4) is defined by limiting the process of liquid viscous flowing in the space between rock grains, whose thickness is usually 10–100 nm.

Applying the Poiseuille equation for value B from Eq. (25.4) gives the next expression [20]:

$$B = 12\eta / \delta P_{\mathrm{cr}} \tag{25.6}$$

where η is the liquid viscosity.

Thus, value $1/B$ is considered to be the effective (conventional) diffusion coefficient. Estimations of $1/B$, conforming to the experiment, gives values of about 10^{-3}–10^{-4} cm^2/s, which are many degrees higher than the diffusion coefficient in solids because of the viscous liquid flow in nanocracks according to PCGM and nanochemistry laws [7, 22].

An established phenomenon (which belongs to spheres of interest of PCGM and geomechanics) in geological and technological aspects appeared to be valuable not only for the development of geomechanics, but also for the eco-security of oil and natural and shale gas production processes. Indeed, infiltration of injected water while extracting oil products from a depth of a few kilometers, even through dense rocks, is possible. Kovzun and Pertsov [19] showed that this process can run a few degrees faster in porous disperse materials than in dense rocks.

Besides the fracturing IASSM mechanism considered, aided by water and processes of liquid phase penetration through grain nanoboundaries, the quasi-spontaneous (nanochemical) dense rock dispersion under the influence of water

and aqueous solutions [20, 23] is possible, as is much more intensive natural and technogenic dispersion of porous materials in various surface-active mediums [11, 18, 19]. Analysis of this mechanism in terms of nanochemical dispersion and PCGM for the next nanostructural phenomena showed that the dispersion process for polydisperse porous iron aluminosilicate and aluminosilicate rocks, while adding the external mechanical load in addition to the availability of the alkalescent pH values of aqueous solutions, can be completed in few hours, i.e., it can be accelerated by many orders of magnitude. Therefore, its kinetics follows the equation [19]:

$$(S - S_0)^2 = \mathrm{kt} \tag{25.7}$$

where S_0 is the initial specific surface of the porous body.

Thus, processes by reactions (25.3), (25.4), (25.5), (25.6), and (25.7) are purely physical. At the same time, while explaining the influence of water on rock dispersion by Eq. (25.4), it relates to the crystallization pressure in nanopores, which can be produced only by the aid of nanochemical reactions of mineral nanophase formation. As mentioned, such reactions are described in Panko et al. [6, 11], but only in general terms. For this reason, more specific mechanisms of crystallization pressure work in nanopores due to nanochemical reactions of iron aluminosilicate, aluminosilicate, and silicate mineral nanophase formation, which wedges nanocracks are considered here, using ideas from Panko et al. [6, 11].

Thus, nanochemical processes, along with reaction (25.1), can occur in nanocracks with sizes 10–100 nm, according to the modified reactions (25.8) and (25.9):

$$\begin{aligned} &\mathrm{Fe_2O_3}\cdot n\mathrm{Al_2O_3}\cdot m\mathrm{SiO_2}\cdot k\mathrm{H_2O} + 4\mathrm{MOH} + (k\text{–}1)\,\mathrm{H_2O} \rightarrow \\ &\rightarrow \mathrm{M_2O}\cdot n\mathrm{Al_2O_3}\cdot k\mathrm{H_2O} + \mathrm{M_2O}\cdot m\mathrm{SiO_2}\cdot k\mathrm{H_2O} + \mathrm{Fe_2O_3}\cdot \mathrm{H_2O} \end{aligned} \tag{25.8}$$

Reaction (25.8) products react next according to the following scheme:

$$\begin{aligned} &\mathrm{M_2O}\cdot n\mathrm{Al_2O_3}\cdot k\mathrm{H_2O} + \mathrm{M_2O}\cdot m\mathrm{SiO_2}\cdot k\mathrm{H_2O} \rightarrow \\ &\rightarrow \mathrm{M_2O}\cdot n\mathrm{Al_2O_3}\cdot m\mathrm{SiO_2}\cdot k\mathrm{H_2O} + 2\mathrm{MOH} + (k\text{–}1)\,\mathrm{H_2O} \end{aligned} \tag{25.9}$$

and along with $Fe_2O_3{\cdot}H_2O$, they take part in nanostructural contact phenomena.

Products formed by reactions (25.8) and (25.9) have a larger volume than the initial product of reaction (25.8). Therefore, the obtained crystallization pressure breaks (chemically wedges) the crack, helped by the concurrent mechanical load. Water, which goes into the mouth of the crack, widened up to micrometers, hydrolytically disintegrating the product of reaction (25.9) with alkali release that diffuses as a solution into a newly formed secondary nanocrack. Thus, the self-dispersion process proceeds and accelerates, which corresponds to conclusions from [20, 23]. The process goes the same way as in the case of liquid phase penetration through grain nanoboundaries, but faster by many orders of magnitude and lasts not years, but hours. This is also helped by other nanochemical interactions in silicate structures, for example, quartz-like structures, that complement interactions (25.1), (25.8), and (25.9) and are characterized by the following reactions [18]:

$$(\equiv \mathrm{SiOH})_n + (\mathrm{OH}^-)_n \rightleftarrows (\equiv \mathrm{SiO}^-)_n + n\mathrm{H_2O} \tag{25.10}$$

$$(\equiv \mathrm{SiOH})_n + (\equiv \mathrm{SiO}^-)_n \rightleftarrows (\equiv \mathrm{Si{-}O{-}Si} \equiv)_n \tag{25.11}$$

These reactions, along with $Fe_2O_3 \cdot H_2O$ (reaction (25.8)), provide a start for nanostructural phenomena of transformation of the fine dispersions formed as a result of coagulation-condensation processes in contact zones of dispersion microparticles. The mechanism of this process is further described here.

Thus, the nanochemical reaction (25.11) is a reaction of polymerization and it leads to the formation of polysilicate nanoclusters on the crack surface or on an internal surface of dispersion microparticles, and released hydroxyl ions thus take part in reaction (25.8) or (25.10), or along with FeOH, in the formation of new phases. Therefore, reactions (25.10) and (25.11) are not only complementary reactions (25.1), they are also intermediate in IASSM transformation processes (25.8) and (25.9). In addition, colloid–chemical interphase interactions occurring at the nanolevel on the solid surface of the formed silicate rock surface are followed by nanochemical transformations and nanostructural phenomena in particle contact zones, with further formation of new coagulation–condensation structures. The process proceeds stepwise [23], which was shown on the model system of iron aluminosilicate with an alkalescent component [24]. As shown in Fig. 25.1, the results prove that the stepwise process proceeds most intensively under conditions of low-agility of porous disperse rock, whereas the stepwise process ceases gradually at an increasing plastic flow rate. This testifies to the partial contact breaking in interphase zones and further system reformatting and the start of restructuring. The mechanism of this process needs further investigation and consideration.

25.3.1.2 Biocolloid Processes

Interphase nanochemical interactions on the contact surface of silicate and aluminosilicate minerals that correspond to the main nanochemical processes (25.1), (25.8), (25.9), (25.10), and (25.11) in iron aluminosilicate minerals, which are composed of ore materials and IASSMs, have more complex features [11, 25, 26]. Proposed models (25.12), (25.13), (25.14), (25.15), (25.16), and (25.17) of interphase nanochemical interactions in iron aluminosilicate minerals from iron oxide silicate (ferro-clay) ore biocolloid materials allow the nanocluster biocolloid mechanisms of such interactions to be estimated more thoroughly. Thus, ferrite formed by reactions (25.8) and (25.9) reacts with the aid of microorganisms according to the following scheme:

$$\mathrm{Fe_2O_3 \cdot H_2O_{(micro)} \xrightarrow[\text{reduction}]{\text{microbiological}} Fe(OH)_2 + Fe(OH)_3 \xrightarrow{CO_2} GR \cdot CO_3^{2-}{}_{(nano)} \rightarrow}$$
$$\xrightarrow{CO_2+H_2O} \mathrm{Fe(HCO_3)_2\ (solution)} \xrightarrow{+O_2} \alpha - \mathrm{FeOOH_{(nano)}\ (goethite)} \tag{25.12}$$

There, the following phase interactions \enlargethispage*{34pt} in contact zones of microparticles take place:

$$\left.\begin{matrix}\mathrm{I}\\ \mathrm{A}\\ \mathrm{S}\\ \mathrm{S}\\ \mathrm{M}\end{matrix}\right| - \left(\begin{matrix} & & \mathrm{OH} \\ & / & \\ \mathrm{O-Fe} & & \\ & \backslash & \\ & & \mathrm{OH}\end{matrix}\right)_{\boldsymbol{n}} + \left(\begin{matrix}\mathrm{HO} & & \\ & \backslash & \\ & & \mathrm{Fe-O} \\ & / & \\ \mathrm{HO} & & \end{matrix}\right)_{\boldsymbol{n}} - \left|\begin{matrix}\backslash & & / \\ \backslash & & / \\ \backslash & \rightarrow & / \\ \backslash & & / \\ \backslash & & /\end{matrix}\right| - \left(\begin{matrix} & \mathrm{O} & \\ & / \quad \backslash & \\ \mathrm{O-Fe} & & \mathrm{Fe-O} \\ & \backslash \quad / & \\ & \mathrm{O} & \end{matrix}\right)_{\boldsymbol{n}} - \left|\begin{matrix}\backslash \\ \backslash \\ \backslash \\ \backslash \\ \backslash\end{matrix}\right| + 2\boldsymbol{n}\mathrm{H_2O} \tag{25.13}$$

$$\left.\begin{matrix}\mathrm{I}\\ \mathrm{A}\\ \mathrm{S}\\ \mathrm{S}\\ \mathrm{M}\end{matrix}\right| \equiv (\mathrm{Si-OH})_n + (\mathrm{HO-Fe-OH})_n + \ (\mathrm{HO-Si})_n \equiv \left|\begin{matrix}\backslash & & \\ \backslash & & / \\ \backslash & \rightarrow & / \\ \backslash & & / \\ \backslash & & \end{matrix}\right| \equiv \left(\mathrm{Si-O-\ Fe\ -O-Si}\right)_n \equiv \left|\begin{matrix}\backslash \\ \backslash \\ \backslash\end{matrix}\right| + 2n\mathrm{H_2O} \tag{25.14}$$

$$\left.\begin{matrix}\mathrm{I}\\ \mathrm{A}\\ \mathrm{S}\\ \mathrm{S}\\ \mathrm{M}\end{matrix}\right| -(\mathrm{Fe-OH})_n + \left(\begin{matrix} & \mathrm{OH} & \\ & | & \\ \mathrm{HO-} & \mathrm{Si} & \mathrm{-OH} \\ & | & \\ & \mathrm{OH} & \end{matrix}\right)_n + (\mathrm{HO-Fe})_n - \left|\begin{matrix}\backslash & & / \\ \backslash & & / \\ \backslash & \rightarrow & / \\ \backslash & & / \\ \backslash & & /\end{matrix}\right| - \left(\begin{matrix} & \mathrm{OH} & \\ & | & \\ \mathrm{Fe-O-} & \mathrm{Si} & \mathrm{-O-Fe} \\ & | & \\ & \mathrm{OH} & \end{matrix}\right)_n - \left|\begin{matrix}\backslash \\ \backslash \\ \backslash \\ \backslash \\ \backslash\end{matrix}\right| + 2n\mathrm{H_2O} \tag{25.15}$$

$$\left.\begin{array}{l}\mathrm{I}\\ \mathrm{A}\\ \mathrm{S}\\ \mathrm{S}\\ \mathrm{M}\end{array}\right| = (\mathrm{Fe-OH})_n + \left(\begin{array}{c}\mathrm{OH}\\ |\\ \mathrm{HO-Si-OH}\\ |\\ \mathrm{OH}\end{array}\right)_n + (\mathrm{HO-Fe})_n = \left|\begin{array}{ccc}\backslash & & /\\ \backslash & & /\\ \backslash & \rightarrow & /\\ \backslash & & /\\ \backslash & & /\end{array}\right|$$

$$= \left(\begin{array}{c}\mathrm{OH}\\ |\\ \mathrm{Fe-O-Si-O-Fe}\\ |\\ \mathrm{OH}\end{array}\right)_n = \left|\begin{array}{c}\backslash\\ \backslash\\ \backslash\\ \backslash\\ \backslash\end{array}\right. + 2n\mathrm{H_2O} \tag{25.16}$$

$$\left.\begin{array}{l}\left|\equiv (\mathrm{Si-OH})_n + (\mathrm{HO-Fe=O})_n \rightarrow\right| \equiv (\mathrm{Si-O-FeO})_n + n\mathrm{H_2O} \rightarrow\\ \equiv \left(\begin{array}{c}\mathrm{OH}\\ /\\ \mathrm{Si-O-Fe}\\ \backslash\\ \mathrm{OH}\end{array}\right)_n\\ \left|\equiv \left(\begin{array}{c}\mathrm{OH}\\ /\\ \mathrm{Si-O-Fe}\\ \backslash\\ \mathrm{OH}\end{array}\right)_n + \left(\begin{array}{c}\mathrm{HO}\\ \backslash\\ \mathrm{Fe-O-Si}\\ /\\ \mathrm{HO}\end{array}\right)_n \equiv\right| \rightarrow \left|\right.\\ \equiv \left(\begin{array}{c}\mathrm{O}\\ /\ \backslash\\ \mathrm{Si-O-Fe\quad Fe-O-Si}\\ \backslash\ /\\ \mathrm{O}\end{array}\right)_n \equiv \left|\right. + 2n\mathrm{H_2O}\end{array}\right\} \tag{25.17}$$

where $(\ldots)_n$ is a nanocluster.

As we can see from models (25.13), (25.14), (25.15), (25.16), and (25.17), the interphase biocolloid interactions are followed by the formation of coagulation–condensation bonds between surfaces of similar or different disperse phases, which leads to the compacting of iron aluminosilicate materials that were dispersed earlier. Such contact interactions testify that interphase interactions with Fe^{3+} are stronger than those with Fe^{2+}, because in the case of Fe(II), described here by models (25.14) and (25.15), a microbiological oxidation of Fe^{2+} up to Fe^{3+} is possible, which leads to interphase bonds –O–Fe–O– breaking with the formation of goethite according to model (25.12). Thus, we can see that the biocolloid mechanism varies from the

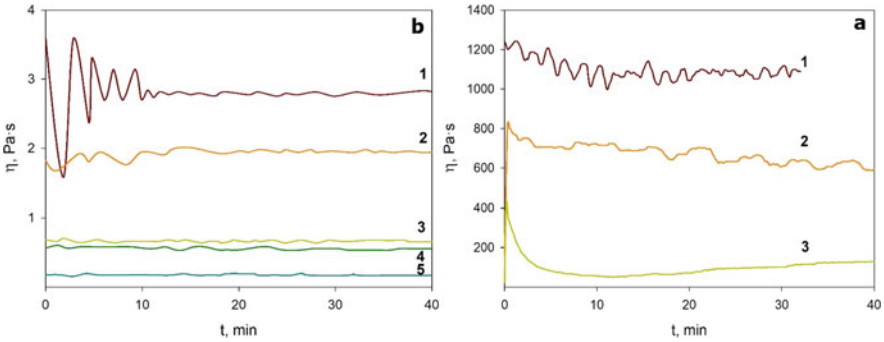

Fig. 25.1 Dispersion flow kinetics. (**a**) At a shear rate of 2453 s^{-1}: 1‘ – polyacrylic gel at $W_{H2O} = 90\%$; 2‘ – polyacrylic gel with the addition of 10% quartz sand at $W_{H2O} = 88\%$; 3‘ – quartz sand ($d < 63$ μ) at $W_{H2O} = 26\%$. (**b**) Iron aluminosilicate rock ($W_{H2O} = 50\%$) with concurrent reactions (25.8) and (25.9) at a shear rate of (s^{-1}): *1* – 1.0; *2* – 1.8; *3* – 3.0; *4* – 27.0; *5* – 81.0

previously described inorganic mechanism [11] by the intermediate formation of green rust (GR).

Analysis of the many-stage process (25.17) of goethite action in contact interactions of disperse phases by inorganic and biocolloid mechanisms shows that this process is almost the same by reaction rate (Fig. 25.1) as one-stage interactions according to model Schemes (25.13) and (25.16) or even faster in some cases.

Besides the previously considered mechanisms of the realization of the Rebinder phenomenon in the Earth crust, the plastification (creeping) of iron silicate rocks is possible under some conditions (small shear rates) [17]. Creep can be realized in two ways. First, the creeping rate can be increased under the influence of surface-active substances by some orders, which is described by an increase in the structural factor (γ) in Eq. (25.2). Second, if the Gibbs–Smith condition is true, then a specific and effective mechanism is possible – where mechanically loaded areas with chemical potential excess are being dissolved according to Eqs. (25.8), (25.9), (25.10), (25.11), (25.12), (25.13), (25.14), (25.15), (25.16) and (25.17), and this dissolved or chemically transformed matter precipitates on other loaded areas. The physical part of this process of theoretical and experimental investigations showed that the creeping rate under conditions of re-crystallization is described by a modified equation [17, 20]:

$$\upsilon = D_{\text{ТЖ}} \omega P c_0 \delta / \mathrm{R}\, T\, \mathrm{d}^2 \tag{25.18}$$

where d is the average grain size in polycrystal.

The results obtained allow the use of PCGM and biocolloid chemistry methods for the analysis of ore formation and technological processes with rocks. The basic aim of the PCGM of ore genesis should be the establishment of conformity and the mechanisms of stepwise changes of the mechanical properties of rock structure

under conditions of complex polychronic ore formation processes, depending on the types of surface interactions on the interphase boundary (interphase interactions), the chemical composition and structure of polymineral ore materials, the temperature and character of the loaded state, and the presence of microorganisms [13]. Thus, according to PCGM, most interesting are various natural and technogenic IASSMs, where surface physicochemical and chemical processes and interactions, determining their lyophilic/lyophobic behavior, play an essential role. Such processes and interactions followed by structural phenomena include nanochemical, microbiological, rheological, mechanical, mechanochemical, adsorption, contact adhesion–cohesion processes and surface interphase interaction. Development of this scientific branch in recent years promoted not only a better understanding of ore genesis in solid, sedimentary, and porous rocks and disperse materials, but also the conditioned development of the respective effective technologies of their transformation, processing, and application in large-scale production processes, and also the development of ideas concerning structural mechanisms of stress phenomena (creeping, earthquakes, etc.).

Considerable advance in that direction received investigations of biocolloid, microbiological, and biochemical processes based on the application of mineral matter and microorganism selective heterocoagulation, described in Prokopenko et al. and Panko et al. [13, 26], and also of ocean concretion recrystallization processes [15]. Further development in these directions provided the possibility of estimating correlations of microbiological, physical–mechanical and nanochemical features of self-dispersion processes of dense, disperse or porous rocks and their derivatives – pelitic sediments, peloids, and their further structural compacting under specific conditions [4, 7, 26]. These processes, especially of secondary compacting in the case of pelitic sediments and peloids substantially depend on the vital activity of microorganisms and the products of their metabolism [4, 26]. Biogeocenosis aggregates are formed according to biochemical ideas, whereas the selective interaction of microorganisms with mineral particles transform them into oolites, which are the basis of sedimentary ore deposits and peloids [13].

However, as shown in works by Pertsov and Panko et al. [7, 26], under the action of surface-active substances – products of microorganism metabolism processes, the secondary dispersion processes of mineral particles in biogeocenosis composition according to established laws of PCGM are possible. In Fig. 25.2 and in Table 25.1 data are given that confirm the summary influence of microorganisms of different ecological and trophic groups (whose number reaches 10 [26]) on the changing of the physicochemical properties of Black Sea pelitic sediments. On the one hand, these data show the ability of pelitic sediments and peloids to restore their biological activity in the case of an increasing number of colony-forming units (lgCFU). On the other hand, the values of effective viscosity and corresponding shear stress with increasing peloid exposure time are growing. This growth correlates with the increase in quantity of bivalent iron (II) in peloid, which is formed as a result of the iron-reducing bacterial activity of biogeocenosis (Fig. 25.2), and correlates with the increase in the number of nanoparticles and decrease of microparticles (Table 25.1). Such data testify that microorganism activity in the composition of

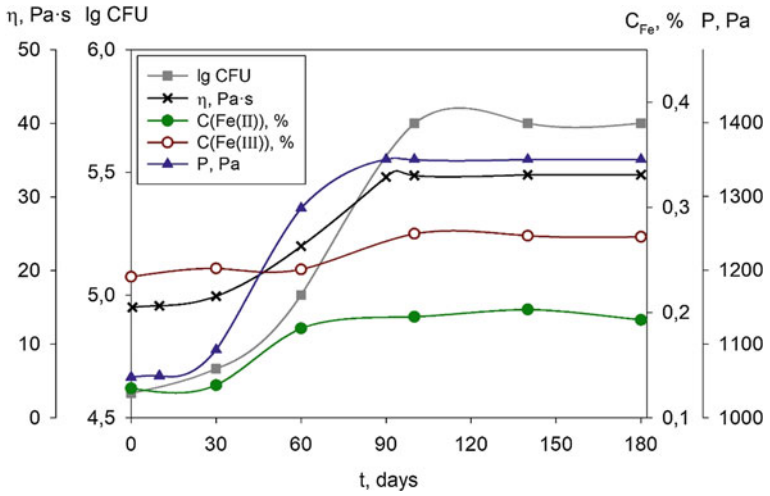

Fig. 25.2 Dependences of viscosity (η), shear stress (P), concentration (C, %) of Fe^{2+} (C(FeII)) and Fe^{3+}(C(FeIII)) and colony forming units (lgCFU) value in marine nanostructured pelagic sediments from the time of their storage, at 46% humidity

Table 25.1 Physicochemical parameters of sea pelagic sediments, at 46% humidity

	Exposure, days				
Parameter	0	10	30	60	100
Liquid phase, pH	7.0	7.1	7.3	7.4	7.4
Shear stress, Pa	1060	1070	1080	1290	1340
Viscosity, Pa·s	15	16	23	33	33
Particle concentration (>250 μm size), %	0.8	0.8	0.7	0.6	0.5
Concentration of nanoparticles, %	0.1	0.1	0.3	0.4	0.4
lgCFU	4.6	4.6	4.7	5.1	5.7

biogeocenosis aggregates leads to the activation of peloid mineral part dispersion according to mechanisms (25.1), (25.8), (25.9), (25.10), and (25.11), and after the end of the peloid activation process after 90–100 days, to the secondary compaction of peloid sediments due to the repeated Fe^{3+} quantity increase in the composition of GR according to the models (25.12), (25.13), (25.14), (25.15), (25.16), (25.17), and the optimal ratio of $FeO:Fe_2O_3$ thus reaches 1:1. This correlation corresponds to the formation of magnetite, whose mechanical characteristics are the highest among iron oxides of different structures. It appears that, owing to the biocolloidal processes, the contact nanofilms in the disperse structure are strongest at the exposure of sediments (Fig. 25.2) within the studied interval of 60–180 days (formation of magnetite type nanostructures). It allows Scheme (25.12) to be presented for the biocolloid process in the following way:

$$\begin{aligned} &Fe_2O_{3(micro)} \xrightarrow[\text{reduction}]{\text{microbiological}} Fe(OH)_2 + Fe(OH)_3 \xrightarrow{CO_2} \\ &\rightarrow GR \cdot CO^{2-}_{3(nano)} \rightarrow FeO \cdot Fe_2O_3(Fe_3O_4)_{(nano)} \end{aligned} \tag{25.19}$$

and reactions (25.15), (25.16), and (25.17) are transformed in the following way:

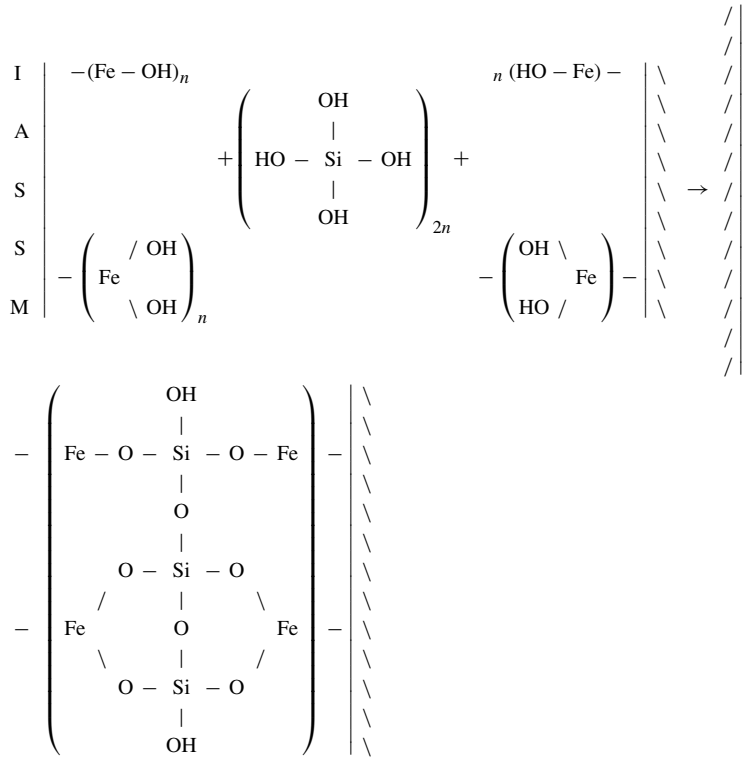

(25.20)

It is clear that structures formed by Schemes (25.19) and (25.20) bond the aggregates of IASSMs, aluminosilicates, and silicate materials in water dispersions most strongly, and this is clearly confirmed by increasing values of viscosity and shear stress.

Thus, biocolloid interactions are activated along with physicochemical and nanochemical processes in dispersions of iron aluminosilicate sediments and peloids under the action of surface-active substances (microorganism metabolites). This influences the formation of nanodispersed structural organo-clay-carbonate products, which enrich bottom pelitic sediments and peloids with organic substances, clays, iron oxides, and calcite [4]. As a result, derivative dense rocks transform into concentrated pasty, watertight compositions of bottom sediments, generally in seas and oceans. Such compositions, being structured with nano- and microparticles of iron oxides, clays, carbonates, and organic substances, form strong coagulation–crystallization nanophase contacts – as a result of the realization of Schemes (25.12),

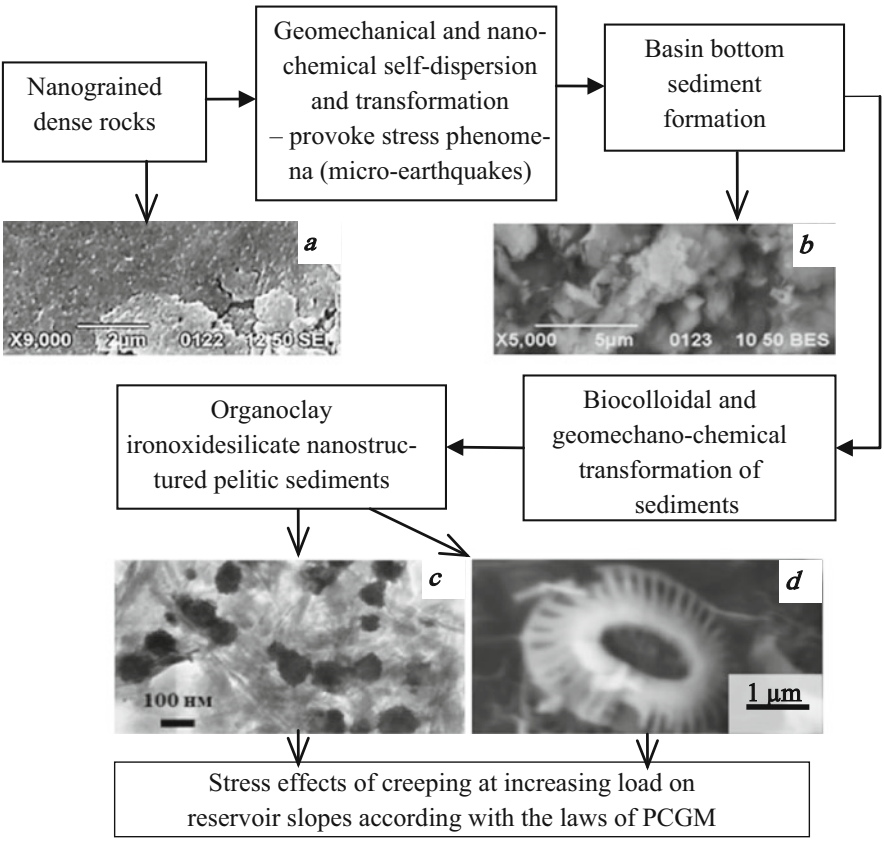

Fig. 25.3 General scheme of rock transformation. Scanning electron microscopy images of (**a**) nanograined rocks; of (**b**) bottom sediments of fractured rocks; (**c**) of pelitic organoclay–iron oxide silicate sediments and peloids; (**d**) of pelitic sediments with carbonate residue of *Foraminifera*

(25.13), (25.14), (25.15), (25.16), (25.17), (25.19), and (25.20). The general scheme of rock transformations is shown in Fig. 25.3, and the rheological behavior of the pelitic sediments formed is reviewed in Panko et al. [11].

25.3.2 Analysis of Nanostructural Phenomena in IASSMs, Related to Rheological Processes

According to the data from Panko et al. [11], most influential on nanostructured IASSM properties are clay minerals, especially montmorillonite, which is one of the bentonite clay [25], and which partially self-disperses up to nanoparticles in aqueous suspensions. The behavior of the latter does not correlate with dispersion water

content (humidity), but has a significant dependence from nanostructuring processes related to nanochemical properties and the chemical structure of montmorillonite nanoparticles. According to Ur'ev and Choy [25], calcium bentonite suspensions at 50% water content are characterized by so-called hyperanomalous viscosity change, and at 75% water-content, the effect of hyperanomalous viscosity is already absent. At the same time, after nanochemical clay processing with formation of sodium bentonite, the effect of hyperanomalous viscosity takes place again, but at 90% suspension humidity. Its appearance is explained by an increasing number of smaller nanoparticles of Na-montmorillonite in bentonite composition owing to the following nanochemical process:

$$\text{Bentonite}^{2-} + \text{Ca}^{2+} + \text{Na}_2\text{CO}_3 \rightarrow 2\left(\text{Bentonite}^{-} \times \text{Na}^{+}\right) + \text{CaCO}_3 \quad (25.21)$$

$$\begin{aligned} &\text{Na}_2\text{CO}_3 + 2\text{H}_2\text{O} \rightleftarrows 2\text{NaOH} + \text{H}_2\text{CO}_3; \\ &\text{Bentonite}^{2-} \times \text{Ca}^{2+} + 2\text{NaOH} \rightleftarrows 2\left(\text{Bentonite}^{-} \times \text{Na}^{+}\right) + \text{Ca(OH)}_2; \\ &\text{Ca(OH)}_2 + \text{H}_2\text{CO}_3 \rightarrow \text{CaCO}_3 + \text{H}_2\text{O} \end{aligned} \quad (25.22)$$

Calcium is usually present in natural bentonites. Therefore, another process of $CaCO_3$ nanoparticle formation is possible concurrently with nanoparticles of Na-montmorillonite, aided by CO_2 from air:

$$\begin{array}{c} \text{laminar flow increasing} \underset{\leftarrow}{(\text{isothermal consensation})} \\ \text{CaCO}_{3(\text{micro})} + \text{CO}_2 + \text{H}_2\text{O} \rightleftarrows \text{Ca(HCO}_3)_2 \rightleftarrows \text{CaCO}_{3(\text{nano})} + \text{H}_2\text{O} \\ \text{Increasing of turbulent flow} \underset{\rightarrow}{(\text{nanochemical recondensation})} \end{array} \quad (25.23)$$

The direct reaction (25.23) of nanochemical recondensation takes place at high turbulent mixing speeds of bentonite suspensions (high shear rate in a rheoviscometer), and the reverse one at low mixing speeds (laminar flow) [26].

Thereby, processes of clay suspensions nanostructuring, nanochemical processes of the formation of nanoparticles in them, biocolloidal processes among them too, and the chemical structure of nanoparticles have a significant influence on the rheological behavior of suspensions.

Based on the above considerations and graphic data for the curves of loading–unloading of elastic–plastic materials [11], which Ur'ev and Choy [25] also refer to as bentonite suspensions under conditions of hyperanomalous viscosity effect appearance, Fig. 13.11 from Panko et al. [11] can be presented in coordinates of viscosity (η) – shear stress (P), as can be seen in Fig. 25.4.

As follows from the curves, hyperanomalous viscosity is usually characterized by curves 1 and 3, and – unknown before the effect of ultra-anomalous viscosity – by curves 1 and 2. Both effects have been experimentally confirmed, but not explained before, by a number of rheograms for different types of clays, pelitic sediments, and peloids, as presented in Wang et al. and Panko et al., [1, 6, 11, 26]. Therefore, from these data, the previous conclusion should be drawn concerning the fact that the effect of hyperanomalous viscosity is more usual for less concentrated suspensions

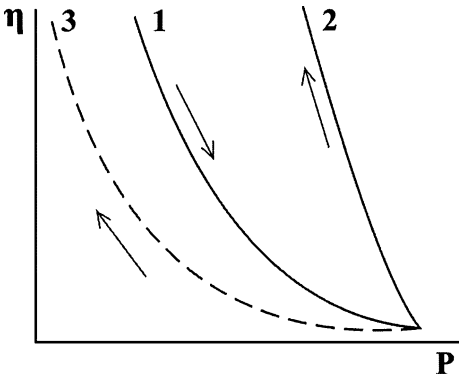

Fig. 25.4 Loading and unloading curves (1, 2 – in accordance) under conditions of the plastic current of elastic–plastic material [11]; 3 – unloading curve under conditions of a viscous hyperanomalous effect [25]

or those with a lower content of iron [26], and the ultra-anomalous viscosity effect for more concentrated suspensions or at lower shear speeds if other previously mentioned factors remain stable. Thus, from Fig. 13.4 in Panko et al. [11] it turns out that at the 65% humidity of the Black Sea pelagic sediment suspension, the dependence $\eta = f(P)$ is characterized by hyperanomalous viscosity at an interval of high shear speeds ($P = 500$–2300 Pa), but at relatively low shear speeds ($P = 50$–500 Pa) by ultra-anomalous viscosity, i.e., it goes into transitional mode [11] (Fig. 13.4a). At a higher humidity of 77% (Fig. 13.4b) [11], the suspension flow is characterized only by a hyperanomalous effect of viscosity. At the same time, the rheogram of IASSMs presented in Panko et al. [26] proves that hyperanomalous viscosity is typical of IASSMs with a high iron content in a form of goethite and at a high humidity of 46%. At a lower humidity of 55% (Fig. 13.5) [11] the flow of another type of Black Sea peloid suspension (Kuyalnitsky estuary) is characterized by the effect of ultra-anomalous viscosity. These data and extensive data received later for various sediments, soils, and sands indicate the significant role of rheological effects in stress processes occurring in the Earth crust. However, these results require additional analysis.

Established regularities for nanostructural phenomena in dense and disperse materials of the Earth's crust were also allowed to develop and implement a number of methods aimed at the control of the structure of IASSMs based on achievements of PCGM, biocolloid chemistry, and laws of nanochemical contact interphase interactions [11]. For example, the methods of control of the physicochemical properties of barrier structures, soils, and rocks were explained by the influence of active natural and technogenic media on them by means of colloid–chemical material science ideas [13, 18, 19].

As an example, Fig. 25.5 indicates the test results of the influence of surface-active inorganic nanostructured medium on the rheological properties of dispersed clayey rock, which was treated with microorganisms for formation of organic surface-active matter, and which was used for the filtration decrease of mineralized water through the bottom of the basin. These results are similar to data of other reports [11, 27]. The data received also provides the possibility of considering

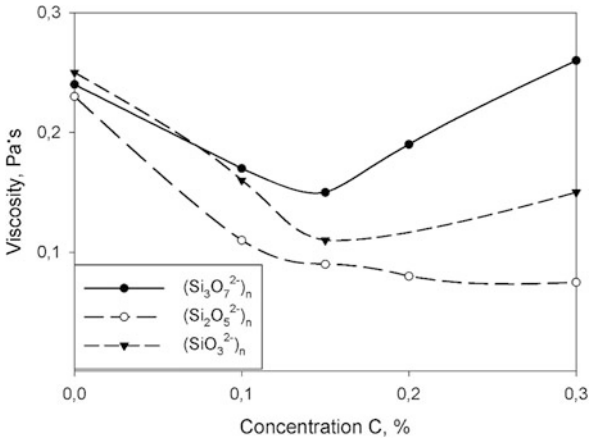

Fig. 25.5 Influence of the chemical structure of a silicate nanocluster on the viscosity of 50% aqueous suspension of dispersed iron aluminosilicate clay rock and correlation with the concentration (*C*) of anionic inorganic nanoclusters of various chemical compositions

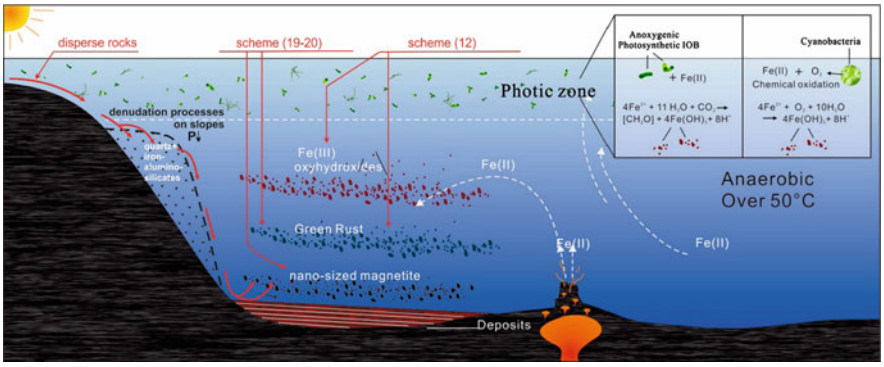

Fig. 25.6 Scheme of the transformation of iron compounds in the Archean ocean [28, 29], and continuing up to the present denudation processes of the land slopes due to creeping of sediments under the action of the pressure (*P*) force of the accumulated mass of quartz and iron aluminosilicates

the denudation processes of marine and ocean land slopes through biogeo- and nanochanges of the elasto-plastic properties of underwater sediments on slopes, and of preventing stress phenomena [3–9, 11–21, 23, 27]. These results agree well with recent conclusions drawn by other authors [28, 29]. Some of their data are presented in Fig. 25.6, added by the denudation process of land slopes that occur to the present day under the action of the increasing mass of the upper layers of the elasto-plastic material of weathering rocks, which generally consist of disperse quartz and iron aluminosilicates. The latter creep when the attained pressure reaches $P > P_{\text{critical}}$ and provoke stress phenomena according to the physicochemical and geomechanical laws of mechanisms previously described in Panko et al. [11].

While summarizing the test result analysis of nanostructural phenomena in iron aluminosilicates of the materials of the Earth's crust, including stress phenomena, and additional experimental data concerning the influence on those phenomena of nanochemical and microbiological processes for rocks and disperse IASSMs, it should be indicated that it is scientifically possible to receive a fairly exact description of nanochemical and rheological mechanisms of general physicochemical stress and catastrophic processes that occur in the Earth's crust and under technogenic conditions.

25.4 Conclusions

Thus, the theoretical investigations carried out and the experimental data obtained permitted the following:

1. Consideration of the thermodynamic basics, kinetics, and mechanisms of rock transformations owing to their self-dispersion aided by nanochemical and microbiological processes with the formation of new disperse structures with thermodynamic stable mineral phases; to develop ideas of rock creeping mechanisms as a result of the recrystallization of mechanically loaded areas, and the nanochemical transport of liquid phase substances through grain boundaries on other loaded surface areas.
2. Disclosure of the general principles of the physico-mechanical and nanochemical regulation of structural properties of disperse porous sediments under natural and technogenic conditions to prevent stress and catastrophic phenomena.
3. The further development of ways of solving the mentioned fundamental problems by applying the received laws in geological sciences, and in colloid and biocolloid chemistry for the development of modern technological processes for their use in environmental protection eco-biotechnologies, ore processing, metallurgical, gas- and-oil producing, ceramics, building, and other industries, in agriculture, and in medicine for the development of new methods of rehabilitation and spa-therapy cures, hemophilia prophylaxis, wound-healing and cosmetic-treatment remedies, etc.

References

1. Wang Y, Wu X, Yang W et al (2011) Aggregate of nanoparticles: rheological and mechanical properties. Nanoscale Res Lett 6:114
2. Karato S (2008) Deformation of earth materials. Cambridge University Press, Cambridge
3. Prokopenko VA, Kovzun IG, Ulberg ZR, Tsiganovich OA, Panko AV (2018) Physicochemical geomechanics and nanochemical processes in natural and technogenic minerals. Her Natl Acad Sci Ukr 2:83–96

4. Kovzun IG, Ulberg ZR, Panko AV et al (2015) Colloid-chemical and nanochemical processes in peloids on basis of ferrous clay minerals. In: Fesenko O, Yatsenko L (eds) Nanoplasmonics, nanooptics surface studies and applications, vol 167. Springer Proceedings in Physics, Heidelberg, pp 233–243
5. Panko AV, Kovzun IG, Prokopenko VA, Tsyganovich OA, Oliinyk VO, Nikipelova OM (2018) Nano- and microstructural disperse rocks in protective barriers, medicine and balneology. Appl Nanosci 8(1–2):1–11. https://doi.org/10.1007/s13204-018-0740-x
6. Panko AV, Kovzun IG, Prokopenko VA et al (2017) Nano- and microdisperse structures in processes of metamorphism, reduction sintering, and component separation of iron-oxide-silicate materials. In: O. Fesenko, L. Yatsenko (eds.) Nanoplasmonics, nanooptics surface studies and applications, Vol 195 Springer Proceedings in Physics, Heidelberg, pp 743–755. https://doi.org/10.1007/978-3-319-56422-7_57
7. Pertsov NV (1998) The Rehbinder effect in the earth's crust (physicochemical geomechanics). Colloid Journal 60(5):578–588
8. Oleinik VA, Panko AV, Kovzun IG et al (2013) Nanochemical processes in solid-phase reduction of ferrioxide-silicate materials. Proc NAP 2(3):03AET10
9. Panko AV, Ablets EV, Kovzun IG, Ilyashov MA (2014) Wasteless solid-phase method for conversion of iron ores contaminated with silicon and phosphorus compounds. Int J Chem Mater Sci Eng 8(1):35–37
10. Nikipelova OM (2011) Colloid-chemical properties of silt peloid and basic principles of their regulation. Dissertation, F.D. Ovcharenko Institute of biocolloid chemistry NAS of Ukraine
11. Panko AV, Kovzun IG, Nikipelova OM, Prokopenko VA, Tsyganovich OA, Oliinyk VO (2018) Nanostructural and nanochemical processes in peloid sediments aided with biogeocenosis. In: Fesenko O, Yatsenko L (eds) Nanochemistry, biotechnology, nanomaterials, and their applications, vol 214. Springer Proceedings in Physics, Cham, pp 215–230. https://doi.org/10.1007/978-3-319-92567-7_13
12. Pertsov NV, Ovcharenko FD (1980) Using the achievements of colloid chemistry in geology. Vistnik Akademii Nauk 1:97
13. Prokopenko VA, Kovzun IG, Ulberg ZR (2014) The creative potential of scientific discovery. Visn Nac Akad Nauk Ukr (10):52–61. https://doi.org/10.15407/visn2014.10.052
14. Pertsov NV (1985) Physico-chemical influence of the environment on the destruction of rocks. In: Physico-chemical mechanics of natural disperse systems. MGU, Moscow, pp 107–117
15. Ovcharenko FD, Pertsov NV, Obushenko IM, Topkina NM (1987) Recrystallization of oceanic nodules. Dopovidi Acad Sci Ukr B 10:42
16. Traskin VY, Pertsov NV, Skvortsova ZN (1988) The contact between adhesive strength and adhesive work of water in polymineral disperse systems. In: Surface films. MGU, Moscow, p 211
17. Traskin VY, Pertsov NV, Kogan BS (1989) Influence of water on the mechanical properties and disperse structure of rocks. In: Water in disperse systems. Nauka, Moscow, p 83
18. Kovzun IG, Protsenko IT, Pertsov NV (2001) Contribution of chemical and physical processes to the formation of alkaline silicate suspensions and their properties. Colloid J 63(2):191
19. Kovzun IG, Pertsov NV (2010) Colloid chemistry process contact self-organization in alkaline silicate composites and relation to formation of Nanosized surface structures. In: Nanoscience colloidal and interfacial aspects. Taylor and Francis Group, London-New York, pp 523–568. https://doi.org/10.1016/j.jcis.2010.07.003
20. Pertsov NV, Kogan BS (1984) Physico-chemical mechanics and lyophilic of natural systems. In: Physico-chemical mechanics and lyophilic of disperse systems. Naukova Dumka, Kyiv, pp 71–78
21. Ivanova NI (1981) The microcracks study of mechanically intense of quartz diorite in the presence of aqueous phases. In: Physico-chemical mechanics and lyophilic of disperse systems. Naukova Dumka, Kyiv, pp 111–114
22. Sergeev GB (2003) Nanochemistry. MGU, Moscow
23. Kovzun IG, Pertsov NV, Protsenko IT (2002) Jumpwise development of the processes with the participation of colloidal systems. Colloid J 64(3):312

24. Kovzun IG, Koryakina EV, Protsenko IT, Pertsov NV (2003) Colloid-chemical processes in the hardening of alkaline compositions based on aluminum silicates and impurities. II. Rheological studies. Colloid J 65(5):589
25. Ur'ev NB, Choy SW (1993) About two types of flow curves of structured disperse systems. Colloid J 55(3):183–190
26. Panko AV, Kovzun IG, Ulberg ZR, Oleinik VA, Nikipelova EM, Babov KD (2016) Colloid-chemical modification of peloids with nano- and microparticles of natural minerals and their practical use. In: Fesenko O, Yatsenko L (eds) Nanophysics, nanophotonics, surface studies, and applications, vol 183. Springer Proceedings in Physics, Cham, pp 163–177. https://doi.org/10.1007/978-3-319-30737-4_14
27. Oleinik VA, Panko AV, Kovzun IG, Prokopenko VA, Ablets EV, Tsyganovitch EA, Nikipelova EM (2016) Processes of metamorphism in iron-oxide-silicate rocks their microbiological, nanochemical and nanostructural transformations. Proc NAP 5(3):02NABM01. https://doi.org/10.1109/NAP.2016.7757285
28. Li W, Beard BL, Johnson CM (2015) Biologically recycled continental iron is a major component in banded iron formations. Proc Natl Acad Sci 112(27):8193–8198
29. Li Y-L, Konhauser KO, Zhai M (2017) The formation of magnetite in the early Archean oceans. Earth Planet Sci Lett 466:103–114

Chapter 26
Two-Dimensional Ordered Crystal Structure Formed by Chain Molecules in the Pores of Solid Matrix

A. N. Alekseev, S. A. Alekseev, Y. F. Zabashta, K. I. Hnatiuk, R. V. Dinzhos, M. M. Lazarenko, Y. E. Grabovskii, and L. A. Bulavin

X-ray diffraction patterns of silicon and silica gel with the pores filled by 1-octadecene were analyzed. It was found that 1-octadecene in the pores of silica gel possesses a two-dimensional crystalline structure. The formation mechanism for such a structure is proposed.

26.1 Introduction

The density function ρ (Eq. 26.1) is applied to create a statistical description of the system's particles location (see, e.g., [1], etc.)

$$\rho = \rho\,(x, y, z) \tag{26.1}$$

where x, y, and z are particle coordinates.

This is a periodic function with the same period as that of the crystal lattice.

A. N. Alekseev · S. A. Alekseev · Y. F. Zabashta · K. I. Hnatiuk (✉) · M. M. Lazarenko
L. A. Bulavin
Taras Shevchenko National University of Kyiv, Physical Faculty, Kyiv, Ukraine
e-mail: alan@univ.kiev.ua; alekseev@univ.kiev.ua; zabashta@univ.kiev.ua; maxs@univ.kiev.ua

R. V. Dinzhos
Mykolaiv V.O. Sukhomlynskyi National University, Mykolayiv, Ukraine

Y. E. Grabovskii
Taras Shevchenko National University of Kyiv, Physical Department, Kyiv, Ukraine

O. Fesenko, L. Yatsenko (eds.), *Nanocomposites, Nanostructures, and Their Applications*, Springer Proceedings in Physics 221,
https://doi.org/10.1007/978-3-030-17759-1_26

In some cases of crystalline systems the function ρ which depends on only two coordinates is possible to exist [1].

$$\rho = \rho\,(x, y) \tag{26.2}$$

The function (26.2) corresponds to a two-dimensional crystal structure in which the particles are randomly located along straight lines parallel to the Z-axis. The points of intersection of these straight lines with a plane perpendicular to the Z-axis form a two-dimensional lattice. Therefore, this function is double-periodic.

The existence of a two-dimensional crystal structure in disk-shape systems of molecules was investigated in the work [2].

The work [3] demonstrates that chain molecules (dodecane) embedded in solid nanopores, form a two-dimensional crystal structure. However, the reason for the formation of this structure has not been discussed.

In this article, we continue to explore such two-dimensional crystal structures. A possible mechanism for the occurrence of investigated structures is also considered.

26.2 Experiment

26.2.1 Studied objects

1. 1-Octadecene, chemical formula ($CH_3(CH_2)_{15}CH = CH_2$);
2. Porous silicon (PSi) samples in the form of "free layers" with a thickness of approximately 50–300 μm were obtained by electrochemical etching of p^{++} type (Ω = 1–3 mΩ cm, orientation (100)) silicon wafers in HF(48%): EtOH (1:1 v:v) mixture according to the procedure described in [4]. The samples possess the porosity of 55% by volume with cylindrical mesopores (D = 20 nm) placed in the sample uniformly and aperiodically. To obtain a composite of PSi with 1-octadecene ($PSi/C_{18}H_{36}$, further denoted as "system A"), the PSi sample was immersed in liquid 1-octadecene under vacuum.
3. Initial KSK 2.5 silica with a pore size 12 nm exists as the glass-like 1–4 nm spheres. To prepare an experimental sample the silica was ground in a porcelain mortar and sieved. The fraction 100–350 μm was refluxed in concentrated HNO_3 for 4 hours in order to remove iron oxide and other impurities, which are present in the initial silica. Then the silica particles were rinsed with distilled water until neutral media. A few decantation rinsing stages were made in order to remove the smallest dust-like silica particles. Rinsed silica sample was dried for 12 hours at 110 °C.

To prepare the sample, further denoted as "system B", the sample of silica was placed into 20% solution of 1-octadecene in n-hexane. Quantity of the solution was taken in order to fill approx. 70–80% of SiO_2 pore volume by 1-octadecene. The

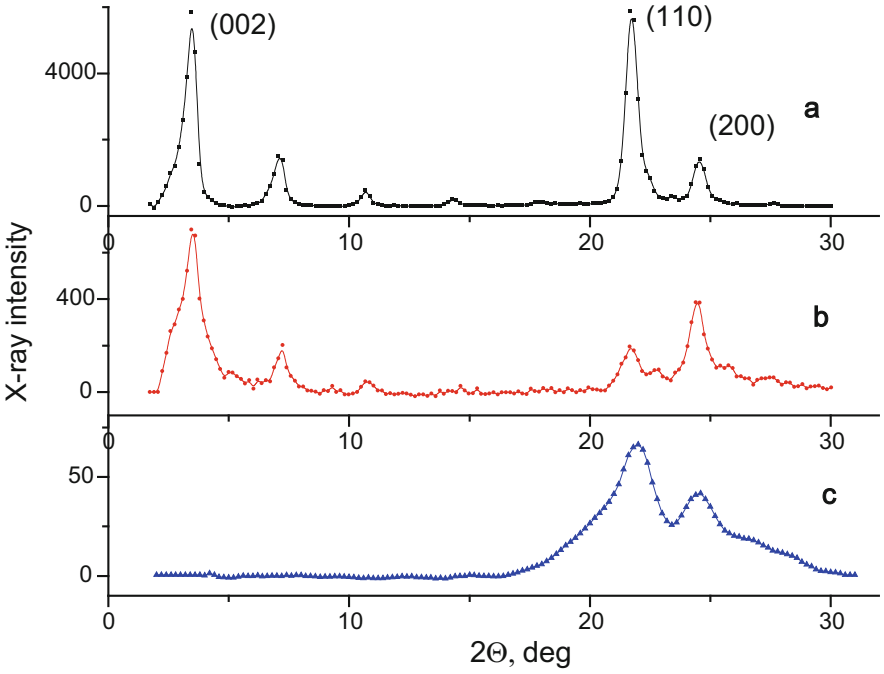

Fig. 26.1 The diffraction angle (2θ) dependence on x-ray diffraction radiation intensity (I): (**a**) 1-Octadecene, (**b**) system A, (**c**) system B

Sample was sonicated to remove any trapped air from the silica pores and then dried in air at 90 °C.

X-ray diffractometer DRON-3 M with a CoKα tube was used to analyze the structure of samples ($\lambda = 1.54178$ Å). The wide-angle X-ray diffraction patterns of the investigated systems are shown in Fig. 26.1.

26.3 Discussion

According to [5], the diffraction peaks at $2\theta = 3.5°$ corresponding to the (200) plane, $2\theta = 21.7°$ – (110) plane, and $2\theta = 24.5°$ – (200) plane. The peaks at 2θ equal to 3.5°, 7.1°, 10.7°, 14.4°, and 17.9° are the diffraction peaks of the 1st, 2nd, 3rd, 4th, and fifth order for the (200) planes (Fig. 26.1). According to Bragg's law, for an angle of $2\theta = 3.5°$, period value of the interplanar distance along the c axis equal to 2.5 nm. For chain molecules, the c axis is the axis of the chain. Based on this, the schematic structure of the 1-octadecene crystal was created (Fig. 26.2a).

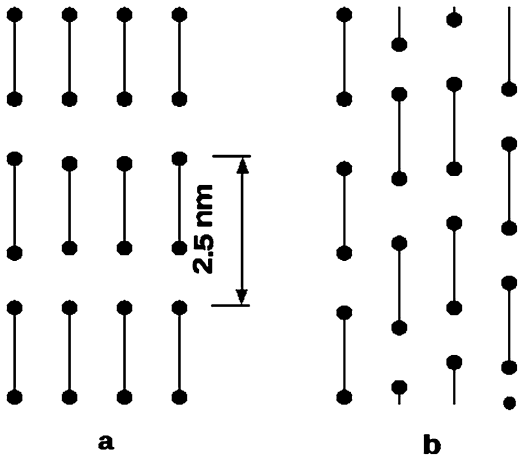

Fig. 26.2 Schematic structure of the 1-octadecene crystal: (**a**) 3D, (**b**) 2D

Fig. 26.3 Location and shape of the pores in the solid matrix of system A (**a**) and system B (**b**)

As it is shown in Fig. 26.1, diffraction peaks of the (200) plane exist for system A and are absent for the system B. This means that system A retains its 3D structure and system B passes to 2D structure during crystallization (Fig. 26.1).

26.4 Pore Model

The shape of the pores in systems A and B is different (Fig. 26.3). System A is a solid silicon plate with a thickness of 300 μm. The shape of the pores in this system is like long holes (Fig. 26.3a). In parallel section of the plate, the pores have the form of flat figures of irregular shape with curved connecting channel. In our model, we assume that the holes have the shape of a circular cylinder with a diameter of $D = 20$ nm.

The location and shape of the pores in the solid matrix of system B are shown in Fig. 26.3b. The pores are 3D figures of irregular shape with connecting channels. In accordance with the idealized model of system A, we will assume that the pores in

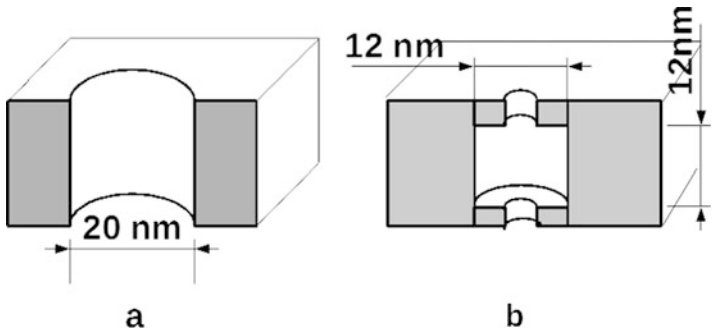

Fig. 26.4 Pore model: (**a**) system A, (**b**) system B

system B also have the shape of a circular cylinder. But height and diameter of this cylinder are the same and equal to $H = 12$ nm. For system A, the cylinder is open, and for system B, the cylinder is closed (connecting through channels is excluded) (Fig. 26.4).

26.5 The Influence of the Curvature of the Pore's Surface on the Location of the Chain

Consider the case when the surface of the pores is absolutely smooth. Therefore, the minimum energy will be reached if the chain is in full contact with the surface of the pore. The pore surface can be considered flat when the condition $l \ll r$ is satisfied (l is the absolute length of the chain, r is the radius of curvature of the surface). In this case, all the locations of the chain, which has an elongated shape, are equivalent. On the other hand, the pore surface cannot be considered flat if the inequality $l \ll r$ is not satisfied.

Consider the possible dispositions of the 1-octadecene chain when it is in contact with the surface of the cylinder. Let's analyze two cases:

1. The chain is directed along the generatrix of the cylinder (Fig. 26.5a).
2. The chain is located in a plane perpendicular to the axis of the cylinder (Fig. 26.5b).

In Fig. 26.5a, the cross sections of the chains are shown as circles. In Fig. 26.5b, the chain is depicted as a curved rectangle.

In the case shown in Fig. 26.5a, only the distance between the chains changes. The deformation in chain is absent.

The average distance between the chains in the initial state is denoted by $AB = h$. The distance between the chains in the current state is denoted by AC (Fig. 26.5a).

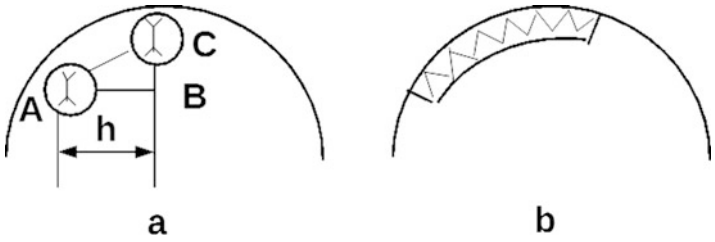

Fig. 26.5 Possible dispositions of the chains in pore: (**a**) along the generatrix of the cylinder; (**b**) in a plane perpendicular to the axis of the cylinder

Figure 26.5a shows that $\Delta h = \mathrm{AC} - \mathrm{AB}$. So, the deformation of the interchain coupling is approximately equal to

$$\Delta h \approx \frac{1}{2}\frac{h^2}{D}. \tag{26.3}$$

Then the increase in energy of the interchain interaction is

$$\Delta W = \frac{1}{2}K(\Delta h)^2 \tag{26.4}$$

Denote by C_1 the distance between the elements along the chain. Then the increase in specific energy ΔA is approximately equal to

$$\Delta A = \frac{\Delta W}{C_1 h^2} \tag{26.5}$$

Substituting formulas (26.3) and (26.4) into Eq. (26.5), we have

$$\Delta A = \frac{1}{8}\frac{K}{C_1}\left(\frac{h}{D}\right)^2 \tag{26.6}$$

Using the results of the experiment for the (110) and (200) planes, as well as the Bragg's law, we obtained the average value of the distance between the chains, $h = 3,9$Å. As is well known [6], break energy U1 of the interchain coupling in order of magnitude is $10 - 20$ J. Given that $K \sim \frac{U_1}{h^2}$, we have $K \sim 0.07\frac{H}{m}$.

From [6] it is known that, for long-chain hydrocarbon, C_1 is equal to 1.27 Å.

Substituting these values in the formula (26.6), we obtain $\Delta A = 0.3 \bullet 10^5$Pa.

The chain is deformed when it is located in a plane perpendicular to the axis of the cylinder (Fig. 26.5b). The specific energy of bending of the chain is determined by the formula

$$\Delta A_1 = \frac{W_1}{lh^2} \tag{26.7}$$

where W_1 represents the energy of bending of the chain and lh^2 represents the chain volume.

According to [7], the bending energy of a beam (model of chain) is equal to

$$W_1 = \frac{M^2}{2EJ} l \tag{26.8}$$

where M is the bending moment, E is the modulus of elasticity in the direction of the axis of the chain (beam), and J is the moment of inertia of the chain (beam).

The bending moment M and the moment of inertia J are related by the expression

$$M = \frac{EJ}{R} \tag{26.9}$$

where $R = \frac{D}{2}$.

The moment of inertia is equal to

$$J = \frac{h^4}{12} \tag{26.10}$$

Substituting the expressions (26.8), (26.9) and (26.10) into formula (26.7), we obtain

$$\Delta A_1 = \frac{1}{24} E \left(\frac{h}{R} \right)^2 \tag{26.11}$$

From [8] it is known that $E = 2 \cdot 10^{11}$ Pa. Given this, we obtain $\Delta A_1 \approx 1.3 \cdot 10^7$Pa. Since ΔA_1 is two orders of magnitude greater than $\Delta A_,$ therefore, it is energetically advantageous for the chains to be located on the surface of the cylindrical pore along the generatrix. In this case, a three-dimensional structure is formed (Fig. 26.2a).

Thus, the chain is not located perpendicular to the pore axis, since in this position the chain experiences a strong bend. This conclusion was obtained because the cross section of the pore is approximately represented as a circle. In the case when the cross section of the pore has the shape of a polygon, the chains, as shown in [9], can be located perpendicular to the axis of the pore on flat faces. Obviously, such a situation is only possible when the length of chain is equal or less than the size of the face.

26.6 The Mechanism of Formation of a Two-Dimensional Crystal Structure

According to the theory of crystallization [10], it can be argued that crystallization in pores begins from the surface. Crystal growth occurs in the direction perpendicular

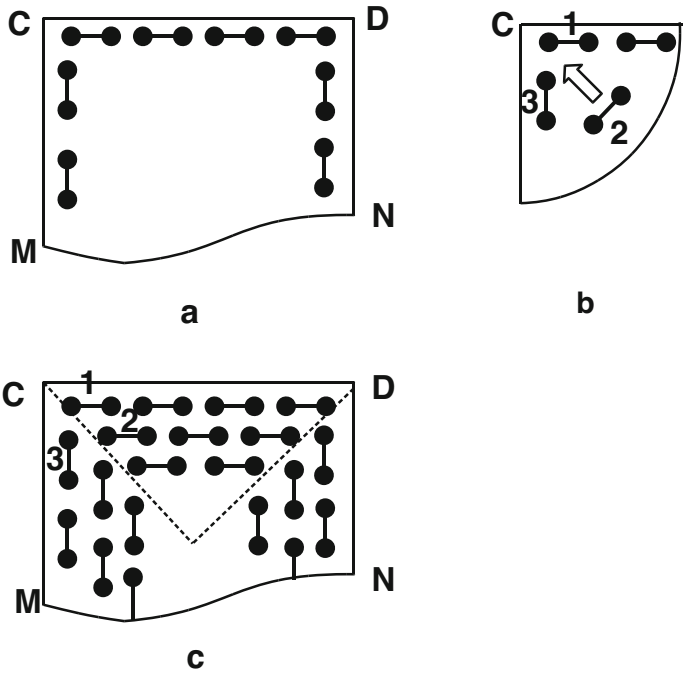

Fig. 26.6 Formation of a two-dimensional crystal structure during crystallization. (CD is the generatrix of the cylinder, the lines CM and DN is located on the bases of cylinder)

to the surface. This leads to the formation of a defective crystal lattice near the bend line of the pore surface.

To carry out the analysis we use Fig. 26.6. Consider the intersection line of the base of the cylinder and its lateral surface (Fig. 26.4b). In a section through the cylinder axis, these lines are projected to points C and D (Fig. 26.6).

The bases of the cylinder are flat. Therefore, the first layer of chains is located parallel to these surfaces (CM and DN in Fig. 26.6a). At the same time, the first layer appears on the lateral surface, where the chains are arranged parallel to the generatrix (CD in Fig. 26.6a).

Then begins the construction of the second layer. In order to form an ideal lattice (Fig. 26.2a), the molecules try to locate exactly above the molecules of the first layer. Thus, for example, molecule 2 should have been located above molecule 1 (Fig. 26.6b). However, molecule 3 interferes with it, therefore molecule 1 shifts in the direction parallel to the surface of the pore (Fig. 26.6c).

This happens for both the CM surface and the DN surface (Fig. 26.6c).

In Fig. 26.6c, it is shown that the original structure is not an ideal lattice. In this structure, disorder arises in the direction of the long axes of molecules. Comparing Figs. 26.6c and 26.2b, we conclude that the structure formed is a two-dimensional crystalline structure.

The proposed mechanism of formation of two-dimensional crystal structure explains the basic result of the experiment. Namely, system A does not have a two-dimensional crystalline structure due to the fact that, in contrast to system B, the pore surface of system A does not contain bends.

26.7 Conclusions

Located in the pores of a solid matrix, chain molecules can form both a two-dimensional and three-dimensional crystal structure. The two-dimensional structure differs from the three-dimensional one in that the periodicity in it disappears along the orientation axis of the chains.

A two-dimensional structure occurs when the surface of the pore contains sharp bends. During crystallization, crystallites grow on the surface areas adjacent to the bend line. The growth direction is normal to the surface. The surface areas are inclined with respect to each other, so the crystals in these areas interfere with each other during their growth. This circumstance leads to the fact that the crystallizing structure is two-dimensional.

References

1. Landau LD, Lifshitz EM (2013) Statistical physics. Elsevier, Butterworth-Heinemann, p 544
2. Chandrasekar S, Sadashiva BK, Suresh KA (1979) Disc-like mesogens. J Phys (France) Coll 40(3)
3. Huber P, Wallacher D, Albers J, Knorr K (2004) Quenching of lamellar ordering in an n-alkane embedded in nanopores. EPL (Europhys Lett) 65(3):351
4. Manilov AI, Alekseev SA, Skryshevsky VA, Litvinenko SV, Kuznetsov GV, Lysenko V (2010) Influence of palladium particles mpregnation on hydrogen behavior in meso-porous silicon. J Alloys Compd 492:466
5. Lazarenko MM, Alekseev AN, Alekseev SA, Grabovsky YE, Lazarenko MV (2011) Phase transitions of alyphatic molecular crystals in confined space. Chem Phys Technol Surf 2(2):128–134
6. Wunderlich B, Baur H (1970) Heat capacities of linear high polymers. Springer, Berlin, Heidelberg, pp 151–368
7. Landau LD, Pitaevskii LP, Kosevich AM, Lifshitz EM (2012) The theory of elasticity, 3rd edn. Elsevier, Butterworth-Heinemann, p 195
8. Sakurada I, Nukushina Y, Ito T (1962) Experimental determination of the elastic modulus of crystalline regions in oriented polymers. J Polym Sci 57(165):651–660
9. Henschel A, Hofmann T, Huber P, Knorr K (2007) Preferred orientations and stability of medium length n-alkanes solidified in mesoporous silicon. Phys Rev E 75(2):021607
10. Frenkel J (1984) Kinetic theory of liquids. Peter Smith Publisher, Gloucester

Chapter 27
Joint Electroreduction of Carbonate and Tungstate Ions as the Base for Tungsten Carbide Nanopowders Synthesis in Ionic Melts

Oleksandr Yasko, Viktor Malyshev, Angelina Gab, and Tetiana Lukashenko

27.1 Introduction

An analysis of the literature shows that high-temperature electrochemical synthesis in ionic melts is a very promising method for obtaining tungsten carbides [1–4]. This method has the following advantages:

- It does not need tungsten and carbon to be powdered.
- It requires lower temperatures than the other methods.
- It uses the most available tungsten and carbon compounds.
- The synthesis is easy to control and can be conducted so as to obtain a coating or a powder with a desired particle size.
- The resulting product is very pure.
- Electrolyte regeneration is possible, making the process wasteless.

An analysis of the state of the art in the high-temperature electrochemical synthesis of tungsten carbide [2, 5] demonstrates that further advancement of this technology is possible only through working out its theory; elucidating the mechanism of electrodeposition; and learning to conduct and control the tungsten and carbon electrodeposition reactions, which are multielectron electrode processes. Since a necessary condition for electrodeposition of a compound is the similarity of the deposition potentials of its components, it is necessary to find ways of ensuring this similarity and the conditions under which the desired electrode reactions will occur simultaneously.

O. Yasko (✉) · V. Malyshev · A. Gab · T. Lukashenko
Institute for Engineering & Technology, University “Ukraine”, Kyiv, Ukraine
e-mail: o.yasko@meta.ua

O. Fesenko, L. Yatsenko (eds.), *Nanocomposites, Nanostructures, and Their Applications*, Springer Proceedings in Physics 221,
https://doi.org/10.1007/978-3-030-17759-1_27

27.2 Simultaneous Electroreduction of the Carbonate and Tungstate Ions in Chloride-Fluoride and Oxide Melts

Tungstate electroreduction in chloride and oxide melts was shown [6] to be possible only in the presence of fairly strong acids such as Mg^{2+}, Al^{3+}, PO_3^-, and MoO_3. Weaker acids (Li^+, Ba^{2+}, Ca^{2+} etc.) should be added in a large excess. On the other hand, the carbonate ion in the presence of excess Li^+ cations decomposes to yield CO_2. For this reason, the simultaneous electroreduction of the carbonate and tungstate ions is difficult to accomplish, requiring a fine control of the melt acidity (basicity).

We studied the simultaneous electroreduction of CO_3^{2-} and WO_4^{2-} in both chloride-fluoride (NaCl-LiF) and oxide (Na_2WO_4) melts [7]. The F^- and WO_4^{2-} ions stabilize the carbonate ions in these systems. Figure 27.1 presents voltammograms for a NaCl-LiF (3:1) melt containing sodium carbonate. The reduction wave of the carbonate ion was detected at Na^+ concentrations as high as 5 wt %. We ascribe the faint and poorly reproducible wave at −0.5 to −0.8 V to the electroreduction of CO_2, which results from CO_3^{2-} decomposition. We observed no reduction wave of the tungstate ion in the NaCl-LiF (3:1) melt (Fig. 27.1). However, as the tungstate concentration is increased, the residual current grows, the voltammetric curve shifts to more positive potentials, and dissolution waves emerge during the reverse potential sweep. Further, we were unable to detect the wave due to the simultaneous reduction of the WO_4^{2-} and CO_3^{2-} ions (Fig. 27.1, curve 4) but observed a positive shift of the voltammetric curve. The product of the potentiostatic electrolysis at −1.4 to −1.5 V was W_2C, WC, or their mixture, depending on

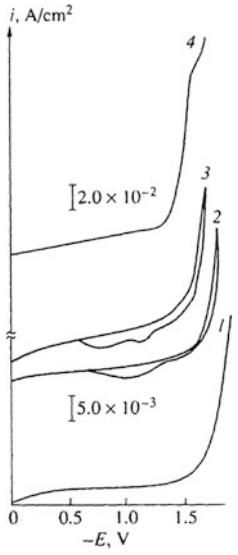

Fig. 27.1 Voltammograms of the NaCl-LiF (3:1) melt containing Na_2WO_4 at $C \times 10^4 =$ (1) 0, (2) 1.6, and (3–4) 2.75 mol/cm^3 and Na_2CO_3 at $C \times 10^4 =$ (1–3) 0, (4) 3.22 mol/cm^3. $T = 1113$ K; potential sweep rate, 0.1 V/s; platinum-oxygen reference electrode; platinum cathode

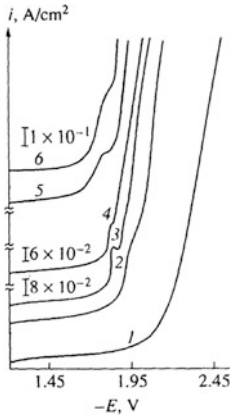

Fig. 27.2 Voltammograms of the Na_2WO_4 melt containing (1) 0, (2) 30, and (3–6) 40 mol % Li_2WO_4 and (1–3) 0, (4) 1.0, (5) 5.0, and (6) 10.0 mol % Li_2CO_3. $T = 1123$ K; potential sweep rate, 0.1 V/s; nickel cathode

Table 27.1 Phase composition of the electrolysis product of the Na_2WO_4-Li_2WO_4 (40 mol %)-Li_2CO_3 melt at various lithium carbonate concentrations C and electrolysis potentials E (vs. Pt, $O_2/(Na_2WO_4–0.2WO_3)$) and $T = 1123$ K

C. mol %	E,V	Phase composition
0	1.90	W
1.0	1.90	W, traces of W_2C
2.5	1.90	W,W_2C, traces of WC
5.0	1.85	W_2C, WC
10.0	1.80	WC, W_2C
15.0	1.80	WC

the concentration ratio of Na_2WO_4 to Na_2CO_3. Thus, our voltammetric studies provided the deposition potentials of tungsten, carbon, and tungsten carbides, which are close to the decomposition potential of the stock melt.

The electroreduction of the carbonate and tungstate ions in a sodium tungstate melt was discussed in [7]. It is difficult to detect the reduction wave of lithium tungstate on the background of Na_2WO_4. Adding lithium tungstate up to 20 mol % gave rise to no waves but caused a positive shift of the voltammetric curve relative to that of pure tungstate (Fig. 27.2). A wave is detectable only at lithium tungstate concentrations above 20 mol %. The reduction wave of lithium tungstate is observed at its concentration 40 mol % and a potential of -1.8 to -1.9 V relative to a Pt, O_2/Na_2WO_4-$0.2WO_3$ electrode. Adding lithium carbonate to the Na_2WO_4-Li_2WO_4 melt initially causes an increase in the height of the lithium tungstate reduction wave. The reduction wave of the carbonate ion, followed by lithium tungstate electroreduction, appears at a lithium carbonate concentration of 10 mol %. At the lithium carbonate concentration of 15 mol %, the tungstate and carbonate reduction waves merge in a single broad electroreduction wave. Potentiostatic electrolysis data, in relation to the Li_2CO_3 concentration, are presented in Table 27.1.

27.3 High-Temperature Electrochemical Synthesis of Tungsten Carbides

27.3.1 Electrochemical Synthesis of Fine Tungsten Carbide Nanopowders from Oxide Melts

From fine tungsten carbide nanopowders with submicron-sized particles, it is sometimes possible to prepare very hard ceramics and cermets [8, 9]. The electrosynthesis of WC and W_2C in a CO_2 atmosphere can be conducted at low current densities (the optimum i value is 0.1 A/cm^2) to obtain carbide particles 2–5 μm large. Smaller particles form at higher i values, which are attainable in alkali-metal tungstate melts containing carbonate ions as the source of carbon. Tungsten carbide was obtained from the electrolyte composed of 10–20 mol % Li_2CO_3, 30–45 mol % Na_2WO_4, and Li_2WO_4 at $T = 1073$–1173 K and $i = 1.0$–1.7 A/cm^2. Varying the concentrations of the melt components modifies the product composition. Melts containing less than 10 mol % Li_2CO_3 yield a WC + W_2C + W mixture with component proportions depending on the carbonate concentration. At Li_2CO_3 concentrations above 20 mol %, the product is contaminated by free carbon. Pure tungsten carbide forms from melts containing 5–45 mol % lithium tungstate. At the other Li_2WO_4 concentrations, the desired product is contaminated by tungsten oxide.

The product composition depends strongly on the synthesis temperature. A WC + W_2C mixture forms below 1073 K, and a W_2C or a W_2C + W mixture results at 1023 K and below. Raising the temperature above 1173 K is inexpedient because of the thermal instability of the carbonate ion and the increasing volatility of the melt components. The cathodic current density is governed by the carbonate concentration in the melt. Striving for finer powders, we conducted the electrosynthesis at the highest possible current densities. In optimal melts, i varied between 1.0 and 1.7 A/cm^2, yielding tungsten carbide powders with a specific surface area of 10–20 m^2/g.

27.3.2 Electrodeposition of Tungsten Carbide Coatings from Tungstate-Halide Melts

In oxide melts, the tungsten concentration is exceedingly high. It can be reduced by using the NaCl-LiF eutectic as a flux for the oxide bath. In this flux, the tungstate-to-tungsten decomposition occurs at a potential 200 mV more negative than the carbonate-to-carbon decomposition (Fig. 27.1). It is almost impossible to obtain a continuous WC deposit, because WC forms in the presence of free carbon, which is known to passivate the growth front of electrodeposits. Therefore, a finer process control is necessary to obtain a continuous WC deposit. Electrosynthesis should be conducted in a melt that is suitable for preparing W_2C, which forms as a continuous

Table 27.2 Cathodic deposits obtained by electrolysis in the NaCl- LiF-Na_2WO_4-Na_2CO_3 system (graphite anode, $T = 1173$ K, $i_{cath} = 0.08$ A/cm^2)

Concentration, wt %				Cathodic deposit
NaCl	LiF	Na_2WO_4	Na_2CO_3	
67.5	22.5	10	–	Tungsten coating W
67.5	22.5	10	–	Non-adherent W-W_2C deposit
71.6	23.7	5	0.2	W_2C-W coating
70.9–71.1	23.6–23.7	5	0.2–0.5	W_2C coating
70.9	23.6	5	0.5	W_2C-C coating
70.5	23.5	5	1.0	Non-adherent WC-C deposit

deposit at 1073–1173 K (Table 27.2). At lower temperatures, W_2C forms as a powder. Adhering coatings on carbon, copper, nickel, tungsten, molybdenum, and steels were deposited at $i = 0.02$–0.15 A/cm^2 and deposition rates no slower than 10 μm/h. The thickness of the coatings was 20 μm.

27.4 Conclusions

1. The conditions were selected experimentally for potential convergence and electroreduction realization of carbonate and tungstate ions in halide and halide-oxide melts.
2. Electrolytes compositions and electrolysis conditions (melt temperature, cathode current density) were elaborated for tungsten carbide electroreduction both in the form of coatings and nanopowders.

References

1. Novoselova IA, Malyshev VV, Shapoval VI, Kushkhov KB, Devyatkin SV (1997) Theoretical foundations of high-temperature electrochemical synthesis technology in ionic melts. Theor Found Chem Eng 31(3):286–295
2. Novoselova IA, Kushkhov KB, Malyshev VV, Shapoval VI (2001) Theoretical foundations and implementation of high-temperature electrochemical synthesis of tungsten carbide in ionic melts. Theor Found Chem Eng 35(2):175–187
3. Kuznetsov SA (2009) Electrochemistry of refractory metals in molten salts: application for the creation of new and functional materials. Pure Appl Chem 81(8):1423–1439
4. Stulov YV, Dolmatov VS, Dubrovskiy AR, Kuznetsov SA (2017) Electrochemical methods for obtaining thin films of the refractory metal carbides in molten salts. Int J Electrochem Sci 12:5174–5184
5. Volkov SV (1990) Chemical reactions in molten salts and their classification. Chem Soc Rev 19:21–28
6. Shapoval VI, Soloviev VV, Malyshev VV (2001) Electrochemically active species and multi-electron electrochemical processes in ionic melts *Russ*. Chem Rev 70(2):161–176

7. Malyshev VV, Soloviev VV, Chernenko LA, Rozhko VN (2015) Management of composition cathodic products in the electrolysis of molydenum-, tungsten- and carbon-bearing halogenide-oxide and oxide melts. Materialwissenschaft und Werkstofftechnik (Mater Sci Eng Technol) 45(11):67–72
8. Ovcharenko VE, Ivanov YF, Mokhovikov AA, Ivanov KV, Ul'yanitsky VY (2016) Nanostructuring and physical properties of metal-ceramic composites with a different content the ceramic components. IOP Conf Ser: Mater Sci Eng 125:012008. https://doi.org/10.1088/1757-899X/125/1/012008
9. do Nascimento RM, Martinelly AE, Buschinelli AJA (2003) Recent advances in metal-ceramic brazing. Cerâmica 49(312):178–198. https://doi.org/10.1590/S0366-69132003000400002

Chapter 28
The Kinetics Peculiarities and the Electrolysis Regime Effect on the Morphology and Phase Composition of Fe-Co-W(Mo) Coatings

Iryna Yu. Yermolenko, Maryna V. Ved', and Nikolay D. Sakhnenko

28.1 Introduction

The formation of functional coatings combining corrosion resistance, hardness, wear resistance, and catalytic activity is determined by the design of new materials. Application of such alloys has contributed to a large extent to the progress in many modern technologies [1, 2].

The advantages of the electrochemical technique for deposition thin-film multicomponent systems compared with other methods are as follows. First of all, there is flexible control of the components' content, the deposition rate, and the surface state using variations in both the composition of the electrolytes and the polarization modes (static or pulsed, reverse current, or potential decrease) [3, 4]. This allows coatings of different qualitative and quantitative composition and with the desired complex of functional properties to be obtained [5–7].

Second, the simplicity of electrochemical deposition and the above process control compared with other methods, in addition to the possibility of creating local technological modules, makes it possible to consider such a method the most convenient and cost-effective [8].

The functional properties and performance characteristics of the electrolytic thin film coatings of iron triads with D^4 elements, in particular molybdenum and tungsten, essentially exceed the characteristics of alloy-forming components [9–11], which attracts the increased interest of researchers.

The problem is to predict the composition and properties that remain a main barrier to the broad introduction of the electrochemical synthesis of binary and ternary alloys of iron and cobalt with tungsten or molybdenum. This is related

I. Y. Yermolenko (✉) · M. V. Ved' · N. D. Sakhnenko
National Technical University "Kharkiv Polytechnic Institute", Kharkiv, Ukraine

O. Fesenko, L. Yatsenko (eds.), *Nanocomposites, Nanostructures, and Their Applications*, Springer Proceedings in Physics 221,
https://doi.org/10.1007/978-3-030-17759-1_28

to relatively complicated and ambiguous processes in the electrolyte, and at the electrolyte/electrode interface at cathode polarization.

Many scientific papers are devoted to the synthesis of binary alloys Fe(Ni, Co)–Mo(W) using the electrolytes of a different qualitative and quantitative composition; however, scientific circles have no common conception of the mechanism of the co-deposition of the above metals into the alloy.

Gómez et al. [12] believe that the most probable mechanism for the co-deposition of cobalt with molybdenum from the citrate electrolyte is the reduction of oxoanion producing intermediate oxide MoO_2 in the presence of citrate cobalt clusters that act in this case as a catalyst:

$$MoO_4^{2-} + 2H_2O + 2e \xrightarrow{CoCit^-} MoO_2 + 4OH^-, \tag{28.1}$$

followed by adsorbed intermediate formation according to the mechanism offered in Podlaha and Landolt [13]:

$$CoCit^- + 2e \rightarrow Co + Cit^{3-} \tag{28.2}$$

$$CoCit^- + MoO_2 \rightarrow [MoO_2\text{–}CoCit^-]_{ad} \tag{28.3}$$

$$[MoO_2\text{–}CoCit^-]_{ad} + 2H_2O + 4e \rightarrow Mo + CoCit^- + 4OH^-. \tag{28.4}$$

Younes et al. [14] surmise that the electrode-active mixed citrate cluster of nickel and tungsten is formed in the solution or on the electrode surface, which is the precursor for nickel and tungsten alloy synthesis. However, they failed to prove the presence of these particles in the solution.

Nevertheless, Younes-Metzler et al. [15] demonstrated indirect evidence for the mixed nickel–tungstate–citrate cluster formation in the reaction:

$$[(Ni)\,(Cit)]^- + [(WO_4)\,(Cit)\,(H)]^{4-} \rightarrow [(Ni)\,(WO_4)\,(Cit)\,(H)]^{2-} + Cit^{3-}. \tag{28.5}$$

Data on gel-chromatographic separation of citrate [16] and gluconate [17] electrolytes into components with different molecular masses also support the hypothesis on the formation of mixed clusters. This allows us to arrive at a conclusion that citrate and multinuclear hetero-metal clusters are formed, which are the precursors of the deposition of cobalt–tungsten alloys.

On the one hand, the proposed mechanisms to a certain extent reflect the scientific views of various electrochemical schools. On the other hand, they are based on the results of studies on specific electrochemical systems of adjusted concentration and ratio of components in the electrolyte pH, etc. Therefore, these mechanisms are not universal and cannot describe all possible reactions during the alloy electrodeposition.

Special attention is paid to the production of electrolytic iron alloys, in particular, Fe-Co-W and Fe-Co-Mo, which are fundamentally different from others by the application of electrolytes based on both iron(II) and iron(III) for deposition [18]. It should be noted that the tendency of iron toward hydrolysis substantially influences the ion equilibrium in the water solution, the electrolyte pH, and consequently the nature of electrode-active particles [19, 20].

For the above-mentioned reasons, issues regarding the control and management of quantitative and phase composition, surface morphology, and the properties of coatings remain relevant.

28.2 Experimental

The kinetics of cathode processes was studied using electrodes made of low-carbon steel with a working area of $7.8 \cdot 10^{-2}$ cm^2 in the solutions with a constant concentration of iron(III) sulfate, cobalt, and sodium citrate. The concentration of sodium molybdate and sodium tungstate varied within the range of 0.004–0.008 mol/dm^3 against a background of 1 M Na_2SO_4 (Table 28.1). The electrolyte solutions were prepared using the certified reagents of chemically pure grade distilled water. The acidity of working solutions was controlled by a pH meter pH 150 M with the glass electrode ESL-6307.

Voltamperometric measurements were taken in the three-electrode glass cell with the chloride-silver reference electrode EV-1 M1 and an auxiliary platinum electrode. This chapter gives all the potentials with regard to a standard hydrogen electrode. The polarization was conducted using the potentiostat PI-50-1.1 with the programmer PR-8; the potential scanning rate varied within the range of $2 \cdot 10^{-3}$–$1 \cdot 10^{-1}$ V/s. Output parameters were registered by the computer using special-purpose "polarization" software.

To analyze the experimental data and define kinetic regularities and the mechanism of cathode reactions, we used kinetic parameters and characteristic criteria [21]: the peak potential E_p and semipeak potential $E_{p/2}$, V; the peak current density i_p, A/dm^2; the product of the transfer coefficient and the electron number αz; the orders of reactions p_i, the Semerano criterion X_s, and the concentration criterion X_c.

Table 28.1 The composition of electrolytes for the study of kinetics

	Concentration, mol/dm^3 for deposits	
Component	Fe-Co-W	Fe-Co-Mo
Na_2SO_4	1	1
Fe^{3+}	0.02	0.02
Co^{2+}		
Cit^{3-}	0.03	0.03
MoO_4^{2-}	–	0.005–0.008
WO_4^{2-}	0.004–0.008	–

To verify the data, the αz product for the irreversible step (stage) was defined using two modes:

– An angle coefficient of the relationship in E_{Π}–lg$s$ coordinates

$$\frac{\Delta E_{\Pi}}{\Delta \lg s} = -\frac{2,303RT}{azF} \tag{28.6}$$

– The Matsuda and Ayabe equation:

$$\mathrm{E}_{\Pi} - \mathrm{E}_{\Pi/2} = -1.85\frac{RT}{azF}. \tag{28.7}$$

where s is the potential scanning rate, V/s; R is the universal gas constant, and T is the thermodynamic temperature, K.

Apparent orders of the reaction p_i were calculated using the concentration relationships of the rate of irreversible electrode reaction as a function of components at a constant content of other components:

$$p_i = \frac{\Delta \lg i_{\mathrm{E}}}{\Delta \lg c_i}, \tag{28.8}$$

where i_{E} is the current density for the prescribed potential and c_i is the concentration of the i-th kind of ions in the solution.

Coatings were deposited onto the substrates of low-carbon steel and the copper from a citrate electrolyte based on iron(III) by a constant and a pulse current (Table 28.2).

The chemical composition and morphology of coatings were defined using the X-ray fluorescent method and portable spectrometer "SPRUT" with a relative standard error of 10^{-3}–10^{-2}, the measurement error of the percentage of components was equal to ±1 wt.%. To verify the data, energy-dispersive X-ray spectroscopy was performed using the electron-probe microanalyzer Oxford INCA Energy 350, integrated into the scanning electron microscopy system [22]. The X-ray radiation was induced by the exposure of specimens to an electron beam of 15 keV. The patterns were obtained by the registration of backscattered secondary electrons with electron beam scanning, which allowed us to study the topography with high resolution and contrast.

In this chapter, the composition of the coatings is given in wt.% (in terms of metal).

The phase composition of coatings was studied using the method of X-ray analysis. The survey was done using the X-ray diffractometer DRON-2.0 in cobalt anode radiation. The diffraction pattern was recorded in the discrete mode every other 0.1° with exposition at each point of 20 s. To define the phase composition, the specimens Fe-Co-W and Fe-Co-Mo on a copper substrate were used with the alloy coating thickness h of at least 20 μm.

Table 28.2 Electrolytes and electrolysis regimes for the deposition of Fe-Co-W(Mo) coatings

Composition of coating, ω, wt.% (in terms of metal):	Composition of electrolyte, mol/dm^3	Electrolysis mode
Fe – 54 Co – 36 W – 10	0.075 $Fe_2(SO_4)_3$•9H_2O 0.200 $CoSO_4$•7H_2O 0.06 Na_2WO_4•2H_2O 0.5 Na_3Cit•2H_2O	$i = 4.5$ A/dm^2
Fe – 54 Co – 35 W – 11		$i = 5$ A/dm^2, $t_{on}/t_{off} = 5$ ms/5 ms
Fe – 31 Co – 31 Mo – 38	0.075 $Fe_2(SO_4)_3$•9H_2O 0.200 $CoSO_4$•7H_2O 0.06 Na_2MoO_4•2H_2O 0.5 Na_3Cit•2H_2O	$i = 3.0$ A/dm^2
Fe – 51 Co – 36 Mo – 13	0.075 $Fe_2(SO_4)_3$•9H_2O 0.200 $CoSO_4$•7H_2O 0.06 Na_2MoO_4•2H_2O 0.3 Na_3Cit•2H_2O	$i = 3.0$ A/dm^2
Fe – 50 Co – 39 Mo – 11		$i = 3$ A/dm^2, $t_{on}/t_{off} = 2$ ms/5 ms

28.3 Theoretical Aspects

Electrodeposition of iron subgroup metals with tungsten and molybdenum into the ternary coating depends on the thermodynamic and crystal–chemical characteristics of the alloy-forming metals, in addition to the kinetic parameters of the cathode process.

Metal potentials, electronegativity and an affinity for oxygen, the ability to form complexes, and the tendency toward hydrolysis are associated with thermodynamic characteristics.

Crystal–chemical parameters reflect the structure and characteristics of the crystal lattice of individual metals, the size of cations and oxometallates, etc., and greatly affect the mutual arrangement and embedding of atoms into the crystal lattice of the alloy.

The ratio of the concentration of alloying metals in the electrolyte, modes, and electrolysis parameters are tools for overcoming the energy and geometric differences of metals, which are co-reduced.

The prerequisites for the formation of ternary coatings are based on the convergence of the potentials for the reduction of iron, cobalt, tungstate, and molybdate, which occurs step by step according to the half-reactions given in Table 28.3.

The competition of metals in the formation of complex compounds with oxygen-containing ligands is due to their acceptor ability, which is quantitatively characterized by electronegativity and affinity for oxygen.

The affinity of the metal to oxygen can be quantified by the metal-oxygen bond energy (Table 28.4).

Table 28.3 Equilibrium potentials of electrode reactions

	Reaction	Electrode potential E, B
1	$Fe^{3+} + e = Fe^{2+}$	$\mathbf{0.77}^{*} + 0.059\ \lg[c(Fe^{3+})/c(Fe^{2+})]$
2	$Fe^{2+} + 2e = Fe^{0}$	$-\mathbf{0.44} + 0.0295\ \lg c(Fe^{2+})$
3	$Co^{2+} + 2e = Co$	$-0.277 - 0.02951\ \lg c(Co^{2+})$
4	$Co(OH)_2 + 2H^{+} + 2e = Co + 2H_2O$	0.095 0.059 pH
5	$MoO_4^{2-} + 4H^{+} + 2e = MoO_2 + 2H_2O$	$\mathbf{0.606} - 0.1182$ pH $+ 0.0295$ $\lg c(MoO_4^{2-})$
6	$MoO_4^{2-} + 8H^{+} + 3e = Mo^{3+} + 4H_2O$	$\mathbf{0.508} - 0.1576$ pH $+ 0.0197$ $\lg[c(MoO_4^{2-})/c(Mo^{3+})]$
7	$MoO_2 + 4H^{+} + 4e = Mo + 2H_2O$	$-\mathbf{0.072} - 0.059$ pH
8	$WO_4^{2-} + 4H^{+} + 2e = WO_2 + 2H_2O$	$\mathbf{0.386} - 0.1182$ pH $+ 0.2951$ lg $c(WO_4^{2-})$
9	$WO_2 + 4H^{+} + 4e = W + 2H_2O$	$-\mathbf{0.119} - 0.0591$ pH

The data are provided by Ved' and Sakhnenko [23]
*Standard red-ox potentials of half-reactions are shown in bold

Table 28.4 The thermodynamic and crystal–chemical characteristics of the alloy-forming metals

Parameter	Fe	Co	Mo	W
$E_{M–O}$, кДж/моль	218.0	238.5	274.5	223.0
Electronegativity, X	1.8	1.9	1.8	1.7
Atomic radius, нм	0.126	0.125	0.139	0.141
The ionization energy, eV	7.87	7.86	7.10	7.98
Lattice structure	Cubic Body-centered	Hexagonal	Cubic Body-centered	Cubic Body-centered
Lattice parameters, Å	2.866	$a = 2.505$, $c = 4.089$	3.147	3.160

Close values of the relative electronegativity of metals indicate almost the same acceptor activity of metals.

Oxygen in oxoanions is an electron donor for hetero-nuclear complexes formed by iron and cobalt. However, the strength of M–O bonds is different because of various bonding energies $E_{M–O}$ (Table 28.4).

In our opinion, the higher the $E_{M–O}$, the higher the probability of heteronuclear complex $[M1^{z}CitM2O_4]^{(z–5)}$ (where M1 – Fe, Co; M2 – Mo, W) formation [23].

Metals are arranged by the strength of the bond $E_{M–O}$ [23]: Fe < W < Co < Mo.

As can be seen from the data analysis (Table 28.4), it is fully justified to assume the competitive reduction of alloying metals into the ternary alloys. In particular, iron is competing with cobalt in addition to iron with tungsten when deposited into the alloy Fe-Co-W. Deposition of a Fe-Co-Mo coating is characterized by the competitive reduction of iron and cobalt, in addition to competition between alloying metals.

The factors required to overcome the energy barrier and to have an effect on the coating composition can be considered to be: the variation of the concentration

of the alloying components in the electrolyte and the ligand addition. The most significant factor is the ratio of the complexing agents and ligand concentration.

The hexagonal, closely packed crystal lattice of cobalt simultaneously with different lattice parameters of alloy-forming metals determines lattice deformation and deceleration of the linear growth of the crystals. In this case, we can expect the formation of spheroid structures.

The atomic radii of molybdenum and tungsten exceed the atomic radii of iron and cobalt by ~10% (Table 28.4); therefore, in formation of the mono-atomic layer, the attached atoms are forced to dislocate from equilibrium positions, thus increasing the probability of "polycrystalline to amorphous" transition in the films of deposited alloys [24].

Amorphization of coatings becomes possible owing to the difference in atomic size and the crystal lattice parameters of the base metal (iron) and the alloying components (Co, Mo, W) when the concentration of the latter reaches values in excess of 20–25 wt.% [24], which causes the transition from crystalline to amorphous states.

The hydrogen discharge at the cathode at the same time as electrodeposition complicates and inhibits the process of crystal structure building [25], and is thus an additional factor in the formation of the amorphous structure multicomponent coatings of iron and cobalt with molybdenum and tungsten.

The close values of the first ionization potentials of iron, cobalt, and tungsten create the background for the formation of donor–acceptor and covalent bonds between metals and metals with ligand. Hence, there is a probability of the co-deposition of these metals into an alloy producing intermetallic compounds.

The energy and time parameters of electrolysis should be considered as the factors influencing the process of nucleation and growth of crystals in such multi-component alloys.

28.4 Electrochemical Behavior of Fe^{3+}–Co^{2+}–WO_4^{2-}–Cit^{3-} and Fe^{3+}–Co^{2+}–MoO_4^{2-}–Cit^{3-} Systems

The Fe^{3+}–Co^{2+}–WO_4^{2-}–Cit^{3-} and Fe^{3+}–Co^{2+}–MoO_4^{2-}–Cit^{3-} systems are extremely complicated and mobile from the standpoint of ion equilibriums. It is impossible to mark out the partial relationships of the reduction of molybdenum and tungsten, because these cannot be reduced independently in the form of individual metals out of water solutions.

The competing reactions of the hydrolysis of iron cations and their complex formation in aqueous solutions, the constants of the instability of iron and cobalt citrate complexes, and the structure of oxometallates are the prerequisites for discharging particles of various natures at the cathode [26].

We analyze the logarithmic concentration diagrams for heterogeneous systems and the instability constants of iron and cobalt citrate complexes, the hydrolysis

constants, and conclude that iron cathodic reduction occur simultaneously from some ionic forms [20]. The contribution of each of the reactions to the overall process is determined by the initial concentration of iron(III) sulfate and the pH of the solution; the cobalt deposition occurs predominantly from the citrate complex.

The kinetics of the electrochemical deposition of the ternary alloys was studied in the electrolytes with constant concentrations of iron(III), cobalt, and citrate ion(III). The concentration of tungstate ions varied within the range 0.004–0.008 mol/dm^3.

The addition of tungstate or molybdate into the electrolyte changes the pH of the solution within the range 4.8–5.3 with an increase in the concentration of oxoanions.

Voltammograms obtained on a steel electrode in the solutions at the same concentration of oxometallates have some differences.

First, the potential of the electrode in a solution containing molybdates is more positive (Fig. 28.1).

Second, the polarization dependences registered in the solution containing molybdates within the potential range of −0.60 to –0.80 V are more gentle, which indicates the influence of adsorption, and an increase in the potential scan rate up to 100 mV/s leads to the peak degeneration.

The slight decrease in current density is observed within the potential range of −0.80 to –0.95 V as being the result of diffusion limitation, namely the reaction products being removed from the electrode/electrolyte interfacial boundary, and adsorption of the atomic hydrogen on the surface of the electrode.

The maximum current density at a concentration of tungsten ions of 0.04 mol/dm^3 in the Fe^{3+}–Co^{2+}–MoO_4^{2-} system (Table 28.5) is observed and the highest rate of the process corresponds to the molybdate concentration of 0.06 mol/dm^3 in the Fe^{3+}–Co^{2+}–MoO_4^{2-} system (Table 28.5).

The analysis of kinetic parameters and characteristic criteria of cathodic reactions gives grounds to consider the mechanism of the co-deposition of metals in the Fe^{3+}–Co^{2+}–WO_4^{2-}–Cit^{3-} and Fe^{3+}–Co^{2+}–MoO_4^{2-}–Cit^{3-} systems to be similar.

Indeed, the Semerano criterion is 0.5, and the linear dependencies in the coordinates $i_p - \sqrt{s}$ indicate the irreversibility of the cathode process (Fig. 28.2).

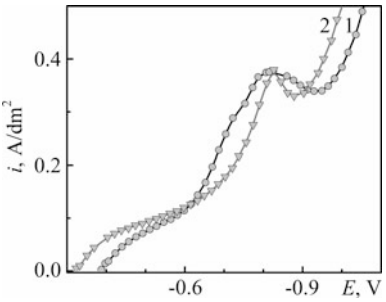

Fig. 28.1 Voltammograms for the steel electrode in the composition of the electrolytes, mol/dm^3: 1 Na_2SO_4, 0.01 Fe^{3+}, 0.02 Co^{2+}, 0.04 Cit^{3-}; 1–0.006 WO_4^{2-} and 2–0.006 MoO_4^{2-}, $s = 2 \cdot 10^{-2}$ B/c

Table 28.5 Kinetic parameters for the system Fe^{3+}–Co^{2+}–WO_4^{2-}–Cit^{3-} and Fe^{3+}–Co^{2+}–MoO_4^{2-}–Cit^{3-}

Electrolyte composition, mol/dm^3	pH	s, V/s	E_p, V	$E_{p/2}$, V	i_p, A/dm^2	αz	X_s
$1Na_2SO_4$ $0.01Fe^{3+}$ $0.02Co^{2+}$ $0.04Cit^{3-}$ **$0.004\ WO_4^{2-}$***	4.8	$2\cdot10^{-3}$	−0.78	−0.65	0.22	0.37	0.42
		$2\cdot10^{-2}$	−0.84	−0.66	0.52	0.27	
		$5\cdot10^{-2}$	−0.96	−0.72	0.84	0.20	
$1Na_2SO_4$ $0.01Fe^{3+}$ $0.02Co^{2+}$ $0.04Cit^{3-}$ **$0.006\ WO_4^{2-}$**	5.1	$2\cdot10^{-3}$	−0.74	−0.65	0.18	0.53	0.34
		$2\cdot10^{-2}$	−0.82	−0.67	0.38	0.32	
		$5\cdot10^{-2}$	−0.83	−0.69	0.53	0.34	
$1Na_2SO_4$ $0.01Fe^{3+}$ $0.02Co^{2+}$ $0.04Cit^{3-}$ **$0.008\ WO_4^{2-}$**	5.3	$2\cdot10^{-3}$	−0.72	−0.62	0.15	0.48	0.42
		$2\cdot10^{-2}$	−0.82	−0.68	0.39	0.34	
		$5\cdot10^{-2}$	−0.85	−0.70	0.57	0.32	
$1Na_2SO_4$ $0.01Fe^{3+}$ $0.02Co^{2+}$ $0.04Cit^{3-}$ **$0.004\ MoO_4^{2-}$**	4.9	$2\cdot10^{-3}$	−0.74	−0.58	0.12	0.30	0.46
		$2\cdot10^{-2}$	−0.80	−0.65	0.31	0.32	
		$5\cdot10^{-2}$	−0.90	−0.75	0.55	0.32	
$1Na_2SO_4$ $0.01Fe^{3+}$ $0.02Co^{2+}$ $0.04Cit^{3-}$ **$0.006\ MoO_4^{2-}$**	5.25	$2\cdot10^{-3}$	−0.76	−0.64	0.14	0.40	0.45
		$2\cdot10^{-2}$	−0.82	−0.71	0.38	0.44	
		$5\cdot10^{-2}$	−0.89	−0.76	0.60	0.37	
$1Na_2SO_4$ $0.01Fe^{3+}$ $0.02Co^{2+}$ $0.04Cit^{3-}$ **$0.008\ MoO_4^{2-}$**	5.35	$2\cdot10^{-3}$	−0.76	−0.60	0.11	0.30	0.42
		$2\cdot10^{-2}$	−0.81	−0.66	0.29	0.32	
		$5\cdot10^{-2}$	−0.84	−0.70	0.42	0.34	

*Concentration of oxometallates in bold

Dependencies in the coordinates $E_p - \sqrt{s}$ for ternary systems are linear as for binary $Fe^{3+}(Co^{2+})$–WO_4^{2-}–Cit^{3-} and $Fe^{3+}(Co^{2+})$–MoO_4^{2-}–Cit^{3-} [20], which confirms the multistage mechanism of the reduction of oxometallates producing the tungsten (molybdenum) oxides of a variable valence in the first step (Figs. 28.3a and 28.4a).

The trend to the characteristic criterion $i_p / \sqrt{s}$ decrease with acceleration of potential scanning rate (Fig. 28.5) and $E_п - \lg s$ dependence deviation from linearity reflects the contribution of a previous chemical reaction at metals codeposition in the ternary systems (Figs. 28.3b and 28.4b).

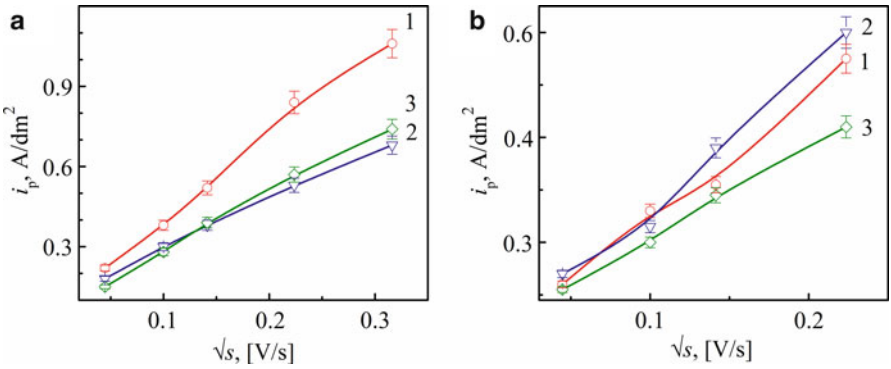

Fig. 28.2 A peak current density versus the potential scanning rate for the reduction of (**a**) the Fe-Co-W and (**b**) Fe-Co-Mo alloys from electrolytes based on 1 M Na_2SO_4 and $c(MO_4^{2-})$, mol/dm^3: 0.004 (1); 0.006 (2); 0.008 (3)

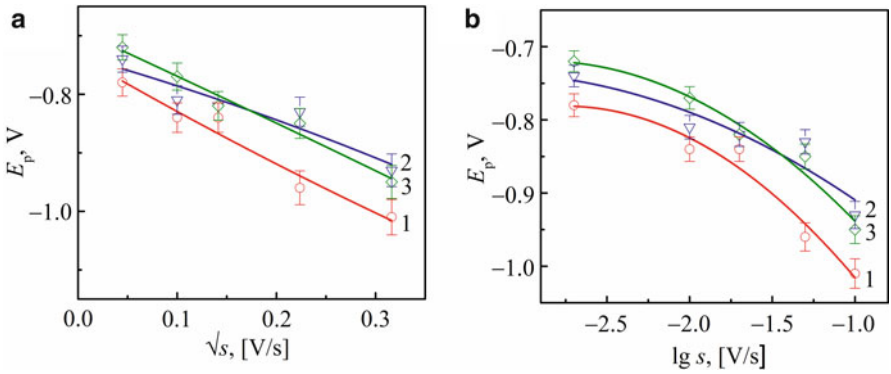

Fig. 28.3 The peak potential versus the potential scanning rate for the reduction of the Fe-Co-W alloy from electrolytes based on 1 M Na_2SO_4 and $c(WO_4^{2-})$, mol/dm^3: 0.004 (1); 0.006 (2); 0.008 (3) in coordinates $E_p - \sqrt{s}$ (**a**) and $E_p - \lg s$ (**b**)

The cathode process mechanism for the $Fe^{3+} - Co^{2+} - MoO_4^{2-}$ system changes when exceeding the limiting concentration of molybdate anions in the solution (0.006 mol/dm^3). As follows from the data on concentration criteria X_c and the apparent reaction order by tungstate and molybdate ions (Table 28.6), the previous chemical reaction contributes to the electrode process. Simultaneously, the previous chemical reaction is one of the steps in metal reduction in the system $Fe^{3+}-Co^{2+}-WO_4^{2-}$ at all the tungstate concentrations investigated.

This difference in the behavior of the $Fe^{3+}-Co^{2+}-WO_4^{2-}$ and $Fe^{3+}-Co^{2+}-MoO_4^{2-}$ systems is related to the trend of oxometallates toward polymerization. Tungstate dimerization apparently begins at lower concentrations than molybdates from electrolytes of the same pH.

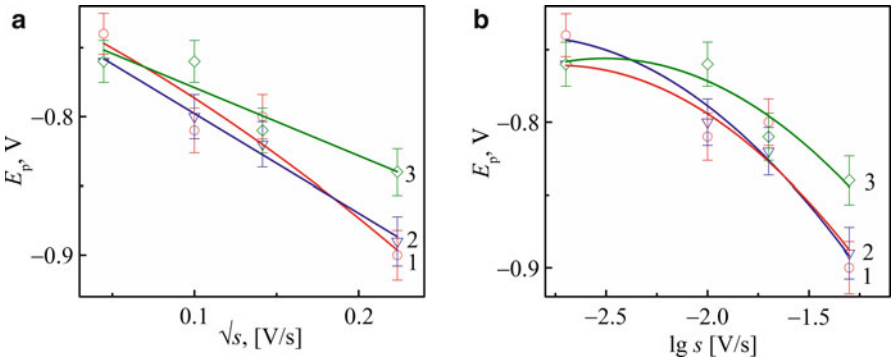

Fig. 28.4 The peak potential versus the potential scanning rate for the reduction of the Fe-Co-Mo alloy from electrolytes based on 1 M Na_2SO_4 and $c(MoO_4^{2-})$, mol/dm^3: 0.004 (1); 0.006 (2); 0.008 (3) in coordinates $E_p - \sqrt{s}$ (**a**) and $E_p - \lg s$ (**b**)

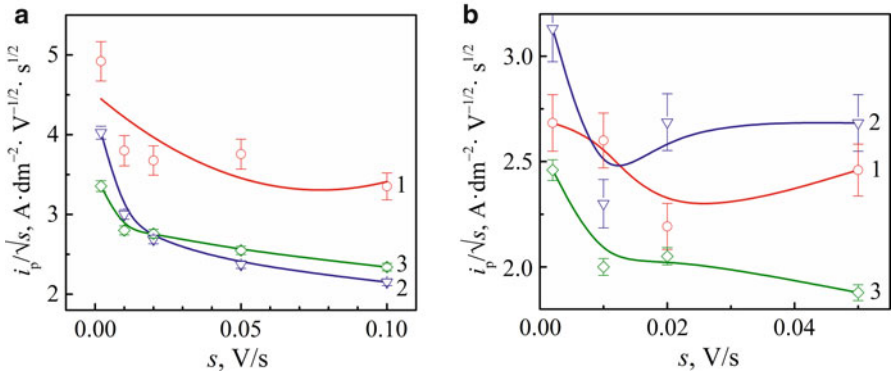

Fig. 28.5 The characteristic criterion $i_п/\sqrt{s}$ versus the potential scanning rate for the reduction of (**a**) the Fe-Co-W and (**b**) the Fe-Co-Mo alloys from electrolytes based on 1 M Na_2SO_4 and $c(MO_4^{2-})$, mol/dm^3: 0.004 (1); 0.006 (2); 0.008 (3)

Table 28.6 Concentration criterion X_c and the apparent reaction order for the $Fe^{3+}-Co^{2+}-WO_4^{2-}-Cit^{3-}$ and $Fe^{3+}-Co^{2+}-MoO_4^{2-}-Cit^{3-}$ systems (based on 1 M Na_2SO_4, $s = 2\cdot10^{-2}$ V/s)

$c(Fe^{3+})$ mol/dm^3	$c(Co^{2+})$ mol/dm^3	$c(Cit^{3-})$ mol/dm^3	$c(MoO_4^{2-})$ mol/dm^3	$c(WO_4^{2-})$ mol/dm^3	X_c	p_i
0.01	0.02	0.04	–	0.004–0.008	−0.5	−1.00[a]
			≤ 0.006	–	0.45	0.67[b]
			> 0.006	–	−1.25	−1.50[b]

[a]By tungstate ions
[b]By molybdate ions

The adsorption stage contributes to the electrode processes of the co-deposition of the ternary systems as follows from the analysis of polarization dependencies in coordinates $i_p/c - c$ and $i_p - c$. The increase in the i_p/c criterion at low concentrations of tungstate and molybdate indicates precisely the adsorption of the reagents (Figs. 28.6 and 28.7). The dependence of peak current density on both the potential scanning rate and the concentration of oxoanions allows us to determine a rational concentration in tungstate electrolytes of 0.004–0.006 mol/dm^3 and molybdate electrolytes of 0.006 mol/dm^3.

The investigation into the reduction of individual components and the electrocrystallization of Fe-Co-W and Fe-Co-Mo coatings allow us to represent the ternary alloy deposition mechanism as a generalized scheme (Fig. 28.8).

The scheme reflects the co-deposition of iron and cobalt with molybdenum and tungsten into the Fe-Co-W and Fe-Co-Mo alloys as the irreversible reduction

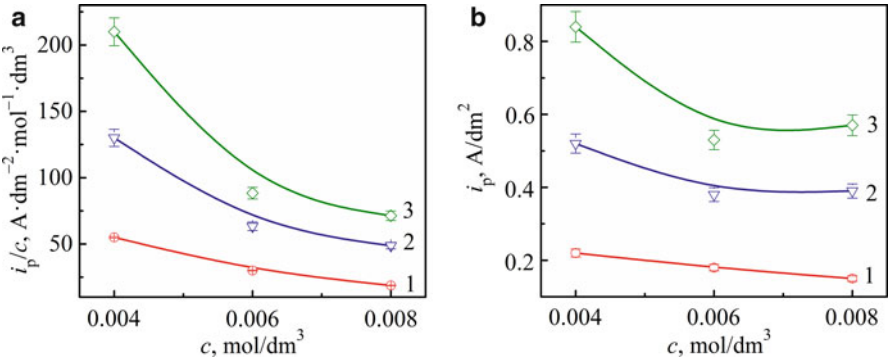

Fig. 28.6 (**a**) The characteristic criterion i_p/c and (**b**) the peak current density versus the concentration of WO_4^{2-} ions in the solution, mol/dm^3: 1 Na_2SO_4. 0.01 Fe^{3+}, 0.02 Co^{2+}, 0.04 Cit^{3-}; *s*, mV/s: 1 – 2, 2 – 20, 3 – 50

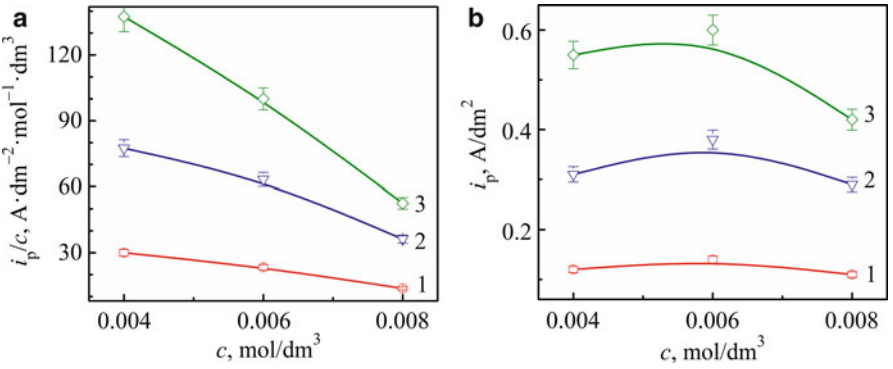

Fig. 28.7 (**a**) The characteristic criterion i_p / c and (**b**) the peak current density versus the concentration of MoO_4^{2-} ions in the solution, mol/dm^3: 1 Na_2SO_4. 0.01 Fe^{3+}, 0.02 Co^{2+}, 0.04 Cit^{3-}; *s*, mV/s: 1 – 2, 2 – 20, 3 – 50

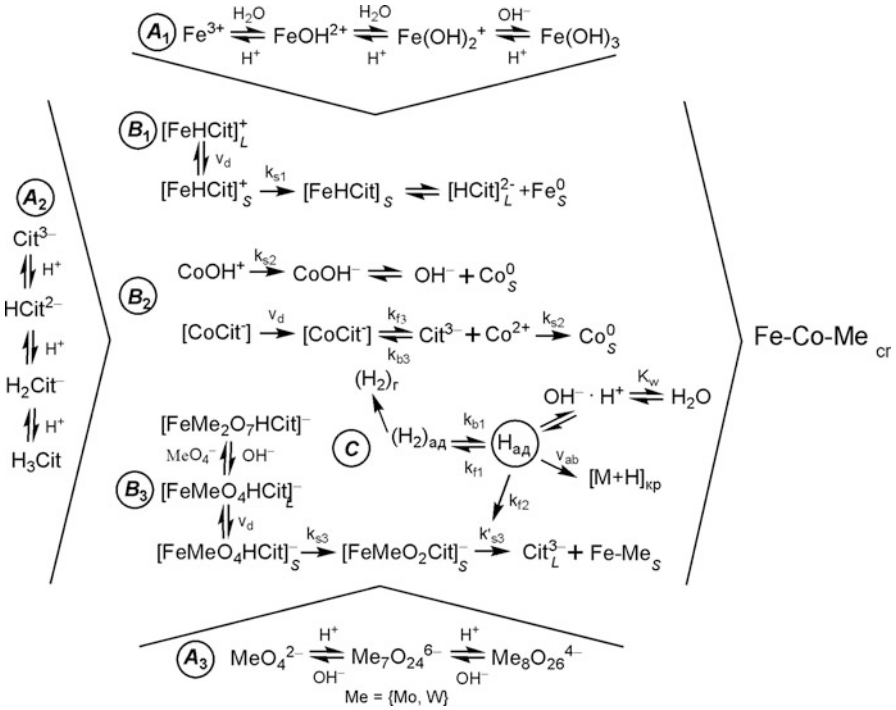

Fig. 28.8 Deposition scheme of Fe-Co-W(Mo) alloys

of intermediates limited by the discharge step and the previous chemical step associated with ligand release. This scheme takes into account ion exchange reactions in the Fe(III) solution, hydrolysis of citrate and oxoanions MoO_4^{2-} (WO_4^{2-}), formation of the clusters and polyanions (Fig. 28.8, routes A1, A2, and A3), the electro-crystallization of iron and cobalt (B1 and B2), the coupled reactions of the reduction of molybdenum and tungsten with iron (B3), the parallel hydrogen evolution reaction, and the chemical reduction of intermediate molybdenum and tungsten oxides by hydrogen adatoms and a possible hydrogen uptake by the coating.

Summarized results and the proposed mechanism form the informational and methodological basis for the development of the composition of electrolytes and the modes of electrochemical synthesis for ternary alloys of iron and cobalt with molybdenum and tungsten [27].

28.5 Composition and Morphology of Fe-Co-W(Mo) Coatings

It has been shown by Yermolenko et al. [4] that the pulse current provides the enrichment of ternary alloys with refractory metals and increases the deposition efficiency up to 80%. The influence of the concentration of the alloying components in the electrolyte in addition to the complexing agents and ligands ratio on the composition and morphology of Fe-Co-W and Fe-Co-Mo coatings were considered in detail by Ved' et al. [27]. In this chapter, we focus on the electrolysis mode effect on the morphology and phase composition of ternary alloys.

The surface morphology of the Fe-Co-W coatings deposited at a direct current 3 A/dm^2 is microglobular with an average grain size of 2–6 μm (Fig. 28.9a) [28]. However, the coatings are high in oxygen content, which increases in the valleys, and the uneven refractory component distribution in the hills and valleys. The porosity of the coating increases with the density of the current.

Coatings obtained by the pulse current are characterized by a decrease in the size of the spheroids up to 2 μm and a more even distribution of elements on the surface. The content of the alloying metals does not substantially change at different

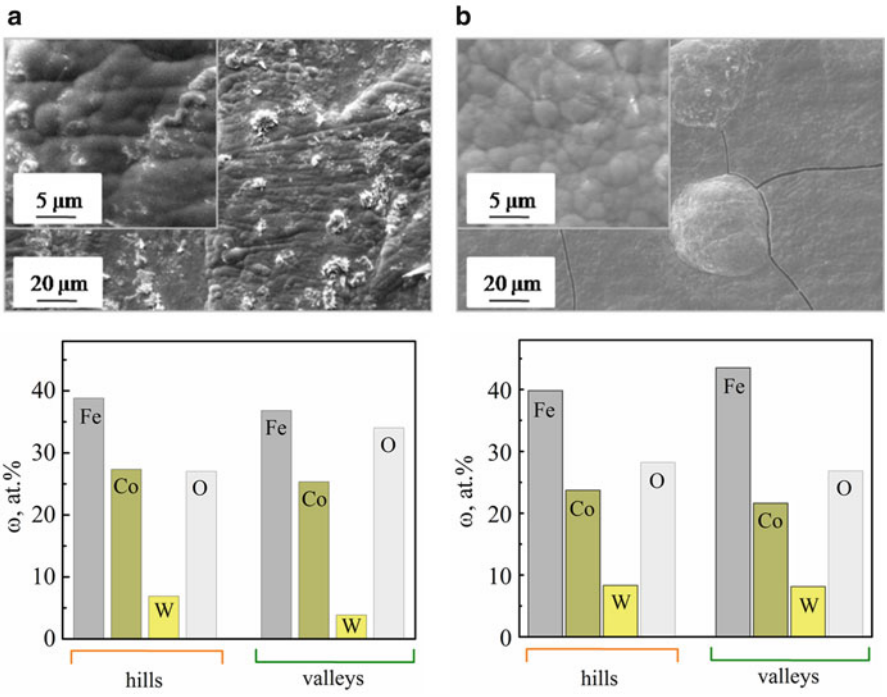

Fig. 28.9 Morphology of the Fe-Co-W alloys obtained by (**a**) direct and (**b**) pulse current, parameters of modes given in Table 28.2

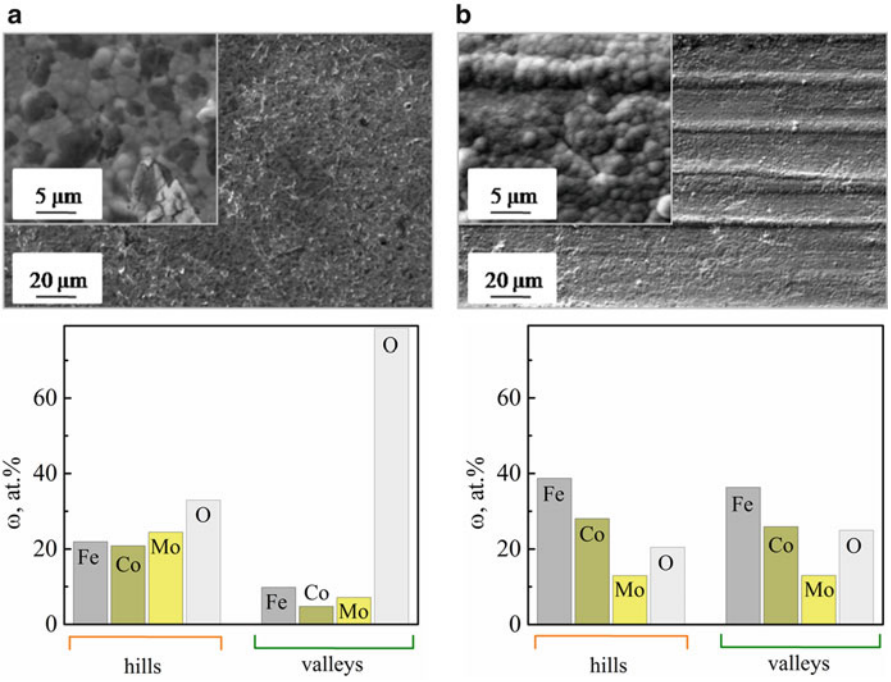

Fig. 28.10 Morphology of the Fe-Co-Mo alloys obtained by (**a**) direct and (**b**) pulse current, parameters of modes given in Table 28.2

sites within the scanning area, and the oxygen content does not exceed 28 wt.%, as shown in Fig. 28.9b.

As follows from Fig. 28.10, the most significant contribution to the formation of the Fe-Co-Mo coating surface morphology is made by the energy factor in comparison with the temporary one, namely the ratio of the on-/off-time duration. As shown by Ved' et al. [27], the morphology of the samples obtained by direct current varies from small crystalline to globular with increasing current density. Increasing the pulse current amplitude provides a denser spheroid-shaped surface of coating.

Such a change in the alloy surface morphology is associated with the peculiarities of the crystallization of alloying metals. As was noted above, the deformation of the alloy lattice and the inhibition of the linear growth of crystals are caused by a difference in the crystal lattice parameters for iron, cobalt, and molybdenum. It is obvious that the deformation of the crystalline lattice is greater as the total content of cobalt and molybdenum in the alloy increases. The globular structure of the surface is typical of deposits with a total content of alloying components higher than 45 wt.%.

The distribution of the components on the Fe-Co-Mo coating surface deposited by a direct current is fairly uneven (Fig. 28.10a). The molybdenum content prevails

on the hills and the oxygen content is minimal owing to the localization at a higher current density and a more complete reduction of intermediate oxides by hydrogen adatoms. The significant increase in the oxygen content in the valleys was found, related first to the incorporation of intermediate molybdenum oxides into the alloy. Second, the possibility of carbon(IV) oxide adsorption into the pores of the coatings deposited under a direct current is not excluded.

A more uniform coating surface with significantly decreasing oxygen content may be obtained by a pulse current (Fig. 25.10b), as follows from morphology and topography analysis. The oxygen content, regardless of the scanning area, varies from 20 to 25 wt.%, which indicates a more complete molybdate reduction to metallic molybdenum during an interruption of polarization, which confirms the advantages of a unipolar pulse current.

28.6 Phase Composition of the Fe-Co-W(Mo) Coatings

It is known that electrolytic alloys may differ in their physical and chemical properties from the alloys obtained using the metallurgical method, and do not correspond with regard to structure to the state phase diagrams of thermal alloys. The conditions of electrodeposition and the composition of electrolytes are factors in the formation of a certain structure of the electrolytic alloys.

The phase composition of ternary coatings with a thickness of 20 μm deposited under a direct current onto a copper substrate was investigated. Figure 28.11 shows the X-ray diffraction (XRD) patterns for the composition of Fe-Co-W alloy, wt.%: Fe, 54; Co, 36; W, 10; deposited under a direct current $i = 4.5$ A/dm^2.

The diffraction patterns of Fe-Co-W deposits are characterized by the presence of copper substrate lines and the lines corresponding to the intermetallic phases of Co_7W_6 and Fe_7W_6, in addition to α-Fe and Fe_3C cementite. The qualitative composition of the intermetallics reflects the reduction of the competitive metals. The detected intermetallic phases of Co_7W_6 and Fe_7W_6 suggest that the competition of iron with cobalt might predominate over the competitive reduction of alloying

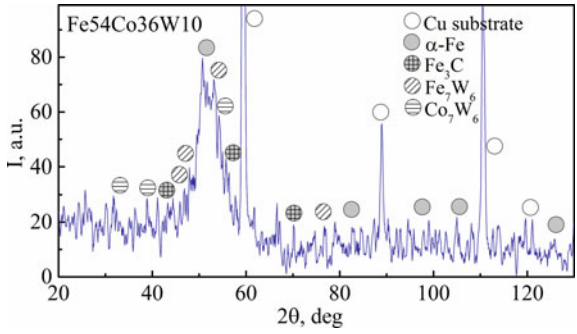

Fig. 28.11 X-ray diffraction patterns for the Fe-Co-W alloy, obtained by a direct current

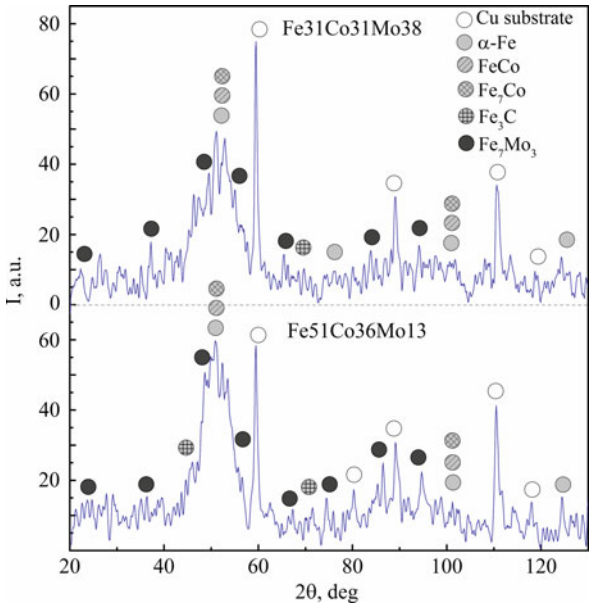

Fig. 28.12 X-ray diffraction patterns for the Fe-Co-Mo alloy, deposited by direct current

components of cobalt with tungsten. A halo of 10° appears at the angles 2θ 50–55°, and the size of the coherent scatter plot is L = 77 Å. Analysis of the results obtained allows us to draw conclusions about the amorphous-crystalline structure of the Fe-Co-W alloy.

Figure 28.12 shows the XRD patterns for the composition of the Fe-Co-Mo alloy, wt.%: Fe, 31; Co, 31; Mo, 38; and Fe, 51; Co, 36; Mo, 13, deposited under a direct current $i = 5$ A/dm^2 from electrolytes of different compositions (Table 28.2).

The Fe-Co-Mo coatings differ somewhat from Fe-Co-W coatings with regard to phase composition. Lines of intermetallic Fe_7Mo, Fe_7Co, and FeCo phases found on the Fe-Co-Mo diffraction pattern obtained by stationary electrolysis, and the absence of intermetallic Co_xMo_y confirm the competitive deposition of alloying metals (cobalt and molybdenum) into the alloy, in addition to the competition between iron and cobalt. Considering that the deposition of the Fe-Co-Mo alloy occurs at potentials more negative for Fe-Co-W, it is fairly obvious that iron wins in the competition for the formation of intermetallic compounds with molybdenum because of the easier and more complete reduction of iron(II). On the other hand, the identical crystalline lattices of iron and molybdenum, in addition to the smaller atomic radius of molybdenum compared with tungsten, are crucial in the formation of intermetallic compounds of molybdenum precisely with iron.

Figure 28.12 shows that the coatings of different compositions, deposited by a direct current from various electrolytes, have the same phase composition. However, the coherent scatter plot is reduced for coatings with a high molybdenum content from 66 Å to 53 Å. It is obvious that the alloy amorphization occurs because of an increase in the refractory metal content, and the change in the ratio of metals

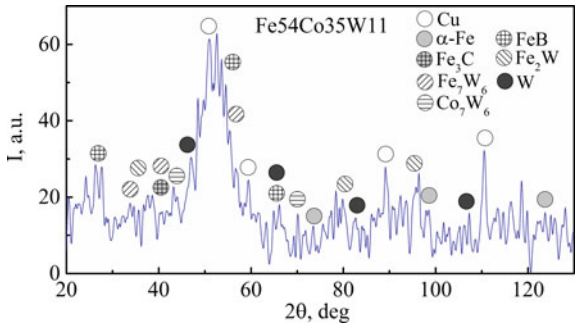

Fig. 28.13 X-ray diffraction patterns for the Fe-Co-W alloy, deposited by a pulse current

contributes to the ratio of different composition phases, which affects the properties of the coating.

Figure 28.13 shows XRD patterns for electrolytic alloys Fe-Co-W deposited by pulse current. The composition of alloys in terms of metal is wt.%: Fe, 54; Co, 35; W, 11.

The XRD patterns of Fe-Co-W coatings obtained by pulsed electrolysis are distinguished by the presence of additional lines corresponding to the crystalline tungsten and the intermetallic phase of Fe_2W (Fig. 28.13). In addition, FeB lines are detected. XRD studies were performed on coating samples with the same content of alloying metals obtained in different polarization modes. Therefore, the phase lines of iron-containing intermetallics, found on the diffractograms of the coatings deposited on the pulse current, give grounds to assert that during the pause there is a more energetically possible common crystallization of metals with the same crystalline lattice as iron and tungsten. Considering that the co-deposition of iron and tungsten in the binary Fe-W alloy occurs with the formation of a solid solution of tungsten in α-Fe [23], it is not necessary to exclude the probability of a combination of intermetallics and a solid solution in the formation of the ternary alloy.

Figure 28.14 shows XRD patterns for the electrolytic alloy Fe-Co-Mo deposited by a pulse current. The composition of alloys in terms of metal is wt.%: Fe, 50; Co, 39; W, 11.

The nonstationary electrolysis substantially affects the phase composition of Fe-Co-Mo coating (Fig. 28.14). The X-ray patterns visualize lines corresponding to metallic cobalt and molybdenum, but the lines of intermetallic iron compounds with cobalt are disappearing.

The phase composition of the coating depends on the refractory component content at the binary deposition of the Fe-Mo and Co-Mo coatings, and the transition from the crystalline (solid solution) to the amorphous structure occurs when the molybdenum content is more than 18–20 wt.% [18, 29, 30]. Consequently, the presence of metallic cobalt and molybdenum reflex, and line of Fe_7Mo on the Fe-Co-Mo alloy diffractograms are indications of the combination of intermetallic and solid solutions at the formation the ternary alloy by a pulse current.

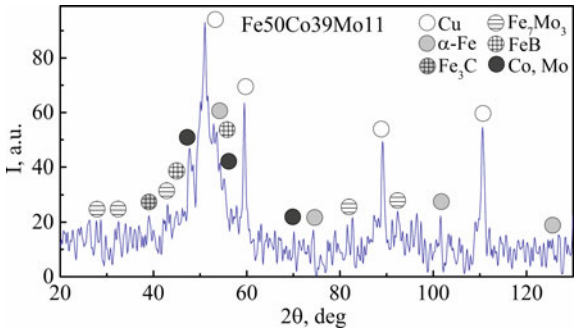

Fig. 28.14 X-ray diffraction patterns for the Fe-Co-Mo alloy, deposited by a pulse current

28.7 Conclusions

The results obtained, first approved the validity of the assumption of the competitive co-reduction of alloy-forming metals and the proposed mechanism the co-deposition of iron and cobalt with molybdenum and tungsten in ternary alloys. Second, the assertion regarding the application of electrolysis regimes as effective instruments for controlling the phase composition of coatings is substantiated.

References

1. Vernickaite E, Tsyntsaru N, Cesiulis H (2016) Electrodeposited co-W alloys and their prospects as effective anode for methanol oxidation in acidic media. Surf Coatings Tech 307:1322. https://doi.org/10.1016/j.surfcoat.2016.07.049
2. Sakhnenko MD, Ved' MV, Ermolenko IY, Hapon YK, Kozyar MO (2017) Design, synthesis, and diagnostics of functional galvanic coatings made of multicomponent alloys. Mater Sci 52(5):680–686. https://doi.org/10.1007/s11003-017-0009-7
3. Ramanauskas R, Gudavičiūtė L, Juškėnas R (2008) Effect of pulse plating on the composition and corrosion properties of Zn–Co and Zn–Fe alloy coatings. Chemija 19(1):7–13
4. Yermolenko I, Ved' M, Karakurkchi A, Proskurina V, Sknar I, Y K, Sverdlikovska O, Sigunov O (2017) Research into influence of the electrolysis modes on the composition of galvanic Fe-Co-Mo coatings. East-Eur J Enterprise Technol Mater Sci 3/12(87):9–15. https://doi.org/10.15587/1729-4061.2017.103100
5. Shao II, Vereecken PM, Chien CL, Cammarata RC, Searson PC (2003) Electrochemical deposition of FeCo and FeCoV alloys. J Electrochem Soc 150:C184–C188
6. Tsyntsaru N, Cesiulis H, Budreika A, Juskenas R, Celis J-P (2012) The effect of electrodeposition conditions and post-annealing on nanostructure of co–W coatings. Surf Coat Technol 206(19–20):4262–4269. https://doi.org/10.1016/j.surfcoat.2012.04.036
7. Grabco DZ, Dikusar IA, Petrenko VI et al (2007) Micromechanical properties of Co–W alloys electrodeposited under pulse conditions. Surf Eng Appl Electrochem 43(1):11–17. https://doi.org/10.3103/S1068375507010024
8. Ved' MV, Ermolenko IY, Sakhnenko ND, Zyubanova SI, Sachanova YI (2017) Methods for controlling the composition and morphology of electrodeposited Fe–Mo and Fe–Co–Mo coatings. Surf Eng Appl Electrochem 53(6):525–532. https://doi.org/10.3103/S1068375517060138

9. Tsyntsaru N, Cesiulis H, Donten M, Sort J, Pellicer E, Podlaha-Murphy EJ (2012) Modern trends in tungsten alloys electrodeposition with iron group metals. Surf Eng Appl Electrochem 48(6):491–520
10. Ćirović N, Spasojević P, Ribić-Zelenović L, Mašković P, Spasojević M (2015) Synthesis, structure and properties of nickel-Iron-tungsten alloy electrodeposits. I: Effect of synthesis parameters on chemical composition, microstructure and morphology. Sci Sinter 47:347–365. https://doi.org/10.2298/SOS1503347C
11. Ved' MV, Sakhnenko MD, Karakurkchi HV, Ermolenko IY, Fomina LP (2016) Functional properties of Fe−Mo and Fe−Mo−W galvanic alloys. Mater Sci 51(5):701–710. https://doi.org/10.1007/s11003-016-9893-5
12. Gómez E, Pellicer E, Vallés E (2003) Influence of the bath composition and the pH on the induced cobalt/molybdenum electrodeposition. J Electroanal Chem 556:137–145
13. Podlaha EJ, Landolt D (1997) Induced codeposition: III. Molybdenum alloys with nickel, cobalt and iron. J Electrochem Soc 144(5):1672–1680
14. Younes O, Zhu L, Rosenberg Y, Shacham-Diamond Y, Gileadi E (2001) Electroplating of amorphous thin films of tungsten/nickel alloys. Langmuir 17(26):8270–8275. https://doi.org/10.1021/la010660x
15. Younes-Metzler O, Zhu L, Gileadi E (2003) The anomalous codeposition of tungsten in the presence of nickel. Electrochim Acta 48(18):2551–2562. https://doi.org/10.1016/S0013-4686(03)00297-4
16. Belevskii SS, Yushchenko SP, Dikusar AI (2012) Anomalous electrodeposition of Co-W coatings from a citrate electrolyte due to the formation of multinuclear Heterometallic complexes in the solution. Surf Eng Appl Electrochem 48(1):97–98
17. Shulman AI, Belevskii SS, Yushchenko SP, Dikusar AI (2014) Role of complexation in forming composition of Co–W coatings electrodeposited from gluconate electrolyte. Surf Eng Appl Elect 50(1):9–17. https://doi.org/10.3103/S106837551401013X
18. Bobanova ZI, Grabko DZ, Danitse Z, Y M, Dikusar AI (2007) Elektroosazhdenie i svoystva splava zhelezo-vol'fram [Electrodeposition and properties of the iron-tungsten alloy]. Elektronnaya Obrab Mater 4:12–21. (in Russian)
19. Danilov FI, Protsenko VS, Ubiikon' AV (2005) Kinetic regularities governing the reaction of electrodeposition of iron from solutions of citrate complexes of iron (III). Russ J Electrochem 41(2):1282–1289
20. Yermolenko IY, Ved' MV, Karakurkchi AV, Sakhnenko ND, Kolupaieva ZI (2017) Electrochemical behavior of Fe^{3+}–WO_4^{2-}–Cit^{3-} and Fe^{3+}–MoO_4^{2-}–WO_4^{2-}–Cit^{3-} systems. Issues Chem Chem Technol 2(III):4–14
21. Budnikov GK, Maystrenko VN, Vyaselev MR (2003) Osnovy sovremennogo elektrokhimicheskogo analiza [Fundamentals of contemporary electrochemical analyzes]. Mir Binom LZ Publishers, Moscow, p 592. (in Russian)
22. Mikhailov IF, Baturin AA, Mikhailov AI, Fomina LP (2016) Perspectives of development of X-ray analysis for material composition. Func Mater 23(1):5–14
23. Ved' MV, Sakhnenko MD (2010) Katalitychni ta zakhysni pokryttia splavamy i skladnymy oksydamy: elektrokhimichnyi syntez, prohnozuvannia vlastyvostei [Tekst]: monohrafiia. NTU «KhPI», Kharkiv, p 272
24. Tochitskiy A, Dmitrieva AE (2013) O mehanizme formirovaniya rentgenoamorfnoy strukturyi plyonok splavov Ni-W [On the mechanism of formation of amorphous structure of Ni-W alloy films]. Metallofiz Noveyshie Tehnol 35(12):1629–1636. (in Russian)
25. Gamburg YD, Zakharov YN (2008) Vliyaniye vodoroda na amorfizatsiyu splavov zhelezo-vol'fram poluchayemykh pri elektrokhimicheskom sinteze [The effect of hydrogen on the amorphization of iron-tungsten alloys obtained by electrochemical synthesis]. Elektrokhimiya 44(6):792–795. (in Russian)
26. Karakurkchi AV, Ved' MV, Ermolenko IY, Sakhnenko ND (2016) Electrochemical deposition of Fe–Mo–W alloy coatings from citrate electrolyte. Surf Eng Appl Electrochem 52(1):43–49. https://doi.org/10.3103/S1068375516010087

27. Ved' MV, Sakhnenko ND, Yermolenko IY, Nenastina TA (2018) Nanostructured functional coatings of Iron family metals with refractory elements. In: Fesenko O, Yatsenko L (eds) Nanochemistry, biotechnology, nanomaterials, and their applications. NANO 2017. Springer proceedings in physics. Springer, Cham, p 214. https://doi.org/10.1007/978-3-319-92567-7_1
28. Yermolenko IY, Ved' MV, Sakhnenko ND, Sachanova YI (2017) Composition, morphology, and topography of galvanic coatings Fe-Co-W and Fe-Co-Mo. Nanoscale Res Lett 12(1):352. https://doi.org/10.1186/s11671-017-2128-3
29. Donten M, Stojek Z, Cesiulis H (2003) Formation of nanofibres in thin layers of amorphous W alloys with Ni, Co and Fe obtained by electrodeposition. J Electrochem Soc 150(2):695–698
30. Yar-Mukhamedova GS, Sakhnenko ND, Ved' MV, Yermolenko IY, Zyubanova SI (2017) Surface analysis of Fe-co-Mo electrolytic coatings. IOP Conf Series: Mater Sci Eng 213:012019. https://doi.org/10.1088/1757-899X/213/1/012019

Chapter 29
Dispersing of Molybdenum Nanofilms at Non-metallic Materials as a Result of Their Annealing in Vacuum

I. I. Gab, T. V. Stetsyuk, B. D. Kostyuk, O. M. Fesenko, and D. B. Shakhnin

29.1 Introduction

When joining many non-metallic materials, in particular oxide and nonoxidic ceramics, single crystals, graphitized carbon, as well as some other metal coatings of various thicknesses deposited at the non-metallic materials are often used [1–5]. The most used materials for brazing are titanium [6–12], niobium, and hafnium [13–22], because the last two metals are of considerable interest for production with their help of high-temperature joints of ceramics with ceramics and metals.

Thin metal films (within the nanothickness range) deposited onto non-metallic inorganic materials are of paramount importance in the processes of joining (brazing) of nonmetals (ceramics, glass, single crystals, carbon materials, superhard materials). The metallization of surfaces of such materials contributes to their sufficient wetting by molten metals which determine the technological possibility of brazed joint formation, as well as the strength and other properties.

Since in the process of brazing or pressure welding metallized nonmetal parts are heated to sufficiently high temperatures (1000–1600 °C), study of the processes of dispersion and coagulation occurring during annealing in these metallic nanofilms 100 nm thick is not only of scientific interest but also of practical value for the development of industrial modes for joining of non-metallic materials.

I. I. Gab (✉) · T. V. Stetsyuk · B. D. Kostyuk
Frantsevich Institute for Problems of Materials Science of National Academy Sciences of Ukraine, Kyiv, Ukraine
e-mail: gab@materials.kiev.ua

O. M. Fesenko
Institute of Physics of National Academy Sciences of Ukraine, Kyiv, Ukraine

D. B. Shakhnin
University “Ukraine”, Kyiv, Ukraine

O. Fesenko, L. Yatsenko (eds.), *Nanocomposites, Nanostructures, and Their Applications*, Springer Proceedings in Physics 221,
https://doi.org/10.1007/978-3-030-17759-1_29

Of widespread application in engineering is molybdenum used for brazing of heterogeneous materials mainly for the electronic and radio industry according to molybdenum-manganese process [23, 24], as well as, in the form of nanofilms coatings, for information storage elements, optical cells, solar cell batteries, molybdenum mirrors etc. [25, 26].

Molybdenum coatings 100–200 nm thickness deposited onto non-metallic materials are of considerable interest for purposes of application of such coatings for further brazing of materials metallized by them.

29.2 Materials and Experimental Methods

In this chapter, the electron-beam method of sputtering of metallic nanofilms done with the help of the electron-beam equipment ELU-5 is discussed.

The thickness of the deposited nanofilms was measured by two methods:

1. The metal of the given mass (calculated for films of the required thickness) was completely evaporated, after which the thickness of the film can be calculated easily according to the law of Lambert [27–29].
2. With the help of a special quartz sensor located in the vacuum spray chamber immediately near the sample onto which the film is deposited.

Solid non-metallic substrates were manufactured both from oxide (quartz glass, leucosapphire, and alumina ceramics) and from non-oxide materials (ceramics based on silicon and aluminum nitrides and also silicon carbide single crystals) as little thin plates of $4 \times 3 \times 2$ mm size. One of the flat surfaces of each sample was well polished to the roughness of $R_z = 0.03$–0.05 μm. After polishing, all samples were carefully made fat-free and annealed in vacuum at a temperature 1100 °C for 1 h.

As a metal deposited on non-metallic surfaces, molybdenum was used. The films were deposited onto all substrates under the same conditions, and their quality was monitored by metallographic microscope XJL-17.

Annealing of non-metallic samples coated by metal films was performed in a vacuum chamber during various time periods from 2 up to 20 min at different temperatures (1200–1600 °C) in vacuum not worse than 2×10^{-3} Pa.

Annealed samples were examined using scanning electron microscopes JCM-6700 and JCM-5000 and an atomic force microscope Nano Scope III with micrographs recording. Using these micrographs the area of substrate surface coated with metal film islands was calculated by planimetric weighting method, i.e., by weighting of metal-coated sample part images cut from micrographs [30]. The data obtained by this method were analyzed as the dependence of sample surface area covered with metal film fragments after annealing on annealing parameters (annealing temperature and time).

29.3 Results and Discussion

The initial molybdenum film onto leucosapphire was solid and remained virtually unchanged during heating up to 1200 °C. The first signs of the disintegration of the film appeared after its 5-min annealing at 1200 °C (Fig. 29.1a); with further increase of exposition time at this temperature, the process of the film dispersing was intensified; and after 20-min annealing, only about 85% of the leucosapphire substrate surface was covered by the film (Fig. 29.2a).

The further increase of the annealing temperature accelerated the process of the film dispersion as usual, and the first signs of its disintegration appeared already after 2-min annealing at 1300 °C. With further exposition time increase up to 10 min, the film was already significantly dispersed; and after 20-min annealing, the film was already divided into separate fragments covering not more than 70% of the substrate surface (Fig. 29.2a).

After the annealing temperature increase up to 1400 °C, clear visible signs of the film dispersion appeared already after 2-min exposition; with further increase of exposition time at this temperature up to 10 min, the film disintegration intensity raised and after 20-min annealing, the film fragments covered only about 60% of the substrate surface (Fig. 29.2a).

With the annealing temperature increase up to 1500 °C the film disintegration rate increased not so much; and after 20-min annealing the film fragments covered only about 50% of the substrate surface (Fig. 29.2a).

The micrograph of this stage of the film disintegration made with the atomic force microscope (Fig. 29.3a) indicates that the film was significantly dispersed and coagulated. Its fragment height increased at some drops up to 300 nm (Fig. 29.3b), but the film adhesion to the substrate still remained.

The process of the film dispersing accelerated significantly with its annealing temperature increase up to 1600 °C. Thus, the film disintegration degree was very

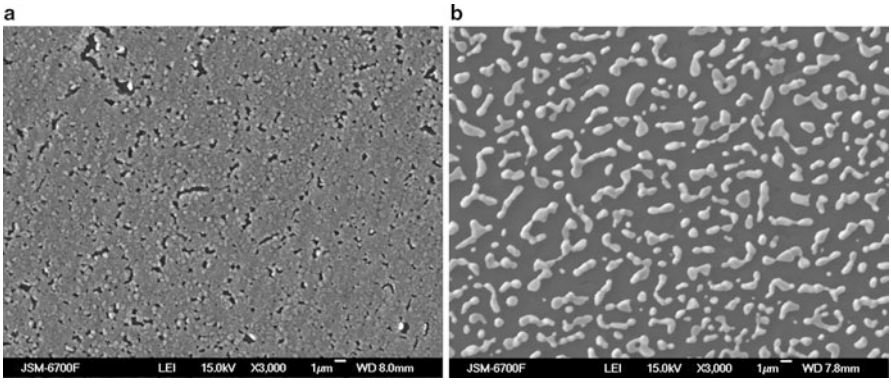

Fig. 29.1 SEM image (×3000) of molybdenum film of 100 nm thickness onto leucosapphire which was annealed in vacuum: (**a**) 1200 °C, 5 min, (**b**) 1600 °C, 2 min

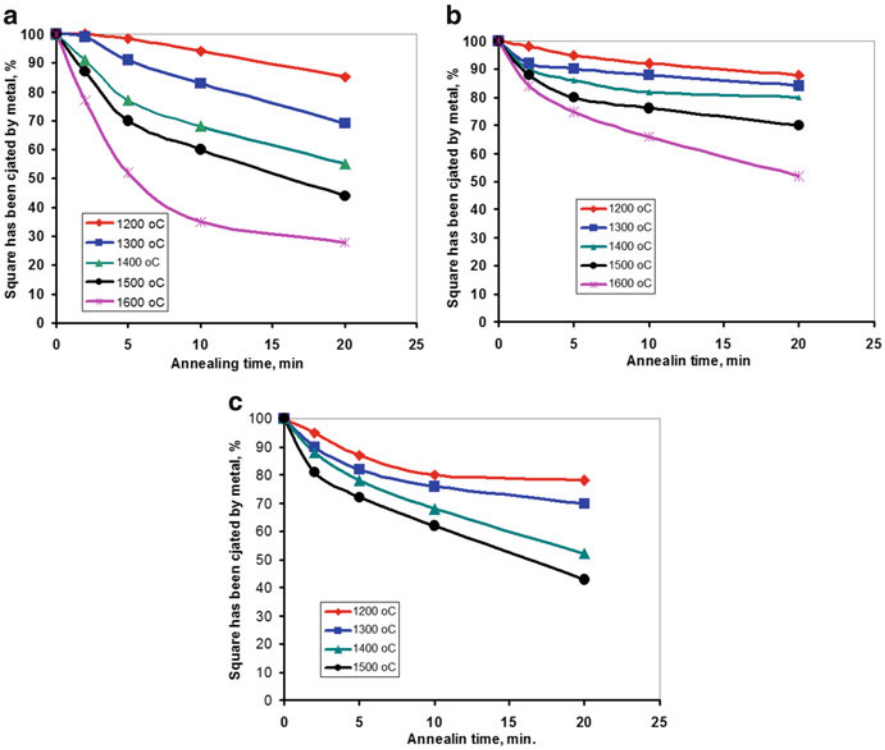

Fig. 29.2 Non-metallic oxide material area covered by molybdenum film depending on annealing time at various temperatures (1200–1600 °C): (**a**) leucosapphire, (**b**) alumina ceramics, (**c**) quartz glass

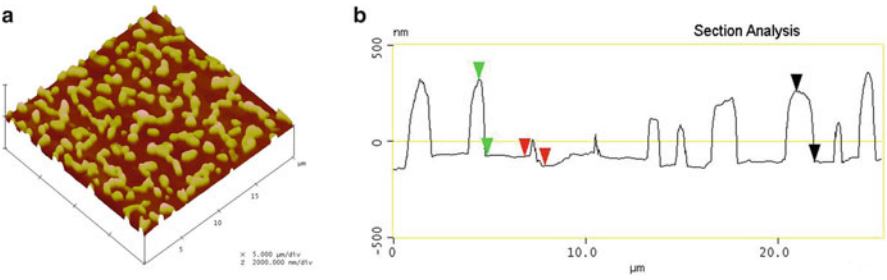

Fig. 29.3 AFM images of molybdenum film of 100 nm thickness onto leucosapphire after annealing at 1500 °C during 20 min in vacuum: (**a**) three-dimensional image. (**b**) film profile

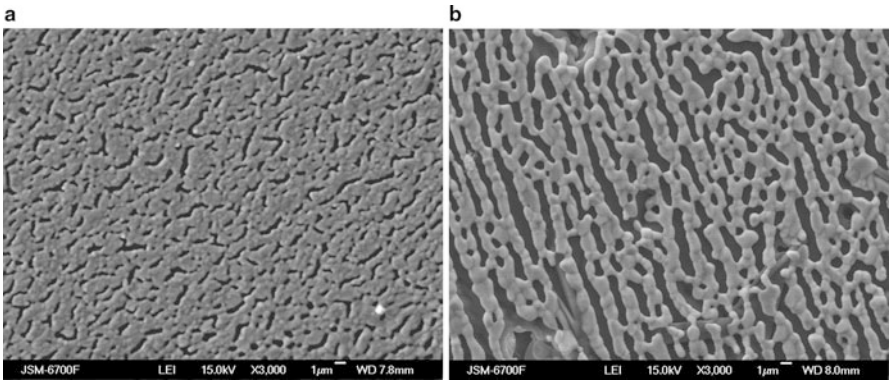

Fig. 29.4 SEM image (×3000) of molybdenum film of 100 nm thickness onto alumina ceramics which was annealed in vacuum: (**a**) 1200 °C, 5 min, (**b**) 1600 °C, 20 min

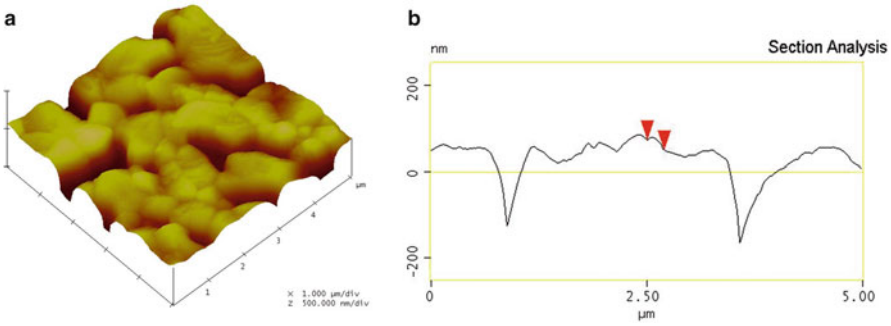

Fig. 29.5 AFM images of molybdenum film of 100 nm thickness onto alumina ceramics after annealing at 1200 °C during 5 min in vacuum: (**a**) three-dimensional image, (**b**) film profile

significant after 2-min exposition at this temperature, and further exposition time increase intensifies film fragmentation significantly (Figs. 29.1b and 29.2a), so that after 20-min annealing film residues covered less than a third of the substrate area (Fig. 29.2a).

The initial molybdenum film onto alumina ceramics, as well as on leucosapphire, was solid. The first signs of the film disintegration appeared after 2-min annealing at 1200 °C, and with the subsequent exposition time increase at this temperature up to 5 min (Fig. 29.4a), the film was not virtually changed. With high magnification degree of the atomic force microscope (Fig. 29.5a), one could notice that the film started to blister slowly and to disintegrate into large conglomerates closely contacting each other. At this stage, the conglomerate thickness remained at the level of the initial film that is 100 nm (Fig. 29.5b). With the exposition time increase at 1200 °C up to 20 min, the film's visual appearance has shown only minor changes.

The temperature increase up to 1300 °C within the exposition time range from 2 up to 10 min did not change significantly the film morphology compared

to annealing at 1200 °C, and only after 20-min exposition the substantial film dispersion occurred (Fig. 29.2b).

Further annealing temperature increase up to 1400 °C, and even to 1500 °C, did not change practically the degree of the film dispersion; only after 10-min exposition at 1500 °C the film started to disperse substantially; and after 20-min annealing, its fragments covered about 70% of the substrate surface (Fig. 29.2b).

Annealing at 1600 °C accelerated significantly the film dispersion which started considerably after 2 min of exposition, and with the subsequent exposition time increase, this process was accelerated, resulting in the significant film disintegration after 20-min exposition at that temperature, when long film fragments covered about half of the substrate area (Figs. 29.4b and 29.2b). In the micrograph of this stage of the film fragmentation, made with the atomic force microscope, one can see that the aforementioned long fragments consisted of shorter ones closely interconnected and making up long chains with a height of 250 nm.

Comparing the kinetics of the molybdenum film dispersion onto alumina ceramics and leucosapphire one can see that the kinetics is quite similar, but onto aluminum oxide the film disperses a bit more slowly, probably due to pores and impurities present in ceramics. According to the results obtained, brazing of aluminum oxide ceramics metallized by molybdenum can be performed at 1500 °C, even with the process duration up to 20 min; and at 1600 °C brazing is possible only if the process time is not longer than 10 min, when the film still covers more than 70% of the substrate surface and there is not very intensive interaction of the molybdenum with ceramics.

The initial continuous molybdenum nanofilm deposited onto quartz glass remained unchanged even after annealing at up to 1200 °C. The first signs of the film dispersion appeared after 2-min annealing at 1200 °C; disintegration became increasingly significant if the exposition time was increased up to 10 (Figs. 29.6a and 29.2c) and then up to 20 min. Taking into account the film

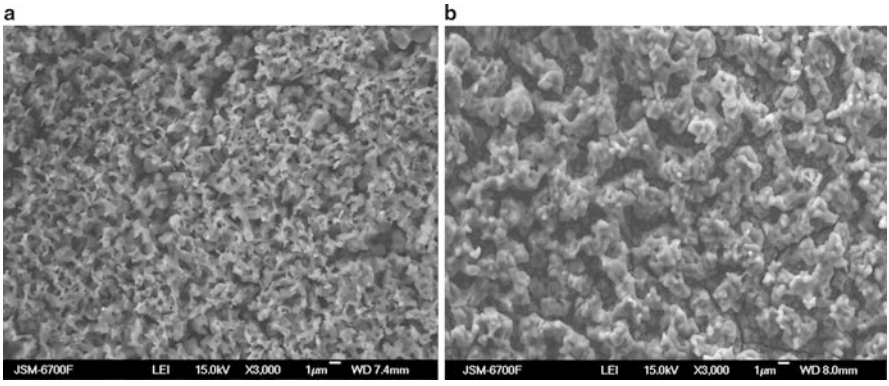

Fig. 29.6 SEM image (×3000) of molybdenum film of 100 nm thickness onto quartz glass which was annealed in vacuum: (**a**) 1200 °C, 10 min, (**b**) 1500 °C, 5 min

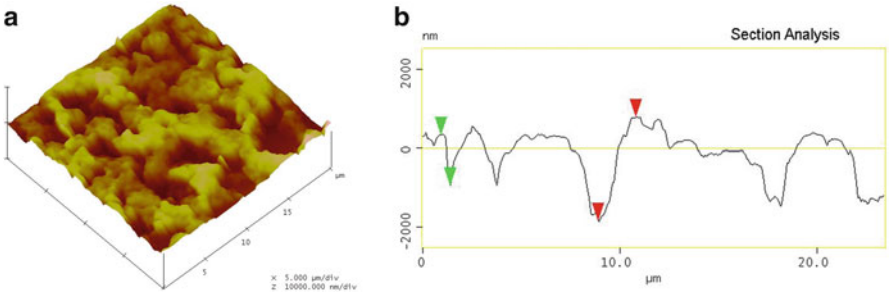

Fig. 29.7 AFM images of molybdenum film of 100 nm thickness onto quartz glass after annealing at 1500 °C during 5 min in vacuum: (**a**) three-dimensional image, (**b**) film profile

destruction form, it is likely that at this temperature there is a certain interaction between the film and the quartz glass surface, and this interaction intensified significantly with further increase of both the annealing temperature and the exposition time at this temperature. After annealing at 1300 °C, the film interaction with the quartz glass surface was observed simultaneously with the film dispersion after the 2-min exposition; and this interaction enhanced with the increase of the exposition time up to 20 min.

The film interaction with the quartz substrate enhanced further after the annealing at 1400 °C, during which it is likely that new phases are formed (Fig. 29.2c). This process reaches the apex after the annealing at 1500 °C, when observed interaction is rapid enough already after 2-min exposition (Fig. 29.2c). After 5-min annealing, this interaction is even more intense (Figs. 29.6b and 29.2c). It is clearly seen with high magnification degree at the film micrograph made with the atomic force microscope (Fig. 29.7a). This photo shows a clearer picture of the molybdenum film interaction with quartz glass substrate resulting in a new phase formation consisting of large closely interconnected conglomerates with blurred contours. Between conglomerates less than 100 nm high, there are large cavities up to 2 mcm wide (Fig. 29.7b).

The initial molybdenum nanofilm deposited onto silicon carbide single crystal was solid and remained virtually unchanged during annealing up to 2 min at 1200 °C. The first signs of the film disintegration appeared after 5-min annealing at 1200 °C in the form of the cracks' grid in it; the number of cracks increased slightly after 10-min exposition and after 20-min annealing local blistering occurred on the entire film surface. With the annealing temperature increase up to 1300 °C, signs of the film disintegration appeared after 2-min exposition, and their amount slightly increased after 5- and 10-min annealing. After 20-min exposition, the film was dispersed into multiple rounded and extended fragments placed quite closely to each other (Fig. 29.8a). The film annealing during 2 min at 1400 °C led to its significant cracking. After 5-min annealing at 1400 °C a significant dispersion of the film occurs leading to its destruction after 10-min exposition (Fig. 29.9a).

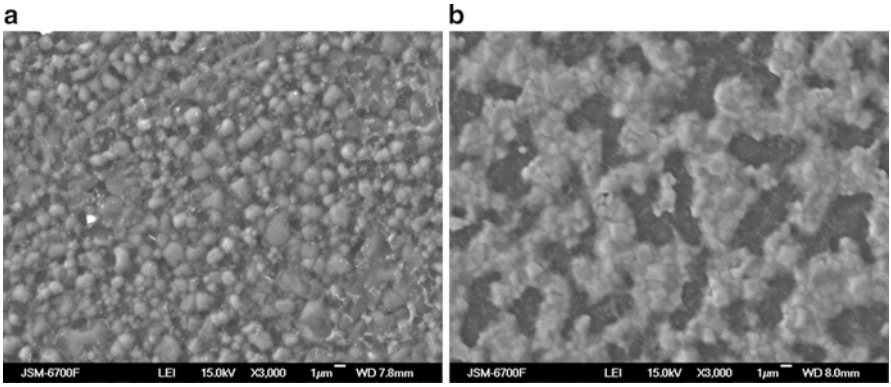

Fig. 29.8 SEM image (×3000) molybdenum film 100 nm thickness onto silicon carbide single crystal which was annealed in vacuum: (**a**) 1300 °C, 20 min, (**b**) 1500 °C, 20 min

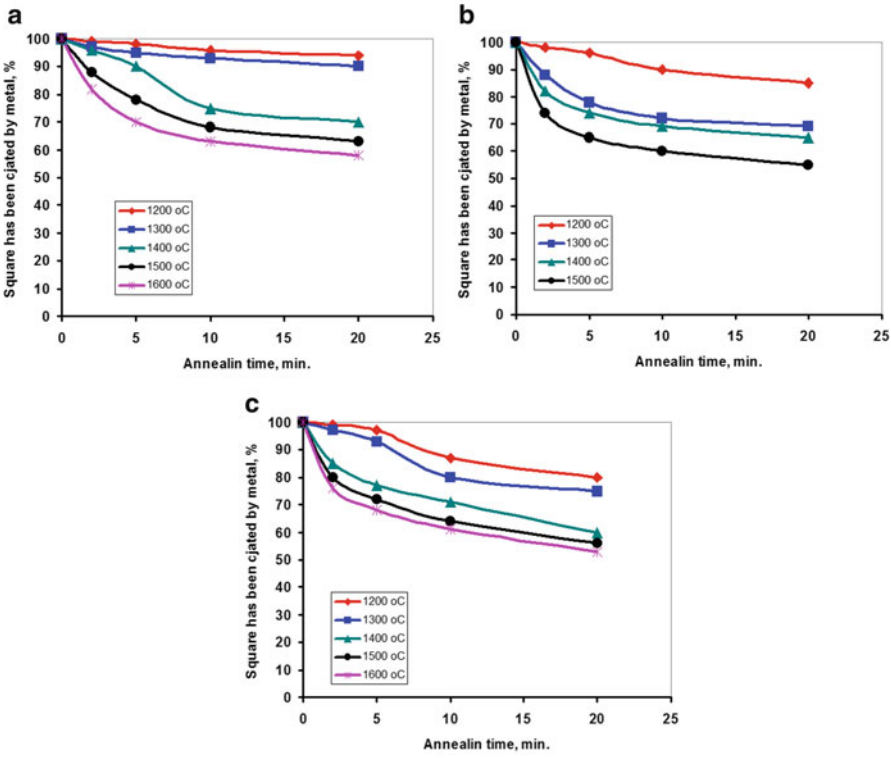

Fig. 29.9 Non-metallic non-oxide materials' area covered by molybdenum film depending on annealing time at various temperatures (1200–1600 °C): (**a**) silicon carbide single crystal, (**b**) nitride silicon ceramics, (**c**) nitride-aluminum ceramics

At a temperature 1500 °C the film destruction processes accelerated considerably. Thus, after 2-min exposition the film blistered strongly and began to disintegrate. This process intensified after 5 min; after 10 min the film disintegrated completely into narrow and rather long fragments, and 20-min annealing ended with the intensive interaction of these fragments with silicon carbide single-crystal substrate with the formation of large conglomerates of, obviously, new phases (Fig. 29.8b).

Figure 29.9, a shows dependences of the area of silicon carbide single-crystal substrate coated by molybdenum film on the annealing time at different temperatures (1200–1600 °C). According to these charts, brazing of silicon carbide metallized by molybdenum can be carried out throughout the studied temperature range.

The initial continuous molybdenum film onto nitride silicon ceramic surface remained virtually unchanged even after 2-min annealing at 1200 °C, the first cracks in it appeared after 5-min exposition, their number increased after 10-min exposition, and after 20-min annealing, the film began to disintegrate (Fig. 29.10a). Two-minute annealing at temperature up to 1300 °C caused significant changes in the film morphology in the form of a significant blistering and the appearance of a large number of cracks which sizes increased with a further increase of annealing time up to 5 and 10 min. After 20-min annealing, at this temperature the film was completely dispersed into rather large conglomerates (Fig. 29.9b).

After 2 min of annealing at 1400 °C, the changes in the film morphology were similar to those occurring after 2-min annealing at 1300 °C. With further increase of the annealing time up to 5 min, the film began not only to disperse, but also to interact with the substrate and this interaction increased significantly after 10-min exposition (Fig. 29.9b), and especially after 20-min annealing.

The increase of the annealing temperature up to 1500 °C significantly intensified the film morphology change process depending on the time of annealing. Thus,

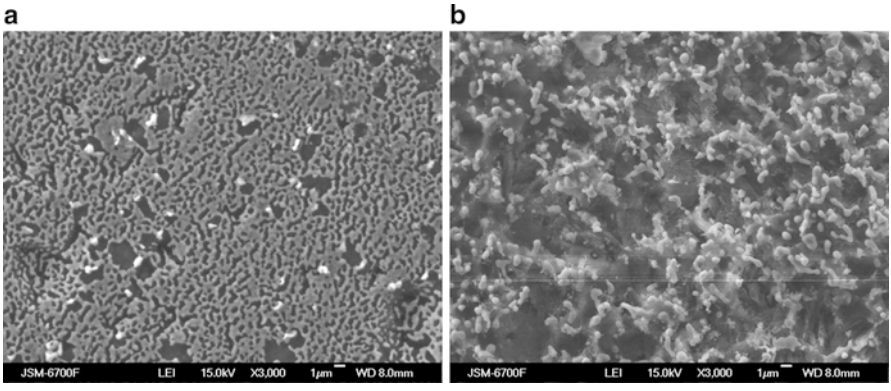

Fig. 29.10 SEM image (×3000) of molybdenum film of 100 nm thickness onto nitride silicon ceramics which was annealed in vacuum: (**a**) 1200 °C, 20 min, (**b**) 1500 °C, 5 min

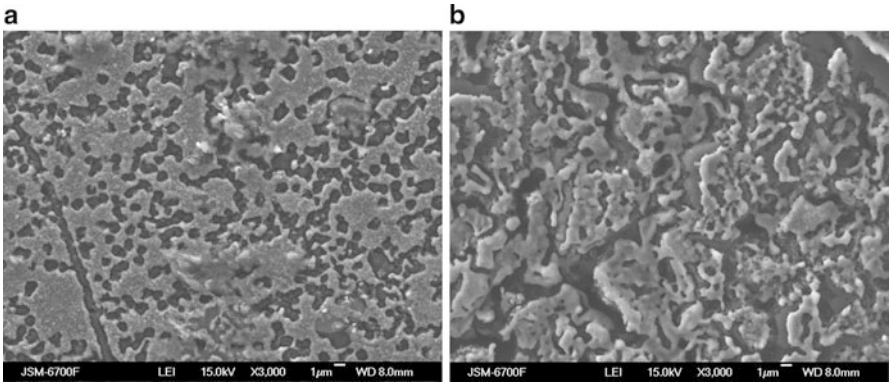

Fig. 29.11 SEM image (×3000) of molybdenum film of 100 nm thickness onto nitride-aluminum ceramics which was annealed in vacuum: (**a**) 1200 °C, 20 min, (**b**) 1600 °C, 20 min

after 2-min annealing the film disintegrated completely into fragments of different sizes and shapes. After 5-min exposition an intensive interaction of the film with the substrate took place (Fig. 29.10b).

Figure 29.9b shows curves of the dependence of the nitride silicon substrate area coated with molybdenum film on the annealing time at different temperatures. According to these charts, brazing of nitride silicon ceramic metallized with molybdenum should be performed at temperatures up to 1200 °C when the molybdenum film covers a sufficiently large area of ceramics (~75%).

Intensive changes in the morphology of the initially continuous molybdenum film deposited onto nitride-aluminum ceramics taking the form of small cracks and pores appeared after 2-min annealing at 1200 °C, and their number increased slightly after 5-min exposition. After 10- and 20-min annealing, the film partially dispersed (Fig. 29.11a) covering about 80% of the substrate in the latter case (Fig. 29.9c). With the annealing temperature increase up to 1300 °C, the nature of the film dispersion remains the same, but only the process of dispersion becomes a little more intense. Thus, after 2-min annealing the film exhibited more pronounced changes compared to 2-min annealing at 1200 °C. With the subsequent exposition time increase, the film dispersed a little more covering about 75% of the substrate area after 20-min annealing.

The temperature increase up to 1400 °C accelerated significantly the film dispersion which began after 2-min exposition. This disintegration intensified after 5- and 10-min exposition; and after 20-min annealing the film was a continuous lace covering at the same time almost 60% of the substrate surface (Fig. 29.9c).

The annealing of the film at 1500 °C led to its rapid disintegration after 2-min exposition. Further increase of the annealing time up to 5 min significantly accelerated the fragmentation process (Fig. 29.9c). Micrograph taken with the atomic force microscope shows that the film does not only decompose, but also coagulate and begin to interact with the substrate surface (Fig. 29.12a). The films

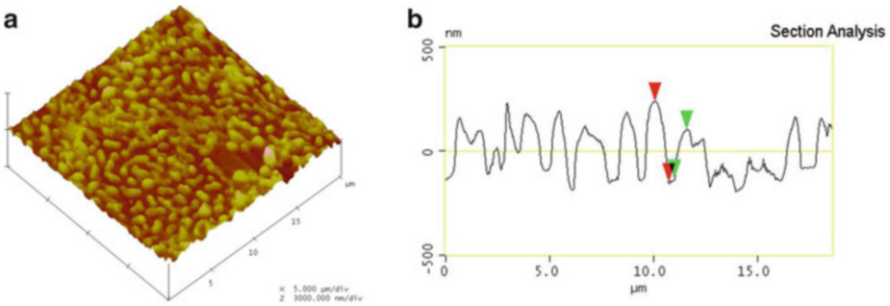

Fig. 29.12 AFM images of molybdenum film of 100 nm thickness onto nitride-aluminum ceramics after annealing at 1500 °C during 5 min in vacuum: (**a**) three-dimensional image, (**b**) film profile

fragments are increased significantly up to 250 nm high, exposing the substrate surface damaged by interaction (Fig. 29.12b), the depth of cavities in which reaching an average of 150 nm from the initial surface level. 10-min annealing accelerated also the process of the film decomposition, which after 20-min exposition ended with the complete disintegration of the film into separate fragments of various shapes, preferably oblong, covering more than 60% of the substrate surface (Fig. 29.9c).

As a result of annealing at 1600 °C, already after 2-min exposition the film began not only to decompose intensively (Fig. 29.9c), but also to interact intensively with the substrate material aluminum nitride.

With the subsequent increase of the annealing time up to 5 min, the interaction of the film with the substrate increased and practically ended after 10-min exposition, slightly changing the appearance of the surface after 20-min annealing (Fig. 29.11b). This indicates that the entire film interacted with the substrate.

Figure 29.9c shows dependences of the alumina nitride ceramic substrate area coated by molybdenum film on annealing time at different temperatures. These chart analyses lead to a conclusion that optimum temperature for brazing of the alumina nitride ceramics metallized by molybdenum is 1400 °C, when film covers more than 70% of the aluminium nitride surface.

29.4 Conclusions

Studying the kinetics of dispersion during annealing in vacuum of molybdenum nanofilms 100 nm thick deposited onto oxide materials (quartz glass, leucosapphire and alumina ceramics) it was established that the first signs of films dispersion appear only after their annealing at 1200 °C. It was found that the most stable is the film on aluminum oxide ceramics, which, even after 20-min annealing at 1600 °C, covers about 50% of the substrate area. The least stable was the film onto the quartz

glass, which begins to disperse intensively and to interact with the substrate surface already at 1300 °C.

It was found that among molybdenum nanofilms deposited onto non-oxide materials (silicon and aluminum nitrides, silicon carbide single crystals), the least stable during annealing is the film at the silicon nitride surface, which decomposes rapidly and begins to interact with the substrate surface already after annealing at 1300 °C. With temperature and annealing time increase, it interacts completely with the substrate. The most stable were films deposited onto aluminum nitride surface which even after 20-min annealing at 1500 °C cover more than 60% of the substrate area, which makes it possible to recommend the soldering of these materials metallized by molybdenum at temperatures up to 1500 °C.

According to the studies' results, the kinetic curves were built for the dispersion of molybdenum nanofilms deposited onto non-metallic inorganic materials (oxides and non-oxides) during their annealing in vacuum within the temperature range 1200–1600 °C on the basis of which process modes for brazing of the studied materials can be developed, namely, the necessary parameters of these modes (temperature, time) can be found.

References

1. Elssner G, Diem W, Wallace JS (1981) Microstructure and mechanical properties of metal-to-ceramic and ceramic-to-ceramic joints. In: Proceedings of (17 Univ. Conf. Ceram. "Surfaces and Interfaces Ceram. and Ceram.–Metal Syst." Berkeley, Calif., July 28 – August 1, 1980), New York/London, p 629
2. Pan WX, Okamoto T, Ning XS (1994) Joining of Al-plasma-sprayed Si_3N_4 ceramics. J Mater Sci 29(6):1436
3. Dalgleish BJ, Tomsia AP, Nakashima K et al (1994) Temperature routes to joining ceramics for high temperature applications (2nd Int Workshop Interfaces, Santiago, Sept 27-29, 1993). Scr Met Et Mater 31(8):1043
4. Hu MZ, Hunt RD, Payzant EA et al (1999) Nanocrystallization and phase transformation in monodispersed ultrafine zirconia particles from various homogeneous precipitation methods. J Amer Ceram Soc 82(9):2313
5. Piticescu RR, Monty C, Taloi D (2001) Hydrothermal synthesis of zirconia nanomaterials. J Eur Ceram Soc 21:2057
6. Naydich YV (1972) Contact phenomena in metallic melts. Naukova Dumka, Kiev
7. Nikolas M (1974) Physical aspect of liquid metals. Ingenierus blad 43(5):139
8. Kang HJ, Kim CH, Park NS, Kim MW (1996) The surface and interface reaction of metal thin film on sapphire substrate. J Appl Surf Sci 100–101:160
9. Koganitskaya EV (1959) Spai keramiki s aktivnymi metallami. Elektronica 4:86. (in Russian)
10. Harding FL, Rossington DR (1970) Wetting of ceramic oxides by molten metals under ultrahigh vacuum. J Am Ceram Soc 53(2):87
11. Naydich YV, Gab II, Zhyravlev VS, Dubrova VF, Gordynya AN (1989) Brazing nonmetallic materials to metals in vacuum brazing solder filled gap. J Welding Tech 2:12. (in Russian)
12. Rhee SK (1971) Wetting ceramic by liquid metals. J Am Ceram Soc 54(7):332
13. Metelkin II, Pavlov MA, Pozdeeva NV (1977) Svarka keramiki s metallami. Metallurgia, Moscow. (in Russian)

14. Melnikov VV, Eremeev SV, Kulkova SE (2011) Izuchenie adhezii plenok niobiya na raznoorientirovanyh poverhnostyah α-Al_2O_3. J Tech Phys 81(10):114. (in Russian)
15. Qiao-ying T, Lai-fei C, Li-tong Z (2004) Infiltration bonding C/SiC composite and niobium [J]. J Aviat Mater 24(1):53
16. Masaaki N, Tohru S, Ikuo O (1988) Bonding behavior between niobium and reaction-sintered SiC. Trans JWRI 17(2):67
17. Shalz ML, Dalgleish BJ, Tomsia AP, Cannon RM, Glaesser AM (1994) Ceramic joining III. Bonding of alumina via Cu/Nb/Cu interlayers. J Mater Sci 29(14):3678
18. Marks RA, Sugar JD, Glaeser AM (2001) Ceramic joining IV. Effect of processing conditions on the properties of alumina joined via Cu|nb|Cu interlayers. J Mater Sci 36(23):5609
19. Marks RA, Chapmen DR, Danielson DT, Glaeser AM (2000) Joining of alumina via copper/niobium/copper interlayers. Acta Mater 48(18):4425
20. Gab II, Zhyravlev VS, Kurkova DI, Stetsyuk TV, Naidich YV (1997) Contact interaction of oxide materials with refractory metals with high-temperature solid phase pressure welding. J Powder Metal 7(8):69. (in Ukranian)
21. Karakozov ES, Kotelkin IS, Matveev GN et al (1968) The formation mechanism of the compound at the solid state welding of ceramics from Al with Nb. J Phys Chem Mater Treat 3:123. (in Russian)
22. Naidich YV, Gab II, Stetsyuk TV et al (2017) Kinetics of fragmentation during annealing in vacuum of titanium nanofilms deposited onto non-metallic materials. J Phys Chem Solid State 18(2):158
23. Naidich YV, Gab II, Stetsyuk TV et al (2017) Influence of annealing in vacuum on dispersion kinetics of palladium and platinum nanofilms deposited onto oxide materials. Springer Proc in Phys 195:457
24. Batygin VN, Metelkin II, Reshetnikov AM (1982) Vacuum dense ceramics and its junctions with metals. Energiya, Moscow. (in Russian)
25. Khryapin VE (1981) Solder handbook. Mashinostroenie, Moscow. (in Russian)
26. Volkov AV, Moiseev OY, Poletaev SD (2013) High-resolution laser recording of contact masks on molybdenum films. J Computernaya Optica 37(2):220
27. Wang SF, Yang HC, Wang SF et al (2014) Characteristics of bilayer molybdenum films deposited using RF sputtering for back contact of thin film solar cells. J Adv Mater Sci Eng:ID 531401
28. Metfessel S (1963) Tonkie plenki, sh szgotovlenie I izmerenie. Gosenergoizdat. Moscow-Liningrad. (in Russian)
29. Khaas G, Tun PE (1968) Thin film physics. Mir, Moscow. (in Russian)
30. Naydich YV, Gab II, Kostyuk BD, Stetsyuk TV, Kurkova DI, Dukarov SV (2007) Investigation of the ceramic materials connection processes (soldering) using metal nanofilms. J Rep Natl Acad Sci Ukr 35:97. (in Ukranian)

Part II
Applications

Chapter 30
Effective Hamiltonians for Magnetic Ordering Within Periodic Anderson-Hubbard Model for Quantum Dot Array

L. Didukh, Yu. Skorenkyy, O. Kramar, and Yu. Dovhopyaty

30.1 Model of an Anderson-Hubbard Material

Modern technologies depend on the synthesis and implementation of novel materials with unique electrical and magnetic properties. Among the most promising of those materials, there are systems with quantum dots [1–3], in which an impurity is embedded into a matrix of the host material. Arrays of nano-sized quantum dots are anticipated to play a central role in a range of breakthrough application, from minimizing energy consumption and providing new effective means of energy harvesting to prospective quantum communication technologies. Experimental techniques of quantum dot array synthesizing have dramatically progressed recently. However, theoretical understanding of a collective behavior of these artificial atom systems lags behind, due to complexity of a model description and a large variety of competing magnetic and nonmagnetic phases.

Theoretical studies of an impurity energy level in a narrowband system have begun with a pioneering work by Anderson [4]. In papers [5, 6] a generalization of the single-site Anderson model for the system of periodically spaced Anderson-Hubbard centers, which is commonly known nowadays as periodic Anderson model, has been proposed. Within this model, in the limit of strong intra-atomic interaction between localized magnetic moments, the indirect exchange interaction, proportional to the fourth power of hybridization, and indirect hopping of electrons in the localized subsystem, proportional to the hybridization integral squared, have been shown to exist. Within the same model, the possibility of the fractional magnetic moment of transition metal atoms, due to the hybridization, has been

L. Didukh · Y. Skorenkyy · O. Kramar (✉) · Y. Dovhopyaty
Ternopil Ivan Puluj National Technical University, Ternopil, Ukraine
e-mail: kramar@tu.edu.te.ua

O. Fesenko, L. Yatsenko (eds.), *Nanocomposites, Nanostructures, and Their Applications*, Springer Proceedings in Physics 221,
https://doi.org/10.1007/978-3-030-17759-1_30

proven, and the observed T^2 and $T^{3/2}$ temperature dependences of magnetization have been derived.

In papers [7, 8] on the basis of single- and two-impurity Anderson models, the electrical conductance of a system with quantum dots has been studied. In the Hamiltonian of paper [8], the processes of Coulomb repulsion and hybridization of band and localized levels have been taken into account and the dependence of the conductivity on strength of Coulomb interaction between localized electrons is investigated. From the results of work [7], it follows that the magnetic order in a system of itinerant electrons plays an important role in the spin-dependent transport through a quantum dot. To investigate an onset of magnetic order within different variants of a generalized Hubbard model, an exact diagonalization approach has been applied for 2D and 3D clusters of quantum dots [9] and 1D interacting QDA [10]. Numerical results of exact diagonalization generally corroborate analysis done within analytical approaches like equation of motion for Green function method [10–14], but the latter provide more flexibility for modeling properties of novel materials for prospective applications [15].

Let us choose a model of the Anderson-Hubbard material which takes into account peculiarities of the electron correlations in narrow bands and describes both the "localized" (d-subsystem) and "itinerant" (s-subsystem) electrons in a form

$$H = H_0 + H_{\text{int}}, \tag{30.1}$$

where

$$H_0 = H_d + \sum_{\vec{k}\,\sigma} \left(\varepsilon_{\vec{k}} - \mu\right) a^{+}_{\vec{k}\,\sigma} a_{\vec{k}\,\sigma}, \tag{30.2}$$

$$H_{\text{int}} = \sum_{i\,\vec{k}\,\sigma} \left(V\left(i\,\vec{k}\right) d^{+}_{i\sigma} a_{\vec{k}\,\sigma} + h.c.\right) + \sum_{\substack{ij\,\vec{k} \\ i \neq j}} \left(V\left(ij\,\vec{k}, -\vec{k}\right) d^{+}_{i\sigma} d^{+}_{j\bar{\sigma}} a_{-\vec{k}\,\sigma} a_{\vec{k}\,\sigma} + h.c.\right), \tag{30.3}$$

Here $\varepsilon_{\vec{k}}$ is the energy of a carrier with wave vector $\vec{k}$, μ stands for chemical potential, $V(i\,\vec{k})$ and $V(ij\,\vec{k}, -\vec{k})$ are matrix elements describing the "single-electron" and "two-electron" hybridization of itinerant and localized subsystems, $d^{+}_{i\sigma}$ and $d_{i\sigma}$ are the operators of creation and annihilation of an electron with spin σ on i-th lattice site in "d"-state, and $a^{+}_{\vec{k}\,\sigma}$ and $a_{\vec{k}\,\sigma}$ are creation and annihilation operators for a conduction electron with spin σ and wave vector $\vec{k}$. H_d describes the "localized" electrons with Hamiltonian

$$H_d = (E_d - \mu)\sum_{i\sigma} d_{i\sigma}^{+} d_{i\sigma} + \sum_{ij\sigma}{}' t_{ij}(n) d_{i\sigma}^{+} d_{j\sigma} + \sum_{ij\sigma}{}' \left(T(ij) d_{i\sigma}^{+} d_{j\sigma} n_{\overline{\sigma}} + h.c.\right) + \\ + U\sum_{i} n_{i\uparrow} n_{i\downarrow} + \tfrac{1}{2}\sum_{ij\sigma\sigma'}{}' J(ij) d_{i\sigma}^{+} d_{j\sigma'}^{+} d_{i\sigma'} d_{j\sigma} + \tfrac{1}{2}\sum_{ij\sigma\sigma'}{}' V(ij) n_{i\sigma} n_{j\sigma'} \tag{30.4}$$

where

$$t_{ij}(n) = t(ij) + n \sum_{\substack{p \neq i \\ p \neq j}} J(ipjp) \tag{30.5}$$

describes the hoppings between the nearest-neighbor sites in the considered model. The model Hamiltonian (30.4) takes into account the main types of interactions in narrow orbitally nondegenerate band; the second and the third sums in (30.4) describe inter-site hopping, the fourth sum describes Coulomb repulsion of the same site, the fifth sum describes the interatomic exchange interaction, and the last sum corresponds to the interatomic Coulomb interaction. The peculiarities of this Hamiltonian are three types of electron transitions and, correspondingly, three types of the hopping integrals, namely, itinerant hopping

$$\sum_{ij\sigma}{}' t_{ij}(n) d_{i\sigma}^{+} d_{j\sigma}, \tag{30.6}$$

correlated hopping of the first type

$$\sum_{ij\sigma}{}' T_1(ij) d_{i\sigma}^{+} d_{j\sigma}, \tag{30.7}$$

and correlated hopping of the second type

$$\sum_{ij\sigma}{}' \left(T(ij) d_{i\sigma}^{+} d_{j\sigma} n_{\overline{\sigma}} + h.c.\right). \tag{30.8}$$

Taking into account the last sum in (30.3) can be justified by the importance of similar term, describing two-electron hopping between anion and neighboring cations (180°-type interaction):

$$\sim \sum_{ijn} \left(J(ijnm) d_{i\uparrow}^{+} d_{j\downarrow}^{+} a_{n\uparrow} a_{n\uparrow} + h.c.\right) \tag{30.9}$$

Here i and j are the nearest cation sites, n numbers the anion site between sites i and j, for stabilization of antiferromagnetic order in materials with narrow energy bands. Taking into account the correlated hopping terms allows to describe the important properties of narrowband systems, namely, the electron-hole asymmetry [16–18] and correlated band narrowing causing effective masses splitting in the external magnetic field [19–21].

H_d in Eq. (30.2) takes into account interactions in d-subsystem, caused by the direct overlapping of the respective wave functions. The representation of H_d in form (30.4) is reasonable only for the description of d-subsystem in $3d$-metals [22]. For alloys of transition metals with other metals; the majority of oxides, sulfides, and selenides of the transition metals; high-temperature superconductors in particular, and rare-earth element compounds, the direct overlap of wave function in the localized electron subsystem is small; therefore, one can neglect all matrix elements except of those describing the interatomic electron hoppings and interatomic exchange interaction and take

$$H_d = (E_d - \mu) \sum_{i\sigma} d^+_{i\sigma} d_{i\sigma} + U \sum_i d^+_{i\uparrow} d_{i\uparrow} d^+_{i\downarrow} d_{i\downarrow}. \tag{30.10}$$

The standard band theory applicable to itinerant subsystem of the Hamiltonian (30.1) raises no doubts for cases of s- or p-electrons in transition metals and alloys and, probably, t_{2g}-electrons in transition metals. However this approach is incapable to provide a proper description of materials with narrow bands, such as SmS, solid solution $Sm_{1\text{-}x}RS$ (R = Ga, Yb, Gd, Nd) and heavy-fermion systems $CeAl_3$, $CeCu_2Si$, $CeCu_6$, $CeIn_3$, UPt and UBe_{13} (see [23, 24]). In the noted materials, unique physical properties are caused by the presence of the narrow conduction band. Therefore, for the description of these systems, one has to take into account the correlation effects. The most straightforward modification of the model for the case of narrow band is to make the following substitution:

$$\sum_{\vec{k}\sigma} \varepsilon_{\vec{k}} a^+_{\vec{k}\sigma} a_{\vec{k}\sigma} \to H_c, \tag{30.11}$$

where H_c has the same structure as Hamiltonian (30.4); in this case the "localized" subsystem Hamiltonian is to be chosen in form (30.10). Thus, for the description of $(c + d)$-subsystem, in distinction form $s + d$-subsystem, described by the Hamiltonian (30.3), one can start with Hamiltonian

$$H = H_c + H_d + H_{cd}, \tag{30.12}$$

where H_{cd} is a generalization of s-d-hybridization in s-d-model

$$H_{cd} = \sum_{ij\sigma} \left(V(ij) c^+_{i\sigma} d_{j\sigma} + h.c. \right) + \sum_{ijnl\sigma} \left(V(ijnl)\, c^+_{i\sigma} c^+_{j\sigma} d_{n\sigma} d_{l\sigma} + h.c. \right). \tag{30.13}$$

In (30.12), as well as in *s-d*-Hamiltonian (30.1), the inter-site exchange interactions are not taken into account. One can show that ferro- or antiferromagnetic ordering in *d*-subsystem can be stabilized by indirect exchange, caused by hybridization, and possibly by translation exchange mechanism in *c*-subsystem. The model (30.12) can be useful for explaining the antiferromagnetic order in metal oxides and peculiarities of their electrical properties [25].

30.2 Configurational Model of Narrowband Material with Anderson Centers

The configurational representation has the peculiarity of a diagonal form for Coulomb on-site repulsion and a correlation effect on electron transfer processes. For both Anderson impurities and Hubbard centers interacting with neighbors through electron hoppings, the configurational representation appears to be very useful.

Let us pass in the Hamiltonian of periodic Anderson model with two-electron hybridization from electron $d_{i\sigma}^{+}$- and $d_{i\sigma}$-operators to X_i^{kl}-operators. One has

$$H = H_0 + H_1 + H_2, \tag{30.14}$$

where

$$\begin{aligned} H_0 = E \sum_i \left(X_i^{\uparrow} + X_i^{\downarrow} + 2X_i^2 \right) + U \sum_i X_i^2 + \sum_{\vec{k}\,\sigma} \varepsilon_{\vec{k}} c_{\vec{k}\,\sigma}^{+} c_{\vec{k}\,\sigma} - \\ - \sum_{ij\sigma} \frac{J(ij)}{2} \left(\left(X_i^{\sigma} + X_i^2 \right) \left(X_j^{\sigma} + X_j^2 \right) + X_i^{\sigma\bar{\sigma}} X_j^{\bar{\sigma}\sigma} \right), \end{aligned} \tag{30.15}$$

$$H_1 = H_a + H_b, \tag{30.16}$$

$$H_2 = H_c + H_d + H_e, \tag{30.17}$$

and

$$H_a = \sum_{i\,\vec{k}\,\sigma} \left(\eta_\sigma V \left(\vec{k}\, i \right) c_{\vec{k}\,\sigma}^{+} X_i^{0\sigma} + h.c. \right), \tag{30.18}$$

$$H_b = \sum_{i\,\vec{k}\,\sigma} \left(V \left(\vec{k}\, i \right) c_{\vec{k}\,\sigma}^{+} X_i^{\sigma 2} + h.c. \right), \tag{30.19}$$

$$H_c = 2 \sum_{ij\,\vec{k}} \left(V \left(ij\,\vec{k}, -\vec{k} \right) X_i^{\uparrow 0} X_j^{\downarrow 0} c_{\vec{k}\uparrow} c_{-\vec{k}\downarrow} + h.c. \right), \tag{30.20}$$

$$H_d = 2\sum_{ij\,\vec{k}} \left(V\left(ij\,\vec{k}, -\vec{k}\right) X_i^{2\uparrow} X_j^{2\downarrow} c_{-\vec{k}\downarrow} c_{\vec{k}\uparrow} + h.c. \right), \tag{30.21}$$

$$H_e = 2\sum_{ij\,\vec{k}} \left(V\left(ij\,\vec{k}, -\vec{k}\right) \left(X_i^{\downarrow 0} X_j^{2\downarrow} c_{-\vec{k}\downarrow} c_{\vec{k}\uparrow} - X_i^{2\uparrow} X_j^{\uparrow 0} c_{-\vec{k}\downarrow} c_{\vec{k}\uparrow} \right) + h.c. \right), \tag{30.22}$$

where $\eta_\uparrow = -1$, $\eta_\downarrow = 1$.

The possible positions of E_d and $(E_d + U)$-levels, which correspond to $|d\sigma>$-, $|d\uparrow\downarrow>$-states can be shown in the energy diagram for the single-impurity Anderson model (Fig. 30.1). This diagram allows drawing some conclusions from the very representation of the Hamiltonian (30.14), which simplifies greatly the system description in comparison with electron representation.

Let us introduce parameters characterizing the relative strength of hybridization, described by components H_a, H_b, H_c, H_d, and H_e:

$$\frac{V\left(\vec{k}\,i\right)}{E_F - E_d} \equiv \vartheta_a\left(\vec{k}\,i\right), \quad \frac{V\left(i\,\vec{k}\right)}{E_d + U - E_F} \equiv \vartheta_b\left(i\,\vec{k}\right), \quad \frac{V\left(\vec{k}, -\vec{k}\,ij\right)}{2(E_F - E_d)} \equiv \vartheta_c\,(k, -kij),$$

$$\frac{V\left(ij, -\vec{k}\,\vec{k}\right)}{2(E_d + U - E_F)} \equiv \vartheta_d\left(ij, -\vec{k}\,\vec{k}\right), \quad \frac{V\left(ij, -\vec{k}\,\vec{k}\right)}{2E_d + U - E_F} \equiv \vartheta_e\left(ij, -\vec{k}\,\vec{k}\right). \tag{30.23}$$

If for one of the parameters ϑ_i $(i = a, b, c, d, e)$ in (30.23) the condition $\vartheta_i << 1$, is fulfilled, then the hybridization interaction which corresponds to H_i part can be taken into account by the perturbation theory, for which a convenient form can be obtained within the configurational representation. The fulfillment of inequalities of type $E_d + U - E_F >> E_F - E_d$ or the opposite one allows neglecting the transfer processes in Hamiltonian (30.14). This conclusion is in accordance with estimates of hybridization matrix elements done in the monograph [26]. This way not only the *s-d*-exchange effect but also the interatomic exchange with parameter, proportional to the fourth power of the hybridization parameter, is obtained. Usefulness of X_i^{kl}-operator representation for Anderson-type models is caused by expediency of the mathematical treatment of such Hamiltonians within the Green function method.

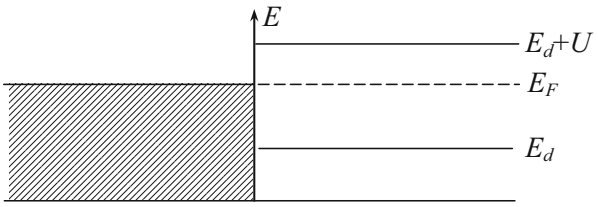

Fig. 30.1 Energy level diagram for $(s + d)$-system

30.3 The Hamiltonian of Strongly Correlated Electron System of Anderson-Hubbard Type

Here we introduce the method of transition by excluding the high-energy $|d\uparrow\downarrow\rangle$ states for strongly correlated electron system models for which a hybridization of the localized $|d\sigma\rangle$ states with conduction band is inherent on the example of single-site Anderson model.

The energy diagram of single-impurity Anderson model in the absence of *s-d*-transitions is represented by Fig. 30.2.

In terms of Hubbard operators, the corresponding Hamiltonian is

$$H_0 = \sum_{\vec{k}\,\sigma} \varepsilon_{\vec{k}} a^{+}_{\vec{k}\,\sigma} a_{\vec{k}\,\sigma} + E_d \left(X^{\uparrow}_d + X^{\downarrow}_d + 2X^2_d \right) + U X^2_d, \tag{30.24}$$

where X^{σ}_d is a number operator for a single occupied d-electron with spin σ state and X^2_d is a number of doubly occupied $|d\uparrow\downarrow\rangle$ sites.

Perturbations related to the transitions between $|d\sigma\rangle$- and $\vec{k}$ -states and between $\vec{k}$ - and $|d\uparrow\downarrow\rangle$-states are

$$H_1 = \sum_{\vec{k}\,\sigma} V\left(\vec{k}\,d\right) a^{+}_{\vec{k}\,\sigma} a_{d\sigma} + h.c.$$

or, in X^{kl}_i-operators

$$H_1 = \sum_{\vec{k}\,\sigma} V\left(\vec{k}\,d\right) a^{+}_{\vec{k}\,\sigma} \left(X^{\bar{\sigma}2} + \eta_\sigma X^{0\sigma} \right) + h.c. \tag{30.25}$$

The representation of the Anderson Hamiltonian in terms of the polar model shows that *s-d*-transitions are connected with creation and annihilation of holes and

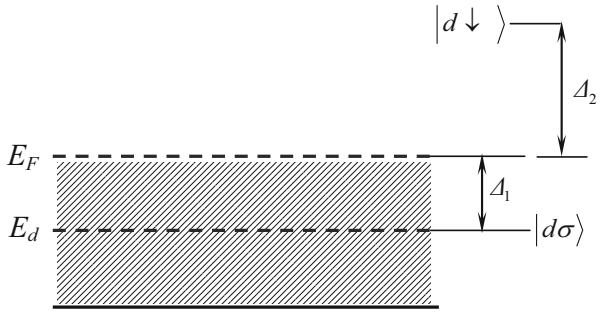

Fig. 30.2 Energy diagram of the single-site Anderson model, $\Delta_1 = E_F - E_d$, $\Delta_2 = E_d + U - E_F$

doublons in d-states, and lead also to the processes with electron spin reversal in d-state.

We assume that the parameters characterizing relative values of hybridization (30.23) comply with the conditions

$$\begin{aligned} &\vartheta_a\left(\overrightarrow{k}\,i\right) << 1, \quad \vartheta_b\left(i\,\overrightarrow{k}\right) << 1, \quad \vartheta_c\left(\overrightarrow{k}\,,-\overrightarrow{k}\,ij\right) << 1, \\ &\vartheta_d\left(ij,-\overrightarrow{k}\,\overrightarrow{k}\right) << 1, \quad \vartheta_e\left(ij,-k\,\overrightarrow{k}\right) << 1 \end{aligned} \tag{30.26}$$

and perform the canonical transformation which excludes from the Hamiltonian the terms of the first order of magnitude in $V\left(i\,\overrightarrow{k}\right)$ and $V\left(ij\,\overrightarrow{k}\,,-\overrightarrow{k}\right)$

$$\tilde{H} = e^{s} H e^{-s}, \tag{30.27}$$

where

$$S = S_a + S_b + S_c + S_d, \tag{30.28}$$

$$\begin{aligned} S_a &= \sum_{i\,\overrightarrow{k}} L_a\left(\overrightarrow{k}\,i\right)\left(a^{+}_{\overrightarrow{k}\,\downarrow} X_i^{0\downarrow} - a^{+}_{\overrightarrow{k}\,\uparrow} X_i^{0\uparrow}\right) + \sum_{i\,\overrightarrow{k}} M_a\left(i\,\overrightarrow{k}\right)\left(X_i^{\downarrow 0} a_{\overrightarrow{k}\,\downarrow} - X_i^{\uparrow 0} a_{\overrightarrow{k}\,\uparrow}\right), \\ S_b &= \sum_{i\,\overrightarrow{k}} L_b\left(\overrightarrow{k}\,i\right)\left(a^{+}_{\overrightarrow{k}\,\uparrow} X_i^{\downarrow 2} + a^{+}_{\overrightarrow{k}\,\downarrow} X_i^{\uparrow 2}\right) + \sum_{i\,\overrightarrow{k}} M_b\left(i\,\overrightarrow{k}\right)\left(X_i^{2\downarrow} a_{\overrightarrow{k}\,\uparrow} + X_i^{2\uparrow} a_{\overrightarrow{k}\,\downarrow}\right), \\ S_c &= \sum_{ij\,\overrightarrow{k}} L_c\left(ij\,\overrightarrow{k}\right) X_i^{\uparrow 0} X_j^{\downarrow 0} a_{\overrightarrow{k}\,\uparrow} a_{-\overrightarrow{k}\,\downarrow} + \sum_{ij\,\overrightarrow{k}} M_c\left(\overrightarrow{k}\,ji\right) a^{+}_{-\overrightarrow{k}\,\downarrow} a^{+}_{\overrightarrow{k}\,\uparrow} X_j^{0\downarrow} X_i^{0\uparrow}, \\ S_d &= \sum_{ij\,\overrightarrow{k}} L_d\left(ij\,\overrightarrow{k}\right) X_i^{2\uparrow} X_j^{2\downarrow} a_{-\overrightarrow{k}\,\downarrow} a_{\overrightarrow{k}\,\uparrow} + \sum_{ij\,\overrightarrow{k}} M_d\left(\overrightarrow{k}\,ji\right) a^{+}_{\overrightarrow{k}\,\uparrow} a^{+}_{-\overrightarrow{k}\,\downarrow} X_j^{\downarrow 2} X_i^{\uparrow 2}, \end{aligned} \tag{30.29}$$

and $L\left(i\,\overrightarrow{k}\right)$, $M\left(\overrightarrow{k}\,i\right)$, $L\left(ij\,\overrightarrow{k}\right)$ and $M\left(\overrightarrow{k}\,ij\right)$ are determined by equations

$$\begin{aligned} &[S_a H_0] + H_a = 0, \ [S_b H_0] + H_b = 0, \ [S_c H_0] + \tfrac{1}{2}[S_a H_a]' + H_c = 0, \\ &[S_d H_0] + \tfrac{1}{2}[S_b H_b]' + H_d = 0. \end{aligned} \tag{30.30}$$

We obtain

$$L_a\left(\overrightarrow{k}\,i\right)=\frac{V\left(\overrightarrow{k}\,i\right)}{\varepsilon_{\overrightarrow{k}}-E_d},\quad M_a\left(i\,\overrightarrow{k}\right)=\frac{V\left(i\,\overrightarrow{k}\right)}{E_d-\varepsilon_{\overrightarrow{k}}},\quad L_b\left(\overrightarrow{k}\,i\right)=\frac{V\left(\overrightarrow{k}\,i\right)}{\varepsilon_{\overrightarrow{k}}-E_d-U},$$

$$M_b\left(i\,\overrightarrow{k}\right)=\frac{V\left(i\,\overrightarrow{k}\right)}{E_d+U-\varepsilon_{\overrightarrow{k}}},\quad L_c\left(ij\,\overrightarrow{k}\right)=\frac{V\left(ij\,\overrightarrow{k},\overrightarrow{k}\right)}{2\left(\varepsilon_{\overrightarrow{k}}-E_d\right)},\quad M_c\left(\overrightarrow{k}\,ij\right)=\frac{V\left(-\overrightarrow{k},\overrightarrow{k},ji\right)}{2\left(E_d-\varepsilon_{\overrightarrow{k}}\right)},$$

$$L_d\left(ij\,\overrightarrow{k}\right)=\frac{V\left(ij\,\overrightarrow{k},-\overrightarrow{k}\right)}{2\left(\varepsilon_{\overrightarrow{k}}-E_d-U\right)},\quad M_d\left(\overrightarrow{k}\,ij\right)=\frac{V\left(-\overrightarrow{k},\overrightarrow{k},ji\right)}{2\left(E_d+U-\varepsilon_{\overrightarrow{k}}\right)},\tag{30.31}$$

So we restrict ourselves to the terms up to terms of the forth order of magnitude (we take $V\left(i\,\overrightarrow{k}\right)$ to be the first order of magnitude, $V\left(ij\,\overrightarrow{k},-\overrightarrow{k}\right)$ of the second order, H_0 of the zeroth order). Then the Hamiltonian takes the following form:

$$\tilde{H}=H+[SH]+\frac{1}{2}[S[SH_0]]+\frac{1}{6}[[S[SH]]]+\frac{1}{24}[S[S[S[SH_0]]]]+\ldots\tag{30.32}$$

Let us take into account that the spin-spin interaction between localized magnetic moments and indirect hopping in localized subsystem attributes only to terms of the fourth order of magnitude. Thus, we can neglect the processes of double creation or annihilation on the same site and the interaction of Bardeen-Cooper-Schrieffer (BCS) type in the itinerant subsystem. Then the effective Hamiltonian is

$$H=\tilde{H}_0+H_1'+H_{sd}+H_{dd}+H_{ss},\tag{30.33}$$

where

$$\tilde{H}_0=H_0+\sum_{ij\sigma}t_0(ij)X_i^{\sigma 0}X_j^{0\sigma}+\sum_{ij\sigma}t_2(ij)X_i^{2\sigma}X_j^{\sigma 2},\tag{30.34}$$

$$H_1'=\sum_{ij}\left(t_{02}(ij)\left(X_i^{2\downarrow}X_j^{0\uparrow}-X_i^{2\uparrow}X_j^{0\downarrow}\right)+e.c.\right),\tag{30.35}$$

$$\begin{aligned}H_{sd}=\sum J_1\left(i\,\overrightarrow{k}\,\overrightarrow{k}'\,i\right)\Big(&a^+_{\overrightarrow{k}\uparrow}a^+_{\overrightarrow{k}'\uparrow}\left(X_i^{\uparrow}+X_i^0\right)+a^+_{\overrightarrow{k}\downarrow}a^+_{\overrightarrow{k}'\downarrow}\left(X_i^{\downarrow}+X_i^0\right)-\\&-a^+_{\overrightarrow{k}\downarrow}a_{\overrightarrow{k}'\uparrow}X_i^{\uparrow\downarrow}-a^+_{\overrightarrow{k}\downarrow}a_{\overrightarrow{k}'\uparrow}X_i^{\downarrow\uparrow}\Big)+\sum J_2\left(ikk'i\right)\Big(a^+_{\overrightarrow{k}\uparrow}a_{\overrightarrow{k}'\uparrow}\left(X_i^{\downarrow}+X_i^2\right)+\\&+a^+_{k\downarrow}a_{k'\downarrow}\left(X_i^{\uparrow}+X_i^2\right)+a^+_{k\downarrow}a_{k'\uparrow}X_i^{\uparrow\downarrow}+a^+_{k\uparrow}a_{k'\downarrow}X_i^{\downarrow\uparrow}\Big),\end{aligned}\tag{30.36}$$

H_{dd} describes the exchange interaction and indirect hopping of $|i0>$ − and $|i\uparrow\downarrow>$ −states, and H_0 describes s-electron subsystem:

$$t_0(ij) = \sum_{\vec{k} > \vec{k}_F} \frac{V\left(i\,\vec{k}\right)\, V\left(\vec{k}\, j\right)}{E_d - \varepsilon_{\vec{k}}}, \tag{30.37}$$

$$t_2(ij) = \sum_{\vec{k} > \vec{k}_F} \frac{V\left(i\,\vec{k}\right)\, V\left(\vec{k}\, j\right)}{E_d + U - \varepsilon_{\vec{k}}}, \tag{30.38}$$

$$t_{02}(ij) = \frac{1}{2}\left(t_0(ij) + t_2(ij)\right), \tag{30.39}$$

$$J_1\left(i\,\vec{k}\,\vec{k}'\,i\right) = \frac{V\left(i\,\vec{k}\right) V\left(\vec{k}'\,i\right)}{2}\left(\frac{1}{\varepsilon_{\vec{k}} - E_d} + \frac{1}{\varepsilon'_{\vec{k}} - E_d}\right), \tag{30.40}$$

$$J_2\left(i\,\vec{k}\,\vec{k}'\,i\right) = \frac{V\left(i\,\vec{k}\right) V\left(\vec{k}'\,i\right)}{2}\left(\frac{1}{\varepsilon_{\vec{k}} - E_d - U} + \frac{1}{\varepsilon'_{\vec{k}} - E_d - U}\right). \tag{30.41}$$

In the above formulae, $t_0(ij)$, $t_2(ij)$, and $t_{02}(ij)$ are the integrals of indirect hopping through the sites with localized electrons (cation subsystem in transition metal compounds, quantum dots, etc.). The magnitudes of these parameters can essentially renormalize the bare band hopping integral $t(ij)$ and enhance localization effects. In figure below, the mechanisms of the band and hybridization hopping mechanisms are shown. Due to the substantial overlapping of the wave functions of electrons in the conduction band, one should expect that not only indirect hopping renormalizes the band hopping but also hybridization exchange has greater magnitude (of order of $\frac{t^4}{\Delta^3}$) than direct exchange interactions.

One can see that taking into account the s-d-hybridization in the perturbation theory leads to the effective Hamiltonian in which there are pronounced effects of the single-electron hybridization: (1) indirect exchange in (σ-0)- and ($\uparrow\downarrow$-σ)-subbands, (2) pair creation and annihilation of holes and doublons, (3) indirect s-d-exchange interaction, and (4) indirect exchange interaction and indirect hopping between localized magnetic moments. Taking into account the two-electron hybridization leads to spin-spin correlation and to the electron interaction in a system of conduction electrons.

When the hybridization is small, the "real" holes are absent at $T = 0$, and for $T > 0$ (for T comparable to the temperature of magnetic ordering or superconducting transition),

$$\left\langle X_i^0 \right\rangle \sim \exp\left(\left(E_d - E_F\right)/kT\right), \tag{30.42}$$

$$\left\langle X_i^2 \right\rangle \sim \exp\left(\left(E_d + U - E_F\right)/kT\right), \tag{30.43}$$

these values are negligible, too, unless the system is doped. Taking into account that in the absence of strong hybridization the narrow (σ-0)-subband lies far below the Fermi level and ($\uparrow\downarrow$-σ)-subband is substantially above the Fermi level, the H_0 renormalization is not to be taken into account. The transitions described by H'_1 form "virtual" holes and doublons. These can be treated within the perturbation theory. This way the effective exchange-like Hamiltonian can be obtained:

$$H'_1 \to \sum_{ij\sigma} \frac{|t_{02}(ij)|^2}{U} \left(X_i^{\overline{\sigma}} X_j^{\overline{\sigma}} - X_i^{\sigma\overline{\sigma}} X_j^{\overline{\sigma}\sigma} \right) \tag{30.44}$$

which may be included in H_{dd}. Therefore, we have the effective Hamiltonian

$$H = H_0 + H_{sd} + H_{cd} + H_{dd} + H_{ss}, \tag{30.45}$$

where H_{cd} describes the indirect interaction between the itinerant and localized subsystems which is analogous to direct s-d-exchange in the s-d-model with one important difference, namely, negativity of the c-d-exchange integral caused by the transitions between $|\sigma > -$ or $|\uparrow\downarrow > -$states and conduction band while the direct s-d-exchange integral is positive. With spin operators $S_i^z = \frac{1}{2}\left(X_i^{\uparrow} - X_i^{\downarrow}\right)$, $S_i^+ = X_i^{\uparrow\downarrow}$, $S_i^- = -X_i^{\downarrow\uparrow}$, $\left\langle X_i^0 \right\rangle = 0$, and $\left\langle X_i^2 \right\rangle = 0$, we have

$$\begin{aligned} H_{cd} = \tfrac{1}{N} \sum_{i\,\vec{k}\,\vec{k}} J\left(kk'\right) \exp\left(i\,\vec{R}_i \left(\vec{k} - \vec{k}' \right) \right) + S_i^z \left(a^+_{\vec{k}\uparrow} a_{\vec{k}'\uparrow} - a^+_{\vec{k}\downarrow} a_{\vec{k}'\downarrow} \right) \\ + S_m^+ a^+_{\vec{k}\uparrow} a_{\vec{k}'\downarrow} + S_i^- a^+_{\vec{k}\downarrow} a_{\vec{k}'\uparrow} \Bigg), \end{aligned} \tag{30.46}$$

where

$$J\left(\vec{k}\,\vec{k}'\right) = \frac{V\left(\vec{k}\right) V\left(\vec{k}'\right)}{2} \left(\frac{1}{\varepsilon_{\vec{k}} - E_d - U} + \frac{1}{\varepsilon'_{\vec{k}} - E_d - U} - \frac{1}{\varepsilon_{\vec{k}} - E_d} - \frac{1}{\varepsilon'_{\vec{k}} - E_d} \right). \tag{30.47}$$

Let us take for the $J\left(\overrightarrow{k}\,\overrightarrow{k}'\right)$ estimate that the main contribution to the indirect *s*-*d*-exchange is done by the conduction electrons with energies close to Fermi level. Then

$$J\left(\overrightarrow{k}_F, \overrightarrow{k}_F\right) = \frac{UV^2\left(\overrightarrow{k}_F\right)}{(E_F - E_d - U)(E_F - E_d)} \tag{30.48}$$

and, if levels $|i\sigma>$ and $|i\uparrow\downarrow>$ have positions shown in Fig. 30.2, then $J\left(\overrightarrow{k}\,\overrightarrow{k}'\right)$ is a negative quantity. In a symmetrical case $E_d + U - E_F = E_F - E_d$, one has

$$J\left(\overrightarrow{k}_F, \overrightarrow{k}_F\right) = -4\frac{V^2\left(\overrightarrow{k}_F\right)}{U}. \tag{30.49}$$

The antiferromagnetic character of *s*-*d*-exchange interaction may lead to specific narrowband effects peculiar to the strongly correlated electron systems. This conclusion supports the results of paper [9] where for half-filled shell the antiferromagnetic Heisenberg exchange has been shown to determine magnetic properties and ferromagnetic coupling between the dots provided the mechanism for magnetic moment saturation for other fillings. We stress also the importance of direct ferromagnetic exchange and kinetic mechanisms [19, 27, 28] for adequate description of the competition between different magnetic ordering types at partial band fillings.

30.4 Narrowband Ferromagnet Case

Let us consider the case of partially filled narrow band, when the system is in the state of doped Anderson-Hubbard insulator, so for $n < 1$ we restrict ourselves to h_σ-subband and in the case $n > 1$ to d_σ-subband. For the less than half-filled band, the effective exchange integral becomes

$$\tilde{J}_{ij} = J_{ij} - \frac{2\left|t_{ij}(n)\right|^2}{U} \tag{30.50}$$

where J_{ij} is the direct (nearest-neighbor) interatomic exchange. The equation for magnetization can be obtained from the Green function

$$G^{\uparrow\downarrow}_{pp'}(E) = \left\langle\left\langle X^{\uparrow\downarrow}_p | X^{\downarrow\uparrow}_{p'}\right\rangle\right\rangle_E, \tag{30.51}$$

which also allows obtaining the Curie temperature. Equation of motion for the Green function (30.51) is

$$EG_{pp'}^{\uparrow\downarrow}(E) = \frac{\delta_{pp'}}{2\pi}m + \sum_i J(ip)\left\langle\left\langle\left(X_i^{\uparrow} - X_i^{\downarrow}\right)X_p^{\uparrow\downarrow}|X_{p'}^{\downarrow\uparrow}\right\rangle\right\rangle_E - \\ - \sum_i J(ip)\left\langle\left\langle\left(X_p^{\uparrow} - X_p^{\downarrow}\right)X_i^{\uparrow\downarrow}|X_{p'}^{\downarrow\uparrow}\right\rangle\right\rangle_E + \sum_i t_{ij}(n)\left\langle\left\langle X_i^{\uparrow 0}X_p^{0\downarrow}|X_{p'}^{\downarrow\uparrow}\right\rangle\right\rangle_E + \\ + \sum_i t_{ij}(n)\left\langle\left\langle X_p^{\uparrow 0}X_i^{0\downarrow}|X_{p'}^{\downarrow\uparrow}\right\rangle\right\rangle_E . \tag{30.52}$$

Using properties of X_i^{kl} operators, we use the identity

$$\left\langle\left\langle X_i^{\uparrow 0}X_p^{0\downarrow}|X_p^{\downarrow\uparrow}\right\rangle\right\rangle_E = \left\langle\left\langle X_i^{\uparrow\downarrow}X_i^{\downarrow 0}X_p^{0\uparrow}X_p^{\uparrow\downarrow}|X_p^{\downarrow\uparrow}\right\rangle\right\rangle_E \tag{30.53}$$

and apply the following mean-field-type approximation

$$\left\langle\left\langle X_i^{\uparrow\downarrow}X_i^{\downarrow 0}X_p^{0\uparrow}X_p^{\uparrow\downarrow}|X_p^{\downarrow\uparrow}\right\rangle\right\rangle_E = G_{pp'}^{\downarrow\uparrow}(E)\left\langle X_i^{\uparrow 0}X_p^{0\uparrow}\right\rangle + G_{pp'}^{\downarrow\uparrow}(E)\left\langle X_i^{\downarrow 0}X_p^{0\downarrow}\right\rangle. \tag{30.54}$$

For the Green function $G_{pp'}^{\downarrow\uparrow}(E)$ in $\vec{k}$ -space, one has

$$G_n(E) = \frac{1}{2\pi}\cdot\frac{m}{E - E\left(\vec{k}\right)}, \tag{30.55}$$

where

$$E\left(\vec{k}\right) = zmJ_{eff}\left(1 - \gamma\left(\vec{k}\right)\right); \tag{30.56}$$

$$J_{eff} = \tilde{J} + \frac{1}{zN}\sum_{ij}\left(\left\langle X_i^{\downarrow 0}X_j^{0\downarrow}\right\rangle - \left\langle X_i^{\uparrow 0}X_j^{0\uparrow}\right\rangle\right) \tag{30.57}$$

where $\gamma\left(\vec{k}\right) = \frac{1}{z}\sum\exp\left(i\vec{k}\,\vec{p}\right)$ (sum goes over the nearest-neighbor sites).

Thus, taking into account the translational motion of magnetically polarized electrons leads to a renormalization of the exchange integral in expression for spin-wave spectrum, which renormalization is determined by the energy difference of spin-up and spin-down electrons per lattice site. From Eq. (30.55) at non-zero temperature $\theta = k_BT$, we obtain a standard equation for the magnetization

$$\frac{n}{m} = \frac{\vartheta}{(2\pi)^3}\int cth\frac{E\left(\vec{k}\right)}{2\theta}d\vec{k}, \tag{30.58}$$

from which the Curie temperature can be obtained

$$\theta_c = \frac{nzJ_{eff}}{C}, \tag{30.59}$$

with constant C dependent on a lattice symmetry.

Mean values of the translational motion energy in the expression for the exchange integral can be calculated at $T = 0$ with magnetic order taken into account. One has

$$\frac{1}{N}\sum_{ij} t_{ij}(n)\left\langle X_i^{\sigma 0} X_j^{0\sigma}\right\rangle = -w(n)\frac{(1-n)\,n_\sigma}{1-n_{\overline{\sigma}}}, \tag{30.60}$$

where w stands for a non-perturbed bandwidths. For temperatures $\theta << \mu$, Eq. (30.60) contains terms, proportional to $(\theta/\varepsilon_F)^2$. For temperatures $\theta \leq \theta_c << w$, the effective exchange integral temperature dependence is weak, therefore

$$zJ_{eff} = z\tilde{J} + \frac{4(1-n)^2 w}{(2-n)^2 - m^2}, \tag{30.61}$$

and we obtain for the Curie temperature

$$\theta_c = \frac{n}{2c}\left[z\tilde{J} + \frac{4(1-n)^2 w}{(2-n)^2}\right]. \tag{30.62}$$

The above result illustrates the peculiarity of the narrow energy band, namely, the mechanism of ferromagnetic order stabilization by translational motion of electrons in a system with strong intra-atomic correlations. At $w >> z\tilde{J}$ in the considered narrowband system, θ_c increases at decreasing electron concentration. It follows from these considerations that narrow partially filled band has both metallic type of conductivity and magnetic properties typical for a system with localized magnetic moments.

30.5 Polar *s-d*-Model Case

The above considerations can be extended for the case of metallic ferromagnet with *s-d*-transfer activated. The generalized equation for magnetization is

$$\frac{1-\left\langle X_i^0\right\rangle - \left\langle X_i^2\right\rangle}{m} = \frac{\vartheta}{(2\pi)^3}\int cth\frac{E\left(\overrightarrow{k}\right)}{2\theta} d\overrightarrow{k}, \tag{30.63}$$

where the polar states concentration is to be calculated for the Hamiltonian (30.1).

Here, in distinction from the previous section, the polar states concentration depends on positions of $E_d + U$ and $E_d - J$ energy levels with respect to Fermi level. If $E_d + U - E_F = E_F - E_d + J$, then $X_i^0 = X_i^2$. Let us restrict ourselves to this case and calculate $\langle X_i^2 \rangle$ from the Green function $\left\langle\left\langle X_i^{\uparrow 2} | X_j^{2\downarrow} \right\rangle\right\rangle$ within approximations used for deriving the magnetization equation above. We obtain

$$G_{ii}(E) = \frac{1}{2\pi} \frac{\langle n_\uparrow \rangle}{E - E_d - U + J \langle n_\downarrow \rangle - \sum\limits_{\vec{k}} \frac{\left| V\left(\vec{k}\, i\right)\right|^2}{E - \varepsilon_{\vec{k}}}}. \tag{30.64}$$

Hence

$$\left\langle X_i^2 \right\rangle = \frac{1}{\pi} \int\limits_{-\infty}^{+\infty} \frac{\Delta \langle n_\uparrow \rangle}{\left(E - E_d - U + J \langle n_\downarrow \rangle\right)^2 + \Delta^2} \frac{dE}{(e^{\frac{E-\mu}{\theta}} + 1)}, \tag{30.65}$$

where

$$\Delta = \pi \sum_{\vec{k}} V\left(\vec{k}\, m\right)^2 \delta\left(E - \varepsilon_{\vec{k}}\right) \tag{30.66}$$

And the energy of d-level renormalization is taken into account:

$$E_d \to E_d - \sum_{\vec{k}} \frac{\left| V\left(\vec{k}\, i\right)\right|^2}{E - \varepsilon_{\vec{k}}}. \tag{30.67}$$

For low temperatures and when E_d and $E_d + U$ levels are symmetrical with respect to the Fermi level, the polar states concentration is

$$\left\langle X_i^2 \right\rangle = \left\langle X_i^2 \right\rangle_0 + \frac{\pi^2}{6} (k_B T)^2 \frac{d\rho_d}{dE}, \tag{30.68}$$

where

$$\left\langle X_i^2 \right\rangle_0 = \frac{1}{\pi} \langle n_\downarrow \rangle arcctg \frac{E_d + U - J \langle n_\uparrow \rangle - E_F}{\Delta} \tag{30.69}$$

is a mean number of doublons per site at $T = 0$

$$\rho_d = \frac{1}{\pi} \cdot \frac{\Delta}{\left(E_F - U + z n_\uparrow J\right)^2 + \Delta^2}. \tag{30.70}$$

Therefore, at low temperature, $n = 1$, $E_d + U - E_F \approx E_F - E_d + J$, the magnetization temperature dependence can be modeled as

$$m = 1 - 2\left\langle X_i^2 \right\rangle_0 - \alpha T^2 - \beta T^{3/2}, \tag{30.71}$$

with constants α and β. It means that the system of localized magnetic moments (quantum dot array) with s-d-hybridization in which the ferromagnetic order is stabilized by the effective exchange interaction has both the properties of a band ferromagnet (fractional magnetic moment and T^2 dependence for magnetization) and those of localized electrons ($T^{3/2}$ dependence).

30.6 Narrowband Antiferromagnet Case

For models of a narrowband antiferromagnet, obtaining the spectrum of magnetic excitations controlled by indirect exchange parameter with correct dependence on quasiparticle momentum has been a long-standing problem. Such calculation is simplified if the effective Hamiltonian in the form (30.33) is chosen. Let us introduce the Green functions

$$G_{pk}(E) = \left\langle\left\langle X_p^{\uparrow\downarrow} | X_k^{\downarrow\uparrow} \right\rangle\right\rangle_E, \tag{30.72}$$

$$T_{lp'}(E) = \left\langle\left\langle X_l^{\uparrow\downarrow} | X_k^{\downarrow\uparrow} \right\rangle\right\rangle_E, \tag{30.73}$$

where $X_p^{\downarrow\uparrow}$ is an antiferromagnon creation operator for lattice site p of sublattice A and $X_l^{\downarrow\uparrow}$ is operator of annihilation for antiferromagnon at site l of sublattice B. Equations for Green function $G_{pk}(E)$ can be written down as

$$(E - zmJ_\alpha)\, G_{pk}(E) = \frac{m}{2\pi}\delta_{pk}p' - m\sum_l J_\alpha(pl)T_{lk} + \sum_l t\left(p'l\right)\left\langle\left\langle\left[X_p^{\uparrow\downarrow}, H_t\right]_- | X_k^{\downarrow\uparrow}\right\rangle\right\rangle_E, \tag{30.74}$$

where the exchange interaction is treated in the mean-field approximation and commutation of $X_p^{\uparrow\downarrow}$ operator with translational part of the Hamiltonian is given by

$$\left[X_p^{\uparrow\downarrow}, H_t\right] = \sum_l t\left(p'l\right)\left(X_p^{\uparrow 0}X_l^{0\downarrow} - X_l^{\uparrow 0}X_p^{0\downarrow}\right). \tag{30.75}$$

Using properties of X_i^{kl} operators, the last term can be represented as

$$\sum_l t\left(p'l\right)\left\langle\left\langle\left(X_p^{\uparrow\downarrow}X_p^{0\downarrow}X_l^{0\downarrow}-X_l^{\uparrow\downarrow}X_l^{\downarrow 0}X_p^{0\downarrow}\right)|X_{p'}^{\downarrow\uparrow}\right\rangle\right\rangle. \tag{30.76}$$

Let us use the linearization procedure for the obtained equation of motion:

$$\left\langle\left\langle X_p^{\uparrow\downarrow}X_p^{0\downarrow}X_l^{0\downarrow}|X_{p'}^{\downarrow\uparrow}\right\rangle\right\rangle\approx\left\langle\left\langle X_p^{\uparrow\downarrow}|X_{p'}^{\downarrow\uparrow}\right\rangle\right\rangle\left\langle X_p^{0\downarrow}X_l^{0\downarrow}\right\rangle,$$

$$\left\langle\left\langle X_l^{\uparrow\downarrow}X_l^{\downarrow 0}X_p^{0\downarrow}|X_{p'}^{\downarrow\uparrow}\right\rangle\right\rangle\approx\left\langle\left\langle X_l^{\uparrow\downarrow}|X_{p'}^{\downarrow\uparrow}\right\rangle\right\rangle\left\langle X_l^{\downarrow 0}X_p^{0\downarrow}\right\rangle. \tag{30.77}$$

For the Green function (30.73), we have the following equation:

$$\left(E+zmJ_\alpha\right)T_{lp'}(E)=\sum_p t(lp)\left(X_l^{\uparrow 0}X_p^{0\downarrow}-X_p^{\uparrow 0}X_l^{0\downarrow}\right)-m\sum_p J_\alpha(pl)G_{pp'}(E)\,. \tag{30.78}$$

Transformation (30.78) allows passing in $\overrightarrow{k}$ space to the system of equations

$$\left(E-zm\tilde{J}_\alpha\right)G_{\overrightarrow{k}}(E)=\frac{m}{2\pi}+m\tilde{J}_\alpha\left(\overrightarrow{k}\right)T_{\overrightarrow{k}}(E),$$

$$\left(E+zm\tilde{J}_\alpha\right)T_{\overrightarrow{k}}(E)=-m\tilde{J}_\alpha\left(\overrightarrow{k}\right)G_{\overrightarrow{k}}(E), \tag{30.79}$$

where $G_{\overrightarrow{k}}(E)$ and $T_{\overrightarrow{k}}(E)$ are the Fourier components of functions (30.72) and (30.73) and $\tilde{J}_\alpha$ is renormalized by translational processes

$$\tilde{J}_\alpha=J_\alpha+\frac{1}{zN}{\sum_{ij}}'t(ij)\left\langle X_i^{\uparrow 0}X_j^{0\uparrow}\right\rangle. \tag{30.80}$$

One can see that the translational processes destabilize antiferromagnetism and a linear $E\left(\overrightarrow{k}\right)$ dependence is obtained.

30.7 Conclusions

On the basis of the canonical transformation method, the effective Hamiltonian of Anderson-Hubbard model taking into account the basic types of interactions in localized and itinerant electron subsystems as well as the hybridization of these subsystems has been obtained for the periodic array of magnetic quantum dots in

conductive matrices. The canonical transformation operator has been chosen in a form which separates processes of Hubbard subband analogues formation and those responsible for the indirect exchange between the magnetic moments.

The obtained effective Hamiltonian allows classifying the processes of indirect exchange and indirect hopping for the systems with Anderson-Hubbard centers, namely, the indirect hopping in (σ-0)- and ($\uparrow\downarrow$-σ)-subbands, the pair creation of holes and doublons, indirect *c*-*d*-exchange interaction, indirect exchange interaction, and indirect hopping between localized magnetic moments. Taking into account the two-electron hybridization leads to spin-spin interaction as well as BCS-type interaction in the itinerant electron subsystem. These results will allow a detailed study of magnetic ordering competitions within comprehensive models of strongly correlated electrons in quantum dot arrays, in analogy to investigations done for similar strongly correlated systems [19, 27–30].

References

1. Chakraborty T (1999) Quantum dots: a survey of the properties of artificial atoms. Elsevier Science, Amsterdam
2. Lan H, Ding Y (2012) Ordering, positioning and uniformity of quantum dot arrays. Nano Today 7:94–123
3. Fesenko O, Yatsenko L (2018) Nanooptics, Nanophotonics, nanostructures, and their applications. NANO 2017. Springer proceedings in physics, vol. Springer, Cham, p 210
4. Anderson PW (1961) Localized magnetic states in metals. Phys Rev 124:41–53
5. Didukh LD, Stasyuk IV (1968) Effective Hamiltonian in the Anderson model. Fiz Met Metalov 26:582–588. [In Russian]
6. Didukh LD, Stasyuk IV [In Russian] (1968) On ferromagnetism theory with account of s-d transfer. Ukr Fiz Zhurn 13:1774–1780. In Russian]
7. Zhang P, Xue Q-K, Wang Y, Xie XC (2002) Spin-dependent transport through an interacting quantum dot. Phys Rev Lett 89:286803
8. Dias da Silva L, Ingersent K, Sandler N, Ulloa SE (2008) Finite-temperature conductance signatures of quantum criticality in double quantum dots. Phys Rev B 78:153304
9. Nikkarila J-P, Koskinen M, Manninen M (2008) Magnetism of quantum dot clusters: a Hubbard model study. Eur Phys J B 64:95–103
10. Hang Xie, Xiao Cheng, Xiaolong Lv (2018) Steady and dynamic magnetic phase transitions in interacting quantum dots arrays coupled with leads. Available via arxiv.org. https://arxiv.org/pdf/1805.04939
11. Didukh L, Kramar O (2005) Metallic ferromagnetism in the systems with strongly correlated electrons. Condens Matter Phys 8:547–564
12. Didukh L, Yu S, Kramar O (2008) Electron correlations in narrow energy bands: modified polar model approach. Condens Matter Phys 11:443–454
13. Górski G, Mizia J, Kucab K (2015) Alternative equation of motion approach applied to transport through a quantum dot. Phys E 73:76–82
14. Górski G, Mizia J, Kucab K (2016) Modified equation of motion approach for metallic ferromagnetic systems with the correlated hopping interaction. Phys Status Solidi B 253:1202–1209
15. Górski G, Kucab K (2018) Effect of assisted hopping on spin-dependent thermoelectric transport through correlated quantum dot. Phys B Condens Matter 545:337–345

16. Didukh L, Skorenkyy Y, Hankevych V, Kramar O (2001) Ground state ferromagnetism in a doubly orbitally degenerate model. Phys Rev B 64:144428
17. Didukh L, Kramar O, Skorenkyy Y (2002) Ground state energy of metallic ferromagnet in a generalized Hubbard model. Phys Status Solidi B 229:1241–1254
18. Didukh L, Kramar O (2002) Metallic ferromagnetism in a generalized Hubbard model. Fizika Nizkikh Temperatur (Kharkov) 28:42–50
19. Didukh L, Kramar O, Yu S (2005) Metallic ferromagnetism in a generalized Hubbard model. In: Murray VN (ed) New developments in ferromagnetism research. Nova Science Publishers Inc, New York
20. Skorenkyy Y, Didukh L, Kramar O, Dovhopyaty Y (2007) Mott transition, ferromagnetism and conductivity in the generalized Hubbard model. Acta Phys Pol A 111:635–644
21. Górski G, Mizia J, Kucab K (2014) New Green's function approach describing the ferromagnetic state in the Hubbard model with correlated hopping. Phys Status Solidi B 251:2294–2301
22. Didukh L (2018) 3d-electrons contribution to cohesive energy of 3d-metals. Condensed Matter Physics 21:13701
23. Izyumov YA, Kurmaev EZ (2008) Materials with strong electron correlations. Physics-Uspekhi 51:23
24. Shishido H et al (2010) Tuning the dimensionality of the heavy fermion compound CeIn3. Science 327:980–983
25. Zaitsev RO, Kuz'min EV, Ovchinnikov SG (1986) Fundamental ideas on metal-dielectric transitions in 3d-metal compounds. Sov Phys Usp 29:322–342
26. Fazekas P (1999) Lecture notes on electron correlation and magnetism. World Scientific Publishing, Singapore
27. Didukh L, Hankevych V, Kramar O, Skorenkyy Y (2002) Itinerant ferromagnetism of systems with orbital degeneracy. J Phys Condens Matter 14:827–835
28. Masuda S, Tan KY, Nakahara M (2018) Spin-selective electron transfer in quantum dot array. Phys Rev B 97:045418
29. Górski G, Mizia J (2009) Hubbard model with intersite kinetic correlations. Phys Rev B 83:064410
30. Skorenkyy Y, Kramar O, Didukh L, Dovhopyaty Y (2018) Electron correlation effects in theoretical model of doped fullerides. In: Fesenko O, Yatsenko L (eds) Nanooptics, nanophotonics, nanostructures, and their applications. NANO 2017. Springer proceedings in physics, vol 210. Springer, Cham

Chapter 31
PET Ion-Track Membranes: Formation Features and Basic Applications

Artem Kozlovskiy, Daryn Borgekov, Inesh Kenzhina, Maxim Zdorovets, Ilya Korolkov, Egor Kaniukov, Maksim Kutuzau, and Alena Shumskaya

31.1 Introduction

Track membranes (TMs) are nanoporous materials with pores of a predetermined size that are obtained as a result of irradiation of thin polymer films by accelerated ions and subsequent chemical etching. The ion-irradiated film undergoes chemical treatment to remove the damaged material and transform the ion tracks into pores with diameters ranging from 10^4 to 10^{10} cm^{-2} [1, 2]. Due to its small thickness, precisely defined structure, simplicity of regeneration, and relatively low cost, TMs have advantages over other types of membranes [3].

Presently, TMs based on polyethylene terephthalate (PET) are the most interesting ones because they are already commercial products embedded with well-developed production technology. The geometry of pores can be controlled by

A. Kozlovskiy · D. Borgekov · I. Kenzhina
Astana branch of the Institute of Nuclear Physics, Nur-Sultan, Kazakhstan

L. N. Gumilyov Eurasian National University, Astana, Kazakhstan

M. Zdorovets
Astana branch of the Institute of Nuclear Physics, Astana, Kazakhstan

L. N. Gumilyov Eurasian National University, Astana, Kazakhstan

Ural Federal University named after the first President of Russia Boris Yeltsin, Ekaterinburg, The Russian Federation

I. Korolkov
Astana branch of the Institute of Nuclear Physics, Astana, Kazakhstan

E. Kaniukov
Institute of Chemistry of New Materials of the NAS of Belarus, Minsk, Belarus

M. Kutuzau · A. Shumskaya (✉)
Scientific-Practical Materials Research Centre, NAS of Belarus, Minsk, Belarus

O. Fesenko, L. Yatsenko (eds.), *Nanocomposites, Nanostructures, and Their Applications*, Springer Proceedings in Physics 221,
https://doi.org/10.1007/978-3-030-17759-1_31

varying the conditions of technological processes such as irradiation by swift heavy ions, sensibilization, and etching [4]. It allows obtaining pores with different shapes (cylindrical, conical, and "hourglass") and small deviation of pore sizes from average values. Depending on the pore parameters, TMs could be used for microfiltration [5], ultrafiltration, nanofiltration [6], forward and reverse osmosis, membrane evaporation, dialysis, electrodialysis, diffusion, gas separation, and template synthesis of nanostructures (NSs) [3, 7–9].

Template synthesis is an interesting and perspective method for the formation of nanostructures. Its unique feature is the ability to control the properties of manufactured nanomaterials [10–12]. Due to physicochemical, magnetic, and electrical properties, ferromagnetic NSs such as nanoparticles, nanowires, and nanotubes classified on the basis of Fe, Co, and Ni are used for catalysis, sensoric applications, the delivery of drug and genes, studying microrheological processes, and as contrast fluids [13–15].

In this connection, the formation features of PET TMs with different geometry and size of pores and their density are considered, and the effect of the formation modes on the characteristics of TMs is analyzed. Special attention is paid to study the possibility of practical applications of TMs for water purification, direct and reverse osmosis, and template synthesis of magnetic nanostructures.

31.2 Methods

Polyethylene terephthalate (PET) films with thicknesses of 12 and 23 μm of the Hostaphan® type, manufactured by Mitsubishi Polyester Film (Germany), were irradiated on the DC-60 cyclotron with Kr ions with energy of 1.75 MeV/nucleon and fluence in the range from 10^4 to 10^9 cm^{-2}. All samples before the etching were sensitized by UV-lamp (UV-C lamp with a wavelength of 253.7 nm) for 30 minutes on each side (for obtaining cylindrical pores) and 12 hours on one side (for obtaining conical pores). Chemical etching was carried out in 2.2 M NaOH solution [16]. After etching, the track membranes were washed in a neutralizing solution (1.0% acetic acid and deionized water) and distilled water.

The surface and lateral edges of TMs were studied using scanning electron microscope JEOL-7500F (SEM). The cross section was obtained by shearing films previously frozen in liquid nitrogen. At least 50 pores were measured on each sample for a set of statistics.

The formation of magnetic nanotubes (NTs) was carried out in the pores of ion-track membranes with a thickness of 12 μm and with a pore density of 4×10^7 cm^{-2} at diameters of 400 nm and 10^9 at diameters of 100 nm. The cathode was covered by gold layer with a thickness of 10 nm, which was deposited by magnetron spraying in a vacuum. With such a thickness of the Au layer, the pores remained open, and the growth of the NSs began at the points of contact of gold with the electrolyte. Electrochemical deposition was carried out in the potentiostatic mode at cathode voltages in the range of 1.5 V using electrolytes: for iron NTs $FeSO_4 \times 7H_2O$ (180 g/l), $FeCl_3 \times 6H_2O$ (5 g/l), H_3BO_3 (25 g/l), $C_6H_8O_6$ (3 g/l); for cobalt:

$CoSO_4 \times 7H_2O$ (120 g/l), H_3BO_3 (45 g/l), $C_6H_8O_6$ (3 g/l); and for nickel: $NiSO_4 \times 6H_2O$ (120 g/l), H_3BO_3 (3 g/l), $C_6H_8O_6$ (1.5 g/l) at a temperature of 25 °C and at pH of the electrolyte 3. The structure and morphology of the synthesized NTs were studied by scanning electron microscopy using the microscope Hitachi TM3030 with the energy dispersive analysis (EDA) system Bruker XFlash MIN SVE at an accelerating voltage of 15 kV. The study of the diameters of pores and internal diameters in PET templates of NTs was carried out by a manometric method for determining gas permeability, based on measuring the change of gas pressure in a closed chamber at a pressure in the range from 8 to 20 kPa in steps of 4 kPa. X-ray diffraction analysis (X-ray diffraction) was performed on a diffractometer D8 ADVANCE using X-ray tube radiation with Cu anode and graphite monochromator on a diffracted bundle. Diffractograms were recorded in the range of angles 30–70° 2θ, step 0.02° 2θ.

The investigation of macromagnetic properties was carried out using the vibrational magnetometer (the Liquid Helium Free High Field Measurement System [Cryogenic Ltd.]). The measurements were made by the induction method, determining the induced electromotive force of the induction in signal coils by a magnetized sample oscillating with a definite frequency at magnetic field $B = \pm 0.5$ T at 300 K.

31.3 Formation Features of PET Ion-Track Membranes with Different Pore Parameters

The production of TMs is a well-known technology, and it is described in [1–3]. Characteristics of TMs are strongly dependent on the conditions of technological processes such as the type of polymers, irradiation by swift heavy ions, sensibilization, and etching modes (Fig. 31.1).

The choice of the base polymer film determines the characteristics of the formation of TMs. For our research, polyethylene terephthalate (PET) was chosen, which is one of the most popular polymers used in well-developed production technology. The scheme of the technological process of the production of PET TMs by ion-track technology is shown in Fig. 31.2.

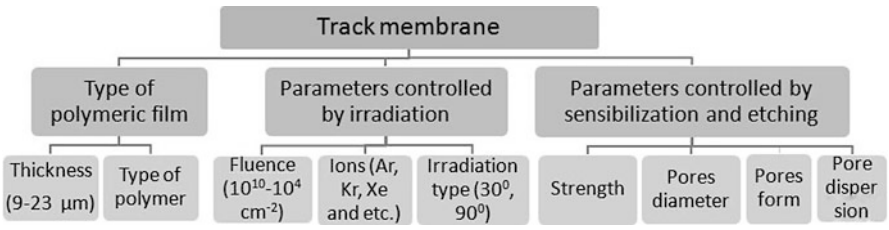

Fig. 31.1 Factors affecting the characteristics of TMs

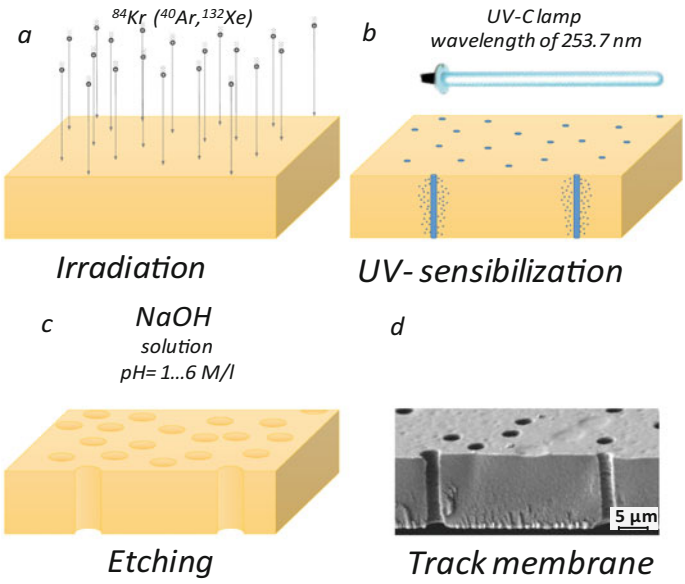

Fig. 31.2 The scheme of the technological process: irradiation (**a**), UV sensibilization (**b**), etching (**c**), the general view of the track membrane (**d**)

Track formation processes are described in detail in [1, 2, 17], and here we are considering only the main aspects of the formation of continuous latent tracks. Thus, due to the transfer of their energy to radiation damage, ions passing through PET films create changes in the material along the trajectory (latent tracks). For formation of latent tracks in PET films, swift heavy ions (Ar, Kr, Xe) with energy more than 1 MeV/nucleon are used.

For the acceleration of the etching process of irradiated material, UV sensibilization is used. UV radiation leads to photooxidation of the surface layer of the polymer. As a result of sensitization of tracks by UV irradiation, the amount of carboxyl groups increases, which contributes to the acceleration of the occurring processes during alkali etching (NaOH, KOH), can be explained by the acidic properties of the carboxyl groups. It is the determining factor for selective etching. During chemical etching, the damaged zone of a latent track is removed and transformed into a hollow channel.

The kinetics of the formation of pores, final dimensions, and shape of pores are determined by the parameters of primary track, the physicochemical parameters of the track-containing substance, the composition [18] of etching solution, its concentration, and temperature. Based on the results presented in [4, 19], the etching process consists of the following steps:

1. Etching of latent track region. Irradiation of polymers leads to the breaking of chemical molecular bonds and modification of substance in the latent track. This fact can explain the increase in the rate of dissolution of the region along the

track. Thus, the ratio $V_t > V_b$ characterizes the process, i.e., the etching rate of the substance in the track (V_t) will always be higher than the etching rate of the polymer outside the irradiated region (V_b).
2. Etching of bulk material with the ratio as $V_t \sim V_b$. In this stage, pores are etched with less velocity nearly equivalent to the etching velocity of membrane surfaces. The etching velocity strongly influence on mechanical properties of TMs.

The characteristics of TMs can be controlled by varying both irradiation parameters and etching modes. The influence of irradiation fluence on the parameters of PET ion-track membranes and optimal ratio of fluence-diameter for practical applications is discussed in Sect. 3.1. The effect of etching time and temperature on the pore diameters and thicknesses of PET ion-track membranes with cylindrical pores is considered Sect. 3.2. The way in which PET ion-track membranes are formed with asymmetric (conical) pores is shown and the effect of etching modes on the pore parameters is discussed Sect. 3.3.

31.3.1 Influence of Irradiation Fluence on the Parameters of PET Ion-Track Membranes

With the use of ion-track technology, it is possible to obtain pores with different shapes and diameters. By varying the geometric features of pores, the surface density of pores can be controlled. The selection of required irradiation fluence makes it possible to form track membranes with optimal characteristics for subsequent applications. In this regard, during the formation of pores with different diameters, it is necessary to select irradiation fluence. Some features of irradiation fluence (Φ) that enhance in the formation of membranes with a pore density up to the percolation threshold are given in [20]. Interrelation of percolation threshold and required diameter (D) can be calculated with the following equation:

$$D = 2\sqrt{\frac{\eta_c}{\pi \Phi}} \tag{31.1}$$

The percolation threshold η_c is the ratio of the total area of all pores to the area of the occupied surface. The equivalent critical area was determined with high accuracy and has the value $\eta_c = 1.128$.

In this work, fluence in the range from 10^4 to 10^9 cm^{-2} was used. It should be mentioned that actually overlapping zones appear when the pore diameter/fluence ratio is significantly less than the theoretical percolation threshold. The theoretical and experimental dependencies of the formation of overlapping zones on irradiation fluence are shown in Fig. 31.3.

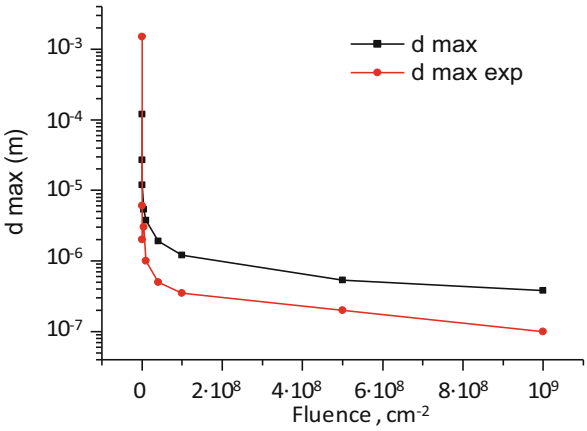

Fig. 31.3 Comparison of the percolation threshold curve and the experimentally obtained ratio of the fluence and the diameter at which overlapping of pores occurs

Porosity ( ), the main characteristic of membranes, could be presented as:

$$\Pi = \frac{\Phi^* S_{\text{pore}}}{S_{\text{sumple}}{}^* 10^{-4}} * 100\% \tag{31.2}$$

It is important to note that the porosity calculated using equation (31.2), in which the overlapping process is observed, is 12–15%, which is dependent on irradiation conditions (uniformity) and etching conditions (diameter dispersion).

From a practical point of view, the limit of effective porosity of TMs should be about 5–15%. In Table 31.1, the results of porosity calculation are shown and zone of optimal fluence/diameter ratio is marked.

31.3.2 Effect of Etching Modes on the Parameters of PET Ion-Track Membranes with Cylindrical Pores

The membranes based on PET, 12 μm thick, irradiated with Kr ions with an energy of 1.75 MeV/nucleon and with a 10^9 cm^{-2} (for time up to 70 seconds) and 10^7 cm^{-2} (for time 150–240 seconds) fluence were used for researching the effect of etching time at 85 ± 0.1 °C on diameter *d*. Examples of TMs produced in selected etch modes, as well as dependence of pore diameters on etching time, are shown in Fig. 31.4.

Figure 31.4a provides examples of membranes with nanoscale pores, for fluence irradiation of 10^9 cm^{-2}. It is obvious, that pore overlapping is significant and overlapping zones are appearing. In Fig. 31.4b , a certain increase in pore-etching rate is noticeable with an increase in diameter more than 50 nm. It is due to an increase in the convective flow of the etching agent inside the pores and an increase

Table 31.1 Optimal fluence/diameter ratio

	Diameter of pores, μm								
Fluence, cm^{-2}	0.1	0.2	1	2	3	4	5	8	10
10^4	10^{-4}	$2 * 10^{-4}$	$8 * 10^{-4}$	$4 * 10^{-3}$	$7.8 * 10^{-3}$	10^{-2}	$2 * 10^{-2}$	$5 * 10^{-2}$	$7.8 * 10^{-2}$
$2 * 10^5$	$2 * 10^{-4}$	$4 * 10^{-3}$	$1.5 * 10^{-2}$	$6 * 10^{-2}$	0.14	0.25	0.4	1.0	1.57
10^6	$8 * 10^{-4}$	$2 * 10^{-2}$	$7.8 * 10^{-2}$	0.31	0.7	1.3	1.96	***5***	***7.8***
$5 * 10^6$	$4 * 10^{-3}$	0.1	0.39	1.57	3.5	***6.3***	***9.8***	25	39
10^7	$7.8 * 10^{-3}$	0.2	0.78	3.14	***7.1***	***12***	19	50	78
$4 * 10^7$	$3 * 10^{-2}$	0.78	3.1	***12.6***	28	50	78	>100	>100
10^8	$7.8 * 10^{-2}$	1.96	***7.8***	31	70	>100	>100	>100	>100
$5 * 10^8$	0.39	***9.8***	39.2	>100	>100	>100	>100	>100	>100
10^9	0.78	***19***	78.5	>100	>100	>100	>100	>100	>100

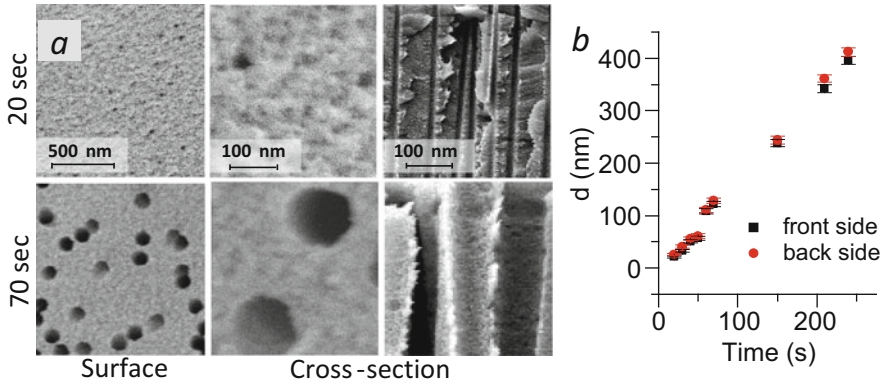

Fig. 31.4 SEM images of the surface and cross section of the PET matrix with different etching times (**a**). The scale is the same for each row. Dependence of the pore diameter (**b**) on the etching time

in ethylene glycol (EG) concentration, which is the product of PET decomposition. EG is an autocatalyst of PET decomposition process, and this is shown in [21].

Figure 31.4 presents the results of etching of TMs with pore diameters up to 250 nm. It should be noted that in the formation of TMs with small pore diameters, change in film thickness could be ignored due to short etching time. During the formation of pores of large diameter up to 10 μm, the thickness of films is important, and this parameter must be controlled in the technological process. Investigation of the dependence of membrane parameters on the etching conditions is represented in Fig. 31.5.

The etching rate strongly depends on the process temperature (Fig. 31.4a) and dramatically increases at the temperature range of about 70–80 °C. It is due to the factors such as PET transition into plastic state (glass transition temperature of 70–80 °C) and an increase in convective flow intensity in the solution. The increase in temperature leads to a significant increase in the process rate; however, in such a case it is much more difficult to predict the diameters of the etched pores (Fig. 31.5c).

Comparing Figs. 31.4 and 31.5b, it can be observed that inclination angles of pore diameter dependencies on the etching time are slightly different. It can be explained by the increase in the convective flow of the etching agent with the increase in pore diameter.

During pore etching more than 1 μm attention should also be paid to the membrane surface etching, which occurs at almost the same rate as pore etching (Fig. 31.5c) and leads to thinning of TMs and loss of its mechanical properties. The results of the thickness measurement after etching of TMs to pore diameters of 10 μm are shown in Fig. 31.5b. Such a study makes it possible to determine the minimum initial PET film thickness for the production of TMs with micro-sized pores.

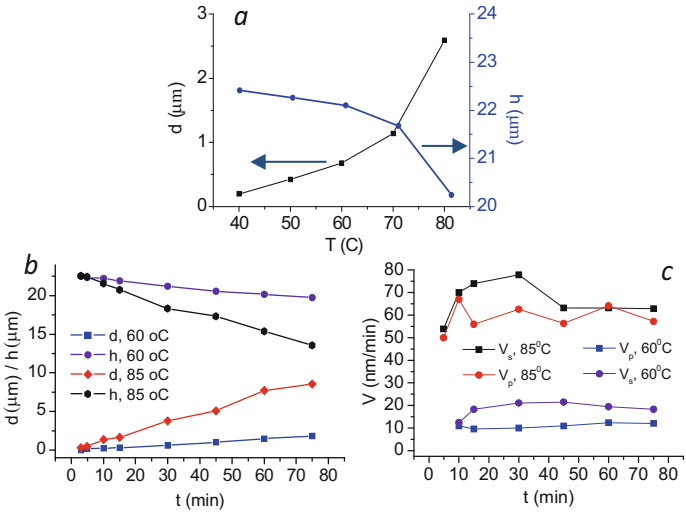

Fig. 31.5 Dependence of pore diameters and thicknesses of TMs on etching temperature at etching time 30 min (**a**); dependence of pore diameters on etching time at temperatures 60 °C and 85 °C (**b**); the etching rate of the substance in the pore (V_t) and the etching rate of the polymer on the membrane surface (V_s) at different etching temperatures (**c**)

31.3.3 Effect of Etching Modes on the Parameters of PET Ion-Track Membranes with Conical Pores

For the formation of TMs with conical pores, films with a fluence of 1×10^6 cm^{-2} were used. Unlike the two-sided etching technique, which is used for producing symmetrical pores, one-sided etching is carried out in a conductometric cell for producing conical pore shape, the scheme of which is shown in Fig. 31.6a.

Figure 31.6b presents the typical chronoamperogram for one-sided etching process, the main stages of which are shown in Fig. 31.6c. The formation of conical-shaped pores can be described as follows: during the initial etching stages, small pits of conical form appear on the PET layer surface, being considerably separated from each other. With longer etching times, an increase in the outer pore diameters, and their height, takes place. The result of one-sided etching process is shown in Fig. 31.6d.

It can be seen from Fig. 31.6b that in the etching period up to 85 minutes, a gradual etching of tracks occurs from one side (Stage 1). For a period of about to 105 minutes, tracks are fully etched (Stage 2), and local electrical breakdowns occur, because ions of the etching agent penetrate into the stop solution and rush to the cathode. A sharp increase in current intensity occurs in this case. In the second stage, slow two-sided pore etching and formation of tracks with given conical geometry take place (Stage 3). Figure 31.6d presents SEM images displaying cross section of track membrane with conical pore geometry. It should be noted that by controlling

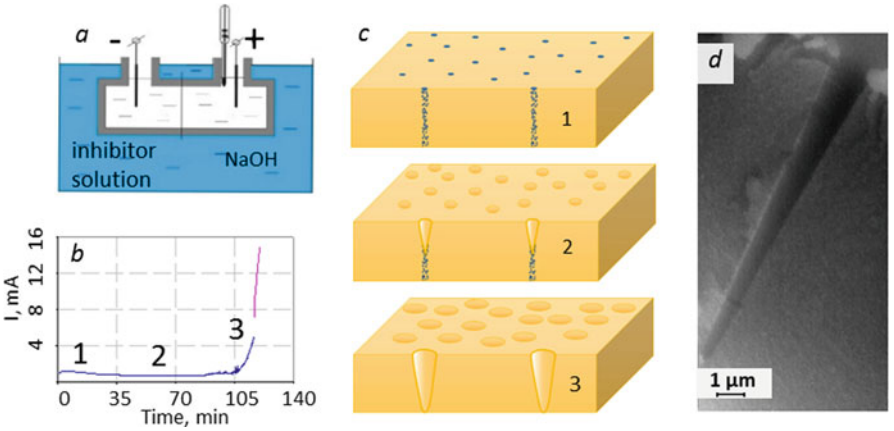

Fig. 31.6 Scheme of conductometric cell (**a**); typical chronoamperogram for one-sided etching process (**b**); schematic illustration of the main stages of the formation of conical-shaped pores (**c**); SEM image of a pore with conical shape (**d**)

Table 31.2 Main characteristics of samples with conical pore shapes

Name	The maximum value of pressure at which the membrane retains its strength properties, MPa	Porosity, %	Contact angle (face/reverse side)
Sample 1	0.61	1.5	57°/73°
Sample 2	0.56	2.4	55°/69°
Sample 3	0.53	3.1	53°/66°

etching modes [22], pores with different values of upper and lower diameters can be obtained.

By determining the dependence of diameters on the etching time, it is possible to control the geometry of the obtained TMs for solving specific filtration problems, including the use of direct and reverse osmosis processes.

TMs with diameters of frustum vertices of 15, 25, and 30 nm were obtained and strength characteristics of TMs were studied. In this research, strength was measured by a method based on the determination of the maximum pressure that the membrane can withstand on a laboratory installation designed for measuring the tensile strength of laboratory samples of track membranes during the loading with a slowly varying pressure. Strength test results are shown in Table 31.2.

An increase in pore diameter, during etching, results in a decrease in strength properties due to an increase in the porosity coefficient.

31.4 Basic Applications of PET Ion-Track Membranes

TMs are used for filtration and separation of various liquids and gases, for example, purification of drinking water, separation of blood into components (plasmaphoresis), isolation of pathogens for medical diagnostics, in chemical, microbiological and cytological research, and in the manufacture of drugs [3, 4, 13]. One of the applications of TMs is the synthesis of nanoscale structures with a large aspect ratio (more than 100). All production features and applications of TMs are not fully studied yet. Each newly obtained task requires theoretical calculation and development of the technological aspects of production. In this chapter, we provide results of the technology of TMs obtained with the required parameters for the following independent tasks:

- Ultrafiltration
- Processes of direct and reverse osmosis
- Template synthesis of nanostructures

31.4.1 Water Purification

TMs with small pore diameters are used for water purification; the main technological aspects of their preparation are described in Sects. 3.1 and 3.2. The filter for water purification based on TMs is a two-stage system. The first is the coarse filtration stage (microfiltration) for the removal of mechanical impurities, where it is possible to use both track membranes with micron-size pores and filter materials of other types. The second is the fine filter stage (ultrafiltration) for the removal of biological objects and submicron contaminants, where track membranes with pore diameters of less than 500 nm are used. The scheme of two-stage water purification is shown in Fig. 31.7.

The transport characteristics of TMs produced according to the recommended ratio of diameters and irradiation fluences are studied in Table 31.1. For comparison,

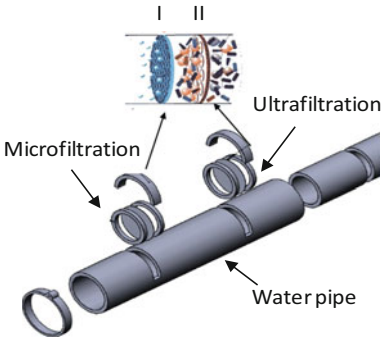

Fig. 31.7 Scheme of two-stage water purification system

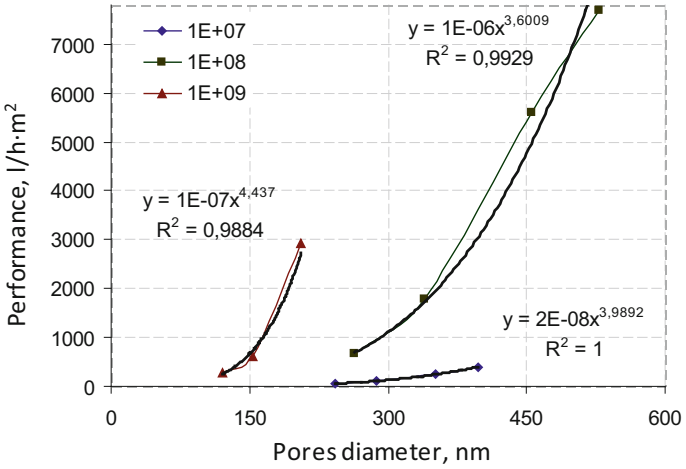

Fig. 31.8 Dynamics of change in water performance for PET ion-track membranes with different pore density/cm^2

TMs were chosen with fluences of 10^7, 10^8 and 10^9 cm^{-2} with increasing pore diameter within the limits indicated in Table 31.1. The measurements were made at different applied water pressure, which is determined by diameter and density of pores.

Figure 31.8 presents the dependence of change in performance of TMs on effective pore diameter at a fixed pore density.

Two ranges of pore diameters of 100–200 nm and 200–600 nm are considered.

In the 200–600 nm range, TMs with irradiation fluence of 10^7 cm^{-2} were less effective, due to low porosity (<0.5%). TMs with irradiation fluence of 10^8 cm^{-2} showed a significant efficiency, expected from the calculation of porosity. In pore diameters with a range of 100–200 nm, TMs with a fluence of 10^9 cm^{-2} were selected, which showed a significant efficiency due to a high porosity of more than 15%.

TMs with asymmetric pore form can be used for water purification with direct and reverse osmosis processes.

31.4.2 Direct and Reverse Osmosis

The process of direct osmosis with the use of TMs is as follows: If a certain substance solution and a pure solvent are separated by a semipermeable membrane, the phenomenon of pure solvent transfer into solution and completion of hydrate shells (if the solvent is water) will be observed. At the same time, the higher the concentration of the dissolved substance in the left vessel, the more molecules of

Table 31.3 Experimental values of base and vertex cone diameters of asymmetric pores

Name	Sample 1	Sample 2	Sample 3
d_b, nm	847 ± 16.3	905 ± 12.7	911 ± 12.1
d_v, nm	15.4 ± 1.3	24.8 ± 1.2	30.0 ± 1.6

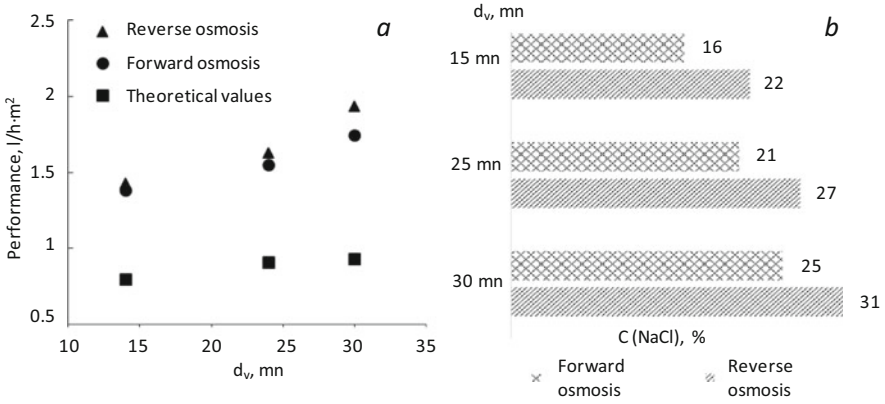

Fig. 31.9 Characteristics of track membranes using the process of direct and reverse osmosis: the dependence of the changing in the flow of liquid J_w on the cone vertex diameter d_b (**a**), the changing in the concentration of NaCl in the solution before and after filtration, depending on the cone vertex diameter d_b (**b**)

water must pass through the membrane into the solution. Water purification with the help of reverse osmosis is the most productive and high-tech process. The principle of this filtration is based on the fact that water from the solution passes through the semipermeable membrane with the help of pressure applied to it, which exceeds natural, osmotic pressure. In this case, the concentration of the dissolved substance in the solution increases.

TMs with an asymmetric (conical) pore shape (Fig. 31.6), observed in Sect. 3.3, were used in direct and reverse osmosis processes. In Table 31.3, experimental values of base and vertex cone diameters of asymmetric pores are presented.

Figure 31.9 presents the performance of track membranes during the direct and reverse osmosis process.

The difference in the values of theoretical calculation and experimental data is due to the geometry of asymmetric tracks. An increase in the productivity of asymmetric membranes is explained by a decrease in eddy currents that occur during the movement of water through the pore channel. As can be seen from the data presented in Fig. 31.4b with a decrease in cone vertex diameter of the pore, an increase in the purification degree is observed due to a decrease in the concentration of NaCl percentage in filtered liquid. At the same time, the purification degree of asymmetric TMs for the processes of direct osmosis is higher, because in filtration and direct osmosis process there is no applied pressure.

31.4.3 Template Synthesis of Magnetic Nanostructures

TMs have advantages over other types of templates due to the simplicity of formation of templates with predetermined pore parameters and the scalability of the technological process. Template synthesis is one of the simplest and well-controlled methods for the formation of nanostructures. By varying the synthesis parameters – temperature, voltage (for electrodeposition), and the composition of the electrolyte – it is possible to obtain structures with different composition and morphology. TMs with 50 ± 500 nm cylindrical pores can be used to synthesize the magnetic nanotubes (NTs) and nanowires (NWs). Nowadays, the aspects of template synthesis of NWs have been considered in detail (e.g., [23–25]), while NTs are not given sufficient attention. In this regard, here the main features of the formation of NTs are considered and their structural and magnetic characteristics are analyzed.

Unique physicochemical, magnetic, and electrical properties of ferromagnetic NSs based on elements of iron group (Fe, Co, Ni) and their alloys create a great interest in them from the academic and manufacturing sectors. It should be noted that not only the material but also the form has a great influence on the properties of NSs. For example, a large aspect ratio of elongated nanoobjects provides an easy-magnetization axis to them, and the hollow form of the NSs, such as NTs, due to the absence of a magnetic core, makes it possible to realize NSs with homogeneous switching fields that guarantee reproducibility of the results. The low bulk density of hollow NSs allows them to float in liquids (including biological) and makes them suitable for use in biotechnology [13, 26, 27].

The growth of NTs is a multistage process [28]. The first stage corresponds to the beginning of filling the pores of the template. When an electric field is introduced at the circular electrode, in the lower part of the pore metal nuclei are formed, which replicate the shape of the electrode and determine the shape of the future NTs (Fig. 31.9a). At the same time, nuclei are formed in the active zones on the surface of the pore walls (containing defects, broken bonds, etc.) formed during chemical or physical activation (e.g., during the formation of pores in ion-track membranes). The intensive formation of nuclei causes a decrease in the concentration of metal ions within the pore (Fig. 31.9b) and, accordingly, a significant decrease in the deposition current.

In the second stage, there is a gradual decrease in I or its practically constant value, which corresponds to the direct growth of NTs inside the pores (Fig. 31.10b) until the membrane surface is reached (Fig. 31.10c). As the diffusion of ions in the pore occurs rather slowly, the growth of NTs is carried out due to the sequential layering of two-dimensional nuclei on the surface of the ring tip.

Taking into account that during electrodeposition, the ion velocity to the active zone is determined by the deposition conditions, increasing both the voltage and the synthesis temperature leads to an acceleration in the growth of NTs. Thus, it increases the release of gas, which accumulates in the inner cavity of NTs and blocks the access of metal ions there. It contributes to the formation of sediment

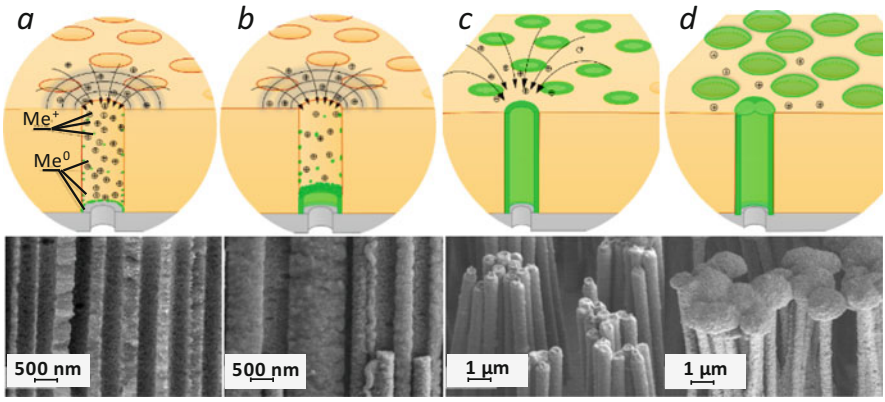

Fig. 31.10 Schematic illustration and SEM images of the stages of the formation of Ni NTs: growth of nuclei (**a**), growth of tube walls (**b**), completion of growth in pores (**c**), formation of "caps" (**d**) [28]

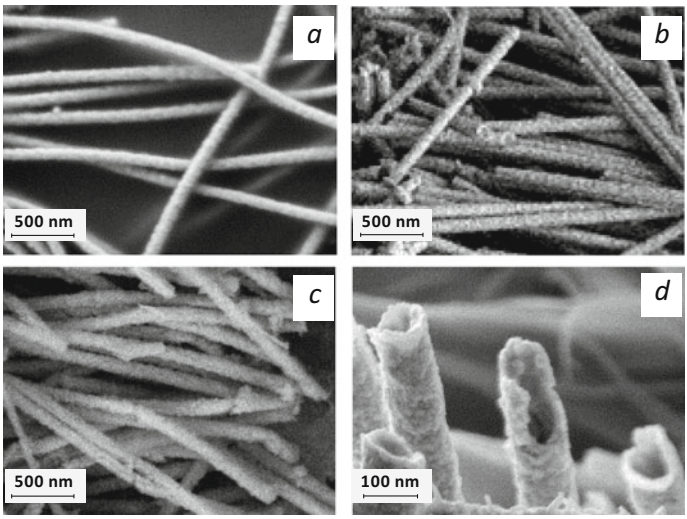

Fig. 31.11 SEM images of ferromagnetic nanotube array after dissolving the PET template: Fe (**a**); Co (**b**); Ni (**c**); breakage of individual Ni nanotubes (**d**)

near the pore walls. Accordingly, increasing the voltage and/ or temperature of the electrochemical synthesis causes a decrease in the thickness of the walls of NTs. It should be noted that by decreasing the potential difference and/or synthesis temperature, it is possible to substantially reduce the hydrogen evolution, thereby obtaining NWs.

SEM images (Fig. 31.11a–c) show that nanostructures obtained from different metals have a similar morphology. The Fe, Co, and Ni NTs synthesized in the

Table 31.4 The main parameters of the crystal structure of nanotubes

Parameter	Fe	Co		Ni
		α-Co	β-Co	
Type of crystal lattice	bcc	fcc	fcc	fcc
The lattice parameter, Å	28,563	25,007	35,428	35,223
Average crystallite size, nm	16.84	18.11		22.64

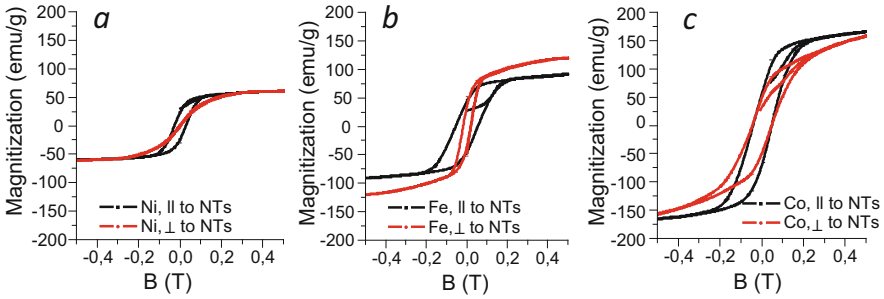

Fig. 31.12 Hysteresis loops of Ni (**a**); Fe (**b**); Co (**c**) nanotubes taken at room temperature. The black continuous line shows the dependencies taken when the field is applied parallel to the main axis of the nanotube, the red dotted line – when the field is applied perpendicular

Table 31.5 The main magnetic characteristics of ferromagnetic nanotubes, taken for a different field direction relative to their main axis

Nanotube materials	Parallel to the nanotube		Perpendicular to the nanotube	
	H_c, Oe	M_r/M_s	H_c, Oe	M_r/M_s
Fe	560	0.46	200	0.41
Co	510	0.14	450	0.25
Ni	300	0.48	20	0.03

pores of PET templates have an outer diameter of 110 ± 10 nm and a length of 12 ± 0.2 μm. From the images of the broken nanostructures, it is found that they have a tubular shape (Fig. 31.11d).

The gas permeability method established that the internal diameters of NTs are 70 ± 10 nm, and it corresponds to a wall thickness of 20 ± 5 nm. The crystal structure of NTs was determined on the basis of the analysis of the X-ray diffraction spectra (Table 31.4).

Measurements of the dependence of the magnetization on the magnetic field M (H) were carried out for a parallel and perpendicular orientation of the field directions relative to the main axis of the NTs (Fig. 31.12). Based on the hysteresis loops, the main magnetic characteristics (H_c – coercivity, M_r/M_s – the squareness factor of the hysteresis loop) were determined, and they are provided in Table 31.5.

Research on the magnetic characteristics of NT arrays of Fe, Co, and Ni shows that for all materials the hysteresis loop has a similar character. The main magnetic parameters of NTs for different directions of the magnetic field relative to the

axis of NTs differ, which indicates the presence of magnetic anisotropy in the samples. From the data in Table 31.5, it can be seen that the coefficient of coercivity and squareness of the loops for Fe and Ni at a parallel orientation is higher than the values for the perpendicular field direction. For Co, the squareness values for the perpendicular orientation exceed the values for the parallel orientation. The anisotropy of the magnetic properties observed in the experiment can be explained either by the crystalline anisotropy, which is confirmed by the X-ray diffraction data, or by the anisotropy of the shape. This happens because in the external magnetic field, NTs with a high aspect ratio (~100) require a higher demagnetization energy when the field is oriented along the axis than in the perpendicular direction.

The dependence of the magnetic properties revealed during the research on hysteresis loops allows us to consider ferromagnetic NTs in the pores of track membranes as sensors for the direction of the magnetic field. Such sensors have not only a simple design but also due to the use of a flexible PET substrate as a base can be used on mobile and complex surfaces. It should also be noted that in the absence of a magnetic core in NTs, two states are energetically favorable (stable): when the magnetic field lines are directed along the axis of the NTs or when they are locked inside the walls in the direction perpendicular to the axis. The presence of two stable states allows us to discuss homogeneous magnetic switching fields. In addition, these stable states can be conditionally assigned the values “1” or “0,” which allows to consider the possibility of using such nanostructures as elements of magnetic memory.

31.5 Conclusion

A comprehensive study of the formation of TMs based on PET films with different diameters and pore shapes (cylinder, cone) was carried out. Based on SEM studies of the surface and cross sections of TMs, the dynamics of the morphology and pore size changes at different etching modes was demonstrated. It was shown that increasing the etching time leads to an increase in pore diameters with a simultaneous decrease in the average distance between them, while the shape of the pores is set at the initial stages of etching. The results of a comprehensive study of TMs indicate a narrow pore diameter distribution. Due to the unique ability to control the parameters of porous patterns, the high degree of control of the etching process and the possibility of producing templates with relatively low cost and high quality, the PET TMs are exceptional materials for various kinds of applications. For example, PET finds application as porous matrices in the template synthesis of NSs, filters for fine purification of gases and liquids, in microfiltration processes for the separation of pathogens, fractionation of colloidal solutions, and in the procedure of hemofiltration and plasmapheresis.

The synthesis and study of the physicochemical properties of NSs on the basis of ferromagnetic metals (Fe, Co, Ni) synthesized in the pores of PET membranes were carried out. The study of the elemental composition showed that NTs do not contain

oxides and impurities, and an analysis of the crystal structure made it possible to establish that NTs have a polycrystalline structure of the walls with a body-centered cubic (iron) and face-centered cubic (cobalt and nickel) crystal lattice. Research on the basic magnetic characteristics of NTs at room temperature made it possible to establish magnetic anisotropy connected with form anisotropy, which is observed at high aspect ratios of nanostructures.

The morphology of NTs, due to the presence of a hollow channel, allows us to consider them as a basic element for the realization within a single pore of the ion-track membrane of multilayer elements in which one tube is placed inside the other. It allows to realize such devices as nanocondensers and sensors, which are sensitive to external influences. The anisotropy of the magnetic properties of NTs makes it possible to consider them as sensors of magnetic field direction, and the absence of magnetic core in NTs will provide predictable magnetic field distribution and homogeneous switching fields when used as magnetic memory elements. Thus, it can be noted that the use of ferromagnetic NTs in the pores of track membranes in the design of flexible electronics elements will simplify the design of many elements and implement devices, which can be used on mobile and complex surfaces.

References

1. Hoppe K, Fahrner WR, Fink D et al (2008) An ion track based approach to nano- and micro-electronics. Nucl Instrum Methods Phys Res B 266:1642–1646. https://doi.org/10.1016/j.nimb.2007.12.069
2. Fink D (2004) Fundamentals of ion-irradiated polymers: fundamentals and applications, vol 1. Springer, Berlin/Heidelberg
3. Stamatialis DF, Papenburg BJ, Gironés M et al (2008) Medical applications of membranes: Drug delivery, artificial organs and tissue engineering. J Membr Sci 308:1–34. https://doi.org/10.1016/j.memsci.2007.09.059
4. Sartowska B, Starosta W, Apel P et al (2013) Polymeric track etched membranes - application for advanced porous structures formation. Acta Phys Pol A 123:819–821. https://doi.org/10.12693/APhysPolA.123.819
5. Korolkov IV, Mashentseva AA, Güven O et al (2015) Enhancing hydrophilicity and water permeability of PET track-etched membranes by advanced oxidation process. Nucl Instrum Methods Phys. https://doi.org/10.1016/j.nimb.2015.10.031
6. Korolkov IV, Gorin YG, Yeszhanov AB et al (2018) Preparation of PET track-etched membranes for membrane distillation by photo-induced graft polymerization. Mater Chem Phys 205:55–63. https://doi.org/10.1016/j.matchemphys.2017.11.006
7. Apel PY, Blonskaya IV, Dmitriev SN et al (2007) Fabrication of nanopores in polymer foils with surfactant-controlled longitudinal profiles. Nanotechnology 18:1–7. https://doi.org/10.1088/0957-4484/18/30/305302
8. Shumskaya AE, Kaniukov EY, Kozlovskiy AL et al (2017) Template synthesis and magnetic characterization of FeNi nanotubes. Prog Electromagn Res C 75:23–30. https://doi.org/10.2528/PIERC17030606
9. Korolkov IV, Borgekov DB, Mashentseva AA (2017) The effect of oxidation pretreatment of polymer template on the formation and catalytic activity of Au/PET membrane composites. Chem Pap 71:2353–2358. https://doi.org/10.1007/s11696-017-0229-1

10. Kaniukov EY, Kozlovsky AL, Shlimas DI et al (2017) Electrochemically deposited copper nanotubes. J Surf Invest X-ray Synchrotron Neutron Tech 11:270–275. https://doi.org/10.1134/S1027451017010281
11. Kaniukov E, Yakimchuk D, Arzumanyan G et al (2017) Growth mechanisms of spatially separated copper dendrites in pores of a SiO2 template. Philos Mag 6435:1–16. https://doi.org/10.1080/14786435.2017.1330562
12. Demyanov SE, Kaniukov EY, Petrov AV, Belonogov EK (2008) Nanostructures of Si/SiO2/metal systems with tracks of fast heavy ions. Bull Russ Acad Sci Phys 72:1193–1195. https://doi.org/10.3103/S1062873808090050
13. Kozlovskiy AL, Korolkov IV, Kalkabay G et al (2017) Comprehensive study of Ni nanotubes for bioapplications : from synthesis to payloads attaching. J Nanomater 2017:1–9. https://doi.org/10.1155/2017/3060972
14. Sivakov V, Kaniukov EY, Petrov AV et al (2014) Silver nanostructures formation in porous Si/SiO2 matrix. J Cryst Growth 400:21–26. https://doi.org/10.1016/j.jcrysgro.2014.04.024
15. Demyanov S, Kaniukov E, Petrov A, Sivakov V (2014) Positive magnetoresistive effect in Si/SiO2(Cu/Ni) nanostructures. Sensors Actuators A Phys 216:64–68. https://doi.org/10.1016/j.sna.2014.04.022
16. Kaniukov EY, Shumskaya EE, Yakimchuk DV et al (2017) Evolution of the polyethylene terephthalate track membranes parameters at the etching process. J Contemp Phys Armenian Acad Sci 52:155–160. https://doi.org/10.3103/S1068337217020098
17. Apel P, Spohr R, Trautmann C, Vutsadakis V (1999) Track structure in polyethylene terephthalate irradiated by heavy ions: Let dependence of track diameter. Radiat Meas 31:51–56. https://doi.org/10.1016/S1350-4487(99)00075-X
18. Korolkov IV, Mashentseva AA, Güven O et al (2014) The effect of oxidizing agents / systems on the properties of track-etched PET membranes. Polym Degrad Stab 107:150–157. https://doi.org/10.1016/j.polymdegradstab.2014.05.008
19. Apel PY, Dmitriev SN (2011) Micro- and nanoporous materials produced using accelerated heavy ion beams. Adv Nat Sci Nanosci Nanotechnol 2:13002. https://doi.org/10.1088/2043-6262/2/1/013002
20. Kaniukov EY, Ustarroz J, Yakimchuk DV et al (2016) Tunable nanoporous silicon oxide templates by swift heavy ion tracks technology. Nanotechnology 27:115305. https://doi.org/10.1088/0957-4484/27/11/115305
21. Mashentseva AA, Orazbaeva DS, Gorin EG et al (2013) Calculation of bulk etch rate's semi-empirical equation for polymer track membranes in stationary and dynamic modes. Kazn Bull Chem Ser 1:69–70
22. Kozlovskiy A, Borgekov K, Zdorovets M et al (2017) Application of ion-track membranes in processes of direct and reverse osmosis. Proc Natl Acad Sci Belarus Phys Ser 1:45–51
23. Martin CR (1994) Nanomaterials: a membrane-based synthetic approach. Science 266:1961–1966. https://doi.org/10.1126/science.266.5193.1961
24. Toimil-Molares ME (2012) Characterization and properties of micro- and nanowires of controlled size, composition, and geometry fabricated by electrodeposition and ion-track technology. Beilstein J Nanotechnol 3:860–883. https://doi.org/10.3762/bjnano.3.97
25. Toimil Molares ME, Buschmann V, Dobrev D et al (2001) Single-crystalline copper nanowires produced by electrochemical deposition in polymeric ion track membranes. Adv Mater 13:62–65. https://doi.org/10.1002/1521-4095(200101)13:1<62::AID-ADMA62>3.0.CO;2-7
26. Son SJ, Reichel J, He B et al (2005) Magnetic nanotubes for magnetic-field-assisted bioseparation, biointeraction, and drug delivery. J Am Chem Soc 127:7316–7317. https://doi.org/10.1021/ja0517365
27. Hillebrenner H, Buyukserin F, Stewart JD, Martin CR (2006) Template synthesized nanotubes for biomedical delivery applications. Nanomedicine (Lond) 1:39–50. https://doi.org/10.2217/17435889.1.1.39
28. Kozlovskiy AL, Shlimas DI, Shumskaya EE, Kaniukov EY (2017) Effect of parameters of electroplating on structural and morphologic features of nickel nanotubes. Phys Metals Metallogr 118:174–179. https://doi.org/10.1134/S0031918X17020065

Chapter 32
Impact of Carbon Nanotubes on HDL-Like Structures: Computer Simulations

Mateusz Pabiszczak, Krzysztof Górny, Przemysław Raczyński, and Zygmunt Gburski

32.1 Introduction

High-density lipoproteins (HDL) are complex aggregates composed of multiple proteins, phospholipids, triglicerides, cholesterol, and cholesterol esters. HDL aggregates transport excess cholesterols from the cells into the liver and thus are important factor concerning atherosclerosis and other cardiovascular events [1]. Nascent high-density lipoproteins (nHDL) are the precursors of HDL transporters and are composed of apoA1 lipoprotein chain, phospholipids, and cholesterols [2, 3]. Liposomes and HDL-like structures can also be considered as drug carriers [4, 5]; thus studying their molecular and mechanical properties is of great interest from both scientific and application point of views.

Developing an efficient tool to perform a nondestructive indentation of such complex biosystem like HDL is a challenging task. Carbon nanotubes have attracted significant attention as an effective system to penetrate the phospholipid bilayer [6–8]. Due to similar molecular composition of HDL and bilayer, it is interesting to test whether the carbon nanotubes can be utilized as an artificial channel allowing to load or unload molecules from HDL-like structures.

In our recent studies, we have investigated the process of nanoindentation of phosphoilipid bilayer by various nanotubes [9–11]. In this work we present the results of molecular dynamics (MD) simulations of nanoindentation of nHDL-like structure by carbon nanotubes. The simulated lipoprotein consists of POPC phospholipids, cholesterols, and single apoA protein. Constant velocity pulling

M. Pabiszczak · K. Górny · P. Raczyński (✉) · Z. Gburski
Institute of Physics, University of Silesia, Katowice, Poland

Silesian Centre of Education & Interdisciplinary Research, Chorzów, Poland
e-mail: przemyslaw.raczynski@us.edu.pl

O. Fesenko, L. Yatsenko (eds.), *Nanocomposites, Nanostructures, and Their Applications*, Springer Proceedings in Physics 221,
https://doi.org/10.1007/978-3-030-17759-1_32

method was applied to study the force and work required to insert carbon nanotube into the nHDL aggregate.

32.2 Materials and Methods

All simulations were performed using NAMD 2.11 simulation package [12]. We have performed a series of steered molecular dynamics (SMD) simulations of insertion of armchair (10, 10) carbon nanotube of 6 nm length into the nHDL structure composed of apolipoprotein A, POPC phospholipids (200 molecules), and cholesterol (20 molecules). The nanotube main axis was aligned along z-axis of the simulation cell. Additionally, we performed a 10 ns reference simulation of single nHDL aggregate. The boron-nitride surface was modeled with CHARMM like potential developed by Won and Aluru [13]. All remaining interactions in the system were modeled using CHARMM 36 force field [14–16]. In the case of all simulations, the time step was set to 0.5 fs. The temperature was fixed at $T = 310$ K by means of Langevin thermostat implemented in NAMD with damping coefficient $\gamma = 1.0\ \mathrm{ps}^{-1}$.

The initial configuration of nHDL structure was obtained from a series of NVT and NPT simulations of nHDL immersed in water box. After obtaining a stable structure, the water was removed from the system, and 15 × 15 nm boron-nitride hexagonal surface was added. Four ns simulation with constant temperature was performed to equilibrate the sample. The carbon nanotube was placed at a distance $d = 2$ nm from the nHDL structure.

Nanoindentation of nHDL was studied by means of SMD simulations. Constant velocity pulling method was applied to push the CNT into the aggregate. Virtual springs were added between the most distant from nHDL ring of CNT carbon atoms (40 atoms) and imaginary points moving with constant velocity $V = 2.5$ m/s along the z-axis. The force constant was set to be equal to 10 kcal mol^{-1} A^{-2}.

32.3 Results

The instantaneous configuration of the nHDL structure obtained from a series of computer simulations is presented in Fig. 32.1.

The cholesterol is embedded within the layer of POPC. The inner cavity of the obtained nHDL structure is cylindrical and relatively small with a diameter approximately 1 nm. We did not observe aggregation of cholesterol in the apoA proximity.

Three configurations of the nHDL during the nanoindentation process are presented in Fig. 32.2. It can be observed on Fig. 32.2a that the nHDL does not completely adhere to the hexagonal boron-nitride surface. We choose the initial position of the carbon nanotube so that it would not be in contact with apoA during

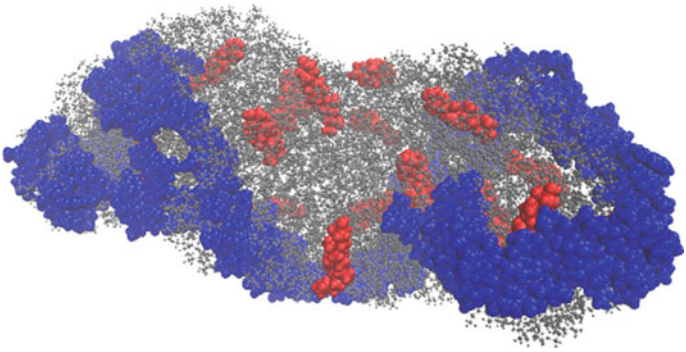

Fig. 32.1 Configuration of the nHDL structure: apoA lipoprotein (blue), phospholipids (gray), and cholesterols (red)

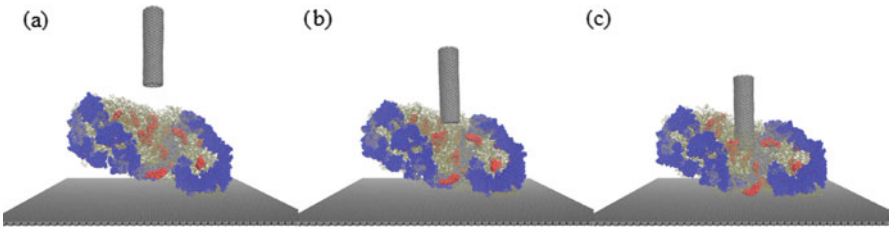

Fig. 32.2 Different stages of the nanoindentation process: (**a**) initial configuration, (**b**) nanotube reaches the nHDL surface, and (**c**) nanotube pierces the first phospholipid layer of the nHDL

the initial stages of the indentation process. During the nanoindentation process, the nHDL is pushed toward the boron-nitride surface.

The force required to push the nanotube into the nHDL structure plotted as a function of indentation depth (reaction coordinate) is presented in Fig. 32.3. The indentation depth $d = 0$ nm describes the point when the nanotube reaches the nHDL upper surface. The highly "noisy" force curve was fitted with a seventh degree polynomial to better visualize the general trend in force curve. The maximal value of force is approximately 4.4 nN. This value is at least three times higher than in the case of nanotube of the same chirality pushed into the phospholipid bilayer with the same indentation speed [11]. This significant difference can be explained, if we take into account that the part of the work performed by the nanotube is used to close up the nHDL into the hexagonal boron-nitride surface. As it can be seen in Fig. 32.2c), even after the nanoindentation process, the nHDL is not completely adhered to the boron-nitride surface. We can observe the monotonic linear increase of the force from $d = 0$ to $d = 2.5$ nm, followed by a slight decrease. Visual inspection of simulation trajectory suggests that this decrease occurs when the nanotube reaches the position of the small inner cavity of the nHDL, pushing two POPC phospholipids into it and causing its collapse. The following increase of the force can be associated with the movement of the entire nHDL aggregate toward the boron-nitride surface.

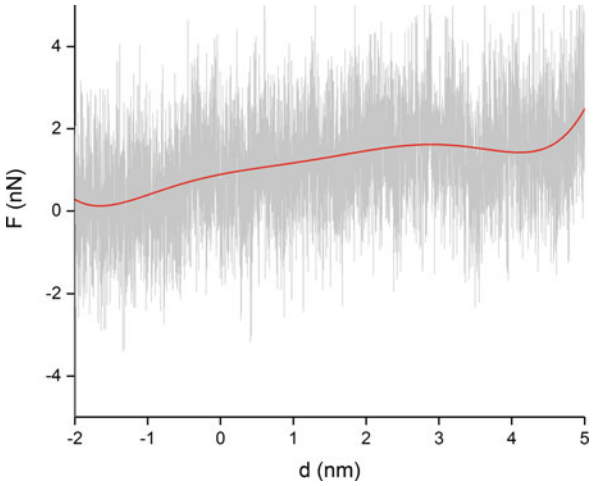

Fig. 32.3 The force required to push the nanotube as a function of indentation depth (the solid thick line represents the seventh degree polynomial fit of the data)

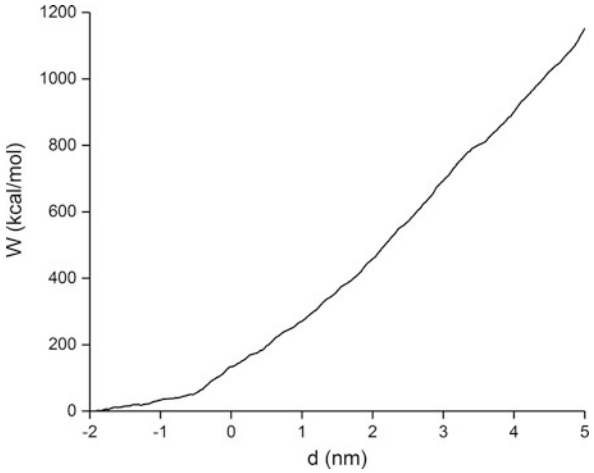

Fig. 32.4 Work performed by the nanotube during the indentation process as a function of indentation depth d

The work required to push the nanotube into the nHDL was calculated using equation

$$W(d) = \int_{z=d_0}^{d} F(z)dz, \tag{32.1}$$

where d_0 is the initial position of the nanotube and $F(z)$ is the force acting on the nanotube. The work plot, presented in Fig. 32.4, reflects the features described for the force curve. The initial region of the work plot represents the energy necessary to put the nanotube in motion, followed by the relatively stable parabolic part (0–2.5 nm) associated with the movement of the carbon nanotube between the phospholipids and cholesterols, flattening the nHDL and collapsing its inner cavity.

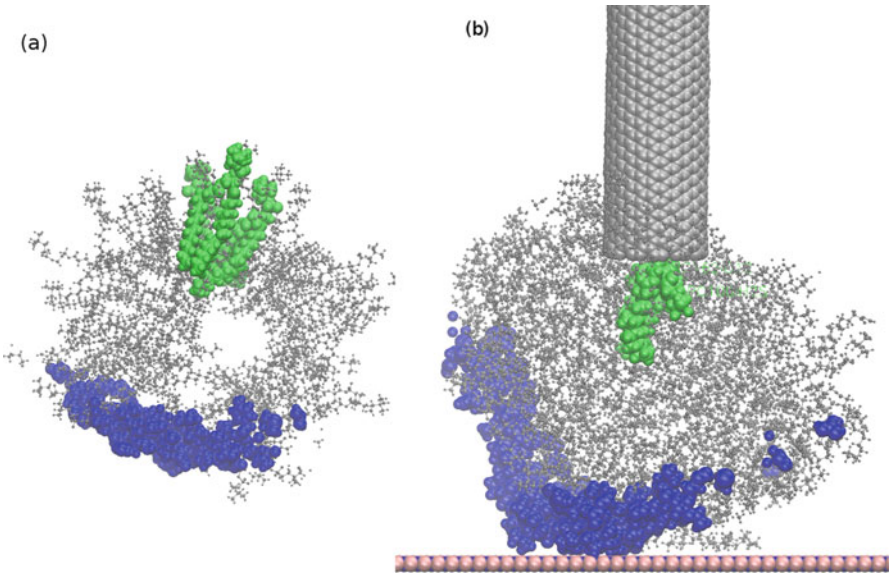

Fig. 32.5 Cross sections of the nHDL structure along the *y*-axis: (**a**) initial configuration and (**b**) configuration at indentation depth $d = 1.4$ nm. Cholesterol and part of the POPC molecules presented in balls and sticks representation, protein and POPC molecules directly pushed by the nanotube in van der Waals spheres representation

The cross section of the nHDL structure during the nanoindentation process is presented in Fig. 32.5. It can be clearly observed that the indentation process leads to the collapse of the inner cavity of the nHDL and pushes lipids into the structure, effectively deforming and flattening the nHDL. This conclusion is strengthened by the plots of linear density of the nHDL along the z-axis, for different indentations depths presented in Fig. 32.6. The linear density plots were calculated by averaging 10 simulations frames corresponding to the indentation depth d. The density near the boron-nitride surface placed at $z = 0$ nm increases during the process. The linear dimension of the nHDL along z-axis is reduced from approximately 7.5–6.4 nm.

The collapse of the inner cavity of the nHDL during the nanoindentation suggests that the nanotube effectively damages the nHDL structure, although it should be noted that the indentation speed $V = 2.5$ m/s is relatively high and far from the speed of the reversible process. Reduction of the nanoindentation speed or nanotube diameter should decrease the deformation of the nHDL introduced by the carbon nanotube as was reported in the case of the phospholipid membranes [11].

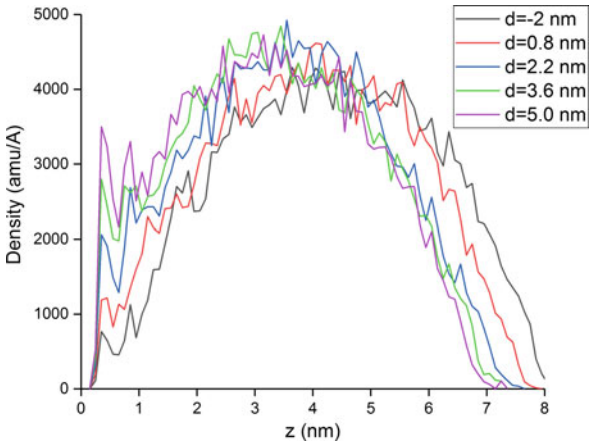

Fig. 32.6 Linear density profiles of the nHDL along the z-axis during the nanoindentation process

32.4 Conclusions

We have performed a series of preliminary computer simulations to investigate the interaction between carbon nanotube and nHDL structure. The presented results might provide some insight into the interaction between aggregates composed of lipids and lipoproteins and nanotubes. The knowledge about interaction between nanotubes and HDL-like structures is particularly important in the context of using nanotubes as drug containers or artificial channels.

The results suggest that the carbon nanotube is able to penetrate the phospholipid layer of nHDL. However it should be noted that it is changing the structure of the aggregate, collapsing its inner niche. The energy required to push the nanotube into the nHDL is in the same order as in the case of breaking the integrity of the phospholipid bilayer. Further investigation of the nanoindentation of nHDLs and liposomes is required to assess whether the nanotubes could be utilized to manipulate such complex structures.

Acknowledgments This research was supported in part by PAAD Infrastructure co-financed by Operational Program Innovative Economy, Objective 2.3.

References

1. Rader DJ, Alexander ET, Weibel GL, Billheimer J, Rothblat GH (2009) The role of reverse cholesterol transport in animals and humans and relationship to atherosclerosis. J Lipid Res 50. Suppl:S189–S194. https://doi.org/10.1194/jlr.R800088-JLR200
2. Jones MK, Zhang L, Catte A, Li L, Oda MN, Ren G, Segrest JP (2010) Assessment of the validity of the double superhelix model for reconstituted high density lipoproteins a combined computational-experimental approach. J Biol Chem 285:41161–41171. https://doi.org/10.1074/jbc.M110.187799

3. Gogonea V, Gerstenecker GS, Wu Z, Lee X, Topbas C, Wagner MA, Tallant TC, Smith JD, Callow P, Pipich V, Malet H, Schoehn G, DiDonato JA, Hazen SL (2013) The low-resolution structure of nHDL reconstituted with DMPC with and without cholesterol reveals a mechanism for particle expansion. J Lipid Res 54:966–983. https://doi.org/10.1194/jlr.M032763
4. Allen TM, Cullis PR (2013) Liposomal drug delivery systems: from concept to clinical applications. Adv Drug Deliv Rev 65:36–48. https://doi.org/10.1016/j.addr.2012.09.037
5. Liu X, Suo R, Xiong S-L, Zhang Q-H, Yi G-H (2013) HDL drug carriers for targeted therapy. Clin Chim Acta Int J Clin Chem 415:94–100. https://doi.org/10.1016/j.cca.2012.10.008
6. Gagner J, Johnson H, Watkins E, Li Q, Terrones M, Majewski J (2006) Carbon nanotube supported single phospholipid bilayer. Langmuir 22:10909–10911. https://doi.org/10.1021/la062038g
7. Jin H, Heller DA, Sharma R, Strano MS (2009) Size-dependent cellular uptake and expulsion of single-walled carbon nanotubes: single particle tracking and a generic uptake model for nanoparticles. ACS Nano 3:149–158. https://doi.org/10.1021/nn800532m
8. Porter AE, Gass M, Bendall JS, Muller K, Goode A, Skepper JN, Midgley PA, Welland M (2009) Uptake of noncytotoxic acid-treated single-walled carbon nanotubes into the cytoplasm of human macrophage cells. ACS Nano 3:1485–1492. https://doi.org/10.1021/nn900416z
9. Raczynski P, Górny K, Pabiszczak M, Gburski Z (2013) Nanoindentation of biomembrane by carbon nanotubes - MD simulation. Comput Mater Sci 70:13–18. https://doi.org/10.1016/j.commatsci.2012.12.031
10. Raczyńska V, Raczyński P, Górny K, Gburski Z (2016) Nanoindentation of DMPC layer by nanotubes of various diameters. Fesenko O, Yatsenko, L. (red.) Nanophysics, nanophotonics, surface studies, and applications 23–31. Springer International Publishing
11. Raczyński P, Górny K, Raczyńska V, Pabiszczak M, Dendzik Z, Gburski Z (2018) On the impact of nanotube diameter on biomembrane indentation – computer simulations study. Biochim Biophys Acta BBA – Biomembr 1860:310–318. https://doi.org/10.1016/j.bbamem.2017.10.030
12. Phillips JC, Braun R, Wang W, Gumbart J, Tajkhorshid E, Villa E, Chipot C, Skeel RD, Kalé L, Schulten K (2005) Scalable molecular dynamics with NAMD. J Comput Chem 26:1781–1802. https://doi.org/10.1002/jcc.20289
13. Won CY, Aluru NR (2008) Structure and dynamics of water confined in a boron nitride nanotube. J Phys Chem C 112:1812–1818. https://doi.org/10.1021/jp076747u
14. Klauda JB, Venable RM, Freites JA, O'Connor JW, Tobias DJ, Mondragon-Ramirez C, Vorobyov I, MacKerell AD, Pastor RW (2010) Update of the CHARMM all-atom additive force field for lipids: validation on six lipid types. J Phys Chem B 114:7830–7843. https://doi.org/10.1021/jp101759q
15. Vanommeslaeghe K, Hatcher E, Acharya C, Kundu S, Zhong S, Shim J, Darian E, Guvench O, Lopes P, Vorobyov I, Mackerell AD Jr (2010) CHARMM general force field: a force field for drug-like molecules compatible with the CHARMM all-atom additive biological force fields. J Comput Chem 31:671–690. https://doi.org/10.1002/jcc.21367
16. Yu W, He X, Vanommeslaeghe K, MacKerell AD (2012) Extension of the CHARMM general force field to sulfonyl-containing compounds and its utility in biomolecular simulations. J Comput Chem 33:2451–2468. https://doi.org/10.1002/jcc.23067

Chapter 33
Approximation of a Simple Rectangular Lattice for a Conduction Electron in Graphene

L. V. Shmeleva and A. D. Suprun

33.1 Introduction

Article [1] shows that the dispersion law of an electron considered as a quasiparticle in the graphene conduction band does not allow its generalized analytic dynamics to be fully constructed. This circumstance makes it difficult to analyze such important physical properties of graphenes as the processes of charge or energy transfer. General theoretical concepts of such processes are developed quite intensively in graphenes [1–6] and in other physical systems [7–11]. Such an analysis may also be relevant for media other than crystalline media [12–15]. However, such analysis is complicated by the fact that in the dispersion law for an electron in the graphene conduction band, both components of the wave vector (wave momentum) enter in such a way that the law itself (which is also the quasiparticle Hamiltonian) cannot be represented as two summands containing only one component of wave vector.

The purpose of the article is to analyze, on the basis of the approximate dispersion law obtained, the general dynamic properties of an electron considered as a quasiparticle in the conduction band of graphene and the peculiarities of their physical properties associated with these properties.

Here, as before [15–19], an analysis of the general dynamic properties of an electron in the graphene conduction band is performed on the basis of one of the main characteristics of the excited states of a condensed medium: on the basis of the energy dispersion dependence on the wave vector. To fulfill this task, a region was found within the first Brillouin zone of graphene, in which the dispersion law can be constructed approximately (with a sufficiently high degree of accuracy) in the form of two summands with separated components of the wave vector. It is

L. V. Shmeleva (✉) · A. D. Suprun
Taras Shevchenko National University of Kyiv, Kyiv, Ukraine
e-mail: lshmel@univ.kiev.ua

O. Fesenko, L. Yatsenko (eds.), *Nanocomposites, Nanostructures, and Their Applications*, Springer Proceedings in Physics 221,
https://doi.org/10.1007/978-3-030-17759-1_33

established that the energy range of an electron injection into the conduction band corresponding to this approximation does not exceed 5 eV. An estimation based on this dispersion law, which has the meaning of the quasiparticle Hamiltonian, makes it possible to find the Louis de Broglie relations between the components of the wave and mechanical momenta. The electron velocity and its effective mass, which are necessary to obtain the Louis de Broglie relation, were also defined. A Lagrangian is constructed for an electron, as a quasiparticle, with respect to its wave description. This Lagrangian, as was shown earlier [16, 18, 19], is a summand in the phase of electron wave function in the quantum description. It is shown that in the absence of an external electrostatic field, the symmetry of the conduction bands leads to the absence of a current. Dynamic characteristics of an alternative description of the classical type were also defined: the mechanical Hamiltonian and the mechanical Lagrangian.

33.2 Preliminary Remarks

As it is known [1, 3, 5, 16, 20, 21], the dispersion law for a conduction electron in graphene has the form:

$$E_{\pm}(\mathbf{k}) = \pm E_{\mathrm{C}}\sqrt{1 + 4\cos^2\left(k_x a\sqrt{3}/2\right) + 4\cos\left(k_x a\sqrt{3}/2\right)\cos\left(3k_y a/2\right)}. \tag{33.1}$$

where E_{C} is the width of conduction band. In [1] this energy was analyzed as a dimensionless Hamiltonian $\varepsilon(\mathbf{p}) = E(\mathbf{k})/E_{\mathrm{C}}$ of dimensionless wave momenta:

$$p_x = k_x a\sqrt{3}; \quad p_y \equiv k_y a. \tag{33.2}$$

Thus, the following expression was analyzed:

$$\varepsilon(\mathbf{p}) = \pm\sqrt{1 + 4\cos^2(p_x/2) + 4\cos(p_x/2)\cos\left(3p_y/2\right)}, \tag{33.3}$$

for the possibility of constructing, in accordance with the definitions, $\mathrm{v}_x = \frac{\partial\varepsilon(\mathbf{p})}{\partial p_x}$, $\mathrm{v}_y = \frac{\partial\varepsilon(\mathbf{p})}{\partial p_y}$, of general analytic dynamics of the conduction electron, as quasiparticle. The term "general analytical dynamics" implies the absence of restrictions for components k_x, k_y (or p_x, p_y) within the first Brillouin zone. It has been shown that in the general case, using the exact expression (33.3), this task cannot be fulfilled. The complexity is related to the fact that it is analytically possible to find only two dynamic characteristics. These are the components of the dimensionless electron velocity:

$$\mathrm{v}_x = \mp S_x(\mathbf{p})\sin(p_x/2); \quad \mathrm{v}_y = \mp S_y(\mathbf{p})\sin\left(3p_y/2\right), \tag{33.4}$$

where the following is designated:

$$S_x(\mathbf{p}) \equiv \frac{2\cos(p_x/2) + \cos(3p_y/2)}{|\varepsilon(\mathbf{p})|}; \quad S_y(\mathbf{p}) \equiv \frac{3\cos(p_x/2)}{|\varepsilon(\mathbf{p})|};$$

$$|\varepsilon(\mathbf{p})| \equiv \sqrt{1 + 4\cos^2(p_x/2) + 4\cos(p_x/2)\cos(3p_y/2)},$$

as well as the components of the inverse effective mass tensor. We do not mention them here, since they have a complex and cumbersome form [1] and will not be used later. But precisely because of their complexity, it is practically impossible to find the tensor of the most effective mass in the analytical form. And this, in turn, does not make it possible to construct a mechanical branch of the dynamic description of an electron, as a quasiparticle. In addition, the relations (33.4) for the velocities are also quite complex for their analytic conversion, that is, for determining the components of the dimensionless wave momentum p_x, p_y, as functions of v_x, v_y are components of the dimensionless velocity. This does not allow constructing a wave branch of the dynamic description of an electron, as a quasiparticle.

All these circumstances resulted in the need to search for approximations, in which the task of constructing generalized analytic dynamics would be solved nevertheless. This makes it possible to adequately describe the processes of energy or charge transfer, important for applications, when an electron is injected into the conduction band of graphene.

In the surveys carried out in [1], a region was found in p-space (in k-space), where the dependences (33.4) for velocities are substantially simplified. Namely, within the uniqueness area completely belonging to the first Brillouin zone, $\{|p_x|, |p_y|\} \le 2\pi/3$, the area $\{|p_x|, \quad |p_y|\} \le \pi/2$ was defined, where the dependences (33.4) approximately reduce to the forms $\mathrm{v}_x \approx \sin(p_x/2)$, $\mathrm{v}_y \approx \sin(3p_y/2)$. Particularly good these approximations are met in the area:

$$\{|p_x|, \quad |p_y|\} \le \pi/3. \tag{33.5}$$

The possibility of such a simplification is related to the fact that in this area the functions $S_x(\mathbf{p})$, $S_y(\mathbf{p})$ are weakly dependent on the components of the wave momentum $\mathbf{p}$. It can be seen from the graphs in Fig. 33.1 that in this area they are practically planes parallel to the plane $(p_x, \quad p_y)$. This allows further application of the average values of factors $S_x(\mathbf{p})$, $S_y(\mathbf{p})$, as constants. These constants will be denoted simply by S_x, S_y. In the meantime, it will be enough for us to consider them as constants.

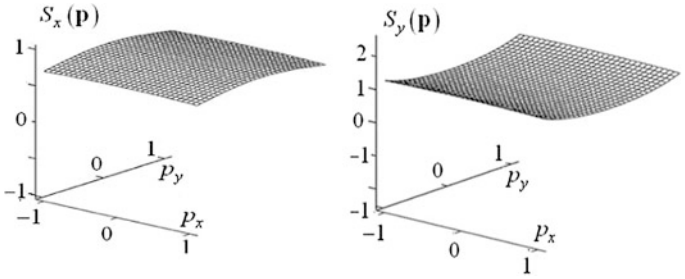

Fig. 33.1 Dependence of factors $S_x(\mathbf{p})$, $S_y(\mathbf{p})$ within the region, $\{|p_x|, \quad |p_y|\} \leq \pi/3$

33.3 Approximation of a Simple Rectangular Lattice in the Dispersion Law (the Quasiparticle Hamiltonian) for a Graphene Conduction Electron

Let's consider the approximation $S_x(\mathbf{p}) \approx S_x$, $S_y(\mathbf{p}) \approx S_y$ in detail. In this case, the dimensionless velocities (33.4), taking into account the definitions, $p_x = k_x a\sqrt{3}$, $p_y \equiv k_y a$, take the form:

$$\mathrm{v}_x = \mp S_x \sin\left(k_x a\sqrt{3}/2\right); \quad \mathrm{v}_y = \mp S_y \sin\left(3k_y a/2\right).$$

From these definitions for velocities it immediately follows that if they have a Hamiltonian origin, then the corresponding wave Hamiltonian (dispersion law) must have a form factorized into two summands. Moreover, each of these summands depends only on one component of the wave vector, either on k_x-component or on k_y-component. Such a form of the dispersion law (Hamiltonian) is important. This is the form of it, suitable for the complete construction of the generalized dynamics of the conduction electron, as a quasiparticle. Let's note that this form is characteristic of simple lattices. That is, one of the purposes of this paper is to construct such a dispersion law. To do this, it is necessary to begin consideration of the dimensional representation (33.1) for the real dispersion law. It will allow, in the final analysis, to correctly formulate the approximate Hamiltonian.

We will start from the definition of the dimensional components of the velocity [16, 18], $V_i(\mathbf{k}) = \frac{1}{\hbar}\frac{\partial E(\mathbf{k})}{\partial k_i}$. Considering only the normal branch of the dispersion $E_-(\mathbf{k})$, the following can be obtained:

$$V_i(\mathbf{k}) = C \left\{ \begin{array}{c} \sqrt{3}\, S_x(\mathbf{p}) \sin\left(k_x a\sqrt{3}/2\right) \\ S_y(\mathbf{p}) \sin\left(3k_y a/2\right) \end{array} \right|,$$

where $i = \left\{ \begin{matrix} x \\ y \end{matrix} \right\}$, and also the notation for the velocity constant is introduced: $C \equiv \frac{a}{\hbar} E_C$. Here, we should recall that $\mathbf{p} = \left\{ p_x, \quad p_y \right\} \equiv \left\{ k_x a\sqrt{3}, \quad k_y a \right\}$. For the abnormal branch, $E_+(\mathbf{k})$, all results are reproduced based on the results for the normal branch, $E_-(\mathbf{k})$, by replacing the signs with the opposite in the velocities components and the effective mass tensor. Considering the approximation:

$$S_x(\mathbf{p}) = S_x, \quad S_y(\mathbf{p}) = S_y, \tag{33.6}$$

the velocity takes the form:

$$V_i(\mathbf{k}) = \left\{ \begin{matrix} C_x \sin\left(k_x a\sqrt{3}/2\right) \\ C_y \sin\left(3k_y a/2\right) \end{matrix} \right|, \tag{33.7}$$

where $C_x = C\,S_x\sqrt{3}$, $C_y = C\,S_y$.

In this approximation, the inverse effective mass tensor is also simplified. This follows from its general definition [16, 18]:

$$m_{ij}^{-1}(\mathbf{k}) = \frac{1}{\hbar}\frac{\partial V_i(\mathbf{k})}{\partial k_j} \equiv \frac{1}{\hbar}\frac{\partial V_j(\mathbf{k})}{\partial k_i}.$$

Since here each component of the velocity depends only on the "own" component of the wave vector, this definition is transformed into the following: $m_i^{-1}(\mathbf{k}) = \frac{1}{\hbar}\frac{\partial V_i(\mathbf{k})}{\partial k_i}$. As a result, we will obtain:

$$m_i^{-1}(\mathbf{k}) = m_0^{-1} \left\{ \begin{matrix} S_x \cos\left(k_x a\sqrt{3}/2\right) \\ S_y \cos\left(3k_y a/2\right) \end{matrix} \right|, \tag{33.8}$$

where both mass constants of the quasiparticle turned out to be identical and the following notation is introduced for them:

$$m_0^x = m_0^y = m_0 \equiv \frac{2}{3}\frac{\hbar^2}{a^2 E_C}. \tag{33.9}$$

When these relations were obtained for the effective mass, the following definitions of the velocity constants were used:

$$C_x = C\,S_x\sqrt{3}; \quad C_y = C\,S_y; \quad C \equiv \frac{a}{\hbar}E_C. \tag{33.10}$$

In the case of a simple rectangular lattice, invariants [16, 18]:

$$m_0^x C_x^2 = m_0^y C_y^2 = E_C$$

are known. In the case considered, when both mass constants turned out to be identical and the velocities are different, for such products we will obtain:

$$m_0 C_x^2 = 2S_x^2 E_C; \quad m_0 C_y^2 = \frac{2}{3} S_y^2 E_C. \tag{33.11}$$

Estimation of the average values of factors $S_x(\mathbf{p})$, $S_y(\mathbf{p})$ in accordance with the standard definition, $S_i = \frac{9}{4\pi^2} \int\limits_{-\pi/3}^{\pi/3} \int\limits_{-\pi/3}^{\pi/3} S_i(\mathbf{p})\, dp_x dp_y$, showed that it is possible to obtain $S_x \approx 1/\sqrt{2}$, $S_y \approx \sqrt{3/2}$ with a satisfactory degree of accuracy. Qualitatively, this can also be seen from the graphs in Fig. 33.1. In this sense, the invariant $m_0^x C_x^2 = m_0^y C_y^2 = E_C$ can be considered fulfilled and assumed as:

$$S_x = 1/\sqrt{2}; \quad S_y = \sqrt{3/2}. \tag{33.12}$$

Next, we define the dimensionless values of wave momenta that are "correct" in the Lagrangian-Hamiltonian sense [16, 18]. Dimensionless representations are convenient for some applied estimations. In particular, such a representation for the wave Lagrangian is directly used for the final detailed definition of the wave function of the injected electron. To find the components of a dimensionless wave momentum, first of all it is necessary to find the dimensional momentum constants $P_i = m_0^i C_i \equiv m_0 C_i$. Considering (33.9) and (33.10), we will obtain:

$$P_x = m_0 C_x = \frac{2}{\sqrt{3}} \frac{\hbar}{a} S_x; \quad P_y = m_0 C_y = \frac{2}{3} \frac{\hbar}{a} S_y. \tag{33.13}$$

If now we take into account the values of the parameters just evaluated in these relations S_x, S_y, specified in (33.12), then we can obtain:

$$P_x = P_y \equiv P = \sqrt{\frac{2}{3}} \frac{\hbar}{a}. \tag{33.14}$$

For the new, in relation to (33.2), dimensionless components of the wave momentum (we denote them by p_{w}^i) in accordance with the general definition:

$$p_{\mathrm{w}}^i = \frac{\hbar k_i}{P_i} \tag{33.15}$$

we can obtain further

$$p_{\mathrm{w}}^x = \sqrt{\frac{3}{2}} k_x a; \quad p_{\mathrm{w}}^y = \sqrt{\frac{3}{2}} k_y a. \tag{33.16}$$

As it can be seen, these components differ from the previously used components (33.2) by the same scale. Now, taking into account (33.2) and (33.12), it is not

difficult to obtain a correlation between the old and new momentum components: $p_{\mathrm{w}}^{x} = S_{\mathrm{x}} p_x$, $p_{\mathrm{w}}^{y} = S_y p_y$. From these definitions it follows, in particular, that in the new components the ranges (33.5) also change. Now they are determined by the inequalities:

$$\left| p_{\mathrm{w}}^{i} \right| \leq \pi \ S_i/3. \tag{33.17}$$

And, as it can be seen, the range by which p_{w}^{x} decreases and p_{w}^{y} increases is in accordance with the values (33.12) for the parameters S_x, S_y.

On the basis of the definitions obtained above, it is possible to construct an effective Hamiltonian, an analogue of the Hamiltonian (33.1), but for the area (33.5) (or the same area (33.17)). This Hamiltonian must be formulated in such a way that the components of the velocity (33.7) and the components of the effective mass (33.8) are accurately reproduced. On the basis of such requirements, we can construct the following expression for the effective Hamiltonian:

$$\tilde{E}\left(\mathbf{k}\right) = -\frac{m_0 \mathrm{C}_x^2}{S_x} \cos\left(\frac{S_x \hbar k_x}{m_0 C_x}\right) - \frac{m_0 \mathrm{C}_y^2}{S_y} \cos\left(\frac{S_y \hbar k_y}{m_0 C_y}\right). \tag{33.18}$$

All quantities included in this expression are given in (33.11), (33.12), and (33.13). The Hamiltonian (33.18) describes only the normal dispersion. Abnormal dispersion is described by the same structure, but with signs "+".

33.4 Reproduction of Velocities and Masses with the Effective Dispersion Law (Quasiparticle Hamiltonian)

By direct substitution of the dispersion (33.18) into the general definition for the velocity components, $V_i\left(\mathbf{k}\right) = \frac{1}{\hbar}\frac{\partial \tilde{E}(\mathbf{k})}{\partial k_i}$, these components can be accurately reproduced in the form (33.7). Indeed, by performing such a substitution, first of all, we obtain the following after differentiation:

$$V_i\left(\mathbf{k}\right) = \left\{ \begin{array}{l} C_x \sin\left(S_x \hbar k_x / m_0 C_x\right) \\ C_y \sin\left(S_y \hbar k_y / m_0 C_y\right) \end{array} \right|. \tag{33.19}$$

Taking into account the general definition for the components of the effective mass of quasiparticles, $m_i^{-1}\left(\mathbf{k}\right) = \frac{1}{\hbar}\frac{\partial V_i(\mathbf{k})}{\partial k_i}$, we can accurately reproduce these components in the form (33.8). Indeed, substituting here the velocity obtained, after differentiation, we will obtain:

$$m_i^{-1}\left(\mathbf{k}\right) = m_0^{-1} \left\{ \begin{array}{l} S_x \cos\left(S_x \hbar k_x / m_0 C_x\right) \\ S_y \cos\left(S_y \hbar k_y / m_0 C_y\right) \end{array} \right|. \tag{33.20}$$

In order that these velocities and masses exactly coincide with (33.7) and (33.8), we consider the arguments $\frac{S_x \hbar k_x}{m_0 C_x}$ and $\frac{S_y \hbar k_y}{m_0 C_y}$ in details. Taking into account (33.12) and (33.13), it can be shown that:

$$S_x \hbar k_x / m_0 C_x = k_x a\sqrt{3}/2, \quad S_y \hbar k_y / m_0 C_y = 3k_y a/2. \tag{33.21}$$

That is, the components of velocities and masses obtained from (33.18) actually reproduce their values (33.7) and (33.8), obtained from (33.1) using the approximation (33.6). Note that when obtaining (33.21), we did not use the explicit values (33.12) for the parameters S_x, S_y.

33.5 Louis de Broglie Ratio and the Estimation of the Energy Range of Electron Injection into Graphene

Louis de Broglie ratio is the ratio between the mechanical and wave momenta for an object of the classical type (material point). The simplest form of this relation, $m_i V_i = \hbar k_i$, corresponds to small momenta. It can be considered as a test. That is, in reality, this ratio should be more complicated, but it should be reduced to its simplest for small momenta.

Here, having definitions of the velocity (33.19) and the mass (33.20) components, as functions of the wave momentum components $\hbar k_i$, it is possible to construct a more general ratio than $mV_i = \hbar k_i$. Introducing the notation $P^i_m \equiv m_i V_i$ for the dimensional components of the mechanical momentum and, similarly to the dimensionless components (33.15), introducing the notation $P^i_{\mathrm{w}} = \hbar k_i$ for the dimensional components of the wave momentum, and also using the definitions (33.19) and (33.20), we obtain the de Broglie relation in the form:

$$P^i_m \equiv \frac{P_i}{S_i} \mathrm{tg}\left(\frac{S_i}{P_i} P^i_{\mathrm{w}}\right), \tag{33.22}$$

where the momentum constants P_i are defined by the general relation, $P_i = m_0 C_i$, and their explicit form is given in (33.13) and (33.14). There are two circumstances, which can confirm the correctness of this relation. The first of these is the case of small momenta in terms of inequality $\frac{S_i}{P_i} P^i_{\mathrm{w}} \ll 1$. Then relation (33.22) takes the simplest form $P^i_m = P^i_{\mathrm{w}}$ (or $m_i V_i = \hbar k_i$). The second circumstance is that when the wave momentum varies within the range of its uniqueness for the function tg(...), $\left|P^i_{\mathrm{w}}\right| < \frac{\pi}{2}\frac{P_i}{S_i}$ (or $\hbar |k_i| < \frac{\pi}{2}\frac{m_0 C_i}{S_i}$), the mechanical momentum $\left|P^i_m\right|$ changes in its natural limits from 0 to ∞.

To estimate the energy range of electron injection in the approximation considered, the dimensionless form of this ratio will be useful in graphene. Taking into account the above updated definition for the dimensionless wave momentum,

$p_{\mathrm{w}}^{i} \equiv \frac{\hbar k_i}{m_0 C_i} \equiv \frac{P_{\mathrm{w}}^{i}}{P_i}$, and also introducing a similar definition for a mechanical momentum:

$$p_m^i = \frac{m_i V_i}{m_0 C_i} \equiv \frac{P_m^i}{P_i}, \tag{33.23}$$

we will obtain:

$$p_m^i \equiv \frac{1}{S_i} \mathrm{tg}\left(S_i\, p_{\mathrm{w}}^i\right). \tag{33.24}$$

Now we can proceed to an estimation of the energy range of an electron injection in graphene, which is valid in the considered approximation. We proceed from the fact that outside the crystal the dimensionless kinetic energy of an electron injected into graphene is determined for each of the components by the relation $w = \sqrt{1 + \left(p_m^i\right)^2} - 1$. In accordance with the law of conservation of momentum, substituting (33.24) here, we obtain a ratio for the injection energy estimation: $0 \leq w \leq \min\limits_{i=x,y}\left(\sqrt{1 + \frac{1}{S_i{}^2}\mathrm{tg}^2\left(S_i\, p_{\mathrm{w}}^i\right)} - 1\right)$. In this case, the expression in parentheses must be the maximum for each value i. And from these two values, it is necessary to choose the minimum. Taking into account the limits (33.17), $\left|p_{\mathrm{w}}^i\right| \leq \pi\ S_i/3$, for such a maximum value, we will obtain $0 \leq w \leq \min\limits_{i=x,y}\left(\sqrt{1 + \frac{1}{S_i{}^2}\mathrm{tg}^2\left(\frac{\pi}{3} S_i{}^2\right)} - 1\right)$. Consistently substituting $S_x = 1/\sqrt{2}$ and $S_y = \sqrt{3/2}$ here, we can confirm that we must choose the first of these two values, since the second gives infinity on the right-hand side of the inequality. For $S_x = 1/\sqrt{2}$, we will obtain $0 \leq w \leq 0.468$. Taking into account that the rest energy of the electron in the conduction band is determined by the relation (33.11) (with allowance for (33.12)), $m_0 \mathrm{C}_x^2 = m_0 \mathrm{C}_y^2 = E_C$, that is, equal to the width of the conduction band, which is of the order of 10 eV [22], we will obtain that the dimensional version of this inequality has the following form: $0 \leq W \leq 4.68$ eV. That is, approximately $0 \leq W \leq 5$ eV.

33.6 Main Characteristics of Analytical Dynamics for a Conduction Electron in Graphene

Part of the dynamic characteristics has been already formulated in the previous sections. First of all, it is a Hamiltonian, which is also a dispersion law. The dimensional representation of its normal branch is given in (33.18). The abnormal branch differs from the normal branch only by the signs in front of each summand. The dimensionless representation (33.18), which is useful in applications and will be used later, has the form:

$$\tilde{\varepsilon}\left(\mathbf{p}_{\mathrm{w}}\right) = -\frac{1}{S_x}\cos\left(S_x\, p_{\mathrm{w}}^x\right) - \frac{1}{S_y}\cos\left(S_y\, p_{\mathrm{w}}^y\right), \tag{33.25}$$

where $\tilde{\varepsilon}\left(\mathbf{p}_{\mathrm{w}}\right) \equiv \frac{\tilde{E}(\mathbf{k})}{E_C}$. In obtaining this dimensionless form, the definition $p_{\mathrm{w}}^i \equiv \frac{\hbar k_i}{m_0 C_i}$ is used, as well as the invariant $m_0^x C_x^2 = m_0^y C_y^2 = E_C$, which reduces to the form:

$$m_0 C_x^2 = m_0 C_y^2 = E_C. \tag{33.26}$$

By direct differentiation of this dimensionless Hamiltonian with respect to the components p_{w}^i of dimensionless momentum $\mathbf{p}_{\mathrm{w}}$, we can obtain the components of the dimensionless velocity $\mathbf{v}$:

$$\mathrm{v}_i = \sin\left(S_i p_{\mathrm{w}}^i\right). \tag{33.27}$$

It is not difficult to verify that this definition coincides with the dimensional definition (33.7) if the components of the dimensionless velocity are determined by the natural relations:

$$\mathrm{v}_i = V_i / C_i, \tag{33.28}$$

and also, taking into account the relations (33.16), from which, taking into account the numerical values (33.12), it follows that:

$$S_x p_{\mathrm{w}}^x = S_x k_x a\sqrt{3/2} = k_x a\sqrt{3}/2, \quad S_y p_{\mathrm{w}}^y = S_y k_y a\sqrt{3/2} = 3k_y a/2.$$

Velocity is one of the most important characteristics, since it directly determines the current density. In particular, if one takes into account that the velocities from the abnormal dispersion have the opposite sign, $\mathrm{v}_i^{an} = -\sin\left(S_i p_{\mathrm{w}}^i\right)$, and the total current density for each component i is proportional to the sums of all velocities for normal and abnormal dispersions $\mathrm{v}_i + \mathrm{v}_i^{an}$, then the current density will be zero. Physically, this is correct, due to the absence of an external field.

We now verify that the components of the dimensionless effective mass tensor, which we denote by μ_i, can be obtained by direct differentiation of (33.27) with respect to the components p_{w}^i, that is, as a result of the operation, $\frac{\partial \mathrm{v}_i}{\partial p_{\mathrm{w}}^i}$, which gives the inverse tensor $\mu_i^{-1} = S_i \cos\left(S_i p_{\mathrm{w}}^i\right)$. As it can be seen, this relation completely coincides with (33.8) if the dimensionless mass is determined by the relation:

$$\mu_i \equiv \frac{m_i\left(\mathbf{k}\right)}{m_0}. \tag{33.29}$$

A peculiarity of the approximation (33.6) used here is that it is not difficult to find the tensor of the effective mass:

$$\mu_i = 1/\left\{S_i \cos\left(S_i p_{\mathrm{w}}^i\right)\right\}, \tag{33.30}$$

in contrast to the general case [1] with the Hamiltonian (33.3). Due to this possibility, it was possible to find the generalized Louis de Broglie ratio (33.24), which allowed the estimation of the permissible energy range of electron injection. Effective mass is a useful characteristic in other applications [23].

In addition to these already discussed dynamic characteristics, we can now obtain and discuss all the remaining. First of all, it is a wave Lagrangian. To construct it we will use the corresponding general definition:

$$l_{\mathrm{w}}(\mathbf{v}) = \mathbf{p}_{\mathrm{w}}\mathbf{v} - \tilde{\varepsilon}(\mathbf{p}_{\mathrm{w}}) \equiv \sum_{i=1}^{2}\left\{p_{\mathrm{w}}^{i}\mathrm{v}_i + \frac{1}{S_i}\cos\left(S_i p_{\mathrm{w}}^{i}\right)\right\}. \tag{33.31}$$

Using (33.27) in terms of representation, $\cos\left(S_i p_{\mathrm{w}}^{i}\right) = \sqrt{1-\mathrm{v}_i^2}$, and the inverse transformation to (33.27), $p_{\mathrm{w}}^{i} = \frac{1}{S_i}\arcsin(\mathrm{v}_i)$, we will obtain the following for the wave Lagrangian: $l_{\mathrm{w}}(\mathbf{v}) = \sum_i \frac{1}{S_i}\left\{\mathrm{v}_i \arcsin(\mathrm{v}_i) + \sqrt{1-\mathrm{v}_i^2}\right\}$. Carrying out direct differentiation, $\frac{\partial l_{\mathrm{w}}}{\partial \mathrm{v}_i}$, we can make sure that $\frac{\partial l_{\mathrm{w}}}{\partial \mathrm{v}_i} = p_{\mathrm{w}}^{i}$, that is, it is indeed a Lagrangian with respect to the wave momentum.

Let's show that this Lagrangian is present in the phase of the wave function of the conduction electron as a separate phase summand. In [1, 16], the wave function for the conduction electron was defined in the form, $A_\alpha \exp\{i[(\mathbf{k}\cdot\mathbf{n}) - \omega t]\}$, where index α takes 2 values and $\mathbf{n}$ is the crystal lattice vector. Since we are interested in the phase factor $(\mathbf{k}\cdot\mathbf{n}) - \omega t$, then, first of all, it is necessary to bring it to a form containing the values introduced here. For this we take into account the definitions of the dimensionless wave momenta given by (33.16). Then multiplying and dividing the first summand $(\mathbf{k}\cdot\mathbf{n})$ in the phase factor by $a\sqrt{3/2}$, it can be shown that $(\mathbf{k}\cdot\mathbf{n}) = (\mathbf{p}_{\mathrm{w}}\cdot\mathbf{r})$, where $\mathbf{r} \equiv \mathbf{n}/\left(a\sqrt{3/2}\right)$ is dimensionless spatial variable. For a product ωt in the phase factor, it is first necessary to take into account that, up to an inessential constant summand, we have $\hbar\omega = \tilde{E}(\mathbf{k})$, where $\tilde{E}(\mathbf{k})$ is defined in (33.18). Further, taking into account the invariant (33.26) and the definition $\tilde{\varepsilon}(\mathbf{p}_{\mathrm{w}}) \equiv \tilde{E}(\mathbf{k})/E_C$, where the dimensionless Hamiltonian $\tilde{\varepsilon}(\mathbf{p}_{\mathrm{w}})$ is defined in (33.25), the product ωt can be reduced to the form $\tilde{\varepsilon}(\mathbf{p}_{\mathrm{w}})\ \tau$. At the same time, a dimensionless time $\tau \equiv E_C t/\hbar$ is introduced.

Thus, the wave function of the conduction electron takes the form $A_\alpha \exp\left\{i\ \left[(\mathbf{p}_{\mathrm{w}}\cdot\mathbf{r}) - \tilde{\varepsilon}(\mathbf{p}_{\mathrm{w}})\ \tau\right]\right\}$. This wave function depends on the spatial variable $\mathbf{r}$, defined in the coordinates of the crystal. Let's define some point $\mathbf{r}_0$ of conditional localization of the electron, as a quasiparticle, and proceed to consider the wave function with respect to this point, that is, to the local coordinates. Then the phase part of the wave function can be represented in the form of two factors:

$$A_\alpha \exp\{i\ (\mathbf{p}_{\mathrm{w}}\cdot\boldsymbol{\rho})\} \exp\left\{i\ \left[(\mathbf{p}_{\mathrm{w}}\cdot\mathbf{r}_0) - \tilde{\varepsilon}(\mathbf{p}_{\mathrm{w}})\ \tau\right]\right\},$$

where $\boldsymbol{\rho} \equiv \mathbf{r} - \mathbf{r}_0$. An important feature of the variable $\mathbf{r}_0$ consists in the fact that, unlike the variable $\mathbf{r}$, it depends on time τ and defines a certain classical trajectory.

In this sense, it is a variable of the classical type, describing the dynamics of a material point. The external fields are not considered here, and the electron has a constant velocity $\mathbf{v}$ with components v_i, which are defined in (33.27). Therefore, the corresponding trajectory has the simplest form $\mathbf{r}_0 = \mathbf{v}\,\tau$. Then the wave function reduces to the form:

$$A_\alpha \exp\{i\ (\mathbf{p}_\mathrm{w} \cdot \boldsymbol{\rho})\} \exp\left\{i\ \left[(\mathbf{p}_\mathrm{w} \cdot \mathbf{v}) - \tilde{\varepsilon}\,(\mathbf{p}_\mathrm{w})\right]\ \tau\right\}.$$

Taking into account the definition (33.31) for the wave Lagrangian $l_\mathrm{w}(\mathbf{v}) = \mathbf{p}_\mathrm{w}\mathbf{v} - \tilde{\varepsilon}\,(\mathbf{p}_\mathrm{w})$, finally, we can reduce the wave function to the form $A_\alpha \exp\{i[(\mathbf{p}_\mathrm{w} \cdot \boldsymbol{\rho}) + l_\mathrm{w}(\mathbf{v})\ \tau]\}$. This analysis is important because it is always necessary to clearly distinguish, in which coordinates the wave function is considered. If in the crystal (laboratory) coordinates, then it has the form $A_\alpha \exp\left\{i\ \left[(\mathbf{p}_\mathrm{w} \cdot \mathbf{r}) - \tilde{\varepsilon}\,(\mathbf{p}_\mathrm{w})\ \tau\right]\right\}$, where $\mathbf{r}$ is a global spatial variable and $\tilde{\varepsilon}\,(\mathbf{p}_\mathrm{w})$ is wave Hamiltonian. In some cases, in the quantum description of an electron in the conduction band, it is necessary to transfer to the local coordinates associated with the point $\mathbf{r}_0$ of its conditional localization, for example, during for the scattering of an electron at a certain center. Then the wave function has the form $A_\alpha \exp\{i[(\mathbf{p}_\mathrm{w} \cdot \boldsymbol{\rho}) + l_\mathrm{w}(\mathbf{v})\ \tau]\}$, where $\boldsymbol{\rho} \equiv \mathbf{r} - \mathbf{r}_0$ is a local spatial variable and $l_\mathrm{w}(\mathbf{v})$ is wave Lagrangian, describing the dynamics of a point $\mathbf{r}_0$. If these features of the description are not taken into account, serious errors can occur.

And, finally, the last two characteristics, which complete the complex construction of the dynamics of the conduction electron, as a quasiparticle, are the mechanical Hamiltonian and the mechanical Lagrangian. They are important, since the dynamics of a free electron, as a particle, is usually described precisely in this dynamic representation. And its use with respect to the injected electron can facilitate the matching of the descriptions outside and inside the crystal. But it should be borne in mind that the mechanical description is less convenient in the crystal than the wave one, since the wave branch is natural (dispersion) for the crystal.

To formulate the mechanical branch of the description, we consider the Hamiltonian (dispersion) (33.25), $\tilde{\varepsilon}\,(\mathbf{p}_\mathrm{w}) = -\sum_{i=1}^{2} \frac{1}{S_i} \cos\left(S_i\, p^i_\mathrm{w}\right)$, and velocity (33.27) $\mathrm{v}_i = \sin\left(S_i\, p^i_\mathrm{w}\right)$. Using the feature $\cos(x) = \sqrt{1 - \sin^2(x)}$, this energy can be represented in the form, $\tilde{\varepsilon}\,(\mathbf{p}_\mathrm{w}) = -\sum_{i=1}^{2} \frac{1}{S_i}\sqrt{1 - \mathrm{v}_i^2}$, where the dependence on $\mathbf{p}_\mathrm{w}$ is mediated through the velocity components v_i. If this energy is considered, as a function of velocity $\mathbf{v}$, then for it, first of all, you need to introduce a different notation, for example, $l_m(\mathbf{v}) = -\sum_{i=1}^{2} \frac{1}{S_i}\sqrt{1 - \mathrm{v}_i^2}$, where index m means that this is a mechanical Lagrangian. And, second, it is clear that this energy, even in its form, largely coincides with the Lagrangian of relativistic mechanics. The fact that this is indeed a mechanical Lagrangian can be verified by differentiating $l_m(\mathbf{v})$ by

velocity components. As a result, we will obtain $\frac{\partial l_m(\mathbf{v})}{\partial \mathrm{v}_i} = \frac{\mathrm{v}_i}{S_i\sqrt{1-\mathrm{v}_i^2}}$. Further, we take into account the definition (33.30) for the dimensionless effective mass tensor, in which we use the transformation $\cos(x) = \sqrt{1-\sin^2(x)}$. Then $\frac{\partial l_m(\mathbf{v})}{\partial \mathrm{v}_i} = \mu_i \mathrm{v}_i$ is the dimensionless mechanical momentum, as defined in (33.23), if we also take into account the definition of the dimensionless velocity (33.28) and the dimensionless mass (33.29). Thus:

$$\mu_i \mathrm{v}_i = p_m^i = \frac{\mathrm{v}_i}{S_i\sqrt{1-\mathrm{v}_i^2}}. \tag{33.32}$$

To complete the consideration of the mechanical branch of the dynamic description of the conduction electron, as a quasiparticle, it remains to formulate a mechanical Hamiltonian. As in the formulation of the wave Lagrangian in (33.31), we also use the general definition:

$$h_m(\mathbf{p}_m) = \mathbf{p}_m \mathbf{v} - l_m(\mathbf{v}). \tag{33.33}$$

In this case, the velocity components must be expressed in terms of the components of the mechanical momentum, $p_m^i = \frac{\mathrm{v}_i}{S_i\sqrt{1-\mathrm{v}_i^2}}$, relative to v_i. Making use of this conversion, we obtain:

$$\mathrm{v}_i = \frac{S_i p_m^i}{\sqrt{1+S_i^2\left(p_m^i\right)^2}}. \tag{33.34}$$

The use of this relation in the Hamiltonian (33.33), finally gives $h_m(\mathbf{p}_m) = \sum_{i=1}^{2} \frac{1}{S_i}\sqrt{1+\left(S_i p_m^i\right)^2}$. The differentiation of this Hamiltonian with respect to the momentum components p_m^i gives the velocity components (33.34). As it was already noted, this branch can be convenient in some applications.

For the transition from the mechanical branch of the dynamic description to the wave branch (or vice versa), it is also necessary to use the Louis de Broglie ratio (33.24).

33.7 Conclusions

The possibility of constructing the general dynamic properties of a conduction electron injected into graphene in the rectangular lattice approximation was analyzed. This approximation is sufficiently accurate within the regions $|k_x|\,a \le \pi/3\sqrt{3}$, $|k_y|a \le \pi/3$, within the first Brillouin zone, where a is a parameter of the graphene lattice (the side of an equilateral hexagon). Numerical-graphical analysis has

shown that in this approximation the exact expression (33.1) for the dimensionless wave Hamiltonian (dimensionless dispersion) can be reduced to the simpler form (33.25) characteristic of crystals with a rectangular lattice. It is shown that the effective Hamiltonian obtained in place of (33.1) makes it possible to construct completely the entire dynamics of an electron injected into the conduction band, as a quasiparticle. This cannot be done in the general case [1] with the use of the Hamiltonian (33.1), but it is possible to do this in fact for only one particular case.

The use of the effective Hamiltonian (33.25) makes it possible to solve this problem within the limits of the above stated limit for wave vector **k**. The following dynamic characteristics were successively defined.

First of all is velocity. This is one of the most important characteristics, since it determines the current. It is shown that the presence of two conduction bands with normal and abnormal (reverse) dispersion leads to a lack of current. Since there are no external fields in the task under consideration, the current from the injected electron should indeed be absent. The appearance of the field should lead to a violation of symmetry of the zones and, as a result, to the appearance of a current.

In addition to the quasiparticle velocity (in fact, the only dynamic characteristic, determined in the general case), it was possible to define its dynamic effective mass tensor, both inverse and direct. Using the exact Hamiltonian (33.1), only the inverse tensor of the effective mass was available for determination, which already at this stage led to a practical impossibility to solve the problem.

Owing to the possibility of determining the effective mass, it was possible to find the mechanical momentum of the quasiparticle defined in (33.23) and (33.32), and also to formulate the generalized Louis de Broglie ratio (33.24). It allows a correct transition from the wave branch of the dynamic description to the mechanical branch or vice versa. This is important, since the dynamics of a free electron outside the crystal is usually considered in terms of a mechanical description with a momentum that has components $m_i V_i$. Whereas, it is more convenient to consider such dynamics in a crystal in terms of a wave description with a momentum having components $\hbar k_i$. In particular, Louis de Broglie ratio allowed estimating the permissible energy range of the electron injection. It was 0 to 5 eV.

On the basis of the definition (33.31), the wave Lagrangian $l_{\mathrm{w}}(\mathbf{v})$ was obtained. This characteristic is important in those cases when, in the quantum description of an electron in the conduction band, it is necessary to transfer to the local coordinates associated with the point of its conditional localization $\mathbf{r}_0$, for example, at the scattering of an electron at a certain center. Then the phase of the wave function contains the summand $l_{\mathrm{w}}(\mathbf{v})\tau$, having the meaning of action.

Finally, a mechanical Hamiltonian and a mechanical Lagrangian were defined. They are important, since the dynamics of a free electron as a particle outside the crystal is usually described precisely in this dynamic representation. And its use with respect to the injected electron can facilitate the coordination of the descriptions outside and inside the crystal. However, as it was already noted, the mechanical representation inside the crystal is less convenient than the wave representation.

References

1. Suprun AD, Shmeleva LV (2017) Features of the generalized dynamics of quasiparticles in graphene. Nanoscale Res Lett 12(187). https://doi.org/10.1186/s11671-017-1940-0
2. Morozovska AN, Eliseev EA, Ievlev AV, Varenyk OV, Pusenkova AS, Chu Y-H, VYa S, Strikha MV, Kalinin SV (2014) Ferroelectric domain triggers the charge modulation in semiconductors. JAppl Phys 116:066817. https://doi.org/10.1063/1.4891346
3. Sarma SD, Adam S, Hwang EH, Rossi E (2011) Electronic transport in two dimensional graphene. Rev Mod Phys 83:407. https://doi.org/10.1103/RevModPhys.83.407
4. Morozovska AN, Pusenkova AS, Varenyk OV, Kalinin SV, Eliseev EA, Strikha MV (2015) Finite size effects of hysteretic dynamics in multi-layer graphene on ferroelectric. Phys Rev B 91:235312. https://doi.org/10.1103/PhysRevB.91.235312
5. Grüneis A, Attaccalite C, Wirtz L, Shiozawa H, Saito R, Pichler T, Rubio A (2008) Tight-binding description of the quasiparticle dispersion of graphite and few-layer graphene. Phys Rev B 78:205425. https://doi.org/10.1103/PhysRevB.78.205425
6. Morozovska AN, Eliseev EA, Strikha MV (2016) Ballistic conductivity of graphene channel with p-n junction on ferroelectric domain wall. Appl Phys Lett 108:232902. https://doi.org/10.1063/1.4953226
7. Davydov AS (1991) Solitons in molecular systems. Kluwer Academic Publishers. 419 p. http://www.worldcat.org/title/solitons-in-molecular-systems/oclc/22505938
8. Natanzon YE, Brizhik LS, Eremko AA (2006) Self-trapping and dynamics of a quasi-particle in a one-dimensional molecular chain under interaction with optical phonons. Ukr J Phys 51(4):413–422. http://archive.ujp.bitp.kiev.ua/files/journals/51/4/510415p.pdf
9. Suprun AD, Shmeleva LV (2014) Alpha-helical regions of the protein molecule as organic nanotubes. Nanoscale Res Lett 9:200. https://doi.org/10.1186/1556-276X-9-200
10. Suprun AD, Shmeleva LV (2015) Primary structure of proteins as a nanowire for metabolic electronic transport. Nanoscale Res Lett 10:121. https://doi.org/10.1186/s11671-015-0763-0
11. Ebrahimnejad H, Sawatzky GA, Berciu M (2014) The dynamics of a doped hole in a cuprate is not controlled by spin fluctuations. Nat Phys 10(12):951–955. https://www.nature.com/articles/nphys3130
12. Filippov AV, Zagorodny AG, Momot AI, Pal' AF, Starostin AN (2009) Screening of a moving charge in a non equilibrium plasma. JETP 108(3):497–515. https://doi.org/10.1134/S1063776109030145
13. Mryglod IM, Kuporov VM (2010) Perturbation theory for collective modes in the dynamics of simple and complex fluids. Ukr J Phys 55(11):1172–1181. http://archive.ujp.bitp.kiev.ua/files/journals/55/11/551103p.pdf
14. Verkhoglyadova OP, Tsurutani BT, Lakhina GS (2013) Theoretical analysis of Poynting flux and polarization for ELF-VLF electromagnetic waves in the Earth's magnetosphere. J Geophys Res Space Physics 118:7695–7702. https://doi.org/10.1002/2013JA019371
15. Suprun AD, Shmeleva LV (2016) Current in the protein nanowires: quantum calculations of the base states. Nanoscale Res Lett 11(74). https://doi.org/10.1186/s11671-016-1269-0
16. Suprun AD, Shmeleva LV (2016) Some aspects of generalized dynamics of quasiparticles in crystals with unit cell of arbitrary complexity. Ukr J Phys 61(6):537–546. https://doi.org/10.15407/ujpe61.06.0537
17. Shmeleva LV, Suprun AD (2015) Features of generalized dynamics of quasiparticles in the presence of an external potential field. Part 1. General analysis of the problem. Funct Mater 22(4):524–534. https://doi.org/10.15407/fm22.04.524
18. Suprun AD, Shmeleva LV (2012) Degeneracy effect of dynamical properties of quasiparticles of electronic origin in semiconductor materials. Funct Mater 19(4):508–519. http://functmaterials.org.ua/contents/19-4/fm194-17.pdf
19. Suprun AD, Shmeleva LV (2014) The centrally-symmetric solutions of electronic excitations of semiconductors in the conditions of relativistic like degeneracy of dynamical properties. Funct Mater 21(1):69–79. https://doi.org/10.15407/fm21.01.069

20. Sitenko YA, Vlasii ND (2007) Electronic properties of graphene with a topological defect. Nucl Phys B 787:241–259. https://doi.org/10.1016/j.nuclphysb.2007.06.001
21. Wallace PR (1947) The band theory of graphite. Phys Rev 71:622–634. https://doi.org/10.1103/PhysRev.71.622
22. Hibino H, Kageshima H, Maeda F, Nagase M, Kobayashi Y, Yamaguchi H (2008) Microscopic thickness determination of thin graphite films formed on SiC from quantized oscillation in reflectivity of low-energy electrons. Phys Rev B 77(7):075413. https://doi.org/10.1103/PhysRevB.77.075413
23. Bose PK, Paitya N, Bhattacharya S, De D, Saha S, Chatterjee KM, Ghatak KP (2012) Influence of light waves on the effective electron mass in quantum wells, wires, inversion layers and superlattices. Quantum Matter 1(2):89–126. https://doi.org/10.1166/qm.2012.1009

Chapter 34
Simulation of the Formation of a Surface Nano-Crater Under the Action of High-Power Pulsed Radiation

L. V. Shmeleva, A. D. Suprun, and S. M. Yezhov

34.1 Introduction

Currently, the mechanisms of solid matter surface corrosion damage due to the action of laser radiation are not fully investigated. The main characteristics of pulsed laser radiation, important for determining the stability of materials to momentum exposure, are the intensity, duration, shape of the momentum, and the frequency of radiation. Momentums of high intensity and corresponding duration, falling on the surface of a solid matter, lead to a significant damage to this surface, hence causing a particular interest [1–15]. The "behavior" of condensed media, which is affected by intense laser momentum, is not unambiguous. The formation of a corrosion crater on the surface of such media depends on both the characteristics of the energy flux and the properties of a particular separate substance.

The purpose of this work is to investigate the theoretical dynamics of a crater formation and all related processes. In the case of destruction, the removal of a substance from a solid matter to a gas phase in real conditions can occur not only directly from the surface in the form of individual atoms but also through micro-clusters and micro-droplets that cannot be formed in the gas phase. Therefore, the model of the destructive process proposed in the work was developed on the basis of a system of heterogeneous equations of continuum mechanics [16].

L. V. Shmeleva (✉) · A. D. Suprun · S. M. Yezhov
Taras Shevchenko National University of Kyiv, Kyiv, Ukraine
e-mail: lshmel@univ.kiev.ua

O. Fesenko, L. Yatsenko (eds.), *Nanocomposites, Nanostructures, and Their Applications*, Springer Proceedings in Physics 221,
https://doi.org/10.1007/978-3-030-17759-1_34

34.2 Dynamics Equations System for the Crater Formation

Based on the basic system of equations [17] and taking into account the influence of the radiation flux on the process of laser-stimulated formation of crater-like surface relief, [18] the boundary conditions for this task were specified on the boundary's two phases, the solid matter, which we denote by the index "os," and gas, which we will denote by the index "s," namely:

– Condition of the mass flow balance:

$$\rho_s \left(\boldsymbol{\upsilon}_s \cdot \mathbf{n}\right) - \rho_{os} \left(\boldsymbol{\upsilon}_{os} \cdot \mathbf{n}\right) = 0. \tag{34.1}$$

– Condition of the momentum flow balance:

$$P_s n_i + \frac{1}{c} \left(\mathbf{n} \cdot \mathbf{q}_s\right) + \rho_s \left(\mathbf{n} \cdot \boldsymbol{\upsilon}_s\right) \left(\upsilon_s^i - \upsilon_{os}^i\right) + P_{ij}^{os} n_j = 0. \tag{34.2}$$

– Condition of the energy flow balance:

$$\begin{aligned} &\left(\mathbf{n} \cdot \boldsymbol{\upsilon}_s\right) \left(\rho_s H_s + \rho_s \frac{\upsilon_s^2}{2}\right) + L_0 \left(\mathbf{n} \cdot \mathbf{q}_s\right) - \\ &- L\lambda_s \left(\mathbf{n} \cdot \operatorname{grad} T\right)_s - \left(\mathbf{n} \cdot \boldsymbol{\upsilon}_s\right) \rho_s U_{os} = 0. \end{aligned} \tag{34.3}$$

Under the boundary conditions (34.1, 34.2, and 34.3), U_{os}, ρ, υ represents the internal energy of the unit mass of the solid media, its density, and the convective velocity vector, respectively; $\mathbf{q}_s$, the superficial part of the flux that has reached the surface; $-\lambda_s(\text{grad}T)_s$, a superficial part of the heat flow in the gas phase; L_0 and L, generalized coefficients of losses in the transition of light and heat fluxes, respectively, through the boundary matter, gas; H_s, Gibbs heat function (enthalpy); and P_s, near-surface pressure.

All boundary conditions are formulated in the local reference system, located on the boundary between the condensed media and the gas phase in the area of the momentum action. It is clear that when the solid surface does not collapse, the reference system will remain stationary relative to the observer. But when destruction occurs, then the chosen system in the area of this destruction is rigidly associated with a certain point of the surface of the solid medium and moves along with it. That is, such a system describes the events directly at each individual point of the surface. Therefore, there is a need to establish a connection between the local and laboratory coordinate systems. The latter is stationary relative to the surface prior to its destruction.

The shape of the crater at each fixed time point is determined as follows [19]: $z(t) = S(t, x(t), y(t))$. Here $S(t, x(t), y(t))$ represents the function of the shape of the surface of the formed crater. For each moment of time, it determines a certain dependence from x and y. In the future, this function will be called the crater shape function.

As a result of coordinate transformations from the laboratory reference system to the local reference system associated with the surface of the crater, the following relations were obtained for the velocities that bind these two systems [19]:

$$\begin{aligned} \upsilon^{(\xi)} &= \frac{\upsilon^{(x)} + S_x \upsilon^{(z)}}{T}, \\ \upsilon^{(\eta)} &= \frac{-S_x S_y \upsilon^{(x)} + T^2 \upsilon^{(y)} + S_y \upsilon^{(z)}}{NT}, \\ \upsilon^{(\zeta)} &= \frac{-S_x \upsilon^{(x)} - S_y \upsilon^{(y)} + \upsilon^{(z)}}{N}, \end{aligned} \tag{34.4}$$

where $S_x \equiv \partial S/\partial x$, $N \equiv \sqrt{1 + {S_x}^2 + {S_y}^2}$, and $T \equiv \sqrt{1 + {S_x}^2}$, $\upsilon^{(i)}$ are components of the vector of velocity in the laboratory reference system at $i = x, y, z$ and components of the velocity vector in the local reference system at $i = \xi, \eta, \zeta$.

The relations (34.4) allow us to switch from the local reference system, in which the conditions (34.1, 34.2, and 34.3) are formulated to a laboratory reference system where the processes associated with destructive processing can be observed. Due to these transformations, one can formulate the equation of the crater formation dynamics relative to the laboratory reference system. To do this we will use the condition of the mass flow balance (34.1). This condition in the local reference system can be written immediately in the form:

$$\rho_s \upsilon_s^{(\zeta)} = \rho_{os} \upsilon_{os}^{(\zeta)}. \tag{34.5}$$

As for the near-surface velocity value $\upsilon_s^{(\zeta)}$ and density ρ_s, they can be defined from a system of equations that describes a solid-gas medium if density ρ and convective velocity υ are considered as functions of pressure P:

$$\begin{cases} P_t + \left(\mathbf{\upsilon} + \frac{\rho}{\rho'}\mathbf{\upsilon}'\right) \cdot \operatorname{grad} P = \frac{R}{\rho'}, \\ P_t + \left(\mathbf{\upsilon} + \frac{\mathbf{\upsilon}}{(\mathbf{\upsilon}\cdot\mathbf{\upsilon}')\rho}\right) \cdot \operatorname{grad} P = \frac{(\mathbf{\upsilon}\cdot\mathbf{f})}{(\mathbf{\upsilon}\cdot\mathbf{\upsilon}')}, \\ P_t + \left(\mathbf{\upsilon} + \kappa P \mathbf{\upsilon}'\right) \cdot \operatorname{grad} P = \frac{PR}{\rho} - (\kappa - 1) \operatorname{div} \mathbf{Q}. \end{cases} \tag{34.6}$$

Here $\mathbf{Q}$ represents the generalized energy flow in a plasma-gas medium, consisting of two independent flows, the radiation flux and the heat flux; P, the pressure acting on the system; and $P_t \equiv \partial P/\partial t$, its partial derivative in time. R is the function of source of mass sinking, due to the presence of volumetric sources mass sinking in the gas phase, associated with the micro-cluster and micro-particle occurrence, when the solids evaporate into the gas phase [16], $\mathbf{f}$ is the mass density of the force acting on the gaseous matter flow from the radiation side [20], and κ represents the polytropic indicator.

Under the condition of the compatibility of system (34.6), we obtain:

$$\upsilon_s^{(\zeta)} = \frac{{P_s}^{\sigma}}{\sigma\sqrt{\kappa a}}, \quad \rho_s = a {P_s}^{\eta}, \tag{34.7}$$

and the system itself (34.6) reduces to one equation:

$$P_t - \frac{\alpha}{\gamma}\sqrt{\frac{\kappa}{a}}P^{\sigma}\,(\mathbf{n}\cdot\operatorname{grad}P) \quad = -\kappa\,\operatorname{div}\mathbf{Q}. \tag{34.8}$$

In (34.7), $\alpha \equiv \kappa + 1$, $\gamma \equiv \kappa - 1$, $\sigma \equiv \gamma/2\kappa$, $\eta \equiv 1/\kappa$, and a is the integration constant. Solutions (34.7) and Eq. (34.8) (after it is solved) make the left part of Eq. (34.5) be defined as a function of time t and coordinates. As for the right side of Eq. (34.5), where $z(t) = S(t, x(t), y(t))$, the component of velocity $\upsilon_{os}^{(z)}$ is apparently equal to $dz/dt \equiv \upsilon_{os}^{(z)} = S_t + S_x\upsilon_{os}^{(x)} + S_y\upsilon_{os}^{(y)}$. Substituting the result obtained in (34.4) and mapping the component $\upsilon_{os}^{(\zeta)}$ on the surface, we will find the following:

$$\upsilon_{os}^{(\zeta)} = S_t/N. \tag{34.9}$$

Let's substitute the solution (34.9) to the right side of Eq. (34.5), and in the left part of this equation, we will substitute the values given in (34.7). After some transformations, we obtain:

$$\frac{\partial S}{\partial t} = \frac{2\sqrt{a\kappa}}{(\kappa-1)\,\rho_{os}}P_s{}^{\beta}\sqrt{1 + S_x^2 + S_y^2}, \tag{34.10}$$

where $\beta \equiv (\kappa + 1)/(2\kappa)$. Equation (34.10) describes the dynamics of the crater formation. Since the near-surface pressure, which is included in the resulting equation, is not a constant value, the boundary condition (34.3) is used to find it. In this condition, the temperature T is replaced by pressure in accordance with the state equation $P = \frac{k_B}{m_a}\rho T$, where k_B is the Boltzmann constant and m_a is the atomic mass of the matter under consideration. The use of Eq. (34.8), mapped on the surface [18], allows us to exclude the construction $(\mathbf{n}\cdot\ \operatorname{grad}P)$ from the condition (34.3). As a result we will obtain:

$$\begin{aligned} P_t = &-\frac{2a^{3/2}\kappa^2\alpha\varphi_o}{\gamma^3 bL}P_s{}^{2\eta+\sigma} - \frac{2\sqrt{a}\kappa^3\alpha^2}{\gamma^5 bL}P_s{}^{2\beta+\sigma} + \\ &+ \frac{1}{N}e_q\vartheta_\tau\frac{a\alpha\kappa^{3/2}q_oL_0}{\gamma^2 bL}P_s{}^{\eta} + \kappa a^{3/2}q_oP^{\eta+\beta}h\,(\omega)\,e_q\vartheta_\tau. \end{aligned} \tag{34.11}$$

In Eq. (34.11), $\vartheta_\tau \equiv \vartheta(\tau - t)$ represents the Heaviside's step function and is the duration of the momentum. Equations (34.10) and (34.11) can lead to dimensionless variables Π, θ, Σ, X, and Y by replacing:

$$P = P_o\Pi, \quad t \equiv t_o\theta, \quad S \equiv S_o\Sigma, \quad x \equiv S_oX, \quad y \equiv S_oY. \tag{34.12}$$

Π, θ, Σ, X, and Y are dimensionless pressure, time, form of crater function, and coordinates, and P_o, t_o, S_o are appropriate scale factors. The Heaviside step function in this case transforms into $\vartheta_\tau \equiv \vartheta(\theta_\tau - \theta)$, where $\theta_\tau \equiv \tau/t_0$.

As a result, the reduction of (34.10) and (34.11) to dimensionless form, taking into account that three of the four coefficients with degrees Π of Eq. (34.11), can

be set equal to units at the expense of three uncertain parameters t_o, P_o, a, and the only coefficient for degree Π of Eq. (34.10) can also be placed equal to an uncertain parameter S_o; we have a system of bounded differential equations in partial derivatives in dimensionless form, which can be conventionally called the crater dynamics equation:

$$\Sigma_\theta = \Pi^\beta \sqrt{1 + {\Sigma_X}^2 + {\Sigma_Y}^2}, \tag{34.13}$$

and the equation of the dynamics of near-surface pressure:

$$\Pi_\theta = \left(-1 + \Lambda e_q \vartheta_\tau\right) \Pi^{\beta+\eta} - \Pi^{\beta+1} + \frac{1}{\sqrt{1 + {\Sigma_X}^2 + {\Sigma_Y}^2}} e_q \vartheta_\tau \Pi^\eta, \tag{34.14}$$

where $\Pi_\theta \equiv \partial\Pi/\partial\theta$, $\Sigma_\theta \equiv \partial\Sigma/\partial\theta$, $\Sigma_X \equiv \partial\Sigma/\partial X$, and $\Sigma_Y \equiv \partial\Sigma/\partial Y$.

In Eq. (34.14) the parameter e_q determines the ratio of the flow that enters the surface of the matter q_s to the output flow q_o, i.e., in dimensionless units $e_q \equiv q_s/q_o = f(x, y) \exp(-\Lambda M \Pi^{\eta+\beta} \Sigma)$, where the function $f(x, y)$ determines the transverse shape of the stimulus momentum and adds to (34.14) an additional dependence on x, y; Λ is the parameter determining the degree of interaction of the evaporable matter with the incident radiation; and M is the dimensionless parameter determined by equality: $M \equiv \frac{q_o(\kappa-1)^2 L^2}{2{\varphi_o}^{3/2}\kappa^2 \rho_{os}(\kappa+1)^{1/2}}$. It is clear that in the presence of the destruction of the surface formed by the corrosion torch at the matter surface will significantly affect the factor e_q, reducing it ($0 \le e_q \le 1$).

34.3 Investigation of the Asymptotic "Behavior" of the Crater Form Function

Equation (34.14) actually holds in two equations that describe essentially different processes. The first describes the dynamics of pressure during the momentum action on the surface ($\vartheta_\tau = 1$):

$$\Pi_\theta = \left(\Lambda e_q - 1\right) \Pi^{\beta+\eta} - \Pi^{\beta+1} + \frac{1}{N} e_q \Pi^\eta. \tag{34.15}$$

The second monitors the "behavior" of near-surface pressure when the momentum action is stopped ($\vartheta_\tau = 0$):

$$\Pi_\theta = -\Pi^{\beta+\eta} - \Pi^{\beta+1}, \tag{34.16}$$

where $N \equiv \sqrt{1 + {\Sigma_X}^2 + {\Sigma_Y}^2}$. Since Eq. (34.13) contains a function of pressure, it is clear that the formation of the crater should take place in two stages. At the first

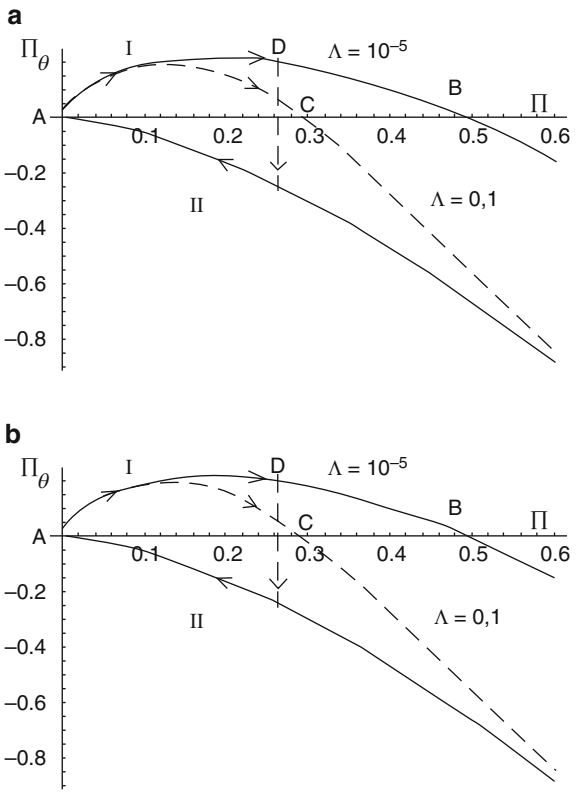

Fig. 34.1 Phase trajectories of the two periods described by Eqs. (34.15) and (34.16): (**a**) curve I corresponds to Eq. (34.15) at $N = 1$, $e_q \sim 1$, and curve II to Eq. (34.16); (**b**) curves for Eq. (34.15) at different e_q and Λ

stage in Eq. (34.13), the function Π will be given by the solution of Eq. (34.15) and on the second by the solution of Eq. (34.16).

To conduct asymptotic estimates of the "behavior" of the crater formation as a function of time, it is convenient to analyze the phase dependence curves Π_θ from Π according to Eqs. (34.15) and (34.16) (Fig. 34.1a). Since e_q and N depend on time θ and the shape of the crater, then in order to investigate the phase curves (trajectories), we consider a situation where the width of the incident beam is much larger than the depth of the crater and the intensity is evenly distributed along its cross-section. This makes it possible to consider $N = 1$, as in Eq. (34.15) and in the crater Eq. (34.13). The value of e_q, as noted earlier, varies with time in the range from 0 to 1. Therefore, in phase analysis, consider some of its principal values. The value $e_q = 0$ means that by absorbing the flow, $q_s = 0$, that is, the outflow does not reach the surface. In this case, the momentum action on this surface stops even when the momentum itself continues to operate. This is confirmed mathematically: Eq. (34.15) automatically takes the form (34.16) (Fig. 34.1b, curve, marked as $e_q = 0$). In view of this we consider for Eq. (34.15) the limiting case $e_q = 1$ (no absorption) and one of the intermediate cases. All the above restrictions in no way apply to Eq. (34.16), because there are no parameters N and e_q in it.

The arrows on Fig. 34.1a designate the direction of the process movement of time pressure development and indicate that the first stage (I) begins with point A, which is unstable for this stage (added derivative Π_θ), so the dependence change Π_θ from Π occurs along curve I to the moment of the momentum ending (indicated by D in the figure), or until the pressure reaches its maximum (Fig. 34.1a – points B or C). These points are stable; as soon as the curve crosses the axis Π, the condition starts to be complied $\Pi_\theta < 0$. This forces the process to return to point B (or C) again. At these points, the gas pressure remains constant until the momentum is reached. As soon as the momentum is over, the transition to curve II occurs, and the process begins to move along the curve until it reaches zero. Figure 34.1a shows a dashed line that conventionally describes the dynamics of the process in the case of large Λ (an increase in this parameter physically means an increase in the interaction of radiation with the plasma-gas torch formed near the surface of matter). As can be seen from Figure 34.1b, with $e_q \cong 1$ there are such values Λ when in the point B, pressure value Π will be larger than unit. Also, for different values Λ at similar e_q (on Fig. 34.1b are two curves that correspond to $e_q \cong 1$) with increase in Λ, the value Π_θ increases in maximum.

As it was noted, for the second stage of the process (Fig. 34.1a), the point is at zero; therefore, for asymptotic evaluation of the formation of a crater after the momentum is complete, it is enough to investigate the behavior Σ for the least power in Eq. (34.16), that is, to consider the equation $\Pi_\theta = -\Pi^{\beta+\eta}$. From here we will obtain:

$$\Pi = ((\beta + \eta - 1) \cdot \theta)^{-\frac{1}{\beta+\eta-1}}. \tag{34.17}$$

The integration constant in the expression for Π is considered as zero, since at the end of the momentum condition, $\Pi \to 0$ is fulfilled. Since we are working in the approximation $N = 1$, then (34.13) is reduced to the form $\Sigma_\theta = \Pi^\beta$. Thus, the asymptotic behavior of the function Σ can be determined from the solution of this equation using dependence (34.17):

$$\Sigma = D + \frac{1}{\eta - 1}((\beta + \eta - 1)\,\theta)^{\frac{\eta-1}{\beta+\eta-1}} = D - \frac{j+2}{2}\left(\frac{j-1}{j+2}\theta\right)^{-\frac{2}{j-1}}. \tag{34.18}$$

In (34.18) it is taken into account that $\beta \equiv (\kappa + 1)/(2\kappa)$ and $\eta \equiv 1/\kappa$, as $\kappa = (j+2)/j$. Parameter j is the number of degrees of freedom of atoms or molecules in the gas. For monatomic gas, $j = 3$; in other cases $j > 3$. Definition of the asymptotic (34.18) through the number of degrees of freedom j clearly demonstrates a strict degree of disengagement θ.

Integration constant D is determined from the equality of values Σ at the moment of momentum ending $\theta_\tau \equiv \tau/t_0$. Value Σ is represent in (34.18) for such moment. In particular for monatomic gas, when $j = 3$, constant D will be the following: $D = {\Pi_c}^\beta \theta_\tau + \frac{25}{4\theta_\tau}$. And the solution (34.18) takes on a specific form: $(\theta \geq \theta_\tau)$. Analyzing this expression we see that when $\theta = \theta_\tau$, the depth of the crater is defined,

as it should be, by equality (34.20): and at $\theta \to \infty$ the depth of the crater increases and asymptotically approaches the value: $\Sigma = {\Pi_c}^{\beta}\theta_\tau + \frac{25}{4\theta_\tau}$.

For intervals of time that do not exceed the length of the stimulus momentum (Eq. (34.15)), the "behavior" of the formation of a crater at the initial moment is also determined by the lowest degree, $\Pi_\theta = \Pi^\eta$, which dominates throughout this interval, at least until the phase trajectory is at point B (Fig. 34.1a). Thus, the asymptotic "behavior" of the crater formation at the beginning of the destructive process will be determined by the power law:

$$\Sigma = \frac{2\theta}{4+j} \cdot \left(\frac{2\theta}{2+j}\right)^{1+\frac{j}{2}}, \tag{34.19}$$

where the integration constant is zero, since the initial condition must determine the form Σ by the time the nano-crater began to be formed.

A special study requires the case when the pressure acquires its maximum value (points B, C in Fig. 34.1). At these points, the value of the derivative $\Pi_\theta = 0$, which corresponds to a fixed time pressure Π_c. Then the equation for the shape of the crater will have the form: $\Sigma_\theta = {\Pi_c}^{\beta}$. As can be seen, the formation rate of the crater will be constant, and the function of the crater form will be described by a linear dependence: $\Sigma = {\Pi_c}^{\beta}\theta$. This means that the increase of Σ in time slows down when compared with the dependence (34.19). Particularly at the moment of momentum ending:

$$\Sigma = {\Pi_c}^{\beta}\theta_\tau. \tag{34.20}$$

As can be seen from Fig. 34.1b, with a sufficiently consistent factor e_q consideration, the maximum value of dimensionless pressure, most likely, does not exceed the unit. But it is impossible to exclude the possibility of realizing the situation when Π will be more 1. This situation is shown in Fig. 34.1b (the very upper curve). In this case, the dynamics of the formation of the crater varies, since at values $\Pi > 1$ in (34.15) dominates the term with the highest degree, and the pressure equation has the form: $\Pi_\theta = -\Pi^{\beta+1}$. The corresponding asymptotic dependence of Σ from time is logarithmic:

$$\Sigma = \frac{(2+j)}{1+j} \ln(\theta/\theta_0). \tag{34.21}$$

That is, it slows even more. Here θ_0 represents the moment of time when pressure Π begins to exceed 1. Dependences (34.19) and (34.21) are shown in Fig. 34.2. Figure 34.2a shows the asymptotic behavior of $\Sigma(\theta)$, according to Eq. (34.19), which indicates the explosive nature of the formation of a crater, and Fig. 34.2b illustrates the dynamics described by Eq. (34.21) and has a slower tendency to increase the crater. It can be seen that with increasing degrees of freedom j, the value Σ reacts more slowly to the external laser effect. According to the figure (Fig. 34.2a) it can be confirmed that at the beginning of the formation of the crater the

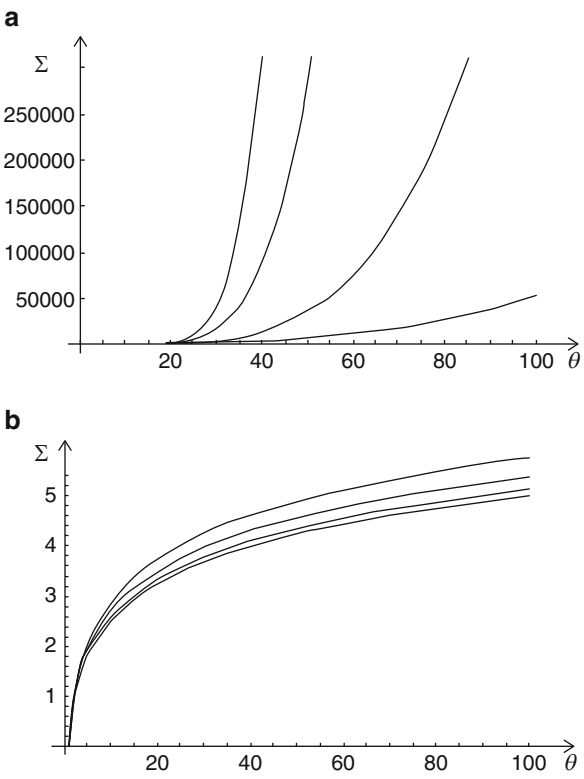

Fig. 34.2 Asymptotic behavior of the formation of a crater under the influence of a laser power momentum according to equation (34.19) (**a**) and according to equation (34.21) (**b**)

process has an explosive, power-law character. When value of pressure reaches the maximum possible value (point B in Fig. 34.1a) crater's formation slows down. At this stage crater is formed by the linear law (Fig. 34.2b).

Upon completion of the momentum action, the crater formation is rapidly stopped, and when the situation is implemented under $\Lambda > 1$, the explosive (Fig. 34.2a) process is gradually transformed into logarithmic and only then becomes linear.

34.4 Conclusions

The dynamics of the formation of a corrosion crater on the surface of material under destructive treatment is considered. This dynamics is determined by the condition (34.1), which reduces to the differential Eq. (34.10), or its dimensionless form (34.13), and is the main subject of research. Since Eq. (34.13) depends on the pressure, the equation is analyzed together with (34.14).

The phase diagrams (Fig. 34.1) for this equation are analyzed. It is shown that the dynamics of crater formation is significantly influenced by parameters Λ and e_q, which determine the interaction of incident radiation with a plasma gas torch. This is expressed in the fact that with decreasing pressure due to interaction, the rate of crater formation also decreases. Since the parameter Λ increases in time, then there is a probability that the formation of a crater for a long-term momentum will stop even before the end of this momentum.

Asymptotic estimations of dynamics of crater development are carried out. It is shown that the function of the shape of the crater surface Σ is stabilized in time after the momentum action ends at arbitrary values of the polytropic index. This indicates the internal consistency of the model.

References

1. Wu Z, Zhang N, Zhu X, An L, Wang G, Tan M (2018) Time-resolved shadowgraphs and morphology analyses of aluminum ablation with multiple femtosecond laser pulses. Chinese Physics B 27(7):077901. http://iopscience.iop.org/article/10.1088/1674-1056/27/7/077901/meta
2. Mann T, Mathieson R, Murray M, Richards B, Jose G (2018) Femtosecond laser ablation properties of Er3+ ion doped zinc-sodium tellurite glass. J Appl Phys 124(4):044903. https://aip.scitation.org/doi/abs/10.1063/1.5040947
3. Shugaev MV, Gnilitskyi I, Bulgakova NM, Zhigilei LV (2017) Mechanism of single-pulse ablative generation of laser-induced periodic surface structures. Phys Rev B 96(20):205429. https://journals.aps.org/prb/abstract/10.1103/PhysRevB.96.205429
4. Pasquier C, Sentis M, Utéza O, Sanner N (2016) Predictable surface ablation of dielectrics with few-cycle laser pulse even beyond air ionization. Appl Phys Lett 109(5):051102. https://aip.scitation.org/doi/abs/10.1063/1.4960152
5. Zhang N, Yang J, Zhu X (2012) Investigation of the ultrafast process of femtosecond laser ablation of highly oriented pyrolytic graphite. Chin J Lasers 39(5):0503002. http://en.cnki.com.cn/Article_en/CJFDTOTAL-JJZZ201205018.htm
6. Suprun AD, Shmeleva LV, Razumova MA (2011) The influence of bulk absorption of substance on the threshold of destruction by the intensive pulse of electromagnetic radiation. Funct Mater 18(2):237–243. http://functmaterials.org.ua/contents/18-2/
7. Nayak BK, Iyengar VV, Gupta MC (2011) Efficient light trapping in silicon solar cells by ultrafast-laser-induced self-assembled micro/nano structures. Prog Photovolt Res Appl 19(6):631–639. https://onlinelibrary.wiley.com/doi/abs/10.1002/pip.1067
8. Byskov-Nielsen J, Savolainen JM, Christensen MS, Balling P (2010) Ultra-short pulse laser ablation of metals: threshold fluence, incubation coefficient and ablation rates. Appl Phys A Mater Sci Process 101(1):97–101. https://link.springer.com/article/10.1007/s00339-010-5766-1
9. Lamela J, Lifante G, Han TPJ, Jaque F, Garcia-Navarro A, Olivares J, Agulló-López F (2009) Morphology of ablation craters generated by fs laser pulses in LiNbO3. Appl Surf Sci 255(7):3918–3922. https://www.sciencedirect.com/science/article/pii/S0169433208019144
10. Corkum PB, Dupont E, Liu HC, Zhu X (2005) Method and apparatus for repair of defects in materials with short laser pulses. U.S. Patent No. 6878900, 12 Apr 2005. https://patents.google.com/patent/US6878900B2/en
11. Itina TE, Vidal F, Delaporte P, Sentis M (2004) Numerical study of ultra-short laser ablation of metals and of laser plume dynamics. Appl Phys A Mater Sci Process Issue 79(4–6):1089–1092. https://link.springer.com/article/10.1007/s00339-004-2647-5

12. Bykov NY, Bulgakova NM, Bulgakov AV, Loukianov GA (2004) Pulsed laser ablation of metals in vacuum: DSMC study versus experiment. Appl Phys A Mater Sci Process Issue 79(4–6):1097–1100. https://link.springer.com/article/10.1007/s00339-004-2654-6
13. Hulin D (2000) La matière condensée. Sciences aux temps ultracourts (de l'attoseconde aux petawatts), rapport sur la science et la technologie $n^0$9. l'Académie des Sciences. Septembre 2000, Londres-Paris-New York, pp 197–222
14. Zhu X, Naumov AY, Villeneuve DM, Corkum PB (1999) Influence of laser parameters and material properties on micro drilling with femtosecond laser pulses. Appl Phys A Mater Sci Process 69:367–371. https://link.springer.com/article/10.1007/s003390051418
15. Lenzner M (1999) Femtosecond laser-induced damage of dielectrics. Int J Mod Phys B 13(13):1559–1578. https://www.worldscientific.com/doi/abs/10.1142/S0217979299001570
16. Alekseev BV (1982) Mathematical kinetics of reacting gases. Nauka, Moscow. 419 p. (in Russian). https://scholar.google.com.ua/scholar?hl=ru&as_sdt=0%2C5&q=Alekseev+B.+V.+Mathematical+Kinetics+of+Reacting+Gases.+Nauka%2C+Moscow%2C+1982&btnG
17. Landau LD, Lifshits EM (1986) Theoretical physics, vol VI, Hydrodynamics. Science. 736 p. (in Russian). https://scholar.google.com.ua/scholar?hl=ru&as_sdt=0%2C5&q=Landau+L.+D.%2C+Lifshits+E.+M.+Theoretical+Physics%2C+V.+VI%2C+Hydrodynamics.+Science.+1986&btnG
18. Shmeleva LV, Yezhov SM, Suprun AD, Shevchenko SY (2006) Theory of plasma dynamics in the case of solid matter surface destruction by pulses of power radiation. Ukrayins'kij Fyizichnij Zhurnal (Kyiv) 51(8):788–794. http://archive.ujp.bitp.kiev.ua/index.php?item=j&id=84
19. Korn GA, Korn TM (2000) Mathematical handbook for scientists and engineers: definitions, theorems, and formulas for reference and review. Courier Corporation, New York. 1097 p. https://books.google.com.ua/books?hl=ru&lr=&id=xUQc0RZhQnAC&oi=fnd&pg=PP1&dq=Korn&ots=QDWUbJ9xI6&sig=N__AgdlGQ-soUjn6QfDIjM_7bE8&redir_esc=y#v=onepage&q=Korn&f=false
20. Fedorchenko AM (1992) Teoretychna fizyka [Theoretical physics], vol 1. Kyiv, Vyshcha shkola, 535 p. (in Ukrainian) https://scholar.google.com.ua/scholar?hl=ru&as_sdt=0%2C5&q=Fedorchenko+A.+M.+%22Teoretychna+fizyka%22+Theoretical+physics%5D.+Kyiv%2C+Vyshcha+shkola+1+%281992%29%3A+535&btnG

Chapter 35
Ballistic Transmission of the Dirac Quasielectrons Through the Barrier in the 3D Topological Insulators

A. M. Korol, N. V. Medvid', A. I. Sokolenko, and I. V. Sokolenko

35.1 Introduction

Topological insulators belong to the new class of substances that have recently been called Dirac materials ([1] and references therein). These include very different objects in their structure, in particular the low- and high-temperature d-wave superconductors, superfluid phases 3He, graphene, and two- and three-dimensional insulators [1].

The key concept that unites these different objects is a linear dispersion relation that describes the low-energy excitations of quasiparticles. Due to the fact that the Dirac materials have a number of nontrivial, interesting properties, they—and topological insulators (TI) among them—are actively studied in the last time [2–10]. The most important characteristic of TI is that they are insulators in their volume, but are capable of conducting the electric current on their surface. These surface states can contribute to charge transport at low energies. Under low energies, the surface states of TI are described by a massless Dirac equation in one or two dimensions, analogous to the equation for quasielectrons in graphene. The dispersion relation for the Dirac particles relates to a cone in the three-dimensional case. Some properties of surface states of TI are expressed in terms of topologically invariant quantities and, importantly, are protected from the influence of perturbations due to the symmetry of inversion of time in the corresponding Hamiltonian. Time reversal invariant perturbations such as lattice imperfections or nonmagnetic moderate

A. M. Korol (✉)
Laboratory on Quantum Theory in Linkoping, ISIR, Linkoping, Sweden

N. V. Medvid' · A. I. Sokolenko · I. V. Sokolenko
National University for Food Technologies, Kyiv, Ukraine

O. Fesenko, L. Yatsenko (eds.), *Nanocomposites, Nanostructures, and Their Applications*, Springer Proceedings in Physics 221,
https://doi.org/10.1007/978-3-030-17759-1_35

disorder do not produce a gap; at the same time, the external magnetic field can produce a gap for the surface states.

Quasielectrons in TI exhibit strong spin-orbital interaction. Due to this and due to the time-reversal symmetry, the surface states of TIs have an odd number of Dirac cones and expose the chiral spin nature (as observed by the angle-resolved photo emission-spectroscopy). Directions of the linear and the spin-angular quasi-momenta of quasielectrons on the surface of TI are interconnected and perpendicular to each other. Also, we should keep in mind that the surface Hamiltonian of the 3D TI deals with the real spin (in contrast with the graphene where the respective Hamiltonian comprises the pseudospin term).

There are two classes of topological insulators: two-dimensional (2D) and three-dimensional (3D) TI. The first ones are also called quantum spin Hall dielectrics, and they can be realized in quantum wells of HgCdTe compounds. Three-dimensional TIs are represented by bismuth compounds Bi_2Se_3, Bi_2Te_3, and similar materials. There are also strong and weak 3D TIs. Surface states in 2D and 3D TIs are one-dimensional and two-dimensional, respectively.

It is known that the Dirac excitations in TI exhibit the Klein tunneling (as in graphene) for the normal incidence of the quasielectrons on the barrier.

It is convenient to control the behavior of fermions in Dirac materials by means of external electric and magnetic fields, and a lot of publications are devoted to the corresponding problem for this reason. At the same time, since the Fermi velocity fully characterizes the Dirac cone slopes, i.e., the linear dispersion relation, it is essential for applications. Therefore, recently one more way for controlling the electronic properties of the Dirac materials, namely, by means of the spatial change of the Fermi velocity (in particular with the help of doping) was offered (e.g., [14]). A lot of propositions to use this control in practice were also published [10–18]. The 2D and 3D TI may be useful in practice in particular in quantum computation and spintronics.

Motivated by the abovementioned statements, we analyze here the transmission of the Dirac quasiparticles through the electrostatic and velocity barriers in the 3D topological insulators.

35.2 Model and Formulae

Let us consider the motion of quasielectrons through the surface states of a topological insulator, and we believe that there is a one-dimensional barrier, located along the axis of 0_x.

A Dirac equation describing a behavior of the massless fermions in the case when the Fermi velocity depends on the position of quasielectrons in space can be written in the form

$$\left\{\sqrt{v\left(\overrightarrow{r}\right)}\,\overrightarrow{\sigma}\left(-i\hbar\nabla\right)+\sigma_0 U\left(\overrightarrow{r}\right)\right\}\sqrt{v\left(\overrightarrow{r}\right)}\psi\left(\overrightarrow{r}\right)=E\psi\left(\overrightarrow{r}\right) \tag{35.1}$$

In this equation, $v\left(\overrightarrow{r}\right)$is the Fermi velocity, which depends on the spatial coordinate $\overrightarrow{r}$, $\overrightarrow{\sigma} = \left(\sigma_x, \sigma_y\right)$ the two-dimensional Pauli matrices associated with the real spin of the electron, and σ_0 is a unitary two-dimensional matrix, and we take into account the presence of the electrostatic field through the scalar potential U. Introducing the auxiliary spinor $E\psi\left(\overrightarrow{r}\right) = \sqrt{v\left(\overrightarrow{r}\right)}\,\varphi\left(\overrightarrow{r}\right)$, the Eq. (35.1) can be expressed as

$$\left\{v\left(\overrightarrow{r}\right)\ \overrightarrow{\sigma}\ (-i\hbar\nabla) + \sigma_0 U\left(\overrightarrow{r}\right)\right\}\phi\left(\overrightarrow{r}\right) = E\phi\left(\overrightarrow{r}\right) \tag{35.2}$$

Then the corresponding effective Hamiltonian for the given problem reads

$$H = \alpha\begin{pmatrix} U & k_y + ik_x \\ k_y - ik_x & U \end{pmatrix} \tag{35.3}$$

where $\alpha = \frac{v_b}{v_0}$ is the ratio of velocities in the barrier (v_b) and in the out-of-barrier (v_0) regions and further we shall assume that $v_0 = 1$; we will also use units of measurement in which $e = \hbar = 1$.

Assuming that the Fermi velocity only depends on the coordinate x, that is, $v\left(\overrightarrow{r}\right) = v(x)$, for boundary conditions it can be obtained from the equation of continuity of the current density (e.g [15]):

$$\sqrt{v_0}\ \psi\left(x_{b0}^{-}\right) = \sqrt{v_b}\ \psi\left(x_{b0}^{+}\right) \tag{35.4}$$

where the indexes b and 0 relate to the barrier and out-of-barrier areas, respectively, and x_{b0} is the coordinate of the interface. If the electron wave moves along the axis 0_x from the left to the right, then for wave functions in the left and the right out-of-barrier regions, it is possible to write, respectively:

$$\psi_e\ (x) = \frac{1}{\sqrt{2}}\begin{pmatrix} 1 \\ f^- \end{pmatrix} e^{ik_x x} + \frac{r}{\sqrt{2}}\begin{pmatrix} 1 \\ f^+ \end{pmatrix} e^{-ik_x x}$$

$$\psi_r\ (x) = \frac{1}{\sqrt{2}}\begin{pmatrix} 1 \\ f^- \end{pmatrix} e^{ik_x x} \tag{35.5}$$

where $f^{\mp} \equiv \frac{\mp k_x + k_y}{E}$; for the barrier area we have

$$\psi_b\ (x) = \frac{a}{\sqrt{2}}\begin{pmatrix} 1 \\ g^+ \end{pmatrix} e^{iq_x x} + \frac{b}{\sqrt{2}}\begin{pmatrix} 1 \\ g^- \end{pmatrix} e^{-iq_x x} \tag{35.6}$$

where $g^{\mp} = \frac{\mp i q_x + k_y}{(E-U)\alpha^{-1}}$;

$$k_x = \sqrt{E^2 - k_y^2}; \quad q_x = \sqrt{\frac{(E-U)^2}{\alpha^2} - k_y^2}; \tag{35.7}$$

$$k_x = E\cos\theta, k_y = E\sin\theta, \quad \varphi = \operatorname{atan}\left(k_y/q_x\right),$$

where θ and φ are the angle of incidence and the refractive angle, respectively. Using the boundary conditions, we find coefficients in expressions for wave functions and hence the transmission coefficient T.

35.3 Results and Discussion

From the above formulas, it is clear that the difference in the values of the Fermi velocity in the barrier and the out-of-barrier regions has a definite influence on the transmission spectra of the structure under consideration. The question is how essential this impact can be.

Consider the case of the presence of the combined Fermi velocity barriers and electrostatic barriers. Figure 35.1 depicts the dependence of the transmission coefficient T on an angle of the quasielectron incidence on the structure θ for their fixed energy $E = 1.5$ for several values of $\alpha = \frac{v_b}{v_0}$, namely, curves 1–4 correspond to values of $\alpha = 0{,}5; 1; 2; 5$, and other parameters are $U = 3$, $D = 3$, D being the widht of the barrier. It is seen that the change in the Fermi velocity in the barrier region has a strong influence on the transmission spectra. The nontrivial feature of the given spectra is the manifestation of the phenomenon of supertunneling, which consists in the fact that for electron energy value equal to half the height of the potential barrier $E = U/2$, the transmission through the barrier region is perfect for any angle of incidence – see line 3 in Fig. 35.1.

We emphasize that for Fermi velocity values in a barrier other than $v_0(\alpha \neq 1)$,the phenomenon of supertunneling also occurs, but for energies other than $E = U/2$. As shown below, for the case $\alpha \neq 1$, there are certain energies for which the transmission is ideal for any angle of incidence.

Figure 35.1 shows also that in the considered structure, in addition to the effect of supertunneling, a phenomenon similar to the Klein tunneling is observed: the barrier transparency is ideal for particles that fall to the barrier normally. Klein tunneling takes place for any values of α, that is, the Fermi velocity barriers are perfectly transparent in the case of normal incidence of particles for any height of the velocity barriers and of the electrostatic barriers.

The value of the transmission rates T for a fixed angle of incidence θ is an oscillating value, depending on the value of α. The region of the angles of incidence

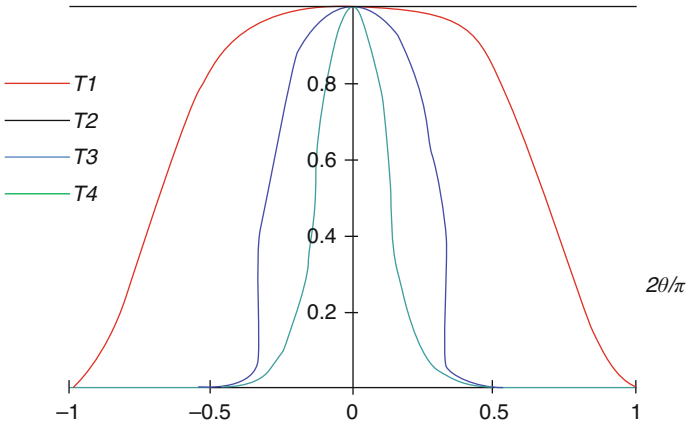

Fig. 35.1 The parameters are $E = 1, 5$, $U = 3$, $D = 3$, $\alpha = 0, 5; 1; 2; 5$, respectively, for the curves *T1*, *T2*, *T3*, *T4*

θ for which $T(\theta)$ is high can be broad; see curve $T1$ in Fig. 35.1 for which $\alpha = 0.5$. Although the general trend is such that, with increasing an angle of incidence the coefficient T decreases on average, but for certain values of α, the value of T can be significant even for large angles of incidence.

Figure 35.2 shows the dependence $T(\theta)$ for the energy close to the electrostatic barrier height for three different values of α: $\alpha_1 = 5$; $\alpha_2 = 1$; $\alpha_3 = 0.5$ for curves 1, 2, and 3, respectively. It is seen that the number of resonance peaks increases with decreasing α (for the case, $T \ll U$, the dependence $T(\theta)$ is described by a smooth line throughout the range of values of angles $-\frac{\pi}{2} < \theta < \frac{\pi}{2}$ (see Fig. 35.1)). For $\alpha > 1$, there is only a narrow range of values of angles θ – in the vicinity of $\theta = 0$ – in which $T(\theta) \neq 0$ and can reach large values. This is explained by the fact that for energies $E \sim U$ for most angles θ the quasi-momentum q becomes imaginary and the electron wave becomes evanescent (see formulae (35.7)). The spectra for the case of large energies (in comparison with the height of the barrier) are characterized by the presence of many resonance peaks which corresponds to the condition for the formation of the resonance states of the Fabry–Perot type:

$$d\sqrt{\frac{(E-U)^2}{\alpha^2} - k_y^2} = n\pi. \tag{35.8}$$

It is obvious from this condition that more resonances are formed at higher energies. The studied transmission spectra are characterized by the presence of a critical angle of the quasiparticles incidence on the structure θ_c. For angles of incidence θ greater than θ_c, the quasiparticles cannot penetrate through the barrier

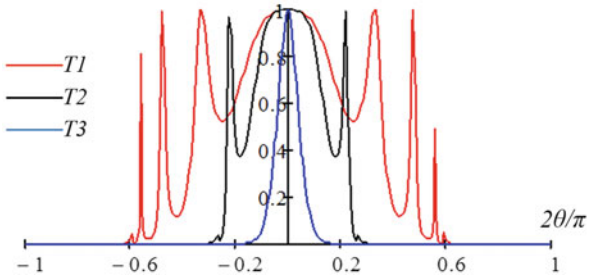

Fig. 35.2 Parameters are as follows: $E = 5$, $U = 3$, $D = 3$, $\alpha = 0.5$; 1; 5, respectively, for the curves *T1*, *T2*, *T3*

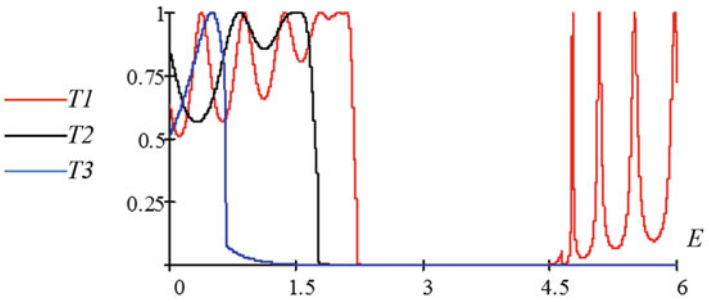

Fig. 35.3 The parameters are $\theta = \pi/4$, $U = 3$, $D = 3$, $\alpha = 0.5$; 1; and 5, respectively, for the curves *T1*, *T2*, *T3*

(see, in particular, spectra 1 and 2 in Figs. 35.1 and 35.2). The value of the critical angle can be found from the Snell law, and it is equal to

$$\varphi_c = \pm \arcsin\left(\frac{|\,E - U\,|}{\alpha E}\right) \tag{35.9}$$

Depending on the particle energy E and on the height of the potential barrier height U, the critical angle may be formed for both cases of $\alpha > 1$ and $\alpha < 1$. The values of $\alpha > 1$ are associated with the barriers for electrons, and in this case, the range of values of E and U for which there is a critical angle is rather broad – unlike for the case $\alpha < 1$ (which is associated with the quantum wells).

The range of angles of incidence θ for which the value of $T(\theta)$ is significant as well as the values of the critical angle θ_c are significantly reduced with increasing α. Figure 35.3 shows the dependence of the coefficient T on energy E for a fixed angle of incidence $\theta = \frac{\pi}{4}$ and values of α_i: $\alpha_1 = 0.5$, $\alpha_2 = 1$, $\alpha_3 = 5$ for the curves 1, 2, and 3, respectively, and in others, the parameters are $U = 3$ and $D = 3$.

It is clearly seen that there exist resonant values of energy E_r for which the transparency of the structure is perfect, that is, $T(E_r) = 1$. For each value α, there

is such an energy for which the phenomenon of supertunneling is realized; we can deduce the expression for this energy from the above formulae and it reads:

$$E_s = \frac{U}{1+\alpha} \tag{35.10}$$

Consequently, the energy position associated with the phenomenon of supertunneling depends essentially on the ratio of the Fermi velocities in the barrier and in the out-of-barrier regions. The value of E_s decreases with increasing α regardless of whether we are dealing with the barriers ($\alpha > 1$) or with the quantum wells ($\alpha < 1$).

Now we can state that the spectra $T(E)$ in general have the following structure:

1. The presence of peaks in the dependence of $T(E)$ (and also on the dependence of $T(\theta)$ indicates that the transmission of quasielectrons in the structure considered has a resonant-tunneling character.
2. For energy, $E_s = \frac{U}{1+\alpha}$, the transmission coefficient $T = 1$ for all θ (the effect of supertunneling).
3. There is a plateau of energies with values of T~1 in the vicinity of the point E_s.
4. There is a wide gap in the vicinity of energy E~U. Its width sharply depends on an angle of incidence θ increasing with increasing θ; this is illustrated by Fig. 35.4, which shows the dependence $T(E)$ for three different values of θ: $\theta_1 = \theta_2 = \theta_3$, the other parameters are the same.
5. There are Fabry–Perot-like resonances with values $T = 1$ in the regions distant from the point E_s under the condition $E < U, E_s$. If conditions for the formation of a critical angle are not fulfilled, similar resonances exist for energies $E > U, E_s$. The Fabry–Perot-type resonances are placed on the axis of energy periodically.
6. If there is a critical angle then T decreases sharply with E increasing. The steepness of the function $T(E)$ depends on the parameters of the problem. The critical energy E_c corresponds to the critical angle θ_c: for the electrons with energy $E > E_c$ the barrier is insurmountable. According to formula (35.9), the critical energy is equal to

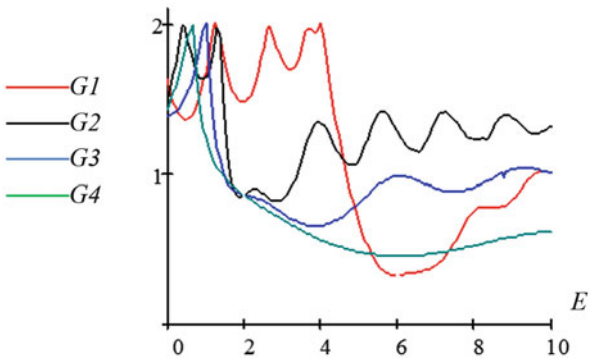

Fig. 35.4 The parameters for the curves are $D = 1$ for all; $U = 6$; $\alpha = 0.5$ for $G1$, $U = 2$ for all other curves, $\alpha = 0.5$ for $G2$, $\alpha = 1$ for $G3$, and $\alpha = 2$ for $G4$, respectively

$$E_c = \frac{U}{\mid \alpha \sin \theta_c - 1 \mid} \tag{35.11}$$

and hence the critical energy exists only for values of $\alpha > 1$, that is, only for the barriers (and not for the wells).

In Fig. 35.4, the dimensionless conductivity G (the quantity that can be measured experimentally) is presented as the function of energy E. It takes into account the combined Fermi velocity barriers and the electrostatic barriers. The values of the parameters for this figure are as follows: $D = 1$ for all curves; $U = 6$; $\alpha = 0.5$ for $G1$, $U = 2$ for all other curves, $\alpha = 0.5$ for $G2$, $\alpha = 1$ for $G3$, $\alpha = 2$ for $G4$, respectively.

First of all, it is noteworthy that the function $G(E)$ has an oscillating character which corresponds to the dependences of the transmission coefficient T on energy E. At the points $E_s = \frac{U}{1+\alpha}$, the maximum values of conductivity due to the effect of supertunneling are realized and the given condition of maxima is performed precisely. In the energy region E~U, there is a fairly wide range of energies in which the function $G(E)$ has a minimal value – this region is associated with the gap in the $T(E)$ dependencies. Its width increases markedly with an increase of α (compare the curves 1, 2, and 3). On average, the growth of α leads to a decrease in conductivity.

At energies somewhat smaller and larger than those corresponding to the minimum $G(E)$, oscillations of conductivity are observed. In the region of smaller energies, the value of $G(E)$ reaches a maximum, and in the right side of the spectra, the value of G is much smaller. These oscillations are related to Fabry–Perot resonances in the dependences $T(E)$. The difference in the regions of smaller and larger energies is explained in this way. In the region of energies, $E < 0,5U$, the half-widths of the resonances are substantially larger than in the region $E \gg 0,5U$ (see Fig. 35.3), and in addition resonances are placed denser on the axis of energies.

35.4 Conclusion

The object of our investigation is a 3D topological insulator the surface states of which are described by the Dirac-like equation. We use the continuum model and the transfer matrix method for our evaluations. The transmission spectra, i.e., the dependencies of the transmission rates on the quasiparticle energy and on the angle of incidence through the Fermi velocity barriers and the electrostatic barrier, are calculated. It is shown that these spectra display the resonant tunneling character. The dependence of spectra on the magnitude of the electrostatic potentials, as well as on the values of the Fermi velocity in the barrier and in the out-of-barrier regions, is studied.

The most characteristic and interesting property of the investigated structures is the manifestation in them of a phenomenon known as the supertunneling: for some energy values, its quantum transparency is perfect for all angles of incidence of quasiparticles on the barrier. For the case of tunneling through the combined

electrostatic and the Fermi velocity barriers, supertunneling takes place for energies not equal to half the electrostatic barrier (as in the case of the absence of the velocity barriers), these values being dependent on the Fermi velocity barrier magnitude. An analytical formula for this dependence is deduced. An important feature is also the presence in the transmission spectra of the critical angle of incidence of quasiparticles on the barriers. In a wide range of parameter values, barriers become opaque for particles that fall on them at an angle that exceeds a critical angle. This feature allows you to use the investigated structures, in particular, as wavevector filters. The conductivity of the structure considered exhibits the features associated with the *T(E)* dependences. The results of our work can be applied for controlling the transmission spectra of the 3D topological insulators.

References

1. Wehling TO, Black-Schaffer AM, Balatsky AV (2014) Dirac materials. Adv Phys 63:1
2. Tanaka Y, Yokohama T, Nagaosa N (2009) Manipulation of the Majorana fermion, Andreev reflection, and Josephson current on topological insulators. Phys Rev 103:107002
3. Fu L (2009) Hexagonal warping effects in the surface states of the topological insulator Bi_2Te_3. Phys RevLett 103:266801
4. Takahashi R, Murakami S (2011) Gapless interface states between topological insulators with opposite Dirac velocities. Phys Rev 107:166805
5. Iurov A, Gumbs G, Roslyak O, Huang D (2012) Anomalous photon-assisted tunneling in graphene. J Phys Condens Matter 24:015303
6. Iurov A, Gumbs G, Roslyak O, Huang D (2013) Photon dressed electronic states in topological insulators: tunneling and conductance. J Phys Condens Matter 25:135502
7. Alos-Palop M, Rakesh P, Blaauboer M (2013) Suppression of conductance in a topological insulator nanostep junction. Phys Rev 87:035432
8. Li H, Shao J, Zhang H, Dao-Xin Y, Yang G (2013) Resonant tunneling in a topological insulator superlattice. J Appl Phys 114:093703
9. Takagaki Y (2016) J Phys Condens Matter 28:025302
10. Zheng YJ, Song JT, Li YX (2016) Topological charge pump by surface acoustic waves. Chin Phys B 25:037301
11. Liu L, Li Y-X, Liu J (2012) Transport properties of Dirac electrons in graphene based double velocity-barrier structures in electric and magnetic fields. Phys Letters A 376:3342
12. Wang Y, Liu Y, Wang B (2013) Strain-tunable Josephson current in graphene-superconductor junction. Phys E 53:186
13. Sun L, Fang C, Liang T (2013) Novel transport properties in monolayer graphene with velocity modulation. Chin Phys Lett 30(4):047201
14. Raoux A, Polini M, Asgari R, Hamilton AR, Fasio R, MacDonald AH (2010) Velocity modulation control of electron-wave propagation in graphene. Phys Rev B 81:073407
15. Concha A, Tešanović Z (2010) Effect of a velocity barrier on the ballistic transport of Dirac fermions. Phys Rev B 82:033413
16. Yuan JH, Zhang JJ, Zeng QJ, Zhang JP, Cheng Z (2011) Tunneling of Dirac fermions in graphene through a velocity barrier with modulated by magnetic fields. Physica B 406:4214
17. Krstajic PM, Vasilopoulos P (2011) Ballistic transport through graphene nanostructures of velocity and potential barriers. J Phys Condens Matter 23:135302
18. Korol AM, Sokolenko AI, Sokolenko IV (2018) The energy spectra of the graphene-based quasi-periodic superlattice. Low Temp Phys 44(8):803

Chapter 36
The Perspective Synthesis Methods and Research of Nickel Ferrites

Iryna Ivanenko, Serhii Lesik, Ihor Astrelin, and Yurii Fedenko

36.1 Introduction

Magnetic nanopowders of spinel nickel ferrites are some of the most important materials of the present, which were first synthesized about 50 years ago. During the last decade, they have attracted great interest among scientists around the world due to their useful electromagnetic characteristics for a huge number of technological applications such as information storage systems, radio frequency coils, transformers, magnetic field in magnetic resonance, sensors, and radio wave absorbing materials. The development of electronic industry requires more compact kernels to operate at higher frequencies. This problem is solved by synthesis of nanoparticles of nickel ferrites.

In the conditions of intensive development of science, nanostructured nickel ferrite, due to the presence of active centers of nickel in its structure, is studied for medical purposes and catalysis. Thus, it is very important to find a simple and cost-effective method for the synthesis of nanoparticles of ferrites with predefined properties.

Actual scientific and practical problem is the receipt of nickel ferrites with high electromagnetic and chemical properties, under the condition of low cost.

Therefore, in order to solve this important task, it is necessary to comprehensively examine the relationship between the conditions of synthesis, the structure and the physical and chemical properties of ferrites, and composites on their basis.

I. Ivanenko (✉) · S. Lesik · I. Astrelin · Y. Fedenko
Department of Inorganic Substances Technology, Water Treatment and General Chemical Engineering of National Technical University of Ukraine "Igor Sikorsky Kyiv Polytechnic Institute", Kyiv, Ukraine

O. Fesenko, L. Yatsenko (eds.), *Nanocomposites, Nanostructures, and Their Applications*, Springer Proceedings in Physics 221,
https://doi.org/10.1007/978-3-030-17759-1_36

36.2 Imaginations About Ferrites

Spinel ferrites are important magnetic materials today due to their magnetic and electrical properties, with high chemical and thermal resistance. These materials are technologically important and have been used in many industries, such as carriers of information, catalysis, medicine, sensors, pigments, magnetic liquids, and others [1–3].

$NiFe_2O_4$ is widely used in electrical devices due to its high permeability at high frequencies, high electrical conductivity, mechanical strength, and chemical resistance. With all these advantages, it is a relatively cheap material. Their properties depend on the shape and size of the particles.

Different methods of synthesis are used for synthesis of nickel ferrites: co-precipitation [4, 5], sol–gel [6–8], hydrothermal [9, 10], microemulsion [11, 12], mechanic, aerolization [13], microwave combustion [14], etc.

Nickel ferrite is a reverse spinel in which an elementary cell consists of eight atoms of $NiFe_2O_4$ molecules. Half of the ions of the iron occupy the tetrahedral regions (A-sides) and the others – octahedral (B-sides). Therefore, nickel ferrite can be represented as the formula $(Fe^{3+})_A(Ni^{2+}, Fe^{3+})_BO_4$, where A and B are tetrahedral and octahedral regions, respectively [15]. High electrical and magnetic properties of $NiFe_2O_4$ depend on the nature, charges, and distribution of metal ions. However, $NiFe_2O_4$ exhibits ferromagnetism, which derives from the magnetic moment of the antiparallel spins between the Fe^{3+} ions on the A-sections and Ni^{2+} in B-regions [16].

In the general case, the structure of the ferrites is depicted as in Figs. 36.1 and 36.2.

The dielectric and magnetic properties of $NiFe_2O_4$ particles are depicted in Figs. 36.3 and 36.4. The study of these properties (at a temperature interval of 293–513 K) showed high dielectric and magnetic properties; the material is easily and quickly heated under the action of an external magnetic field and the conduction of electric current. It has been found that energy absorption and heat conversion have a stronger effect in a stronger magnetic field. But with increasing magnetic field also energy losses partly increase [18].

Chinese scientists have demonstrated the fact (in the example of three different samples of $NiFe_2O_4$) that there is no direct correlation between the parameters of the grains of nickel ferrite (Table 36.1) and the magnetic properties (Tables 36.2, 36.3, and 36.4 and Figs. 36.5, 36.6, and 36.7), which is explained by the A–B structure of $NiFe_2O_4$. Nickel ferrite retains its high magnetic properties in the form of porous and granular nanoparticles [18].

The particles obtained with the sol–gel method have high phase purity, chemically homogeneous, and flexible to control the morphology of grains. This is the most effective method for obtaining nanoparticles with controlled by shape and size.

To calculate the parameters of $NiFe_2O_4$, there are many equations. Let us look at some of them.

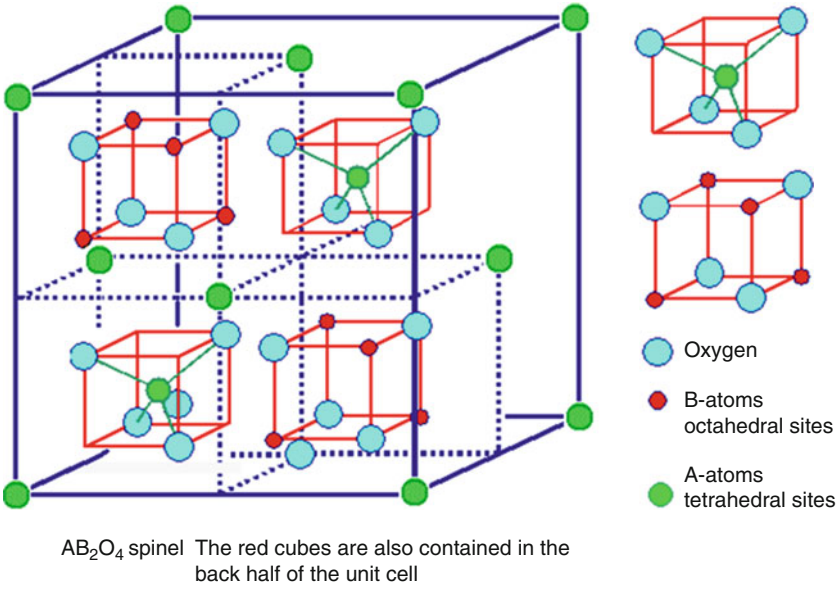

Fig. 36.1 Schematic structure of ferrites [17]

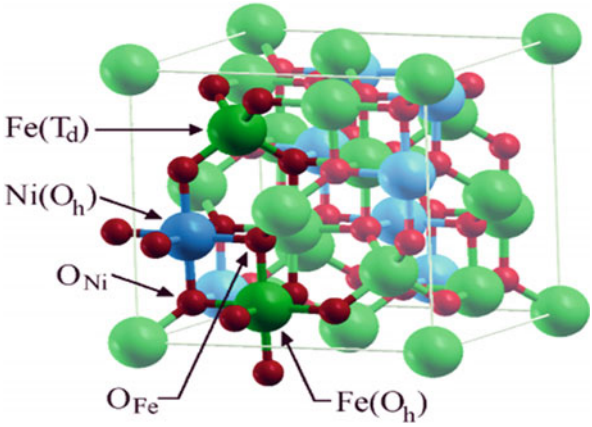

Fig. 36.2 Model of ferrites structure [17]

The average size of the crystal (D, nm) for (311) XDR peak calculates using the Scherer equation [19]:

$$D = \frac{k\lambda}{B \sin\theta}, \tag{36.1}$$

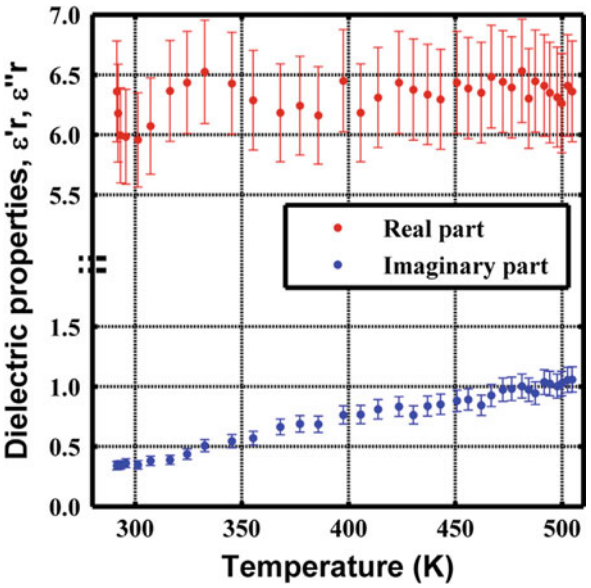

Fig. 36.3 Dielectric properties of $NiFe_2O_4$ [18]

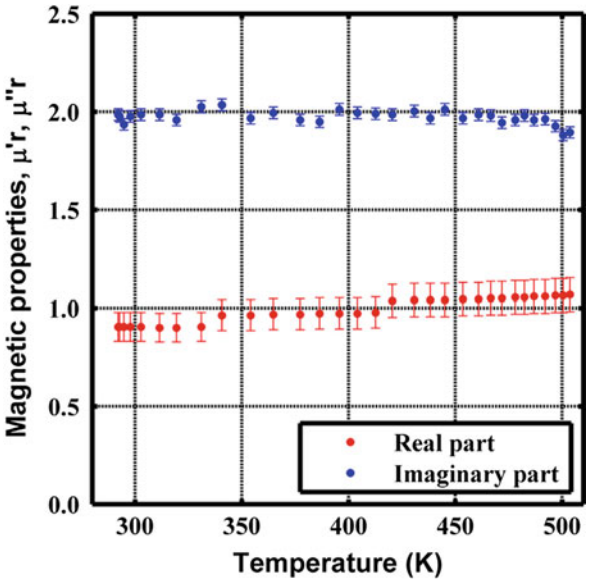

Fig. 36.4 Magnetic properties of $NiFe_2O_4$ [18]

where k is the constant of Scherer (0.89), B full width of half-maximum of diffraction peak, and θ angle of Bragg.

The interplanar space ($d_{(311)}$) calculates by the Bragg equation:

$$d_{(311)} = \frac{\lambda}{2 \sin \theta_{(311)}}. \tag{36.2}$$

Table 36.1 Average size of crystallites (D), interplanar space ($d_{(331)}$), and specific surface area (∂) of $NiFe_2O_4$ [16]

Sample	1#	2#	3#
D, nm	35.1	32.8	30.9
$d_{(311)}$, nm	2.516	2.514	2.510
∂, m^2/g	20.1	55.7	48.6

Table 36.2 The main magnetic properties of different samples of nickel ferrite [16]

Sample	1#	2#	3#
M_s, emu/g	57.4	65.5	66.6
M_r, emu/g	14.4	12.7	15.9
H_c, Oe	241.0	137.7	161.6

Table 36.3 The parameters using at evaluation of critical size of nickel ferrite grains [16]

Parameter	T_c	α	M_s	K_1	ε_p	d_{cr}
Dimension	K	sm	Gs	erg/cm^3	erg/cm^2	nm
Value	855	$8.34 \cdot 10^{-8}$	390	$7 \cdot 10^{-4}$	0.44	41

Table 36.4 The data about the loss of hysteresis and specific rate of heating of $NiFe_2O_4$ samples [16]

Sample	1#	2#	3#
The loss of hysteresis, kJ/m^3	6.70	6.92	6.95
The specific rate of heating, K/s	1.64	1.69	1.72

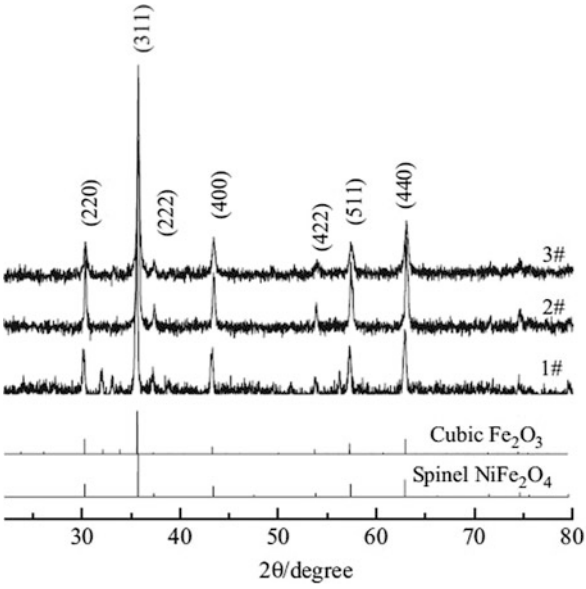

Fig. 36.5 XRD of $NiFe_2O_4$ [16]

The critical diameter with (GHS value) [20]:

$$d_{cr} = \frac{9\varepsilon_p}{2\pi M_s^2}, \tag{36.3}$$

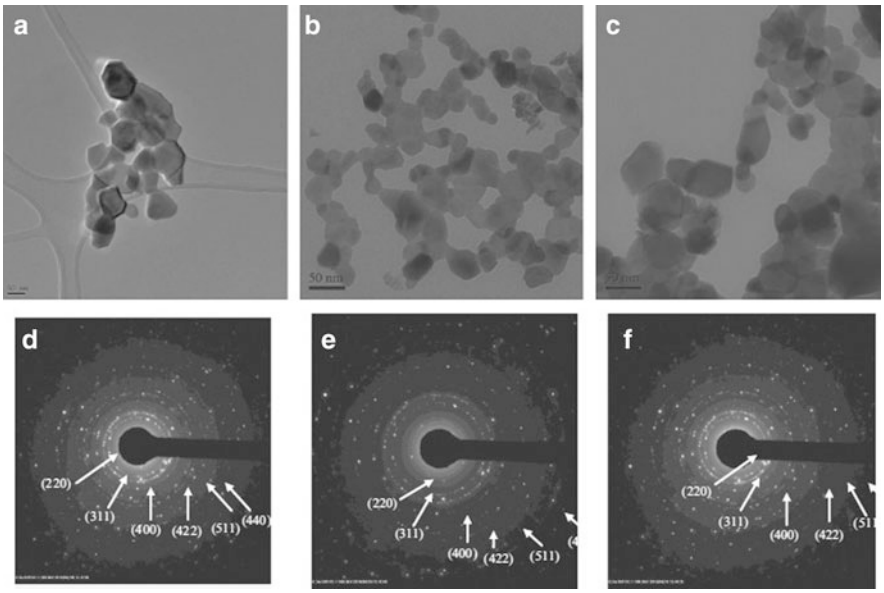

Fig. 36.6 TEM images (**a**–**c**) and selected area (electron) diffraction (SAED) (**d**–**f**) of nickel ferrite [16]

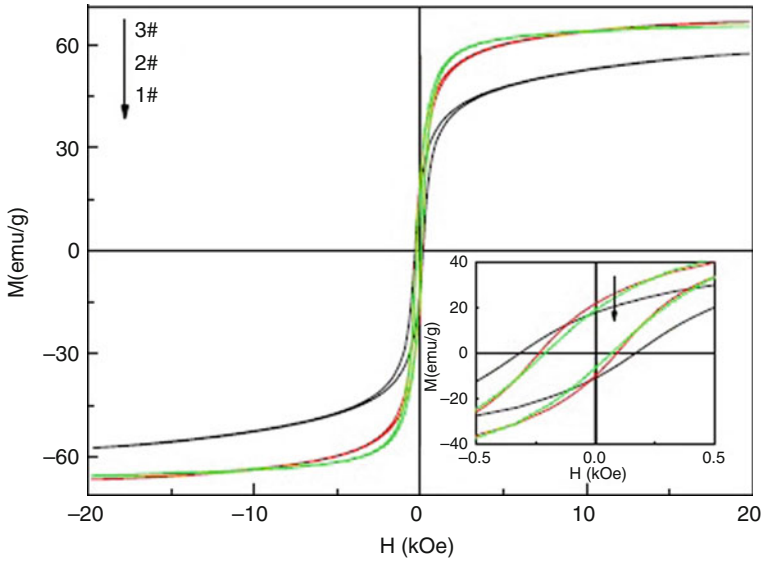

Fig. 36.7 The curve of magnetic hysteresis of different samples of nickel ferrite. The addition demonstrates detailed curves close to coercivity [16]

where ε_p is the the surface energy of domain wall:

$$\varepsilon_p = \left(\frac{2k_B T_c K_1}{a}\right)^{0.5}, \tag{36.4}$$

where k_B is the the Boltzmann constant, T_c the Kurri temperature, a latent parameter, and K_1 absolute value of magnetocrystalline anisotropy constant.

The critical diameter of the nickel ferrite is greater than its grain size. For ultra-thin grains smaller than the critical diameter, the ratio of H_c to D^6 is as follows [21, 22]:

$$H_c = p_c \frac{K_1^4 D^6}{M_s A}, \tag{36.5}$$

where p_c is the dimensionless factor and A exchange of constants.

36.2.1 The Microwave Combustion

Iron (III) nitrate ($Fe(NO_3)_3 \cdot 9H_2O$), nickel (III) nitrate ($Ni(NO_3)_2 \cdot 6H_2O$), trisodium citrate ($Na_3C_6H_5O_7$), and sodium hydroxide (NaOH) had been used. Nickel ferrite crystals had been obtained using a microwave process burning process using trisodium citrate as a fuel. An aliquot of 0.1 mol of trisodium citrate was dissolved in 100 cc of distilled water and then 0.1 mol of $Ni(NO_3)_2 \cdot 6H_2O$ was added to form solution 1. Similarly, 0.2 mol of trisodium citrate was dissolved in 100 cc of distilled water and then 0.2 mol $Fe(NO_3)_3 \cdot 9H_2O$ was added to obtain solution 2. The molar ratio of nickel to iron nitrate was 1:2, and the nitrates to citrate trisodium were 1:1. Then, the finished solutions 1 and 2 were mixed under strong magnetic stirring at 80 °C. The aqueous solution of 2 M NaOH was used to adjust the pH to about 13. The resulting mixture was placed in a microwave oven (2.45 GHz, 700 W) and irradiated for 30 minutes. The mixture is first boiled and then subjected to dehydration with subsequent combustion with the release of a large number of gases, turning into a solid black mass. The resulting mass is crushed into powder [14].

Identification of the crystalline phase of the sample was carried out by comparing the experimental XRD scheme with the standard data compiled by the International Center for Diffraction Data (ICDD). The characteristic of the synthesized XRD sample is shown in Fig. 36.8, which is in good agreement with the data of the Joint Committee for Standards of Powder Diffraction (JCPDS) for Nickel Ferrite (JCPDS File No. 74-2081). This indicates that the prepared sample is a nickel ferrite having a cubic inversion structure of the spinel. Characteristic XRD has typical diffraction peaks (220), (311), (222), (400), (511), and (440) of Miller planes at 30.24, 35.60, 37.26, 43.18, 57.32, and 63.20°, respectively [14].

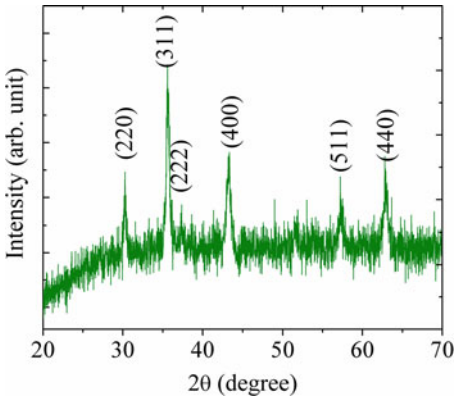

Fig. 36.8 XRD of $NiFe_2O_4$ crystal phases [13]

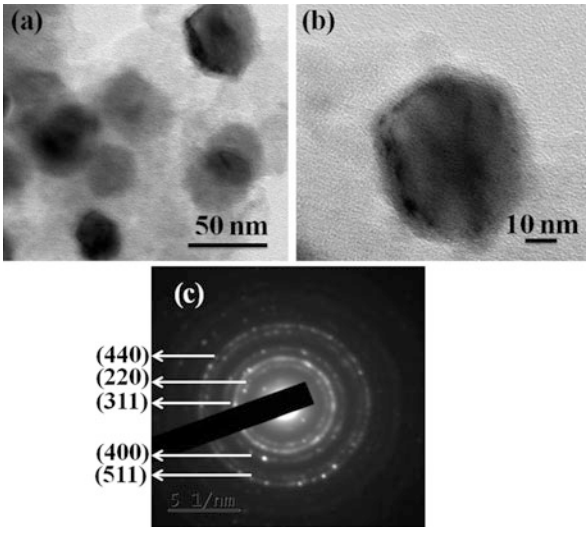

Fig. 36.9 TEM image of $NiFe_2O_4$ [14]

Figure 36.9a shows the transmission electron micrograph (TEM) image of the prepared sample, which indicates that the sample consists of 40–50 nm nanoparticles. This size is well consistent with the size of the crystallite obtained with the XRD. Figure 36.9b is an enlarged image that shows the morphology and size of one particle. The SAED picture (Fig. 36.9c) shows continuous rings around the spot showing the polycrystalline nature of the prepared sample.

Magnetic histogram of $NiFe_2O_4$ is depicted in Fig. 36.10. The obtained dependence indicates a high ferromagnetic magnetization of nickel ferrite.

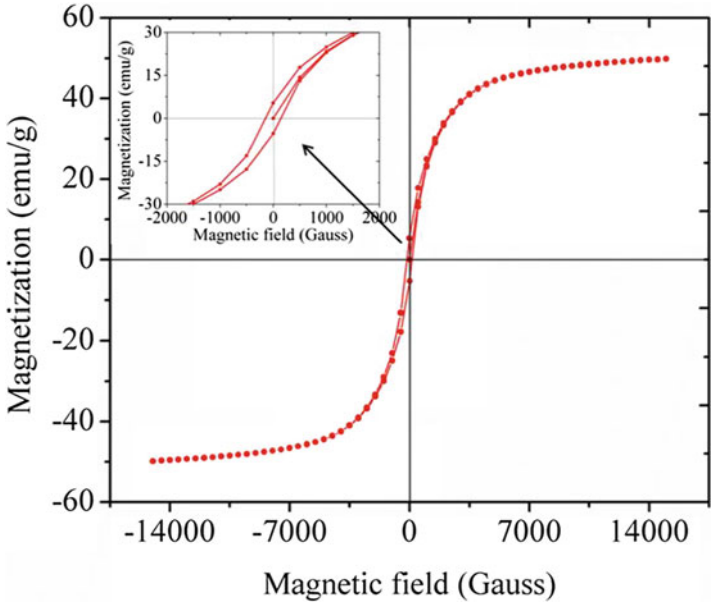

Fig. 36.10 The curve of magnetic histogram of $NiFe_2O_4$ [14]

36.2.2 Sol–Gel Method

The salts $Ni(NO_3)_2$ and $Fe(NO_3)_3$ with molar ratio $[Ni^{2+}]/[Fe^{3+}] = 1/2$ were completely dissolved in deionized water. The aqueous solution containing Ni^{2+} and Fe^{3+} was poured into citric acid with a total ratio of cations/citric acid = 1/1. Ammonium hydroxide was added to the mixed solutions in aqueous form and the pH of the solutions was adjusted to about 7. The mixture was stirred and slowly evaporated at 80 °C to form a gel. The gel was dried at 230 °C for more than 3 hours to form xerogel. The samples of nanoparticles were obtained after the firing of products at 350, 500, and 700 °C for 2 hours [23].

To study the formation of xerogel from a gel, a thermal analysis of the gel product was performed. The differential thermal analysis (DTA) curve shows the presence of two exothermic peaks. The first exothermic peak of about 230 °C in DTA, accompanied by a large loss in TG, is probably due to the decomposition of the precursor of metallic citrate with the release of CO and CO_2. The temperature range of the schedule is 210–253 °C with a maximum temperature of 230 °C. This is confirmed by the results of previous studies on some ferrites, where it has been shown that the first exothermic peak with a high weight loss is due to the decomposition of metal citrate. The second exothermic peak at 345 °C along the DTA curve is associated with the formation and crystallization of the ferrite phase.

The formation of the cubic phase of the spinel oxide in three samples is confirmed by the XRD models shown in Fig. 36.11. For samples fired at 350 and 500 °C,

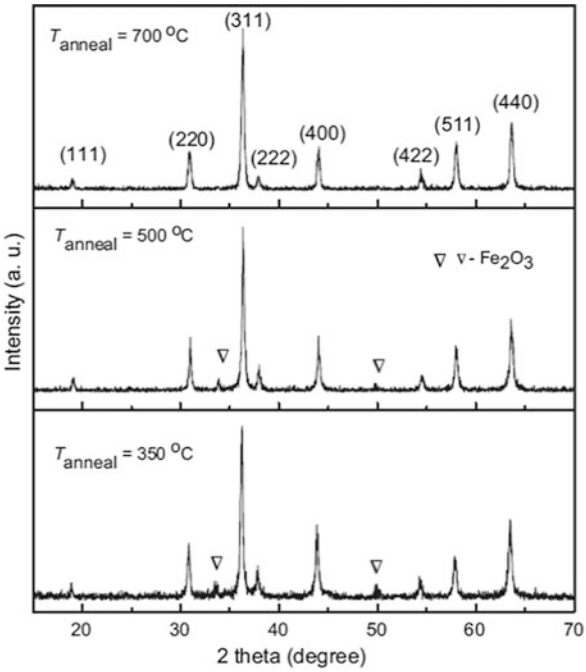

Fig. 36.11 XRD of nanoparticles of nickel ferrite [23]

Table 36.5 The lattice constant (a) and average crystallite size (D_{XRD}) of nickel ferrite calcined at temperature 350, 500, and 700 °C [23]

Temperature, °C	a, Å	D_{XRD}, nm
300	8.332	28.55
500	8.333	28.50
700	8.331	26.18

there is a small amount of impurities that can be identified as the Fe_2O_3 phase. The lattice parameters were calculated using distance d and corresponding (h, k, l) parameters. Wide lines of XRD show that the particles have a nanoscale range. The average particle size for each sample was calculated according to the Debye-Scherrer formula. The structural parameters are listed in Table 36.5. It was found that the values of the samples are in good agreement with the ones indicated for bulk materials (8.33 Å), and the average size is in the range 26.18–28.55 nm, which does not significantly change at calcination temperatures.

The shape, size, and morphology of single-phase particles were investigated by direct observation using electron microscopy. The TEM of the sample (Fig. 36.12a) shows that the particles have a roughly spherical shape. A histogram of particle size (sample of about 300 particles) from different TEM is shown in Fig. 36.12b. Particle size values are distributed in the range of 21.0–82.5 nm. The most likely diameter is DTEM 55.4 nm.

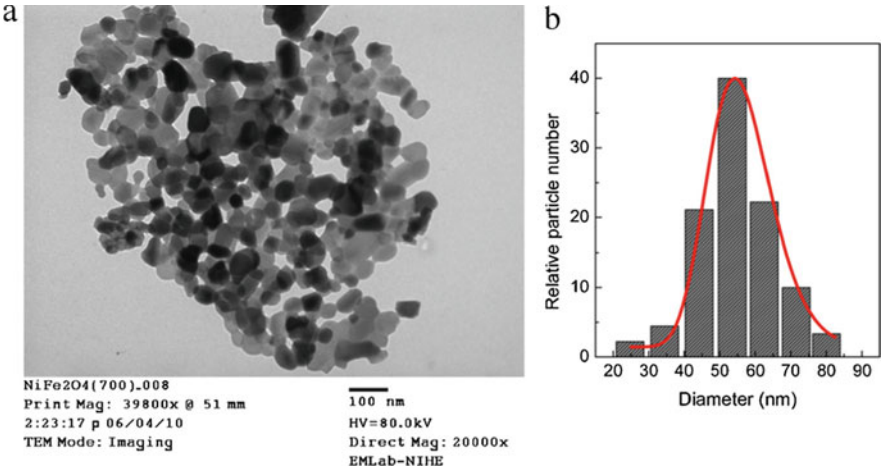

Fig. 36.12 TEM of nickel ferrite nanoparticles obtained at 700 °C (**a**) and the histogram of particles sizes distribution (**b**) [23]

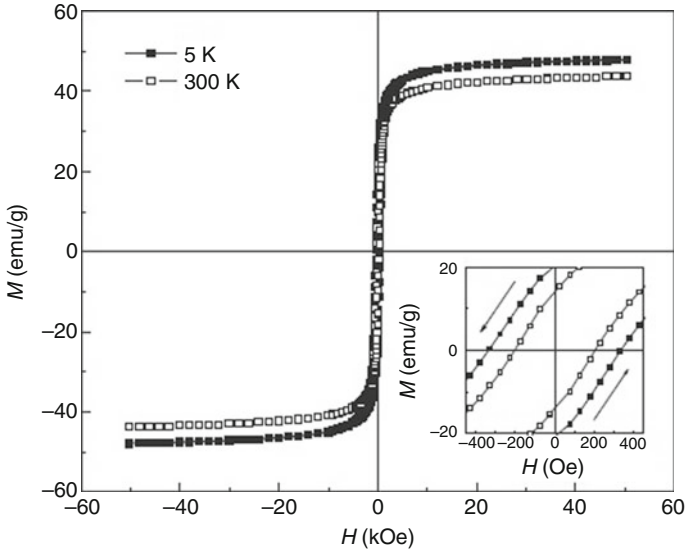

Fig. 36.13 The hysteresis loop of $NiFe_2O_4$ [23]

The magnetic isotherms of nickel ferrites were performed at temperatures from 5 to 300 K. The hysteresis loop of $NiFe_2O_4$ is presented in Fig. 36.13. The common feature of the loop at different temperatures is that the magnetization approaches the saturation of about 13 kOe and then slow increases in magnetization with the subsequent increase in the magnetic field. This behavior is usually observed in many systems of ferrite nanoparticles and is the result of the formation of rotating or

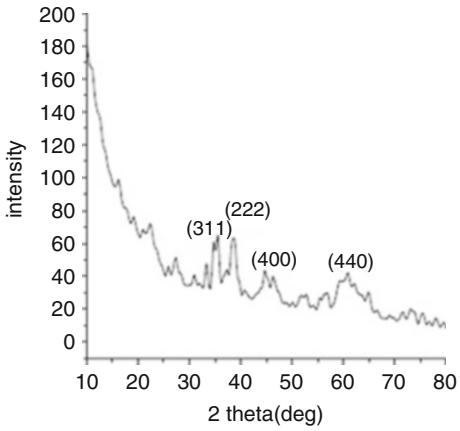

Fig. 36.14 XRD of calcined at 100 °C ferrite [24]

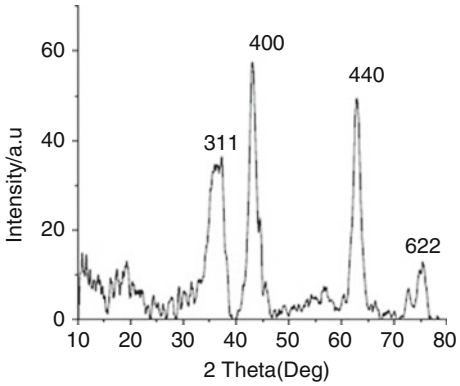

Fig. 36.15 XRD of calcined at 400 °C ferrite [24]

disordered spins on the surface shell. The spontaneous magnetization of the Ms ferromagnetic core is determined by extrapolating the linear part of the high field of the magnetization curve to a zero field [23].

36.2.3 The Investigation of Calcination Temperature

The study was conducted on the basis of nickel ferrite obtained by sol–gel method. The resulting gel was calcined at temperatures of 100, 400, 600, and 800 °C. Transmission electron micrographs were taken for the samples obtained to study the factors of particle size [23].

Figures 36.14, 36.15, 36.16, and 36.17 show XRD powder samples after sintering at various temperatures of 100, 400, 600, and 800 °C, respectively. The XRD data were used to calculate the structural parameters of the crystallites size, lattice parameter, and crystal deformation and dislocation density of the prepared sample given in Table 36.6 [24].

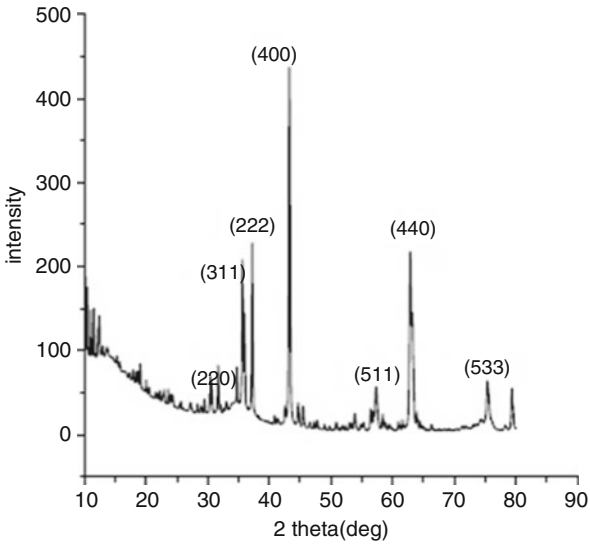

Fig. 36.16 XRD of calcined at 600 °C ferrite [24]

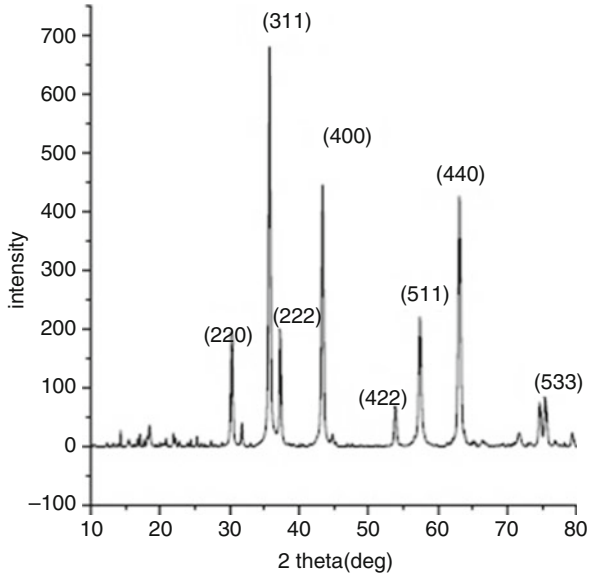

Fig. 36.17 XRD of calcined at 800 °C ferrite [24]

Table 36.6 The lattice parameter (a), strain density (E), and dislocation (δ) for $NiFe_2O_4$ in depends on calcination temperature [24]

T, °C	a, Å	E	δ	D, nm
100	8.3857	$6.60 \cdot 10^{-4}$	$4.5 \cdot 10^{14}$	26
400	8.3354	$5.58 \cdot 10^{-4}$	$2.7 \cdot 10^{14}$	37
600	8.3540	$5.18 \cdot 10^{-4}$	$2.3 \cdot 10^{14}$	42
800	8.3253	$8.28 \cdot 10^{-4}$	$5.3 \cdot 10^{14}$	28

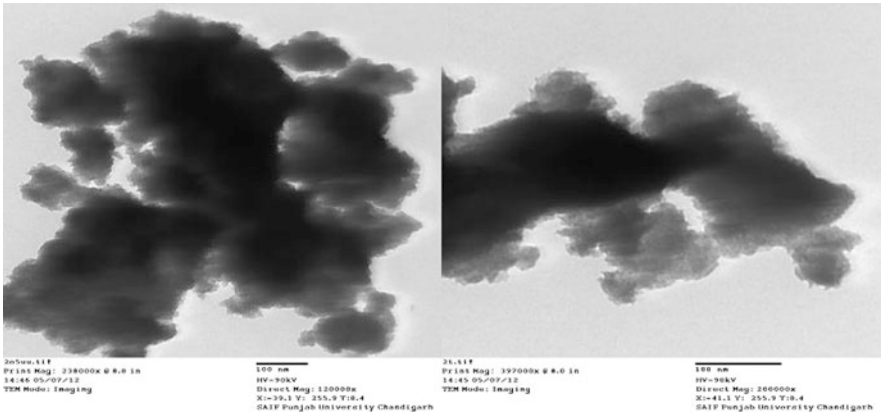

Fig. 36.18 TEM of calcined at 100 °C nickel ferrite [24]

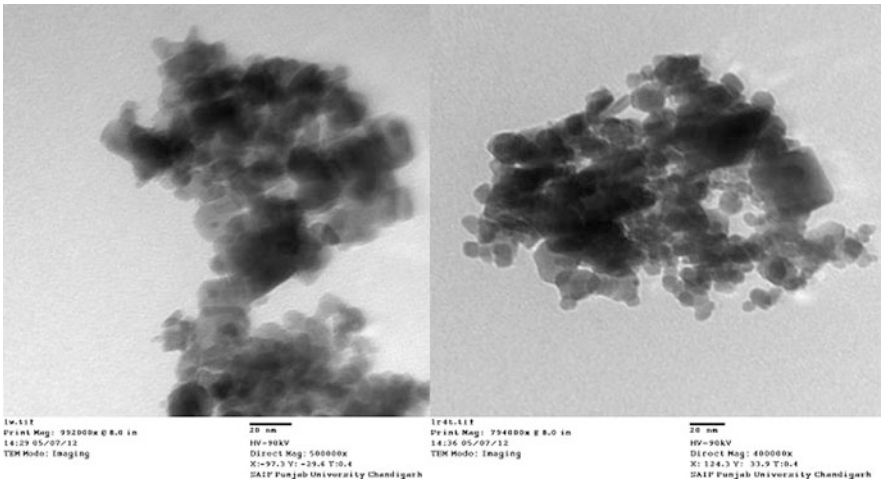

Fig. 36.19 TEM of calcined at 800 °C nickel ferrite [24]

TEM images of $NiFe_2O_4$ powder are shown in Figs. 36.18 and 36.19. The morphology of the prepared sample is mainly cubic with some agglomeration. The average particle size is estimated at about 10 nm for the powders calcined at temperatures of 100, 400, 600, and 800 °C during 4 hours. TEM image of nickel ferrite powder calcined at 100 °C, which is shown in Fig. 36.18, is not clear. It shows a cloud-like appearance, what is consistent with the XRD of this sample without an intense peak (see Fig. 36.14). This may be due to the presence of moisture and impurities in this sample. But the microphotographs calcined at 800 °C nickel ferrite, shown in Fig. 36.19, are clear and have a cubic structure, which confirms the results of XRD (see Fig. 36.17) [24].

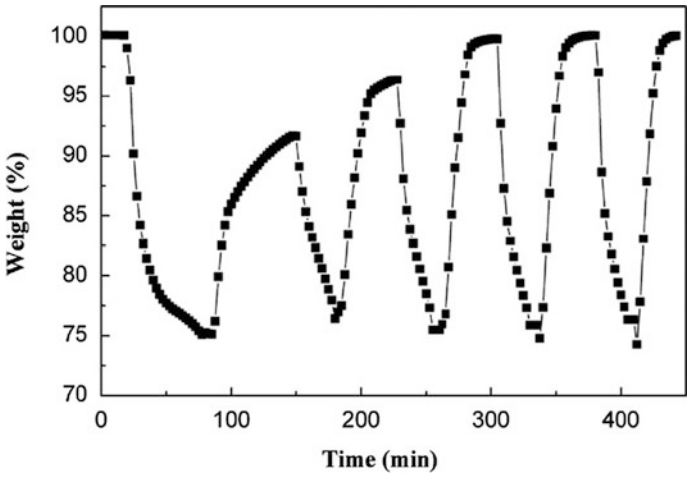

Fig. 36.20 Reaction cyclic characteristics of oxygen carriers in $NiFe_2O_4$ [26]

36.3 Applications of Ferrites

36.3.1 Catalysts Based on Nickel Ferrite

Nanoparticles of nickel ferrite were used in Sonogashira reaction. This is the reaction for producing carbon–carbon triple bonds. Various types of aryl and alkyl halides have been successfully combined with phenylacetylene under optimized reaction conditions with high yield and selectivity in a short time. Ferrite is easily restored and can be reused for several cycles [25].

Taiwanese scientists proved and found out that the result was a mechanism of chemical-cyclic conversion of natural gas (Fig. 36.20) [26]:

$$NiFe_2O_4 + CH_4 = Fe(Ni) + Fe + CO_2 + H_2O;$$

$$Fe(Ni) + Fe + H_2O = Fe_3O_4 + Ni + H_2;$$

$$Ni + Fe_3O_4 + O_2 = NiO + Fe_2O_3 = NiFe_2O_4.$$

It is also possible to use a cobalt–nickel ferrite composite as a catalyst for steam reforming of methanol with the chemical formula $Ni_{1-x}Cu_xFe_2O_4$:

$$CH_3OH + H_2O = 3H_2 + CO_2 \ \Delta H^0_{298\ K} = 49.5\ \text{kJ/mol}.$$

To reduce the degree of conversion of CO_2 into CO, a number of studies of the selectivity of the catalyst of different compositions were carried out (Fig. 36.21) [27].

The predecessors of these studies were French scientists who put the basic knowledge about the catalytic activity toward natural gas [28]. Studies of catalytic

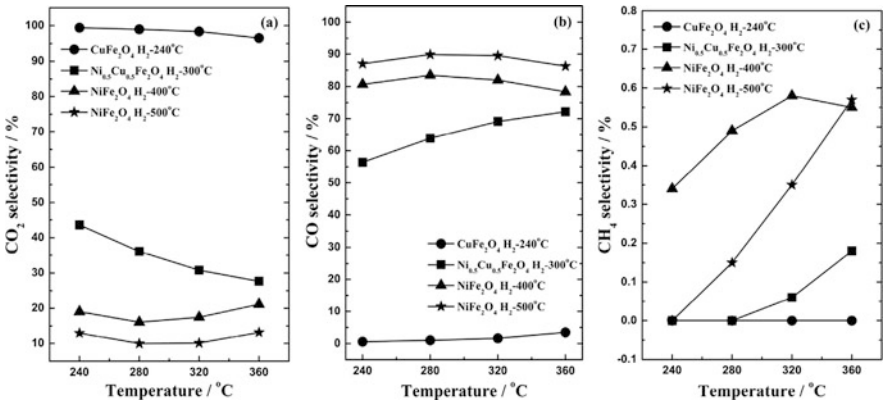

Fig. 36.21 Selectivity of CO_2 (**a**), CO (**b**), and CH_4 (**c**) as a function of reaction temperature for steam reforming of methanol over Cu-Ni ferrite [30]

properties on the examples of chlorinated organic matter [29] and the production of dyes [30] were also carried out.

36.3.2 Nickel Ferrites for Gas Sensing

For studies of the sensory properties, ferrite derived from nitroethane was used [31]. The temperature resistance study showed a linear character (Fig. 36.22a) expected for the semiconductor nature of the material. From the diagram, the activation energy is calculated as 0.41 eV.

Figure 36.22b shows the response measurements for gas reactions at different temperatures for liquefied natural gas, acetone, ethanol, and ammonia. Best reaction to methane. The reaction itself is a surface-controlled process that does not depend on the amount of adsorbed oxygen. Figure 36.22c shows the dependence of material response on methane concentration.

In general, nickel ferrite showed high sensitivity to the studied gases, especially to liquefied natural gas, which increases with its increase. At the same time, Chinese scientists studied the ultra-fast electronic sensorics of ferrite [32].

36.3.3 Nickel Ferrites in Water Treatment

The use of ferrites in water treatment has recently gained wide interest in the scientific community. One of these studies involved Argentine scientists who studied the removal of dipyrone from the wastewater of the pharmaceutical industry [33].

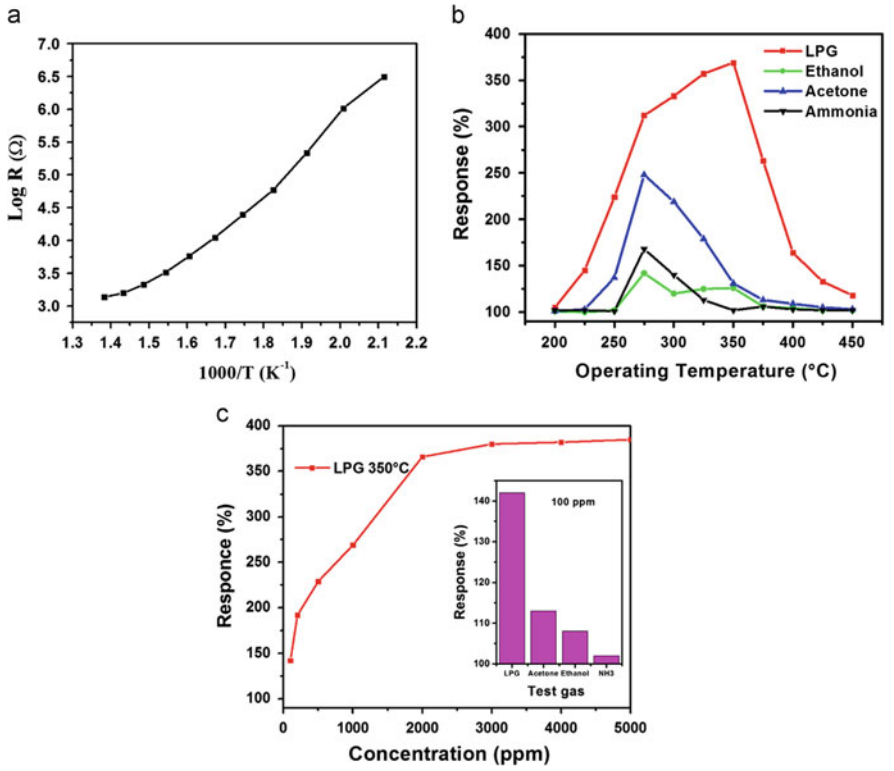

Fig. 36.22 Diagram of $NiFe_2O_4$ resistance in dependence on temperature (**a**); response of the ferrite for different gases with a concentration of 0.2% depending on the temperature (**b**); response of the ferrite for liquefied natural gas depending on the concentration (**c**) [31]

They have obtained excellent results that open a new branch of ferrite application in the industry to the world (Fig. 36.23).

36.4 Conclusions

Contrary to the well-established opinion on the use in processes based on the magnetic properties of nickel ferrites, they can be used in other areas. Nickel ferrites successfully applied as sensing layers, electrode mass catalysts, sorbents and other in gas sensing, fuel cells, lithium batteries, water purification, and waste water treatment processes. And this is not a complete list of possible practical application of functional materials based on ferrites.

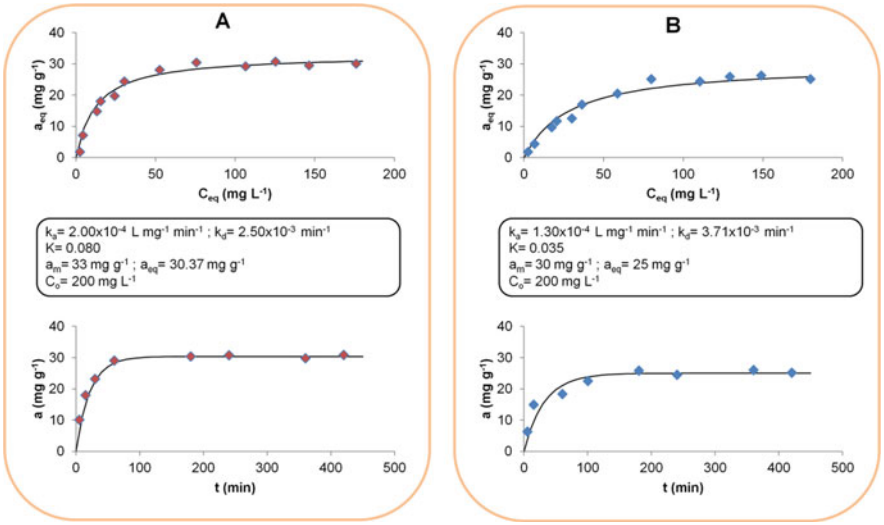

Fig. 36.23 Kinetics of dipyrone adsorption and adsorption isotherms at pH = 6.0 (**a**) and pH = 4.0 (**b**) [33]

Acknowledgments The authors thank the National Technical University of Ukraine "Igor Sikorsky Kyiv Polytechnic Institute" for the opportunity to carry out this research.

References

1. Pileni MP et al (2001) Magnetic fluids: fabrication, magnetic properties, and organization of nanocrystals. Adv Funct Mater 11:323
2. Sugimoto M (1999) The past, present, and future of ferrites. J Am Ceram Soc 82:269
3. Song Q et al (2004) Shape control and associated magnetic properties of spinel cobalt ferrite nanocrystals. J Am Chem Soc 126:6164
4. Ceylan A et al (2009) Investigation of nickel ferrite formation in a binary Fe(III)-Ni(II) hydroxide precipitate containing H_2O with or without Li_2O doping. J Alloys Compd 486:824
5. Doh SG et al (2004) Characteristics and synthesis of Cu-Ni ferrite nanopowders by coprecipitation method with ultrasound irradiation. J Magn Magn Mater 272:2238
6. Chen DH et al (2001) Synthesis of nickel ferrite nanoparticles by sol-gel method. Mater Res Bull 36:1369
7. Chatterjee A et al (1993) Synthesis of nanocrystalline nickel-zinc ferrite by the sol-gel method. J Magn Magn Mater 127:214
8. George M et al (2006) Finite size effects on the structural and magnetic properties of sol-gel synthesized $NiFe_2O_4$ powders. J Magn Magn Mater 302:190
9. Huo JZ et al (2009) Characterization and magnetic properties of nanocrystalline nickel ferrite synthesized by hydrothermal method. Mater Lett 63:1183
10. Zhou J et al (2005) Low temperature synthesis of $NiFe_2O_4$ by a hydrothermal method. J Am Ceram Soc 88:2135
11. Fand J et al (2003) Ultrafine $NiFe_2O_4$ powder fabricated from reverse microemulsion process. J Appl Phys 93:7483

12. RDK M et al (2003) Synthesis of nanocrystalline nickel and zinc ferrites by microemulsion technique. Mater Sci Technol 19:826
13. Elmasry MA et al (1997) Preparation of nickel ferrite using the aerosolization technique: Part I: aerosolization behaviour of individual raw material solutions. Powder Technol 90:161
14. Venkatesh M et al (2016) Microwave assisted combustion synthesis and characterization of nickel ferrite nanoplatelets. Mod Electron Mater 2:74
15. Goldman A (1993) Modern ferrite technology, 2nd edn. Marcel Dekker, New York, p 438, ISBN 978-0387281513
16. Li D et al (2014) Structural and magnetic properties of nickel ferrite nanoparticles synthesized via a template-assisted sol-gel method. Ceram Int 40:16529
17. Perron H et al (2007) Structural investigation and electronic properties of the nickel ferrite $NiFe_2O_4$: a periodic density functional theory approach. J Phys Condens Matter 19:346219
18. Polaert I et al (2015) Dielectric and magnetic properties of $NiFe_2O_4$ at 2.45 GHz and heating capacity for potential uses under microwaves. J Magn Magn Mater 374:731
19. Cullity BD (1978) Elements of X-ray diffraction. In: Cohen M (ed) Addison-Wesley series in metallurgy and materials, 2nd edn. Addison-Wesly Publishing Co. Inc., Massachusetts - Menlo Park, California London - Amsterdam - Don Mills, Ontario – Sydney, p 531, ISBN 978-0201610918
20. Rahman IZ et al (2005) A study on Cu substituted chemically processed Ni-Zn-Cu ferrites. J Magn Magn Mater 290:1576
21. Herzer G (1990) Grain size dependence of coercivity and permeability in nanocrystalline. IEEE Trans Magn 26:1397
22. Xia A et al (2014) Facile hydrothermal synthesis of core/shell-like composite $SrFe_{12}O_{19}$/(Ni,Zn)Fe_2O_4 nanoparticles and their magnetic properties. RSC Adv 4:18885
23. Nguyet DTT et al (2011) Crystallization and magnetic behavior of nanosized nickel ferrite prepared by citrate precursor method. J Alloys Compd 0925:8388
24. Emdadul SKI et al (2014) Synthesis and characterization of nickel ferrite: role of sintering temperature on structural parameters. J Elect Phys 30:926
25. Moghaddam FM et al (2015) A copper-free Sonogashira reaction using nickel ferrite as catalyst in water. Catal Commun 60:82
26. Yu LK et al (2013) Assessment of redox behavior of nickel ferrite as oxygen carriers for chemical looping process. Ceram Int 39:5459
27. Huang YH et al (2015) Catalysts prepared from copper–nickel ferrites for the steam reforming of methanol. J Power Sources 281:138
28. Rafik B et al (2012) Nickel ferrite spinel as catalyst precursor in the dry reforming of methane: synthesis, characterization and catalytic properties. J Nat Gas Chem 21:595
29. Divya SN et al (2017) Catalytic peroxide oxidation of persistent chlorinated organics over nickel-zinc ferrite nanocomposites. J Wat Process Eng 16:69
30. Petrisor S et al (2017) Remarkable catalytic properties of rare-earth doped nickel ferrites synthesized by sol-gel auto-combustion with maleic acid as fuel for CWPO of dyes. Appl Catal Environ 202:21
31. Patil JY et al (2014) Synthesis of glycine combusted $NiFe_2O_4$ spinel ferrite: a highly versatile gas sensor. Mater Lett 475:144
32. Zhou T et al (2018) Structure-driven efficient $NiFe_2O_4$ materials for ultra-fast response electronic sensing platform. Sens Actuators B Chem 255:1436
33. Springer V et al (2016) Magnetic nickel ferrite nanoparticles for removal of dipyrone from aqueous solutions. J Environ Chem Eng 4(4):3882

Chapter 37
Electron Irradiation of Carbon Nanotubes

H. Yu. Mykhailova and M. M. Nischenko

Recently, the production of effective thermoelectric materials has been associated with nanostructures. It is based on the use of physical effects that were found in nanostructures, such as size quantization, charge carrier tunneling, phonon scattering on nanostructure surfaces, which is necessary to increase the thermoelectric figure of merit (ZT) of thermal to electrical energy converters. The possibility of increasing ZT in superlattices was theoretically shown for the first time in Hicks and Dresselhaus [1]. The possibility of developing effective thermoelectric materials on the basis of nanostructures is predicted in Shevelkov et al., Dmitriev and Zvyagin, and Vineis et al. [2–4]. The approach based on the creation of bulk nanostructured thermoelectric materials have great interest [5]. Theoretical calculations were performed in Eletsky and Bulat and Millet-Severin [6, 7], demonstrating the possibility of increasing ZT due to electron tunneling through the gap between nanoparticles, in addition to the occurrence of conditions under which the phonon mean free path is limited by the size of structural units or the gap between particles. In Shevelkov [2], the increase in ZT values is attributed to the effective dispersion of phonons at numerous grain interfaces in nanomaterials, leading to a stronger decrease in lattice thermal conductivity, compared with a decrease in electrical conductivity, which is necessary to increase the σ/λ ratio [8–10].

In this regard, carbon nanotubes (CNTs), which have a unique anisotropy of properties, are of interest.

Carbon nanotubes always have defects that can be formed during synthesis and under external influences. The main types of defects are: Stone–Wales (pairs 5–7), double vacancies, ad-dimer defect, and combinations of these [11, 12]. External influences can heal defects.

H. Y. Mykhailova (✉) · M. M. Nischenko
G. V. Kurdyumov Institute for Metal Physics of the NAS of Ukraine, Kiev, Ukraine

O. Fesenko, L. Yatsenko (eds.), *Nanocomposites, Nanostructures, and Their Applications*, Springer Proceedings in Physics 221,
https://doi.org/10.1007/978-3-030-17759-1_37

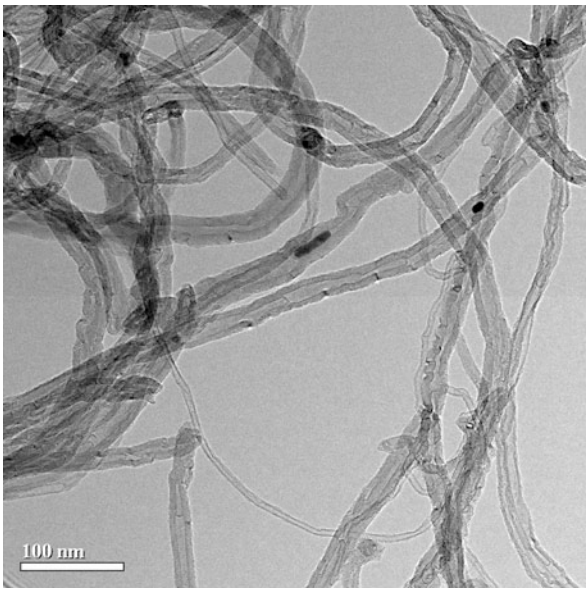

Fig. 37.1 Transmission electron microscopy images of the carbon nanotube (CNT)

Dislocations arise in the multiwall carbon nanotubes and change the number of layers in CNTs [13]. Heating to a temperature of up to 2773 K can induce topological defects to disappear.

Thus, growth and radiation defects of CNTs change the electronic structure and properties in different ways.

Multilayer CNTs with a diameter of 18 ± 7 nm were obtained by chemical vapor deposition (CVD) and identified by transmission electron microscopy (TEM) using a JEM-100CX11 instrument (Japan). The irradiation was carried out on a Myktron-St cyclic accelerator with an electron energy of 21 MeV and doses of $0.89 \cdot 10^{17}$ and $2.21 \cdot 10^{17}$ electrons/cm^2.

A TEM image of a nanotube is shown in Fig. 37.1. In this method, the intensity of the contrast of images is directly dependent on the amount of the scattering substance, and the darker areas on the positive prints correspond to the thicker areas of the sample or the heavier atoms present in the sample. The narrow dark bands observed refer to the walls of the nanotube. Statistical analysis of their size distribution showed that the diameters of most CNTs are within the range 10–25 nm. Dark particles of the remaining catalyst Al_2O_3–Fe_2O_3–MoO_3 can be seen inside some CNTs.

In bulk, CNTs do not conduct electrical current. However, with a little uniaxial compression, they become conductors. Therefore, it was necessary to measure the electrical conductivity of an array of CNTs in a dielectric cylinder under the piston. The piston and the bottom of the cylinder, made of copper, served as electrodes.

Thermo electromotive force (EMF) was measured using the standard method [14]. In this work, the branches of the differential chromel–alumel thermocouple

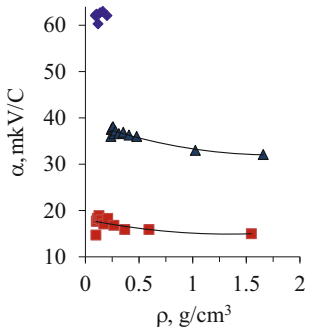

Fig. 37.2 Electromotive force (EMF) of the CNT. ■ Radiation, ■ initial, ■ growth

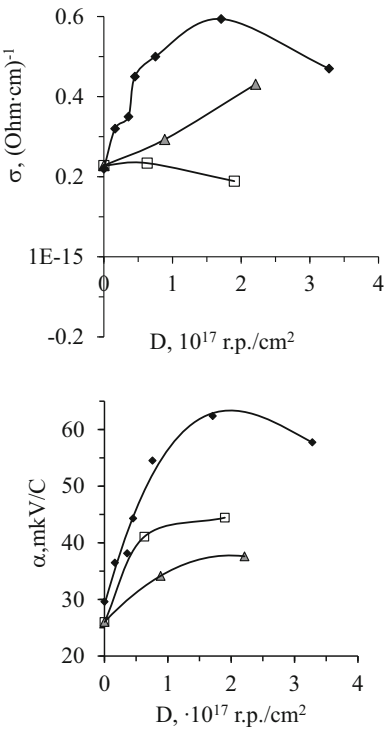

Fig. 37.3 Conductivity and the coefficient of thermo-EMF of the CNT after electron irradiation

were in contact with the heated piston and the bottom of the cylinder, which served as a thermostat. The range of temperature difference between the electrodes (junctions) ΔT varied from 0 to 20 the coefficient of electromotive force for different types of influence of carbon nanotubes are presented in Fig. 37.2.

On Fig. 37.3 conductivity of the CNT array and the coefficient of thermo EMF are present. For the CNT array, the sign of the Seebeck coefficient α is positive, which indicates the contribution of the hole to the electrical conductivity. Radiation defects lead to an additional capture of electrons, and a decrease in the concentration of conduction electrons.

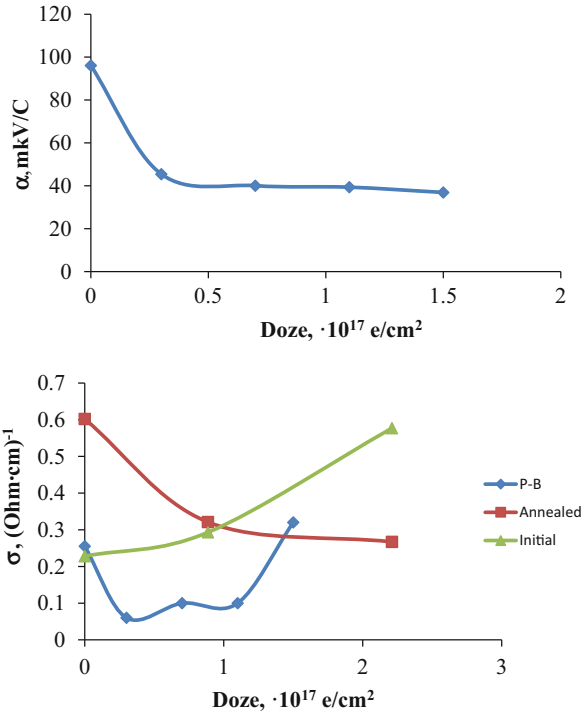

Fig. 37.4 Conductivity and the coefficient of thermo EMF of the CNT with voorloper propan-butan

For both types of matched samples α is increase with the dose D and for the maximum dose $D = 2.21 \cdot 10^{17}$ el/cm^2, α is 38 μV/K for an unannealed sample and 35 μV/K for annealed material. This increase in the coefficient α is also associated with the appearance of radiation defects of an acceptor type when exposed to high-energy electrons. Under the conditions of the temperature gradient required to realize the Seebeck effect, these defects become additional centers of "emission" of the conduction electrons that they previously captured, which leads to an increase in the coefficient α (Fig. 37.4).

It is established that the value of the coefficient of thermo EMF decreases with an increase in the radiation dose by 10%; the conductivity after irradiation is reduced for the smallest dose by 24%, and then, with an increase in the dose of radiation, it begins to increase to 18%. Such behavior is caused by the formation, destruction, and reclamation of defects to radiation and radiation in the array of CNT.

Defects of different genesis reject the form of the CNT from the straight and forms a topological disorder, which changes the electrical conductivity and increases the coefficient of the thermo EMF, but their combined effect reduces this disorder as a result of the interaction of defects leading to the annihilation of defects and/or "healing."

References

1. Hicks LD, Dresselhaus MS (1993) Effect of quantum-well structures on the thermoelectric figure of merit. Phys Rev B 47(19):727–731
2. Шевельков АВ (2008) Химические аспеты создания термоэлектрических материалов. Успехи химии 77(1):3–21
3. Дмитриев АВ, Звягин ИП (2010) Современные тенденции развития физики термоэлектрических материалов. УФН 180(8):821–838
4. Vineis CJ, Shakouri A, Majumdar A, Kanatzidis MG (2010) Nanostructured thermoelectric: big efficiency gains from small features. Adv Mater 22:3970–3980
5. Снарский АА, Сарычев АК, Безсуднов ИВ, Лагарьков АН (2012) Термоэлектрическая добротность объмных наноструктурированных композитов с распределнными параметрами. Физика и техника полупроводников 46(5):677–683
6. Елецкий АВ (2002) Углеродные нанотрубки и их эмиссионные свойства. УФН 172(4):401–438
7. Булат ЛП, Пшенай-Северин ДА (2010) Влияние туннелирования на термоэлектричекую эффективность объмных наноструктурированных материалов. ФТТ 52(3):452–458
8. Булат ЛП, Бочкова ЛВ, Нефедоваа ИА, Ахыска Р (2014) НАНОСТРУКТУРИРОВАНИЕ КАК СПОСОБ ПОВЫШЕНИЯ ЭФФЕКТИВНОСТИ ТЕРМОЭЛЕКТРИКОВ. Научно-технический вестник информационных технологий, механики и оптики (4):48–56
9. Kajiura H, Nandyala A, Bezryadin A (2005) Quasi-ballistic electron transport in as-produced and annealed multiwall carbon nanotubes. Carbon 43:1317–1339
10. Азаренко НА, Береснев ВМ, Погребняк АД. Наноматериалы, нанопокрытия, нанотехнологии: Учебное пособие. Харьков: ХНУ им. В.Н. Каразина. – 2009. – 209с
11. Charlier JC (1996) Structural and electronic properties of pentagon-heptagon pair defects in carbon nanotubes. Phys Rev B 53(16):11108–11113
12. Нищенко ММ (2003) Збірник наукових праць: “Наносистеми, наноматеріали, нанотехнології”. Академперіодика 1(1):193–259
13. Нищенко ММ (2004) Збірник наукових праць: “Наносистеми, наноматеріали, нанотехнології”. Академперіодика 2(3):983–991
14. Анатычук ЛИ (1979) Термоэлементы и термоэлектрические устройства. К.: Наук. Думка. p 228

Chapter 38
Influence of Irradiation with Deuterium Ions on the Magnetic Properties and Structure of Nickel

Oleksandr Mats, Nikolay Chernyak, Oleksandr Morozov, and Volodymyr Zhurba

38.1 Introduction

The investigation into regularities of hydrogen interaction with metals and alloys over a wide range of temperatures and pressures still remains a currently central problem in material physics from both the scientific and practical standpoints [1–9]. The hydrogen accumulation in structural and functional materials is an extremely hazardous phenomenon, which leads to hydrogen degradation of materials and to possible unforeseen equipment failures [10–14]. Degradation of materials increases due to hydrogen interaction with the whole range of crystal structure imperfections of solids such as interstitial and substitutional impurities, vacancies and their complexes, dislocations and their pileups, subgrain and grain boundaries, and phase components [11, 15, 16].

The results of studies related to the capture, retention, and desorption of ion-implanted deuterium in nickel are presented in [17]. It is shown that the structure of the desorption spectrum, the distribution of the amount of isolated deuterium, is a function of the irradiation dose. It is believed that the peaks of thermal desorption are due to diffusion of hydrogen and its release from various types of traps – interstices and crystal lattice defects that arise during irradiation. In this chapter, the results of studies on the formation of a defect structure and elastic stresses in polycrystalline nickel after irradiation of deuterium with various doses are presented.

O. Mats · N. Chernyak · O. Morozov (✉) · V. Zhurba
National Science Center "Kharkiv Institute of Physics and Technology", Kharkiv, Ukraine
e-mail: morozov@kipt.kharkov.ua

O. Fesenko, L. Yatsenko (eds.), *Nanocomposites, Nanostructures, and Their Applications*, Springer Proceedings in Physics 221,
https://doi.org/10.1007/978-3-030-17759-1_38

38.2 Methods

Polycrystalline nickel samples with a purity of 99.98 wt.%. Samples look like disks with a diameter of 10 mm and a thickness of 0.05 mm. It is carved from foil, which was annealed. They were fixed in the target device, which cools the sample to 78 K in the dose range from 8×10^{14} to 2.7×10^{18} D/cm^2. Irradiation with deuterium (D^+) was carried out at the facility [18]. The samples were irradiated with a beam of ions with an energy of 12 keV. The low temperature was chosen to restrict the diffusion mobility of deuterium in the samples and to investigate its behavior in a wide range of concentrations produced in the implantation layer. The field dependences of the magnetization at 78 K were taken according to the permeameter scheme in a closed magnetic circuit. The structure was examined for clearance by means of an electron microscope.

The TDS technique has been used to investigate the kinetics of spectrum development for deuterium desorption from nickel versus the implanted deuterium dose. The chamber is partitioned into two separate, nearly equal in volume compartments: analytical and pumping. At the center of the partition wall, there is an iris diaphragm with the aperture variable in the range from 10 to 50 mm. That permits one to control the rate of pumping of the analytical compartment and to increase, if necessary, the sensitivity of the analyzer registering the partial gas pressure in the chamber. The opening of the diaphragm is controlled from the outside of the chamber by means of the magnetic system. In our TDS measurements, we have used the Type APPM-1 monopolar mass-spectrometer. In our experiments, to reduce the impact of background hydrogen being present in the samples and in the target chamber, we have used deuterium as the hydrogen isotope. After irradiation, the samples implanted to the pre-assigned dose were heated in the same measurement chamber at a rate of ~3.5 K/s to a temperature of ~1700 K, with simultaneous registration of the D_2 ion desorption spectrum (4 amu). The heating of samples was turned on immediately after the ion beam was switched off. The temperature was measured by the Tungsten-Rhenium thermocouple, WRe 5/20 fixed to the sample. The total amount of deuterium released from the sample was determined from the area lying under the gas-release curve.

38.3 Results and Discussion

The magnetic properties of ferromagnets strongly depend on the defectiveness of the crystal structure; this causes the appearance of magnetic hysteresis and magnetic consequences. Irradiated crystals are affected by both dislocations and damage zones [19]. Information on the coercive force Hc makes it possible to judge not only the degree of defectiveness of the ferromagnetic, but also the dominant type of defects and their distribution.

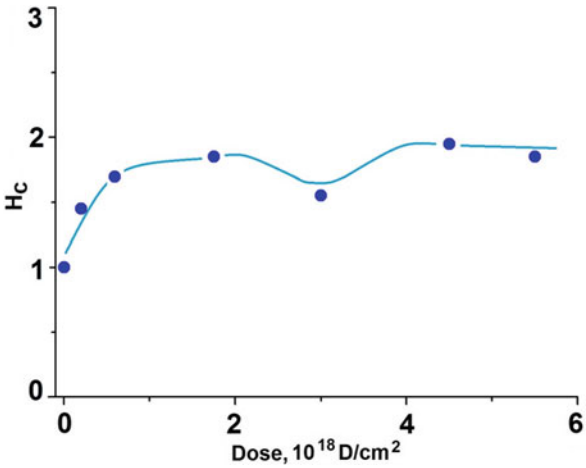

Fig. 38.1 Relative dependence of the coercive force H_c of nickel on the dose of implanted deuterium. The coercive force of the initial annealed Ni is taken as unity

Figure 38.1 shows the dependence of the coercive force on the dose D of implanted deuterium. When irradiated with a dose of more than 2×10^{18} D/cm^2 there is inhomogeneous distribution spectrum of released deuterium that is associated with an increase in non-uniformly distributed defects of radiation origin, such as clusters of dislocations or other local distortions. In the interval up to 2×10^{18} D/cm^2, the dependence obeys the law $H_c \sim D^{1/2}$, which agrees well with the rate of accumulation of dislocation groups—$H_c \sim V_n$, where n is the density of these groups [20]. The subsequent of inhomogeneous distribution spectrum of released deuterium in Fig. 38.1 is due to the development of competing processes of accumulation and relaxation of radiation-stimulated elastic stresses.

It is believed that when a solid is irradiated by charged particles with small energies, all of their energy is absorbed in a relatively thin surface layer. However, studies, for example, of the mechanical characteristics of materials irradiated with energies of 10–150 keV and doses of 10^{16}–10^{20} D/cm^2, indicate the spreading of the modifying effect to depths substantially exceeding the layers of expected ion runs [21].

At low irradiation temperatures ($T < 300$ K) at anomalously large distances from the surface, local concentrations of radiation defects and elastic distortions arise. These defects affect the change in properties, presumably, according to athermal mechanisms. This explains the relevance of structural studies of irradiated nickel at 78 K at various doses.

Electron microscope studies have shown that as a result of the deuterium bombardment, extended areas of elastic distortion appear in the Ni crystal structure (in the pictures this is the flexural contours—Fig. 38.2a). This is a consequence of the synchronous shift of atoms from equilibrium positions in the planes of light slip. Such regions can be classified as cascades of displacements, which relax by the occurrence of walls of like dislocations. In the course of the research, we estimated the dislocation density (ρ) in the contours, the azimuthal components

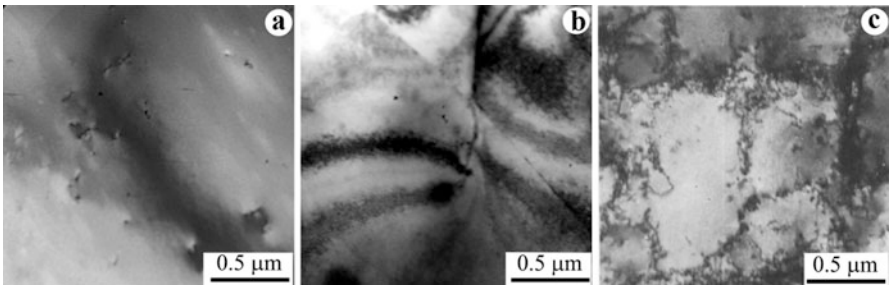

Fig. 38.2 Microstructure of nickel: (**a**) prior to and after irradiation with deuterium ions to the doses; (**b**) 1.7×10^{18} D/cm^2; (**c**) 2.4×10^{18} D/cm^2

(ω) of the misorientations of the microregions separated by the bending contours, the values of the tangential stresses (τ) in the contours along the radius of curvature and at a distance from the stress source along the bend of a detached dislocation. (Fig. 38.2c).

Thus, for $D = 1.75 \times 10^{18}$ D/см^2 and the maximum value of H_c, ρ is 3×10^{11} cm^{-2}, ω reaches 5°, τ in the circuit is 240–250 MPa, and at a distance of 150–180 MPa (Fig. 38.2b). An increase in the dose of implantation to 3×10^{18} D/cm^2 leads to a decrease in the coercive force. Relaxation processes are fixed in the structure, it is sufficiently justified to associate with the interaction of vacancies of radiation origin with dislocations and annihilation of the latter. ρ does not exceed 10^{11} cm^{-2}, misorientations decrease to 2°, and residual stresses in free places do not exceed 80 MPa. The origin of small-angle boundaries is noted, as the initial stage of cellular structure formation.

Further irradiation again leads to the accumulation of defects, which is removed by reducing the stored energy. It can be argued that the structure of irradiated Ni is due to the following interrelated processes: the radiation formation of defects, the exchange of energy between the incident particles and lattice electrons, and the relaxation of elastic distortions. The totality of these processes explains the development of radiation-stimulated diffusion, ordering, aggregation, formation of compounds (hydrides), amorphization, and cracking.

Figure 38.3 shows the spectra of thermal desorption of deuterium implanted in Ni, obtained for different doses of irradiation. It can be seen that at low doses above 2.1×10^{18} D/см^2, low-temperature desorption peaks appear, that is, the rate of diffusion of the interstitial ions to the surface sharply increased. This fact cools with the reduction of distortions in the crystal lattice and the appearance of dislocation boundaries, as active diffusion paths. Desorption at higher temperatures at low deuterium concentrations in Ni should probably be attributed to its retention in highly visualized regions (Fig. 38.2c).

At doses higher than 6.5×10^{17} D/cm^2, the deuterium thermodesorption spectrum qualitatively changes, this being manifested in the appearance of a low-temperature region of deuterium desorption, which testifies to the emergence of a

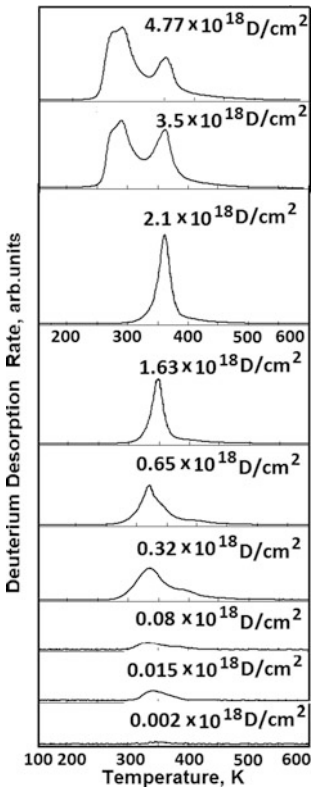

Fig. 38.3 Deuterium TD spectra from nickel samples implanted with different doses of deuterium ions: (1)—2×10^{15} D/cm^2; (2)—1.5×10^{16} D/cm^2; (3)—8×10^{16} D/cm^2; (4)—3.2×10^{17} D/cm^2; (5)—6.5×10^{17} D/cm^2; (6)—1.63×10^{18} D/cm^2; (7)—2.1×10^{18} D/cm^2; (8)—3.5×10^{18} D/cm^2; (9)—4.77×10^{18} D/cm^2

new phase state; that may be considered as a hydride formation. The conclusion about hydride formation was made on the basis of our data obtained when studying the deuterium thermodesorption spectra from Pd, Ti [22, 23], and austenitic stainless steel [24]. It was indicated there that in the deuterium thermodesorption spectrum, the hydride formation showed itself as the occurrence of lower temperature peaks.

Using the deuterium thermodesorption spectra from the Ni samples exposed to different doses, we have plotted the total amount of deuterium $C(F)$ desorbed from the sample as a function of the radiation dose F. This function is presented in Fig. 38.4.

The linear dependence of the amount of implanted deuterium on the irradiation dose value persists until the dose $F = 1.3 \times 10^{18}$ D/cm^2 is reached. Then, we observe an abrupt departure from the linearity and the tendency for attaining saturation at a dose of 1.5×10^{18} D/cm^2.

The concentrations of implanted deuterium were estimated with due regard for both the amount of metal atoms in the implanted layer and the amount of implanted deuterium. In this case, it was assumed that implanted deuterium had low diffusion mobility in the Ni cooled down to 100 K, and practically all deuterium was in the implantation layer. The estimation has shown that saturation of Ni with deuterium is

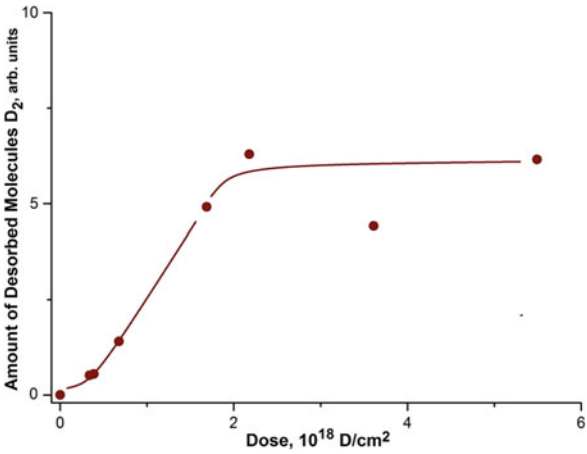

Fig. 38.4 Amount of desorbed deuterium versus irradiation dose for nickel implanted at 100 K

attained at deuterium concentration C (at.D/at.met.) ≈ 1.0. When plotting the $C(F)$ curve, it was taken into account that the Ni surface reflection coefficient for the D^+.

When considering the mechanism of phase transformations during ion bombardment, it is necessary to take into account the specific factors of ion implantation, as a very nonequilibrium process. This is, first, replacing collisions of atoms, collective processes in displacement cascades and thermal peaks, high instantaneous concentration of point defects against the background of extended dislocation formations, fluxes of point defects in the fields of internal distortions, excitation of the electronic system that affects the interatomic bond, the behavior of atoms matrix and embedded atoms. Second, it is necessary to take into account the long-range factor, when physical processes and the laws of their course are realized in an area much larger than the scales shot through by ions. These factors must be taken into account when studying the hydrodization of nickel, the formation of stable compounds in large volumes of irradiated samples.

38.4 Conclusions

The chapter considers the evolution of the structure of the Ni surface layer under the action of deuterium ions with increasing radiation dose it is shown.

Formed structure controls the rate and temperature of desorption of the implanted ions.

The concentration of diffuse paths, but not the level of the elastically deformed state of the Ni crystal lattice, causes the deuterium ions to move to the surface.

References

1. Alefeld G, Völkl J (1978) Hydrogen in metals I. Springer, Verlag, Berlin, Heidelberg, New York
2. Alefeld G, Völkl J (1978) Hydrogen in metals II. Springer, Verlag, Berlin, Heidelberg, New York
3. Wipf H (1997) Hydrogen in metals III. Properties and applications. Springer, Berlin, Heidelberg, New York
4. Gel'd PV, Ryabov RA, Kodes ES (1979) Hydrogen and metal structure imperfections (in Russian). Metallurgiya, Moskow
5. Ageyev VN, Bekman IN, Gol'tsov VA (1987) Hydrogen interaction with metals (in Russian). Nauka, Moskow
6. Lewis FA, Aladjem A (2000) Hydrogen in metal systems II. Trans Tech Publications, Pfaffikon
7. Varin RA, Czujko T, Wronski ZS (2009) Nanomaterials for solid state hydrogen storage. Springer, New York
8. Zuttel A, Borgschulte A, Schlapbach L (2008) Hydrogen as a future energy carrier. WILEY-VCH, Weinheim
9. Broom DP (2011) Hydrogen storage materials. The characterization of their storage properties. Springer, London
10. Kolachev BA (1985) Hydrogen embrittlement of metals (in Russian). Metallurgiya, Moskow
11. Gol'tsov VA (2001) Progress in hydrogen treatment of materials. Kassiopeya Ltd, Donetsk
12. Borchers C, Michler T, Pundt A (2008) Effect of hydrogen on the mechanical properties of stainless steels. Adv Eng Mater 10:11
13. Touge M, Miki T, Ikeya M (1983) Effects of X-ray irradiation on hydrogen-induced phase transformations in stainless steel. Metall Mater Trans A 14A:151
14. Neklyudov IM, Ozhigov LS, Shilyayev BA, Laptev IN, Parkhomenko AA, Morozov AN et al (2003) Hydrogen in stainless steel in-vessel components of the WWER-1000 reactor (in Russian). Voprosy At Nauki i Tekhniki, Series: Fizika radiats povr i radiats materialoved 83:47
15. Myers SM, Baskes MI, Birnbaum HK, Corbett JW, DeLeo GG, Estreicher SK et al (1992) Hydrogen interactions with defects in crystalline solids. Rev Mod Phys 64:559
16. Gavriljuk VG (2006) Austenite and martensite in nitrogen-, carbon- and hydrogen-containing iron alloys: similarities and difference. Mater Sci Eng A438–440:75
17. Kulish VG, Gunn VV, Neklyudov IM, Morozov AN, Pistryak SV, Rybalko VF (1992) Thermodesorption of deuterium implanted in Ni at T = 100 K (in Russian). Voprosy At Nauki i Tekhniki, Series: Fizika radiats povr i radiats materialoved 58–59:66
18. Ruzhitsky VV, Gribanov YA, Rybalko VF, Khazan SM, Morozov AN, Martynov IS (1989) Multi-purpose experimental installation «SKIF» (in Russian). Voprosy At Nauki i Tekhniki, Series: Fizika radiats povr i radiats materialoved 51:84
19. Voyevodin VN, Neklyudov IM (2006) Evolution of the structural-phase state and radiation resistance of structural materials. Naukova Dumka, Kiev
20. Trouble G, Zeger A (1969) Influence of crystal lattice defects on magnetization processes in ferromagnetic single crystals. In: Berner R, Kronmuller G (eds) Plastic deformation of single crystals. Mir, Moskow
21. Shalaev AM, Adalinko AA (1977) Radiation-stimulated change in the electronic structure (in Russian). Atomizdat, Moskow
22. Rybalko VF, Morozov AN, Neklyudov IM, Kulish VG (2001) Observation of new phases in Pd-D systems. Phys Lett 287A:175
23. Neklyudov IM, Morozov AN, Kulish VG (2005) Temperature ranges of hydride phase stability of the TiD system (in Russian). Materialovedeniye 11:45
24. Morozov O, Zhurba V, Neklyudov I, Mats O, Rud O, Chernyak N, Progolaieva V (2015) Structural transformations in austenitic stainless steel induced by deuterium implantation: irradiation at 100 K. Nanoscale Res Lett 10:154

Chapter 39
Formation of VI-B Group Metal Silicides from Molten Salts

Konstantin Rozhalovets, Dmytro Shakhnin, Viktor Malyshev, and Julius Schuster

39.1 Introduction

Transition metal disilicides demonstrate exceptional properties at elevated temperatures: high electrical conductivity, temperature stability, strength, and corrosion resistance. Such specific properties of disilicides are due to their crystal structure and the presence of covalent bonds M-Si and Si-Si in their structure [1]. Because of its unique properties, disilicides of VI-B group became the most intensively investigated transition metal silicides. For example, $CrSi_2$ is a promising thermoelectric material used for energy conversion at high temperature [2] or as anode material for Li-ion batteries [3]. Due to low density, $MoSi_2$ is one of the lightweight refractory materials for the aerospace engine [4]. The nanocrystal WSi_2 is used as a new nonvolatile flash memory devices (NVM) [5]. $CrSi_2$, $MoSi_2$, and WSi_2 are among the most advanced high-temperature structural materials of the next generation, especially as protective coatings for construction materials operated at high temperatures [6].

K. Rozhalovets (✉) · D. Shakhnin · V. Malyshev
Institute for Engineering & Technology, University "Ukraine", Kyiv, Ukraine
e-mail: rozhalovets@meta.ua

J. Schuster
Faculty of Chemistry, University of Vienna, Vienna, Austria
e-mail: julius.schuster@univie.ac.at

O. Fesenko, L. Yatsenko (eds.), *Nanocomposites, Nanostructures, and Their Applications*, Springer Proceedings in Physics 221,
https://doi.org/10.1007/978-3-030-17759-1_39

A large number of works regarding silicon currentless deposition in ionic melts on metals surface were performed [7]. The authors have found that the addition of NaF in the chloride-fluoride melts contributes to the binding of silicon in fluoride complexes and causes the formation of lower oxidation state of silicon ions. As silicon can penetrate only into the surface of the metal with the consequent formation of the corresponding silicide on the surface of the metal, the improvement of physicochemical properties takes place without any mechanical damage to the total volume of metal.

So, our work purpose was the synthesis of MSi_2 (M – Cr, Mo, W) disilicide coatings in molten salt and investigation of their microstructure.

39.2 Experimental

MSi_2 coatings were obtained by currentless deposition of Si onto pure metal substrate in molten KCl-NaCl-NaF-Na_2SiF_6 system containing elemental Si. Pure Cr, Mo, or W plate was immersed into the molten salt (Fig. 39.1).

Temperatures of processes were 700–800 °C. Syntheses were realized during 10–12 h under Ar atmosphere. The morphology, cross section, and the impurity of the obtained samples were investigated by scanning electron microscopy (SEM). The structure was investigated by X-ray microanalyzer JEOL Superprobe 733 (Japan) in characteristic radiation. The thermogravimetric analysis (TGA/DTA) was performed on a thermal analyzer NETZSCH STA 449 F1 Jupiter below 1000 °C in the air at a rate of 10 °C·min^{-1} to study the oxidation behavior of $CrSi_2$.

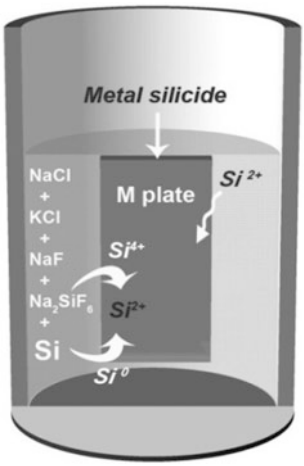

Fig. 39.1 Formation of silicide coating on the metal surface

39.3 Results and Discussion

Figure 39.2 shows SEM the cross section of the obtained coating on chromium surface (a) and the same sample in the characteristic radiation (b). Three zones can be separated: chromium substrate area, Kirkendall zone, and silicide layer. In the characteristic radiation, these zones differ from each other by the ratio of chromium and silicon in their composition. By means of elemental analysis, it was found that the Kirkendall zone contains minor impurities of Al, Na, Cl, and Fe. These imprities are a possible cause of voids formation. The thickness of silicide coating is >25 μm. Identified by X-ray analysis on the chromium surface was a formed layer of disilicide. Furthermore, authors [8–10] reported that the Si-rich phases formed on the surface of metals of VI-B group. This related with the diffusivity of metal inside the deposition layers that is different from that of silicon.

Mechanism of deposition was described earlier in [11]. Due to proportionation-disproportionation reactions between Si (Si powder) and Si^{4+} (Na_2SiF_6) ions (1), Si is deposited onto metal plate, and MSi_2 phase is formed at its surface (2). Reaction process:

$$Si + 6F^- + SiF_6^{2-} \rightarrow 2SiF_6^{4-} \tag{39.1}$$

$$4Si_6^{4-} + M \rightarrow MSi_2 + 12F^- + 2SiF_6^{2-} \tag{39.2}$$

Then, deposited Si diffuses into MSi_2 phase and reacts with the substrate. After the disilicide phase thick layer formation, Si supply to the interface is slowed down, and lower silicides are formed. So, inhomogeneity of silicide coating obtained on chromium surface (Fig. 39.3) becomes clear. Lower silicides Cr_5Si_3 and CrSi formed closer to the metallic base and $CrSi_2$ layer formed at the surface. The coating composition is presented in Table 39.1.

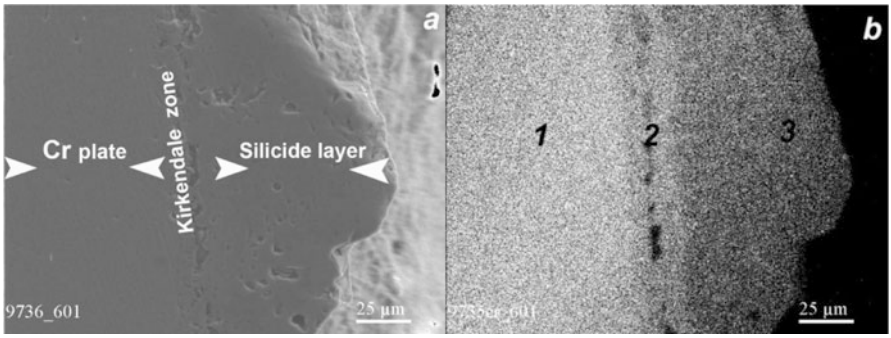

Fig. 39.2 Cross-sectional image SEM of the silicide layer deposited on Cr (**a**), in characteristic radiation of chromium (**b**)

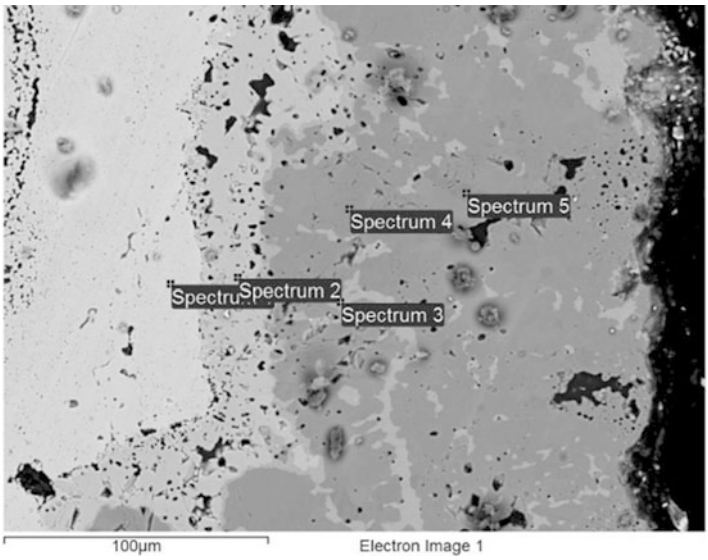

Fig. 39.3 Cross-sectional image SEM of the silicide layer deposited on Cr

Table 39.1 The composition of silicide coating obtained at chromium surface

Spectrum[a]	Si (in at. %)	Cr (in at. %)	Formula
1	–	100	Cr
2	37.19	62.81	Cr_5Si_3
3	50.21	49.79	CrSi
4	65.75	34.25	$CrSi_2$
5	65.62	34.38	$CrSi_2$

[a]Spectrum shown in Fig. 39.3.
in at. % – atomic content chromium and silicon in obtained coating

Molybdenum and tungsten disilicide (Fig. 39.4a, b) coatings are homogeneous in characteristic radiation. The thickness of obtained coatings was 10–20 μm. In both cases, only the phases of $MoSi_2$ and WSi_2 were found, respectively. It should be mentioned that adhesion of $MoSi_2$ and WSi_2 coatings to metallic substrate is higher in comparison with silicide coatings obtained on the Cr substrate.

To describe diffusion processes in M-Si system, growth constant, k^2, was calculated as follows (Eq. 39.3):

$$k^2 = \frac{d^2}{t} \tag{39.3}$$

d^2 – the thickness of silicide layer
t – the reaction time

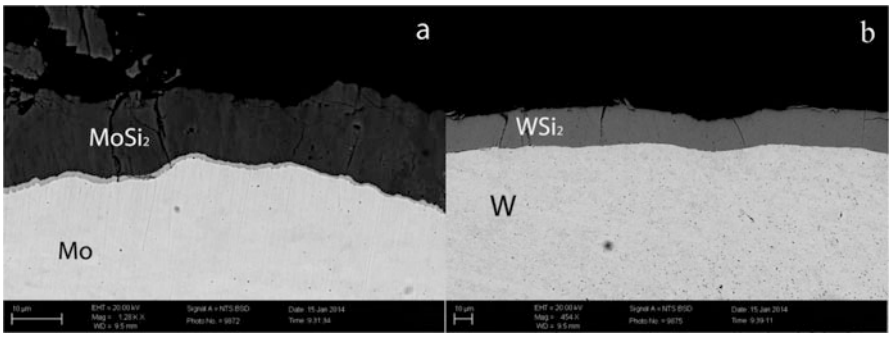

Fig. 39.4 SEM of obtained molybdenum (**a**) and tungsten (**b**) silicide coating composition according to characteristic radiation data

Table 39.2 Growth constant, k^2, of the VI-B group silicides

Formula	$k^2 \cdot 10^{-16}$ $m^2 \cdot s^{-1}$
$CrSi_2$	1512
$MoSi_2$	238
WSi_2	52.2

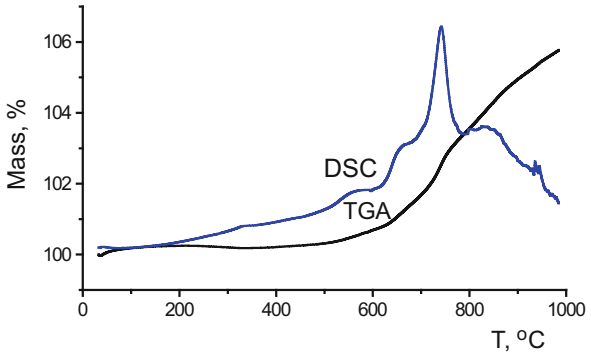

Fig. 39.5 DSC/TGA curves heated in air for $CrSi_2$

The following value of k^2 was represented in Table 39.2.

Higher diffusion rate in Cr-Si system can be related to the presence of higher concentration of vacancies at the sublattice of $CrSi_2$ compared with $MoSi_2$ and WSi_2 sublattices [12].

TGA and DSC results (Fig. 39.5) show that the mass of synthesized $CrSi_2$ to a temperature of 600–650 °C does not change. At a temperature of about 700 °C in the DSC curve observed a major exothermic peak. A slight increase in samples weight up to 5.27% was found (TGA curve). The process of oxidation occurs at a temperature of about 700 °C, which is consistent with literature data for this compound [13, 14]. Later on the surface, a protective oxide layer SiO_2 was formed.

39.4 Conclusions

MSi_2 (M – Cr, Mo, W) could be deposited at 700–800 °C on a pure metal substrate, using the disproportional reaction between Si^{4+} and the Si powder in the molten salt composed of NaCl-KCl-NaF-Na_2SiF_6.

In case of Mo and W plates siliconizing, only single phase, MSi_2, was formed. The silicide coating thickness was about 10–20 μm. The silicide coating obtained on chromium surface is inhomogeneity. Phases CrSi and Cr_5Si_3 were additionally formed.

The mechanism of coating growth during siliconizing has been suggested. It was found that there were higher growth constants (k^2) in the Cr-Si system due to the presence of higher concentration of vacancies at the $CrSi_2$ sublattice.

TGA and DSC results show that the oxidation process for chromium disilicide occurs at a temperature of about 700 °C.

Due to high oxidation resistance, obtained samples could be used as heat-resistant details and coating for devices working at elevated temperatures.

References

1. Zhang X, Wang Z, Qiao Y (2011) Prediction of stabilities, mechanical properties and electronic structures of tetragonal 3d transition metal disilicides: a first-principles investigation. Acta Mater 59:5584–5592. https://doi.org/10.1016/j.actamat.2011.05.033
2. Nonomura T, Wen C, Kato A, Isobe K, Kubota Y, Nakamura T, Yamashita M, Hayakawa Y, Tatsuoka H (2011) Thermoelectric properties of group VI metal silicide semiconductors. Phys Procedia 11:110–113. https://doi.org/10.1016/j.phpro.2011.01.039
3. Courtel FM, Duguay D, Abu-Lebdeh Y, Davidson IJ (2012) Investigation of $CrSi_2$ and $MoSi_2$ as anode materials for lithium-ion batteries. J Power Sources 202:269–275. https://doi.org/10.1016/j.jpowsour.2011.11.047
4. Yokota H, Kudoh T, Suzuki T (2003) Oxidation resistance of boronized $MoSi_2$. Surf Coat Technol 169–170:171–173. https://doi.org/10.1016/S0257-8972(03)00221-4
5. Seo KB, Lee DU, Han SJ, Kim EK, You H-W, Cho W-L (2010) Electrical properties of WSi_2 nanocrystal memory with $SiO_2/Si_3N_4/SiO_2$ tunnel barriers. Curr Appl Phys 10:e5–e8. https://doi.org/10.1016/j.cap.2009.12.002
6. Mikula M, Grančič B, Drienovský M, Satrapinskyy L, Roch T, Hájovská Z, Gregor M, Plecenik T, Čička R, Plecenik A, Kúš P (2013) Thermal stability and high-temperature oxidation behavior of Si–Cr–N coatings with high content of silicon. Surface Coatings Technol 232:349–356. https://doi.org/10.1016/j.surfcoat.2013.05.034
7. Ilyushchenko NG, Anfinigenov AI, Shurov II (1991) Interaction of metals in ionic melts. Science, Moskow
8. Suzuki RO, Ishikawa M, Ono K (2000) $MoSi_2$ coating on molybdenum using molten salt. J Alloys Compd 306:285–291. https://doi.org/10.1016/S0925-8388(00)00792-1.
9. Suzuki RO, Ishikawa M, Ono K (2002) $NbSi_2$ coating on niobium using molten salt. J Alloys Compd 336:280–285. https://doi.org/10.1016/S0925-8388(01)01879-5.
10. Tatemoto K, Ono Y, Suzuki RO (2005) Silicide coating on refractory metals in molten salt. J Phys Chem Sol 66:526–529. https://doi.org/10.1016/j.jpcs.2004.06.043
11. Gay AG, Quakernaat J (1975) A study of electroless siliconizing of nickel. J Less-Common Met 40:21–28. https://doi.org/10.1016/0022-5088(75)90178-2

12. Roy S, Paul A (2013) Diffusion in tungsten silicides. Intermetallics 37:83–87. https://doi.org/10.1016/j.intermet.2013.01.014
13. Strydom WJ, Lombaard JC, Pretorius R (1985) Thermal oxidation of the silicides $CoSi_2$, $CrSi_2$, $NiSi_2$, PtSi, $TiSi_2$ and $ZrSi_2$. Thin Solid Films 131:215–231. https://doi.org/10.1016/0040-6090(85)90142-7
14. Lu J, Yang H, Liu B, Han J, Zou G (1999) Preparation and physical properties of nanosized semiconducting $CrSi_2$ powders. Mater Chem Phys 59:101–106. https://doi.org/10.1016/S0254-0584(99)00018-8

Chapter 40
The Structure of Reinforced Layers of the Complex Method

Andrew E. Stetsko, Yaroslav B. Stetsiv, and Yaryna T. Stetsko

40.1 Introduction

It is possible to increase the resources of machine parts in several ways. Among them are economically feasible methods of surface reinforcement of parts made from low-cost structural materials.

The stability of these parts increases 2–3 times after use of the complex method.

The complex method of chemical deposition and titanium (Ti) diffusion forms on the parts made of structural steel, a reinforced layer with a thickness of 150–170 μm, and a microhardness of 12–16 GPa.

The objective was to create a new complex method of strengthening steel surfaces of friction pairs by chemical sedimentation and Ti diffusion that strengthens them for manufacture or restoration of machine parts.

40.2 Materials and Methods

Titanium is a pure, silvery gray metal that is relatively soft, but Ti alloys such as Ti-3%Al-8%V-6%Cr-4%Zr-4%Mo can be very strong and because of the relatively low density of Ti, they have a much better specific strength than many steels. Ti and its alloys are also resistant to oxidation and corrosion. Perversely, the resistance to

A. E. Stetsko (✉) · Y. B. Stetsiv
Ukrainian Academy of Printing, Lviv, Ukraine

Y. T. Stetsko
Ivan Franko National University of Lviv, Lviv, Ukraine

O. Fesenko, L. Yatsenko (eds.), *Nanocomposites, Nanostructures, and Their Applications*, Springer Proceedings in Physics 221,
https://doi.org/10.1007/978-3-030-17759-1_40

degradation arises because Ti is very reactive and rapidly forms adherent Ti dioxide, TiO_2, which prevents further environmental attack on the underlying metal [1, 2].

Titanium is light (density approximately midway between aluminum and iron) and has a high strength ratio. It has good corrosion resistance because of a protective surface TiO_2 film [3].

Prospective materials are composite materials [4, 5]. Ti matrix composites (TMCs) have a bottleneck problem of extreme brittleness and a low strengthening effect surrounding TMCs fabricated by means of powder metallurgy has recently been solved by designing network microstructures that yield both high strength and superior ductility. As such, network structured TMCs will increasingly offer materials characterized by low weight, high strength, high temperature resistance, and superior deformability. The authors systematically address the design, fabrication, microstructure, properties, modification, and toughening mechanisms of these composites, which will help us to find innovative solutions to a range of current and future engineering problems.

Developed TMCs consist of a Ti matrix containing continuous reinforcing fibers [6]. Reinforced TMCs have about twice the ultimate strength and stiffness of conventional Ti alloys, measured parallel to the fiber direction. In principle, this makes them among the most structurally efficient engineering materials known. In practice, it is often difficult to fully capitalize on the unidirectional capability of TMCs in a component, because off-axis loads are usually present. This lessens the impact of TMCs. Moreover, as is often the case, there are many other aspects of a successful material introduction than just one or two material properties (in this case UTS and E). Included are the additional considerations of the reproducibility and variability of the properties, the cost and availability of the material, and the cost of the finished components made from the material. There is also the question of design methods when the material is significantly different from those that it might replace. Because of the fiber reinforcement, TMCs are extremely anisotropic, which creates the challenge of maximizing the benefits of the longitudinal properties while minimizing the penalties associated with the lower transverse properties. When this design situation is achieved, TMCs have much to offer.

The authors [7] consider excellent resistance to high-temperature oxidation in composite materials based on Ti carbonitride and double Ti-chromium carbide with metal binders. In addition to Ti carbonitride with an aluminum nitride additive, with and without a binder are very good.

From the work analyzed, we can draw the following conclusions. The surface layers covered hard phase-type borides, nitrides, etc. It is very difficult to provide high efficiency across a large number of defects that cause a significant concentration of stress. In addition, the diffusion surface layer is thin, which is not sufficient for abrasion wear. In this regard, there is a need to use a new method for hardening machines, which would provide the opportunity to obtain hardened layers of increased thickness that were quite plastic, in the process of economic strengthening, and allowed re-recovery of such parts.

40.3 Discussion

Titanium is used to increase the corrosion, cavitation, and also surface hardness and wear resistance of steels, pig-iron, and nonferrous metals.

After Ti, a layer of Ti carbide is formed that has a high degree of microhardness, wear resistance, and corrosion resistance. The microhardness of Ti carbides is higher than that of other metal carbides – from 30,000 to 45,000 MPa. This high microhardness is also explained by the fine-grained structure. Ti carbon steel can be replaced by high-alloy stainless steels, alloys of Ti, nonferrous metals, and alloys that work under corrosion, cavitation, and mechanical wear.

After the process of Ti diffusion, thin layers (10–15 μm) are formed on the surface of the parts. These diffusion layers are destroyed because of different temperature coefficients of bulk expansion of the layer and the base metal when there is a sharp temperature change (Figs. 40.1 and 40.2). Also, these layers are not continuous.

To eliminate such disadvantages in diffusion thinning, the technology of processing by a complex method (Fig. 40.3) should be used. The method is carried out in two main stages: chemical coating and Ti diffusion [4, 8–14].

Experiments were carried out with samples made of steel (0.45%C and 1.2%C).

The samples were mechanically treated to the desired size before applying the Ni-Co-P coating. After that, they were cleaned, degreased, and digested. The chemical deposition was carried out in a water solution according to Fig. 40.1 at a temperature of 85–95°C, and solutions pH 9–9.5; deposition time was 45–

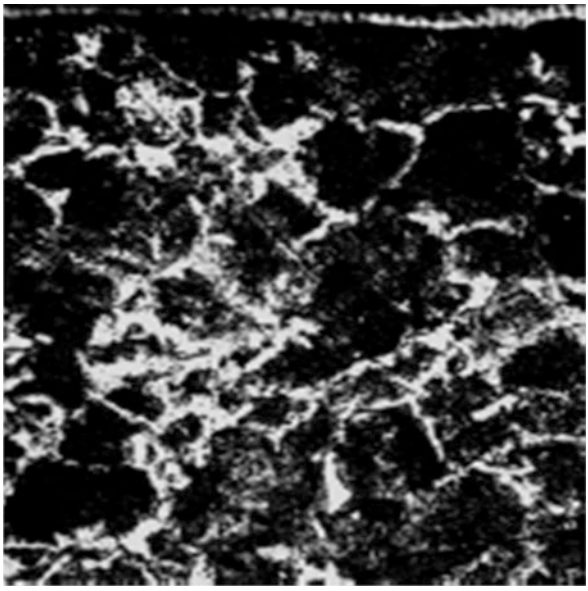

Fig. 40.1 The microstructure of a hardened diffusion layer of steel (0.45%C) for the diffusive saturation of Ti for 6 h at a temperature of 950 °C; magnification ×450

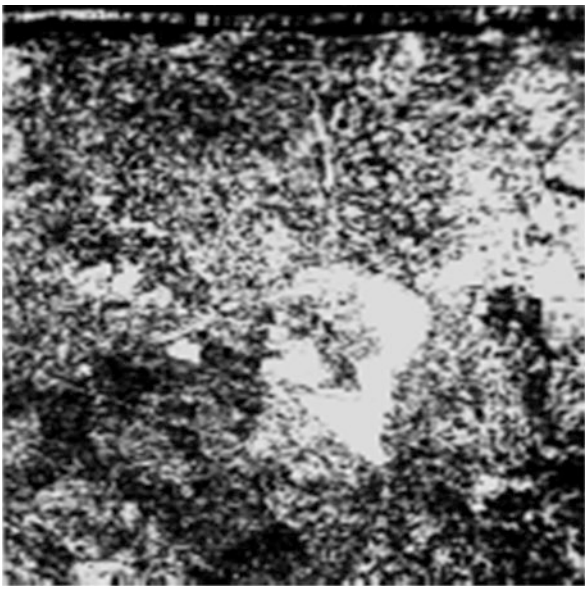

Fig. 40.2 The microstructure of a hardened diffusion layer of steel (1.2%C) for diffusive saturation of Ti for 6 h at a temperature of 950 °C; magnification ×450

Fig. 40.3 Operations of the complex method

60 min. The composition of the chemical solution for precipitation was as follows (Fig. 40.4):

Cobalt(II) sulfate $CoSO_4$ – 30 g/l
Nickel(II) sulfate $NiSO_4$ – 30 g/l
Ammonium chloride NH_4Cl – 50 g/l
Kalium hypophosphorosum $K_2H_2PO_2$ – 30 g/l
Succinic acid disodium salt hexahydrate $Na_2C_4H_4O_4$ – 100 g/l

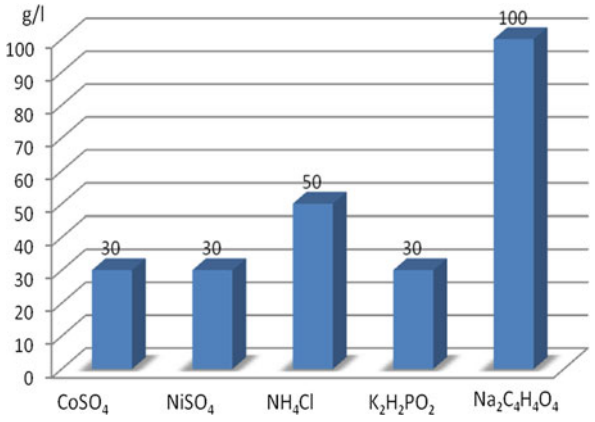

Fig. 40.4 Diagram elements of chemical sedimentation

Chemical deposition was carried out in water solutions with a loading density of 4 l/dm^2 higher than the industrial value, but allowed the time of deposition to be reduced from 120 to 60 min, at a precipitation temperature of 85–95 °C and a pH of maintained medium of 9–10.

Titanium diffusion was carried out in a retort with a fused gate for 1, 3, and 6 h in powder mixtures: ferrotitanium – 60 mass%, aluminum oxide – 35 mass%, and ammonium chloride – 5 mass%. During heating, when the temperature reached 882 °C, an hourly isothermal endurance.

Conducted microstructural studies revealed that the formed layer after complex processing (chemical sedimentation and Ti diffusion) at all endurances in all samples is uniform and continuous throughout the surface of the samples. It is much larger than the layer obtained in the same modes after normal Ti (Figs. 40.5, 40.6, 40.7, 40.8, 40.9, and 40.10) and consists of two zones: the gray upper zone 1 and the white lower zone 2 (after etching in 4% nitric acid solution). The upper composite zone 1 with small dark inclusions is thinner than zone 2 (Table 40.1).

As can be seen from Table 40.1, an increase in the holding time does not lead to a significant increase in the thickness of the composite diffusion zones. The optimal shutter speed for these steels is 3 h.

More precise analysis of diffusion layers was investigated by X-ray spectral and X-ray methods.

The diffusion layer of 0.45%C and 1.2%C steel after Ti diffusion consists mainly of carbides: for 1.2%C steel, the content of carbides is higher, because there is more carbon. In the diffusion layer of 0.45%C steel, after the Ti, there is additionally a small amount of ε-phase (Fe_2C) and α-iron.

Phase composition studies showed that after the chemical precipitation and Ti diffusion of 0.45%C and 1.2%C steel, the diffusion layer consists of two zones. The upper (outer) zone is composite. It consists of Ti carbides, small amounts of FeNi, NiTi, and Ti_2Ni intermetallic, ε-phase (Fe_2C) and solid Ni and Co in α-Fe. Also, there is a small amount of Ti oxide (TiO_2) and iron oxide (FeO; Table 40.2).

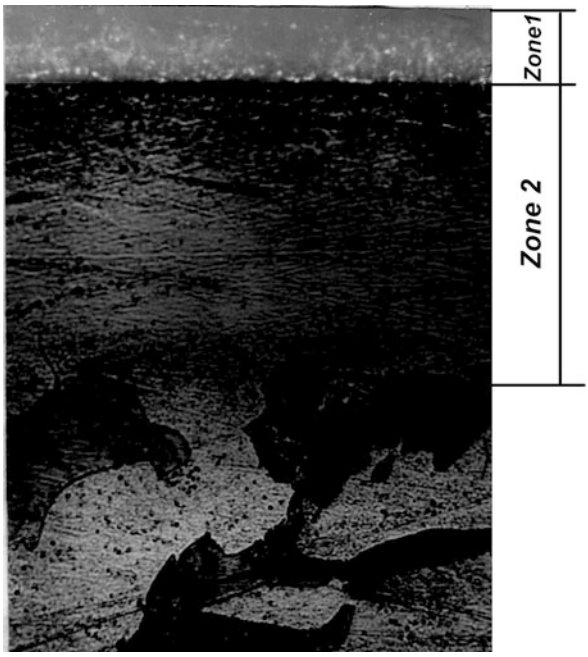

Fig. 40.5 The microstructure of the hardened diffusion layer of steel (0.45%C) of chemical Ni-Co-P coating and for the Ti diffusion modes: diffusive saturation of Ti for 1 h at a temperature of 950 °C; magnification ×450

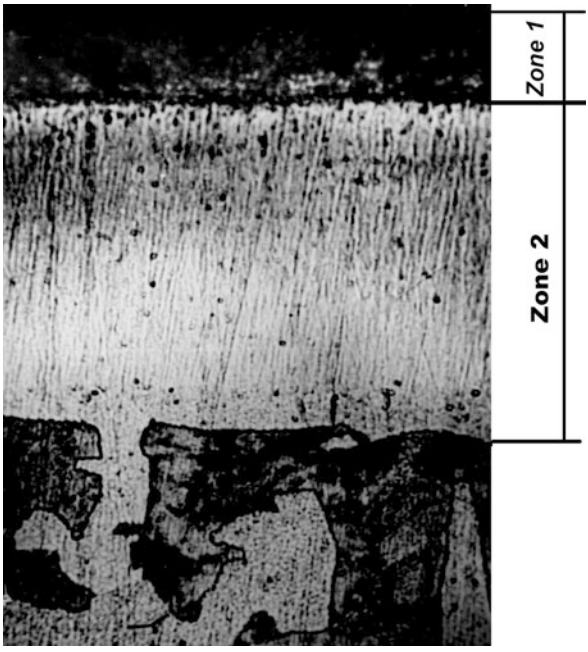

Fig. 40.6 The microstructure of the hardened diffusion layer of steel (0.45%C) of chemical Ni-Co-P coating and for the Ti diffusion modes: diffusive saturation of Ti for 3 h at a temperature of 950 °C; magnification ×450

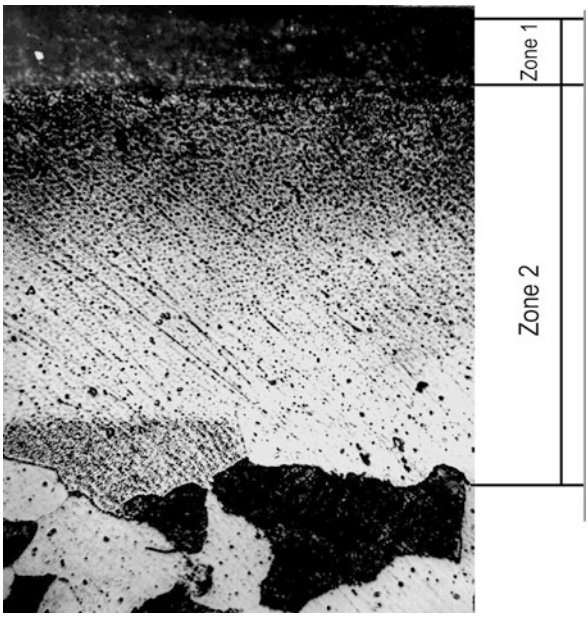

Fig. 40.7 The microstructure of the hardened diffusion layer of steel (0.45%C) of chemical Ni-Co-P coating and for the Ti diffusion modes: diffusive saturation of Ti for 6 h at a temperature of 950 °C; magnification ×450

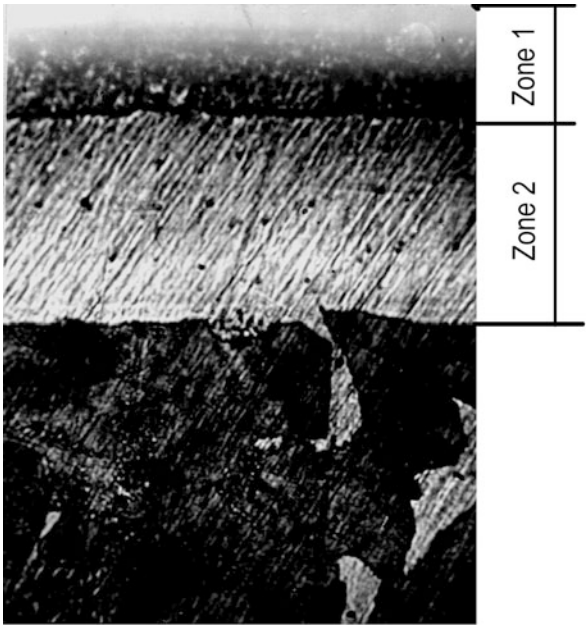

Fig. 40.8 The microstructure of the hardened diffusion layer of steel (1.2%C) of chemical Ni-Co-P coating and for the Ti diffusion modes: diffusive saturation of Ti for 1 h at a temperature of 950 °C; magnification ×450

The second zone of the diffusion layer is homogeneous and consists of a solid solution of Ni and Co in α-Fe. But here there is a small amount of Ti carbide, which confirms the presence of ultrafine inclusions of TiC (Table 40.2).

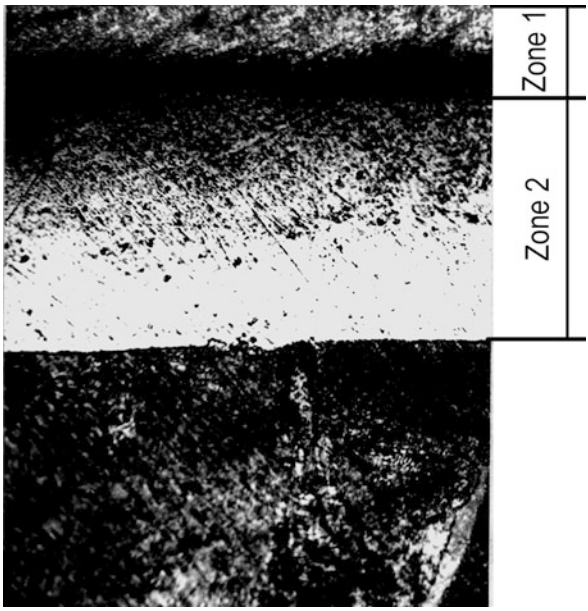

Fig. 40.9 The microstructure of the hardened diffusion layer of steel (1.2%C) of chemical Ni-Co-P coating and for the Ti diffusion modes: diffusive saturation of Ti for 3 h at a temperature of 950 °C; magnification ×450

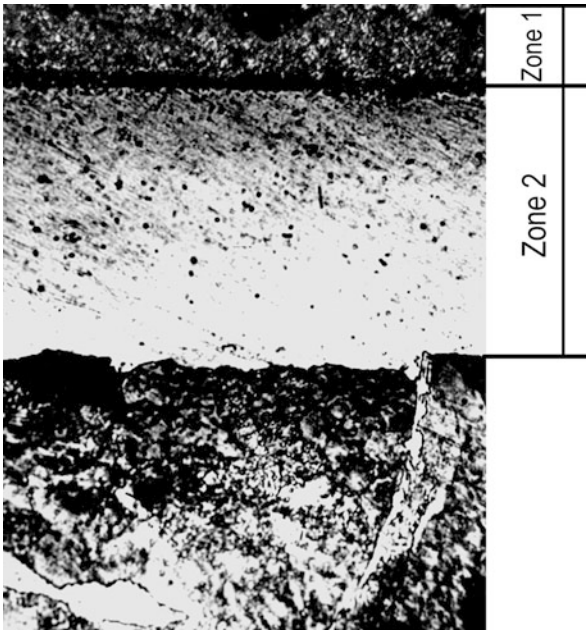

Fig. 40.10 The microstructure of the hardened diffusion layer of steel (1.2%C) of chemical Ni-Co-P coating and for the Ti diffusion modes: diffusive saturation of Ti for 6 h at a temperature of 950 °C; magnification ×450

Table 40.1 Dependence of the thickness of the diffusion layers on the time of diffusion saturation with a complex method of strengthening

Material	Time of diffusion saturation (h)	Thickness of the diffusion layers (μm)	
		Zone 1	Zone 2
Steel (0.45%C)	1	28	131
	3	30	154
	6	30	157
Steel (1.2%C)	1	37	92
	3	39	106
	6	39	110

Table 40.2 The phases of diffusion layers of 0.45%C and 1.2%C steel after Ti diffusion and after the complex method

Material	Method of hardening	Phases
Steel (0.45%C)	Ti diffusion, 6 h	TiC, ε-Fe_2C, α-Fe
Steel (1.2%C)	Ti diffusion, 6 h	TiC
Steel (0.45%C), zone 1	Ni-Co-P sedimentation and Ti diffusion for 1 h	TiC, α-Fe, Ti_2Ni, FeNi, NiTi, ε-Fe_2C
Steel (1.2%C), zone 1	Ni-Co-P sedimentation and Ti diffusion for 1 h	TiC, α-Fe, Ti_2Ni, FeNi, NiTi, ε-Fe_2C, TiO_2

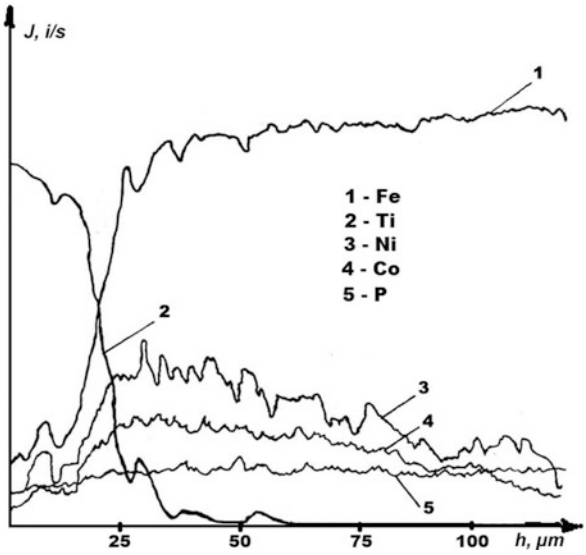

Fig. 40.11 Diffusion concentration distribution of the element diffusion layer of hardened diffusion layer steel (0.45%C) of chemical Ni-Co-P coating and for the Ti diffusion modes: diffusive saturation of Ti for 3 h at a temperature of 950 °C

Data from X-ray spectral studies at the "Cameca" plant (Figs. 40.11 and 40.12). There is only a quantitative difference in the percentage of Ti in the upper zone of the layer, which is somewhat higher for 1.2%C steel than for 0.45%C steel. This is confirmed by the data on microhardness, where the microhardness of the first zone of 1.2%C steel is greater than for 0.45%C steel (owing to more Ti carbides).

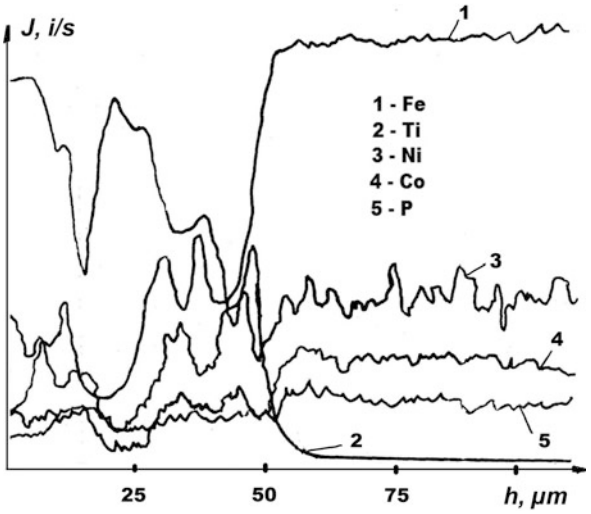

Fig. 40.12 Diffusion concentration distribution of the element diffusion layer of hardened diffusion layer steel (1.2%C) of chemical Ni-Co-P coating and for the diffusion Ti modes: diffusive saturation of Ti for 3 h at a temperature of 950 °C

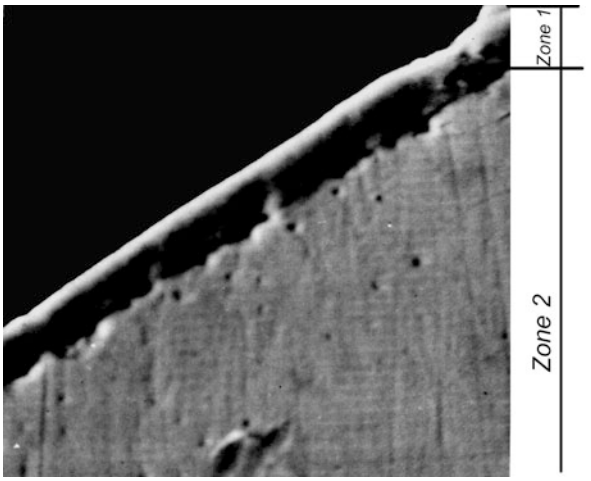

Fig. 40.13 The microstructure of a hardened diffusion layer of steel (0.45%C) for the diffusive saturation of Ti for 6 h at a temperature of 950 °C; magnification ×1200

The thickness of the first composite zone in 0.45%C steel (due to less carbon) is less than that of 1.2%C steel. The thickness of the second zone – the area of the solid solution in 0.45%C steel is greater than in the 1.2%C steel, because a smaller amount of carbon makes it possible for Ni and Co to diffuse deeper into the depth during a period when the temperature of the medium is greater than the critical point. In addition, a large amount of carbon from this zone goes to the carbide formation in zone 1.

Patterns of the formation of diffusion layers of 0.45%C and 1.2%C steel are shown in the photo taken on an electron microscope (Figs. 40.13, 40.14, 40.15, 40.16, 40.17, and 40.18).

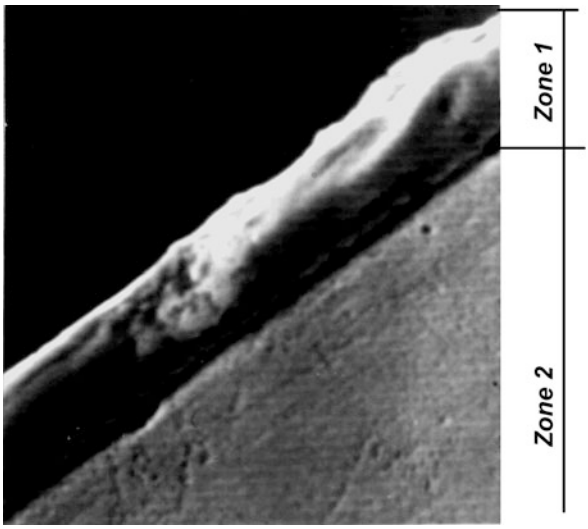

Fig. 40.14 The microstructure of a hardened diffusion layer of steel (1.2%C) for the diffusive saturation of Ti for 6 h at a temperature of 950 °C; magnification ×1200

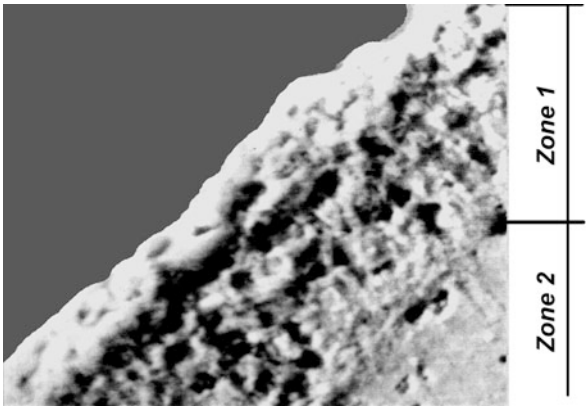

Fig. 40.15 The microstructure of a hardened diffusion layer of steel (0.45%C) of chemical Ni-Co-P coating and the diffusive saturation of Ti for 1 h at a temperature of 950 °C; magnification ×1200

Studies have shown that after 3 h Ti diffusion changes in morphology and a significant increase in the strengthened zone 1 is not observed.

The percentage of the elements of the diffusion layer of 0.45%C and 1.2%C steel is shown in Table 40.3.

Microhardness data are presented in the graphs shown in Figs. 40.19 and 40.20. The microhardness of zone 1 indirectly indicates that it contains a large percentage of Ti carbides. It ranges from 12 to 18 GPa, depending on the content of the carbide component in the local area of the zone.

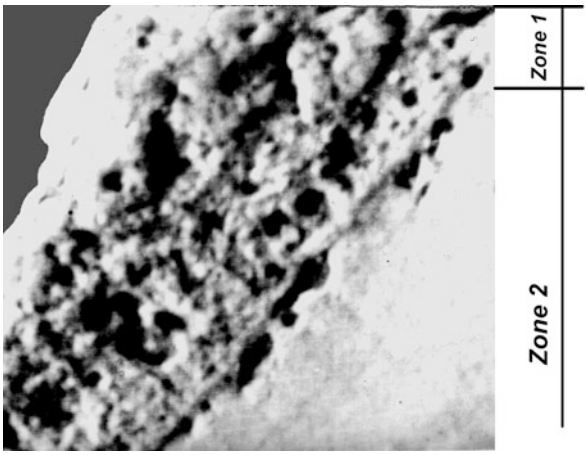

Fig. 40.16 The microstructure of a hardened diffusion layer of steel (1.2%C) of chemical Ni-Co-P coating and the diffusive saturation of Ti for 1 h at a temperature of 950 °C; magnification ×1200

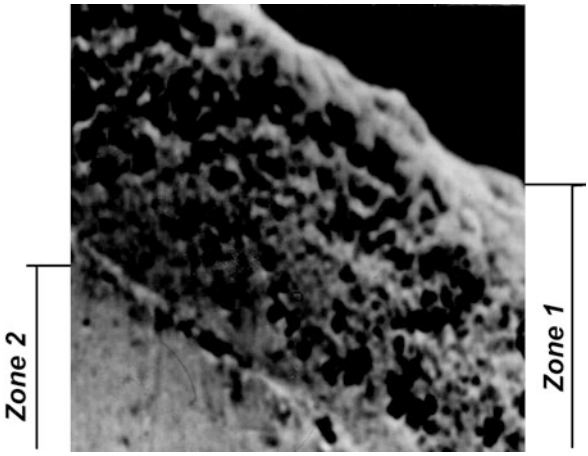

Fig. 40.17 The microstructure of a hardened diffusion layer of steel (0.45%C) of chemical Ni-Co-P coating and the diffusive saturation of Ti for 6 h at a temperature of 950 °C; magnification ×1200

The microhardness of the lower zone (zone 2) is much smaller than in the first zone. For 1.2%C steel it is 3–5 GPa and for 0.45%C steel it is 3–2.5 GPa, indicating the presence of solid solution. Ti carbides in the second zone are very small or they are completely absent.

40.4 Conclusions

1. The implementation of a complex method for improving the quality characteristics of the working surfaces of machine parts made of medium carbon and high carbon steels allows reinforced diffusion layers of a composite structure to be obtained, which can be clearly divided into zones.

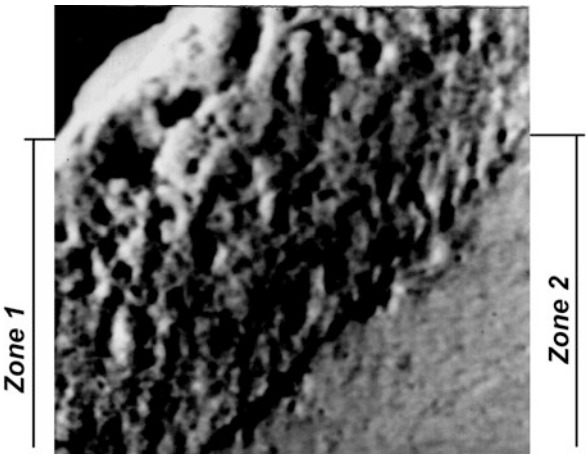

Fig. 40.18 The microstructure of a hardened diffusion layer of steel (1.2%C) of chemical Ni-Co-P coating and the diffusive saturation of Ti for 6 h at a temperature of 950 °C; magnification ×1200

Table 40.3 Quantitative analysis of diffusion layers of 0.45%C and 1.2%C steel after Ti diffusion and the complex method

Material	Method of hardening	Quantities of elements
Steel (0.45%C), diffusion layer	Ti diffusion, 6 h	70%Ti, 4%Fe
Steel (1.2%C), diffusion layer	Ti diffusion, 6 h	80%Ti, 8%Fe
Steel (0.45%C), zone 1	Ni-Co-P sedimentation and Ti diffusion for 1 h	60%Ti, 20%Fe, 1%Ni, 1.5%Co, 0.5%P
Steel (1.2%C), zone 1	Ni-Co-P sedimentation and Ti diffusion for 1 h	70%Ti, 30%Fe, 1%Ni, 1%Co, 1%P
Steel (0.45%C), zone 2	Ni-Co-P sedimentation and Ti diffusion for 1 h	85%Fe, 2%Ni, 2%Co, 1%P
Steel (1.2%C), zone 2	Ni-Co-P sedimentation and Ti diffusion for 1 h	95%Fe, 1%Ni, 1%Co, 0.5%P

2. The optimal mode for any of these steels is the shutter speed for 3 h at a temperature of 950 °C, which, in comparison with the classical option (diffusion titanification for 10 h), provides considerable advantages, namely: time-saving, energy-saving, and the avoidance of significant growth of the grain of the core, thus avoiding additional heat treatment.
3. The noncarbonated zone on the samples is not observed, which allows you to work under conditions of corrosion–mechanical wear, as there is no danger of compression of the diffusion layer.
4. A large number of Ti carbides in the composite zone 1 were found, in addition to a homogeneous zone of solid solution (zone 2), in which there is a relaxation of deformation stresses with a possible change in the load sign on the friction surface in a rigid wear regime (for example, a reversible friction mode), which provides the ability to apply such composite layers under conditions of corrosion–mechanical wear.

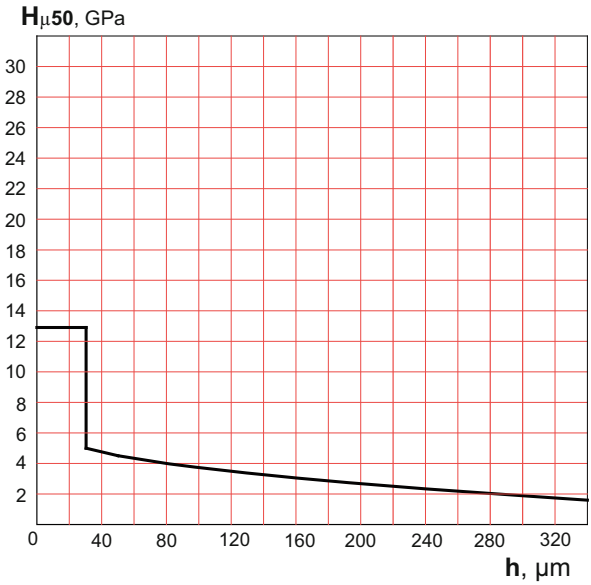

Fig. 40.19 Microhardened layer of steel (0.45%C) obtained for the hardened diffusion layer of chemical Ni-Co-P coating and for the Ti diffusion modes: diffusive saturation of Ti for 6 h at a temperature of 950 °C

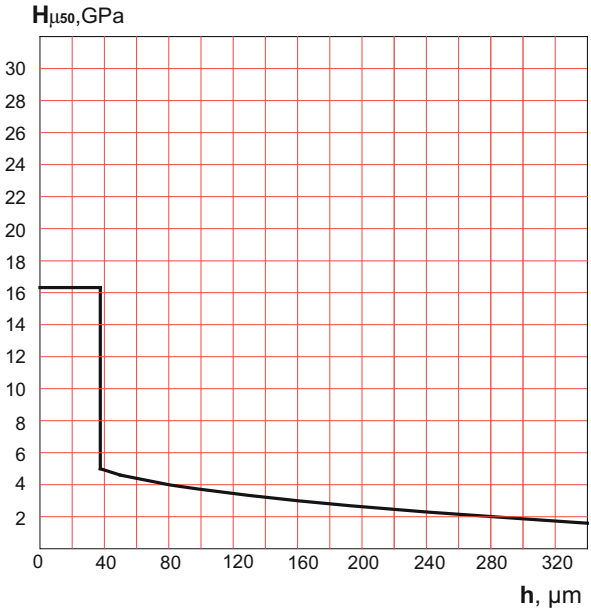

Fig. 40.20 Microhardened layer of steel (1.2%C) obtained for the hardened diffusion layer of chemical Ni-Co-P coating and for the Ti diffusion modes: diffusive saturation of Ti for 6 h at a temperature of 950 °C

References

1. Thomas JB (2016) Titanium. In: White W (ed) Encyclopedia of geochemistry. Encyclopedia of earth sciences series. Springer, Cham
2. Baker I (2018) Titanium. In: Fifty materials that make the world. Springer, Cham
3. Meetham GW, Van de Voorde MH (2000) Titanium. In: Materials for high temperature engineering applications. Engineering materials. Springer, Berlin, Heidelberg
4. Stetsko A (2016) Composite coatings formed by complex methods of surface hardening. In: Fesenko O, Yatsenko L (eds) Nanophysics, nanophotonics, surface studies, and applications. Springer proceedings in physics, vol 183. Springer, Cham
5. Huang L et al (2017) Discontinuously reinforced titanium matrix composites. Microstructure design and property optimization, 1st edn. Jointly published with National Defense Industry Press, Beijing, ISBN 978-981-10-4449-6, VII, 178 p 138 illus
6. Lütjering G, Williams JC (2007) Titanium matrix composites. In: Titanium. Engineering materials, processes. Springer, Berlin/Heidelberg
7. Umanskii AP, Lavrenko VA, Chuprov SS et al (2006) High-temperature oxidation of composites based on titanium carbonitride and double titanium-chromium carbide. Refract Ind Ceram 47:246. https://doi.org/10.1007/s11148-006-0099-5
8. Stetsko AE (2016) Composite coatings are formed by complex methods. Universal J Mater Sci 4:75–81. https://doi.org/10.13189/ujms.2016.040401
9. Stetsko AE (2017) Effect of chemical vapor deposition on the morphology of the nanocomposite layer in the complex method. In: Fesenko O, Yatsenko L (eds) Nanophysics, nanomaterials, interface studies, and applications. NANO 2016. Springer Proceedings in Physics, vol 195. Springer, Cham
10. UA 112714, C23C 22/63, C23C 22/52, 10 Oct 2016
11. UA 112601, C23C 22/63, C23C 22/52, 26 Sept 2016
12. UA 112605, C23C 22/05, C23C 10/40, C23C 10/32, C23C 10/02, 26 Sept 2016
13. UA 117077, C23C 10/02, C23C 10/40, 11 June 2018
14. UA 115383, C23C 10/26, C23C 22/60, 25 Oct 2016

Chapter 41
Technology and the Main Technological Equipment of the Process to Obtain N_4HNO_3 with Nanoporous Structure

A. E. Artyukhov and N. O. Artyukhova

41.1 Introduction

Porous ammonium nitrate (PAN) is an essential component of the industrial explosives without triton (ammonium nitrate/fuel oil, ANFO in particular) [1–3]. The quantity of fuel oil, efficiently absorbed and retained by PAN, depends on the sizes, the number, and the volume of pores, the configuration of the pores network on the surface and the pre-surface layers of a granule [4–6]. More specifically:

- A size of pores: a minimal size must be commensurate with the size of the fuel oil molecule.
- The number and the volume of pores must provide the proper absorbing ability of a granule.
- The configuration of the pores network: the surface straight pores available for the free penetration of fuel oil into a granule and the tortuous deep pores available for efficient binding of fuel oil inside a granule.

The nanoporous structure is formed at the stage of thermal processing after the moisturization of a granule [7]. Therefore, it is important to create the conditions favorable for the uniform contact of the drying agent and granules in the active hydrodynamic regime. The main challenge of this stage is that the turbulization of the drying agent flow and its vortex motion (theoretical description of this process was shown in works [8–10], program realization of calculation – in works [11–13]) may lead to the reduced strength of the granule's core and its possible destruction. After the destruction, such granules are still able to absorb fuel oil (ANFO is made

A. E. Artyukhov (✉) · N. O. Artyukhova
Processes and Equipment of Chemical and Petroleum-Refineries Department, Sumy State University, Sumy, Ukraine
e-mail: a.artyukhov@pohnp.sumdu.edu.ua

O. Fesenko, L. Yatsenko (eds.), *Nanocomposites, Nanostructures, and Their Applications*, Springer Proceedings in Physics 221,
https://doi.org/10.1007/978-3-030-17759-1_41

from any nonstandard granules) [14]. However, when transporting, almost all of fuel oil is discharged from the granule; it flows down from it. This fact significantly reduces the ANFO explosive properties [15].

The aim of the work is to review and to analyze the main author's constructions of the vortex granulators that can be applied for thermal processing of the common ammonium nitrate granules after moisturizing (as well as during moisturizing directly in the workspace of the vortex granulator).

41.2 The Review and the Analysis of the Main Constructions of Vortex Granulators

The main objective of the constructive solutions on forming the directional drying agent flow is to stabilize the motion of the two-phase vortex flow of common ammonium nitrate granules after the moisturization. This objective is achieved through the use of various combinations of gas distribution and stabilizing devices. Such devices installed serve to distribute damp granules uniformly within the workspace of the vortex granulator. Herewith, the uniformity of the vortex fluidized bed increases, and the distribution of granules in fractions becomes more precise. This leads to the provision of the necessary contact time for the drying agent and granules (the minimal drying time without the destruction of the granule's core).

The main disadvantages of the existing methods of the granule's structure formation in the fluidized bed apparatuses and the ways to constructively elimination of these disadvantages.

Designation of flows: I, gas flow for ejection of granules; II, liquid material; III, drying agent; IV, drying agent for additional contact with the granules; V, spent drying agent; and VI, granules.

Granulation of the intermediate fraction product and the complete formation of the commodity granule structure are carried out in the same workspace of the apparatus. The impossibility of processing the intermediate fraction product for successful drying and crystallization before recontacting the spraying liquid and further growing to the commodity fraction (with a simultaneous contact of commodity granules with the drying agent for the final structure formation) leads to the irregular fractional processing of granules and obtaining of the final product with the heterogeneous granule composition of lower quality. Collision of granules of different fractions with the nonfinal surface and further agglomeration of single granules also contribute to the violation of the commodity granule's shape, which increases its polydispersity and reduces the quality (Fig. 41.1).

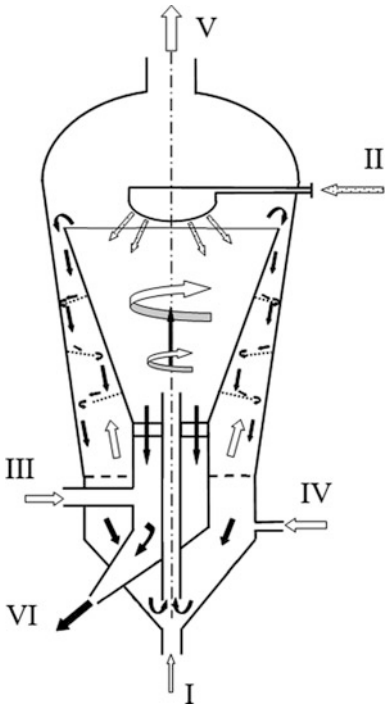

Fig. 41.1 A vortex granulator with a sectioned annulus [16]

The less intensive vortex motion of the gas flow and, consequently, the absence of the spiral-like motion of granules are observed outside the location of the accelerating elements of the vortex gas distribution hub on the periphery of the lower part of the additional cone. Granules from this zone are characterized by the disordered motion or even absence of it. The nonuniform motion of granules in the zone above the distribution hub (the so-called fluidized bed active zone) with the maximum intensive heat exchange leads to possible underheating of granules and sudden drop in the formation of the solid layer on the granule after filming with solution or melt. This results in the destroyed shape of the granule (some areas with solution or melt film do not have enough time to harden and break away from the granule) and the lower degree of monodispersity of the commodity granules (Fig. 41.2).

The heat-transfer agent is supplied in the zone where the granules are simultaneously removed. Herewith, the removal of granules is irregular, which prevents the uniform distribution of the heat-transfer agent before it enters the vortex gas distribution hub. The absence of the heat-transfer agent redistributor, which is at the same time the redistributor for the discharged granules, leads to the fact that the heat-transfer agent does not pass through the entire vortex gas distribution hub and its peripheral part particularly. It is followed by the formation of the stagnant zones in the lower part of the workspace (on the periphery mostly) and the absence of the intensive side mix in the same part of the apparatus. The stagnant zones and the

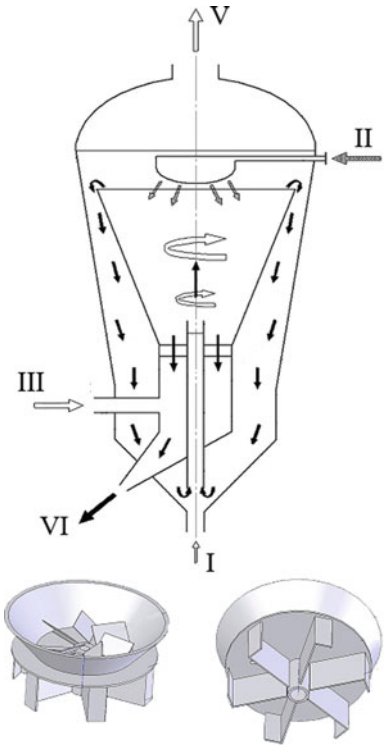

Fig. 41.2 A vortex granulator with a two-zone swirler [17]

absence of the side mix lead to the temperature differences in the fluidized bed that reduce the uniformity of solid filming with solution or melt on the granule's surface and decrease strength of the final product and the degree of its monodispersity (Fig. 41.3).

Inside the inner cone, the maximum length of the granules' trajectory corresponds to the maximum height of the cone. Since the trajectory of granules does not exceed the maximum length, there occurs a drastic reduction of the residence time of granules in the cone, which results in less intensive crystallization and drying. Thus, the structure of granules is not completely formed, the quality of the final product is lower, and the apparatus is not efficient enough (Fig. 41.4).

The maximum length of the fine granules' trajectory corresponds to the maximum height of the annulus in its location. Considering that the heat-transfer agent flows in laminar conditions and does not resist falling of the fine granules, the trajectory of their motion does not exceed the maximum length, which results in the reduced residence time of granules in this zone and, thus, less intensive heat and mass exchange processes (Fig. 41.5).

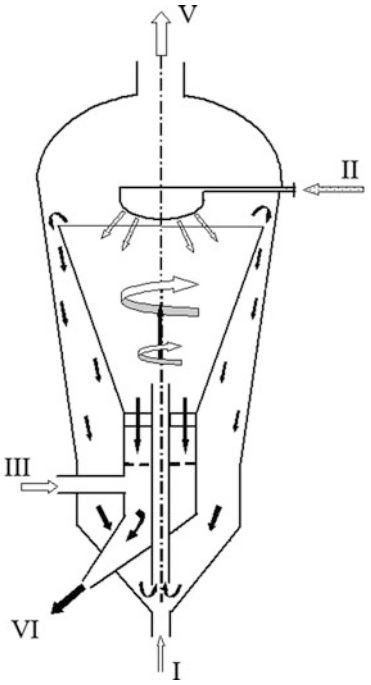

Fig. 41.3 A vortex granulator with a stabilization zone for the drying agent upward flow [18]

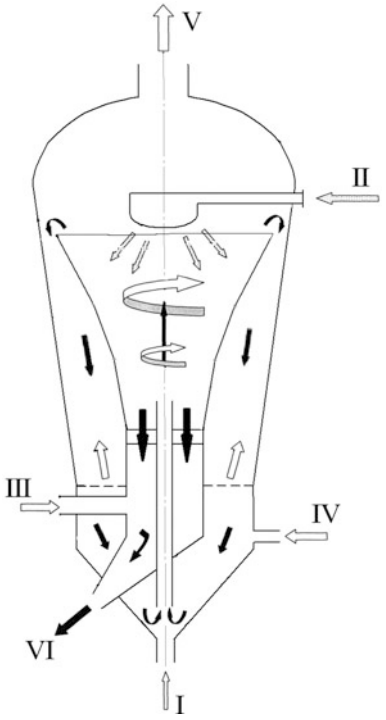

Fig. 41.4 A vortex granulator with a drying agent re-distributor in an annulus [19]

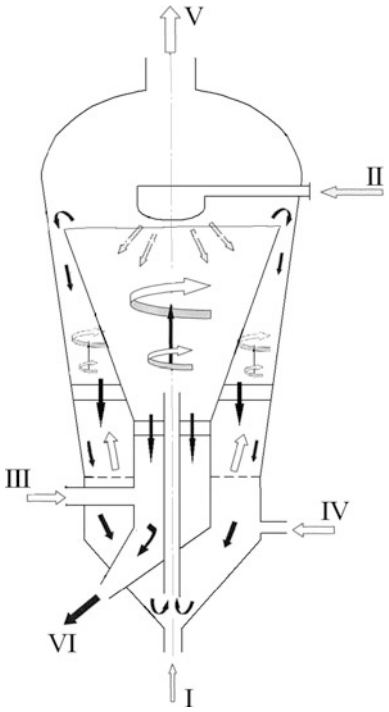

Fig. 41.5 A vortex granulator with double guides of the drying agent in the annulus [20]

41.3 An Influence of the Constructions of Vortex Granulators on the PAN Granules' Structure

The above-described constructional solutions make the uniform contact of the drying agent with granules possible. As a result, the formation of the nanoporous structure of granules becomes controlled and predicted. Then, depending on the selected operational regime of the granulator and temperature and moisture characteristics of the drying agent, we can obtain various configurations of nanopores:

- Short-term thermal processing with the high-temperature drying agent flow in the active hydrodynamic regime – straight shallow pores (Fig. 41.6)
- Long-term thermal processing with the high-temperature drying agent flow in the active hydrodynamic regime – straight deep pores (Fig. 41.7)
- Short-term thermal processing with the low-temperature drying agent flow in the active hydrodynamic regime – tortuous shallow pores (Fig. 41.8)
- Short-term thermal processing with the high-temperature drying agent flow in the active hydrodynamic regime – tortuous deep pores (Fig. 41.9)
- A combination of different regimes for thermal processing with the drying agent of various temperature potentials (for instance, in the apparatus depicted in Fig. 41.2) – surface straight-line macropores and deep tortuous meso- and micropores in the pre-surface layers of the granule (Fig. 41.10)

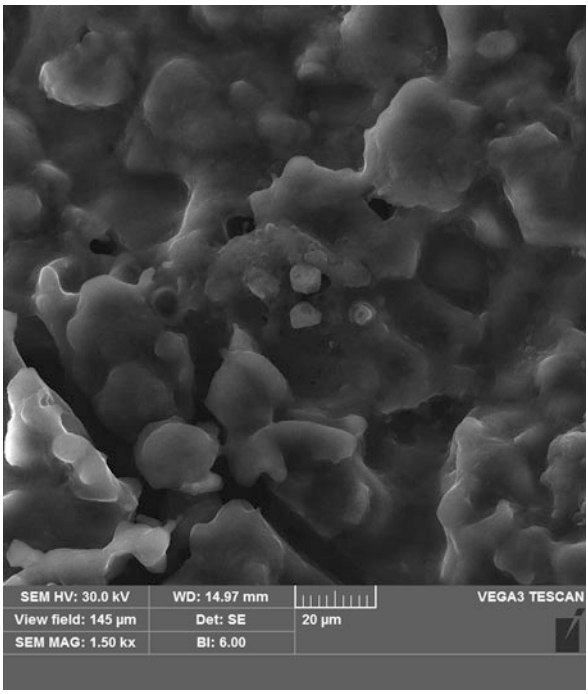

Fig. 41.6 PAN sample (short-term thermal processing with the high-temperature drying agent flow in the active hydrodynamic regime)

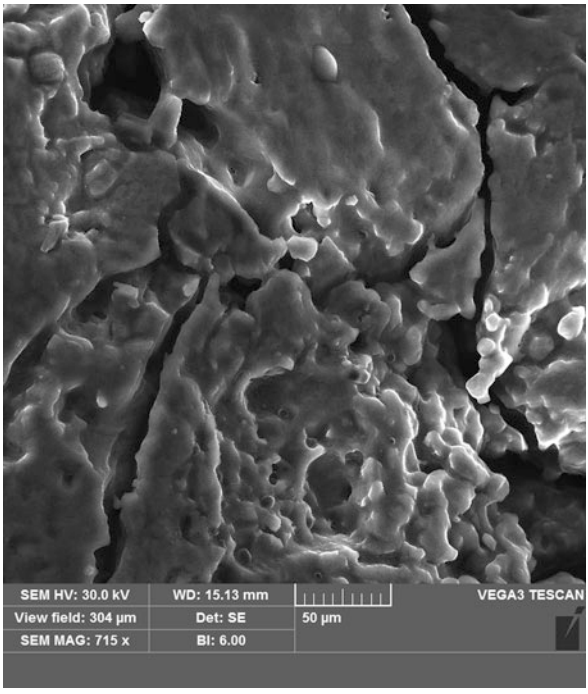

Fig. 41.7 PAN sample (long-term thermal processing with the high-temperature drying agent flow in the active hydrodynamic regime)

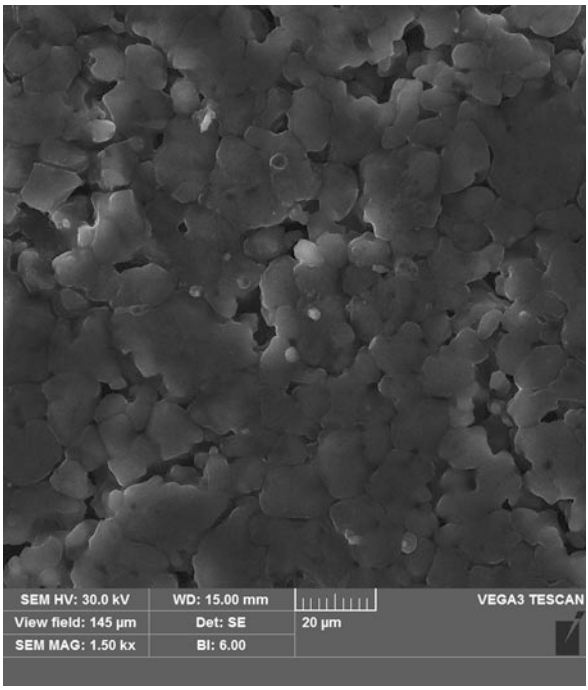

Fig. 41.8 PAN sample (short-term thermal processing with the low-temperature drying agent flow in the active hydrodynamic regime)

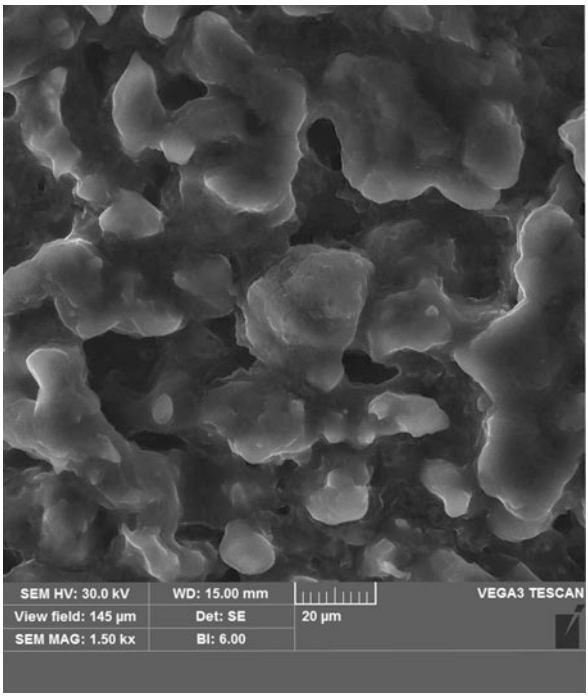

Fig. 41.9 PAN sample (long-term thermal processing with the low-temperature drying agent flow in the active hydrodynamic regime)

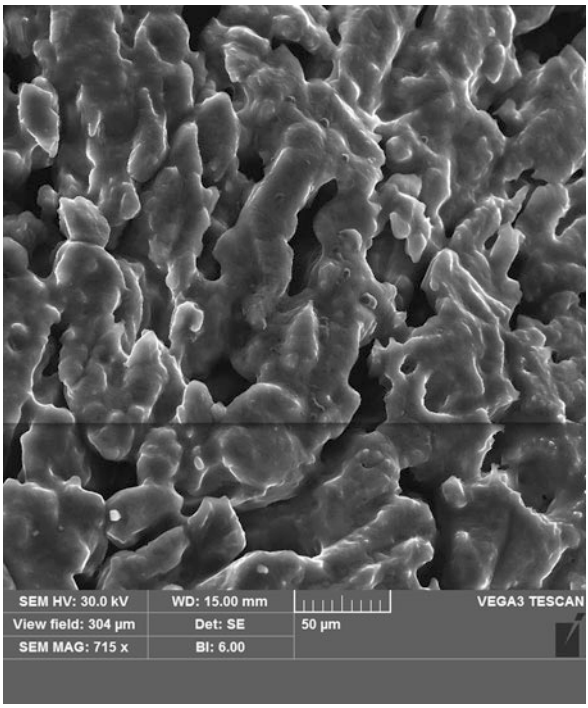

Fig. 41.10 PAN sample (a combination of different regimes for thermal processing with the drying agent of various temperature potentials)

41.4 Conclusions

The results of investigations on the crystal structure of PAN granules show that the above-described methods of the nanopores formation can be further applied in the industrial production. Moreover, the developed network of granules enables the standard quantity of fuel oil (in terms of the granule's volume) to be absorbed and bound during the transportation. The preserved strength properties of granules make it possible to have the same volume of nanopores and stable detonation characteristics. The selection of the certain construction of the granulator (or a possible combination of several constructions) can be predetermined by the temperature and moisture characteristics of the drying agent (or rather minimum costs for achieving the proper temperature potential under minimal moisture) and the capacities of the granulation unit for the heat utilization and recuperation.

References

1. Lipinska K et al (2005) Demilitarized propellants as ingredients in commercial explosives. European federation of explosives engineers: Brighton conference proceedings, Brighton, pp 493–498

2. Zygmunt B, Buczkowski D (2007) Influence of ammonium nitrate prills' properties on detonation velocity of ANFO. Propellants Explos Pyrotech 32(5):41–414
3. Erode GM (2013) Ammonium nitrate explosives for civil applications: slurries, emulsions and ammonium nitrate fuel oils. Wiley-VCH Verlag & Co, Weinheim
4. Artyukhov AE, Sklabinskyi VI (2016) 3D nanostructured porous layer of ammonium nitrate: influence of the moisturizing method on the layer's structure. J Nano- Electron Phys 8(4):04051–1–04051–5
5. Artyukhov AE, Sklabinskyi VI (2016) Thermodynamic conditions for obtaining 3D nanostructured porous surface layer on the granules of ammonium nitrate. J Nano- Electron Phys 8(4):04083–1–04083–5
6. Artyukhov AE, Sklabinskyi VI (2017) Investigation of the temperature field of coolant in the installations for obtaining 3D nanostructured porous surface layer on the granules of ammonium nitrate. J Nano- Electron Phys 9(1):01015–1–01015–4
7. Artyukhov AE, Voznyi AA (2016) Thermodynamics of the vortex granulator's workspace: the impact on the structure of porous ammonium nitrate. In: Abstracts of the 6th international conference nanomaterials: application & properties (NAP-2016), vol 5(2), p 02NEA01
8. Artyukhov AE, Sklabinskyi VI (2013) Experimental and industrial implementation of porous ammonium nitrate producing process in vortex granulators. Nauk Visnyk Nats Hirnychoho Univ 6:42–48
9. Artyukhov AE, Sklabinskyi VI (2015) Theoretical analysis of granules movement hydrodynamics in the vortex granulators of ammonium nitrate and carbamide production. Ch&ChT 9(2):175–180
10. Artyukhov AE, Sklabinskyi VI (2015) Hydrodynamics of gas flow in small-sized vortex granulators in the production of nitrogen fertilizers. Ch&ChT 9(3):337–342
11. Artyukhov A et al (2016) Application software products for calculation trajectories of granules movement in vortex granulator. CEUR workshop proceedings (1761), p 363–373
12. Artyukhov A et al (2016) Software for calculation of vortex type granulation devices. CEUR workshop proceedings (1761), p 374–385
13. Artyukhov AE et al (2015) Classification and separation of granules in vortex granulators. Chem Pet Eng 51(5–6):311–318
14. Weber PW et al (2015) Numerical simulation of a 100-ton ANFO detonation. Shock Waves 25(2):127–140
15. Artyukhov AE (2016) Kinetics of heating and drying of porous ammonium nitrate granules in the vortex granulator. In: Abstracts of the 6th international conference nanomaterials: application & properties (NAP-2016), vol 5(2), p 02NEA02
16. Artyukhov AE et al (2016) Sposib oderzhannya hranul u zvazhenomu shari ta prystriy dlya yoho zdiysnennya (Method for producing granules in a suspended layer and a device for its implementation). UA Patent 110992, 25 Mar 2016
17. Artyukhov AE et al (2016) Prystriy dlya hranulyuvannya u vykhrovomu zvazhenomu shari (Device for granulation in the vortex suspended layer). UA Patent 111592, 10 Nov 2016
18. Artyukhov AE et al (2016) Vykhrovyy hranulyator zvazhenoho sharu (Suspended layer vortex granulator). UA Patent 112293, 12 Dec 2016
19. Artyukhov AE et al (2017) Vykhrovyy hranulyator zvazhenoho sharu (Suspended layer vortex granulator). UA Patent 114517, 3 Mar 2017
20. Artyukhov AE et al (2017) Vykhrovyy hranulyator zvazhenoho sharu (Suspended layer vortex granulator). UA Patent 114521, 3 Mar 2017

Chapter 42
Study of Structural Changes in a Nickel Oxide Containing Anode Material During Reduction and Oxidation at 600 °C

Ye. V. Kharchenko, Z. Ya. Blikharskyy, V. V. Vira, and B. D. Vasyliv

42.1 Introduction

Fuel cells are electrochemical devices that transform the chemical energy of fuel directly into electric energy or heat, with a high electrical efficiency and a low level of emission. A solid oxide fuel cell (SOFC) seems to be the most versatile as compared to other types of fuel cells. It may use all known types of fuel and is only slightly affected by the purity of fuel. Typical SOFC anodes are fabricated from a nickel oxide/yttria-stabilized zirconia (YSZ) ceramic composite and are reduced in situ, during operation, to form a YSZ–Ni cermet. However, the nickel component of the anode may be reoxidized in a SOFC for various reasons [1–3]. In order to use a reoxidized cell, it must be reduced once more. For this reason, SOFC anode material should be resistible against cyclic reduction/oxidation (redox) action.

It is known that oxygen from air may react with the remaining hydrogen followed by formation of high-pressure water vapor atmosphere in small pores of the anode material. There is the contradictory evidence of water vapor effect on structural integrity and electrical conductivity of YSZ–Ni cermet anodes [4–7].

It is also known that the electrochemical oxidation is strongly influenced by the steam content in the fuel. Small amount of water (few %) significantly decreases anode polarization resistance, while its too large amount can degrade anode performance especially at high electrical load and low H_2 concentrations in the fuel [4]. The mechanism of water vapor influence on the anode oxidation reaction is still not well stated. There is the contradictory evidence as to whether the adsorption of

Ye. V. Kharchenko · Z. Ya. Blikharskyy · V. V. Vira
Institute of Building and Environmental Engineering, Lviv Polytechnic National University, Lviv, Ukraine

B. D. Vasyliv (✉)
Karpenko Physico-Mechanical Institute of the NAS of Ukraine, Lviv, Ukraine

O. Fesenko, L. Yatsenko (eds.), *Nanocomposites, Nanostructures, and Their Applications*, Springer Proceedings in Physics 221,
https://doi.org/10.1007/978-3-030-17759-1_42

oxygen from water on the ceramic part of a cermet anode or the metal part of the anode plays the key role in reaction promoting. It is also known that redistribution of Ni in the YSZ–Ni cermet occurs under anodic operation in the presence of high water vapor content [5].

The aim of this work is to study the substructure changes in the YSZ–NiO anode material during its reduction and oxidation at 600 °C, basing on the microstructural analysis, in order to develop an appropriate mode of its redox treatment.

42.2 Materials and Methods

The 8YSZ–50NiO anode ceramics (ZrO_2 stabilized by 8 mol% Y_2O_3 with the addition of 50 wt% NiO) have been investigated. The sintering temperature was 1450 °C. Resulting grain size of the ceramics was in the range of 1–2 μm, and the porosity was 29%. The beams were cut of square anode plates (50 per 50 mm) and used as specimens for testing. A series of the specimens of 1 × 5 × 25 mm in size were subjected to three treatment modes at 600 °C (see Table 42.1), namely: (1) one-time reduction in a hydrogenous atmosphere (the Ar–5 vol% H_2 mixture) for 4 h at the pressure of 0.15 MPa (Fig. 42.1a); (2) redox cycling (five cycles), each redox cycle comprises the stages of isothermal dwell for 4 h in the hydrogenous atmosphere at 0.15 MPa and for 4 h in laboratory air, followed by one-time reduction after mode 1; and (3) redox cycling (five cycles) with extra stages of degassing, followed by one-time reduction after mode 1 (Fig. 42.1b) [8]. Two extra modes (4 and 5, see Table 42.1) were used to simulate the behavior of materials in a water

Table 42.1 The treatment modes for the materials tested

Mode marking	Mode
1	One-time reduction for 4 h in the Ar–5 vol% H_2 mixture at 600 °C under the pressure of 0.15 MPa (Fig. 42.1a)
2	Redox cycling (five cycles), each redox cycle comprises a stage of isothermal dwell for 4 h at 600 °C in the Ar–5 vol% H_2 mixture under the pressure of 0.15 MPa and a stage of isothermal dwell for 4 h at 600 °C in laboratory air (Fig. 42.1b without a stage of degassing), followed by one-time reduction after mode 1
3	Redox cycling (five cycles), each redox cycle comprises a stage of isothermal dwell for 4 h at 600 °C in the Ar–5 vol% H_2 mixture under the pressure of 0.15 MPa, a stage of degassing at 600 °C and a stage of isothermal dwell for 4 h at 600 °C in laboratory air (Fig. 42.1b), followed by one-time reduction after mode 1
4	Treatment according to mode 3 followed by dwelling for 4 h in "water vapor – the Ar–5 vol% H_2 mixture" atmosphere at 600 °C under the pressure of 0.15 MPa (water vapor pressure 0.03 MPa)
5	Treatment according to mode 3 followed by dwelling for 4 h in "water vapor – the Ar–5 vol% H_2 mixture" atmosphere at 600 °C under the pressure of 0.15 MPa (water vapor pressure 0.148 MPa)

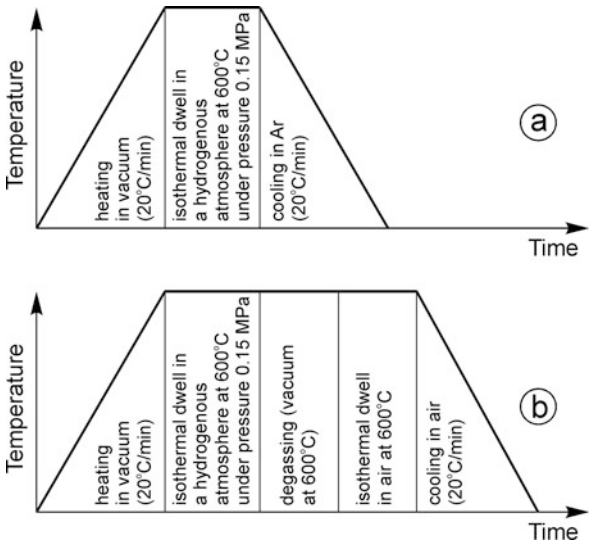

Fig. 42.1 The treatment schemes. (**a**) One-time reduction in a hydrogenous atmosphere. (**b**) A cycle of redox treatment

vapor-containing atmosphere [7]. The treatment of specimens was performed in a special hermetic chamber providing the conditions of pressure that range from 0.1 to 1 MPa and temperature range from 20 to 600 °C. A mechanical test was performed under a three-point bend.

Material microstructure and fracture surface morphology of the specimens were studied using SEM Carl Zeiss EVO-40XVP. The detailed microstructural analysis was performed using a scanning transmission electron microscope (STEM) Hitachi-HD2700, equipped with the Cs corrector and operated at 200 kV. Bright field and annular dark field (Z-contrast) were used for imaging. Chemical analysis was carried out using the X-ray energy dispersive spectroscopy (EDS) and electron energy loss spectroscopy (EELS) techniques.

The modelling of the substructure changes during the reduction and oxidation half-cycles (at 600 °C) has been performed basing on the nano- and microstructural analysis.

42.3 Results and Discussion

According to our preliminary results [8–10], there had not been a substantial difference in cermet structures after the first and second cycle of the redox treatment of YSZ–NiO ceramics. Similar to that, we have not found any discernible difference in structures of specimens treated for 1 cycle after both modes 2 and 3 (Figs. 42.2a and 42.3a, respectively).

Increased porosity, along with an increased amount of reduced Ni, has been revealed in specimens after mode 2 test (Fig. 42.2e). In case of such treatment,

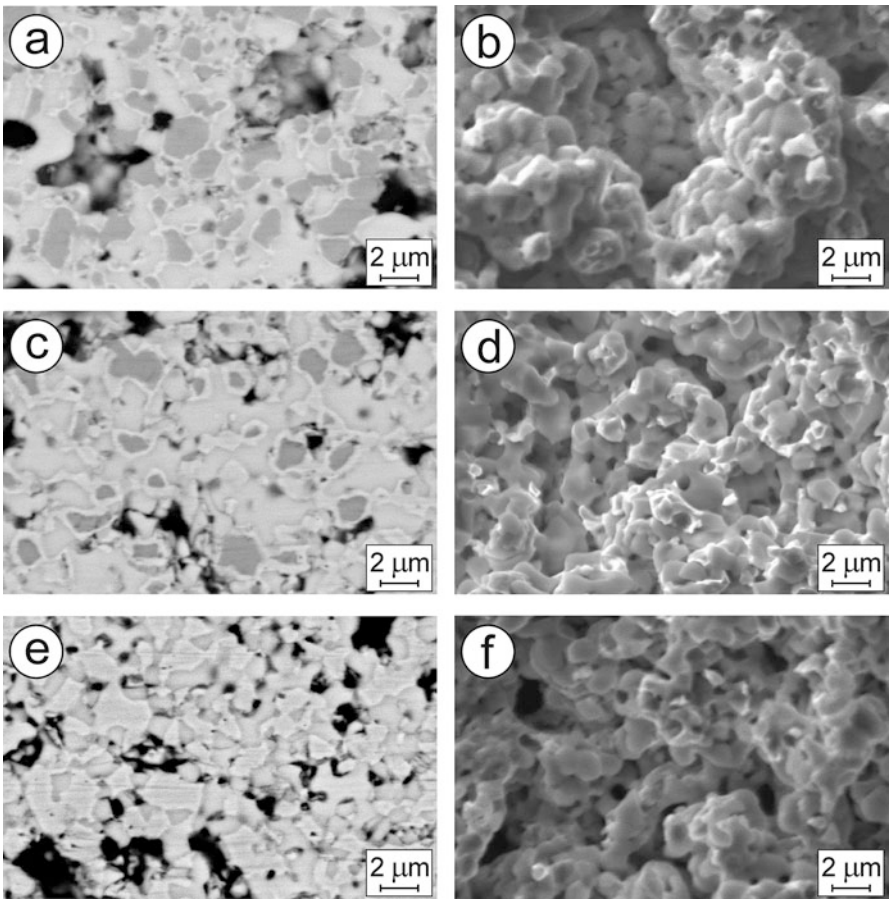

Fig. 42.2 SEM (**a**, **c**, **e**) structures and (**b**, **d**, **f**) fractographies of specimens treated according to mode 2 test for (**a**, **b**) one cycle (**c**, **d**) two cycles, and (**e**, **f**) five cycles, followed by a stage of reduction in the Ar–5 vol% H_2 mixture (see Table 42.1)

a reaction of oxygen with the remaining hydrogen on the stage of isothermal dwell in air at 600 °C takes place followed by a substantial increase of water vapor local pressure [11]. Such high-pressure conditions occur in small pores (Fig. 42.4c) causing nucleation of microcracks on three-phase ("nickel phase-zirconium phase-pore") boundaries (Fig. 42.4d). Such effect of water vapor is probably one of the main reasons of structural degradation of the cermet [12]. The presence of the remaining hydrogen in small pores does not allow complete reoxidation to be reached during the oxidation half-cycle. So finally we obtained a cermet structure with completely reduced Ni particles (Fig. 42.3e).

After mode 3 test of specimens, it was revealed that the stage of degassing between half-cycles of reduction and oxidation plays a substantial role in the

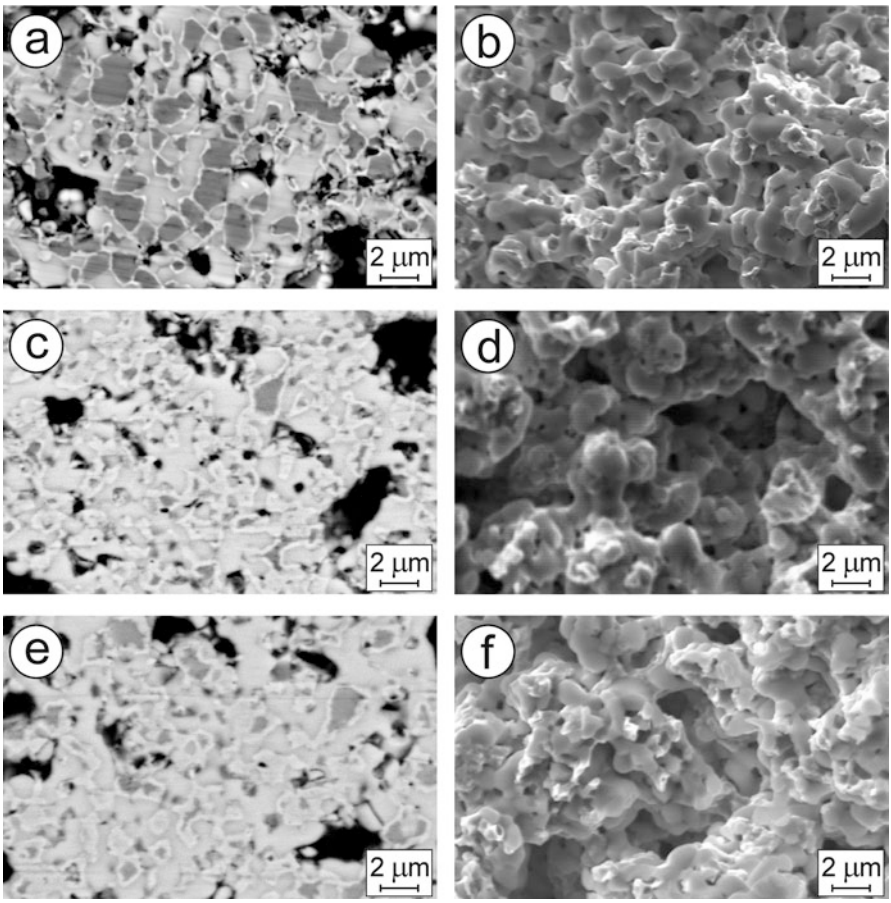

Fig. 42.3 SEM (**a**, **c**, **e**) structures and (**b**, **d**, **f**) fractographies of specimens treated according to mode 3 test for (**a**, **b**) one cycle (**c**, **d**) two cycles, and (**e**, **f**) five cycles, followed by a stage of reduction in the Ar–5 vol% H_2 mixture (see Table 42.1)

formation of Ni-network. We found that upon redox cycling, exposition of the material at 600 °C for 4 h in air resulted in complete oxidation of preliminary reduced Ni edgings (Fig. 42.3a) on NiO particles by diffusion mechanism [12]. After five cycles of the redox treatment at 600 °C with final reduction stage (mode 3), most of NiO particles were reduced completely. They formed a continuous network of electrically conducting material in zirconia skeleton (Fig. 42.3e), which resulted in high electrical conductivity. Fragmentation of coarse grains of nickel phase resulted in a more fine structure of the material treated. The mixed fracture micromechanism (Fig. 42.3f) corresponds to higher cohesive strength between the particles of zirconia and nickel phase as compared to the singly reduced material (Fig. 42.3b).

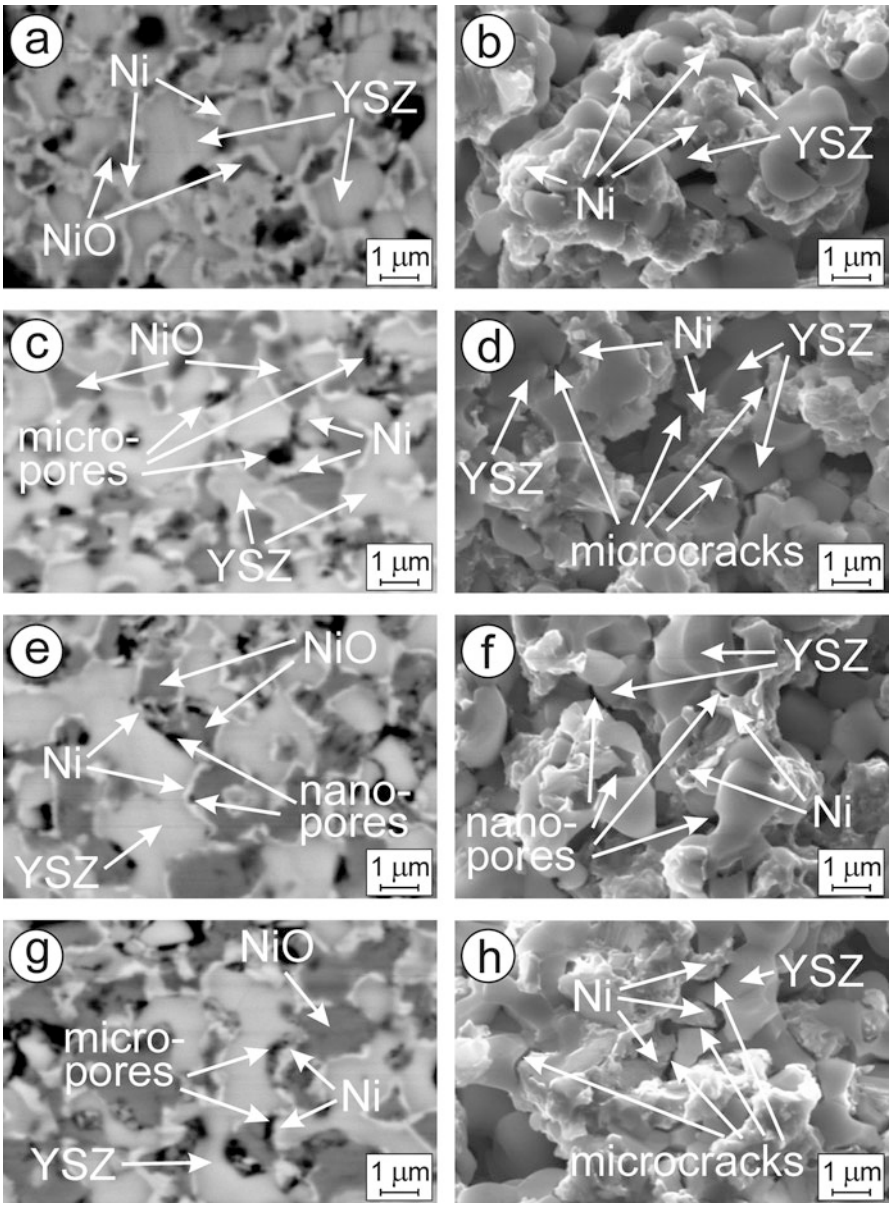

Fig. 42.4 SEM (**a**, **c**, **e**, **g**) structures and (**b**, **d**, **f**, **h**) fractographies of specimens treated according to (**a**, **b**) mode 3 and (**c**, **d**) mode 2 tests for five cycles, followed by a stage of reduction in the Ar–5 vol% H_2 mixture, and (**e–h**) mode 3 test for five cycles followed by a stage of reduction in (**e**, **f**) a water vapor-depleted atmosphere (water vapor pressure 0.03 MPa) and (**g**, **h**) a water vapor-enriched atmosphere (water vapor pressure 0.148 MPa) (see Table 42.1)

Modes 4 and 5 (see Table 42.1) were used to simulate the behavior of materials in a hydrogenous atmosphere containing water vapor [7]. We recognized better resemblance between pictures which correspond to a redox-treated specimen without degassing stage (Fig. 42.4c) and a redox-treated specimen with aging in water-enriched (water vapor pressure 0.148 MPa) hydrogenous atmosphere (Fig. 42.4e). The structure of a redox-treated specimen with aging in water-depleted (water vapor pressure 0.03 MPa) hydrogenous atmosphere (Fig. 42.4g) has little resemblance to the mentioned above structures.

Based on microstructural analysis, the modelling of the substructure changes during the reduction and oxidation half-cycles (at 600 °C) has been performed. The goal of this modelling was to estimate how water vapor affects a Ni-containing cermet structure after the specimen is subjected to the redox treatment.

As mentioned above, in case of a redox treatment without degassing stage, water vapor is formed as a result of reaction of the inlet air with the remaining hydrogen. Such a complex atmosphere, in contrast to dry air, allows more intensive reduction of the nickel phase instead of its oxidation during the oxidation half-cycle.

Bright-field (BF) STEM image of the cermet structure obtained after mode 2 (Fig. 42.5a) displays strong Ni phase shrinkage as a result of the complete transformation of NiO into Ni confirmed by EDS and EELS analyses. This transformation is followed by the formation of nanopores (inner pits) inside the Ni grain and reduction of its size. Nanopores are uniformly distributed in the whole Ni grain, and their diameters are in the range of 20–100 nm (Fig. 42.5a). The core of the Ni grain is like a single crystal which is enveloped by Ni subgrains having its own nanocrystalline structure. The porous core area and its nanocrystalline envelope have the same contrast, i.e., the same composition.

The Ni phase shrinkage is followed by the formation of clearly visible microcracks between the nickel and zirconium phases. This results in the loss of structural integrity of the cermet.

Assuming that after the first reduction half-cycle the nickel phase of a cermet consists of nonreduced NiO core (of dark color, see Fig. 42.5b) enveloped by

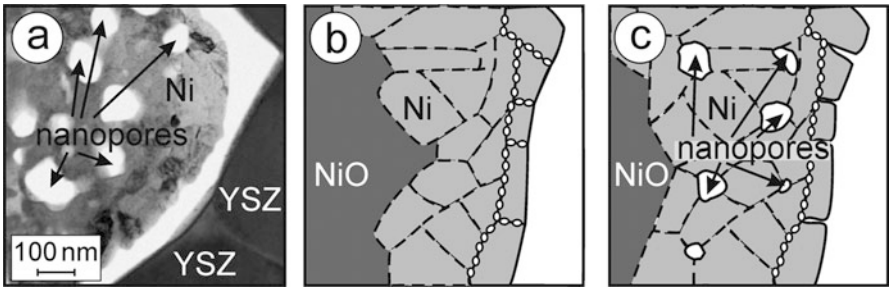

Fig. 42.5 Bright-field (BF) STEM image of the cermet structure (**a**) and model presentations (**b, c**) of corresponding nanostructural changes in the material treated according to mode 2 test for (**b**) one cycle and (**a**, **c**) five cycles (see Table 42.1)

reduced Ni (of bright color) like in Fig. 42.2a, we can further develop a concept of stepwise Ni gain on nickel phase grains after each half-cycle. As mentioned above, the atmosphere of water vapor formed as a result of the reaction of air with the remaining hydrogen allows more intensive reduction of the nickel phase instead of its oxidation during the oxidation half-cycle. Finally, mode 2 allows a cermet structure to be obtained with completely reduced porous Ni particles (Fig. 42.5c).

In case of a redox treatment with degassing stage, no water vapor is formed when air is introduced into the material being degassed. Annular dark-field (ADF) STEM image of the cermet structure obtained after mode 3 (Fig. 42.6a) does not indicate any discernible shrinkage of the Ni phase because of the incomplete transformation of NiO into Ni. In general, nano-sized NiO particles are fully transformed into Ni ones. Larger particles of diameter above 1 μm consist of nonreduced NiO core (of dark color, see Fig. 42.6a) enveloped by reduced Ni (of bright color), which is confirmed by EDS and EELS analyses. The NiO core is like a single grain, whereas the Ni nanocrystalline envelope consists of many subgrains (each of them is smaller than 200 nm) oriented randomly. No pores except a few small ones are visible inside the Ni grain (Fig. 42.6a). The porosity of grains of the Ni phase in the specimen treated after mode 3 is much lower than that in the specimen treated after mode 2. No shrinkage accompanying NiO to Ni phase transformation has been indicated. This is why the structural integrity of the cermet was not lost.

Assuming similar to mode 2 that after the first reduction half-cycle the nickel phase of a cermet consists of nonreduced NiO core (of dark color, see Fig. 42.6b) enveloped by reduced Ni (of bright color) like in Fig. 42.3a, we should change the nickel phase reduction concept developed for mode 2, because of the change in oxidation conditions. During oxidation half-cycle, a complete oxidation of preliminary reduced Ni phase envelope subgrains occurs caused by diffusion of oxygen from air [13–15]. The improved performance of this process is because of degassing (low partial pressure inside the material). With the increasing number of redox cycles, the closer are the subgrains to the grain surface, the more are their boundaries distinguished. This is because of the formation of a network of

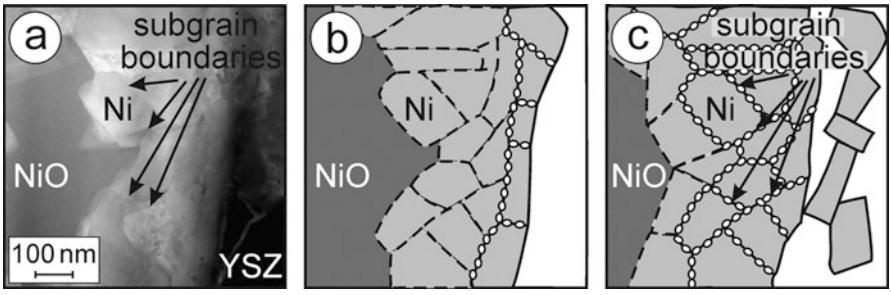

Fig. 42.6 Annular dark-field (ADF) STEM image of the cermet structure (**a**) and model presentations (**b**, **c**) of corresponding nanostructural changes in the material treated according to mode 3 test for (**b**) one cycle and (**a**, **c**) five cycles (see Table 42.1)

nanopores in the particle outer layer on the subgrain boundaries [16]. Thin layer of reduced Ni subgrains is being occasionally separated. In such a way, the initial size of the Ni grain is decreased, and the grain reduction becomes deeper (Fig. 42.6c). Separated tiny Ni particles coagulate forming a continuous network of electrically conducted Ni in the zirconia skeleton.

So in contrast to mode 2, the following structural changes, peculiar for mode 3, can be marked: (1) formation of a network of nanopores in the outer layer of Ni particle; (2) reduction of Ni-phase particle size by separating Ni clusters of the particle outer layer; (3) redistribution of fine Ni particles that allows the porosity to be partially decreased; and (4) formation of a network of reduced Ni particles that improves electrical conductivity and structural strength of the cermet.

42.4 Conclusions

Cyclic treatment technique (redox cycling) comprising stages of material exposition in reducing and oxidizing high-temperature gas environments and intermediate degassing between these stages has been used to improve the structural integrity and electrical conductivity of YSZ–NiO ceramic anode substrates for solid oxide fuel cells. With applying of the developed treatment mode, the following structural changes have occurred: formation of a network of nanopores in the outer layer of Ni particle; reduction of Ni-phase particle size by separating Ni clusters of the particle outer layer; decreasing porosity of the cermet by redistribution of fine Ni particles; and formation of a network of reduced Ni particles. All these changes allow improving the electrical conductivity and structural strength of the cermet. The developed treatment technique promises to enhance the operational efficiency of SOFCs.

References

1. Ettler M, Timmermann H, Malzbender J et al (2010) Durability of Ni anodes during reoxidation cycles. J Power Sources 195:5452–5467
2. Sarantaridis D, Atkinson A (2007) Redox cycling of Ni-based solid oxide fuel cell anodes: a review. Fuel Cells 3:246–258
3. Faes A, Nakajo A, Hessler-Wyser A et al (2009) Redox study of anode-supported solid oxide fuel cell. J Power Sources 193:55–64
4. Kim P, Brett D, Brandon N (2009) The effect of water content on the electrochemical impedance response and microstructure of Ni-CGO anodes for solid oxide fuel cells. J Power Sources 189(2):1060–1065
5. Primdahl S (1999) Nickel/yttria-stabilised zirconia cermet anodes for solid oxide fuel cells. Dissertation, University of Twente, Faculty of Chemical Technology, The Netherlands, and Riso National Laboratory, Materials Research Department, Denmark
6. Dees DW, Balachandran U, Dorris SE et al (1989) Interfacial effects in monolithic solid oxide fuel cells. SOFC I: The Electrochemical Society Proceedings Series. Pennington, pp 317–321

7. Vasyliv B, Podhurska V, Ostash O (2017) Preconditioning of the YSZ-NiO fuel cell anode in hydrogenous atmospheres containing water vapor. Nanoscale Res Lett 12:265. https://doi.org/10.1186/s11671-017-2038-4
8. Vasyliv BD, Ostash OP, Podhurska VY et al (2013) Method of treatment of NiO-containing anodes of a solid oxide fuel cell [in Ukrainian]. Patent of Ukraine No. 78992. Published on 10.04.13, Bulletin No. 7
9. Vasyliv BD (2010) Improvement of the electric conductivity of the material of anode in a fuel cell by the cyclic redox thermal treatment. Mater Sci 46(2):260–264
10. Vasyliv BD, Podhurs'ka VY, Ostash OP et al (2013) Influence of reducing and oxidizing media on the physicomechanical properties of ScCeSZ–NiO and YSZ–NiO ceramics. Mater Sci 49(2):135–144
11. Maruyama T, Fukagai N, Ueda M et al (2004) Chemical potential distribution and void formation in magnetite scale formed in oxidation of iron at 823K. Mater Sci Forum 464:807–814
12. Faes A, Hessler-Wyser A, Zryd A et al (2012) A review of RedOx cycling of solid oxide fuel cells anode. Membranes 2(3):585–664. https://doi.org/10.3390/membranes2030585
13. Wood A, Waldbillig D (2011) Preconditioning treatment to enhance redox tolerance of solid oxide fuel cells. US Patent 8,029,946 B2, 4 Oct 2011
14. Peraldi R, Monceau D, Pieraggi B (2002) Correlations between growth kinetics and microstructure for scales formed by high-temperature oxidation of pure nickel. I. Morphologies and microstructures. Oxid Met 58:249–273
15. Podhurska V, Vasyliv B, Ostash O et al (2016) Influence of treatment temperature on microstructure and properties of YSZ–NiO anode materials. Nanoscale Res Lett 11:93. https://doi.org/10.1186/s11671-016-1306-z
16. Clemmer RMC, Corbin SF (2009) The influence of pore and Ni morphology on the electrical conductivity of porous Ni/YSZ composite anodes for use in solid oxide fuel cell applications. Solid State Ionics 180:721–730

Index

O. Fesenko, L. Yatsenko (eds.), *Nanocomposites, Nanostructures, and Their Applications*, Springer Proceedings in Physics 221,
https://doi.org/10.1007/978-3-030-17759-1